

Medical 3D technology

From bench to bedside



Koen Willemsen

Medical 3D technology

From bench to bedside

Koen Willemsen

Medical 3D technology,

From bench to bedside

K. Willemsen, 2022

Doctoral thesis, Utrecht University, Utrecht, The Netherlands

Cover design: Koen Willemsen

Design chapter pages & lay-out: Koen Willemsen

Printed by: Proefschriftmaken.nl

ISBN: 978-94-6423-847-1

DOI: 10.33540/527

© Copyright 2022 Koen Willemsen

All rights reserved. No part of this thesis may be reproduced, stored in a retrieval system, or transmitted in any form or by any means without prior permission of the author.

Financial support for the production of this thesis was provided by: Diergeneeskunde Universiteit Utrecht, Rita Leibinger GmbH & Co. KG, Oceanz B.V., MRlguidance, Amnovis BV, Stichting ETB-BISLIFE, Materialise NV, Baat Medical Products B.V., The Dutch Spine Society, Sectra, Anna Fonds te Leiden en Xilloc Medical Int B.V.

I declare that the text and the work presented in this document are original and that no sources other than those mentioned in the text and its references have been used in creating it.

Medical 3D technology

From bench to bedside

Medische 3D technologie
Van het lab naar de kliniek
(met een samenvatting in het Nederlands)

PROEFSCHRIFT

Ter verkrijging van de graad van doctor aan de
Universiteit Utrecht
op gezag van de
rector magnificus, prof.dr. H.R.B.M. Kummeling,
ingevolge het besluit van het college voor promoties
in het openbaar te verdedigen op

dinsdag 12 juli 2022 des middags te 4.15 uur

Door

Koen Willemsen

Geboren op 2 februari 1991 te Tilburg

Promotor:

Prof. dr. ir. H. Weinans

Prof. dr. B.P. Meij

Copromotor:

Dr. B.C.H van der Wal

Dr. R.J.B. Sakkers

Leden van de promotiecommissie

Prof. dr. L. van Rhijn (voorzitter)

Prof. dr. W.J.A. Dhert

Prof. dr. L.C. Heyligers

Dr. S.H.A.J. Tytgat

Prof. dr. P.R. van Weeren

Content page

Part 1:	SCOPE	09
Chapter 1:	General Introduction & thesis outline	11
Chapter 2:	Long-term outcomes of the hip shelf arthroplasty in adolescents and adults with residual hip dysplasia: a systematic review	29
Chapter 3:	Good long-term outcomes of the hip Chiari osteotomy in adolescents and adults with hip dysplasia: a systematic review	47
Chapter 4:	Comparing hip dysplasia in dogs and humans: a review	63
Chapter 5:	Magnetic resonance imaging versus computed tomography for three-dimensional bone imaging of musculoskeletal pathologies: a review	89
Part 2:	BENCH	135
Chapter 6:	Patient-specific 3D-printed shelf implant for the treatment of hip dysplasia: anatomical and biomechanical outcomes in a canine model	137
Chapter 7:	3D-printed regenerative magnesium phosphate implant ensures stability and restoration of hip dysplasia	155
Chapter 8:	A novel treatment for anterior shoulder instability: a biomechanical comparison between a patient-specific implant and the Latarjet procedure	179
Chapter 9:	Deformable titanium for acetabular revision surgery: a proof of concept	195
Part 3:	ONE MEDICINE (TRANSLATION)	219
Chapter 10:	Patient-specific 3D-printed shelf implant for the treatment of hip dysplasia tested in an experimental animal pilot in canines	221
Chapter 11:	Acetabular rim extension using a patient specific implant for the treatment of hip dysplasia in dogs	241
Chapter 12:	Additive manufacturing of titanium implants for skull reconstruction in canine oncological surgery	265
Chapter 13:	Additive titanium manufacturing to repair critically-sized antebrachial bone defects in dogs	279

Part 4:	BEDSIDE	299
Chapter 14:	MRI-based synthetic CT shows equivalence to conventional CT for the morphological assessment of the hip joint	301
Chapter 15:	3D-printed saw guides for lower arm osteotomy, a comparison between a synthetic CT and CT-based workflow	323
Chapter 16:	Challenges in the design and regulatory approval of 3D-printed surgical implants: a two-case series	343
Chapter 17:	The vital role of an in-house 3D lab to create unprecedented solutions for challenges in spinal surgery, practical guidelines and clinical case series	365
Part 5:	CLOSINGS	389
Chapter 18:	Three-dimensional manufacturing of personalized implants in orthopedic trauma surgery, feasible future or fake news?	391
Chapter 19:	Summary, general discussion, future perspectives and concluding remarks	397
Part 6:	APPENDICES	417
	Dutch Summary / Nederlandse Samenvatting	421
	List of publications	433
	Non-scientific communication	439
	PhD-Portfolio	441
	Acknowledgements	445
	Curriculum Vitae	451



The background is a solid blue color. It features several sets of parallel diagonal lines. One set of lines is in the top-left corner, another set is in the bottom-left corner, and a single line runs from the top-right towards the bottom-left. The lines are thin and light blue, creating a subtle geometric pattern.

PART 1

SCOPE



The background is a solid blue gradient. On the left side, there are several sets of parallel diagonal lines. One set is grey and runs from the top-left towards the bottom-right. Another set is yellow and runs from the bottom-left towards the top-right. A third set is grey and runs from the bottom-left towards the top-right, parallel to the yellow lines.

CHAPTER 1

General Introduction &
Thesis outline

General Introduction

Background

Technology has been growing exponentially since the first introduction of the planar silicon transistor in 1959.[1], [2] These technologies have led to a rapid change in how we perceive our world. Now, computers, the internet, smartphones, software applications, videoconferencing and social media affect us all during our daily routine.

In the medical domain this advancement in technology has enabled many improvements and refinements. Older techniques such as X-rays, first discovered in the 1895 by Wilhelm Röntgen, developed under influence of computer technology to the first commercially available Computed Tomography (CT) scanner made by Sir Godfrey Hounsfield in 1972 (Fig. 1A). Furthermore other imaging techniques were introduced such as the first in-vivo acquired MRI-scan made in 1977 (Fig. 1B).[3]

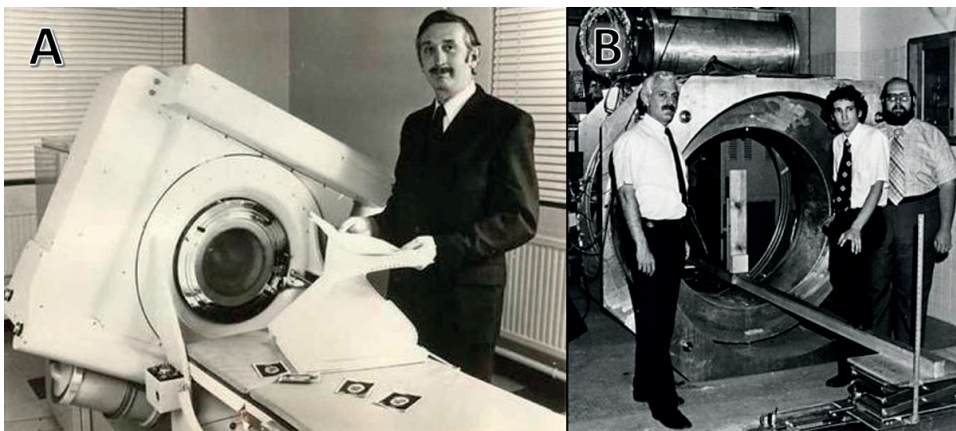


Figure 1. A) Sir Godfrey Hounsfield with the first clinical CT scanner. B) The development of the first in-vivo MRI-scan

Prior to these devices the medical field was restricted to the focal plane tomography; the anterior-posterior coronal X-ray view and the lateral sagittal X-ray view (Fig. 2A). Therefore, the introduction of the CT and MR scanner allowed physicians to view the axial plane of patients and therefore “enter into” the third dimension; also known as 3D (Fig. 2D). The introduction of the third dimension to medical practice proved to be of much help for identifying cancer or brain abnormalities (e.g. aneurysms and cysts) that were hard to discover using plain orthogonal radiographs.[4]

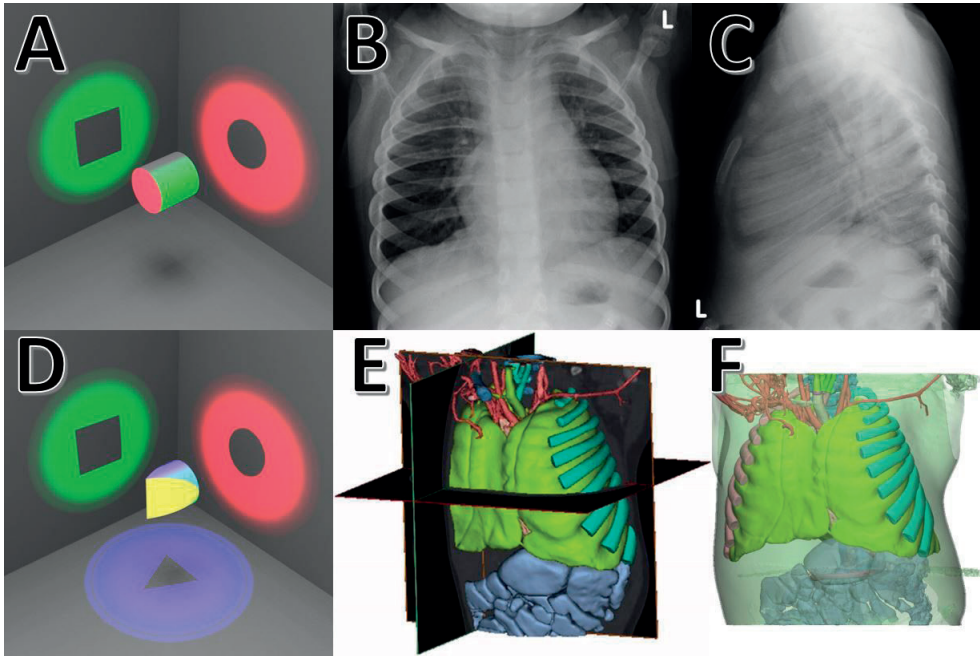


Figure 2. A) The projection of images in two directions gives a rough prediction of the object in the middle. B) Anterior-posterior radiograph of the thorax. C) Lateral radiograph of the thorax D) In comparison to figure 2A, when a third projection is introduced a more precise prediction can be made of the true object. Using the third dimension allows physicians to appraise anatomical structures in a more precise manner. E. & F) Using CT-imaging data from the same patient as in Fig. 2B, now multiple structures can be segmented and appreciated.

One other industry that evolved by using the third dimension was Computer Aided Design (CAD) software (1968)(Fig. 3A) and 3D printing industry (1983)(Fig. 3B). 3D printing is one of the technological advancements that has grown fast over the last three decades and became established primarily in the manufacturing industry as a form of additive manufacturing technique.[5] 3D Technology, and additive manufacturing in specific, has enabled industrial users to create virtually anything; as additive manufacturing is not as limited by tool size as compared to the subtractive manufacturing workflow. Therefore, additive manufacturing is capable of creating more complex structures.[5], [6] Moreover, 3D printing can be used to reduce waste by using fewer raw materials, require fewer manufacturing steps to come to a final product and can be produced closer to the required location, therefore also reducing transportation costs.[5], [7] Essentially, 3D printing can be used for small low volume prototypes to entire houses destined for living.[8] Additive manufacturing or three-dimensional (3D) printing of metal implants can provide novel solutions for difficult-to-treat conditions, yet legislation concerning patient-specific implants complicates the implementation of these techniques in daily practice. In this

Article, we share our acquired knowledge of the logistical and legal challenges associated with the use of patient-specific 3D-printed implants to treat spinal instabilities.

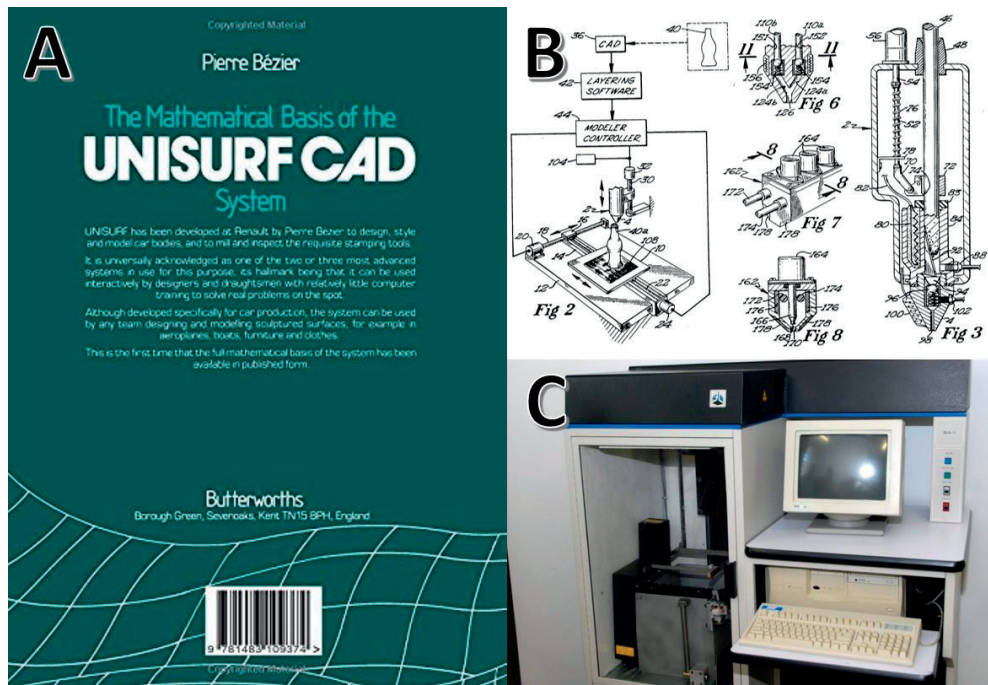


Figure 3. A) The first true 3D computer added design (CAD) software developed by Pierre Bézier (Engineer at Renault) B) The patent for an extrusion 3D printer in 1984 C) First 3D printer developed in 1983 by Chuck Hull, later co-founder of 3D Systems.

Medical 3D technology

In the manufacturing industry the 3D printers are often used for fast-prototyping or to create identical copies of one specific design. However, in the medical industry 3D printers can also be used to print the unique anatomy of each patient or create unique devices or instruments unique for their geometry and usability.[9] These medical devices include anatomical models (3D-printed or virtual)(Fig. 2E & 2F), instruments (e.g., guides to guide a drill direction or cutting plane or a guide to assist with proper surgical placement of a device), or even custom-made devices with complex geometry or features that match patient's unique anatomy.[10] The last decade these new developments in medical additive manufacturing had a great significant impact on teaching of medical professionals[11] and treatment of patients[10] (Fig. 4). 3D printing allows for printing of (micro)porous structures or scaffolds[12], which can promote (bone) ingrowth into an implant or scaffold which increases the amount of secondary fixation.[13] Besides polymers and metals there

are more (biological) materials capable of being 3D-printed and these will be discussed at the end of this chapter.



Figure 4. An schematic example of a 3D-technology enhanced pathway for the restoration of an antebrachia fracture.

In medicine, these 3D technologies have only been introduced in clinical practice during the last few years because there were still many challenges when using these techniques in patient care. Due to recent technological progress, numerous manufacturers are now capable of using the virtually endless possibilities of 3D technology for the production of (3D-printed) medical devices. A new law, the Medical Device Regulation (MDR), was introduced in 2021 in the European Union to protect patients from low quality device manufacturers.[14] Due to the novelty of the MDR and the lack of precedent and jurisprudence it is difficult for hospitals and medical device manufacturers to comply with the MDR. In this thesis insight is given in the development and implementation of medical 3D technology from bench to bedside. New medical devices are being sorted in different risk-classes (I-II-III) dependent on the complexity and invasiveness of the medical device. Also when devices are part of assembly or have an active component this can increase risk class. In the next section examples of various 3D-derived products with different risk-classes are given and difficulties in the conversion from 2D to 3D are discussed.

A low complex and low invasive application of 3D technology is the use of 3D anatomical models (risk-class I).[14] First segmentation software is used to derive anatomical data from CT and MRI scans by selecting a region of interest on each slice and recombining all these data points to a 3D object.[15] Those 3D objects then visualize an anatomical structure, a tumor or even a congenital malformation that is hard to decipher on 2D images. These models can be presented to a physician to prepare for surgery or just get a better understanding of a challenging condition. The models can be visualized by using regular 2D monitors or even visualized in 3D with augmented reality or virtual reality.[16] Moreover, if needed, the model can be materialized into a physical model by 3D printing in order for a surgeon to dry-practice a certain procedure before the actual surgery, or present the model to a patient to increase awareness in the disease condition (Fig. 5).[17] However, with these new possibilities also many questions arise. Which type of software package should one use to generate a design?[15] Is MRI equivalent to CT to make bone models and is CT equivalent to MRI when it comes to soft-tissue models, and how useful are MRI derivatives such as synthetic-CTs? Are virtual reality goggles safe to use and permitted in medical care? Do 3D printers need a defined accuracy or certification to be used for medical care? How should quality control of the work process be organized? What are the consequences of errors in the image processing? What are the consequences of an incorrectly 3D-segmented representation of an aneurysm of the abdominal aorta with outcome parameters that reach the 5.5mm threshold value for major invasive surgery with high mortality, in a case in which the true anatomical situation is (well) below the threshold value? And who should be held accountable for such errors, the clinician, the software company or the engineer/technician responsible for the technical analysis? How can the risks be kept to a minimum with preservation of optimal quality? In order

to address all these questions research is needed to develop these new techniques and translate them in a safe, manageable and sustainable method from bench to bedside.

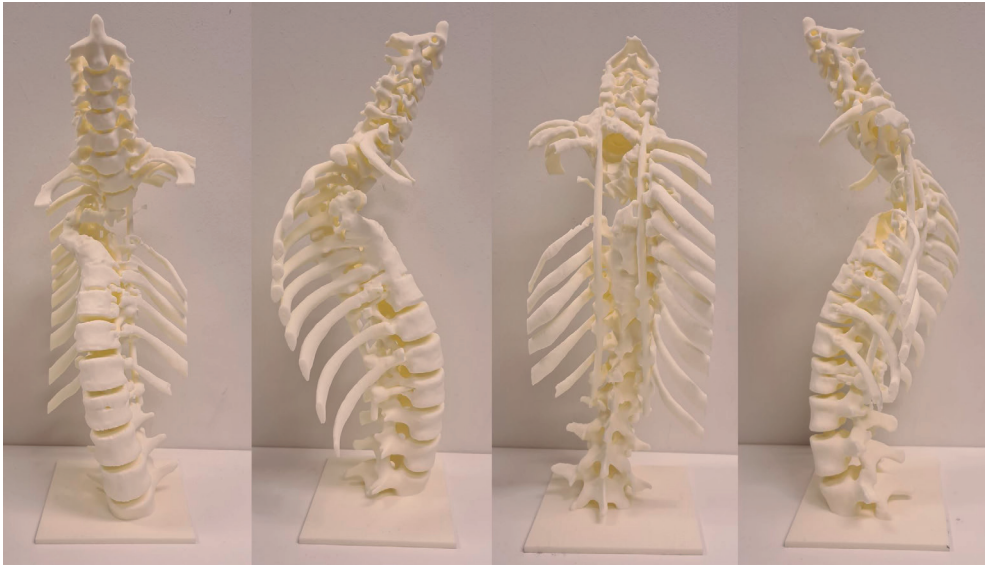


Figure 5. Example of a 3D-printed anatomical model of a severe scoliotic spine.

A more complex application of 3D technology is the use of 3D cutting and drilling guides (risk-class II) to guide surgeons during surgery.[18] In the case of e.g. resection a tumor or realignment of a misaligned bone, the surgeon can now choose to use drilling or cutting guides to perform these tasks to the highest precision.[18] To do so, segmented 3D anatomical models are transferred to a CAD/CAM modelling program in which cutting guides can be made using straight-forward engineering principles.[18] However, with these new possibilities also many questions arise. For a tumor resection guide it is usually what needs to be resected, a margin is determined and a resection guide can be made beyond those borders. In other cases the introduction of the third dimension might deliver new unforeseen problems, especially when the gold standard treatment methods are based on conventional 2D imaging. An illustrative example is the planning of a tibia plateau levelling osteotomy that has a clear planning consensus on how to determine the optimal biomechanical axis on the gold standard full leg (2D) radiograph in weight bearing standing position.[19], [20] However, when the weight bearing full leg radiograph is replaced by a (non-weightbearing) 3D-CT examination there is not yet clear consensus on how to do the preop planning because the points and lines drawn on a 2D projection image are difficult to convert to reformatted CT slices or even 3D models (Fig. 6).[21]

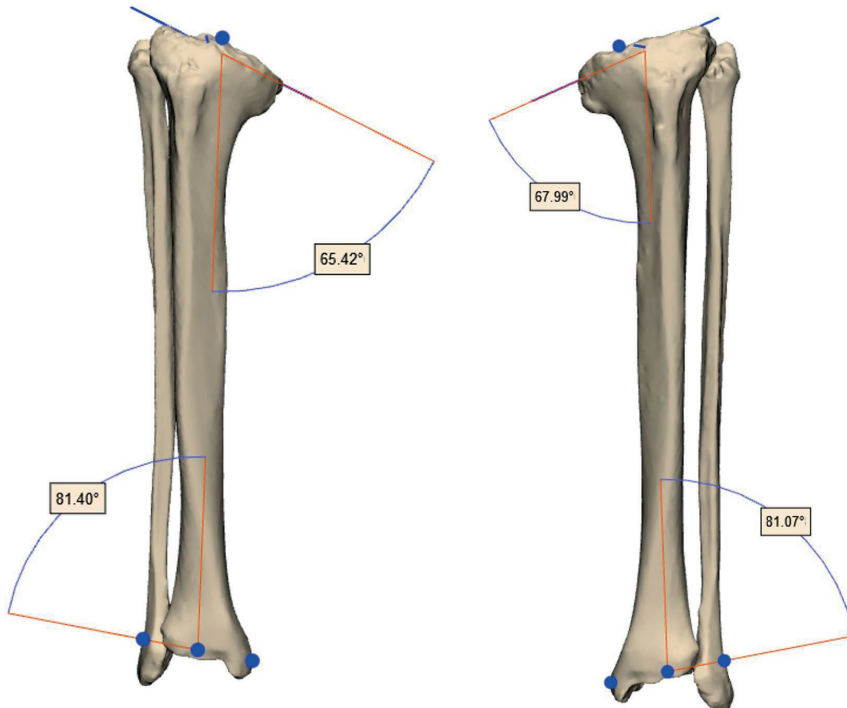


Figure 6. Examples of leg measurements to evaluate the eligibility of a patient for tibia plateau levelling osteotomy surgery.

Another example of difficulties with 2D to 3D conversion is the measurement of the cup positioning in total hip arthroplasty. The parameters for the ‘anteversion’ and ‘inclination’ are routinely acquired from AP and lateral radiographs.[22] However, when reviewing the different methods used to measure anteversion and inclination it has been shown that, despite looking similar, all studies used different angles when converted back to vectors in actual 3D space.[23] Therefore new protocols, techniques and terminology need to be introduced and validated to assure that what is defined in literature can also be planned and realized in 3D.

Concluding, the transition from old unguided and 2D planned methods to novel guided 3D planned methods is not without challenges and certain questions need to be asked and answered. Can CAD/CAM software be used for all medical purposes, even when there is no validated (gold) standard in 3D? Is any 3D printer suited for printing guides for invasive / sterile use? How do CT and MRI compare for creating (bone) saw or drill guides? What are the margins that should be used for a guide to exactly fit to the bone? What are

the consequences of a surgery guide that is not correctly used or placed? Hence, research is needed to develop these new techniques from bench to bedside.

An even more complex application of 3D technology is the use of 3D-printed patient-specific implants (risk-class III) to treat individual patients, e.g., cranial plates[24] and acetabular implants[25]. There are at least two different pathways for patient-specific implants, both with a different approach. The first pathway that is frequently used is for patients who have no options left within conventional procedures that use off-the-shelf implants (Fig. 7). A multidisciplinary team will decide that conventional treatment options will not solve the patients problem and that there is an indication for a patient-specific implant treatment. In these cases the patient-specific implant is considered good clinical practice and needs less scientific proof than the cases that can be solved with conventional implants. Nevertheless, these cases have to comply with the procedural rules and regulations (MDR) that are not always that obvious.[26] For each implant a technical file need to be prepared which essentially has the same substrate as an Investigational Medical Device Dossier and the documentation . This will be further discussed in this thesis.

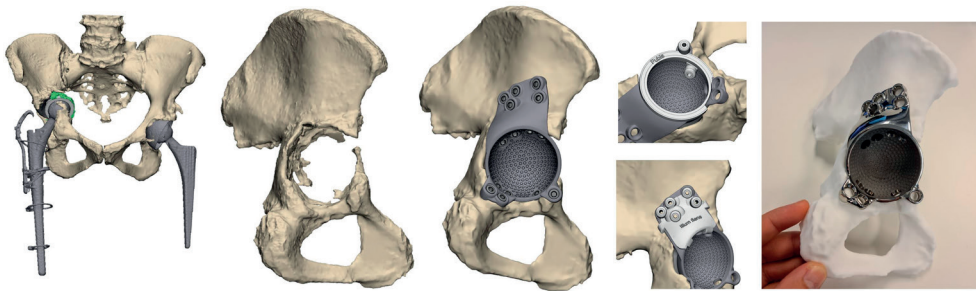


Figure 7. Example patient with THA failure and severe pelvic discontinuity that needed a patient-specific approach for restoration of the pelvis because no conventional off-the-shelf products were available.

The second pathway for patient-specific implants is to improve on surgical procedures that were previously not performed in a patient-specific manner. For example, an improvement can be made at the correction of (developmental) hip dysplasia by pre-planning designs for improving the joint socket.[27], [28] Moreover, it is proven that the success of current hip dysplasia interventions is overestimated when measuring the amount of head coverage on post-operative 2D anterior-posterior radiographs.[29] To get a better approximation and representation the amount of femoral head coverage can be calculated in 3D on CT images.[30] The gold standard is still measured on projection radiographs, and we do not exactly know the importance of head coverage in the most

anteromedial acetabular subsection when measured on CT.[30] Another question is the importance of the graft (shelf) shape and placement accuracy for the survival of the hip joint. This has never been systematically documented. However, it can be expected that a better fit realizes improved clinical performance and a higher survival rate of the hip, and therefore a 3D-designed patient-specific shelf implants might benefit patients with a pathological malformation of their pelvic bone. These kind of 3D improvements of conventional hip treatments should be investigated and if successful these techniques might find translation to other joints, e.g. shoulder instability where 3D printing may be used to precisely correct any (traumatic) loss of glenoid or humeral bone.[27], [28] However, new reference standards need to be developed and proven when designing 3D products to improve formerly 2D diagnosed and treated diseases. When these patient-specific implants are used to improve on conventional methods, extensive evidence is needed to support their use. Generally, a research and development pathway includes in silico, ex vivo, biomechanical and in vivo animal testing before translating the idea to humans.

Other questions that need to be addressed are: what materials are biomechanically and biologically suited for implantation? How will implant reliability be ensured? How do you make sure that an implant is positioned as designed? How to comply with rules and regulations?[14], [31] What legislation is needed to allow patient-specific implants for (human) clinical applications? What is necessary to develop new medical technology?

Further acceptance

Clinically, certain areas seem more swayed by the new 3D printing movement than others. [32] For example, the use of 3D-printed acetabular triflange cups for complicated total hip arthroplasty revisions is frequently implemented in regular practice. (Fig. 7).[33] This type of custom-made implants were quickly accepted as suited treatment for patients with large bone defects (high Paprosky classifications) that could not be solved with the conventional arthroplasty cups. For these commonly used 3D-printed acetabular cups improvement is still possible. The current cups are generally printed with a (micro) porous scaffold[12] on the posterior side to encourage bone ingrowth at the implant-bone interface to increase the amount of secondary fixation.[13] Due to segmentation uncertainties (e.g. due to metal artefacts at the planning CT-scan) a large error-margin is deemed necessary to not oversize the cup for the already big acetabular defect. Therefore, the implant is often not press-fit to parts of the bone, leaving a gap with unloaded bone that resorbs over time[34]. This problem that occurs often with regular (3D-printed) implants could find its solution in new performances in 3D printing. New developments lead to printing of even more complex and ultra-thin struts in titanium resulting in so-called metamaterials.[35], [36] These (e.g. titanium) structures can deform in many ways thereby e.g. filling gaps or expand under pressure and creating a more surgeon and

patient-friendly implant that deforms or shapes itself to the bone (defect) of the patient. [35] Next, due to the novelty of these techniques, the hypothesis need to be tested in a basic research setting to close the gap to the bedside.

Continuous improvement of 3D imaging techniques is needed parallel to the development of the 3D technology[15]. Next to the 3D reconstruction images provided by the CT scanner, MR images are also used to visualize anatomy in 3D without the use of damaging radiation. Segmenting anatomical data from MRI data is currently still time-consuming as the intensity contrast distribution on MRI is different compared to density contrast distribution by Hounsfield units on a CT scan. To speed up the process and improve the image quality for skeletal reconstruction, an increasing amount of effort is being put in creating machine learning algorithms that convert MRI data into CT data, also known as synthetic-CT[37]. These models are currently being validated to confirm that the anatomical references are the same in both imaging modalities and to assess if synthetic-CT can be used for 3D diagnosis and preplanning (Fig. 8).

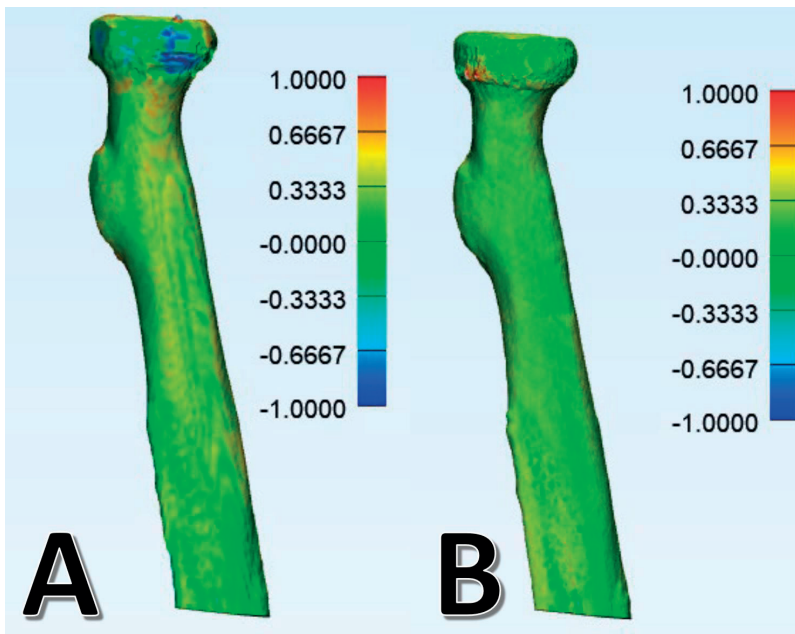


Figure 8. A) The surface distance between a MRI-derived (synthetic-CT) model and the micro-CT model. B) The surface distance between a CT derived model and the ground-truth micro-CT derived model and

As the technology behind 3D printing is developing fast, new 3D printable biofabricated materials are under development to ultimately print entire tissues and organs to facilitate the regenerative medicine movement. For these materials, tests for regulatory approval are especially difficult.[38] Each of these constructs needs the same regulatory approval as e.g. metal implants and polymer saw guides but with the extra notion of their bioactive and bioresorbable nature.

This new era of technological advancements enables many practice-changing modifications of conventional clinical medicine. However not every technological transformation will instantaneously be adopted in medical practice. The purpose of this thesis is to help physicians, clinical physicist and medical engineers with examples of how to develop and implement new medical 3D technology in direct patient care.

Outline of this thesis

Part 1, Scope

In **Chapter 1** of this thesis the current background and development of 3D technology is addressed as well as the challenges and options for improvement.

In **Chapters 2 and 3** respectively the shelf arthroplasty and Chiari osteotomy, are systematically reviewed as both might find options for improvement within 3D technology. Both these interventions are commonly used hip dysplasia treatments that solely rely on the surgeon's craftsmanship and therefore could benefit from 3D additive manufacturing technology. Moreover, both treatments are extra-articular which means that they are less-invasive compared to the presently often performed peri-acetabular osteotomies. In these systematic reviews the primary aim was to measure the survival time until conversion to total hip arthroplasty. As secondary parameters the indications, complications and possible factors that influence the survival were examined. In **Chapter 4** a comparison is made between human hip dysplasia and canine hip dysplasia. Dogs have a high incidence of naturally occurring hip dysplasia and therefore might be a suitable animal to test technological improvements made to hip dysplasia treatment methods.

Until recently skeletal pathologies were most often diagnosed using CT imaging, however with the rise of 3D technology and machine learning, new MRI-based imaging methods find their way to the clinic. However, how do they compare to CT? In **Chapter 5** a review is made comparing different MRI and CT methods for the three-dimensional bone imaging of different musculoskeletal pathologies.

Part 2, Bench

In the second part of this thesis more basic research questions are being tested. In **Chapter 6** a proof of concept is being tested to improve shelf arthroplasty treatment (reviewed in chapter 2) by designing, implanting and biomechanically testing a 3D-printed and patient-specific titanium shelf implant in an ex-vivo canine model with hip dysplasia. Thereafter in **Chapter 7** the same concept is being tested as in chapter 3 but then with a 3D-printed biodegradable hip dysplasia implant.

In **Chapter 8** the idea of a 3D-printed hip dysplasia implant is being translated to also repair and restore stability in the shoulders with >20% bone loss. This concept is also biomechanically tested in human cadaveric specimens and compared to the gold standard Latarjet procedure.

Most 3D-printed titanium implants are rigid and therefore induce stress-shielding in underlying bony tissue. In **Chapter 9** an improvement to the 3D-printed titanium porous structures is examined. Strut diameters of the porous implant are minimized and elongated to allow exceptional (clay-like) deformability of the scaffold material, which will enable the implant to form itself to the shape of the bone while still transferring stress to the underlying bone.

Part 3, One Medicine (translational)

In the third part of the thesis a translation is being made from bench and *ex vivo* research to *in vivo* animal studies. In **Chapter 10** the hip dysplasia implant that was biomechanically tested in chapter 3 was implanted in a pilot trial of dogs (N=3) to ensure feasibility and safety, needed to allow subsequent dog patient treatment in the out-patient clinic. In **Chapter 11** the data of the first patient cohort of 42 implanted 3D shelf implants is being presented as a first-in-dog application of the hip dysplasia implant, designed and tested in Chapters 6 and 10.

In **Chapter 12** two applications of additive manufactured titanium implants for skull reconstruction in canine oncological surgery are presented. In **Chapter 13** another application of additive manufacturing of titanium implants is described. In this chapter two dogs with critically sized- bone defects due to non-union are treated by reconstruction of the ulna with 3D-printed implants.

Part 4, Bedside

In the fourth part, the translation of 3D technology to the human clinic (bedside) is being made. In **Chapter 14** a comparison is made between CT and synthetic-CT to visualize and interpret pelvic landmarks from CT and MRI derived data. This is important for the implementation of MRI derived diagnostics. In **Chapter 15** a CT derived workflow is compared to an MRI derived synthetic-CT workflow to create saw guides for lower arm osteotomies. Subsequently, both these saw guides are compared to the gold standard (micro-CT) for their placement accuracy to evaluate their clinical value.

Chapter 16 illustrates the first-in-man application of a 3D-printed multi-segment vertebrae bridging spinal implant. This chapter includes the required rules and regulations that needed to be documented, providing a workflow that allows clinicians a swifter process in future comparable cases. In **chapter 17** the importance of an in-house multi-disciplinary 3D lab is stressed by presenting two unrepresented solutions that were developed in an academical hospital in close collaboration with a tertiary spine unit and a point-of-care team for 3D innovations.

Part 5, Closings

In **Chapter 18** an invited commentary is given on the usability and applicability of novel 3D technology for (trauma) surgery. Finally, in **Chapter 19**, a short summary is provided and the chapters are discussed in cohesion and the value of this thesis is being reviewed for future research.

References

1. C. A. MacK, "Fifty years of Moore's law," in *IEEE Transactions on Semiconductor Manufacturing*, May 2011, vol. 24, no. 2, pp. 202–207. doi: 10.1109/TSM.2010.2096437.
2. G. E. Moore, "Cramming more components onto integrated circuits," *Electronics*, vol. 38, no. 8, p. 114, 1965.
3. R. Damadian, M. Goldsmith, and L. Minkoff, "Nmr in cancer: Xvi. fonar image of the uve human body," *Physiological chemistry and physics*, vol. 9, no. 1, pp. 97–100, 1977.
4. W. H. Oldendorf, "The quest for an image of brain: a brief historical and technical review of brain imaging techniques," *Neurology*, vol. 28, no. 6, p. 517, 1978.
5. M. Attaran, "The rise of 3-D printing: The advantages of additive manufacturing over traditional manufacturing," *Business Horizons*, vol. 60, no. 5, pp. 677–688, 2017.
6. D. Lin *et al.*, "Three-dimensional printing of complex structures: man made or toward nature?," *ACS nano*, vol. 8, no. 10, pp. 9710–9715, 2014.
7. M. Gebler, A. J. M. S. Uiterkamp, and C. Visser, "A global sustainability perspective on 3D printing technologies," *Energy Policy*, vol. 74, pp. 158–167, 2014.
8. M. Sakin and Y. C. Kiroglu, "3D Printing of Buildings: Construction of the Sustainable Houses of the Future by BIM," *Energy Procedia*, vol. 134, pp. 702–711, 2017.
9. N. J. Mardis, "Emerging technology and applications of 3D printing in the medical field," *Missouri medicine*, vol. 115, no. 4, p. 368, 2018.
10. Q. Yan *et al.*, "A review of 3D printing technology for medical applications," *Engineering*, vol. 4, no. 5, pp. 729–742, 2018.
11. K. H. C. Li *et al.*, "The role of 3D printing in anatomy education and surgical training: A narrative review," *MedEdPublish*, vol. 6, 2017.
12. S. M. Ahmadi *et al.*, "Mechanical behavior of regular open-cell porous biomaterials made of diamond lattice unit cells," *Journal of the mechanical behavior of biomedical materials*, vol. 34, pp. 106–115, 2014.
13. J. van der Stok *et al.*, "Enhanced bone regeneration of cortical segmental bone defects using porous titanium scaffolds incorporated with colloidal gelatin gels for time- and dose-controlled delivery of dual growth factors," *Tissue Engineering Part A*, vol. 19, no. 23–24, pp. 2605–2614, 2013.
14. EUR-Lex, *Regulation (EU) 2017/745 of the European parliament and of the council of 5 April 2017 on medical devices, amending Directive 2001/83/EC, Regulation (EC) No 178/2002 and Regulation (EC) No 1223/2009 and repealing Council Directives 90/385/EEC and 93/42/EE*. 2017. [Online]. Available: <https://eur-lex.europa.eu/legal-content/EN/TXT/PDF/?uri=CELEX:32017R0745&from=EN>
15. D. J. Withey and Z. J. Koles, "A review of medical image segmentation: methods and available software," *International Journal of Bioelectromagnetism*, vol. 10, no. 3, pp. 125–148, 2008.
16. J. Sutherland *et al.*, "Applying modern virtual and augmented reality technologies to medical images and models," *Journal of digital imaging*, vol. 32, no. 1, pp. 38–53, 2019.

17. R. Petzold, H.-F. Zeilhofer, and W. A. Kalender, "Rapid prototyping technology in medicine—basics and applications," *Computerized Medical Imaging and Graphics*, vol. 23, no. 5, pp. 277–284, 1999.
18. H. Hoekstra, W. Rosseels, A. Sermon, and S. Nijs, "Corrective limb osteotomy using patient specific 3D-printed guides: a technical note," *Injury*, vol. 47, no. 10, pp. 2375–2380, 2016.
19. O.-S. Lee, E. S. Lee, and Y. S. Lee, "Disparity between preoperative target correction amount and postoperative correction amount in open wedge high tibial osteotomy," *Knee surgery & related research*, vol. 31, no. 2, p. 126, 2019.
20. Y. Akasaki *et al.*, "Patient-specific prediction of joint line convergence angle after high tibial osteotomy using a whole-leg radiograph standing on lateral-wedge insole," *Knee Surgery, Sports Traumatology, Arthroscopy*, vol. 28, no. 10, pp. 3200–3206, 2020.
21. H. O. Gbejuade, P. White, M. Hassaballa, A. J. Porteous, J. R. Robinson, and J. R. Murray, "Do long leg supine CT scanograms correlate with weight-bearing full-length radiographs to measure lower limb coronal alignment?," *The Knee*, vol. 21, no. 2, pp. 549–552, 2014.
22. M. P. Abdel, P. von Roth, M. T. Jennings, A. D. Hanssen, and M. W. Pagnano, "What safe zone? The vast majority of dislocated THAs are within the Lewinnek safe zone for acetabular component position," *Clinical Orthopaedics and Related Research*®, vol. 474, no. 2, pp. 386–391, 2016.
23. T. E. Snijders, K. Willemsen, S. M. van Gaalen, R. M. Castelein, H. Weinans, and A. de Gast, "Lack of consensus on optimal acetabular cup orientation because of variation in assessment methods in total hip arthroplasty: a systematic review," *HIP International*, vol. 29, no. 1, 2019, doi: 10.1177/1120700018759306.
24. E.-K. Park *et al.*, "Cranioplasty enhanced by three-dimensional printing: custom-made three-dimensional-printed titanium implants for skull defects," *Journal of Craniofacial Surgery*, vol. 27, no. 4, pp. 943–949, 2016.
25. M. Baauw, G. G. Van Hellemond, M. L. Van Hooff, and M. Spruit, "The accuracy of positioning of a custom-made implant within a large acetabular defect at revision arthroplasty of the hip," *The bone & joint journal*, vol. 97, no. 6, pp. 780–785, 2015.
26. K. Willemsen, R. Nizak, H. J. Noordmans, R. M. Castelein, H. Weinans, and M. C. Kruyt, "Challenges in the design and regulatory approval of 3D-printed surgical implants: a two-case series," *The Lancet Digital Health*, vol. 1, no. 4, 2019, doi: 10.1016/S2589-7500(19)30067-6.
27. G. Welsch *et al.*, "CT-based preoperative analysis of scapula morphology and glenohumeral joint geometry," *Computer Aided Surgery*, vol. 8, no. 5, pp. 264–268, 2003.
28. L. Bockhorn *et al.*, "Application of three-dimensional printing for pre-operative planning in hip preservation surgery," *Journal of hip preservation surgery*, vol. 6, no. 2, pp. 164–169, 2019.
29. K. Klaue, M. Sherman, S. M. Perren, A. Wallin, C. Looser, and R. Ganz, "Extra-articular augmentation for residual hip dysplasia Radiological assessment after Chiari osteotomies and shelf procedures," *Journal of Bone and Joint Surgery - Series B*, vol. 75, no. 5, pp. 750–754, 1993, doi: 10.1302/0301-620x.75b5.8376432.

30. C. M. Larson *et al.*, "Are normal hips being labeled as pathologic? A CT-based method for defining normal acetabular coverage," *Clinical Orthopaedics and Related Research*, vol. 473, no. 4, pp. 1247–1254, 2015, doi: 10.1007/s11999-014-4055-2.
31. A. Christensen and F. J. Rybicki, "Maintaining safety and efficacy for 3D printing in medicine," *3D printing in medicine*, vol. 3, no. 1, pp. 1–10, 2017.
32. K. C. Wong, "3D-printed patient-specific applications in orthopedics," *Orthopedic research and reviews*, vol. 8, p. 57, 2016.
33. M. Scharff-Baauw, M. L. Van Hooff, G. G. Van Hellemond, P. C. Jutte, S. K. Bulstra, and M. Spruit, "Good results at 2-year follow-up of a custom-made triflange acetabular component for large acetabular defects and pelvic discontinuity: a prospective case series of 50 hips," *Acta Orthopaedica*, pp. 1–7, 2021.
34. J. Wolff, *The law of bone remodelling*. Springer Science & Business Media, 2012.
35. H. M. A. Kolken *et al.*, "Additively manufactured space-filling meta-implants," *Acta Biomaterialia*, vol. 125, pp. 345–357, 2021.
36. H. M. A. Kolken, S. Janbaz, S. M. A. Leeftang, K. Lietaert, H. H. Weinans, and A. A. Zadpoor, "Rationally designed meta-implants: a combination of auxetic and conventional meta-biomaterials," *Materials Horizons*, vol. 5, no. 1, pp. 28–35, 2018.
37. M. C. Florkow *et al.*, "Deep learning-based MR-to-CT synthesis: The influence of varying gradient echo-based MR images as input channels," *Magnetic Resonance in Medicine*, vol. 83, no. 4, 2020, doi: 10.1002/mrm.28008.
38. R. Levato, J. Visser, J. A. Planell, E. Engel, J. Malda, and M. A. Mateos-Timoneda, "Biofabrication of tissue constructs by 3D bioprinting of cell-laden microcarriers," *Biofabrication*, vol. 6, no. 3, p. 35020, 2014.



CHAPTER 2

Long-term outcomes of the hip shelf arthroplasty in adolescents and adults with residual hip dysplasia: a systematic review

Koen Willemsen | Christiaan J Doelman | Ali SY Sam | Peter R Seevinck |
Ralph JB Sakkers | Harrie Weinans | Bart CH van Der Wal

Published in Acta orthopaedica 91.4 (2020): 383-389
<https://doi.org/10.1080/17453674.2020.1747210>

Abstract

Background and purpose: The shelf arthroplasty was the regular treatment for residual hip dysplasia before it was substituted by the peri-acetabular osteotomy. Yet, evidence regarding the survival of shelf arthroplasty surgery has never been systematically documented. Hence, we investigated the survival time of the shelf procedure until revision to THA in patients with primary hip dysplasia. Factors that influenced survival and complications were also examined, along with the accuracy of correcting radiographic parameters to characterize dysplasia.

Material and methods: The inclusion criteria were studies of human adolescents and adults (> 16 years) with primary or congenital hip dysplasia who were treated with a shelf arthroplasty procedure. Data were extracted concerning patient characteristics, survival time, complications, operative techniques, and accuracy of correcting radiographic parameters.

Results: Our inclusion criteria were applicable to 9 studies. The average postoperative Center-Edge Angle and Acetabular Head Index were mostly within target range, but large variations were common. Kaplan–Meier curves (endpoint: conversion to THA) varied between 37% at 20 years' follow-up and 72% at 35 years' follow-up. Clinical failures were commonly associated with pain and radiographic osteoarthritis. Only minor complications were reported with incidences between 17% and 32%.

Interpretation: The shelf arthroplasty is capable of restoring normal radiographic hip parameters and is not associated with major complications. When carefully selected on minimal osteoarthritic changes, hip dysplasia patients with a closed triradiate cartilage may benefit from the shelf procedure with satisfactory survival rates. The importance of the shelf arthroplasty in relation to peri-acetabular osteotomies needs to be further (re) explored.

Introduction

The concept of shelf arthroplasty as a treatment for hip dysplasia was introduced by Franz König (1891); autologous bone is transplanted extra-articularly to extend the coverage of the femoral head by the acetabulum. Nowadays, shelf arthroplasty that relies on fibrocartilaginous changes of the capsule has mostly been replaced by treatments that reorient the patient's own hyaline cartilage, the peri-acetabular osteotomy (PAO) being one of the most frequently used treatments (Clohisy et al. 2009). However, evidence proving the superiority of the PAO over shelf arthroplasty is lacking. A systematic review of Clohisy et al. (2009) including 13 studies concerning PAO treatment displayed conversion rates to THA between 0% and 17% during, respectively, an average follow-up of 3 and 11 years. Moreover, the PAO is a relatively invasive procedure that necessitates a long rehabilitation period, requires a long learning curve, and has major complication rates reaching as high as 37% (Clohisy et al. 2007).

A systematic review concerning shelf arthroplasty survival in adolescent and adult patients has never been made. Therefore, the primary objective of this study is to systematically evaluate the long-term survival of shelf arthroplasty in adolescents and adults. As a secondary objective we evaluated factors that influence survival, the amount and type of complications, and the ability to correct radiologically dysplastic parameters to normal levels.

Method

For this systematic review, we consulted the databases Pubmed, Embase, and Cochrane, per search date of November 2019. The term 'shelf' was separately combined with the term 'arthroplasty' including all known synonyms to minimize the chance of missing articles (see Supplementary data). Obtained articles were imported into a RefWorks database (ProQuest, Ann Arbor, MI, USA). After removal of duplicates the abstracts were read separately by 2 authors (CD, AS) in search of the inclusion criteria (Figure 1).

Inclusion criteria were studies reported in the English language, population human subjects with an average age of 16 years and older with mainly primary (congenital) hip dysplasia, treated with a shelf procedure, and with follow-up of at least 8 years. Studies concerning $\geq 50\%$ secondary hip dysplasia, e.g., due to Down syndrome, Trevor's disease, Perthes disease, or cerebral palsy were excluded. Studies that used $\geq 50\%$ combined dysplasia treatments, e.g., additional osteotomies, were also excluded because the influence of the combined treatment on the results is not clear. In addition, studies with an average follow-up of less than 8 years, case reports, and reviews were excluded. Studies were excluded only when there was consensus between authors (KW, CD, AS). Finally, cross-referencing was done in the bibliographies of the included studies.

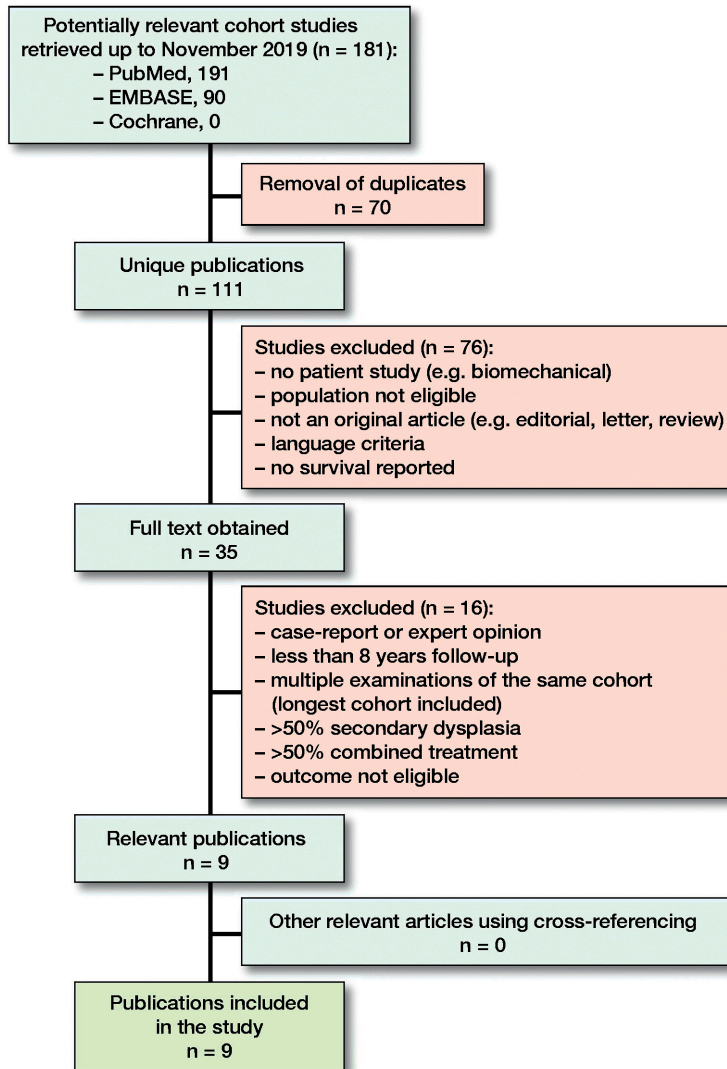


Figure 1. From the 111 unique publications that were found in the systematic literature search, only 9 publications were eligible for this systematic review.

Each published full article was reviewed separately by 3 of the authors (KW, CD, AS). Items reviewed included age, sex, number of patients and hips, study type, level of evidence, type of shelf procedure, type of graft used, amount of patients who were lost to follow-up, combination with other treatments, previous operations, preoperative osteoarthritic state (with scale), failure definition, survival-rates, complications, used surgical indication, amount of conversions to total hip arthroplasty at final follow-up, and the change in hip score (with scale). If documented pre- and postoperatively, the 2 hip parameters (Center

Edge Angle=CEA, and Acetabular Head Index=AHI) were also reviewed and displayed graphically. Furthermore, the Newcastle Ottawa Scale (NOS) was used to assess the quality of each study and the average between 2 observers (CD and AS) was documented (Tables 1 and 2).

Preoperative advanced osteoarthritis was recorded and dichotomized because different scales were used: the Tönnis and Heinecke (1999), De Mourgues and Patte (1978), Japanese Orthopedic Association (Takatori et al. 2010) and Oxford Hip Scores (Dawson et al. 1996). Because of the heterogeneity of this parameter, we distinguished between mild and advanced osteoarthritis. Therefore, on every scale the level that corresponds to advanced osteoarthritis was identified after which the number of patients who were in an advanced state of osteoarthritis were identified (Table 1). Differences in extracted information were discussed between the 3 reviewers and consensus was reached regarding the aspect in question at all times. Authors of included studies were not contacted in the event of missing data.

Results

111 unique publications were found in the databases Pubmed, Cochrane, and Embase. 9 studies remained after inclusion and exclusion criteria were applied. Cross-referencing offered no additional articles, resulting in 9 studies analyzed in this study (Tables 1 and 2).

All the studies, except for Berton et al. (2010), are observational retrospective cohort studies without a control group. Berton et al. is a prospective cohort that stratified for the existence of labral tears.

In all studies autologous cortical bone was used and placed superiorly and extra-capsularly to create an extra weight-bearing area and increase joint stability (Nishimatsu et al. 2002, Migaud et al. 2004, Fawzy et al. 2005, Berton et al. 2010, Hirose et al. 2011, Bartoniček et al. 2012, Tanaka et al. 2018). The bone was harvested from the iliac crest (Nishimatsu et al. 2002, Migaud et al. 2004, Bartoniček et al. 2012), the iliac inner (Fawzy et al. 2005) or outer (Hirose et al. 2011, Tanaka et al. 2018) fossa. Unicortical grafts were used by 2 studies (Migaud et al. 2004, Tanaka et al. 2018) and both uni- and bicortical grafts were used by 1 study (Fawzy et al. 2005). A tectoplasty was performed in 2 studies by raising a vertical flap and filling the space with cancellous bone (Nishimatsu et al. 2002, Hirose et al. 2011). Cancellous bone was packed above the shelf by 3 studies (Fawzy et al. 2005, Bartoniček et al. 2012, Tanaka et al. 2018). Migaud et al. (2004) contained the cortical shelf by securing it with a small bent plate. The operation time of 55 minutes (35–75) was only documented by Bartoniček et al. (2012). Some studies combined the shelf arthroplasty in a minor part of their total population with a varus or valgus osteotomy of the proximal

Table 1. Study characteristics

Reference	NOS score	Study design ^a	Level of evidence	Type of shelf procedure	Analyzed hips/patients	Male/female	Mean age (range)	Combination with other treatment n (%)	Previous operation n (%)	OA scale ^b	Preop. advanced OA n (%)
<i>Bartoniček et al. (2012)</i>	8	R	IV	Bosworth (1961)	25/18	1/17	31 (16–52)	0 (0)	2 (8)	TH	2 (8)
<i>Berton et al. (2010)</i>	8	P	III	Modified Roy-Camille (1968)	17/17	NR	34 (20–49)	(100) ^c	NR	TH	4 (14)
<i>Fawzy et al. (2005)</i>	8	R	IV	NR	76/67	14/53	33 (17–60)	6 (8)	≥ 7	MP	>32 (42)
<i>Hamanishi et al. (1992)</i>	6.5	R	IV	Spitzky (1933)	124/113	12/101	24 (10–53)	33 (27)	8 (7)	NR	NR
<i>Hirose et al. (2011)</i>	7.5	R	IV	Mizuno (1970)	28/26	0/26	34 (17–54)	6 (21)	NR	JOA	0 (0)
<i>Migaud et al. (2004)</i>	7	R	IV	NR	56/48	NR	32 (17–56)	NR	NR	MP	32 (57)
<i>Nishimatsu (2002)</i>	7	R	IV	Spitzky (1933)	119/108	3/105	25 (1–56)	27 (26)	NR	JOA	58 (48)
<i>Saito et al. (1986)</i>	8	R	IV	Mizuno (1970)	27/24	3/21	25 (11–55)	NR	11 (41)	NR	6 (22)
<i>Tanaka et al. (2018)</i>	7	R	IV	Modified Spitzky (1933)	35/32	2/30	31 (19–49)	NR	(0)	TH	0 (0)

NOS = Newcastle Ottawa Scale for assessing study quality

NR = Not reported;

^a = Study design: P = prospective, R = retrospective

^b = OA scales: JOA = Japanese Orthopedic Association (Takatori et al. 2010) and Oxford Hip Scores (Dawson et al. 1996); MP = De Mourguès and Patte (1978); TH = Tönnis and Heinecke (1999);

^c = Diagnostic arthroscopy

Table 2. Study characteristics

<i>First author</i>	<i>Study country</i>	<i>Analyzed hips/ patients</i>	<i>Years follow-up mean (range)</i>	<i>Conversions to THA during follow-up, n (%)</i>	<i>Clinical outcome scale^a</i>	<i>Hip score pre- (range)</i>	<i>Hip score post- (range)</i>	<i>Final score (years)</i>	<i>Lost to follow-up n (%)</i>
<i>Bartoniček</i>	Czech Republic	25/18	15 (10–23)	4 (16)	HHS	68 (56–82)	90 (76–100)	NR	NR
<i>Berton</i>	France	17/17	16 (16–18)	8 (47)	PMA	NR	NR	NR	1/18 (6)
<i>Fawzy</i>	England	76/67	11 (6–14)	22 (30)	OHS	NR	NR	NR	NR
<i>Hamanishi</i>	Japan	124/113	10 (5–25)	2 (2)	JOA	73	NR	86 (10)	NR
<i>Hirose</i>	Japan	28/26	25 (20–32)	5 (18)	JOA	76	NR	92 (5) > 80 (20)	29/57 (51)
<i>Migaud</i>	France	56/48	17 (15–30)	25 (45)	PMA	NR	NR	NR	5/53 (9)
<i>Nishimatsu</i>	Japan	119/108	24 (15–41)	11 (9)	JOA	NR	80	68 (NR)	NR
<i>Saito</i>	Japan	27/24	13 (5–19)	2 (7) ^b	PMA	13	16	15 (18)	7/31 (23)
<i>Tanaka</i>	Japan	35/32	26 (16–36)	10 (28)	JOA	82	> 90	86 (25)	NR

^a = Outcome scales: HHS = Harris Hip Score (Harris 1969); JOA = Japanese Orthopaedic Association (Tanaka 1978, Takeda et al. 2006); PMA = The Postel;

Merle d'Aubigné (Merle d'Aubigné 1990); OHS = Oxford Hip Score (Dawson et al. 1996)

^b = Additional undefined surgery

NR = Not reported

femur (8–27%) (Hamanishi et al. 1992, Nishimatsu et al. 2002, Hirose et al. 2011). Berton et al. (2010) combined the shelf procedure with diagnostic arthroscopy solely to image the labral condition. No surgical alterations were made.

Preoperative indications varied widely (Table 3). Early arthritis secondary to dysplasia was used as indication in 3 studies (Hamanishi et al. 1992, Nishimatsu et al. 2002, Hirose et al. 2011). Pain was used as a preoperative indication by Fawzy et al. (2005) and Bartoníček et al. (2012). Radiographic parameters were used for preoperative indications by 4 studies (Migaud et al. 2004, Berton et al. 2010, Bartoníček et al. 2012, Tanaka et al. 2018); the diagnosis ‘congenital dislocation and subluxation of the hip’ was used by 1 study (Saito et al. 1986).

Table 3. Indications for the shelf procedure and negative survival predictors as suggested by the authors

Reference	Surgical indication shelf	Significant negative survival factors
<i>Bartoníček et al. (2012)</i>	Dysplastic centered hip, without osteoarthritic changes, even in patients who are 60 years old	Asphery, decentration, osteoarthritic changes.
<i>Berton et al. (2010)</i>	Age over 18 years, dysplastic hip, ($0^\circ < \text{CE angle} < 20^\circ$), hip centered with regard to the Shenton line	Osteoarthrosis, CE angle $< 0^\circ$, subluxation, labral tears (in positive-angle acetabular dysplasia)
<i>Fawzy et al. (2005)</i>	Mild/moderate dysplasia, minimal secondary arthritis	Advanced osteoarthritis, moderate/severe incongruency
<i>Hamanishi et al. (1992)</i>	Age under 30, pre-/early osteoarthritis, stable hip joint, with intact or uninverted labrum	Age above 30, bilateral dysplasia
<i>Hirose et al. (2011)</i>	Moderate dysplasia, without severe osteoarthritis; however, advanced osteoarthritis in combination with femoral valgus osteotomy might be possible	None found
<i>Migaud et al. (2004)</i>	If peri-acetabular osteotomy is not possible because of severe subluxation or incongruency	Severe dysplasia (CE angle $< 15^\circ$), advanced stage osteoarthrosis
<i>Nishimatsu et al. (2002)</i>	Younger age (however not < 6 years)	Older age, advanced osteoarthritis, height of the shelf
<i>Saito et al. (1986)</i>	Age under 30, no or early degenerative change	Age above 30, severe degenerative changes
<i>Tanaka et al. (2018)</i>	Moderate dysplasia without severe osteoarthritis	Incorrect graft placement (too high)

CE angle = center-edge angle.

Kaplan–Meier survival analysis with THA as endpoint (Figure 2) was documented by 5 studies (Migaud et al. 2004, Fawzy et al. 2005, Berton et al. 2010, Hirose et al. 2011, Tanaka et al. 2018). Fawzy et al. (2005) analyzed 76 hips from 67 patients with an average age of 33. From those shelf procedures, 86% lasted 5 years, 70% lasted 7.5 years, and 46% lasted 10 years until revision to THA. However, many hips showed advanced narrowing of the joint space preoperatively with 32 hips graded as grade IV on the De Mourgues and Patte scale (1978) (> 50% joint space narrowing). When the 44 hips with preoperative grade 3 or less only were analyzed, they found a substantially higher survival percentage of 97% at 5 years and 75% at 10 years..

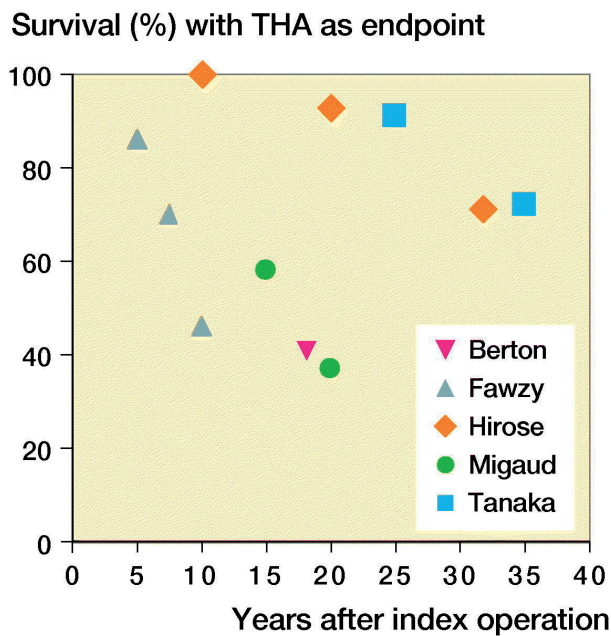


Figure 2. Survival of shelf arthroplasties with years to THA as endpoint. Data for these Kaplan–Meier survival analysis results were extracted from the articles.

Berton et al. (2010) used a prospective trial to investigate the effect of the CE angle and labral tears on the shelf arthroplasty survival in a small group of patients. From the 18 patients with an average age of 34 years, 8 hips were converted to a total hip replacement at 18 years' follow-up. This was significantly higher in the group with labral tears with 7 hips (85%) converted in 18 years of follow-up, as compared with the group without labral tears with 1 hip (17%) converted in 18 years of follow-up.

Migaud et al. (2004) analyzed 56 hips in 48 patients with an average age of 32 at the time of shelf arthroplasty. From their hips, 58% survived 15 years, and 37% managed to

survive for 20 years. Similarly to Fawzy et al. (2005), Migaud et al. (2004) treated 32 hips at baseline with grade III or higher on the De Mourgues and Patte scale (1978). These 32 severely osteoarthritic hips had a significant lower survival than the 24 lower graded hips, respectively 27% and 83% survival at 18 years.

Hirose et al. (2011) analyzed 28 hips in 26 patients with an average age of 34 years. All had some amount of osteoarthritis but not one was graded as severe. 29 patients (51%) were lost to follow-up and were therefore not included in the analysis. All hips lasted to the 10-year mark, 93% lasted 20 years, and 71% lasted until 32 years' follow-up. Hirose et al. (2011) undertook additional survival analysis for clinical evaluation and stage of joint space narrowing of 28 hips. The survival with joint space narrowing < stage 3 on the (0–4) scale of the JOA as an endpoint was 79% at 10 years, 54% at 20 years, and 21% at 32 years. Survival with a pain score of 20 (scale 0–40) as an endpoint was 100% at 10 years, 86% at 20 years, and 51% at 32 years.

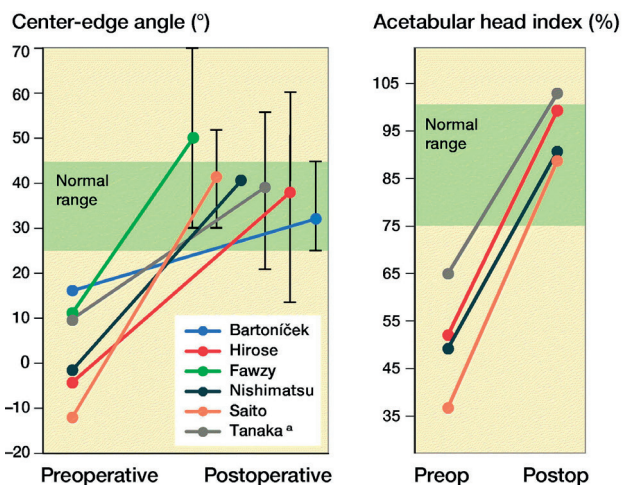


Figure 3. The left panel) displays the average center-edge (CE) angle and the right panel the acetabular head index (AHI) pre(operative) and post(operative). Whiskers display postoperative center-edge angle ranges in relation to the healthy normal/target zone (green areas). a No range reported, 2 SD was taken as alternative.

Tanaka et al. (2018) analyzed 35 hips in 32 patients with an average age of 31 years and no cases of advanced osteoarthritis at the time of shelf arthroplasty. The hip survival with conversion to THA as the endpoint was 91% at 25 years and 72% at 35 years. The survival with a Tönnis osteoarthritis score of 3 or higher as the endpoint was 74% at 25 years' follow-up.

All articles reported the number of conversions to THA but only in regard to their average follow-up. This ranged from 2% conversions in 10 years to 47% conversions in 16 years (Table 2). Fawzy et al. (2005) and Migaud et al. (2004) stratified their outcomes for the grade of preoperative osteoarthritis and Saito et al. (1986) for severe degenerative changes. All found a negative effect of preoperative advanced osteoarthritis on the outcome of the shelf arthroplasty.

In general, functional outcomes between studies were difficult to compare because of heterogeneous clinical scoring methods and patient characteristics (Table 2). Moreover, evaluation time points in relation to the surgery or the number of patients per evaluation were often not reported. The average functional outcome improved postoperatively (Saito et al. 1986, Hamanishi et al. 1992, Hirose et al. 2011, Bartoniček et al. 2012, Tanaka et al. 2018) and this improvement lasted up to the final follow-up (Saito et al. 1986, Hamanishi et al. 1992, Hirose et al. 2011) even after 25 years of follow-up (Tanaka et al. 2018).

Most studies documented radiological angles. Perioperative CE angles were documented in all studies and the AHI was measured in 5 studies (Saito et al. 1986, Nishimatsu et al. 2002, Berton et al. 2010, Hirose et al. 2011, Tanaka et al. 2018). All studies that documented both preoperative and postoperative values found a postoperative increase in average CE angle and/or AHI (Figure 3). However, the range of surgical correction achieved was not always within the target values (Figure 3). Both radiographic parameters and functional outcomes were documented in 4 manuscripts (Nishimatsu et al. 2002, Hirose et al. 2011, Bartoniček et al. 2012, Tanaka et al. 2018), yet no relation between radiographic scores and function was reported.

Rehabilitation and postoperative weightbearing was documented in 6 studies with no clear consensus between the different studies (Saito et al. 1986, Hamanishi et al. 1992, Fawzy et al. 2005, Hirose et al. 2011, Bartoniček et al. 2012, Tanaka et al. 2018). Non-weightbearing walking started at 2 days to 6 weeks, partial weightbearing started at 6 to 8 weeks and full weightbearing started at 10 weeks to 6 months.

The complication rate and the background information on the complications were reported by 4 articles. No major complications were encountered (Table 4).

Table 4. Reported complications of shelf procedure

Reference	n (%)	Complications
<i>Bartoniček et al. (2012)</i>	5 (20)	Paresthesia lateral femoral cutaneous nerve (disappeared over time)
	2 (8)	Too large a graft (limited external rotation of 1 hip) Partial resorption of graft (still sufficient coverage)
	1 (4)	Extra screw fixation Non-displacement fracture of graft (after a fall)
<i>Fawzy et al. (2005)</i>	10 (13)	Meralgia paraesthetica
	4 (5)	Nonunion and graft breakage
	3 (4)	Superficial wound infection
	2 (3)	Bursa over metalwork (femoral osteotomy)
	1 (1)	Wound hematoma, knee stiffness after traction, flexion contracture, deep venous thrombosis, heterotopic ossification, pulmonary edema
<i>Migaude et al. (2004)</i>	5 (9)	Non-unions
	2 (4)	Temporary peroneal palsies
	2 (4)	Sacroiliac pain
<i>Saito et al. (1986)</i>	2 (7)	Fracture of the base of the reflected outer cortex of the ilium
	2 (7)	Wrong shelf placement

Discussion

The aim of this systematic review of the shelf arthroplasty was to describe long-term survival, the ability to correct hip dysplasia radiologically, complications, and surgical indications used. The shelf arthroplasty is considered a simple procedure with a THA-free survival of up to 72% over a 35-year period, provided the right surgical indication is used.

The THA-free survival of the shelf procedure reported in this review is comparable to those of the PAO while not being associated with major complications (Clohisy et al. 2009). However, different approaches of the PAO such as the adductor-sparing approaches could result in better recovery of the patient and fewer complications, yet long-term follow-up is still sparse (Murphy and Millis 1999). When evaluating the 5 out of 9 articles that undertook a Kaplan–Meier analysis as part of their survival analysis, the shelf procedure shows surprisingly high survival results (Figure 2). Especially so when noting that both Migaude et al. (2004) and Fawzy et al. (2005) had a high number of patients with severe preoperative osteoarthritis and Berton et al. (2010) had many cases with an existing labral tear. Both the advanced osteoarthritic and labral tear patients had significantly inferior results as compared with patients without osteoarthritis or labral tears. When fewer patients with advanced osteoarthritis were included, as in the studies of Hirose et al. (2011) and Tanaka et al. (2018), the THA-free survival percentage even reached 72% at 35 years of follow-up. These survival results are in line with a recent study by Holm et al.

(2017), who reported very long shelf survival rates in children and adolescents. That study was not included in this systematic analysis because the average age of 56 patients (70 hips) was only 12 years (5–22), an average age that was too low for the inclusion criteria. Holm et al. (2017) reported a THA-free survival percentage of 100% at 20 years, 83% at 30 years, and up to 22% at 50 years. In a separate report from the same hospital, Terjesen (2018) made a sub-analysis for the age group > 12 years (average age 16.1 years). The Kaplan–Meier analysis showed a survival of 100% at 20 years, 72% at 30 years, and 32% at 40 years of follow-up. However, because it concerned a sub-analysis many specifics were not given (e.g., number of patients, sex, average follow-up, combinations with other treatment, previous operations, preoperative osteoarthritis scale, clinical hip score, and lost-to-follow up) and therefore the study was not included in this review. The shelf survival values resemble or are even better than PAO survival in the long term (Schramm et al. 2003, Hasegawa et al. 2014, Lerch et al. 2017). Nonetheless, the shelf arthroplasty is considered a salvage procedure, while the peri-acetabular osteotomy is considered to be joint-preserving surgery. Once again, this raised the question as to whether the shelf procedure should be reconsidered in the palette of treatment options for residual hip dysplasia.

Klaue et al. (1993) noticed that a normal CE angle on a radiograph after a shelf arthroplasty is commonly an overestimation when compared with the true femoral coverage on a CT scan. Therefore, parameters such as the CE angle and the AHI might be overestimated. Nevertheless, new 3D planning and evaluation techniques can overcome difficulties in graft placement and improve the effectiveness of correcting the radiological dysplastic parameters in all dimensions (Figure 3). However, it should be noted that the shelf arthroplasty does not change the hyaline cartilage but rather induces fibrocartilaginous metaplasia of the joint capsule to increase the amount of weight-bearing tissue.

Evaluation of the literature shows substantial limitations. First, the level of evidence was low: 8 out of 9 articles were retrospective with level IV evidence and only Berton et al. (2010) was prospective with level III evidence (Table 1). Low-level evidence is common in orthopedics studies as different surgical techniques are often difficult to compare (Obremsky et al. 2005). The included studies used 6 different modifications of the shelf procedure and all had a different postoperative rehabilitation process. The effects of these differences on the outcome were not clear. Second, the investigated population could be considered a limitation as 5 out of 9 studies were completed in Japan, which has a population with a well-known higher incidence of hip dysplasia (Nakamura et al. 1989). Furthermore, far more women participated in the studies investigated, which could have influenced the results, but none of the included studies stratified for sex.

Another limitation could be the search syntax. Additional unknown nomenclature for the shelf arthroplasty could have influenced the effectiveness of the search syntax. However, cross-referencing did not provide any additional articles, causing the impact of this aspect to be low, presumably.

Lost to follow-up was not documented in Fawzy et al. (2005) and Nishimatsu et al. (2002). Therefore, selection bias could have occurred. Only 2 studies documented the number of patients who died before final follow-up. Berton et al. (2010) reported 2 “unrelated” deaths and Migaud et al. (2004) noted 2 deaths without further explanation.

Another type of selection bias may arise from the lack of consensus on the correct indication for performing a shelf procedure. For example, studies that included patients with incongruency and advanced osteoarthritis showed lower survival of the shelf arthroplasty (Migaud et al. 2004, Fawzy et al. 2005). Saito et al. (1986), Berton et al. (2010) and Bartoníček et al. (2012) included only a few patients with severe osteoarthritis (8–22%), Nishimatsu et al. (2002), Migaud et al. (2004) and Fawzy et al. (2005) included roughly half of their patients with severe osteoarthritis (42–57%), while Hirose et al. (2011) and Tanaka et al. (2018) included no patients with severe osteoarthritis. Differences were also found in inclusion of aspheric hips (Migaud et al. 2004) or spheric hips (Bartoníček et al. 2012), younger patients (Saito et al. 1986, Hamanishi et al. 1992, Nishimatsu et al. 2002) or older patients (Berton et al. 2010) even up to their 6th decade (Bartoníček et al. 2012). An additional evident selection bias was introduced by Migaud et al. (2004) who considered shelf arthroplasty as salvage only in patients not eligible for a peri-acetabular osteotomy.

Conclusion

The shelf arthroplasty is competent in restoring radiographic hip parameters to normal levels, increases functional outcomes, and is not associated with major complications. When selected on minimal osteoarthritic changes, adolescent and adult hip dysplasia patients may benefit from the shelf procedure with satisfactory survival rates. Therefore, based on the findings in this review, the indications for shelf arthroplasty should more often be considered in the treatment of residual hip dysplasia, especially with regard to the difficult-to-perform peri-acetabular osteotomy surgery. Given the constant development of 3D-planning techniques, shelf placement can even be further optimized and therefore may increase its clinical effectiveness.

Supplementary Data

<http://dx.doi.org/10.1080/17453674.2020.1747210>

References

- Bartoniček J, Vávra J, Chochola A. Bosworth hip shelf arthroplasty in adult dysplastic hips: ten to twenty-three year results. *Int Orthop* 2012; 36(12): 2425–31.
- Berton C, Bocquet D, Krantz N, Cotten A, Migaud H, Girard J. Shelf arthroplasties long-term outcome: influence of labral tears. A prospective study at a minimal 16 years' follow-up. *Orthop Traumatol Surg Res* 2010; 96(7): 753–9.
- Bosworth D M, Fielding JW, Ishizuka T, Ege R. Hip-shelf operation in adults. *J Bone Joint Surg* 1961; 43(1): 93–106.
- Clohisy J C, Nunley R M, Curry M C, Schoenecker P L. Periacetabular osteotomy for the treatment of acetabular dysplasia associated with major aspherical femoral head deformities. *J Bone Joint Surg–Ser A* 2007; 89(7): 1417–23.
- Clohisy J C, Schutz A L, John L S, Schoenecker P L, Wright R W. Periacetabular osteotomy: a systematic literature review. *Clin Orthop Relat Res* 2009; 467(8): 2041–52.
- Dawson J, Fitzpatrick R, Carr A, Murray D. Questionnaire on the perceptions of patients about total hip replacement. *J Bone Joint Surg Br* 1996; 78(2): 185–90.
- De Mourgues G, Patte D. Résultats, après au moins 10 ans, des ostéotomies d'orientation du col du fémur dans les coxarthroses secondaires peu évoluées chez l'adulte: symposium. *Rev Chir Orthop* 1978; 64(7): 525-9.
- Fawzy E, Mandellos G, De Steiger R, McLardy-Smith P, Benson M K D, Murray D. Is there a place for shelf acetabuloplasty in the management of adult acetabular dysplasia? *Bone Joint J* 2005; 87(9): 1197–202.
- Hamanishi C, Tanaka S, Yamamuro T. The Spitzzy shelf operation for the dysplastic hip retrospective 10 (5–25) year study of 124 cases. *Acta Orthop Scand* 1992; 63(3): 273–7.
- Harris W H. Traumatic arthritis of the hip after dislocation and acetabular fractures: treatment by Mold arthroplasty. An end-result study using a new method of result evaluation. *J Bone Joint Surg Am* 1969; 51(4): 737.
- Hasegawa Y, Iwase T, Kitamura S, Kawasaki M, Yamaguchi J. Eccentric rotational acetabular osteotomy for acetabular dysplasia and osteoarthritis: follow-up at a mean duration of twenty years. *J Bone Joint Surg* 2014; 96(23): 1975–82.
- Hirose S, Otsuka H, Morishima T, Sato K. Long-term outcomes of shelf acetabuloplasty for developmental dysplasia of the hip in adults: a minimum 20-year follow-up study. *J Orthop Sci* 2011; 16(6): 698–703.
- Holm A G V, Reikerås O, Terjesen T. Long-term results of a modified Spitzzy shelf operation for residual hip dysplasia and subluxation: a fifty-year follow-up study of fifty-six children and young adults. *Int Orthop* 2017; 41(2): 415-21.
- Klaue K, Sherman M, Perren S M, Wallin A, Looser C, Ganz R. Extra-articular augmentation for residual hip dysplasia: radiological assessment after Chiari osteotomies and shelf procedures. *Bone Joint J* 1993; 75(5): 750–4.

- König F. Osteoplastische Behandlung der congenitalen Hüftgelenkluxation. *Verh Deutsch Ges Chir* 1891; 20: 75–80.
- Lerch TD, Steppacher SD, Liechti EF, Tannast M, Siebenrock KA. One-third of hips after periacetabular osteotomy survive 30 years with good clinical results, no progression of arthritis, or conversion to THA. *Clin Orthop Relat Res* 2017; 475(4): 1154–68.
- Merle d'Aubigné R. Cotation chiffrée de la fonction de la hanche. *Rev Chir Orthopédique* 1990; 76(6): 371–4.
- Migaud H, Chantelot C, Giraud F, Fontaine C, Duquennoy A. Long-term survivorship of hip shelf arthroplasty and Chiari osteotomy in adults. *Clin Orthop Relat Res* 2004; (418): 81–6.
- Mizuno S. *Short Lectures in Orthopaedic Surgery, Illustrated*. Tokyo: Ishiyaku Publishers 1970. PP: 27–39.
- Murphy S B, Millis M B. Periacetabular osteotomy without abductor dissection using direct anterior exposure. *Clin Orthop Relat Res* 1999; (364): 92–8.
- Nakamura S, Ninomiya S, Nakamura T. Primary osteoarthritis of the hip joint in Japan. *Clin Orthop Relat Res* 1989; (241): 190–6.
- Nishimatsu H, Iida H, Kawanabe K, Tamura J, Nakamura T. The modified Spitzzy shelf operation for patients with dysplasia of the hip. *Bone Joint J* 2002; 84(5): 647–52.
- Obremskey WT, Pappas N, Attallah-Wasif E, Tornetta III P, Bhandari M. Level of evidence in orthopaedic journals. *J Bone Joint Surg* 2005; 87(12): 2632–8.
- Roy-Camille R. Butée ostéoplastique armée de hanche. Technique permettant la marche au 21e jour. *Press Med* 1968; 76: 273–5.
- Saito S, Takaoka K, Ono K. Tectoplasty for painful dislocation or subluxation of the hip: long-term evaluation of a new acetabuloplasty. *Bone Joint J* 1986; 68(1): 55–60.
- Schramm M, Hohmann D, Radespiel-Troger M, Pitto R P. Treatment of the dysplastic acetabulum with Wagner spherical osteotomy: a study of patients followed for a minimum of twenty years. *J Bone Joint Surg* 2003; 85(5): 808–14.
- Spitzzy H. Kunstliche Pfannendachbildung: Benutzung von Knochenbolzen zur temporären Fixation. *Z Orthop Chir* 1933; 58: 470–86.
- Takatori Y, Ito K, Sofue M, Hirota Y, Itoman M, Matsumoto T, Hamada Y, Shindo H, Yamada H, Yasunaga Y. Analysis of interobserver reliability for radiographic staging of coxarthrosis and indexes of acetabular dysplasia: a preliminary study. *J Orthop Sci* 2010; 15(1): 14–19.
- Takeda H, Kamogawa J, Sakayama K, Kamada K, Tanaka S, Yamamoto H. Evaluation of clinical prognosis and activities of daily living using functional independence measure in patients with hip fractures. *J Orthop Sci* 2006; 11(6): 584–91.
- Tanaka H, Chiba D, Mori Y, Kuwahara Y, Baba K, Yamada N, Fujii G, Itoi E. Long-term results of a modified Spitzzy shelf operation for developmental dysplasia of the hip in adults and adolescents. *Eur J Orthop Surg Traumatol* 2018; 28(7): 1341–7.
- Tanaka S. Surface replacement of the hip joint. *Clin Orthop Relat Res* 1978; 134:75–9.
- Terjesen T. Current concepts review—residual hip dysplasia: is there a place for hip shelf operation? *J Child Orthop* 2018; 12: 358–63.
- Tönnis D, Heinecke A. Current concepts review-acetabular and femoral anteversion: relationship with osteoarthritis of the hip. *J Bone Joint Surg* 1999; 81(12): 1747–70.



CHAPTER 3

Good long-term outcomes of the hip Chiari osteotomy in adolescents and adults with hip dysplasia: a systematic review

Koen Willemsen | Menco J. S. Niemeyer | Netanja I. Harlianto |
Said Sadiqi | Peter R. Seevinck | Ralph J. B. Sakkers | Harrie Weinans |
Bart C. H. van der Wal

Published in Acta Orthopaedica 93 (2022): 296
<https://doi.org/10.2340/17453674.2022.2031>

Abstract

Background and purpose: The Chiari osteotomy was a regular treatment for developmental hip dysplasia before it became mostly reserved as a salvage therapy. However, the long-term survival of the Chiari osteotomy has not been systematically investigated. We investigated the survival time of the Chiari osteotomy until conversion to total hip arthroplasty (THA) in patients with primary hip dysplasia, and factors which correlated with survival, complications, and the improvement measured in radiographic parameters.

Patients and methods: Studies were included when describing patients (> 16 years) with primary hip dysplasia treated with a Chiari osteotomy procedure with 8 years' follow-up. Data on patient characteristics, indications, complications, radiographic parameters, and survival time (endpoint: conversion to THA) were extracted.

Results: 8 studies were included. The average postoperative center–edge angle, acetabular head index, and Sharp angle were generally restored within the target range. 3 studies reported Kaplan-Meier survival rates varying from 96% at 10 years to 72% at 20 years' follow-up. Negative survival factors were high age at intervention and pre-existing advanced preoperative osteoarthritis. Moreover, reported complications ranged between 0% and 28.3 %.

Interpretation: The Chiari osteotomy has high reported survival rates and is capable of restoring radiographic hip parameters to healthy values. When carefully selected by young age, and a low osteoarthritis score, patients benefit from the Chiari osteotomy with satisfactory survival rates. The position of the Chiari osteotomy in relation to the periacetabular osteotomies should be further (re-)explored.

Introduction

Patients with developmental dysplasia of the hip (DDH) are prone to develop osteoarthritis (OA) of the hip at a young age [1]. A variety of osteotomy procedures have been described to prevent secondary OA and to relieve pain, including the Chiari pelvic osteotomy, which distinctively augments the dysplastic acetabulum by transverse medial displacement made just proximal to the acetabular rim. The effective lateral displacement of the superior iliac fragment covers the femoral head, creating support for the capsule, increasing hip stability, enlarging the effective weightbearing surface, and increasing hip joint stability [2-4].

Chiari osteotomy historically has been considered a reasonable mainline treatment option for acetabular dysplasia [2]. In recent decades, however, as powerful acetabular redirection osteotomies and total hip replacements have proved effective, the Chiari osteotomy has become a salvage option, limited to use in very severe dysplasia or in hips with aspherical femoral heads [5]. However, redirection osteotomies can be quite invasive [6] and total hip replacements may need (multiple) revisions, especially when placed in young and active patients [7]. Therefore, procedures that can postpone a total hip replacement, such as the Chiari osteotomy, should be reconsidered, though no recent joint survival analysis has been performed, as is done for other hip dysplasia treatment options, e.g., the “shelf arthroplasty” [8] and the “redirectional (peri-acetabular) osteotomy” [6], nor is there a clear consensus on indications for Chiari osteotomy [5,9].

Thus, the primary aim of this study was to perform a systematic review of the long-term THA-free survival of Chiari pelvic osteotomy. The secondary aim was to evaluate reported factors that correlated with survival, the surgical indications, surgical approach, reported complications, and clinical and radiological parameters.

Method

For this systematic review, the databases Pubmed, Embase, and Cochrane were searched and queried until February 2021. The term “Chiari” was separately combined with the term “osteotomy” including all known synonyms to minimize the chance of missing articles (see Supplementary data). Obtained articles were imported into a RefWorks database (<https://refworks.proquest.com/>). After removal of duplicates the abstracts were read and assessed as per MOOSE guidelines [10] for quality independently by 2 authors (MN, SS) (Figure 1).

Inclusion criteria were studies in the English language, human subjects aged ≥ 16 years with primary or secondary hip dysplasia treated with Chiari procedure, and a minimum

follow-up of 8 years. Studies concerning $\geq 50\%$ patients with secondary hip dysplasia, e.g., due to Down syndrome, Trevor's disease, Perthes disease, or cerebral palsy, were excluded. Studies in which $\geq 50\%$ of the patients received a combined dysplasia treatment, e.g., additional osteotomies, were also excluded as we considered that in those cases the influence on the results of the Chiari osteotomy is not clear. Study inclusion was done by 3 reviewers (KW, MN, SS). Cross-references were made in the bibliographies of the included studies.

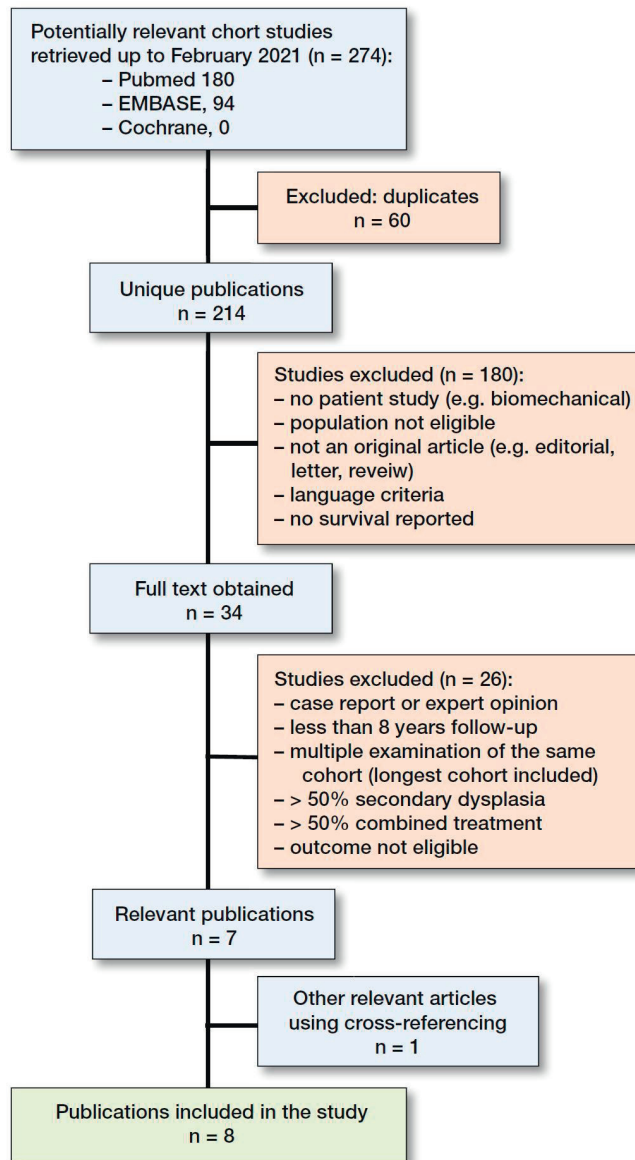


Figure 1. From the 214 unique publications found in the systematic literature search, only 8 publications were eligible for this systematic review.

Each article was reviewed independently in full text (KW, MN, SS). Items reviewed included age, sex, number of patients and hips, study type, level of evidence, number of patients who were lost to follow-up, combination with other treatments, previous operations, preoperative OA (with scale), failure as defined by the authors (see below), survival rates (conversion to THA), complications, surgical indication, and the change in hip score (with scale). The preoperative and postoperative hip parameters (center–edge angle = CEA, Sharp angle = SA, and acetabular head index = AHI) were reviewed and visualized. The Newcastle Ottawa Scale (NOS) was used to assess the quality of each study and the average between the 2 scores of the independent observers (MN and NIH) was documented (Table 1).

Preoperative OA was recorded and dichotomized between mild and advanced OA because different scales were used: the Tönnis [11], De Mourgues and Patte (DMP) [12], Japanese Orthopedic Association [13], and Kellgren–Lawrence (K–L) [14]. Therefore, in every scale the level that corresponds to advanced OA was identified, after which the number of patients who were in an advanced state of OA were identified (Table 1). Differences in extracted information were discussed between the reviewers and consensus was reached at all times regarding the aspect in question. Authors of included studies were not contacted in the event of missing data.

No statistics were used due to the heterogenous data available.

Results

180 studies were identified, of which 8 remained after inclusion and exclusion criteria were applied. Results are summarized in Table 1. All included studies were of observational retrospective cohort design (level IV evidence), without the use of a control group.

In all cases, the osteotomy was extracapsular, located just superior to the hip joint. The osteotomy was specified as straight in 1 study [15], while in 3 other studies it was specified as curved [16–18], and in 4 studies the shape of the osteotomy was not stated [19–22]. The osteotomy height was performed at 5.5–9.0 mm height from the articular surface [15,16,18,19]. Furthermore, the osteosynthesis was fixated by a plate in 1 study [17], and with Steinman pins in a second study [15]. 2 studies specified the usage of graft material [17,19], while 1 other study only used graft material following complications of non-union [20]. 5 studies combined the Chiari procedure with a varus or valgus osteotomy of the proximal femur (3.1–25%) [16,18–21], and 2 studies combined the Chiari procedure with a trochanter osteotomy (1.3–1.9%) [19,20].

Table 1, part 1. Included studies, all retrospective

Reference [ref. #] (year)	Type of procedure	Stratified for ^a	Analyzed hips/ patients	Male/female	Mean age (range)/(SD)	Combination with other treatment n (%)	Previous hip operation n (%)	OA scale ^b	Preop. Advanced OA, n (%)
Calvert et al. [15] (1987)	Chiari (30)		49/45	7/38	20 (3-41)	NA	28 (57)	Own	NA
Kotz et al. [22] (2009)	Chiari (4)		80/66	9/57	23 (2-50)	NA	NA	Tönnis	NA
Migaud et al. [17] 2004	Chiari (31)		89/82	NA	34 (17-56)	NA	9 (10)	MP	67 (75)
Nakano et al. [18] (2007)	Modified Labrectomy (+)		20/20	3/17	35 (16-54)	5 (16)	1 (3)	JOA	4 (20)
Nakata et al. [16] (2001)	Chiari (21)	Labrectomy (-)	11/11	3/8	37 (21-52)	48 (50)	8 (8)	JOA	6 (55)
	Dome modified		96/87	8/79	29 (16-55)				23 (24)
	Chiari (32)								
Ohashi et al. [20] (2000)	Chiari (4)	POA	86/78	12/66	18 (6-48)	41 (40)	3 (3)	JOA	0 (0)
Rozkydal et al. [21] (2003)	Chiari (4)	AOA	17/15	1/14	37 (11-54)	10 (8)	NA	K-L	17 (100)
			130/130	5/125	29 (15-52)				10 (8)
Yanagimoto et al. [19] (2005)	Chiari (4)	Total	74/69	6/63	31 (6-64)	12 (16)	NA	JOA	38 (51)
		Early, spherical	16/NA	NA	23 (14)	NA	NA	NA	0
		Early, flat	20/NA	NA	18 (6.7)	NA	NA	NA	0
		Advanced, spherical	17/NA	NA	43 (8.8)	NA	NA	NA	17 (100)
		Advanced, flat	21/NA	NA	39 (7.5)	NA	NA	NA	21 (100)

^a POA = pre- or early osteoarthritis; AOA = advanced osteoarthritis; NA = Not available.

^b Tönnis [11]; MP = De Mourses and Patte [12]; JOA = Japanese Orthopedic Association [13]; K-L = Kellgren-Lawrence [14].

Table 1, part 2. Included studies

Reference	NOS score ^c	Stratified for	Analyzed hips/ patients	Follow-up years, mean (range)	Conversions to THA n (%)	Clinical outcome scale ^d	Pre.	Hip score mean (range)/(SD) Post.	At follow-up	Patients lost to follow-up, ratio (%)
<i>Calvert et al. [15]</i>	7		49/45	14 (10-19)	3 (6)	HHS	NA	NA	76 (33-76)	27/72 (38)
<i>Kotz et al. [22]</i>	6.5		80/66	32 (27-48)	32 (40)	HHS	NA	NA	79 (37-100)	384/450 (8)
<i>Migaud et al. [17]</i>	8		89/82	14 (6-25)	23 (26)	PMA	NA	NA	NA	10/99 (10)
<i>Nakano et al. [18]</i>	5	Labrectomy (+)	20/20	16 (10-23)	1 (5)	JOA	72	NA	83	3/34 (9)
		Labrectomy (-)	11/11	15 (10-21)	0					
<i>Nakata et al. [16]</i>	7		96/87	13 (10-18)	4 (4)	PMA	14	NA	17	35/122 (29)
<i>Ohashi et al. [20]</i>	7	POA	86/78	17 (4-37)	1 (1)	JOA	79 (8)	NA	89 (13)	20/113 (18)
		AOA	17/15	16 (1-27)	4 (24)		63 (8)	NA	84 (12)	
<i>Rozkydal et al. [21]</i>	7		130/130	22 (15-30)	50 (38)	HHS	42 (36-55)	NA	68	100/230 (43)
<i>Yanagimoto et al. [19]</i>	5.5	Total	74/69	13 (10-20)	2 (3)	JOA	72	NA	87	33/102 (32)
		Early, spherical	16/NA	NA	NA	JOA	79	NA	95	NA
		Early, flat	20/NA	NA	NA	JOA	81	NA	96	NA
		Advanced, spherical	17/NA	NA	NA	JOA	66	NA	71	NA
		Advanced, flat	21/NA	NA	NA	JOA	61	NA	84	NA

^c Newcastle Ottawa Scale, calculated by taking the average of each age category.^d HHS = Harris Hip Score [14]. JOA = Japanese Orthopedic Association [32,33]. PMA = Postel and Merle d'Aubigne [17].

Preoperative indications and negative survival factors varied widely among all 8 studies (Table 2).

Table 2. Indications for the Chiari procedure and negative survival predictors as suggested by the authors

Reference	Inclusion criteria	Significant negative survival factors
<i>Calvert et al. [15]</i>	Congenital hip dislocation Acetabular dysplasia	None reported
<i>Kotz et al. [22]</i>	High-grade dysplasia without signs of OA	Age at the time of operation
<i>Migaud et al. [17]</i>	Acetabular dysplasia Preoperative stage of OA and CEA > 0°	Age before operation
<i>Nakano et al. [18]</i>	OA secondary to congenital subluxation or acetabular dysplasia	Reduced volume of the interposed soft tissues: capsule and the remaining labrum. Presence of labrum interposed between the new acetabular roof and the femoral head
<i>Nakata et al. [16]</i>	Pain and disability attributable to OA	Preoperative stage of OA
<i>Ohashi et al. [20]</i>	Subluxation of the hip and OA	None reported
<i>Rozkydal et al. [21]</i>	DDH	Level of osteotomy (high or low). Severe deformity of femoral head
<i>Yanagimoto et al. [19]</i>	DDH	Advanced DDH. Spherical femoral head

CEA = center–edge angle, DDH = developmental dysplasia of the hip, OA = osteoarthritis.

All studies documented radiological angles and all studies that documented both preoperative and postoperative values found a postoperative increase in average CEA and AHI, while the SA decreased postoperatively (Figure 2). Migaud et al. [17] reported a positive relation between improved radiographic scores and postoperative function and Nakata et al. [16] reported that hips with lower angles subsequently correlated with progression to terminal OA, whereas Calvert et al. [15] reported no correlation between achieved postoperative CEA and hip score.

All articles reported the number of conversions to THA in regard to average follow-up, ranging from 1% conversions in 17 years to 40% conversions in 32 years (Table 1).

Kaplan–Meier survival analysis with radiological progression of OA as endpoint was documented in 3 studies using the Japanese Orthopedic Association scale [16,18,20]. Ohashi et al. [20] analyzed 62 hips with Chiari osteotomy alone, and recorded a 84% survival rate at 10 years and 69% at 20 years. The survival rate for 24 hips using a combined

Chiari procedure with a varus or valgus osteotomy was 82% and 44% at 10 and 20 years, respectively.

Nakata et al. [16] reported survival rates in 56 patients (63 hips) at 10 and 15 years follow-up of 92% and 78%. Respectively, Nakano et al. (18) analyzed 20 patients (20 hips) with labrectomy, and 11 patients (11 hips) without labrectomy at a mean age of 35 years. Survival rates for the labrectomy group were 80% at 10 years' and 67% at 15 years' follow-up. For the group without labrectomy this was 100% and 83%, respectively.

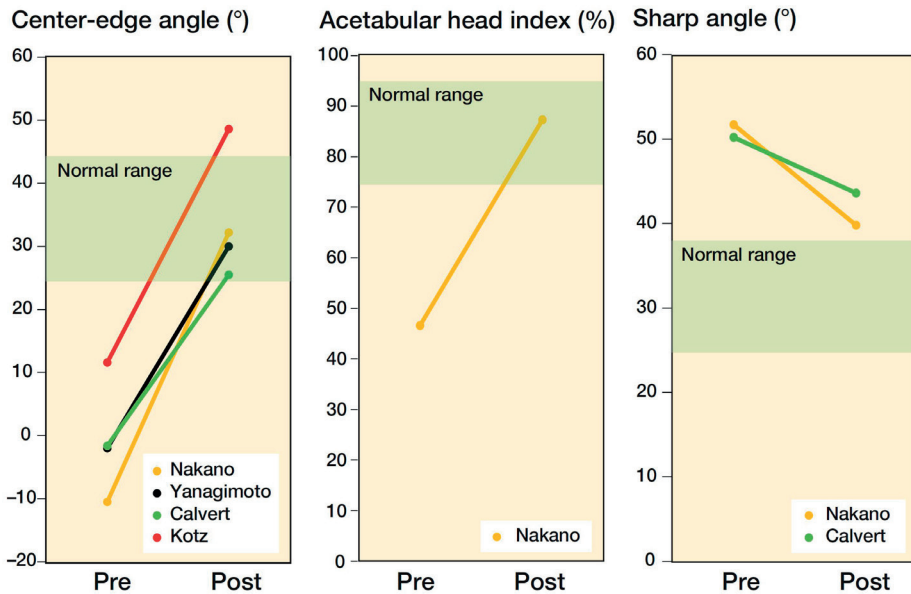


Figure 2. Displays the average preoperative and postoperative radiological values. (A) Center–edge (CE) angle: (B) Acetabular head index (AHI), and (C) Sharp angle. Green areas display the operative target values.

Kaplan Meier survival analysis with conversion to THA as endpoint (Figure 3) were documented by 3 studies [16,17,20]. First, Ohashi et al. [20] reported THA as endpoint in the advanced OA group, which consisted of 17 hips in 15 patients with a mean age of 39 (range 11–54). The survival rate after 10 years was 88%, and 72% at 20 years. Second, Nakata et al. [16] analyzed 96 hips from 87 patients with an average age of 29 (range 16–55). Of these, 96% lasted 10 years, and 82% survived 15 years until conversion to THA. Third, Migaud et al. [17] analyzed 99 hips in 92 patients with an average age of 34 (SD 11) and found a survival rate of 84% at 10 years' and 68% at 18 years' follow-up. The survival rates for DMP grade 2, 3, and 4 OA were documented as 94%, 74%, and 54% at 18

years. Additionally, severe arthrosis (DMP grade 3 and 4) in combination with a positive preoperative CEA ($> 0^\circ$) was significantly ($p < 0.05$) associated with a higher conversion to THA. 2 other studies reported non-Kaplan–Meier survival percentages with THA as failure definition. Survival ranged from 55% to 60% with a mean time interval between 17.6 and 26.0 years [21,22].

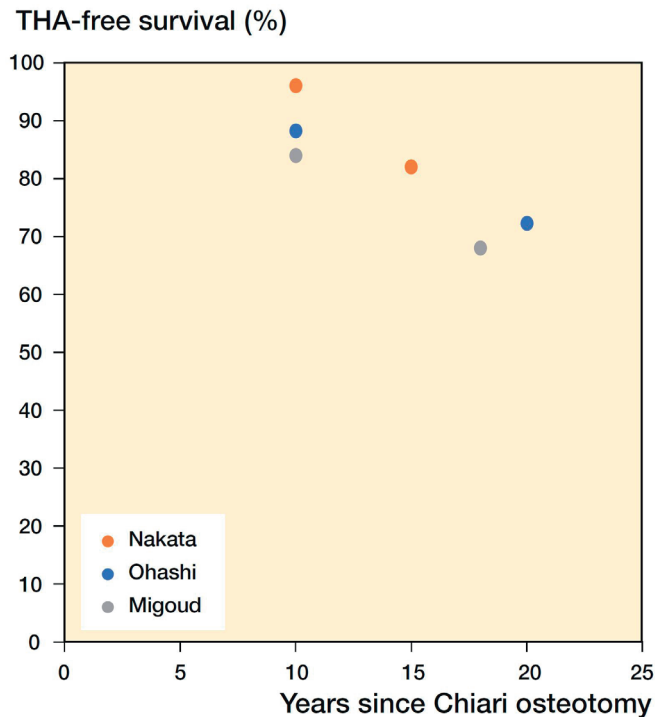


Figure 3. Survival of Chiari osteotomy with years to THA as endpoint. The data for these Kaplan–Meier survival analysis results was extracted from the articles.

Rehabilitation outcomes and postoperative weightbearing were documented in 4 studies Postoperatively, non-weightbearing was done with a hip spica cast [16,18,21] or with crutches [21,22]. Partial weightbearing started at 6 weeks [16,18,22], and full weightbearing after 12 weeks postoperatively [16,18,21].

The complication rate and the background information on the complications were reported by all articles, except for Nakano et al. [18] and Kotz et al. [22] (Table 3).

Discussion

This study reviews survival rates after the Chiari procedure and aimed to evaluate factors that influence survival, and reported indications, complications, and functional and radiological parameters. The included studies with a minimal follow-up of at least 8 years showed good survival outcomes after surgery varying between 68% at 18 years' and 86% at 30 years' follow-up. Furthermore, the Chiari procedure may also be able to increase hip scores and restore radiological angles within normal ranges, with minimal occurrences of major complications.

Careful selection of patients is important for the success of any surgery. However, the outcomes between the included studies were difficult to compare, because of heterogeneous patient characteristics due to differences in inclusion (Tables 1 and 2), ranging from pain, and/or dysplasia with and without concurrent OA, to avascular necrosis of the femoral head and with a negative or positive preoperative CEA. Migaud et al. [17] recommend that the Chiari osteotomy should be done in patients with severe arthrosis and low CEA regardless of present subluxation or the loss of congruency. However, higher levels of arthrosis by itself are again a negative survival factor (Table 2) [16,19]. Moreover, patients with deformities of the femoral head were reported to be more vulnerable to the progression of OA [19,21], as it can be associated with bone atrophy, poor repair, or the presence of acetabular labral tears [19]. Yet again, the Chiari osteotomy is preferred over the peri-acetabular osteotomy (PAO) in hips with dysplasia where pelvic remodeling is restricted due to extreme dysplasia or aspheric femoral heads [5,9,23]. This lack of consensus makes it difficult to appraise the Chiari osteotomy in relation to other procedures.

In the included studies, often a combination was made between the Chiari osteotomy and, e.g., a femoral osteotomy, making it difficult to ascribe the success of the survival time solely to the value of the Chiari osteotomy, and differences in the THA conversion endpoints amplify this effect. However, in 1 study by Ito et al. [24], 87% of all Chiari procedures were combined with a varus osteotomy, they did not find a significant difference between the group with or without femur osteotomy, and survival was also negatively affected by high age and the stage of OA [16,24].

Nonetheless, the Chiari procedure shows surprisingly high survival rates, in the four studies that reported Kaplan–Meier analysis with THA conversion as endpoint (Figure 2). Taking into account the high survival rates, complication rates, and radiological and functional improvements, this raises the question as to whether the Chiari osteotomy should be reconsidered in the palette of treatment options for developmental hip dysplasia.

The number of reported complications ranged from 0% to 28%, when excluding the number of patients with “thigh numbness” reported by Calvert et al. [15], which may be regarded as a direct and inevitable result of iatrogenic injury to the cutaneous nerves. It should be noted that after the Chiari osteotomy there is a potential decrease in pelvis diameter and if this (transverse mid-pelvic) diameter is < 9.5 cm the likelihood of a Caesarean section is increased [25]. Moreover, despite it not being scored as a complication, some patients keep a persisting limp after the Chiari osteotomy. These factors should be explained to the patient when the Chiari procedure is considered as a treatment method. When the Chiari osteotomy is performed but needs to be converted to a THA it is good to mention that the salvage THA has comparable results to a primary THA [26].

The reviewed literature showed considerable limitations. First, all included articles were of level IV evidence with retrospective design and relatively small numbers, no control groups were present, and therefore it was difficult to make a comparison with a nonoperative, PAO, or shelf treatment. Moreover, evaluation time points in relation to the surgery or the number of patients per evaluation were often not reported. Second, the research population largely included females, but none of the included studies stratified for sex, which could have influenced results, and this could limit generalization to a male population, although the incidence of hip dysplasia is higher in women.

Nevertheless, in this era of advanced technology [27] and complex acetabular osteotomies [28,29], it may be useful to reassess the role of historical procedures such as the Chiari osteotomy, which may still have a role in selected clinical situations. Moreover, due to technological progression, additive manufacturing techniques are also being considered to treat hip dysplasia [28,30,31] and might help in planning and evaluating to increase the success of the Chiari osteotomy [29].

Conclusion

The Chiari osteotomy has often yielded long-term hip preservation rates, can improve hip coverage, and hip functional parameters to near-normal values, and has a relatively low reported major complication rate. Moreover, when carefully selected for patients of young age, or minimal preoperative OA, patients may benefit from the Chiari osteotomy with satisfactory survival rates.

Supplementary Data

<https://doi.org/10.2340/17453674.2022.2031>

References

1. Weinstein S L. Natural history and treatment outcomes of childhood hip disorders. *Clin Orthop Relat Res* 1997; (344): 227-42.
2. Reynolds D A. Chiari innominate osteotomy in adults: technique, indications and contra-indications. *J Bone Joint Surg Br* 1986; 68(1): 45-54.
3. Chiari K. Results of pelvic osteotomy as of the shelf method acetabular roof plastic. *Zeitschrift fur Orthopadie und ihre Grenzgebiete* 1955; 87(1): 14-26.
4. Chiari K. Medial displacement osteotomy of the pelvis. *Clin Orthop Relat Res* 1974; (98): 55-71.
5. Otani T, Kawaguchi Y, Fujii H, Hayama T, Marumo K. Indications for shelf acetabuloplasty and rotational acetabular osteotomy for developmental dysplasia of the hip. In: *Revival of shelf acetabuloplasty*. Dordrecht: Springer; 2018. p. 83-96.
6. Clohisy J C, Schutz A L, John L S, Schoenecker P L, Wright R W. Periacetabular osteotomy: a systematic literature review. *Clin Orthop Relat Res* 2009; 467(8): 2041-52.
7. Papachristou G, Hatzigrigoris P, Panousis K, Plessas S, Sourlas J, Levidiotis C, et al. Total hip arthroplasty for developmental hip dysplasia. *Int Orthop* 2006; 30(1): 21-5.
8. Willemsen K, Doelman C J, Sam A S Y, Seevinck P R, Sakkars R J B, Weinans H, et al. Long-term outcomes of the hip shelf arthroplasty in adolescents and adults with residual hip dysplasia: a systematic review. *Acta Orthop* 2020; 91(4): 383-9.
9. Turgeon T R, Phillips W, Kantor S R, Santore R F. The role of acetabular and femoral osteotomies in reconstructive surgery of the hip: 2005 and beyond. *Clin Orthop Relat Res* 2005; 441: 188-99.
10. Stroup D F, Berlin J A, Morton S C, Olkin I, Williamson G D, Rennie D, et al. Meta-analysis of observational studies in epidemiology: a proposal for reporting. *JAMA* 2000; 283(15): 2008-12.
11. Tönnis D, Heinecke A. Current concepts review: Acetabular and femoral anteversion: relationship with osteoarthritis of the hip. *J Bone Joint Surg Am* 1999; 81(12): 1747-70.
12. de Mourgues G, Patte D. Résultats, après au moins 10 ans, des ostéotomies d'orientation du col du fémur dans les coxarthroses secondaires peu évoluées chez l'adulte: symposium. *Rev Chir Orthop* 1978; 64(7): 525-9.
13. Takatori Y, Ito K, Sofue M, Hirota Y, Itoman M, Matsumoto T, et al. Analysis of interobserver reliability for radiographic staging of coxarthrosis and indexes of acetabular dysplasia: a preliminary study. *J Orthop Sci* 2010; 15(1): 14-19.
14. Kellgren J H, Lawrence J. Radiological assessment of osteoarthrosis. *Ann Theum Dis* 1957; 16(4): 494.
15. Calvert P T, August A C, Albert J S, Kemp H B, Catterall A. The Chiari pelvic osteotomy: a review of the long-term results. *J Bone Joint Surg Br* 1987; 69(4): 551-5.
16. Nakata K, Masuhara K, Sugano N, Sakai T, Haraguchi K, Ohzono K. Dome (modified Chiari) pelvic osteotomy: 10- to 18-year followup study. *Clin Orthop Relat Res* 2001; (389): 102-12.
17. Migaud H, Chantelot C, Giraud F, Fontaine C, Duquenois A. Long-term survivorship of hip shelf arthroplasty and Chiari osteotomy in adults. *Clin Orthop Relat Res* 2004; (418): 81-6.

18. Nakano S, Nishisyo T, Hamada D, Kosaka H, Yukata K, Oba K, et al. Treatment of dysplastic osteoarthritis with labral tear by Chiari pelvic osteotomy: outcomes after more than 10 years follow-up. *Arch Orthop Trauma Surg* 2008; 128(1): 103-9.
19. Yanagimoto S, Hotta H, Izumida R, Sakamaki T. Long-term results of Chiari pelvic osteotomy in patients with developmental dysplasia of the hip: indications for Chiari pelvic osteotomy according to disease stage and femoral head shape. *J Orthop Sci* 2005; 10(6): 557-63.
20. Ohashi H, Hirohashi K, Yamano Y. Factors influencing the outcome of Chiari pelvic osteotomy: a long-term follow-up. *J Bone Joint Surg Br* 2000; 82(4): 517-25.
21. Rozkydal Z, Kovanda M. Chiari pelvic osteotomy in the management of developmental hip dysplasia: a long term follow-up. *Bratislavske lekarske listy* 2003; 104(1): 7-13.
22. Kotz R, Chiari C, Hofstaetter J G, Lunzer A, Peloschek P. Long-term experience with Chiari's osteotomy. *Clin Orthop Relat Res* 2009; 467(9): 2215-20.
23. Lack W, Windhager R, Kutschera H P, Engel A. Chiari pelvic osteotomy for osteoarthritis secondary to hip dysplasia. Indications and longterm results. *J Bone Joint Surg Br* 1991; 73(2): 229-34.
24. Ito H, Tanino H, Yamanaka Y, Nakamura T, Minami A, Matsuno T. The Chiari pelvic osteotomy for patients with dysplastic hips and poor joint congruency: long-term follow-up. *J Bone Joint Surg Br* 2011; 93(6): 726-31.
25. Loder R T. The long-term effect of pelvic osteotomy on birth canal size. *Arch Orthop Trauma Surg* 2002; 122(1): 29-34.
26. Schneider E, Stamm T, Schinhan M, Peloschek P, Windhager R, Chiari C. Total hip arthroplasty after previous Chiari pelvic osteotomy: a retrospective study of 301 dysplastic hips. *J Arthroplasty* 2020; 35(12): 3638-43.
27. Willemsen K, Nizak R, Noordmans H J, Castelein R M, Weinans H, Kruyt M C. Challenges in the design and regulatory approval of 3D-printed surgical implants: a two-case series. *Lancet Digit Health* 2019; 1(4): e163-e171.
28. Wang X, Liu S, Peng J, Zhu Z, Zhang L, Guan J, et al. Development of a novel customized cutting and rotating template for Bernese periacetabular osteotomy. *J Orthop Surg Res* 2019; 14(1): 1-10.
29. Otsuki B, Takemoto M, Kawanabe K, Awa Y, Akiyama H, Fujibayashi S, et al. Developing a novel custom cutting guide for curved peri-acetabular osteotomy. *Int Orthop* 2013; 37(6): doi: 10.1007/s00264-013-1873-x.
30. Willemsen K, Tryfonidou M, Sakkers R, Castelein R M, Zadpoor A A, Seevinck P, et al. Patient-specific 3D-printed shelf implant for the treatment of hip dysplasia: anatomical and biomechanical outcomes in a canine model. *J Orthop Res* 2021 Jun 30. doi: 10.1002/jor.25133. Online ahead of print.
31. Golafshan N, Willemsen K, Kadumudi F B, Vorndran E, Dolatshahi-Pirouz A, Weinans H, et al. 3D-printed regenerative magnesium phosphate implant ensures stability and restoration of hip dysplasia. *Adv Healthc Mater* 2021; 10(21): e2101051.

32. Takeda H, Kamogawa J, Sakayama K, Kamada K, Tanaka S, Yamamoto H. Evaluation of clinical prognosis and activities of daily living using functional independence measure in patients with hip fractures. *J Orthop Sci* 2006; 11(6): 584-91.
33. Tanaka S. Surface replacement of the hip joint. *Clin Ortho Relat Res* 1978; (134): 75-9.



CHAPTER 4

Comparing hip dysplasia in dogs and humans: A review

Koen Willemsen | Michelle M. Möring | Netanja I. Harlianto |
Marianna A. Tryfonidou | Bart C. H. van der Wal | Harrie Weinans |
Björn P. Meij | Ralph J. B. Sakkera

Published in
Frontiers in Veterinary Science, Veterinary Regenerative Medicine (2021): 1491.
<https://doi.org/10.3389/fvets.2021.791434>

Abstract

Hip dysplasia (HD) is common in both humans and dogs. This interconnection is because humans and dogs descended from a common ancestor and therefore have a similar anatomy at micro- and macroscopic levels. Furthermore, dogs are the animals of choice for testing new treatments for human hip dysplasia and orthopedic surgery in general. However, little literature exists comparing HD between the two species. Therefore, the aim of this review is to describe the anatomy, etiology, pathogenesis, diagnostics, and treatment of HD in humans and dogs. HD as an orthopedic condition has many common characteristics in terms of etiology and pathogenesis and most of the differences can be explained by the evolutionary differences between dogs and humans. Likewise, the treatment of HD shows many commonalities between humans and dogs. Conservative treatment and surgical interventions such as femoral osteotomy, pelvic osteotomy and total hip arthroplasty are very similar between humans and dogs. Therefore, future integration of knowledge and experiences for HD between dogs and humans could be beneficial for both species.

Introduction

Dogs and humans have developed from a common ancestor. Both species are vertebrates and terrestrial mammals, with a very similar homologous musculoskeletal structure (Figure 1). Because of this resemblance in body structure, certain diseases in both species have a common ground. One of these diseases is hip dysplasia (HD). HD was first described in dogs in the 1930's [1] and in humans as early as Hippocrates [2]. HD is better known as canine hip dysplasia (CHD) in dogs, and developmental dysplasia of the hip (DDH) in humans. The prevalence of HD in humans varies between 0.1 and 10%, depending on the population and definition [3, 4]. In dogs, the prevalence varies between 0 and 73.4%, depending on the breed [5–8].

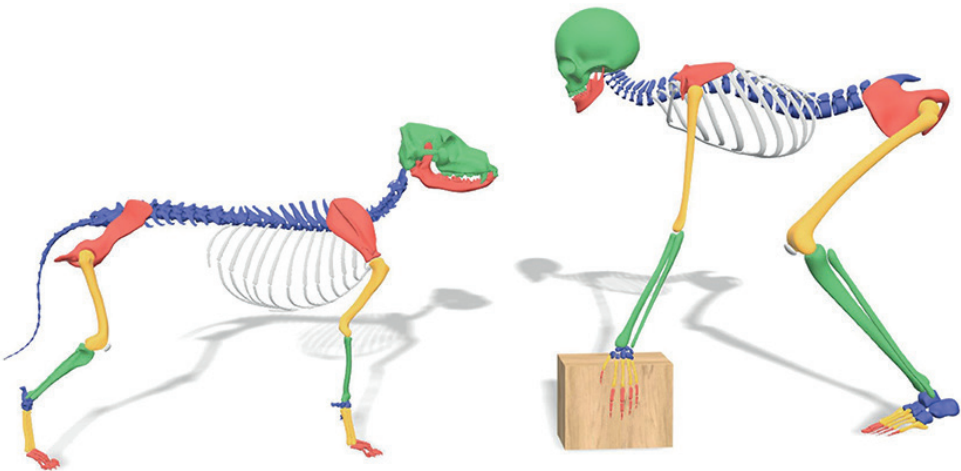


Figure 1. Comparison skeletal structure between dog and human

There are similar characteristics for HD in humans and dogs. In both species the acetabular cover of the femoral head is insufficient, either because the acetabulum [5, 9, 10] or the femoral head [5, 9, 10] is deformed, or joint laxity [2, 5] is present. This disturbed femuro-acetabular relationship causes abnormally high peak forces [1, 6, 10] with or without joint instability and (sub)luxation [2, 5, 9] resulting in osteoarthritic changes [2, 5, 9]. The body tries to counter the sequela of HD in both species by thickening and stiffening of the joint capsule [10–12] in order to reduce the laxity [11, 12]. However, HD will eventually induce osteoarthritis (OA) resulting in pain [6, 13], lameness [14], and loss of limb function [6, 13], reducing quality of life.

While CHD and DDH show numerous similar characteristics, disease management is not always the same for both species. In this review we give an overview of the anatomy,

etiology, development, diagnostics and treatment of HD in humans and dogs. This will provide veterinarians and physicians a perspective and incentive to share the combined translational knowledge.

Anatomy

Initially, the anatomy of humans and dogs may seem very different. For instance, an obvious difference between dogs and humans is that dogs have a quadruped (four-legged) gait while humans have adopted a bipedal (two-legged) gait. While some anatomical differences have developed due to this difference in gait, dogs and humans have more in common than one might think (Figure 1).

The human biped gait has a smaller base of support (less point of ground contact) and an elevated center of mass [15, 16]. To balance the body, humans have developed a lumbar lordosis so the center of mass (head, arms and trunk) is directly above the point of ground contact. This is also more energy efficient [17, 18]. Similarly, a wider pelvis with more laterally oriented iliac crests (as opposed to the coronal plane in dogs) allowed for some changes in musculature, improving balance on one leg, energy efficiency, and increasing stride length [16–18].

While the load orientation [19] of the hip is very similar in dogs and humans, the difference between biped and quadruped gait gives different load distribution between limbs. Humans distribute their bodyweight between two legs while dogs distribute their weight over four legs, with the front legs carrying approximately 60–65% of the bodyweight [20–22]. Because of the dominance of the front legs over the hind legs, dogs are capable of compensating for hip abnormalities (e.g., HD) by lowering their neck and increasing the load on the non-affected side [20]. Humans can also reduce load on the affected sides by using instruments such as a cane or a stroller [23].

The canine and human anatomy is not just similar on a macroscopic level. Human and canine hips have a similar cortical microstructure [24, 25] and long bone vascularization [25, 26]. Because of these external and internal similarities, the dog has long since been (one of) the animal(s) of choice for orthopedic research aimed at humans [24, 27, 28].

Etiology and Pathogenesis

While the exact etiology of HD for both humans and dogs remains unknown [10, 29], the general agreement is that both genetic and environmental factors influence the development of CHD and DDH [4, 8]. First the genetic factors are discussed, followed by environmental factors and finished with the pathogenesis.

Some examples of common genetic factors that influence the occurrence of HD in both species include breed [1, 6] ethnicity [29], increased anteversion angle of the femur [2, 30, 31], neck shaft angle of the femur [2, 31], and collagen composition [1, 4]. Because of these high genetic factors, family anamnesis is important for discovering HD in humans and improving breeding programs in dogs. However, not all genetic factors have an known influence on both species, e.g., a clear genetic factor such as female sex in humans is known for a higher incidence of HD (4:1, Female:Male) [3, 9], while no such relation is known for dogs [8, 32].

Besides genetic factors there are many different environmental factors influencing the development and incidence of HD. Some common environmental factors concern the nutritional state such as diet [33], obesity [14, 34, 35] and high birth weight [5, 36]. Furthermore, environmental factors such as to seasonal influence [4, 7] and hormone levels have an association with HD [4, 37]. Other environmental factors concern disturbances of the biomechanical equilibrium in the pelvic area, e.g., transitional vertebrae [38] can change the forces flowing through the hip. This also happens with restrictive swaddling of babies which is common in certain human cultures. Swaddling limits the abduction and therefore reduces the required force on the triradiate growth plate [39, 40].

Most of previous mentioned factors are identical between both species, however factors surrounding birth do differ between species. Humans have only one baby at a time, while dogs have several pups in their litter, meaning intra-uterine mechanical factors are different. For instance, breech presentation in humans is associated with a high incidence of DDH in single child pregnancies, but no relation has been found in twin pregnancies [3, 41]. Similarly, other factors like oligohydramnios [42], breach position, being first born [3, 4] and even the preference for the left hip are commonly described in humans, but not in dogs who are typically born in a litter. The preference for the left hip in humans might be explained as the left hip is often positioned against the mother's spine in the womb, which limits abduction [5, 9] and reduces force on the developing triradiate cartilage.

Besides genetic and environmental factors, there is a clear developmental aspect in both DDH and CHD. Both species need the femoral head to be centered on the triradiate cartilage of the acetabulum in order to develop normal joint morphology [5, 9, 10]. Well balanced

supporting structures of the joint like the pelvic muscles [2, 43], the joint capsule, and the femoral head ligament are important to maintain joint congruity [5]. A larger amount of pelvic muscle mass is associated with a lower incidence of CHD [2, 10]. Similarly, weak pelvic muscles in dogs are associated with adverse joint changes [2]. For humans, weak pelvic muscles have also been theorized to cause dysplasia and degenerative joint change [43].

Human newborns with normal hips might develop HD later in life [44]. Of newborns with perceptible HD, 88% will develop into normal hip joints by the age of 8 weeks, without any intervention [9, 39, 45]. However, the older the infant is, the less likely it will be that natural normalization occurs [9]. The abnormal stress on the hip joint caused by HD can cause pain even before degenerative changes start. Patients with HD can already present with OA in adolescents and young adults [46]. In CHD, the hips are typically normal at birth [2, 10]. However, early signs such as edematous and slightly torn ligaments of the femoral head can already be seen around 4 weeks of age [47, 48]. Subsequently, further dysplastic joint changes develop such as joint laxity and deformity of the acetabulum and femur [47]. This deformity eventually leads to cartilage changes, pain and lameness. Some dogs start showing clinical signs around 3–12 months of age [10, 49], while other dogs remain asymptomatic and present long after full maturation.

Diagnosis

Early detection of HD in humans and dogs can lead to earlier interventions, which is important for disease management [9, 50]. To ensure early detection in humans, many countries have developed and implemented screening programs aimed at diagnosing DDH in infancy [51]. In dogs early detection of HD is usually driven by the occurrence of clinical signs from age of 4 to 5 months, which will stimulate owners to seek veterinary advice for diagnostic testing, usually with radiography. However, screening programs for CHD in dogs are recommended for breeding, and is globally implemented. However, the minimum age for screening using radiographs is commonly set at skeletally mature age of 1 year for most breeds and at 18 months for selected large to giant breeds. Since HD in young dogs is commonly asymptomatic this will prevent early detection of HD in dogs. While the details might differ, the clinical diagnostics in dogs and humans are very comparable, generally consisting of physical examination and imaging.

Physical Examination

Early observational findings during physical examination in humans are restricted abduction and difference in leg length in case of hip (sub)luxation [9, 39]. Asymmetric gluteal folds who were once thought to be of high clinical significance did not have a high predictive value and are therefore not used anymore [52]. In a child of walking age the Trendelenburg sign can be seen with or without asymmetries, like a proximal thigh crease, posterior knee crease, wide perineum, prominent hip curvature, and limping [39, 53]. With bilaterally affected hips this asymmetry is usually absent, but bilateral Trendelenburg sign, waddling gait [9, 39] and bilateral limited abduction [9] can be seen. Dogs should be observed in rest, during activity, and after exercise [54]. The main finding in young dogs with hip joint laxity is lameness that increases during exercise [1], but also hip atrophy, reduced range of motion and pain during flexion and extension may be present. Hip pain in dogs is usually noted by abnormal behavior like bunny hopping with pelvic limbs, difficulty to rise, and less playfulness together with grunting, whimpering, or whining [55]. The combined pain assessment by both the owner and the veterinarian seems to work best [55], but there is no consensus on a gold standard [1, 55]. Furthermore, dogs do not need a pain free full range of motion for a normal gait [11], typically dogs with no or minimal clinical signs could have severe dysplastic hips [12].

For examining the depth of the acetabulum and joint laxity, the following clinical tests are performed: the Barlow test, the Barden test, the Galeazzi test, and the Ortolani test, all of which were originally developed for use in humans [1, 9]. The Ortolani test is most commonly used in both humans [9, 51](Figure 2) and dogs [1, 54](Figure 3). The Barlow test is also commonly used in dogs [1, 54]. It should be noted that while on human infants and dogs these tests can be directly performed, these tests often require sedation or general anaesthesia when dogs are not cooperative [54] (Figures 2, 3).

Since DDH and CHD develop at different rates, a positive result has slightly different implications. In humans a positive result indicates subluxation or dislocation of the femoral head typically due to decreased coverage [9, 51]. A positive Ortolani test in young dogs usually points to joint laxity [1, 54] which is a sign of HD in development [58].

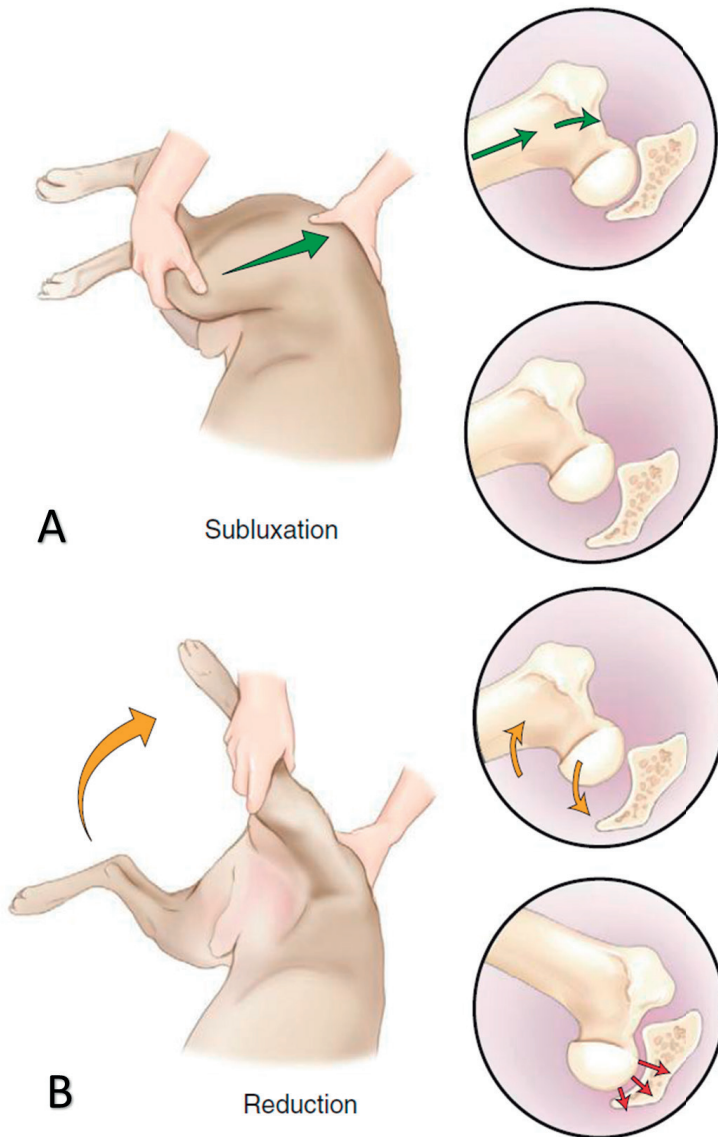


Figure 2. The Barlow and Ortolani test in dogs.

(A) “Barlow” (subluxation) test. The dog is positioned in lateral or dorsal recumbency. In lateral recumbency, the examiner is caudal to the dog with one hand on the distal stifle (flexed to 90 degrees) and the other is dorsal to the pelvis, with the thumb resting over the greater trochanter. The limb is in an adducted position, and force is applied toward the dorsum of the dog up through the femur (green arrow), causing dorsal subluxation in a hip with joint laxity. (B) Ortolani (reduction) test. The limb is slowly abducted (yellow arrow) while force along the axis of the femur is maintained. A positive Ortolani sign is felt when a click or clunk is heard or palpated as the subluxated femoral head reduces into the acetabulum (red arrow). Figure reproduced without modification from [56] under the Creative Commons Attribution 4.0 International License ().

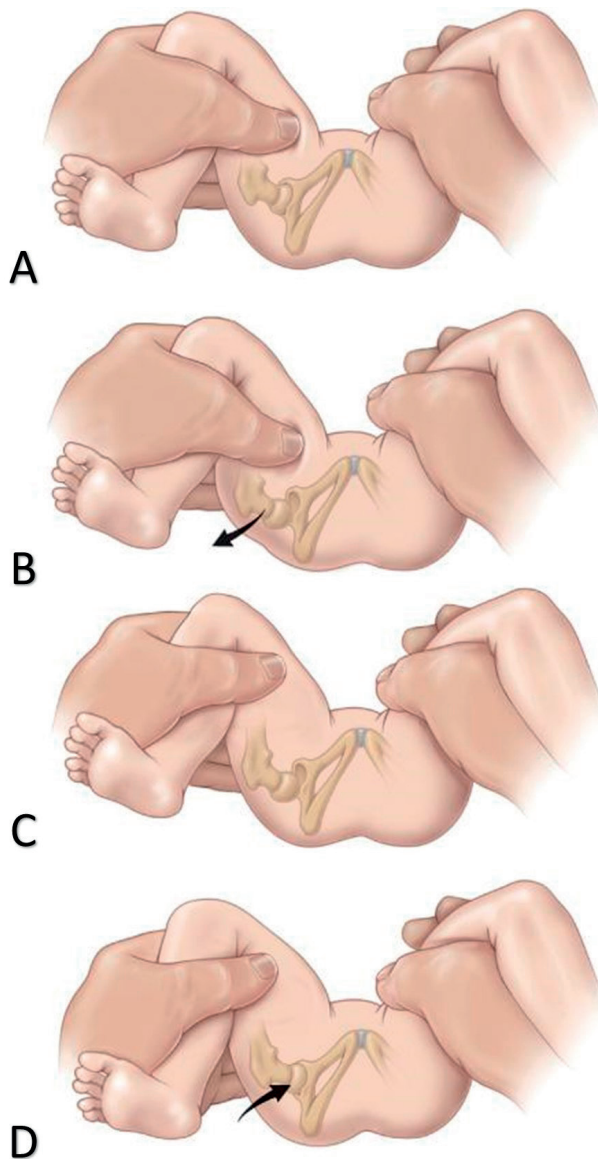


Figure 3. The Barlow and Ortolani test in Humans.

The Barlow test for developmental dislocation of the hip in a neonate. (A) With the infant supine, the examiner holds both of the child's knees and gently adducts one hip and pushes posteriorly. (B) When the examination is positive, the examiner will feel the femoral head make a small jump (arrow) out of the acetabulum (Barlow's sign). When the pressure is released, the head is felt to slip back into place. The Ortolani test for developmental dislocation of the hip in a neonate. (C) The examiner holds the infant's knees and gently abducts the hip while lifting up on the greater trochanter with two fingers. (D) When the test is positive, the dislocated femoral head will fall back into the acetabulum (arrow) with a palpable (but not audible) "clunk" as the hip is abducted. [Reprinted with permission from Tachdjian's *Pediatric Orthopedics* [57], Elsevier Publishing].

Imaging

Radiography is the golden standard for diagnosing HD in dogs [1]. Historically, pelvic and hip radiography has been used for diagnosing HD in humans [9, 59]. However, in some parts of the worlds X-rays have been partially replaced by ultrasound imaging for young patients [60] as classification of HD on X-rays is currently considered less reliable before ossification of the femoral head center occurs at 4–6 months [9, 39]. Although there are widely accepted ultrasound classifications, ultrasound images still has drawbacks, such as: high variability and low agreement [61]. In dogs the ossification starts at 8 weeks, which makes ultrasound less useful as the ossification distorts the view of the acetabulum on ultrasound [54]. The way radiographs are attained and measured is remarkably alike, both in dogs and humans the radiographs are taken in ventrodorsal and anterior-posterior position to measure the center-edge (CE)-angle and the Norberg angle (Figure 4)[59, 62–64]. Besides the CE-angle and the Norberg angle, other radiographic parameters can be measured to increase the validity of the diagnosis. However the CE-angle is the most renown [65].

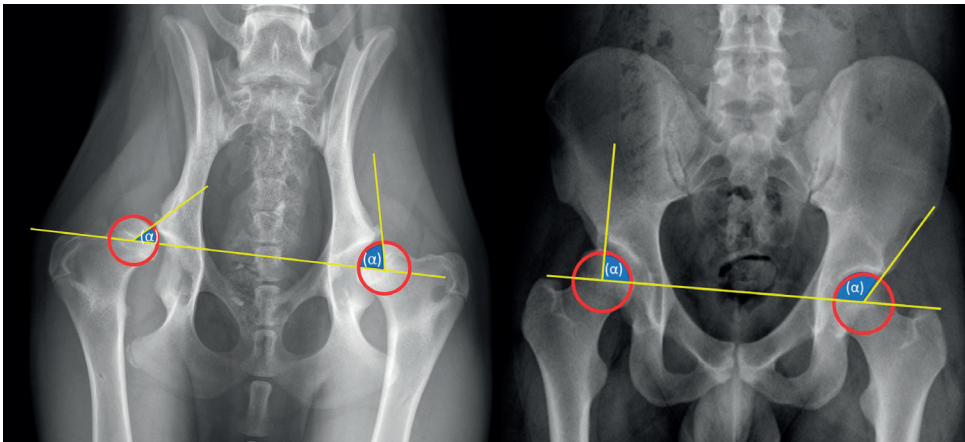


Figure 4. Radiographic diagnostics.

Left: Norberg-Angle, take the center of each femoral head (hip ball) and draw a line between them. Then take the center of the femoral head and draw a line to the outer point of the pelvis. The angle between these lines is the Norberg angle. The Norberg angle is calculated for each hip joint. A normal Norberg Angle ranges from 100/105 to 115 degrees. <100 degrees is dysplastic. Right: CE-angle, take the center of each femoral head (hip ball) and draw a line between them. Then take the center of the femoral head and draw a line to the center of the acetabulum. The angle between these lines is the CE angle. The CE-angle is calculated for each hip joint. A normal CE Angle ranges from 110/115 to 130 degrees. <110 degrees is dysplastic.

Treatment

The available treatments for HD in humans and dogs change when patients develop toward skeletal maturity [39]. Young patients have soft and pliable bone with good remodeling capabilities due to growth. Therefore, HD treatment can focus on stimulating growth by redirecting the femoral head to the center of the triradiate growth plate of the acetabulum in order to create a stable well-covered hip joint [9]. As the patient matures the growth potential of bone decreases and the ability to correct the joint relationships with it. When forming a congruent well-covered joint is no longer an option, osteoarthritis might develop.

Skeletal maturity is reached around 15–18 years in humans [43] and 1–1.5 years in dogs [66]. The triradiate cartilage (acetabular growth plate) closes around 14 years of age in humans [67] and around 6 months of age in dogs. There is no clearly defined separation between treatment options for certain ages and stages of bone development. Therefore, in order to accommodate this review a separation is made between “early” and “late” treatment.

Early Non-surgical Treatment

Early treatment of hip dysplasia in humans distinguishes between a (sub-)luxated and a non-luxated hip. A luxated hip needs repositioning first before the acetabular dysplasia can be treated.

When a dysplastic hip is diagnosed with (sub)luxation of the femoral head, a Pavlik harness is most often applied as first treatment. The Pavlik harness uses several straps to flex the hips and knees and prevent adduction, while movement is still possible [9, 68]. In a child treated within the 1 weeks after birth this position forces the femoral head into the acetabular socket and onto the triradiate cartilage. After creation of a stable joint, the harness is still worn for 23 h per day until a morphologically normal hip joint is found on imaging [39, 68]. When a stable reduction of the hip is not reached within 3–4 weeks, reposition of the hip under full relaxation under anesthesia might be tried, with or without adductor tenotomy, followed by a plaster cast usually for 3 months [9, 68]. If repositioning of the hip fails under anesthesia, open reposition of the hip should follow, usually after the age of 6–9 months [9]. There is no consensus about optimal treatment length [9, 69]. The Pavlik harness has not been described for dogs, since they do not easily accept external hip coaptation devices. However, a somewhat similar concept was used in puppies with genetic predisposition for CHD that were raised in a small cage (1 m³) until they finished growing. This caused them to sit more often with their hind limbs spread

(flexion and abduction) and reduced the prevalence of CHD. This method prevents dogs from socializing and is therefore not used in daily practice [48, 54].

In young dogs with CHD that start to show clinical signs, usually from age 4 to 5 months, the non-surgical treatment measures are similar to those at older age and therefore will be discussed in more detail in section Late Non-surgical Treatment.

Early Surgical Treatment

If non-surgical treatments are ineffective or the child gets older than 9–18 months, open reduction of the hip joint can be performed [9, 46]. Open reduction focuses on reducing the subluxated or dislocated hip and creating a stable hip joint, similar to closed reduction. Open reduction of the hip is usually combined with capsular reefing and the release of the transverse acetabular ligament, and may be combined with an acetabular or femoral osteotomy in order to create a stable well-centered hip [9]. After the open reduction, the child is treated with a spica cast to maintain the position of the hips [9]. In dogs open reduction for a luxated hip due to severe HD is never performed. Hip luxation in young dogs with HD, called the luxoid hip, is usually an indication for early euthanasia, femoral head and neck resection or total hip replacement from age 7–9 months.

In the older child with residual hip dysplasia, an acetabuloplasty, e.g., the Dega, or Pemberton acetabuloplasty is commonly used to improve centering and acetabular coverage of the femoral head [70, 71]. While both procedures are different, both are curved partial osteotomies of the ilium, with a small (bone) graft placed in the osteotomy. This partial osteotomy causes a hinging effect in the horizontal line of the triradiate cartilage and will reshape the acetabulum, reducing its diameter, yet increasing depth [72]. The Pemberton acetabuloplasty improves anterior and lateral femoral head coverage, but not coverage of the posterior femoral head. The Dega acetabuloplasty increases the anterior, lateral, and posterior femoral head coverage [72]. Acetabuloplasties give the best results when used on patients 2–8 years old [46].

Another common technique for pelvic osteotomies in young children is the Salter osteotomy [9, 72]. This technique is based on a complete osteotomy of the ilium bone just superior of the acetabulum and redirection of the existing acetabulum [73, 74]. Therefore, the Salter osteotomy does not alter the shape of the acetabulum. A possible complication described in the Salter osteotomy is instability [71, 74] and another complication for the Salter and Pemberton acetabuloplasty [71] is overcorrection, leading to excessive coverage of the femoral head resulting in femoral acetabular impingement [71, 74].

The majority of early surgical treatments, like the Pemberton and Salter osteotomy used in humans are not applicable in dogs simply because CHD is not detected early enough in the dog's life. The only comparable treatment in dogs is juvenile pubic symphysiodesis (JPS). The JPS is an early surgical treatment for CHD, and to our knowledge has not been used in humans. JPS is a relatively simple surgery in which the cartilage of the pubic symphysis is destroyed through electrocauterization. The heat causes the chondrocytes to become necrotic, resulting in premature closure of the pubic symphysis. Since other parts of the pelvis continue to grow, the acetabulum is rotated ventrolateral, similarly to the human Pemberton and Salter osteotomy, which allows for greater femoral head coverage [12, 54, 66]. To be effective, JPS should be performed before week 18 in small dogs or week 22 in large breed dogs [12, 66].

Osteotomies of the femur are frequently used in humans and infrequently in dogs. In dogs aged ½–2 years the intertrochanteric femoral osteotomy is used to reduce the neck shaft angle (varisation) and anteversion angle, which are often increased in dysplastic hips. The femoral head is moved more medially [12, 75, 76] which helps redirect the femoral head into the acetabulum [75, 76]. This is achieved by removing a bone wedge from the proximal femur and the bone is then stabilized by a hook plate [12, 75, 76]. In humans, a femoral osteotomy can be performed sub- or intertrochanteric. The osteotomy also aims to reduce the anteversion (also called derotational osteotomy) and neck-shaft angle. Femoral osteotomies in humans are often combined with open reduction and acetabular osteotomies, between the ages of 2–14 years [69].

Late Non-surgical Treatment

There are various late non-surgical treatments for dogs and humans with hip dysplasia. To decrease pain (1, 77), reduce lameness (14), and delay onset of osteoarthritis [1, 66] a variety of treatments are available including medication like NSAIDs [1], reducing body weight [34, 77], life style changes including training of pelvic muscles, exercise programs and the limiting sudden explosive movements (like throwing a ball for dogs). On average, weight loss in dogs delays surgery for another 3 years [10] and in overweight dogs and humans 10% body weight reduction is associated with a relieve in symptoms and signs [14, 77]. Another non-surgical intervention is the nutraceutical market, which is especially big in the veterinary market. Nutraceuticals are food additives or supplements that are purported to have a disease modifying potential in hip dysplasia and osteoarthritis, but also other conditions. An example of a nutraceutical is Polysulfanated glycosaminoglycans (PSGAGs) which proposedly stimulates collagen synthesis and inhibits the breakdown of collagen [13] which may help reduce subluxation [54].

Another option for early non-surgical treatment is physiotherapy [78, 79]. In both dogs and humans physiotherapy and hydrotherapy is an important component first as a conservative treatment option but also as an important aspect in post-surgical rehabilitation [78, 79].

Late Surgical Treatment

Originally designed for humans with HD, triple pelvic osteotomy (TPO) has also become a successful procedure for dogs with HD [12, 80](Figure 5). This surgery can be used in young dogs [1, 54, 81], but more often in adolescents [46, 82, 83] and young adults [82, 83] without or with minimal degenerative joint damage [1, 49, 54, 83]. In dogs, the surgery is preferably performed before full skeletal maturity is reached, while in humans it can be used both before and after the triradiate cartilage closes [9, 83]. However, humans have more early surgical treatments available (e.g., Salter & Pemberton), deferring the more invasive TPO to older patients. Over the years there have been many changes in specific surgical techniques, but the general outline of TPO remains the same. Osteotomies are made in the pubic, ischial, and iliac bones, and the acetabulum is subsequently rotated ventrally to improve femoral head coverage and increase the load bearing area [80] (Figure 5). The acetabulum is then fixated in place by plates, screws, or K-wire. Clinical reduction of lameness after TPO, and improvement in weight bearing of 86–92% is reported in dogs [75, 76, 81]. The joint laxity is reduced following TPO in dogs [80, 81], but degenerative changes cannot be stopped completely [81]. In humans, TPO causes a long term reduction of pain and improvement of function [84] and a (total hip free) survival of 68% after 25 years is reported. Recently, dual pelvic osteotomy (DPO) has been recommended in dogs [75, 85], it has also been described in humans [72]. DPO is similar to TPO, with a faster post-operative recovery, as there is no osteotomy of the ischium and therefore no pelvic discontinuity [75, 85].



Figure 5. Canine left and human right triple pelvic osteotomies (purple planes) are made in the pubic, ischial and iliac bones and subsequently the acetabulum is rotated ventrally (dogs) or anteriorly (humans) to improve femoral head coverage and increase the load bearing area.

Shelf arthroplasty is a commonly used salvage procedure for HD in humans [86]. It involves the placement of an autologous bone graft outside of the joint capsule superior to the acetabulum [87, 88]. The graft can be impacted into the bone or be held in place by a screw [88], improving the support structure of the joint [9]. Capsular metaplasia causes the improvement of the articulating surface. The improved support and improved femoral head coverage helps improve the weight bearing surface [9] and delays the progression of OA. This procedure is preferably performed in younger patients with minimal arthritic changes, however it is mostly reserved as a salvage procedure as other treatments are not eligible. The survival of the shelf procedure can be up to 72% at 35 years of follow-up [86]. A similar procedure called the biocompatible osteoconductive polymer (BOP) procedure has been described as an alternative to TPO in adolescent dogs [12, 75, 76]. Instead of autologous bone graft, biocompatible osteoconductive fibers were used to increase coverage, because the fibers were expected to promote bony ingrowth [12, 75, 76]. Despite that the shelf procedure was successful in humans, BOP in dogs never became a common procedure because of uncontrolled bone growth [75, 76]. New procedures involving 3D-printed titanium shelves [89] or 3D-printed biodegradable magnesium phosphate shelves [90] are still being developed in dogs and when successful these procedures hopefully find their way back to the human clinic.

While being one of the most effective procedures, total hip arthroplasty (THA) in humans and dogs [12] is often postponed as the last treatment option (Figure 6). When young patients with a demanding lifestyle receive a THA they may need one or more revisions in their lifetime due to implant wear. However, every revision is more difficult to perform due to fibrosis in the perioperative area. Therefore, in humans, the need for THA is preferably

postponed beyond the age of 60 to prevent revisions in the long term. Although THA has been available for dogs for three decades, it remains an expensive treatment option, especially when the owners have no insurance [49]. Also, THA in humans can become technically demanding due to anatomical differences in dysplastic hips making it difficult to ream a large enough bony bed to support an acetabular cup [91]. In dogs the procedure is technically demanding due to breed anatomic differences but can be used in dogs of any size or shape when aged 9 months or older [12].

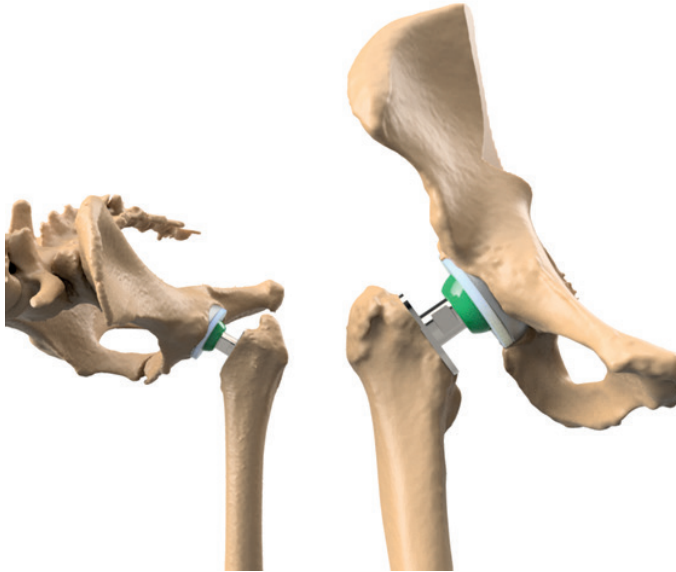


Figure 6. The comparable set-up of the total hip arthroplasty in humans and dogs. On the left the set-up in dogs and on the right the set-up in humans.

It is good to note that implant improvements have benefited for cross species research. For example, due to the active nature of dogs, the THA materials demand is high and companies specializing in canine THA have benefited from the prosthetic knowledge being researched and developed for human medicine. For example, similar durable materials developed for human cups and stems are translated to the dog THA allowing dogs to perform without the need for revision beyond a decade lifetime, with a biomechanically demanding lifestyle asking for more cyclic loading of their implants than humans. Vice versa, in dogs new products are developed e.g., to decrease stem loosening, because dogs demand immediate full weightbearing after surgery due to their non-compliance to life style restrictions. One example of a successful concept in THA surgery in dogs (Zürich cementless THA) is the immediate stem screw fixation at the medial femoral cortex instead

of press fit fixation [92]. Likewise, in a few years more developments might be translated back from the veterinary to the human market.

One of the least performed in humans but most commonly executed salvage procedures in dogs is the femoral head and neck excision [75, 76]. The surgery is relatively easy to perform and has low costs, and is most effective in dogs with low body weight [75, 93]. The removal of the femoral head and neck leads to a fibrotic pseudoarthrosis (false joint), allowing for relative pain free movement [12, 49]. Femoral head and neck excision generally has good results in relieving pain, however possible side effects are extensive rehabilitation, decreased range of motion, muscle atrophy and limping due to decreased limb length [12, 75, 76, 93]. Important factors in the outcome are body size [12, 75, 76], dog temperament and activity [12, 94]. This procedure performed in humans is called a “Girdle stone” procedure, but only as the last option [94].

Conclusion

In this review we described the anatomy, etiology, development, diagnostics and treatment of HD in humans and dogs. Humans and dogs have similar anatomy on micro- and macroscopic levels. HD as an orthopedic condition has many overlying characteristics in humans and dogs in terms of etiology and pathogenesis. Likewise, treatment of HD shows many similarities. There is much parallel use of early and after growth (conservative) treatments and interventions. Moreover, many of the surgical treatments for HD that were developed for humans have first been tested in experimental dogs. Procedures that became successful in humans found their way to the veterinary field and are now commonly used in companion animal clinics. We suggest that further exchange between research on HD in humans and dogs can be beneficial for the treatment of HD in humans and dogs.

References

1. Lopez M, Schachner E. Diagnosis, prevention, and management of canine hip dysplasia: a review. *Vet Med Res Reports*. (2015) 6:181. doi: 10.2147/VMRR.S53266
2. Olmstead ML, Linda LD. *Small Animal Orthopedics*. St. Louis: Mosby (1995). p. 365–8.
3. Stein-Zamir C, Volovik I, Rishpon S, Sabi R. Developmental dysplasia of the hip: risk markers, clinical screening and outcome. *Pediatr Int*. (2008) 50:341–5. doi: 10.1111/j.1442-200X.2008.02575.x
4. Rhodes AML, Clarke NMP. A review of environmental factors implicated in human developmental dysplasia of the hip. *J Child Orthop*. (2014) 8:375–9. doi: 10.1007/s11832-014-0615-y
5. VandenBerg-Foels WS, Todhunter RJ, Schwager SJ, Reeves AP. Effect of early postnatal body weight on femoral head ossification onset and hip osteoarthritis in a canine model of developmental dysplasia of the hip. *Pediatr Res*. (2006) 60:549–54. doi: 10.1203/01.pdr.0000243546.97830.a0
6. Roberts T, McGreevy PD. Selection for breed-specific long-bodied phenotypes is associated with increased expression of canine hip dysplasia. *Vet J*. (2010) 183:266–72. doi: 10.1016/j.tvjl.2009.11.005
7. Worth AJ, Bridges JP, Cave NJ, Jones G. Seasonal variation in the hip score of dogs as assessed by the New Zealand Veterinary Association hip dysplasia scheme. *N Z Vet J*. (2012) 60:110–4. doi: 10.1080/00480169.2011.636730
8. Rettenmaier JL, Keller GG, Lattimer JC, Corley EA, Eilersieck MR. Prevalence of canine hip dysplasia in a veterinary teaching hospital population. *Vet Radiol Ultrasound*. (2002) 43:313–8. doi: 10.1111/j.1740-8261.2002.tb01010.x
9. Kotlarsky P, Haber R, Bialik V, Eidelman M. Developmental dysplasia of the hip: what has changed in the last 20 years? *World J Orthop*. (2015) 6:886–901. doi: 10.5312/wjo.v6.i11.886
10. Smith GK, Karbe GT, Agnello KA, McDonald-Lynch MB. Pathogenesis, diagnosis and control of canine hip dysplasia. In: *Veterinary Surgery: Small Animal*. 1st ed. St. Louis: Elsevier (2012). p. 824–48.
11. Barr ARS, Denny HR, Gibbs DC. Clinical hip dysplasia in growing dogs: the long-term results of conservative management. *J Small Anim Pract*. (1987) 28:243–52. doi: 10.1111/j.1748-5827.1987.tb03879.x
12. Anderson A. Treatment of hip dysplasia. *J Small Anim Pract*. (2011) 52:182–9. doi: 10.1111/j.1748-5827.2011.01049.x
13. Kirkby KA, Lewis DD. Canine hip dysplasia: reviewing the evidence for nonsurgical management. *Vet Surg*. (2012) 41:2–9. doi: 10.1111/j.1532-950X.2011.00928.x
14. Impellizeri JA, Tetrack MA, Muir P. Effect of weight reduction on clinical signs of lameness in dogs with hip osteoarthritis. *J Am Vet Med Assoc*. (2000) 216:1089–91. doi: 10.2460/javma.2000.216.1089
15. Bonneau N, Baylac M, Gagey O, Tardieu C. Functional integrative analysis of the human hip joint: the three-dimensional orientation of the acetabulum and its relation with the orientation of the femoral neck. *J Hum Evol*. (2014) 69:55–69. doi: 10.1016/j.jhevol.2013.12.013

16. Hogervorst T, Bouma HW, De Vos J. Evolution of the hip and pelvis. *Acta Orthop.* (2009) 80:1–39. doi: 10.1080/17453690610046620
17. Lovejoy CO. The natural history of human gait and posture. *Part 1 Spine and pelvis Gait Posture.* (2005) 21:95–112. doi: 10.1016/j.gaitpost.2004.01.001
18. Gruss LT, Schmitt D. The evolution of the human pelvis: changing adaptations to bipedalism, obstetrics and thermoregulation. *Philos Trans R Soc Lond B Biol Sci.* (2015) 370:20140063. doi: 10.1098/rstb.2014.0063
19. Bergmann G, Siraky J, Rohlmann A, Koelbel R. A comparison of hip joint forces in sheep, dog and man. *J Biomech.* (1984) 17:907–21. doi: 10.1016/0021-9290(84)90004-6
20. Soontornvipart K, Chalayon P, Tangwongsan C. Standing analysis of healthy and abnormal canines using force platform system. In: *2013 10th International Conference on Electrical Engineering/Electronics, Computer, Telecommunications and Information Technology.* IEEE (2013) p. 1–6.
21. Brookhart JM, Parmeggiani PL, Petersen WA, Stone SA. Postural Stability in the Dog. *Am J Physiol.* (1965) 208:1047–57. doi: 10.1152/ajplegacy.1965.208.6.1047
22. Nunamaker DM, Blauner PD. *Normal and Abnormal Gait. Textbook Small Anim Orthop.* Ithaca, NY: International Veterinary Information Services (IVIS) (1985).
23. Byrne DP, Mulhall KJ, Baker JF. Anatomy & Biomechanics of the Hip. *Open Sport Med J.* (2010) (4):51–7. doi: 10.2174/1874387001004010051
24. Pearce AI, Richards RG, Milz S, Schneider E, Pearce SG. Animal models for implant biomaterial research in bone: a review. *Eur Cell Mater.* (2007) 13:1–10. doi: 10.22203/eCM.v013a01
25. Eitel F, Klapp F, Jacobson W, Schweiberer L. Bone regeneration in animals and in man. A contribution to understanding the relative value of animal experiments to human pathophysiology. *Arch Orthop Trauma Surgery.* (1981) 99:59–64. doi: 10.1007/BF00400911
26. Rhinelander FW, Nelson CL, Stewart RD. Experimental reaming of the proximal femur and acrylic cement implantation: vascular and histologic effects. *Clin Orthop Relat Res.* (1979) (141):74–89. doi: 10.1097/00003086-197906000-00009
27. Goel VK, Drinker H, Panjabi MM, Strongwater A. Selection of an animal model for implant fixation studies: anatomical aspects. *Yale J Biol Med.* (1982) 55:113–22.
28. Aerssens J, Boonen S, Lowet G, Dequeker J. Interspecies differences in bone composition, density, and quality: potential implications for in vivo bone research. *Endocrinology.* (1998) 139:663–70. doi: 10.1210/endo.139.2.5751
29. Ibrahim T, Riaz M, Hegazy A. The prevalence of developmental dysplasia of the hip in idiopathic clubfoot: a systematic review and meta-analysis. *Int Orthop.* (2015) 39:1371–8. doi: 10.1007/s00264-015-2757-z
30. Sankar WN, Neuberger CO, Moseley CF. Femoral anteversion in developmental dysplasia of the hip. *J Pediatr Orthop.* (2009) 29:885–8. doi: 10.1097/BPO.0b013e3181c1e961
31. Sugano N, Noble PC, Kamaric E, Salama JK, Ochi T, Tullos HS. The morphology of the femur in developmental dysplasia of the hip. *J Bone Joint Surg Br.* (1998) 80:711–9. doi: 10.1302/0301-620X.80B4.0800711

32. Krontveit RI, Nødtvedt A, Sævik BK, Ropstad E, Skogmo HK, Trangerud C, et al. Prospective study on canine hip dysplasia and growth in a cohort of four large breeds in Norway (1998-2001). *Prev Vet Med.* (2010) 97:252–63. doi: 10.1016/j.prevetmed.2010.09.015
33. Kealy RD, Olsson SE, Monti KL, Lawler DF, Biery DN, Helms RW, et al. Effects of limited food consumption on the incidence of hip dysplasia in growing dogs. *Journal-American Vet Med Assoc.* (1992) 201:857.
34. Karlson EW, Mandl LA, Aweh GN, Sangha O, Liang MH, Grodstein F. Total hip replacement due to osteoarthritis: the importance of age, obesity, and other modifiable risk factors. *Am J Med.* (2003) 114:93–8. doi: 10.1016/S0002-9343(02)01447-X
35. Smith GK, Paster ER, Powers MY, Lawler DF, Biery DN, Shofer FS, et al. Lifelong diet restriction and radiographic evidence of osteoarthritis of the hip joint in dogs. *J Am Vet Med Assoc.* (2006) 229:690–3. doi: 10.2460/javma.229.5.690
36. Atalar H, Gunay C, Yavuz OY, Camurdan AD, Uras I, Eren A. Maternal height and infant body mass index are possible risk factors for developmental dysplasia of the hip in female infants. *Acta Med Okayama.* (2015) 69:349–51.
37. Steinetz BG, Williams AJ, Lust G, Schwabe C, Büllsbach EE, Goldsmith LT. Transmission of relaxin and estrogens to suckling canine pups via milk and possible association with hip joint laxity. *Am J Vet Res.* (2008) 69:59–67. doi: 10.2460/ajvr.69.1.59
38. Flückiger MA, Steffen F, Hässig M, Morgan JP. Asymmetrical lumbosacral transitional vertebrae in dogs may promote asymmetrical hip joint development. *Vet Comp Orthop Traumatol.* (2017) 30:137–42. doi: 10.3415/VCOT-16-05-0072
39. Schwend RM, Shaw BA, Segal LS. Evaluation and treatment of developmental hip dysplasia in the newborn and infant. *Pediatr Clin North Am.* (2014) 61:1095–107. doi: 10.1016/j.pcl.2014.08.008
40. Kutlu A, Memik R, Mutlu M, Kutlu R, Arslan A. Congenital dislocation of the hip and its relation to swaddling used in Turkey. *J Pediatr Orthop.* (1992) 12:598–602. doi: 10.1097/01241398-199209000-00006
41. De Pellegrin M, Moharamzadeh D. Developmental dysplasia of the hip in twins: the importance of mechanical factors in the etiology of DDH. *J Pediatr Orthop.* (2010) 30:774–8. doi: 10.1097/BPO.0b013e3181fc35c0
42. Manoukian D, Rehm A. Oligohydramnios: Should it be considered a risk factor for developmental dysplasia of the hip? *J Pediatr Orthop Part B.* (2019) 28:442–5. doi: 10.1097/BPB.0000000000000624
43. Ford CA, Nowlan NC, Thomopoulos S, Killian ML. Effects of imbalanced muscle loading on hip joint development and maturation. *J Orthop Res.* (2016) 35:1128–36. doi: 10.1002/jor.23361
44. Klisic PJ. Congenital dislocation of the hip—a misleading term: brief report. *J Bone Joint Surg Br.* (1989) 71:136. doi: 10.1302/0301-620X.71B1.2914985
45. Sakkars R, Pollet V. The natural history of abnormal ultrasound findings in hips of infants under six months of age. *J Child Orthop.* (2018) 12:302–7. doi: 10.1302/1863-2548.12.180056
46. Wenger DR, Bomar JD. Human hip dysplasia: evolution of current treatment concepts. *J Orthop Sci.* (2003) 8:264–71. doi: 10.1007/s007760300046

47. Tobias KM, Johnston SA. Veterinary surgery: small animal-E-BOOK: 2- volume set. *Elsevier Health Sciences*. (2013).
48. Read RA. Conservative management of juvenile canine hip dysplasia. *Aust Vet J*. (2000) 78:818–9. doi: 10.1111/j.1751-0813.2000.tb10494.x
49. Rawson EA, Aronsohn MG, Burk RL. Simultaneous bilateral femoral head and neck ostectomy for the treatment of canine hip dysplasia. *J Am Anim Hosp Assoc*. (2005) 41:166–70. doi: 10.5326/0410166
50. Gatineau M, Dupuis J, Beauregard G, Charette B, Breton L, Beauchamp G, et al. Palpation and dorsal acetabular rim radiographic projection for early detection of canine hip dysplasia: a prospective study. *Vet Surg*. (2012) 41:42–53. doi: 10.1111/j.1532-950X.2011.00926.x
51. Shorter D, Hong T, Osborn DA. Screening programmes for developmental dysplasia of the hip in newborn infants. *Cochrane database Syst Rev*. (2011) (9):CD004595. doi: 10.1002/14651858.CD004595.pub2
52. Kang MS, Han GW, Kam M, Park S-S. Clinical significance of asymmetric skin folds in the medial thigh for the infantile screening of developmental dysplasia of the hip. *Pediatr Neonatol*. (2019) 60:570–6. doi: 10.1016/j.pedneo.2019.02.004
53. Kamath SU, Bennet GC. Does developmental dysplasia of the hip cause a delay in walking? *J Pediatr Orthop*. (2004) 24:265. doi: 10.1097/01241398-200405000-00005
54. and preventive management of canine hip dysplasia: a review. *Vet J*. (2010) 184:269–76. doi: 10.1016/j.tvjl.2009.04.009
55. Hielm-Björkman AK, Kuusela E, Liman A, Markkola A, Saarto E, Huttunen P, et al. Evaluation of methods for assessment of pain associated with chronic osteoarthritis in dogs. *J Am Vet Med Assoc*. (2003) 222:1552–8. doi: 10.2460/javma.2003.222.1552
56. Kyriazis A, Prassinou NN. Canine hip dysplasia: part i: aetiopathogenesis & diagnostic approach. *Hell J Companion Anim Med*. (2016) 5:22–47.
57. Herring JA. *Tachdjian's Pediatric Orthopaedics: From the Texas Scottish Rite Hospital for Children E-Book*. Philadelphia, PA: Elsevier (2020).
58. Ginja MMD, Ferreira AJ, Jesus SS, Melo-Pinto P, Bulas-Cruz J, Orden MA, et al. Comparison of clinical, radiographic, computed tomographic, and magnetic resonance imaging methods for early prediction of canine hip laxity and dysplasia. *Vet Radiol Ultrasound*. (2009) 50:135–43. doi: 10.1111/j.1740-8261.2009.01506.x
59. Wiberg G. Studies on dysplastic acetabula and congenital subluxation of the hip joint: with special reference to the complication of osteoarthritis. *Acta Chir Scand*. (1939) 83:53–68.
60. Storer SK, Skaggs DL. Developmental dysplasia of the hip. *Am Fam Physician*. (2006) 74:1310–6.
61. Quader N, Schaeffer EK, Hodgson AJ, Abugharbieh R, Mulpuri K, A. systematic review and meta-analysis on the reproducibility of ultrasound- based metrics for assessing developmental dysplasia of the hip. *J Pediatr Orthop*. (2018) 38:e305–11. doi: 10.1097/BPO.0000000000001179
62. Murphy SB, Ganz R, Müller ME. The prognosis in untreated dysplasia of the hip. A study of radiographic factors that predict the outcome. *J Bone Jt Surg Am*. (1995) 77:985–9. doi: 10.2106/00004623-199507000-00002

63. Murphy SB, Kijewski PK, Millis MB, Harless A. Acetabular dysplasia in the adolescent and young adult. *Clin Orthop Relat Res.* (1990) 261:214–23. doi: 10.1097/00003086-199012000-00023
64. Werner CML, Ramseier LE, Ruckstuhl T, Stromberg J, Copeland CE, TurenCH, et al. Normal values of Wiberg's lateral center-edge angle and Lequesne's acetabular index—a coxometric update. *Skeletal Radiol.* (2012) 41:1273–8. doi: 10.1007/s00256-012-1420-7
65. Monazzam S, Bomar JD, Cidambi K, Kruk P, Hosalkar H. Lateral center-edge angle on conventional radiography and computed tomography. *Clin Orthop Relat Res.* (2013) 471:2233–7. doi: 10.1007/s11999-012-2651-6
66. Vezzoni A, Dravelli G, Vezzoni L, De Lorenzi M, Corbari A, Cirila A, et al. Comparison of conservative management and juvenile pubic symphysiodesis in the early treatment of canine hip dysplasia. *Vet Comp Orthop Traumatol.* (2008) 21:267–79. doi: 10.1055/s-0037-1617372
67. Parvaresh KC, Pennock AT, Bomar JD, Wenger DR, Upasani VV. Analysis of acetabular ossification from the triradiate cartilage and secondary centers. *J Pediatr Orthop.* (2018) 38:e145–50. doi: 10.1097/BPO.0000000000001120
68. Tibrewal S, Gulati V, Ramachandran M. The Pavlik method: a systematic review of current concepts. *J Pediatr Orthop B.* (2013) 22:516–20. doi: 10.1097/BPB.0b013e328365760e
69. Cooper AP, Doddabasappa SN, Mulpuri K. Evidence-based management of developmental dysplasia of the hip. *Orthop Clin North Am.* (2014) 45:341–54. doi: 10.1016/j.ocl.2014.03.005
70. López-Carreño E, Carillo H, Gutiérrez M. Dega vs. Salter osteotomy for the treatment of developmental dysplasia of the hip. *J Pediatr Orthop B.* (2008) 17:213–21. doi: 10.1097/BPB.0b013e32830850eb
71. Castañeda P, Vidal-Ruiz C, Méndez A. How often does femoroacetabular impingement occur after an innominate osteotomy for acetabular dysplasia? *Clin Orthop Relat Res.* (2016) 474:1209–15. doi: 10.1007/s11999-016-4721-7
72. Sales de Gauzy J. Pelvic reorientation osteotomies and acetabuloplasties in children. Surgical technique. *Orthop Traumatol Surg Res.* (2010) 96:793–9. doi: 10.1016/j.otsr.2010.07.004
73. Wang CW, Wang TM, Wu KW, Huang SC, Kuo KN. The comparative, long-term effect of the Salter osteotomy and Pemberton acetabuloplasty on pelvic height, scoliosis and functional outcome. *Bone Joint J.* (2016) 98:1145–50. doi: 10.1302/0301-620X.98B8.37215
74. Wang C-W, Wu K-W, Wang T-M, Huang S-C, Kuo KN. Comparison of acetabular anterior coverage after Salter osteotomy and Pemberton acetabuloplasty: a long-term followup. *Clin Orthop Relat Res.* (2014) 472:1001–9. doi: 10.1007/s11999-013-3319-6
75. Raghuvir HB, Shivrajsinh KJ, Dipak NS, Harit DB, Chirag AB, Naresh HK. Treatment of canine hip dysplasia: a review. *J Anim Sci Adv.* (2013) 3:589–97.
76. Remedios AM, Fries CL. Treatment of canine hip dysplasia: a review. *Can Vet J = La Rev vétérinaire Can.* (1995) 36:503–9.
77. Bliddal H, Leeds AR, Christensen R. Osteoarthritis, obesity and weight loss: evidence hypotheses and horizons - a scoping review. *Obes Rev.* (2014) 15:578–86. doi: 10.1111/obr.12173

78. Bockstahler B, Levine D, Maier J, Millis D, Wittek K. *Essential Facts of Physical Medicine, Rehabilitation and Sports Medicine in Companion Animals*. Babenhausen: VBS GmbH (2019).
79. Retchford TH, Crossley KM, Grimaldi A, Kemp JL, Cowan SM. Can local muscles augment stability in the hip? A narrative literature review. *J Musculoskelet Neuronal Interact.* (2013) 13:1–12.
80. Hara Y, Harada Y, Fujita Y, Taoda T, Nezu Y, Yamaguchi S, et al. Changes of hip joint congruity after triple pelvic osteotomy in the dog with hip dysplasia. *J Vet Med Sci.* (2002) 64:933–6. doi: 10.1292/jvms.64.933
81. McLaughlin RM, Miller CW, Taves CL, Hearn TC, Palmer NC, Anderson GI. Force plate analysis of triple pelvic osteotomy for the treatment of canine hip dysplasia. *Vet Surg.* (1991) 20:291–7. doi: 10.1111/j.1532-950X.1991.tb01270.x
82. de Kleuver M, Kapitein PJ, Kooijman MA, van Limbeek J, Pavlov PW, Veth RP. Acetabular coverage of the femoral head after triple pelvic osteotomy: no relation to outcome in 51 hips followed for 8–15 years. *Acta Orthop Scand.* (1999) 70:583–8. doi: 10.3109/17453679908997846
83. Mimura T, Mori K, Kawasaki T, Imai S, Matsusue Y. Triple pelvic osteotomy: Report of our mid-term results and review of literature. *World J Orthop.* (2014) 5:14–22. doi: 10.5312/wjo.v5.i1.14
84. van Stralen RA, van Hellemond GG, Ramrattan NN, de Visser E, de Kleuver M. Can a triple pelvic osteotomy for adult symptomatic hip dysplasia provide relief of symptoms for 25 years? *Clin Orthop Relat Res.* (2013) 471:584–90. doi: 10.1007/s11999-012-2701-0
85. Vezzoni A, Boiocchi S, Vezzoni L, Vanelli AB, Bronzo V. Double pelvic osteotomy for the treatment of hip dysplasia in young dogs. *Vet Comp Orthop Traumatol.* (2010) 23:444–52. doi: 10.3415/Vcot-10-03-0034
86. Willemsen K, Doelman CJ, Sam ASY, Seevinck PR, Sakkers RJB, Weinans H, et al. Long-term outcomes of the hip shelf arthroplasty in adolescents and adults with residual hip dysplasia: a systematic review. *Acta Orthop.* (2020) 91:383–9. doi: 10.1080/17453674.2020.1747210
87. Migaud H, Chantelot C, Giraud F, Fontaine C, Duquennoy A. Long-term survivorship of hip shelf arthroplasty and Chiari osteotomy in adults. *Clin Orthop Relat Res.* (2004) (418):81–6. doi: 10.1097/00003086-200401000-00014
88. Bartoniček J, Vávra J, Chochoła A. Bosworth hip shelf arthroplasty in adult dysplastic hips: ten to twenty three year results. *Int Orthop.* (2012) 36:2425–31. doi: 10.1007/s00264-012-1665-8
89. Willemsen K, Tryfonidou M, Sakkers R, Castelein RM, Zadpoor AA, Seevinck P, et al. Patient-specific 3D-printed shelf implant for the treatment of hip dysplasia: Anatomical and biomechanical outcomes in a canine model. *J Orthop Res.* (2021). doi: 10.1002/jor.25133
90. Golafshan N, Willemsen K, Kadumudi FB, Vorndran E, Dolatshahi-Pirouz A, Weinans H, et al. 3D-printed regenerative magnesium phosphate implant ensures stability and restoration of hip dysplasia. *Adv Healthc Mater.* 10:e 101051. doi: 10.1002/adhm.202101051
91. Bicanic G, Barbaric K, Bohacek I, Aljinovic A, Delimar D. Current concept in dysplastic hip arthroplasty: Techniques for acetabular and femoral reconstruction. *World J Orthop.* (2014) 5:412–24. doi: 10.5312/wjo.v5.i4.412

92. Vezzoni L, Vezzoni A, Boudrieau RJ. Long-term outcome of Zürich cementless total hip arthroplasty in 439 cases. *Vet Surg.* (2015) 44:921–9. doi: 10.1111/vsu.12371
93. OffW, Matis U. Excision arthroplasty of the hip joint in dogs and cats. clinical, radiographic, and gait analysis findings from the department of surgery, veterinary faculty of the ludwig-maximilians-university of munich, germany. 1997. *Vet Comp Orthop Traumatol.* (2010) 23:297–305.
94. Olsson SE, Figarola F, Suzuki K. Femoral head excision arthroplasty. A salvage operation in severe hip dysplasia in dogs. *Clin Orthop Relat Res.* (1969) 62:104–12. doi: 10.1097/00003086-196901000-00013



CHAPTER 5

Magnetic resonance imaging versus computed tomography for three-dimensional bone imaging of musculoskeletal pathologies: a review

Mateusz C. Florkow | Koen Willemsen | Vasco V. Mascarenhas |
Edwin H.G. Oei | Marijn van Stralen | Peter R. Seevinck

Published in Journal of Magnetic Resonance Imaging (2022)
<https://doi.org/10.1002/jmri.28067>

Abstract

Magnetic resonance imaging (MRI) is increasingly utilized as a radiation-free alternative to computed tomography (CT) for the diagnosis and treatment planning of musculoskeletal pathologies. MR imaging of hard tissues such as cortical bone remains challenging due to their low proton density and short transverse relaxation times, rendering bone tissues as nonspecific low signal structures on MR images obtained from most sequences. Developments in MR image acquisition and post-processing have opened the path for enhanced MR-based bone visualization aiming to provide a CT-like contrast and, as such, ease clinical interpretation. The purpose of this review is to provide an overview of studies comparing MR and CT imaging for diagnostic and treatment planning purposes in orthopedic care, with a special focus on selective bone visualization, bone segmentation, and three-dimensional (3D) modeling. This review discusses conventional gradient-echo derived techniques as well as dedicated short echo time acquisition techniques and post-processing techniques, including the generation of synthetic CT, in the context of 3D and specific bone visualization. Based on the reviewed literature, it may be concluded that the recent developments in MRI-based bone visualization are promising. MRI alone provides valuable information on both bone and soft tissues for a broad range of applications including diagnostics, 3D modeling, and treatment planning in multiple anatomical regions, including the skull, spine, shoulder, pelvis, and long bones.

Introduction

Magnetic resonance imaging (MRI) is a radiation-free, noninvasive imaging modality that provides three-dimensional (3D) visualization of tissues. Its superior soft tissue contrast has made it a preferential diagnostic tool for the imaging of various organ systems, including the musculoskeletal system. Osseous structures are, however, usually visualized using radiography or computed tomography (CT). For imaging complex structures, CT is preferred as it offers high-resolution 3D images with a radiodensity contrast that highlights bony tissues. Building upon the characteristic high X-ray attenuation of cortical bone, dedicated (semi-)automatic bone segmentation tools have been developed for CT images. Resulting 3D bone renderings have proven valuable in the diagnosis and treatment of bone pathologies. Consequently, pathologies affecting both soft and hard tissues, including skull,[1,2] spine,[3-5] and joint disorders,[7,7] often warrant the acquisition of both MR and CT images. Such a multimodal workflow is logistically complex and induces an adverse radiation burden inherent to CT imaging, especially harmful in young population.[8]

Recent advances in MR image acquisition and processing, facilitated by the development of new hardware and the increase in computing power, have enabled the improvement of bone contrast on MR images. If reliable, MRI could be a radiation-free alternative to CT for the diagnosis and treatment planning of certain musculoskeletal pathologies. Transforming a CT-MR multimodal workflow into a simplified radiation-free MR-only workflow, as previously proposed in radiotherapy treatment planning,[9] could lead to less hospital visits, lower costs, allow for the fusion of soft tissue and bone information, and reduce the time under sedation for younger patients.[10, 11] This review will discuss comparative studies of MRI and CT for the diagnosis and treatment planning of bone pathologies in musculoskeletal diseases in multiple anatomical regions, including the skull, the spine, the shoulder, and the pelvis. Four main subjects will be described: MRI-based techniques for bone imaging, MRI for bone segmentation and 3D reconstruction, MRI for the diagnosis of bone pathologies, and the remaining challenges faced by MRI in the context of bone visualization. Applications in the fields of radiotherapy and positron emission tomography–magnetic resonance (PET-MR) will not be covered as they have been thoroughly reviewed in the past few years.[12-15]

MRI-Based Visualization of the Bone Morphology

Cortical bone imaging is challenging with MRI due to its low free-water content. The MR signal that originates from cortical bone is mostly emitted by bound water, causing the signal decay to be rapid. Consequently, in conventional MRI sequences, cortical bone appears as a structure with low signal intensity that is not specific to bone. Although valuable for structural imaging, the poor visualization of cortical bone on conventional

sequences has motivated the development of dedicated imaging techniques that facilitate bone visualization and segmentation. The remainder of this section briefly discusses several MR sequences and processing techniques used for bone imaging. The resulting MR images are compiled in Fig. 1 which provides an overview of multiple anatomical regions and in Fig. 2 which displays ankle images of a single patient. For each sequence, Table 1 provides the reported acquisition parameters, and Table 2 summarizes their characteristics and fields of study.

Conventional Clinical MR Sequences

Within the field of musculoskeletal imaging, T1- and proton density (PD)-weighting is often acquired for structural bone imaging whereas T2-weighting is acquired for imaging functional and pathophysiological processes. T1-weighted (T1w) images have been acquired to detect structural lesions using spin-echo (SE) or gradient-echo (GRE) sequences. SE images and their derivatives are routinely acquired in musculoskeletal radiology owing to their excellent soft tissue contrast. Compared to GRE, SE sequences are also less prone to susceptibility, chemical shift, and field inhomogeneity artifacts but are nonetheless affected by geometrical distortions, especially at low receiver bandwidth and in regions far from the bore isocenter.⁶⁶ On the other hand, GRE sequences are usually faster owing to a shorter minimal repetition time (TR) as shown in the pulse sequence chronograms in Fig. 3. In addition, GRE sequences are more versatile and are increasingly investigated for musculoskeletal radiology using radiofrequency spoiled gradient-echo (S-GRE also known as vendor-specific acronyms FLASH [fast low angle shot], SPGR [spoiled gradient-recalled], or T1-FFE [T1 fast field echo]), or volumetric radiofrequency spoiled gradient-echo (VS-GRE also known as vendor-specific acronyms VIBE [volumetric interpolated breath-hold examination], LAVA [liver acquisition with volume acquisition], or THRIVE [T1-weighted high-resolution isotropic volume examination])[67] that enable post-acquisition multiplanar reformatting.

For bone morphology visualization, these sequences have been proposed in combination with fat-saturation [37, 39, 47] or water excitation [16] to suppress the signal from adipose tissues and render bone as structures with a uniform low intensity. Alternatively, water-only images can be generated by acquiring a GRE sequence with specific echo times to perform a Dixon water–fat separation.[25, 28, 29, 68, 69]

Dedicated MR Sequences

To further improve bone visualization, sequences have been developed to enhance bone specificity by providing a uniform soft tissue contrast, or by aiming at a CT-like contrast.

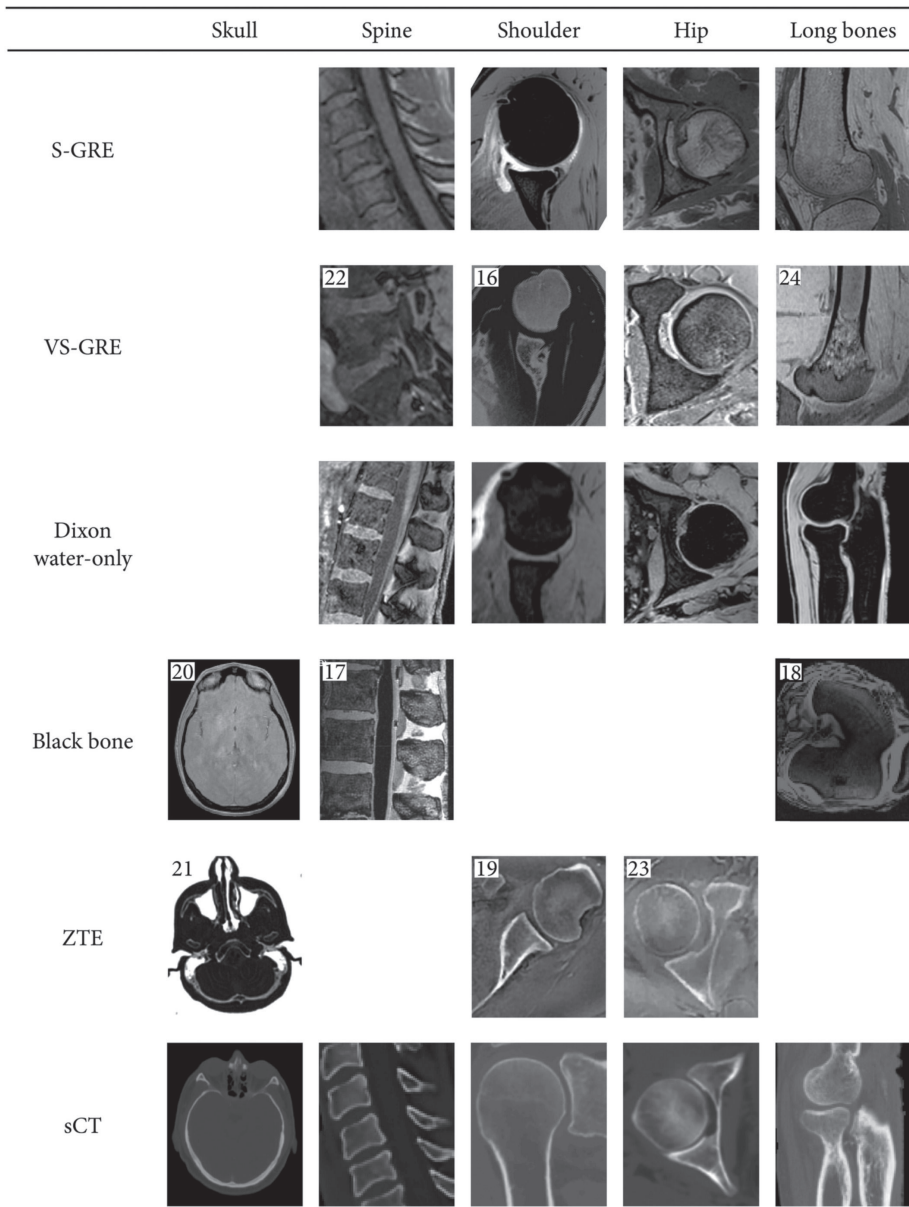


Figure 1. Illustrations of the various MR contrasts used for bone visualization in multiple anatomies. Some of the images were fat-suppressed (eg, S-GRE of the shoulder) or post-processed (eg, VS-GRE of the shoulder). Some images are reprinted with permissions from the reference given in the top left-hand corner of the images.¹⁶⁻²⁴ Black bone/skull was reprinted by permission from Springer Nature.²⁰ Original images were all cropped to only show the region of interest. MR = magnetic resonance; sCT = synthetic computed tomography; S-GRE = radiofrequency spoiled gradient-echo; VS-GRE = volumetric radiofrequency spoiled gradient-echo; ZTE = zero echo time.

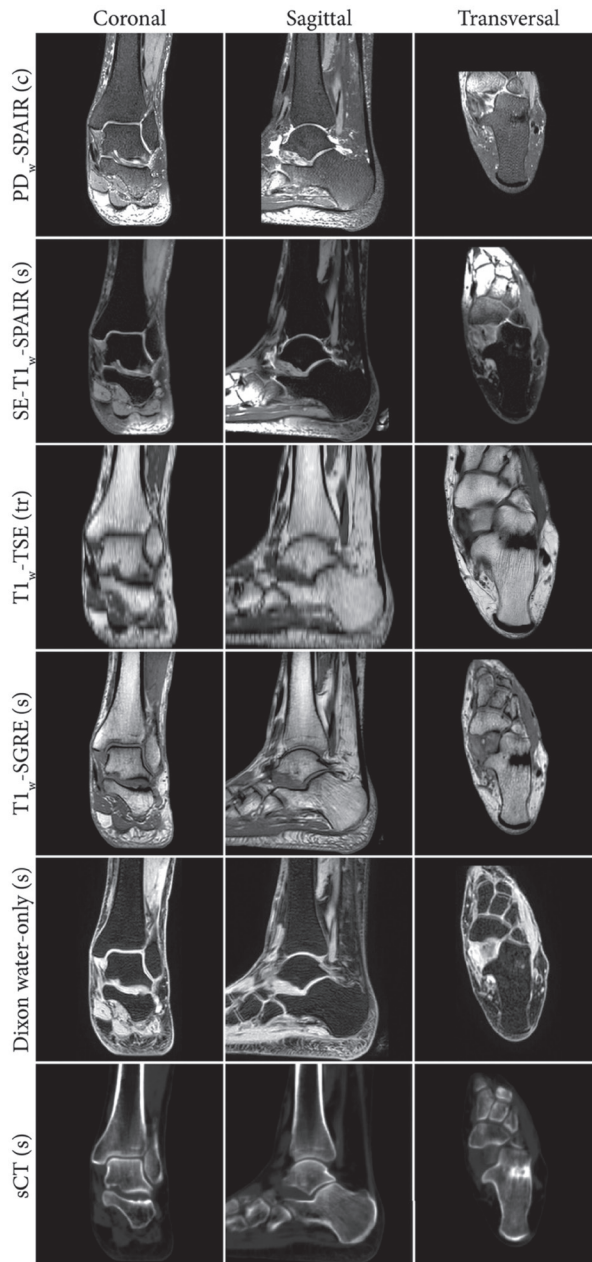


Figure 2. Example of coronal, sagittal, and transversal slices of the same anatomical region obtain from MRI.

The letters between brackets indicate the acquisition plane (c: coronal, s: sagittal, tr: transversal). Dixon water-only and synthetic CT (sCT) images were based on the T1w-S-GRE image. PDw = proton density-weighted; T1w = T1-weighted; SPAIR = spectral attenuated inversion recovery (fat suppression); SE = spin-echo; TSE = turbo spin-echo; S-GRE = radiofrequency spoiled gradient-echo; MRI = magnetic resonance imaging.

Table 1. Acquisition parameters of the MR sequences reported in this review

Sequence Type	Anatomies	Field Strength (T)	Resolution (mm)	FOV (mm)	Acquisition Time	TE	TR	Flip Angle (°)	Bandwidth
Dixon-T1w-GRE	Hip ²⁵ shoulder ²⁶	1.5	0.9 × 0.9 × 0.9	288 × 288	7 minutes 33 seconds	2.4/4.8	7.4	9	490 Hz/px
Dixon—S-GRE	Hip ²⁷	1.5	0.6 × 0.6 × 0.67^b	270 × 270 × 120	4 minutes 38 seconds	2.0/4.3	6.7	20	541 Hz/px
	Hip ²⁷	3	0.97 × 0.97 × 1^a	435 × 435 × 160	2 minutes 38 seconds	2.1/3.5	6.5	10	1122 Hz/px
	Hip ²⁸	3	1 × 1 × 1^a	200	3 minutes 28 seconds	2.4/7	10	145	350 Hz/px
	Shoulder ²⁹	3	1 × 1 × 1^a	200	3 minutes 28 seconds	2.4/3.7	10	10	400 Hz/px
Dixon—VS-GRE	Hip ³⁰	3	1.2 × 1.2 × 1	175 × 320 × 192	32 seconds	1.27/2.5	3.9	9	NA
S-GRE	Long bone ³¹	1.5	0.45 × 0.45 × 1	NA	20 minutes	4.9	11	15	NA
	Long bone ³²	1.5	0.39 × 0.39 × 1 ^a	200 × 200 ^b	NA	4	17	25	NA
	Long bone ³³	1.5	0.39 × 0.39 × 1 ^a	NA	NA	5	20	12	NA
	Shoulder ³⁴	1.5	0.7 × 0.7 × 0.7	NA	NA	5.1	23	50	NA
	Shoulder ³⁵	1.5	0.31 × 0.625 × 1 ^b	160 × 160	3.5 minutes	4.38	1290	15	NA
	Shoulder ³⁵	3	0.54 × 0.68 × 1.5 ^b	100 × 100	3.5 minutes	2.3	5.1	30	NA
	Hip ³⁰	3	1 × 1 × 1	170 × 170	16 minutes (3 scans)	3.3	15	4/24	NA
	Spine ³⁶	3	0.28 × 0.28 × 0.75 ^c	70 × 160 × 250	5 minutes 7 seconds	2.3	7.8	8	NA
	Spine ³⁷	3	0.94 × 0.94 × 2 ^{ab}	240	6 minutes 43 seconds	7	27	30	20.8 kHz
VS-GRE	Long bone ³⁸	3	0.31 × 0.31 × 0.7	160 × 160	3 minutes 34 seconds	5.4	11.6	NA	NA
	Long bone ²⁴	3	0.47 × 0.47 × 1	240 × 120	9 minutes 37 seconds	1.83	11	NA	NA
	Spine ³⁹	3	? × ? × 2	200	4 minutes	2.45	7	NA	NA
	Spine ²²	1.5	0.94 × 2.4 × 1.7	240	NA	2.4	6.52	NA	NA
	Shoulder ¹⁶	3	0.7 × 0.7 × 0.7	180 × 180	4 minutes 16 seconds	3.5	10.5	12	300 Hz/px
	Shoulder ⁷	3	0.9 × 0.9 × 0.9	180	<2 minutes	4.9	12.3	10	NA
	Shoulder ⁴⁰	3	0.6 × 0.6 × 0.6	160 × 160	3 minutes 14 seconds	4.9	12.2	10	NA
	Shoulder ⁴¹	3	0.82 × 0.82 × 0.89	210 × 210 × 100	5 minutes	2.66	7.16	10	300 Hz/px
	SI joint ⁶	1.5	? × ? × [0.89–1]	NA	3–5 minutes	7	25	NA	NA
	SI joint ⁴²	3	0.6 × 0.6 × 0.6	154 × 154 ^b	3 minutes	5.2	11.7	10	NA
	Hip ⁴³	1.5	1 × 1 × 1	NA	4 minutes	2.88	7.67	NA	NA
	Hip ⁴⁴	3	0.8 × 0.8 × 0.8	160 × 160 × 102 ^b	9 minutes	3.3	15	4 and 24	NA
	Hip ⁴⁵	3	0.8 × 0.8 × 0.8	180 × 340	6 minutes 33 seconds	4.9	10.8	NA	NA

Sequence Type	Anatomies	Field Strength (T)	Resolution (mm)	FOV (mm)	Acquisition Time	TE	TR	Flip Angle (°)	Bandwidth
GRE	Long bone ⁴⁶	0.3	0.39×0.39×1	160	11–15 minutes	NA	NA	NA	NA
	Long bone ⁴⁷	1.5	0.39×0.39×0.7 ^a	200×200	NA	NA	NA	NA	NA
	Long bone ⁴⁸	3	0.3×0.3×0.5	[120–150]	5 minutes 30 seconds to 6 minutes 45 seconds	2.7	10	8	NA
UTE	Skull ^{49,50}	1.0	0.9×0.9×1^a	230×230 ^b	NA	6.9	25	NA	NA
	Long bone ⁵¹	3	0.25×0.25×2	400	7 minutes	0.032	100	10	NA
	Skull ²	1.5	0.5×0.5×[1, 2] ^{a,b}	256×256×140	[6–8] minutes	[0.08–0.35]/[2.3–4.6]	[8–12]	25	NA
ZTE	Skull ⁵³	3	0.7×0.7×0.7	246	5 minutes 15 seconds	0.07	5	NA	355 Hz/px
	Skull ⁵⁴	3	1.1×1.1×1.1	280×280×280	6 minutes	0.06/2.46	7	12	NA
	Spine ³⁶	3	0.28×0.28×0.75 ^a	279×259×250	6 minutes 18 seconds	0.14	6.3	5	NA
	Spine ³⁷	3	0.94×0.94×2 ^b	240	3 minutes 12 seconds	0.05	44.3	2	125 kHz
	Spine ⁵⁵	3	0.8×0.8×1.2	230×230×119	8 minutes 56 seconds	0.2/4.6	10.2	10	NA
	Shoulder ⁵⁶	3	0.83×0.83×[3, 4]	160	3–4.5 minutes	0.03	134	18	NA
	Skull ⁵⁷	3	0.69×0.69×1 ^b	180×180	~5 minutes	0	785	4	31.25 kHz
Skull ²¹	3	0.85×0.85×0.85	220	6 minutes 12 seconds	0	NA	1.2	62.5 kHz	
Skull ²¹	3	1.35×1.35×1.35	260	2 minutes 53 seconds	0	NA	1.2	62.5 kHz	
Skull ⁵⁸	3	1.4×1.4×1.4	260×260×260	2 minutes 52 seconds	0	NA	1	62.5 kHz	
Spine ⁵	3	1×1×1	320	~5 minutes	0	417	1	62.5 kHz	
Shoulder ⁵⁹	1.5/3	[0.625–1.2]×[0.625–1.2]×1.4	[200–300]	4–6 minutes	[25–40]	[1.375–1.629]	1	62.5 kHz	
Shoulder ¹⁹	3	1×1×1	200	3–4 minutes	0	[0.8–1.1]	1	62.5 kHz	
Shoulder ¹⁹	3	0.7×0.7×0.7	200	10–13 minutes	0	[0.8–1.1]	1	62.5 kHz	
Hip ²³	3	~[1.1–1.4]×[1.1–1.4] ^b	[360–440]	5 minutes	0	[425–528]	1	62.5 kHz	

Sequence Type	Anatomies	Field Strength (T)	Resolution (mm)	FOV (mm)	Acquisition Time	TE	TR	Flip Angle (°)	Bandwidth
BB-MRI	Long bone ¹⁸	3	1 x 1 x 1	401 x 401	10 minutes	3.69	10	5	NA
	Skull ^{2b,60-62}	1.5	0.94 x 0.94 x 1.2 ^b	240	4 minutes	4.2	8.6	5	31.25 kHz
	Skull ⁶³	3	0.47 x 0.47 x 2 ^{a,b}	240	7 minutes 50 seconds	2.2	6.7	5	610 Hz/px ^b
	Skull ⁶⁴	3	1.6 x 1.6 x 3	? x 7 x 240	~3 minutes	[1.51-1.55]	[3.5 6 - 3.62]	12	[590-610] Hz/px
BB-MRI-VS-GRE	Spine ¹⁷	3	0.625 x 0.325 x 0.6 ^b	240 x 144	6 minutes	3.1	7.4	NA	62.5 kHz
	Skull ⁶⁴	3	1 x 1 x 0.9	192 x 192	~3 minutes	In-phase	25	3 and 5	[590-610] Hz/px
BB-MRI-UTE	Skull	1.5/3	1.1 x 1.1 x 1^b	250 x 250	4 minutes	0.07	3.32	NA	NA
	Skull ⁶⁵	3	0.53 x 0.53 x 0.53	171 x 171	7 minutes 1 second	5.8	800	NA	625
	Spine ²²	1.5	0.87 x 3.5 x 3	280	NA	19	624	NA	NA

In red = acquisition time longer than 5 minutes.

In bold = nearly isotropic acquisition.

GRE = gradient-echo; S-GRE = radiofrequency spoiled gradient-echo; UTE = ultrashort echo time; ZTE = zero echo time; BB = black bone; BB = field of view; TE = echo time; TR = repetition time; MRI = magnetic resonance imaging.

Question mark and NA indicate the information was not available.

^a Indicates this is the reconstructed resolution.

^b Indicates that the parameter was not directly given and computed using other parameters reported in the manuscript.

Table 2. Characteristics and fields of applications of multiple MR acquisition and processing techniques

	GRE	BB	UTE	ZTE	sCT
<i>Generation</i>	Acq.	Acq.	Acq.	Acq.	Processing
<i>Hardware requirement</i>	Low	Low	High	High	Low
<i>Software requirement</i>	Low	Low	High	High	High
<i>Availability</i>	High	High	Low	Low	Medium
<i>Pros</i>	- Fast 3D (isotropic) acquisition	- Uniform soft tissue contrast	- Acquisition of cortical bone signal	- Fast 3D isotropic silent acquisition - Not sensitive to motion - Acquisition of cortical bone signal	- Quantitative (Hounsfield units)
<i>Cons</i>	- Low signal acquired in cortical bone	- Low signal acquired in bone	- Susceptible to gradient inhomogeneity - Spatially nonselective 3D excitation	- Spatially nonselective excitation	- Questionable reliability
<i>Applications</i>	- Fracture detection - Structural changes - Morphometric parameters assessment	- Fracture detection - Skull suture assessment - Surgical planning	- Structural changes - Fracture detection	- Structural changes - Morphometric parameters assessment	- Structural changes - Morphometric parameters assessment - Surgical planning
<i>Anatomical regions</i>	- Skull - Spine - Shoulder - Hip - Long bones	- Skull - Spine - Long bones	- Skull - Spine - Shoulder - Long bones	- Skull - Spine - Shoulder - Hip	- Spine - Pelvis - Long bones

GRE = gradient-echo; BB = black bone; UTE = ultrashort echo time; ZTE = zero echo time; sCT = synthetic computed tomography; Acq. = acquisition; MR = magnetic resonance.

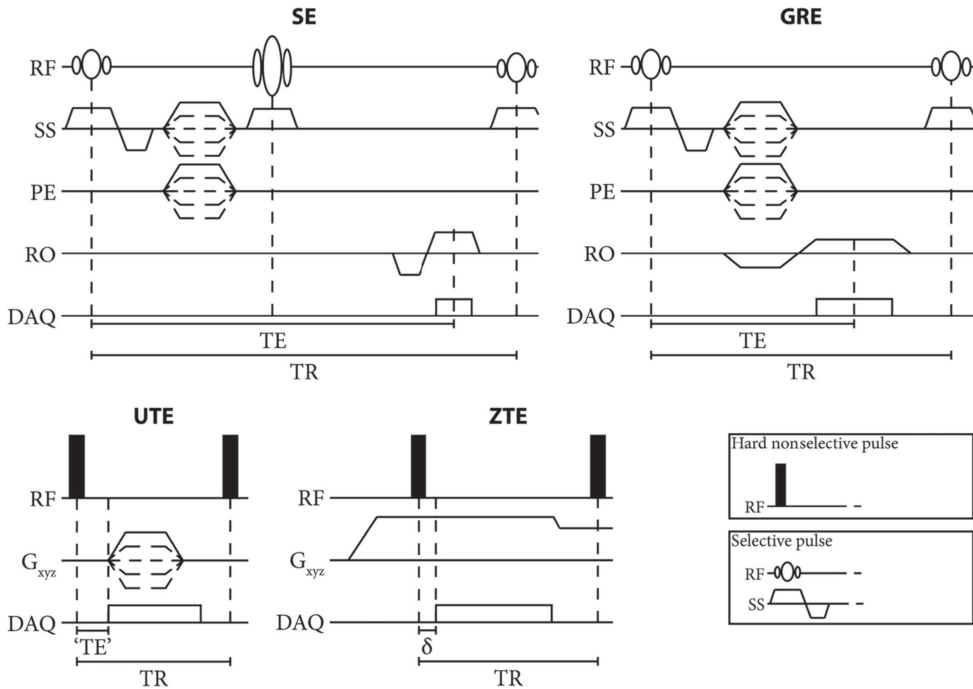


Figure 3. Chronograms of basic spin-echo (SE) gradient-echo (GRE), ultrashort echo time (UTE), and zero echo time (ZTE) pulse sequences.

Note the difference in echo time (TE) and repetition time (TR) between the sequences. Typical values of TE in the UTE sequence are in the range of $100\ \mu\text{s}$ and of δ in the ZTE sequence in the range of $10\ \mu\text{s}$. In particular, in the UTE sequence, there is a fast gradient switching between TR's and the acquisition starts during the gradient ramp up. In the ZTE sequence, gradient switching is smooth and the gradient is on before the excitation but there is a delay between the excitation and the acquisition. In this basic UTE sequence, a free induction echo is acquired but more complex sequences can acquire gradient-recalled echoes. RF = radiofrequency; SS = slice selection; PE = phase encoding; RO = readout; DAQ = data acquisition.

BLACK BONE IMAGING

The gain in bone specificity was achieved in "black bone" (BB) sequences by applying a low flip angle and short echo time (TE) and TR to GRE-like sequences,[60] including VS-GRE[64] and ultrashort echo time (UTE)[70] sequences. With such parameters, cortical bone appears as a low-intensity structure whereas soft tissues have a uniform intermediate intensity. Originally developed for craniofacial imaging,[60] BB-MRI has been further applied to image the spine,[17, 71] and long bones.[18]

ULTRASHORT AND ZERO ECHO TIME IMAGING

Subsequently, the development of new hardware, which enabled faster transmit/receiving switching coils and more demanding gradients, permitted a drastic lowering of the echo time resulting in UTE sequences. In such sequences, the signal is usually acquired radially, soon after the end of the excitation, before a T₂-induced signal decay and minimal T₂* signal decay. An image with a CT-like contrast containing signal mainly in short T₂ components can then be obtained by suppressing the long T₂ signal.[72] However, the fast gradient switching between TR's and the acquisition during the gradient ramp up (Fig. 3) renders UTE sequences prone to Eddy currents and susceptible to gradient delays, potentially resulting in imaging artifacts.

With further developments, zero echo time (ZTE) images have been acquired for which the signal is sampled (usually radially) directly after the application of the radiofrequency (RF) pulse. To that end, readout gradients are on during the RF excitation. However, because of the delay in switching from transmit to receive modes, there is a dead time during which the center of the k-space is not sampled (Fig. 3). Consequently, to reduce the dead time, hard short RF pulses need to be used, which put constraints on the achievable flip angles and bandwidths. ZTE images are acquired only with free induction decay readout, and a CT-like contrast can be obtained by applying an inverse-logarithmic rescaling.[72] Since gradient switching is smooth (Fig. 3), ZTE acquisitions are rather silent, and the short achievable TR makes them fast.

Image Processing Techniques

In addition to the advances in image acquisitions, image analysis and processing techniques have been applied to enhance bone visualization, usually aiming to create images with a CT-like contrast. The simplest processing steps consisted in inverting the intensities or subtracting water intensities from the entire image, thus highlighting low signal in the MR images which is hypothesized to reflect the presence of cortical bone. Such a technique has been applied on standard GRE,[48] VS-GRE,[16] or Dixon water-only images.[26, 29] More advanced processing has been searched to convert MR image intensities to CT Hounsfield units (HU), creating so-called synthetic CT (sCT). The most promising sCT generation models are deep learning-based and rely on various network architectures, including UNet,[73] generative adversarial network,[74] and their derivatives.[75] The use of sCT images has already been reviewed multiple times for radiotherapy purposes and PET-MR[9, 12-14] but their use for orthopedic purposes is rare. sCT generation models for orthopedic care have mainly been developed for the pelvis,[27, 76, 77] sacroiliac joint,[78] spine,[79, 80] and long bones.[81, 82]

MRI for Three-Dimensional Bone Modeling

Three-dimensional bone renderings are gaining popularity in orthopedic care as they provide an overview of the bone morphology, enable kinematic analyses,[30, 41] and allow for the patient-specific design of surgical guides and implants.[63, 82] Hence, 3D bone models facilitate the clinical diagnosis and improve surgical outcomes,[26, 43, 70, 83-85] motivating their use in the treatment management of pathologies in the skull, shoulder, and hip.[43, 83-85] Therefore, to be a CT surrogate for bone visualization, MRI should provide images on which bone can be segmented within a time and with a level of accuracy similar to or better than what can be achieved on CT. This section describes approaches for bone segmentation on MRI and provides results on segmentation geometrical accuracy and segmentation time with applications related to surgical planning.

Bone Segmentation

Regardless of the acquired MR contrast, there is a lack of MR-dedicated, automated software for bone segmentation as exists for CT images. Bone segmentation on MR is mainly manual, or with extensive manual editing,[16, 17, 25, 28-30, 33, 41, 47, 54, 70, 86] although some (semi-)automated methods based on thresholding,[7, 26] region growing,[32] or ray casting[19] can be applied. The development of fully automated segmentation approaches is complicated by structures in the vicinity of bones that share the same intensity as (cortical) bone and that can consequently be wrongly included in the bone segmentation. The problematic anatomical areas depend on the acquisition sequence but usually include air,[54, 58, 70] and soft tissues like tendons, ligaments, or labrum. [7, 31, 81] sCT images are a special case for segmentation as they are quantitative and reproduce HU from CT images. Hence, sCT can benefit from HU-based segmentation and CT-dedicated software[27, 81, 82] as demonstrated by the segmentations of the knee bones obtained from S-GRE, Dixon water-only, sCT, and CT images in Fig. 4.

In total, MR segmentation of bone lasted from 33 seconds to 5 hours[16, 19, 29, 32, 47] in the reported literature and were made on standard of care fat-suppressed MR,[47] GRE-MR,[86] S-GRE,[31-33, 46] VS-GRE,[7, 30, 41] processed GRE-derived,[16, 25, 26, 28, 29, 43] BB,[17, 18, 54, 63, 70] ZTE,[19, 59] and sCT[27, 77, 81, 82] images. This duration depends on the anatomy, the user's experience,[16, 19, 30, 86] the segmentation method, and the desired quality of the segmentation, which hinders comparisons between studies. However, compared to CT-based segmentation within the same study, segmentation on MR images was usually more time-intensive,[16, 19, 29, 54, 86] sometimes requiring more than twice the time.[30, 43, 47] As an example, Fig. 5 presents timed segmentations of ankle bones obtained from CT and Dixon water-only images. Nevertheless, when the segmentation was done by experts or companies, no difference was noted in segmenting bone from MR or CT images in terms of processing time.[19, 63] To alleviate the impact of user's experience on bone segmentation, automated methods based on deep learning

are being developed[44, 87] and are becoming commercially available for limited applications (eg, Mimics Innovation Suite 24, Materialize, Leuven, Belgium or CoLumbo, SmartSoft, Varna, Bulgaria).

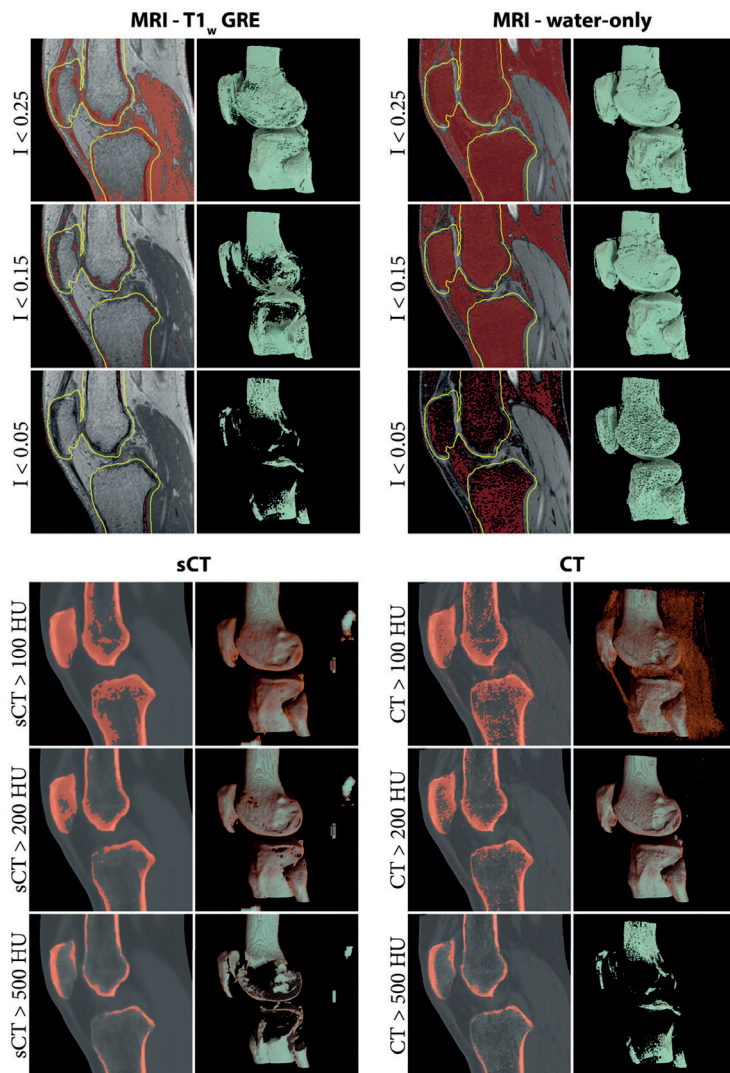


Figure 4. Bone segmentation and corresponding renderings obtained through the application of a simple threshold on magnetic resonance imaging (MRI) and computed tomography (CT) images. The low signal on acquired MR images is not specific to bone and other structures are included in the segmentation when thresholding is used alone. Therefore, for the T1-weighted gradient-echo (T1w-GRE) and water-only images, renderings were computed only in a region of 5 mm around the ground truth bones (yellow line) to focus on the bony region and hide most segmented soft tissues. Synthetic CT (sCT) images, by representing Hounsfield units (HU) enable a quick segmentation of bone, similar to what can be obtained on CT.

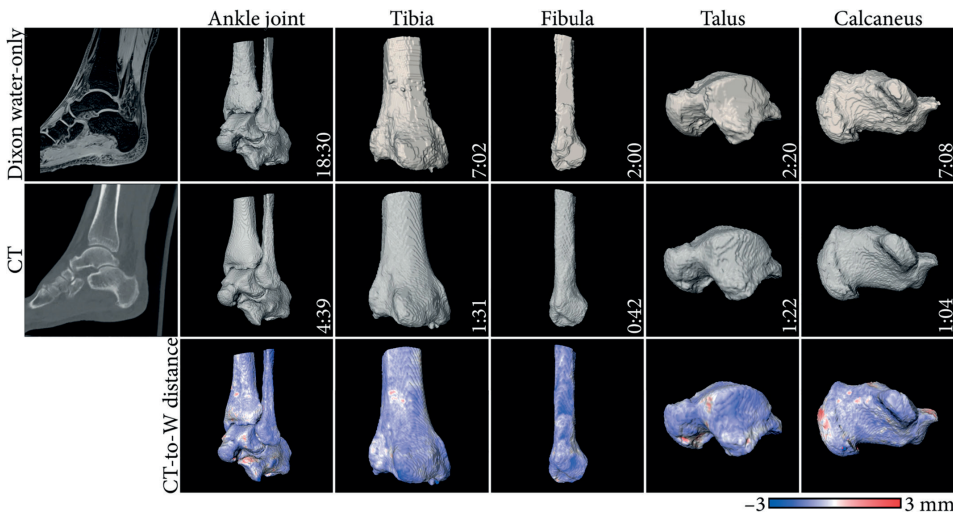


Figure 5. Example segmentations obtained from bone Dixon reconstructed water-only (W) and computed tomography (CT) images of the ankle joint.

Segmentations were performed by a junior engineer using Slicer 4.11 (<https://www.slicer.org/>). The time required to perform the segmentation is reported in the format mm:ss. Surface distance maps from CT to magnetic resonance imaging (MRI)-based bone renderings are displayed. Negative values indicate the CT-based segmentation is larger.

Bone Geometrical Accuracy

Regions prone to motion or magnetic field inhomogeneity could compromise the geometrical accuracy of the bone as seen on MR images. The geometrical integrity of the image can also be altered by nonlinear encoding gradients that may introduce compression or stretching of parts of the image. Because geometrical distortions could alter bone morphology, and consequently MR diagnostic capabilities, the overall geometry of the bone as visualized using MRI has been compared to physical ex vivo specimens and in vivo to CT, which is reviewed below.

COMPARISON TO BONE CADAVERIC SPECIMENS

The geometrical accuracy of bone segmentation has been evaluated on long bones and vertebrae in ex vivo studies so that MR segmentation could be compared to the physical bone shape using 3D printing,⁴⁷ mechanical contact/optical scanners,^[18, 31-33] or micro-CT.^[31, 82] Bone specimens were processed to remove soft tissues, resulting in a potential shrinkage of the gold standard compared to the bone as scanned using MRI and CT.^[18, 25, 33, 82]

On average, CT segmentation overestimated the actual bone shape, whereas MR segmentation mostly underestimated it,^[31-33, 47] although not consistently.^[25, 82] Nevertheless, surface distances between the MR-based segmentation and the

cadaveric specimen were on average submillimeter,[17,25 31,33,82] with mean absolute surface distances ranging from 0.23 mm to 0.41 mm for MR-segmentations and from 0.15 mm to 0.51 mm for CT-based segmentations.[17,25,31 33] Similarly, root mean square error (RMSE) was mainly submillimeter,[18,31,33] although it could reach 1.2 mm³² in the knee for MRI models (vs. 0.5 mm for CT models).

When the CT-based segmentation was used as a reference, the MR-based bone segmentation also showed a submillimeter accuracy. In ex vivo long bones, absolute surface distances ranging from 0.23 mm to 0.61 mm were reported,[31, 38, 81] with limits of agreement of the signed surface distance within ± 0.72 mm,[18] and RMSE of 1.1 mm.[88] In ex vivo skulls, which can be harder to register and segment, BB-MRI segmentations deviated on average by ± 1.4 mm from CT segmentations.[63]

Larger differences were generally observed between the reference and MRI models near the joints in the proximal and distal bone ends,[31, 82] although not always with statistical significance.[18] Such differences resulted from the multiple soft tissues present at these locations (muscle, tendons, cartilage, and ligaments) which induce partial volume effects that hinder bone segmentation and warrant manual editing.[31, 81] Alternatively, errors were observed at the edge of the field of view (FOV), where there is less signal.[33]

COMPARISON TO CT-BASED BONE SEGMENTATION IN VIVO

The average submillimeter accuracy of bone segmentations compared to bone specimens shows that MR images have the ability to provide geometrically accurate bone models. To take into account soft tissue, evaluate more complex anatomies, and to make comparisons in an in vivo setting, MR segmentations were compared to CT segmentations. In in vivo hip joints, MR bone models differed on average by 0.4–0.9 mm from CT models,[27, 30] with average RMSE under 1.8 mm[30] for VS-GRE Dixon images and under 0.81 mm for sCT images.[77] When considering in vivo knees, there was no difference in the width and volume of the medial tibial plateau, with highly consistent measurements between standard of care PDw MR and CT images.[89]

This geometrical accuracy was influenced by the MR sequence acquired to perform the segmentation. Compared to other MR sequences, VS-GRE offered the best correspondence to CT in the knee, with up to 45% differences in surface distance between VS-GRE and balanced steady-state GRE or spin-echo derived images.[38] VS-GRE sequences had a better soft-tissue-to-bone contrast, offering easier and more reproducible segmentations. Unfortunately, studies did not often report on registration parameters and acquisition parameters, such as the receiver bandwidth (see Table 1) or the built-in distortion correction that can affect surface distance measurements and geometrical accuracy,⁶⁶ preventing further comparisons between sequences and studies.

Surgical Planning

Bone models obtained from segmentations can serve as a diagnostic tool in the therapeutic decision-making, but also for surgical planning by allowing the design of customized surgical guides and implants.

In the lower arm, saw guides for osteotomy were designed from CT and MR-based sCT images and placed on cadaveric bones.[82] The average saw guides positioning errors compared to the virtual planning were 2.4 mm and 3.8° for CT-based guides and 2.8 mm and 4.9° for sCT-based guides. More specifically, there were no intermodal statistically significant differences in the guides positioning. In addition, the intermodal rotational and translational limits of agreements were within the interobserver limits of agreement, suggesting the interchangeability of CT and sCT for the design of guides for long bone osteotomy. As an example, Fig. 6 shows saw guides positioning differences between CT and sCT.

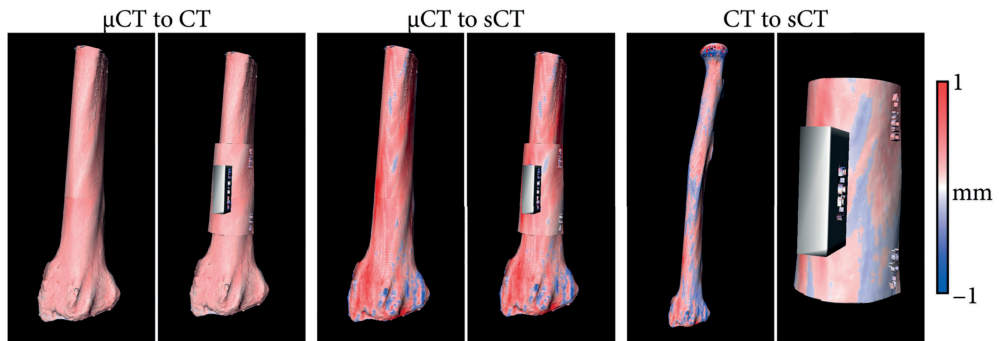


Figure 6. Example of an ex vivo radius used for evaluating different modalities for osteotomy planning. Bone renderings were generated from micro-CT (μ CT), CT, and synthetic CT (sCT) images and were used to design saw guides in identical locations. The color map indicates the surface distance between the bone renderings/saw guides obtained from the different modalities. Negative values indicate the μ CT/CT is larger.

In the skull, deviations of ± 1.4 mm were reported between BB-MR and CT segmentations.⁶³ The surgical guides resulting from the corresponding bone models were positioned on the skull with errors within ± 0.6 mm for CT-guides and ± 0.8 mm for MR-guides relative to their respective virtual planning. Given such differences, the average deviation from planned postoperative craniofacial reconstruction was within ± 1.3 mm when using CT-based guides and ± 1.5 mm when using BB-MRI-based guides, with no statistical differences between the two modalities.[63]

MRI for Diagnosing Bone Pathologies

Bone visualization and diagnosis on MR images can be hampered by the presence of water-fat interfaces, specific soft tissues like tendons, or air pockets in the vicinity of the bone since they may share the same low signal (Fig. 4). Therefore, the advantages and challenges of employing MRI for diagnosing bone-related pathologies are anatomy-specific. Multiple regions, including the skull, spine, shoulder, and pelvis have been assessed in recent years and are discussed in this section. For each anatomical region, the focus has been placed on two aspects: the potential of MRI for 1) detecting structural changes and for 2) measuring morphometric parameters of the bone. Structural changes include the detection of fractures, bone erosion, or sclerosis. On the other hand, morphometric parameters offer a quantitative assessment of bones which provides a standardized discrimination between “normal” and pathological regions and can influence therapeutic decision-making.

Skull

The development of MR protocols for skull visualization was favored by the routine acquisition of MR images for a wide range of clinical indications. In the standard of care, CT is indicated for trauma patients and for detecting osseous lesions, whereas MR images can be acquired for the detection of intracranial pathologies such as hemorrhage, ischemic changes, tumor, or other neurological disorders.[1, 2, 52, 53, 57, 70]

STRUCTURAL CHANGES

Skull composition and anatomy vary between stages of life, resulting in an age-dependent diagnostic power of MRI and CT. Infants under 6 months have a thin skull (~1 mm thick) with high water content.[64] In children under 2 years of age, sutures are wider[61, 83] and harder to distinguish from trauma-induced fractures.[61, 70] Lastly, cranial sutures tend to be less conspicuous in adults than children on BB-MRI[20] and UTE-MRI[54] as compared to CT because of a lower suture-to-skull contrast in adults.

Nonetheless, the premature fusion of cranial sutures could be evaluated in infants and children with good to excellent inter- and intraobserver variability.[20, 64] For detecting skull fractures in children, BB-MRI had an overall sensitivity of 66.7% and specificity of 87.5%, with errors originating from confusion between linear fractures and sutures, mainly in children under 2 years of age.[61] However, the addition of BB-MRI-based 3D skull renderings increased the sensitivity to 83% and the specificity to 100% in a different cohort of patients under 30 months.[70] Skull renderings obtained from MRI as shown in Fig. 7 were stated to be valuable for diagnosis in most patients,[70] which is in line with results obtained in CT images.[83] When UTE-MR images were used, promising results were reported for the detection of fractures in patients aged from 1 month to 71 years. [52] Sensitivity, specificity, and accuracy were all higher than 90%.[52] The length and depth of the fractures could be measured on UTE-MR images with no statistical difference

compared to measurements made on CT images. For both UTE and BB-MRI,[52, 70] good to excellent inter and intraobserver agreement was reported for detecting fractures. Moreover, MRI could detect other pathologies such as edema, axonal injuries, and fractures accompanied by hemorrhages that were not visible on CT.[52, 61]

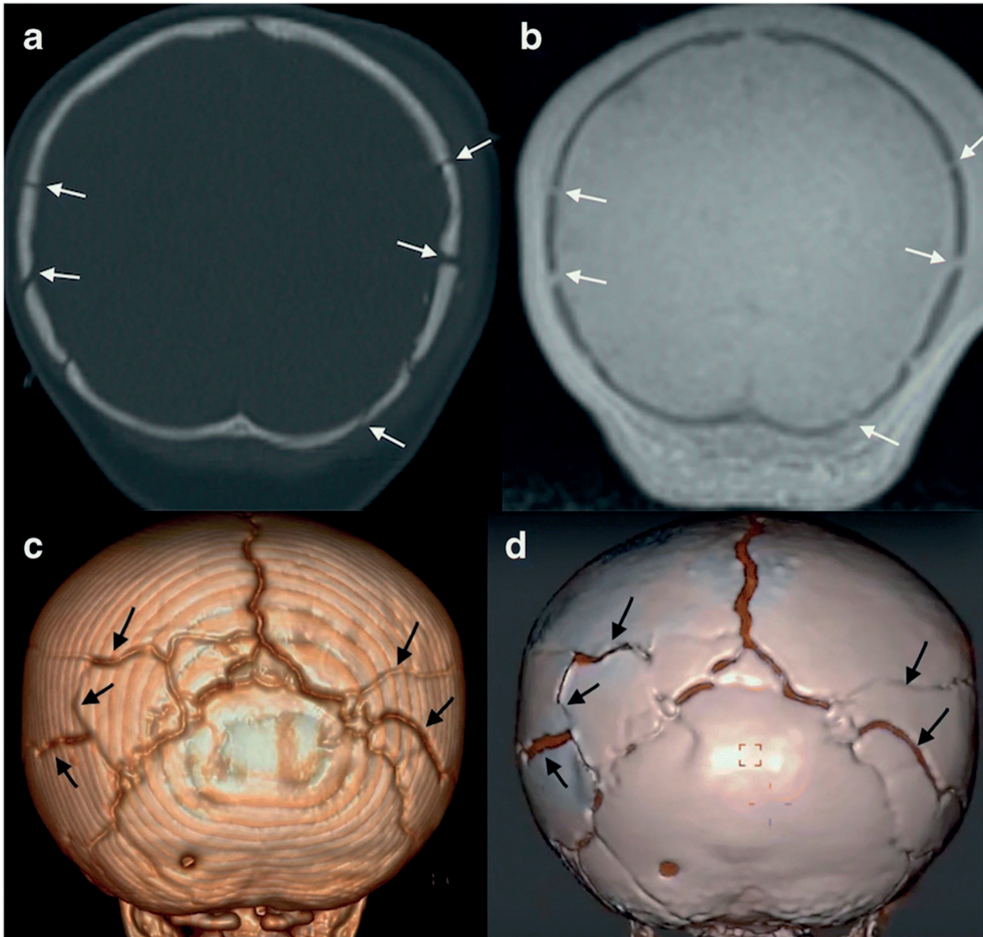


Figure 7. A 9-month-old with multiple skull fractures (arrows) demonstrated on coronal head computed tomography (CT) (a), and coronal black bone magnetic resonance imaging (MRI) (b) and the corresponding 3D rendering (c, d). Reprinted by permission from Springer Nature from reference 70.

With regard to the temporomandibular joint and mandible, other structural differences were visible on UTE- and ZTE-MRI with good to excellent inter- and intraobserver variability,[53, 57] benefitting from a good UTE/ZTE-to-CT voxelwise intensity correlation in healthy and diseased bones.[21, 53] ZTE-MRI revealed flattening and osteophytes in the mandibular condyles with near-perfect agreement to cone beam CT[57] whereas

intermodal agreement for detecting medullary sclerosis was excellent on ZTE and moderate on UTE images.[53, 57] However, erosions, osteolysis, and periosteal reactions were more difficult to diagnose with only moderate intermodal agreement. In particular, periosteal reactions could be confused with air pockets on UTE images as both bone and air share similar intensities.[53]

Overall, all MR images suffered from misdiagnoses at interfaces between bone and air. Air and bone share similar intensities, making the bone/air interface difficult to distinguish. [52, 54, 61, 70] Particularly difficult regions were the mastoid process,[52, 61, 70] the paranasal sinuses,[52, 70] and complex bone/fluid interfaces with high anatomical details like the inner ear.[58] Such interfaces can cause misdiagnoses[58, 61] and complicate automated processes for segmentation.[54, 87] To facilitate the distinction between tissues and air, phase information could complement the magnitude images,[90] although the processing of phase images is complex and can be error prone.[90, 91]

MORPHOMETRIC ASSESSMENT

Following the diagnosis, morphometric analysis of the mandible and cranium can be performed to plan craniofacial or maxillofacial surgeries.[54, 65] However, the measurement of such local parameters on MR images was not consistent between studies.[54, 65] On UTE-based skull segmentations, intermodal differences of up to 2 mm and average deviation to cadaveric measurements of up to 4 mm were reported for eight anatomical parameters.[54] By comparison, on SE-derived images, performances were deemed statistically equivalent to cone beam CT, with average differences under 0.61 mm and 0.65° for 27 parameters[65] and BB-based bone segmentations deviated by ± 1.4 mm from CT segmentations.[63] Such differences might be due to differences in resolution as the voxel size was twice as small on T1w-SE and BB-MRI images as on UTE images (~ 0.5 mm vs. 1.1 mm).[54, 63, 65] The T1w-SE and BB acquisitions also had high receiver bandwidth (>610 Hz/px—Table 1) to maintain geometrical integrity.

Spine

When imaging the spine, MRI is the modality of choice in many applications as it offers valuable information on the neural structures, the intervertebral discs, bone marrow, and the surrounding soft tissues.[17, 36] CT is typically acquired to assess the osseous involvement of soft tissue pathologies, for assessing bony abnormalities such as fractures, spondylosis, spondylolysis, or for surgical planning,[5, 17, 39] owing to the superior cortical bone contrast and to the isotropic resolution of CT that enables multiplanar reformatting. [5]

STRUCTURAL CHANGES

When patients are suspected of having a vertebral fracture, CT images are routinely acquired to depict the extent of fracture. In addition, CT imaging is preferred in patients for whom a quick assessment is required, eg, patients who suffered high-velocity accidents. Additional MRI is sometimes acquired, mainly to rule out occult injuries and to identify spinal cord lesions.[4] In this context, MRI can also aid in distinguishing acute from old fractures,[3] and can help diagnose specific types of fractures, such as stress fractures.³⁹ Diagnostic performance statistics for detecting acute or stress fractures on MRI were excellent for S-GRE, VS-GRE, and UTE images with specificity, sensitivity, and accuracy above 90% when CT was used as ground truth.[36, 37, 39] The interobserver agreement was good to excellent[36, 37, 39] and was comparable between CT and MRI. [37, 39] For standard of care SE images, the specificity and accuracy for detecting fractures was above 95% while the sensitivity was 75% for incomplete fractures and 91% for complete fractures.[22]

Overall, GRE images, including S-GRE and VS-GRE seemed to outperform standard of care SE images for detecting fractures,[22, 37] demonstrating a higher sensitivity in the delineation of the fracture line, probably owing to their thinner slices (see Table 1). Regarding S-GRE and UTE images, differences are more questionable. In a cadaveric study,[37] S-GRE was reported as the most decisive standard of care sequence for detecting fractures in the pars interarticulares but observers were more confident in their diagnosis and missed fewer fractures when using UTE-MRI. In particular, UTE imaging demonstrated a better interobserver agreement thanks to its CT-like characteristics and a better contrast between the bone and fracture gap.[37] On the other hand, in patients with suspected acute vertebral fractures, S-GRE images outperformed UTE images in terms of the intermodal and interobserver agreements for detecting fractures, which was also the case for sclerosis, osteophytes, and joint degeneration.[36] The difference in diagnostic quality between UTE and S-GRE images between the cadaveric[37] and in vivo³⁶ studies might have several sources. In vivo, despite the radial k-space sampling, the UTE images were reported to be prone to pulsation and motion artifacts[36] that were not present ex vivo. In addition, the presence of multiple tissue types and air in the surrounding of the spine could result in susceptibility artifacts, especially seen in UTE images, more than GRE or ZTE images.[5, 36] A comparison between S-GRE, UTE, and CT images for the detection of acute fractures and osteophytes is given in Fig. 8.

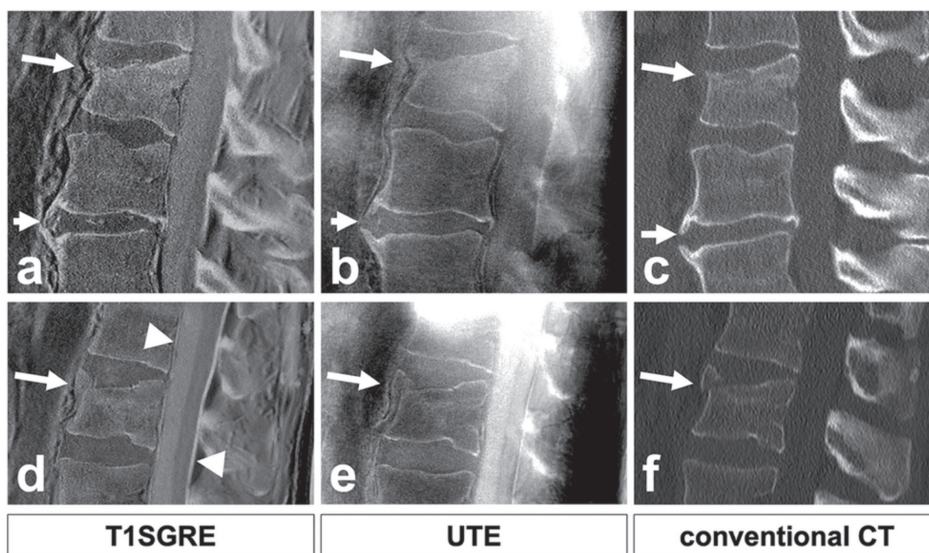


Figure 8. Comparison of T1SGRE-derived CT-like images (a, d), UTE images (b, e), and conventional CT images (c, f). In one patient (a–c), a wedge-compression fracture of L1 with signs of an acute pathology such as a compaction zone can be depicted (upper arrows), as well as ventral and small dorsal osteophytes on level L2/3 (lower arrows). In another patient (d–f), another wedge-compression fracture of L2 with a triangular teardrop-like fragment can be identified (arrows). Also note the thin hyperintense line running longitudinally along the posterior walls of vertebral bodies representing the posterior longitudinal ligament as well as the thicker hyperintense line posterior to the dural sac representing the ligamenta flava (arrowheads; d), which are not depicted on CT (f), and must not be misinterpreted as ligament calcifications. Figure reproduced without modification from reference 36 under the Creative Commons Attribution 4.0 International License (<http://creativecommons.org/licenses/by/4.0/>). T1SGRE = T1 radiofrequency spoiled gradient-echo; UTE = ultrashort echo time; CT = computed tomography.

SE, S-GRE, VS-GRE, and UTE sequences all misdiagnosed fractures in some patients,[22, 36, 39] in part because of the misinterpretation of areas of bone sclerosis. These could be confused with subtle fractures or edema-like changes,[36, 39] or could mask fractures.[22] However, the addition of a fluid-sensitive MR sequence like short tau inversion recovery could reveal bone marrow edema and enable the detection of stress reactions that are invisible on CT images[22, 36, 39] but can potentially change the patient's clinical management.[39] For diagnosing sclerosis, GRE images seemed superior to UTE images[36] or SE images as seen in the sacroiliac joint.[42, 92]

Other structural anomalies, including degenerative changes in the craniocervical junction[55] and in the cervical spine[5] that can cause neck pain were also investigated. In these cases, MRI is suitable for detecting ligamentous or intervertebral disc pathologies whereas CT can detect stenosis of the cervical spinal canal or neuroforamina.[5] In both the craniocervical junction and cervical spine, degenerative changes were graded with

good intermodal agreement,[5, 55] similar to the interobserver agreement on CT.[5] This was facilitated by multiplanar reformatting possible on isotropic ZTE images.[5] Overall, good to excellent inter- and intraobserver agreement was reported with MRI.[5, 55] However, when using MR images with inverted intensities, care needs to be taken not to misinterpret the apparent high signal intensity of ligaments, or of the gas accumulation in the intervertebral discs as calcifications[36] as seen in Fig. 8.

MORPHOMETRIC ASSESSMENT

The diagnosis of degenerative changes can also be made quantitatively by measuring morphometric parameters including vertebral body and intervertebral disc parameters. Despite a good to excellent intermodal agreement in measuring vertebral body height on UTE, S-GRE, and sCT images, and an excellent interobserver agreement,[36, 79] the accuracy of morphological vertebral assessment was highly dependent on the MR acquisition. Average differences in the vertebral height of 0.26mm were reported in the sCT[80] with limits of agreement within ± 2 mm for S-GRE images[36] and within 6–10mm for UTE images.[36] For intervertebral disc heights, limits of agreement of ± 2 –3 mm were reported between S-GRE and CT images and of ± 4 mm between UTE and CT images.[36] Similarly, CT/UTE intermodal limits of agreements were within ± 1 mm for the distance between the cranium and C1 and within ± 2 –4 mm between the cranium and C2.[55] However, these intermodal differences in the distances between the cranium and cervical spine were not significant and may partly originate from the differences in resolution between MR (0.8 mm \times 0.8 mm \times 1.2 mm) and CT (<0.6 mm \times 0.6 mm \times 0.6 mm).

Shoulder

In the shoulder, MR examinations are commonly performed to examine the ligaments, the rotator cuff, the labrum, and the joint capsule, eg, after shoulder dislocation. [7, 35, 93] However, standard of care T1w-SE images have similar low intensity for cortical bone and labrum,[40] warranting a CT examination to assess the glenohumeral bone architecture and review bone changes. In particular, the amount of glenoid bone loss, and to a lesser extent humeral deformity, often associated with shoulder dislocation, determines the clinical management plan.[86]

STRUCTURAL CHANGES

On MR images acquired with[35, 40] or without[94] intra-articular contrast injection, a strong correlation ($r > 0.8$) was found between MR and CT for the glenoid width and percentage bone loss. The mean glenoid bone loss error was under 2.5% for both modalities,[94] with intermodal differences not statistically different.[35, 40] Furthermore, MR and CT measurements had good correlation with arthroscopy as percentage bone loss differences under 3% were reported between MR and arthroscopy and under 1% between CT and arthroscopy.

When MR-based 3D bone renderings were compared to CT, bone defects were also equivalently visible on the bone reconstructions[16] with no statistically significant differences between MR- and CT-based renderings,[7, 29, 86] good to excellent intermodal correlation,[7, 86] excellent intermodal agreement,[19, 26] and submillimeter/<1% average defect size difference.[7, 19, 29] Although small on average, some intermodal differences could reach up to 3 mm/10% difference in glenoid bone loss,[19, 86] potentially influencing clinical management for a minority of patients. However, such large differences were not systematically reported, with some maximal differences within $\pm 7.5\%$. [26, 35, 40]

In addition to diagnosing bone loss, MR was used to detect fractures in the humerus and scapula with good intermodal agreement, and excellent sensitivity and specificity (>90%) [40, 59] using ZTE-MR and VS-GRE images. Fracture extent was measured equivalently on MR and CT.[16] ZTE-MR images were able to reveal bone depression, bone resorption, and bone fragments better than standard of care PDw images in most patients, along with a good ZTE-to-CT intermodal agreement for detecting bone fragments and osteoarthritis. [59] Moreover, ZTE-MRI surpassed CT in revealing cortical bone and intraosseous lesions within a single image.[59] In particular, bone marrow edema and cysts that remained undetected in CT were visible on ZTE images. As cysts indicate regions of lower bone quality, it is important to accurately detect them, particularly when the images are used for guidance of surgical planning.[59]

MORPHOMETRIC ASSESSMENT

Treatment planning of shoulder instability might include the measurement of morphometric parameters of the glenoid on 2D images or 3D renderings. The glenoid morphometric accuracy on MRI was comparable to CT as demonstrated by an excellent intermodal agreement with no statistical difference in the measurement on glenoid vault[59] and glenoid version angle,[59, 93, 95] using ZTE[59] or standard of care MR images.[93, 95] Intermodal agreement was good when comparing certain shoulder-specific parameters, with limits of agreements within 6 mm for measuring glenoid vault depth[59] and within 5° for the version angle[59, 95] for most patients. However, for some patients, these measurements could differ drastically due to blurring and reduced FOVs on the MR images.[59, 95] The intermodal limits of agreements were within the interobserver limits of agreement.[59]

In a similar way, the geometrical accuracy of MR-based 3D bone renderings was compared to CT. Measuring glenoid/humeral width, height, and surface areas was equivalent between CT and MRI, although some statistically significant differences could be found[16] but not systematically.[7, 29] In particular, the average intermodal differences in glenoid

and humeral surfaces were within $\pm 10\%$, [7, 29] and in glenoid/humeral width and height were within ± 1 mm. [16, 29]

Based on bone rendering and radiography, kinematic analysis of joints can also be performed to quantify changes to the joint position and contact points. [41, 46] Hence, using S-GRE or CT-like VS-GRE images, digitally reconstructed radiographs (DRR) have been generated and registered to radiography images for shoulder and knee kinematic analyses. [41, 46] Registration errors and kinematics measurements errors were larger for MR-based DRRs than CT-based DRR and showed an RMSE under 2.2 mm and 2.6° (vs. 1.6 mm and 2.2° for CT). [41, 46] Because CT and radiography share the same contrast mechanism, intensity-based metrics can be used for the CT-DRR to radiograph registration whereas only edge-information was used for the MRI-DRR to radiograph registration, [41] potentially explaining the larger registration errors of MRI-based DRRs.

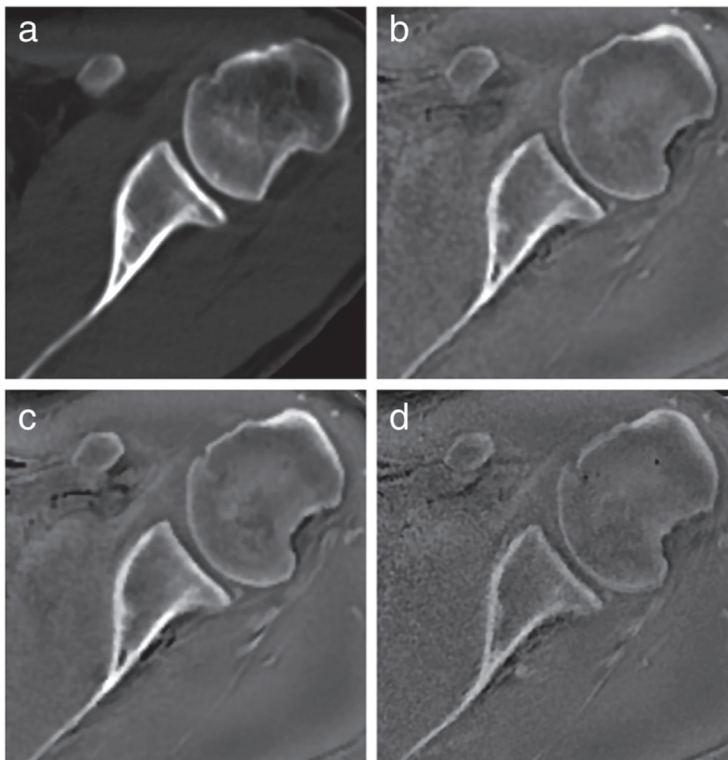


Figure 9. Axial computed tomography and zero echo time magnetic resonance imaging of left shoulder in a 38-year-old man. Axial images obtained by computed tomography (a) and zero echo time magnetic resonance imaging at 1.0 mm^3 (b), 0.8 mm^3 (c), and 0.7 mm^3 (d) all show high-contrast imaging of the osseous structures, including the glenoid and glenohumeral joint. Reprinted with permission from reference 19.

Overall, MR and CT showed good to excellent inter- and intraobserver variability in diagnosing bone pathologies or performing morphometric measurements in the shoulder,[19,26,35,40,93,95] with good to excellent intermodal agreement.[19,26,59,86] Figure 9 compares the CT image of a shoulder to the corresponding ZTE images acquired at different resolutions.

Pelvis

The pelvic bone connects the upper body to the lower limbs through the sacroiliac and hip joints. Both joints can be subjected to degenerative osteoarthritic changes, affecting the bone and the surrounding soft tissues. In the sacroiliac joint, spondyloarthritis induces bone marrow edema and inflammatory lesions that can be detected with MRI, and structural lesions such as erosions, sclerosis, or ankylosis that may be detected with MRI,[96, 97] but are better defined on CT.[6, 97, 98] In the hip joint, hip dysplasia and femoroacetabular impingement are morphological hip conditions that affect bone, and soft tissues including but not limited to cartilage and labrum. For these conditions, clinical care usually includes morphometric assessment of the joint made on radiograph, with optional addition of CT or MRI for diagnosis, a soft tissue evaluation with MRI and a bone rendering based on CT for surgical planning. To limit adverse ionizing radiation, MR has been investigated as a diagnostic tool for detecting structural bone lesions and performing bone morphometric assessments and 3D renderings.

STRUCTURAL CHANGES

In the sacroiliac joint, SE, GRE, and sCT images were used to assess structural changes. T1w-SE images were shown to strongly correlate with low-dose CT for detecting erosions and were able to reveal 88% of erosions.[92] However, standard MRI missed some cases of axial spondyloarthritis when used alone.[92] On more dedicated images to visualize bone, including VS-GRE or sCT images, higher diagnostic accuracy and diagnostic confidence were achieved for detecting erosions,[6, 42, 78] especially when sclerosis was present. [42] In particular, the sensitivity and specificity for detecting erosions increased between standard and dedicated images, reaching a sensitivity above 70%,[6, 42, 78] a specificity around 90%,[6, 42, 78] and an accuracy above 90%.[78] A qualitative comparison between T1w, VS-GRE, and CT images for diagnosing erosions is presented in Fig. 10.

Standard MR images were also able to detect 92% of joint space alterations, and to a lesser extent sclerosis,[92] while sCT could diagnose sclerosis and ankylosis with accuracies higher than 90%.[78] Dedicated MR imaging was also reliable owing to a good to excellent interobserver agreement[6, 78] and repeatable with good intraobserver agreement,[78] in accordance with CT imaging.[6, 78] Moreover, observers were more confident when scoring VS-GRE images than low-dose CT images because of the noise of low-dose CT[42] and equally confident when scoring sCT compared to CT images.[78] Some

erosions were only visible on dedicated MR images and not on CT images,[6, 42] especially in young patients⁶ and for small lesions.[42] As no erosions were detected in healthy controls,[42] this suggests that the observed destructive changes were no artifact and that MR was superior in revealing those erosions.

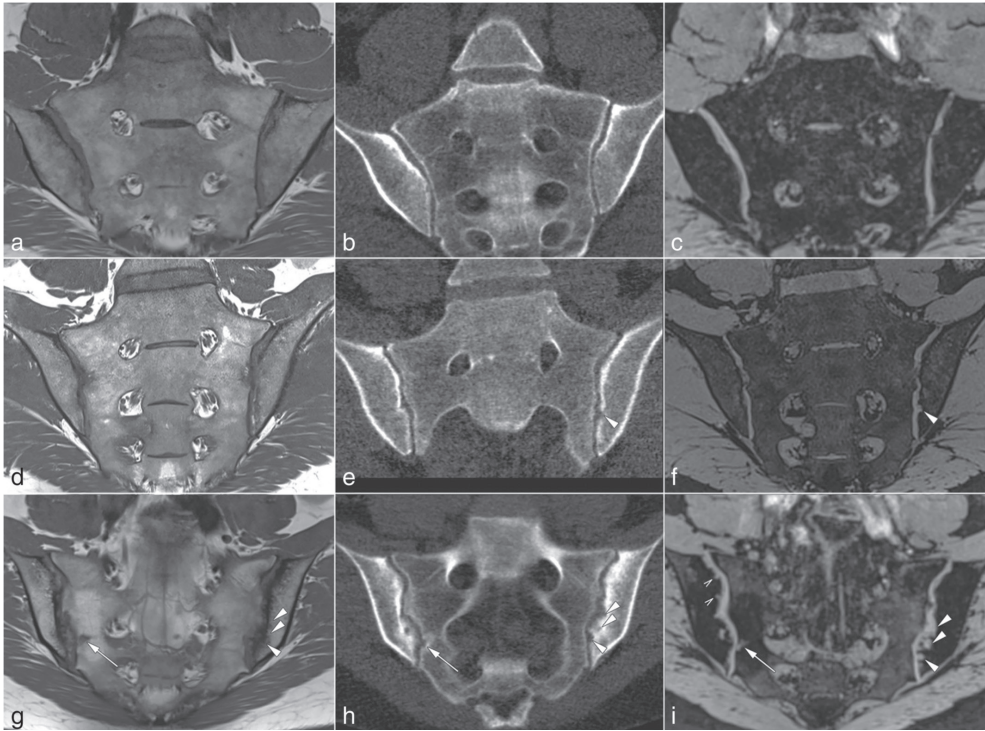


Figure 10. Imaging examples. (a, d, and g) Oblique coronal MR-T1 sequence; (b, e, and h) low-dose CT images in oblique coronal reconstruction; (c, f, and i) oblique coronal MR-VIBE sequence. Slice positions and orientation are identical for T1 and VIBE. Low-dose CT was reconstructed to match orientation and position. (a–c) normal findings in the sacroiliac joint without erosions. (d–f) Patient with axial spondyloarthritis with a single but prominent erosion of the left iliac surface that is shown by low-dose CT and MR-VIBE (arrowheads) but not by MR-T1. (g–i) Patient with axial spondyloarthritis and multiple erosions. Some erosions (arrow) are depicted by all modalities. However, some larger erosions are hardly seen with MR-T1 due to sclerosis, while they are more conspicuous using low-dose CT and MR-VIBE (arrowheads). The smallest erosions are only depicted with MR-VIBE (open arrowheads). MR = magnetic resonance; CT = computed tomography; VIBE = volumetric interpolated breath-hold examination. Reprinted with permission from reference 42.

In addition, MR images have been acquired to describe fractures in the hip joint. MRI has been shown to perform better than CT for the detection of fractures in the hip in elderly patients,[99, 100] but also in adolescents[101] and children.[101-103] All fractures detected on CT were also detected on MR[100, 101] and some fractures were visible on MR but not CT,[101] or misdiagnosed on CT resulting in changes in the clinical

management plan,[100] especially regarding instructions for weight bearing. In patients under the age of 13 years, the posterior acetabular wall is not fully ossified[103] and the MRI findings of traumatic hip dislocations with acetabular fractures were better correlated with intraoperative findings than CT findings,[102] which did not always directly detect acetabular fractures.[103] Some soft tissue defects, oblivious to CT, were also identified on MRI. These included entrapment of labra and posterior acetabular cartilage fractures. The detection of entrapment of labra, in particular, had an influence on the patient clinical management.[101]

MORPHOMETRIC ASSESSMENT

The measurement of morphometric parameters is especially important in the hip joint for the diagnosis of hip dysplasia and femoroacetabular impingement and has been investigated on VS-GRE,[43, 45] ZTE,[23] sCT,[77] or intermediate-weighted images.[43] All imaging techniques found good to excellent intermodal agreement for measuring the acetabular version[23, 43, 45, 77] with excellent inter- and intraobserver agreements[23, 45, 77] and statistically equivalent measures given an acceptable error below 4.3°.[45, 77] The reported limits of agreements were, however, mixed. On VS-GRE and sCT images, intermodal limits of agreements were in line with the intraobserver variability, within $\pm 4.2^\circ$. [45, 77] On ZTE images, on the other hand, intermodal limits of agreements of acetabular version reached 11.3°, higher than the 8° obtained for the interobserver variability on CT.[23] These differences might originate from the fact that pelvic tilt was not standardized in the ZTE study.[23] Other parameters that were compared include the lateral center edge and alpha angles. The intermodal agreement was good to excellent[23, 43] with intermodal limits of agreements roughly within 12°[23, 43, 77] and bounded by the interobserver limits of agreement achieved on CT.[23]

Femoral parameters such as the femoral anteversion were also measured and compared between CT and MRI. In two studies using standard clinical sequences,[104, 105] a strong correlation between CT and MR measurements was reported with correlation coefficients of 0.77 and 0.80 between the two modalities. However, the intermodal absolute agreement was poor with biases ranging from 5° to 10°, probably because of interscan positioning differences. The MR examination being long (30–45 minutes), patients might be given knee wedges[105] to bend the knee, or can relax into greater external rotation of the hip, possibly explaining such differences. When measured in infants with developmental dysplasia of the hip[106] on CT and T1w-SE images, the intermodal, intraobserver, and interobserver agreements for the femoral version were all excellent (intraclass correlation coefficient >0.9), demonstrating the reliability and reproducibility of the methods. In such a young population, MRI had the advantage over CT that it was able to visualize the not fully ossified femoral condyle in infants under the age of 6 months. In these cases, the condylar plane could be defined more accurately on MR than CT.

Using bone renderings, the measurement of local morphometric parameters, including the center-edge angle and acetabular version was similar between CT and MR, with average intermodal differences under 4° . [28, 30, 44] Hip range of motion measurements were also compared between CT and MR with average differences under 4° for all rotations and with limits of agreements within $\pm 6^\circ$. [30] All measurements had excellent intermodal correlation, intermodal agreement, and interobserver agreement. [30, 44] Correspondingly, such models were able to diagnose femoroacetabular impingement or hip dysplasia with 100% agreement reported between MR and CT for the presence and location of cam deformity, [28] and good to excellent intermodal and interobserver agreements. [43] Figure 11 presents 3D bone reconstructions as obtained from CT and sCT.

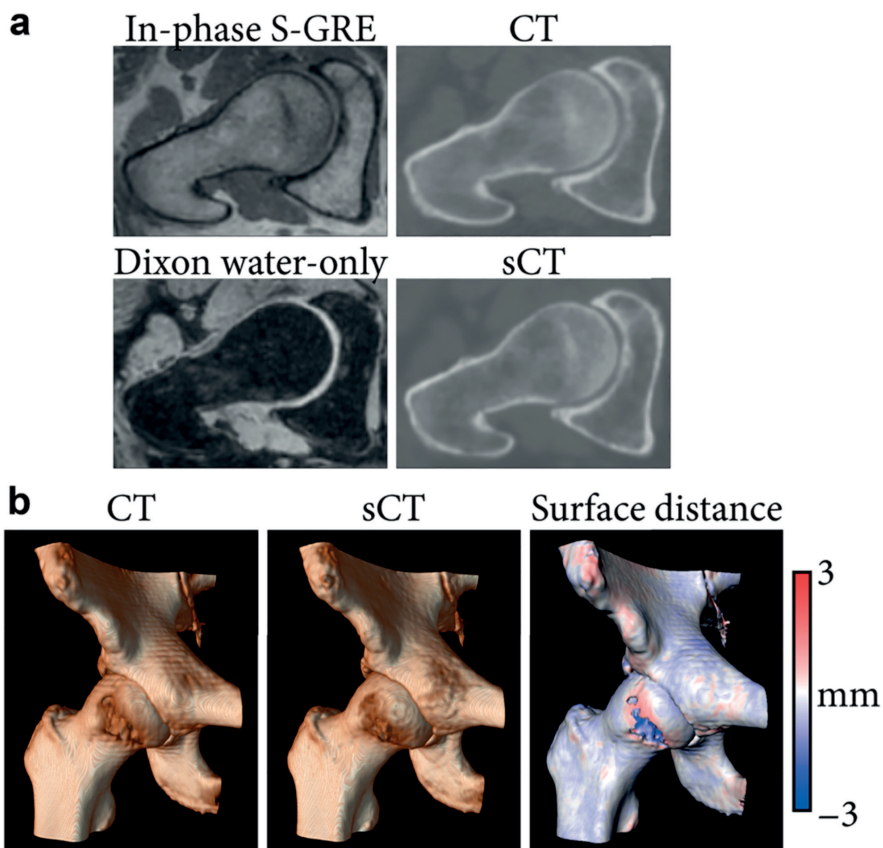


Figure 11. Magnetic resonance imaging (MRI)- and computed tomography (CT)-based hip imaging. (a) Radial reformats of in-phase radiofrequency spoiled gradient-echo (in-phase S-GRE), Dixon reconstructed water-only, CT, and synthetic CT (sCT) images. (b) Bone renderings obtained by applying a 150 Hounsfield unit threshold on CT and sCT images of a hip joint. Surface distance between the CT- and sCT-based renderings was computed and mapped on the CT-based rendering. Negative values indicate the CT is larger.

Remaining Challenges

Overall, the use of MRI as a radiation-free alternative to CT for bone visualization has received a lot of attention in the last decade and has been valued by multiple editorials[107-109] and overviews.[110, 111] Although promising, MRI does suffer from challenges related to data acquisition and accessibility to novel technologies. This section describes these challenges and discusses how they might affect the adoption of MRI for bone imaging in clinical practice.

Challenges in the Acquisition

When planning an MRI scan, a trade-off has to be made between the FOV, the resolution, the signal-to-noise ratio (SNR), and the acquisition time. The MRI sequences used for bone visualization pose different constraints to this trade-off which may limit their applicability in specific situations. These constraints are related to several external factors, including the size of the region to be imaged, or also the intrinsic tissue-specific factors like magnetic susceptibility. In this section, we address these aspects in relation to their use for bone visualization.

FIELD OF VIEW

In general, a limited FOV is chosen when planning MRI acquisitions to reduce scan time. However, some sequences like UTE or ZTE have spatially nonselective excitations which induce large fields of view and reduce their flexibility regarding other acquisition parameters (eg, spatial resolution) to keep a reasonable scan time.

For other sequences, the freedom to reduce the FOV has two constraints. First, the FOV must be large enough to make a proper diagnosis. This includes the visualization of landmarks for post-acquisition image standardization (eg, correction of the anterior pelvic plane for hip imaging) and of a sufficiently large region for the measurement of morphometric parameters (eg, scapula for measuring the glenoid version in the shoulder[95] and femoral shaft and condyles for measuring the femoral neck shaft angle[23, 43]). Second, care needs to be taken to avoid the edge of the FOV where the lower signal and field inhomogeneity may compromise the measurements.[33] As a solution, MR images can be acquired in multiple blocks, overlapping or not, to obtain the necessary information. [18, 24, 30-32] Such multi-station acquisitions are, however, susceptible to slight changes in position between individual acquisitions that can compromise the geometric integrity of the bone.[24]

SPATIAL RESOLUTION

Image resolution was often lower on MRI than on CT, with voxel sizes usually ranging between 0.6mm and 1 mm in the reviewed literature (see Table 1). Note that some of the reported resolutions are reconstructed resolutions and not acquired resolutions. Low-

resolution images induce more partial volume effects that can mask[54] or, on the contrary, enlarge structures of interest, potentially resulting in the under- or over-segmentation of bone on MR images.[58] Furthermore, for 3D bone modeling, low resolutions result in high interpolation uncertainty and can cause stair-step artifacts.[47, 59, 112] However, increasing the resolution is not always beneficial as it is accompanied by a decrease in SNR or an increase in acquisition time without necessarily improving the diagnostic capabilities of the images.[19, 36, 38]

MR images usually had an (almost) isotropic resolution in the literature assessed for this review (Table 1). The voxel isotropy enables multiplanar reformatting of the images for an improved visualization of the vertebrae, of the glenoid, or of the femoral neck for the measurement of morphometric parameters in these regions. In addition, for 3D bone modeling, voxel isotropy makes the interpolation uncertainty equal in all directions, facilitating bone models interpretation and the subsequent modeling of surgical tools.

ACQUISITION TIME

Long acquisition times are problematic as they induce higher costs and potential motion artifacts. In children, in particular, motion artifacts could compromise the diagnostic quality of the MR images.[20, 70] Voluntary motion in the youngest patients can be avoided, by either using immobilization,[70] or sedation which includes the feed-and-sleep method[64] or general anesthesia.[61, 64] Although also sometimes required for CT acquisition, deeper sedation is usually needed during MRI acquisition because of the longer acquisition time. The use of anesthesia is however not risk-free, especially on repeated occurrences.[113] In addition, uncontrolled motion was seen in the spine,[36] and the jaw,[53] and is common in clinical care of the shoulder, weakening the diagnostic power of MRI. Nonetheless, motion artifacts can be reduced by using motion insensitive acquisition methods, including breath holds,[67] interleaved scanning, increased parallel imaging with higher signal averaging, or radial sampling of the k-space.[21, 55, 64, 70]

SUSCEPTIBILITY ARTIFACTS

MRI can also be impaired by magnetic susceptibility-related distortions due to the shape of the body, or the presence of air or of implanted devices. Areas of concern for such artifacts are the spine, where the bone is surrounded by multiple magnetically differing soft tissues, air and/or metal instrumentation, the jaw which can contain orthodontic devices,[53, 65] but also long bones with screw fixations[30] or the skull with ventriculoperitoneal shunts.[61] When expected, susceptibility artifacts can be partly mitigated by choosing the adequate MR sequence and acquisition parameters. At equivalent acquisition parameters, GRE sequences are more prone to susceptibility artifacts than SE sequences, and sequences such as UTE are more prone to field inhomogeneity artifacts than S-GRE[36] or ZTE.[5] The geometrical distortions induced

by susceptibility artifacts can be mitigated by increasing the receiver bandwidth at the cost of SNR, by applying the scanner's built-in distortion correction, or by limiting the FOV around the scanner's isocenter, but they are never completely removed.[66] In addition, although 3 T acquisitions are usually equivalent or better than 1.5 T acquisitions for bone visualization and segmentation,[43, 114] lower field acquisitions should be favored when inhomogeneity artifacts are expected.[36, 61] Low-field MRI (<0.5 T) in particular could be acquired to diagnose pathologies associated with orthopedic hardware,[115] given the assumption that low-field MRI is not overly impacted by susceptibility artifacts and is able to image soft tissues in the vicinity of the implant. Other advantages of low-field MRI include its low cost (purchase and maintenance), and, when considering musculoskeletal radiology, the ability to scan in weight-bearing position.[115] This, however, comes at the expense of SNR and resolution.

Challenges in MRI Access

MR CONTRAINDICATIONS

Compared to CT, MRI suffers from a multitude of contraindications that make it unavailable for some patients. For trauma patients, the access to an MRI can be limited by obstacles related to diagnostic speed, transport of the patient to the MRI, MRI incompatibility with life-support or monitoring equipment, and patient implants. Metallic MR-compatible devices are problematic when in the vicinity of the region of interest as they can generate susceptibility artifacts hampering the diagnosis. Devices that are not MR-compatible, including some pacemakers and cochlear implants, preclude any MR acquisition. In addition, claustrophobic patients or patients unable to stay motionless might require sedation to undergo MRI, complicating the workflow, potentially causing adverse effects,[113] and hindering compliance with the breathing instructions required for some sequences. Overall, in an emergency department, more than a quarter of the elderly patients coming after a trauma could have at least one contraindication for MRI.[99]

AVAILABILITY

Another issue of MRI is its availability for acquisition. CT being faster, it is more accessible, especially in cases of emergency.[70, 99] When an MR system is acquired, the choice of the MR sequence might be driven by the available hardware. The sequences described in this review are not commonly present on all scanners. Dixon reconstruction is now usually built in the scanner,[68] but sequences like UTE and ZTE might require modern hardware or specific chargeable licensing. They tend to be increasingly available and offered as standard sequences[19] but as an example, all ZTE images presented in this review were obtained only on GE scanners. Tools for sCT generation from GRE-derived images are also becoming commercially available.[78]

Discussion

CT is considered the modality of choice for visualizing cortical bone in 3D. However, its adverse radiation burden[8] has motivated the research into alternative modalities with lower radiation doses, including radiography-based,[116] low-dose CT-based,[117] or MR-based methods. In this competition, despite some challenges in the acquisition, MRI has favorable properties including its superior soft tissue contrast that can be exploited to concurrently assess the soft tissue involvement of musculoskeletal pathologies without the need for image registration, and the complete absence of ionizing radiation.

The utility of MRI as an imaging modality for visualizing bone has been shown in many areas of the human body. Overall, the CT-to-MR intermodal agreement for the diagnosis of osseous pathologies and for the measurement of anatomical parameters was good to excellent with multiple reports of statistical equivalence.[16, 45, 65, 77] In addition, MRI could provide 3D bone renderings, critical in the clinical care for the skull, shoulder, or hip, with a submillimeter accuracy compared to CT, although in general representing an underestimation of the actual bone size.

MRI presented several advantages compared to CT in the diagnosis of musculoskeletal pathologies. First, immature bone as seen in the femur and pelvis of young children was better visualized on MR than on CT images.[101, 106] Second, MRI can acquire soft tissue and bone information in a single examination. Sequences like VIBE, UTE, or multi-echo steady state (MESS) can provide bone structural information while providing complementary information on other tissue, including cartilage.[118-121] This can promote joint biomechanical and kinematic modeling by limiting the need for registration. [18, 32, 122] Some of the dedicated images also revealed fractures and lesions, like cysts or edema, that can improve patients' clinical management but which were not visible on CT. Furthermore, MRI can be used to generate simulated radiographs with a diagnostic quality similar to CT for imaging bone tumors, while providing additional information on tumor architecture and soft tissue extension.[48] Lastly, MR sequences for imaging bone can also be combined with other sequences for specific imaging such as venous[64] or fluid-sensitive[36, 39] imaging, magnetic resonance angiography, or quantitative susceptibility mapping[123] for a more comprehensive diagnosis within a single modality.

The use of an MR-based bone visualization could in the future be extended to facilitate clinical care motivated by the benefits of CT/MR fusion. Such fusions could be useful for the design of patient-specific implants by combining bone and joint capsule information[124] and have proven their potential for diagnostic and treatment purposes, by easing the diagnosis for junior readers,[125] and by facilitating treatment guidance[9, 126] and surgical navigation.[49, 50, 127, 128] However, fusing MR and CT requires an intermodal registration that is not necessarily straightforward. With MR

providing a CT-like visualization of bone, visualization of soft tissues and bones can be obtained in one scanning session with similar body geometry, offering new perspectives for diagnosis, treatment planning, and guidance. Fusion of MRI with radiography has also been performed for kinematic analysis.[41, 46]

Is one sequence better than the other? VS-GRE and ZTE sequences seemed to stand out with validation in multiple anatomies, owing to their rather fast acquisition offering isotropic images with good cortical bone-to-bone marrow and cortical bone-to-muscles contrasts that facilitate bone segmentation. VS-GRE sequences are also robust to respiratory motion through breath holds while ZTE acquisitions are robust to motion in general thanks to their radial k-space sampling. In parallel, sCT is gaining interest for orthopedics[77, 78, 82] building upon its CT-like HU, although care still needs to be taken in interpreting such artificial intelligence-based images. In addition, the validity and robustness of single sCT generation models need to be carefully assessed across multiple MR vendors and sites. In general, awareness of the possible artifacts and MR image specificities, especially regarding air, ligaments, tendons, or water/fat interfaces, is required for all anatomical regions and MR sequences.[5, 20, 30, 36, 57, 61, 81] However, getting acquainted with the use of MR images for measurements and diagnosis might be easier and faster on images with a CT-like contrast, like ZTE or sCT, that have a high correspondence to CT images.[21, 27, 53, 80] As of now, only a few studies compared multiple MR sequences[6, 22, 36-38, 42, 55, 78] with equivalent acquisition parameters to CT, complicating definite conclusions, which might be specific to an anatomical region.

To conclude, MRI is a promising radiation-free alternative to CT for the diagnosis and treatment planning of bone pathologies. The recent advances in hardware and software provide MR images with a spatial resolution and contrast that are similar to CT images for the detection of structural and degenerative bone changes. MRI will probably not replace CT for all its applications in the near future, especially not in emergency settings. However, for clinical indications where both bone and soft tissue information are required, these new approaches open new perspectives for comprehensive protocols that facilitate bone and soft tissue visualization and fusion, for diagnosis, treatment planning, and surgical guidance.

References

1. Hudgins PA, Baugnon KL. Head and neck: Skull base imaging. *Clin Neurosurg* 2018;82:255-267. <https://doi.org/10.1093/neuros/nyx492>.
2. Douglas DB, Ro T, Toffoli T, et al. Neuroimaging of traumatic brain injury. *Med Sci* 2019;7:2. <https://doi.org/10.3390/MEDSCI7010002>.
3. Lenchik L, Rogers LF, Delmas PD, Genant HK. Diagnosis of osteoporotic vertebral fractures: Importance of recognition and description by radiologists. *Am J Roentgenol* 2004;183:949-958. <https://doi.org/10.2214/ajr.183.4.1830949>.
4. Adams JM, Cockburn MIE, Difazio LT, Garcia FA, Siegel BK, Bilaniuk JW. Spinal clearance in the difficult trauma patient: A role for screening MRI of the spine. *Am Surg* 2006;72:101-105. <https://doi.org/10.1177/000313480607200126>.
5. Argentieri EC, Koff MF, Breighner RE, Endo Y, Shah PH, Sneag DB. Diagnostic accuracy of zero-echo time MRI for the evaluation of cervical neural foraminal stenosis. *Spine (Phila Pa 1976)* 2018;43:928-933. <https://doi.org/10.1097/BRS.0000000000002462>.
6. Baraliakos X, Hoffmann F, Deng X, Wang YY, Huang F, Braun J. Detection of erosions in sacroiliac joints of patients with axial spondyloarthritis using the magnetic resonance imaging volumetric interpolated breath-hold examination. *J Rheumatol* 2019;46:1445-1449. <https://doi.org/10.3899/jrheum.181304>.
7. Vopat BG, Cai W, Torriani M, et al. Measurement of glenoid bone loss with 3-dimensional magnetic resonance imaging: A matched computed tomography analysis. *Arthroscopy* 2018;34:3141-3147. <https://doi.org/10.1016/j.arthro.2018.06.050>.
8. Huang R, Liu X, He L, Zhou PK. Radiation exposure associated with computed tomography in childhood and the subsequent risk of cancer: A meta-analysis of cohort studies. *Dose Response* 2020;18: 155932582092382. <https://doi.org/10.1177/1559325820923828>.
9. Jonsson J, Nyholm T, Söderqvist K. The rationale for MR-only treatment planning for external radiotherapy. *Clin Transl Radiat Oncol* 2019;18:60-65. <https://doi.org/10.1016/j.ctro.2019.03.005>.
10. Maspero M, Bentvelzen LG, Savenije MHF, et al. Deep learning-based synthetic CT generation for paediatric brain MR-only photon and proton radiotherapy. *Radiation Oncol* 2020;153:197-204. <https://doi.org/10.1016/J.RADONC.2020.09.029>.
11. Florkow MC, Guerreiro F, Zijlstra F, et al. Deep learning-enabled MRI-only photon and proton therapy treatment planning for paediatric abdominal tumours. *Radiation Oncol* 2020;153:220-227. <https://doi.org/10.1016/j.radonc.2020.09.056>.
12. Edmund JM, Nyholm T. A review of substitute CT generation for MRI-only radiation therapy. *Radiat Oncol* 2017;12:28. <https://doi.org/10.1186/s13014-016-0747-y>.
13. Hoffmann A, Oborn B, Moteabbed M, et al. MR-guided proton therapy: A review and a preview. *Radiat Oncol* 2020;15:129. <https://doi.org/10.1186/s13014-020-01571-x>.

14. Hofmann M, Pichler B, Schölkopf B, Beyer T. Towards quantitative PET/MRI: A review of MR-based attenuation correction techniques. *Eur J Nucl Med Mol Imaging* 2009;36:93-104. <https://doi.org/10.1007/s00259-008-1007-7>.
15. Spadea MF, Maspero M, Zaffino P, Seco J. Deep learning based synthetic-CT generation in radiotherapy and PET: A review. *Med Phys* 2021;48:6537-6566. <https://doi.org/10.1002/MP.15150>.
16. Stillwater L, Koenig J, Maycher B, Davidson M. 3D-MR vs. 3D-CT of the shoulder in patients with glenohumeral instability. *Skeletal Radiol* 2017;46:325-331. <https://doi.org/10.1007/s00256-016-2559-4>.
17. Kanawati A, Rodrigues Fernandes RJ, Gee A, Urquhart J, Bailey C, Rasoulinejad P. Geometric and volumetric relationship between human lumbar vertebrae and “black-bone” MRI-based models. *Int J Med Robot Comput Assist Surg* 2021;17:1-11. <https://doi.org/10.1002/rcs.2220>.
18. Stephen JM, Calder JDF, Williams A, El Daou H. Comparative accuracy of lower limb bone geometry determined using MRI, CT, and direct bone 3D models. *J Orthop Res* 2020;1-7:1870-1876. <https://doi.org/10.1002/jor.24923>.
19. de Mello RAF, Ma Y-J, Ashir A, et al. Three-dimensional zero echo time magnetic resonance imaging versus 3-dimensional computed tomography for glenoid bone assessment. *Arthroscopy* 2020;36:2391-2400. <https://doi.org/10.1016/j.arthro.2020.05.042>.
20. Eley KA, Watt-Smith SR, Sheerin F, Golding SJ. “Black bone” MRI: A potential alternative to CT with three-dimensional reconstruction of the craniofacial skeleton in the diagnosis of craniosynostosis. *Eur Radiol* 2014;24:2417-2426. <https://doi.org/10.1007/s00330-014-3286-7>.
21. Wiesinger F, Sacolick LI, Menini A, et al. Zero TE MR bone imaging in the head. *Magn Reson Med* 2016;75:107-114. <https://doi.org/10.1002/mrm.25545>.
22. Ganiyusufoglu AK, Onat L, Karatoprak O, Enercan M, Hamzaoglu A. Diagnostic accuracy of magnetic resonance imaging versus computed tomography in stress fractures of the lumbar spine. *Clin Radiol* 2010; 65:902-907. <https://doi.org/10.1016/j.crad.2010.06.011>.
23. Breighner RE, Bogner EA, Lee SC, Koff MF, Potter HG. Evaluation of osseous morphology of the hip using zero echo time magnetic resonance imaging. *Am J Sports Med* 2019;47:3460-3468. <https://doi.org/10.1177/0363546519878170>.
24. Rathnayaka K, Cowin G, Schuetz MA, Sahama T, Schmutz B. Correction of step artefact associated with MRI scanning of long bones. *MedEng Phys* 2013;35:988-993. <https://doi.org/10.1016/j.medengphy.2012.09.010>.
25. Malloy P, Gasienica J, Dawe R, et al. 1.5 T magnetic resonance imaging generates accurate 3D proximal femoral models: Surgical planning implications for femoroacetabular impingement. *J Orthop Res* 2020;38:2050-2056. <https://doi.org/10.1002/jor.24596>.
26. Lansdown DA, Cvetanovich GL, Verma NN, et al. Automated 3-dimensional magnetic resonance imaging allows for accurate evaluation of glenoid bone loss compared

- with 3-dimensional computed tomography. *Arthroscopy* 2019;35:734-740. <https://doi.org/10.1016/j.arthro.2018.10.119>.
27. Florkow MC, Zijlstra F, Willemsen K, et al. Deep learning-based MR- to-CT synthesis: The influence of varying gradient echo-based MR images as input channels. *Magn Reson Med* 2020;83:1429-1441. <https://doi.org/10.1002/mrm.28008>.
 28. Samim M, Eftekhary N, Vigdorich JM, et al. 3D-MRI versus 3D-CT in the evaluation of osseous anatomy in femoroacetabular impingement using Dixon 3D FLASH sequence. *Skeletal Radiol* 2019;48:429-436. <https://doi.org/10.1007/s00256-018-3049-7>.
 29. Gyftopoulos S, Yemin A, Mulholland T, et al. 3DMR osseous recon- structions of the shoulder using a gradient-echo based two-point Dixon reconstruction: A feasibility study. *Skeletal Radiol* 2013;42:347-352. <https://doi.org/10.1007/s00256-012-1489-z>.
 30. Lerch TD, Degonda C, Schmaranzer F, et al. Patient-specific 3-D magnetic resonance imaging-based dynamic simulation of hip impingement and range of motion can replace 3-D computed tomography- based simulation for patients with femoroacetabular impingement: Implications for planning open hip preservation surgery and hip arthroscopy. *Am J Sports Med* 2019;47:2966-2977. <https://doi.org/10.1177/0363546519869681>.
 31. Rathnayaka K, Momot KI, Noser H, et al. Quantification of the accu- racy of MRI generated 3D models of long bones compared to CT generated 3D models. *Med Eng Phys* 2012;34:357-363. <https://doi.org/10.1016/j.medengphy.2011.07.027>.
 32. Campanelli V, Howell SM, Hull ML. Morphological errors in 3D bone models of the distal femur and proximal tibia generated from mag- netic resonance imaging and computed tomography determined using two registration methods. *Comput Methods Biomech Biomed Eng Imaging Vis* 2020;8:31-39. <https://doi.org/10.1080/21681163.2018.1559101>.
 33. Van den Broeck J, Vereecke E, Wirix-Speetjens R, Vander SJ. Seg- mentation accuracy of long bones. *Med Eng Phys* 2014;36:949-953. <https://doi.org/10.1016/j.medengphy.2014.03.016>.
 34. Stecco A, Guenzi E, Cascone T, et al. MRI can assess glenoid bone loss after shoulder luxation: Inter- and intra-individual comparison with CT. *Radiol Med* 2013;118:1335-1343. <https://doi.org/10.1007/s11547-013-0927-x>.
 35. Lee RKL, Griffith JF, Tong MMP, Sharma N, Yung P. Glenoid bone loss: Assessment with MR imaging. *Radiology* 2013;267:496-502. <https://doi.org/10.1148/radiol.12121681>.
 36. Schwaiger BJ, Schneider C, Kronthaler S, et al. CT-like images based on T1 spoiled gradient-echo and ultra-short echo time MRI sequences for the assessment of vertebral fractures and degenerative bone changes of the spine. *Eur Radiol* 2021;31:4680-4689. <https://doi.org/10.1007/s00330-020-07597-9>.
 37. Finkenstaedt T, Siritwanangsun P, Achar S, et al. Ultrashort time-to- echo magnetic resonance imaging at 3 T for the detection of spondylolysis in cadaveric spines:

- Comparison with CT. *Invest Radiol* 2019;54:32-38. <https://doi.org/10.1097/RLI.0000000000000506>.
38. Neubert A, Wilson KJ, Engstrom C, et al. Comparison of 3D bone models of the knee joint derived from CT and 3T MR imaging. *Eur J Radiol* 2017;93:178-184. <https://doi.org/10.1016/j.ejrad.2017.05.042>.
 39. Ang EC, Robertson AF, Malara FA, et al. Diagnostic accuracy of 3-T magnetic resonance imaging with 3D T1 VIBE versus computer tomography in pars stress fracture of the lumbar spine. *Skeletal Radiol* 2016;45:1533-1540. <https://doi.org/10.1007/s00256-016-2475-7>.
 40. Tian CY, Shang Y, Zheng ZZ. Glenoid bone lesions: Comparison between 3D VIBE images in MR arthrography and nonarthrographic MSCT. *J Magn Reson Imaging* 2012;36:231-236. <https://doi.org/10.1002/jmri.23622>.
 41. Akbari-Shandiz M, Lawrence RL, Ellingson AM, Johnson CP, Zhao KD, Ludewig PM. MRI vs CT-based 2D-3D auto-registration accuracy for quantifying shoulder motion using biplane video-radiography. *J Biomech* 2019;82:375-380. <https://doi.org/10.1016/j.jbiomech.2018.09.019>.
 42. Diekhoff T, Greese J, Sieper J, Poddubnyy D, Hamm B, Hermann KGA. Improved detection of erosions in the sacroiliac jointson MRI with volumetric interpolated breath-hold examination (VIBE):Results from the SIMACT study. *Ann Rheum Dis* 2018;77:1585-1589. <https://doi.org/10.1136/annrheumdis-2018-213393>.
 43. Yan K, Xi Y, Sasiponganan C, Zerr J, Wells JE, Chhabra A. Does 3DMR provide equivalent information as 3DCT for the pre-operative evaluation of adult hip pain conditions of femoroacetabular impingement and hip dysplasia? *Br J Radiol* 2018;91:20180474. <https://doi.org/10.1259/bjr.20180474>.
 44. Zeng G, Schmaranzer F, Degonda C, et al. MRI-based 3D models of the hip joint enables radiation-free computer-assisted planning of periacetabular osteotomy for treatment of hip dysplasia using deep learning for automatic segmentation. *Eur J Radiol Open* 2021;8: 100303. <https://doi.org/10.1016/j.ejro.2020.100303>.
 45. Goronzy J, Blum S, Hartmann A, et al. Is MRI an adequate replacement for CT scans in the three-dimensional assessment of acetabular morphology? *Acta Radiol* 2019;60:726-734. <https://doi.org/10.1177/0284185118795331>.
 46. Moro-Oka TA, Hamai S, Miura H, et al. Can magnetic resonance imaging-derived bone models be used for accurate motion measurement with single-plane three-dimensional shape registration? *J Orthop Res* 2007;25:867-872. <https://doi.org/10.1002/jor.20355>.
 47. White D, Chelule KL, Seedhom BB. Accuracy of MRI vs CT imaging with particular reference to patient specific templates for total knee replacement surgery. *Int J Med Robot Comput Assist Surg* 2008;4: 224-231. <https://doi.org/10.1002/rcs.201>.
 48. Gersing AS, Pfeiffer D, Kopp FK, et al. Evaluation of MR-derived CT-like images and simulated radiographs compared to conventional radiography in patients with benign

- and malignant bone tumors. *Eur Radiol* 2019;29:13-21. <https://doi.org/10.1007/s00330-018-5450-y>.
49. Nemeč SF, Donat MA, Mehraïn S, et al. CT-MR image data fusion for computer assisted navigated neurosurgery of temporal bone tumors. *Eur J Radiol* 2007;62:192-198. <https://doi.org/10.1016/j.ejrad.2006.11.029>.
 50. Nemeč SF, Pelosček P, Schmook MT, et al. CT-MR image data fusion for computer-assisted navigated surgery of orbital tumors. *Eur J Radiol* 2010;73:224-229. <https://doi.org/10.1016/j.ejrad.2008.11.003>.
 51. Jerban S, Ma Y, Jang H, et al. Water proton density in human cortical bone obtained from ultrashort echo time (UTE) MRI predicts bone microstructural properties. *Magn Reson Imaging* 2020;67:85-89. <https://doi.org/10.1016/j.mri.2020.01.004>.
 52. Wu H, Zhong Y-M, Nie Q-M, et al. Feasibility of three-dimensional ultrashort echo time magnetic resonance imaging at 1.5 T for the diagnosis of skull fractures. *Eur Radiol* 2016;26:138-146. <https://doi.org/10.1007/s00330-015-3804-2>.
 53. Huber FA, Schumann P, Von Spiczak J, et al. Medication-related osteonecrosis of the jaw – Comparison of bone imaging using ultra- short echo-time magnetic resonance imaging and cone-beam computed tomography. *Invest Radiol* 2020;55:160-167. <https://doi.org/10.1097/RLI.0000000000000617>.
 54. Zhang R, Lee H, Zhao X, et al. Bone-selective MRI as a nonradiative alternative to CT for craniofacial imaging. *Acad Radiol* 2020;27:1515-1522. <https://doi.org/10.1016/j.acra.2020.03.001>.
 55. Deininger-Czermak E, Villefort C, von Knebel DN, et al. Comparison of MR ultrashort echo time and optimized 3D-multiecho in-phase sequence to computed tomography for assessment of the osseous craniocervical junction. *J Magn Reson Imaging* 2021;53:1029-1039. <https://doi.org/10.1002/jmri.27478>.
 56. Ma Y-J, West J, Nazaran A, et al. Feasibility of using an inversion-recovery ultrashort echo time (UTE) sequence for quantification of glenoid bone loss. *Skeletal Radiol* 2018;47:973-980. <https://doi.org/10.1007/s00256-018-2898-4>.
 57. Lee C, Jeon KJ, Han S-S, et al. CT-like MRI using the zero-TE technique for osseous changes of the TMJ. *Dentomaxillofac Radiol* 2020; 49:20190272. <https://doi.org/10.1259/dmfr.20190272>.
 58. Delso G, Wiesinger F, Sacolick LI, et al. Clinical evaluation of zero-echo-time MR imaging for the segmentation of the skull. *J Nucl Med* 2015;56:417-422. <https://doi.org/10.2967/jnumed.114.149997>.
 59. Breighner RE, Endo Y, Konin GP, Gulotta LV, Koff MF, Potter HG. Zero echo time imaging of the shoulder: Enhanced osseous detail by using MR imaging. *Radiology* 2018;286:960-966. <https://doi.org/10.1148/radiol.2017170906>.
 60. Eley KA, Mcintyre AG, Watt-Smith SR, Golding SJ. "Black bone" MRI: A partial flip angle technique for radiation reduction in craniofacial imaging. *Br J Radiol* 2012;85:272-278. <https://doi.org/10.1259/bjr/95110289>.

61. Dremmen MHG, Wagner MW, Bosemani T, et al. Does the addition of a “black bone” sequence to a fast multisequence trauma MR proto-col allow MRI to replace CT after traumatic brain injury in children? *Am J Neuroradiol* 2017;38:2187-2192. <https://doi.org/10.3174/ajnr.A5405>.
62. Eley KA, Watt-Smith SR, Golding SJ. “Black bone” MRI: A novel imaging technique for 3D printing. *Dentomaxillofac Radiol* 2017;46: 20160407. <https://doi.org/10.1259/dmfr.20160407>.
63. ESuchyta MA, Gibreel W, Hunt CH, Gorny KR, Bernstein MA, Mardini S. Using black bone magnetic resonance imaging in craniofacial virtual surgical planning: A comparative cadaver study. *Plast Reconstr Surg* 2018;141:1459-1470. <https://doi.org/10.1097/PRS.0000000000004396>.
64. Saarikko A, Mellanen E, Kuusela L, et al. Comparison of black bone MRI and 3D-CT in the preoperative evaluation of patients with cranio-synostosis. *J Plast Reconstr Aesthet Surg* 2020;73:723-731. <https://doi.org/10.1016/j.bjps.2019.11.006>.
65. Juerchott A, Freudlsperger C, Weber D, et al. In vivo comparison of MRI- and CBCT-based 3D cephalometric analysis: Beginning of a non-ionizing diagnostic era in craniomaxillofacial imaging? *Eur Radiol* 2020;30:1488-1497. <https://doi.org/10.1007/s00330-019-06540-x>.
66. Walker A, Liney G, Metcalfe P, Holloway L. MRI distortion: Considerations for MRI based radiotherapy treatment planning. *Australas PhysEng Sci Med* 2014;37:103-113. <https://doi.org/10.1007/s13246-014-0252-2>.
67. Rofsky NM, Lee VS, Laub G, et al. Abdominal MR imaging with a volumetric interpolated breath-hold examination. *Radiology* 1999;212: 876-884. <https://doi.org/10.1148/radiology.212.3.r99se34876>.
68. Eggers H, Brendel B, Duijndam A, Herigault G. Dual-echo Dixon imaging with flexible choice of echo times. *Magn Reson Med* 2011; 65:96-107. <https://doi.org/10.1002/mrm.22578>.
69. Dixon WT. Simple proton spectroscopic imaging. *Radiology* 1984; 153:189-194. <https://doi.org/10.1148/radiology.153.1.6089263>.
70. Kralik SF, Supakul N, Wu IC, et al. Black bone MRI with 3D reconstruction for the detection of skull fractures in children with suspected abusive head trauma. *Neuroradiology* 2019;61:81-87. <https://doi.org/10.1007/s00234-018-2127-9>.
71. Robinson AJ, Blaser S, Vladimirov A, Drossman D, Chitayat D, Foetal RG. “Black bone” MRI: Utility in assessment of the foetal spine. *Br J Radiol* 2015;88:20140496. <https://doi.org/10.1259/bjr.20140496>.
72. Du J, Carl M, Bydder M, Takahashi A, Chung CB, Bydder GM. Qualitative and quantitative ultrashort echo time (UTE) imaging of cortical bone. *J Magn Reson* 2010;207:304-311. <https://doi.org/10.1016/j.jmr.2010.09.013>.
73. Ronneberger O, Fischer P, Brox T. U-net: Convolutional networks for biomedical image segmentation. In: Navab N, and Hornegger J, and Wells WM, and Frangi AF, editors. *Lecture*

- notes in computer science*. Vol. 9351. Cham: Springer International Publishing; 2015. pp. 234– 241. doi: https://doi.org/10.1007/978-3-319-24574-4_28.
74. Goodfellow I, Pouget-Abadie J, Mirza M, et al. Generative adversarial nets. *27th International Conference on Neural Information Processing Systems*. Montreal, Canada: MIT Press; 2014. <https://doi.org/10.1017/CBO9781139058452>.
 75. Wang T, Lei Y, Fu Y, et al. A review on medical imaging synthesis using deep learning and its clinical applications. *J Appl Clin Med Phys* 2021;22:11-36. <https://doi.org/10.1002/acm2.13121>.
 76. Leynes AP, Yang J, Wiesinger F, et al. Zero-echo-time and Dixon deep pseudo-CT (ZeDD CT): Direct generation of pseudo-CT images for pelvic PET/MRI attenuation correction using deep convolutional neural networks with multiparametric MRI. *J Nucl Med* 2018;59:852- 858. <https://doi.org/10.2967/jnumed.117.198051>.
 77. Florkow MC, Willemsen K, Zijlstra F, et al. MRI-based synthetic CT shows equivalence to conventional CT for the morphological assessment of the hip joint. *J Orthop Res* 2021. <https://doi.org/10.1002/JOR.25127>.
 78. Jans LBO, Chen M, Elewaut D, et al. MRI-based synthetic CT in the detection of structural lesions in patients with suspected sacroiliitis: Comparison with MRI. *Radiology* 2021;298:343-349. <https://doi.org/10.1148/RADIOL.2020201537>.
 79. van der Kolk B, van Stralen M & Podlogar M et al. Reconstruction of osseous structures in MRI scans of the cervical spine with BoneMRI: A quantitative analysis. In: 58th Annual Meeting of the American Society of Neuroradiology, Boston, USA; 2019. p (abstract 3636).
 80. Staartjes VE, Seevinck PR, Vandertop WP, van Stralen M, Schröder ML. Magnetic resonance imaging-based synthetic computed tomography of the lumbar spine for surgical planning: A clinical proof-of-concept. *Neurosurg Focus* 2021;50:1-7. <https://doi.org/10.3171/2020.10.FOCUS20801>.
 81. Zijlstra F, Willemsen K, Florkow MC, et al. CT synthesis from MR images for orthopedic applications in the lower arm using a conditional generative adversarial network. *SPIE, medical imaging 2019: Image processing*, Vol 10949. San Diego, CA; SPIE - International Society for Optics and Photonics; 2019. p 54. <https://doi.org/10.1117/12.2512857>.
 82. Willemsen K, Ketel MHM, Zijlstra F, et al. 3D-printed saw guides for lower arm osteotomy, a comparison between a synthetic CT and CT-based workflow. *3D Print Med* 2021;7:13. <https://doi.org/10.1186/s41205-021-00103-x>.
 83. Orman G, Wagner MW, Seeburg D, et al. Pediatric skull fracture diagnosis: Should 3D CT reconstructions be added as routine imaging? *J Neurosurg Pediatr* 2015;16:426-431. <https://doi.org/10.3171/2015.3.PEDS1553>.
 84. Bishop JY, Jones GL, Rerko MA, Donaldson C, MOON Shoulder Group. 3-D CT is the most reliable imaging modality when quantifying glenoid bone loss shoulder. *Clin Orthop Relat Res* 2013;471:1251- 1256. <https://doi.org/10.1007/s11999-012-2607-x>.

85. Rerko MA, Pan X, Donaldson C, Jones GL, Bishop JY. Comparison of various imaging techniques to quantify glenoid bone loss in shoulder instability. *J Shoulder Elbow Surg* 2013;22:528-534. <https://doi.org/10.1016/j.jse.2012.05.034>.
86. Yanke AB, Shin JJ, Pearson I, et al. Three-dimensional magnetic resonance imaging quantification of glenoid bone loss is equivalent to 3-dimensional computed tomography quantification: Cadaveric study. *Arthroscopy* 2017;33:709-715. <https://doi.org/10.1016/j.arthro.2016.08.025>.
87. Eley KA, Delso G. Automated segmentation of the craniofacial skeleton with "black bone" magnetic resonance imaging. *J Craniofac Surg* 2020;31:1015-1017. <https://doi.org/10.1097/SCS.00000000000006552>.
88. Lee YS, Seon JK, Shin VI, Kim GH, Jeon M. Anatomical evaluation of CT-MRI combined femoral model. *Biomed Eng Online* 2008;7:6. <https://doi.org/10.1186/1475-925X-7-6>.
89. Watanabe G, Hoshi K, Kurose Y, Gamada K. High validity of measuring the width and volume of medial meniscal extrusion three-dimensionally using an MRI-derived tibial model. *J Exp Orthop* 2020; 7:1. <https://doi.org/10.1186/s40634-019-0216-2>.
90. Zheng W, Kim JP, Kadbi M, Movsas B, Chetty IJ, Glide-Hurst CK. Magnetic resonance-based automatic air segmentation for generation of synthetic computed tomography scans in the head region. *Int J Radiat Oncol* 2015;93:497-506. <https://doi.org/10.1016/j.IJROBP.2015.07.001>.
91. Karsa A, Shmueli K. SEGUE: A speedy region-growing algorithm for unwrapping estimated phase. *IEEE Trans Med Imaging* 2019;38:1347-1357. <https://doi.org/10.1109/TMI.2018.2884093>.
92. Diekhoff T, Hermann KGA, Greese J, et al. Comparison of MRI with radiography for detecting structural lesions of the sacroiliac joint using CT as standard of reference: Results from the SIMACT study. *Ann Rheum Dis* 2017;76:1502-1508. <https://doi.org/10.1136/annrheumdis-2016-210640>.
93. Lowe JT, Testa EJ, Li X, Miller S, DeAngelis JP, Jawa A. Magnetic resonance imaging is comparable to computed tomography for determination of glenoid version but does not accurately distinguish between Walch B2 and C classifications. *J Shoulder Elbow Surg* 2017;26:669-673. <https://doi.org/10.1016/j.jse.2016.09.024>.
94. Gyftopoulos S, Hasan S, Bencardino J, et al. Diagnostic accuracy of MRI in the measurement of glenoid bone loss. *Am J Roentgenol* 2012;199:873-878. <https://doi.org/10.2214/AJR.11.7639>.
95. Parada SA, Shaw KA, Antosh IJ, et al. Magnetic resonance imaging correlates with computed tomography for glenoid version calculation despite lack of visibility of medial scapula. *Arthroscopy* 2020;36:99-105. <https://doi.org/10.1016/j.arthro.2019.07.030>.
96. Mandl P, Navarro-Compan V, Terslev L, et al. EULAR recommendations for the use of imaging in the diagnosis and management of spondyloarthritis in clinical practice. *Ann Rheum Dis* 2015;74:1327-1339. <https://doi.org/10.1136/ANNRHEUMDIS-2014-206971>.

97. Lambert RGW, Bakker PAC, Van Der Heijde D, et al. Defining activesacroiliitis on MRI for classification of axial spondyloarthritis: Update by the ASAS MRI working group. *Ann Rheum Dis* 2016;75:1958-1963. <https://doi.org/10.1136/ANNRHEUMDIS-2015-208642>.
98. Jans L, Egund N, Eshed I, Sudol-Szopin ska I, Jurik AG. Sacroiliitis in axial spondyloarthritis: Assessing morphology and activity. *Semin Musculoskelet Radiol* 2018;22:180-188. <https://doi.org/10.1055/s-0038-1639470>.
99. Eggenberger E, Hildebrand G, Vang S, Ly A, Ward C. Use of CTvs. MRI for diagnosis of hip or pelvic fractures in elderly patients after low energy trauma. *Iowa Orthop J* 2019;39:179-183.
100. Lubovsky O, Liebergall M, Mattan Y, Weil Y, Mosheiff R. Early diagnosis of occult hip fractures: MRI versus CT scan. *Injury* 2005;36:788- 792. <https://doi.org/10.1016/j.injury.2005.01.024>.
101. Thanacharoenpanich S, Bixby S, Breen MA, Kim YJ. MRI is better than CT scan for detection of structural pathologies after traumatic posterior hip dislocations in children and adolescents. *J Pediatr Orthop* 2020;40:86-92. <https://doi.org/10.1097/BPO.0000000000001127>.
102. Rubel IF, Kloen P, Potter HG, Helfet DL. MRI assessment of the posterior acetabular wall fracture in traumatic dislocation of the hip in children. *Pediatr Radiol* 2002;32:435-439. <https://doi.org/10.1007/s00247-001-0634-y>.
103. Mayer SW, Stewart JR, Fadell MF, Kestel L, Novais EN. MRI as a reliable and accurate method for assessment of posterior hip dislocation in children and adolescents without the risk of radiation exposure. *Pediatr Radiol* 2015;45:1355-1362. <https://doi.org/10.1007/s00247-015-3317-9>.
104. Tomczak RJ, Guenther KR, Rieber A, Mergo P, Ros PR, Brambs HJ. MR imaging measurement of the femoral antetorsional angle as a new technique: Comparison with CT in children and adults. *Am J Roentgenol* 1997;168:791-794. <https://doi.org/10.2214/ajr.168.3.9057536>.
105. Botser IB, Ozoude GC, Martin DE, Siddiqi AJ, Kuppuswami S, Domb BG. Femoral anteversion in the hip: Comparison of measurement by computed tomography, magnetic resonance imaging, and physical examination. *Arthroscopy* 2012;28:619-627. <https://doi.org/10.1016/j.arthro.2011.10.021>.
106. Mao C, Liang Y, Ding C, et al. The consistency between measurements of the femoral neck anteversion angle in DDH on three-dimensional CT and MRI. *Acta Radiol* 2016;57:716-720. <https://doi.org/10.1177/0284185115603244>.
107. Fritz J. Automated and radiation-free generation of synthetic CT from MRI data: Does AI help to cross the finish line? *Radiology* 2021;298: 350-352. <https://doi.org/10.1148/RADIOL.2020204045>.
108. Lansdown DA, Padoia V. Editorial commentary: Can we evaluate glenoid bone with magnetic resonance imaging? Yes, if you have the right sequence. *Arthroscopy* 2020;36:2401-2402. <https://doi.org/10.1016/j.arthro.2020.07.029>.

109. Tokish JM. Editorial commentary: Measurement of glenoid bone loss with computed tomography scan versus magnetic resonance imaging. *Arthroscopy* 2018;34:3148-3149. <https://doi.org/10.1016/j.arthro.2018.08.020>.
110. Katakura M, Mitchell AWM, Calder JD, Lee JC. Is it time to replace CT with T1-VIBE MRI for the assessment of musculoskeletal injuries? *Bone Joint J* 2020;102B:1435-1437. <https://doi.org/10.1302/0301-620X.102B11.BJJ-2020-0383.R1>.
111. Roy Chong L, Lee K, Yang SF. 3D MRI with CT-like bone contrast – An overview of current approaches and practical clinical implementation. *Eur J Radiol* 2021;143:109915. <https://doi.org/10.1016/J.EJRAD.2021.109915>.
112. Chhabra A, Nordeck S, Wadhwa V, Madhavapeddi S, Robertson WJ. Femoroacetabular impingement with chronic acetabular rim fracture – 3D computed tomography, 3D magnetic resonance imaging and arthroscopic correlation. *World J Orthop* 2015;6:498-504. <https://doi.org/10.5312/wjo.v6.i6.498>.
113. Warner DO, Zaccariello MJ, Katusic SK, et al. Neuropsychological and behavioral outcomes after exposure of young children to procedures requiring general anesthesia: The mayo anesthesia safety in kids (MASK) study. *Anesthesiology* 2018;129:89-105. <https://doi.org/10.1097/ALN.0000000000002232>.
114. Rathnayaka K, Momot KI, Coulthard A, et al. Anatomical MR imaging of long bones: Comparative performance of MRI at 1.5 T and 3 T. *Biomed Spectrosc Imaging* 2013;2:21-35. <https://doi.org/10.3233/BSI-120030>.
115. Schröder FF, Post CE, van Raak SM, et al. The diagnostic potential of low-field MRI in problematic total knee arthroplasties – A feasibility study. *J Exp Orthop* 2020;7:1-10. <https://doi.org/10.1186/S40634-020-00274-2>.
116. Wybier M, Bossard P. Musculoskeletal imaging in progress: The EOS imaging system. *Joint Bone Spine* 2013;80:238-243. <https://doi.org/10.1016/j.jbspin.2012.09.018>.
117. Su AW, Hillen TJ, Eutsler EP, et al. Low-dose computed tomography reduces radiation exposure by 90% compared with traditional computed tomography among patients undergoing hip-preservation surgery. *Arthroscopy* 2019;35:1385-1392. <https://doi.org/10.1016/j.arthro.2018.11.013>.
118. Bae WC, Du J, Bydder GM, Chung CB. Conventional and ultrashort time-to-echo magnetic resonance imaging of articular cartilage, meniscus, and intervertebral disk. *Top Magn Reson Imaging* 2010;21: 275-289. <https://doi.org/10.1097/RMR.0B013E31823CCEBC>.
119. Zheng ZZ, Shan H, Li X. Fat-suppressed 3D T1-weighted gradient-echo imaging of the cartilage with a volumetric interpolated breath-hold examination. *Am J Roentgenol* 2010;194:W414-W419. <https://doi.org/10.2214/AJR.09.2423>.
120. Zijlstra F, Seevinck PR. Multiple-echo steady-state (MESS): Extending DESS for joint T2 mapping and chemical-shift corrected water-fat separation. *Magn Reson Med* 2021;86:3156-3165. <https://doi.org/10.1002/MRM.28921>.

121. Shao H, Chang EY, Pauli C, et al. UTE bi-component analysis of T2* relaxation in articular cartilage. *Osteoarthr Cartil* 2016;24:364-373. <https://doi.org/10.1016/j.joca.2015.08.017>.
122. Harris MD, Cyr AJ, Ali AA, et al. A combined experimental and computational approach to subject-specific analysis of knee joint laxity. *J Biomech Eng* 2016;138:0810041. <https://doi.org/10.1115/1.4033882>.
123. Jerban S, Lu X, Jang H, et al. Significant correlations between human cortical bone mineral density and quantitative susceptibility mapping (QSM) obtained with 3D cones ultrashort echo time magnetic resonance imaging (UTE-MRI). *Magn Reson Imaging* 2019;62:104-110. <https://doi.org/10.1016/j.mri.2019.06.016>.
124. Willemsen K, Berendes TD, Geurkink T, et al. A novel treatment for anterior shoulder instability: A biomechanical comparison between a patient-specific implant and the Latarjet procedure. *J Bone Joint Surg Am* 2019;101:e68. <https://doi.org/10.2106/JBJS.18.00892>.
125. Hui WY, Li G, Han MR, et al. Diagnostic efficacy of CBCT, MRI, and CBCT-MRI fused images in distinguishing articular disc calcification from loose body of temporomandibular joint. *Clin Oral Investig* 2021; 25:1907-1914. <https://doi.org/10.1007/s00784-020-03497-w>.
126. Noorda YH, Bartels LW, Huisman M, Nijenhuis RJ, Van Den Bosch MAAJ, Pluim JW. Registration of CT to pre-treatment MRI for planning of MR-HIFU ablation treatment of painful bone metastases. *Phys Med Biol* 2014;59:4167-4179. <https://doi.org/10.1088/0031-9155/59/15/4167>.
127. Leong JL, Batra PS, Citardi MJ. CT-MR image fusion for the management of skull base lesions. *Otolaryngol Head Neck Surg* 2006;134: 868-876. <https://doi.org/10.1016/j.otohns.2005.11.015>.
128. Maduri R, Bobinski L, Duff JM. Image merge tailored access resection (IMTAR) of spinal intradural tumors. Technical report of 13 cases. *World Neurosurg* 2017;98:594-602. <https://doi.org/10.1016/j.wneu.2016.05.092>.



The background is a solid blue color. It features several sets of parallel diagonal lines. One set of lines is in the top-left corner, another set is in the bottom-left corner, and a single line runs from the top-right towards the bottom-left. The lines are thin and light blue, creating a subtle geometric pattern.

PART 2

BENCH



CHAPTER 6

Patient-specific 3D-printed shelf implant for the treatment of hip dysplasia: Anatomical and biomechanical outcomes in a canine model

Koen Willemsen | Marianna Tryfonidou | Ralph J. B. Sakkers | René M.
Castelein | Amir A. Zadpoor | Peter R. Seevinck | Harrie Weinans | Björn P.
Meij | Bart C. H. van der Wal

Published in Journal of Orthopaedic Research® (2021)
<https://doi.org/10.1002/jor.25133>

Abstract

A solution for challenging hip dysplasia surgery could be a patient-specific 3D-printed shelf implant that is positioned extra-articular and restores the dysplastic acetabular rim to normal anatomical dimensions. The anatomical correction and biomechanical stability of this concept were tested in a canine model that, like humans, also suffers from hip dysplasia. Using 3D reconstructed computed tomography images the 3D shelf implant was designed to restore the radiological dysplastic hip parameters to healthy parameters. It was tested *ex vivo* on three dog cadavers (six hips) with hip dysplasia. Each hip was subjected to a biomechanical subluxation test, first without and then with the 3D shelf implant in place. Subsequently, an implant failure test was performed to test the primary implant fixation. At baseline, the dysplastic hips had an average Norberg angle of $88 \pm 3^\circ$ and acetabular coverage of $47 \pm 2\%$ and subluxated at an average of $83 \pm 2^\circ$ of femoral adduction. After adding the patient-specific shelf implants the dysplastic hips had an average Norberg angle of $122 \pm 2^\circ$ and acetabular coverage of $67 \pm 3\%$ and subluxated at an average of $117 \pm 2^\circ$ of femoral adduction. Implant failure after primary implant fixation occurred at an average of 1330 ± 320 Newton. This showed that the patient-specific shelf implants significantly improved the coverage and stability of dysplastic hips in a canine model with naturally occurring hip dysplasia. The 3D shelf is a promising concept for treating residual hip dysplasia with a straightforward technology-driven approach; however, the clinical safety needs to be further investigated in an experimental proof-of-concept animal study.

Introduction

One of the oldest and most straightforward treatments for hip dysplasia is the shelf arthroplasty.[1] The shelf procedure uses (autograft) bone harvested from the iliac crest placed in an extra-capsular slot on top of the hip capsule to increase femoral head coverage.[2] In time, the interposed hip capsule is thought to transform into fibrocartilaginous tissue that acts as a load-bearing surface.[3-7] Recent, long term follow-up studies on the shelf arthroplasty[1, 2] report similar long-term results as the periacetabular osteotomy.[8] This might shed new light on the shelf arthroplasty when compared to the highly invasive periacetabular osteotomy, as the latter is associated with a long learning curve, long rehabilitation periods and major complications (6%–37%).[8] However, despite the promising results of the shelf arthroplasty, there are still some limitations to the technique. The traditionally well-placed shelves show good superior femoral head coverage on radiographs but deficient coverage in the anterior and posterior quadrants on postoperative CT analysis.[9] Furthermore, graft positioning is critical for the success of the shelf arthroplasty.[9, 10] When the bone graft is placed too high, it might resorb due to lack of mechanical loading.[10-12] When the bone graft is placed too low or is too large, impingement of the femoral head and neck will occur.[11, 13] Reasonably, the better the fit and size, the better the long-term outcome might be,[10, 14, 15] and therefore the success of the shelf arthroplasty could be improved by creating a better three dimensional (3D) fit and positioning of the shelf implant.

With the current progress in 3D printing technologies,[16] a personalized 3D-printed shelf implant could enable a seamless fit to the hip socket and increase femoral coverage in all load-bearing quadrants.[17] The use of a pre-planned and 3D printed titanium shelf implant to treat hip dysplasia is novel to the authors' knowledge based on extensive screening of the literature. Therefore, a large animal dog model, based on naturally occurring hip dysplasia, was used to investigate this concept.[18] Dogs frequently have hip dysplasia and undergo diagnosis and treatments procedures similar to humans including pelvic osteotomies, total hip replacements and the shelf arthroplasty.[7] Therefore dogs are considered the animal model of choice for studying hip dysplasia.[18] In dogs the shelf arthroplasty has been previously performed using biocompatible orthopedic polymers (BOP).[19,20] During this so-called BOP procedure, bioresorbable osteo-inductive fibers were used to create a shelf on the dorsal acetabular rim, this procedure was not pre-planned in 3D and was therefore entirely dependent on the intraoperative experience of the surgeon. The initial clinical results were promising. However, the fibers induced uncontrolled bone proliferation resulting in poor anatomic remodeling of the dorsal acetabular rim.[19, 20]

This paper presents the anatomical and biomechanical outcomes of a first of its kind pre-planned and personalized 3D-printed titanium shelf implant in an ex vivo dog study employing cadaveric dysplastic hips. Moreover, the hypothesis is tested that the 3D shelf implant statistically increases the amount of femoral coverage and dislocation potential at the 12.00 o'clock position by comparing the native acetabulum to the condition after the 3D shelf intervention.

Method

Animals

For this biomechanical study the hips of three mongrel dogs (25 ± 2 kg) that were terminated for other non-orthopedic related experiments were used (Ethical approval nr.2016.II.529.002). Together the three dogs had six ortolani positive dysplastic hips, resulting in six data sets; data are presented as mean \pm standard deviation (*SD*). Hips 1–3 had moderate dysplasia and hips 4–6 had severe dysplasia according to the Fédération Cynologique Internationale (FCI).[21]

Image analysis

The Norberg angle,[21] and the percentage of acetabular coverage were measured on respectively ventrodorsal radiographs and CT scans (Siemens Somatom Definition AS, Siemens Healthcare) with the following standardized parameters: 120 kV, 250 mas, 0.6 mm slice thickness. For the measurement of the acetabular coverage the method of Larson et al. (2015) was used.[22] The CT images were reformatted through all acetabular clockface positions and for each position it was measured, similar to the Norberg angle, how many degrees the femoral head was covered by the dorsal acetabular rim and graphically displayed in a clockface graph. The total acetabular coverage was expressed as the percentage ($\% = \text{degrees}/180^\circ \times 100$) of the weightbearing part of the femoral head (10:00 to 02:00 o'clock positions) covered by the acetabulum. The whole image analysis process was scripted and took around 5 min per patient.

After image analysis, a simmering maceration process²³ was used on the pelvis and femora, cleaning the skeleton of all soft tissues to better visualize the bony anatomy.

Implant design

The implants were designed on an anatomical 3D model segmented from the CT images (Figure 1A). The segmentation was done semi-automatically using standardized bone threshold values (HU 226—upper boundary) on imaging processing software, Mimics Medical 21.0 (Materialise).

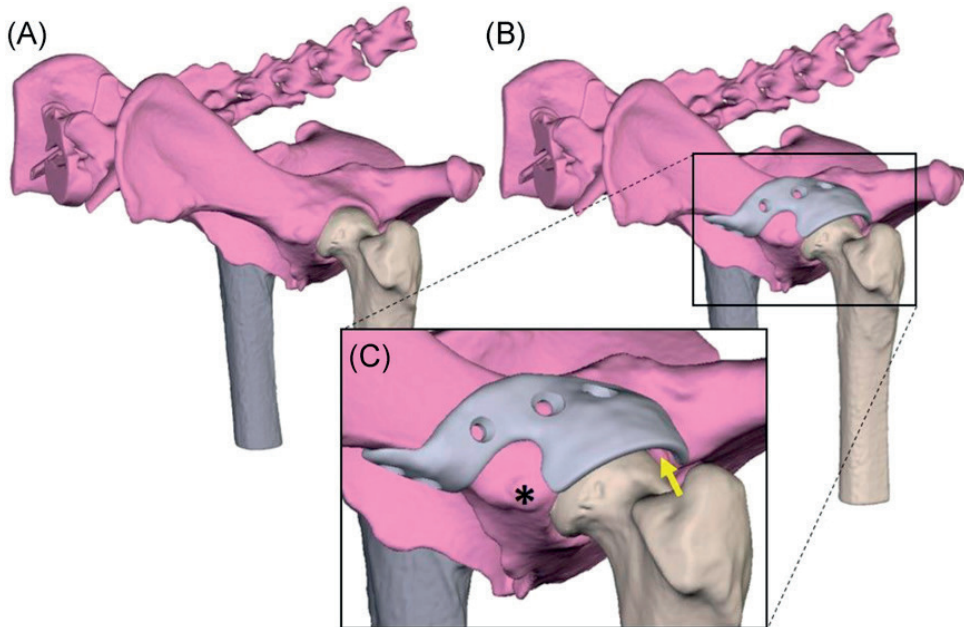


Figure 1. (A) rendering of a canine pelvis with hip dysplasia. (B) Rendering of a 3D-designed acetabular rim extension implant. (C) Detailed picture of the implant design. The base is designed around the rectus femoris muscle attachment(*). Also it is visible that there is 2 mm space between the implant and femoral head (yellow arrow) to prevent impingement of the hip capsule and act as weight bearing surface.

The 3D-printed acetabular rim implants were designed using Freeform Plus software (Geomagic, 3D Systems) (Figure 1B). The implant's rim extension was designed to increase the acetabular 12.00 o'clock CE-angle with a minimum of 30° using the diagnostic method of Larson et al. (2015) (Figure 2).[22] The effect of the implant's rim extension in each acetabular clock position was calculated using an in silico range of motion (ROM) simulation in all three degrees of rotational freedom. Subsequently, a board certified veterinary surgeon decided what was the optimal trade-off between the added acetabular extension and remaining ROM.

The approved rim extension followed the acetabular curvature with an external offset off 2 mm to allow the hip capsule to be interposed between the implant and the femoral head (Figure 1C). Then, to connect the rim extension to the bone a base was designed with an additional offset along the first 5 mm of the base allowing the insertion of a hip capsule to stay unharmed (Figure 2A). Additionally, the shape of the base was designed in such a way that muscle attachments, for example the rectus femoris cranial to the acetabulum, was spared if a dorsolateral approach to the hip joint was used (Figure 1C).

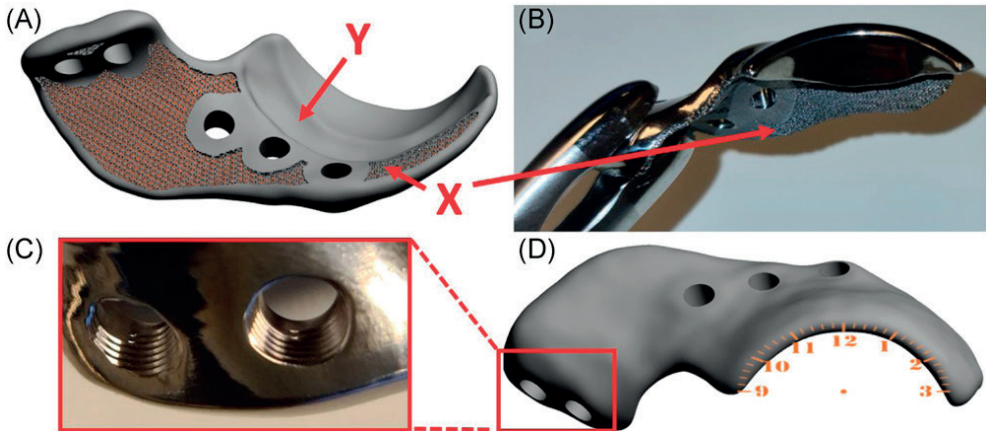


Figure 2. Digital rendering and photos of a 3D shelf implant.

(A) Shows a digital rendering of the inside of the implant. Marker 'X' shows the porous inner surface of the shelf implant facilitating bone ingrowth for osseous integration and secondary implant fixation and marker 'Y' indicates the internal offset of 2 mm on the implant base that to prevent impingement of the acetabular insertion of the hip capsule. (B) Shows a front view of the manufactured implant with the porous scaffold 'X' visible. (C) Shows a close-up of two milled 3.5 mm locking screw holes. (D) Illustrates the external implant surface with a point of view projection of a clockface on the rendered implant.

After the implant's rim and base were determined, the screw holes were planned for primary implant fixation with five 3.5 mm cortical self-tapping locking screws (DePuy Synthes) (Figure 2C). The screw trajectories were planned in such a way that they did not interfere with the acetabulum but at the same time acquired the maximal possible bone stock for the preferred screw length. The screws were placed bicortical and preferably not parallel to each other. Additionally, the implant–bone interface was made partially porous (70%) to allow bone ingrowth and therefore facilitates permanent (secondary) implant fixation in an in vivo situation (Figure 2A and B). The whole implant design process was scripted and took around 5 min per hip.

Implant production

The implants were manufactured from medical grade titanium alloy Ti-6Al-4V ELI grade 23 by direct metal printing using a ProX DMP320 machine (3D Systems). Postprocessing included chronologically: hot-isostatic-pressing, screw wiretapping, polishing, manual cleaning, and autoclave sterilization. The implant production made use of a clinical implant production route (3D Systems) which takes around 14 days per order.

Biomechanical study

The biomechanical study aimed to determine two parameters: (1) the femoral vector angle (degrees) at which joint subluxation occurred without and with shelf implant, and (2) the implant failure load (N).

Subluxation potential test

The subluxation potential test was designed in such a way that it mimicked the Barlow[24] and Ortolani[25] tests conducted in veterinary practice. The cranial and caudal ends of each hemi pelvis were embedded in epoxy resin (poly-pox THV 500, Poly-Service B.V.) in a neutral position (no angulation). The middle pelvic section surrounding the acetabulum was not embedded to allow the hip joints to move freely during testing and enable fixation of the implant (Figure 3). Furthermore, two holes were drilled in the femur shaft perpendicular to the anatomical axis of the femur. Using two bolts, the femur was attached parallel to the distal end of a hollow aluminum bar. Eight nuts were used to lock the bolts, the femur, and the aluminum bar in place. This aluminum bar was then placed in a custom testing jig designed for use with a universal testing machine (Lloyd instruments LR5K). The testing machine raised the proximal end of the metal bar by raising the pulley (5 mm/min) and simulating a movement from abduction to adduction (Figure 3). To simulate a load bearing situation, a constant force vector of 100 N was generated on the pulley by adding a calibrated weight. The vector angle at subluxation was expressed as the degrees (on the lateral side) between the anatomical axis of the femur in relation to the mediolateral axis of the pelvis which can also be measured using the angle (F in Figure 3) between the aluminum bar (H) and the vertical column of the testing machine. The test started with the pulley in its lowest position, corresponding to a femoral vector angle of 60° (30° of abduction) which points towards the acetabulum and is therefore still a stable position (Figure 3I). By raising the pulley, the femur slowly adducted and the 100 N force vector slowly surpassed the rim of the acetabulum and joint subluxation occurred marked by a sudden drop in resistance, leading to a preprogrammed stop of the testing machine (Figure 3II).

Each acetabulum was tested three times and then rotated around the mediolateral axis to five different rotational positions simulating different amount of femoral flexion, resulting in a total of 15 subluxation tests in the native dysplastic hip. The resulting force vectors were aimed at the main weightbearing directions of the acetabulum (10:00, 11:00, 12:00, 01:00, 02:00 clock position) (Figure 2D) as these positions contribute most to joint stability and utilized cartilage surface during normal gait.[26, 27]

After the first round of tests the shelf implants were fixed to the acetabular rim by a board certified veterinary surgeon followed by another CT to evaluate the new acetabular coverage. Thereafter the series of 15 subluxation tests were repeated.

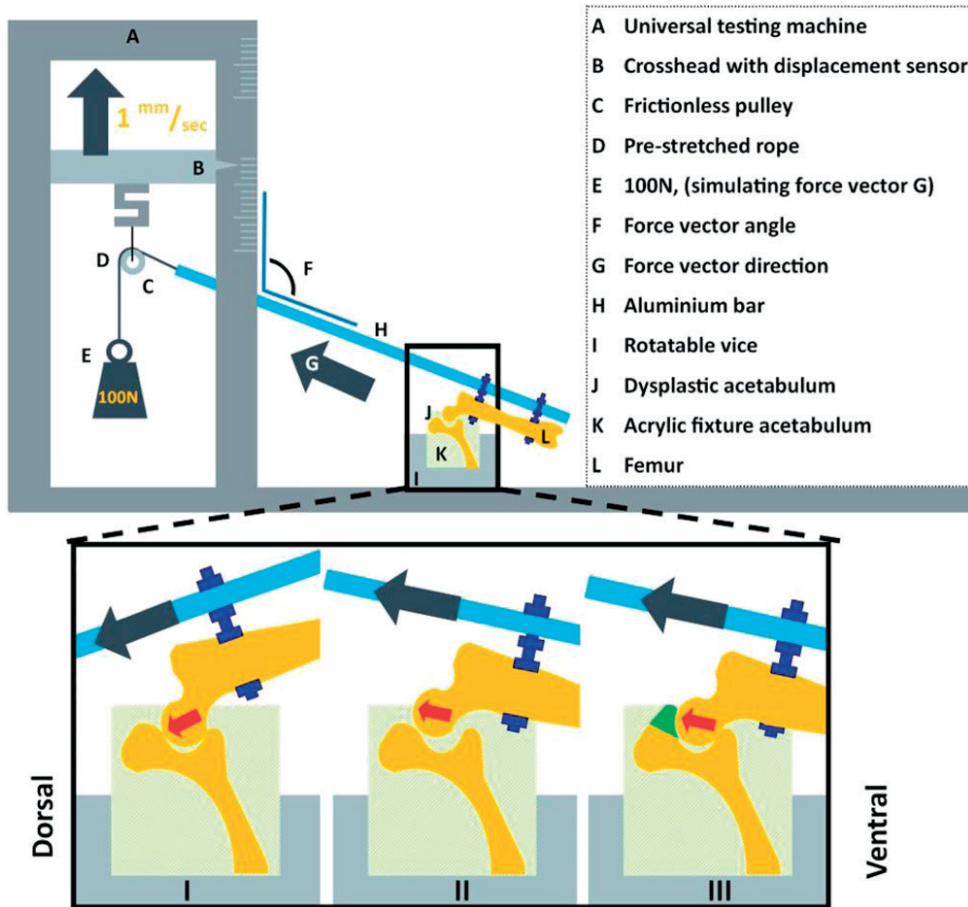


Figure 3. Schematic diagram of the custom-made set-up for measuring the dislocation potential of the canine hip joint mimicking the Ortolani test applied in the clinic.

I. Dysplastic acetabulum with abducted femur, hip is still centralized because the force vector is directed towards the acetabulum. The test continues by further adducting the femur and increasing the force vector angle (F). II. Dysplastic acetabulum with adducted femur, hip is decentralized (subluxated) because the force vector is directed outwards of the acetabulum. The vector angle at subluxation is measured when the resistance drops. III. Dysplastic acetabulum with implant in situ with adducted femur in same position as in II. Note that the hip remains centralized. The force vector is directed outwards of the acetabulum but the resistance remains intact due to the acetabular rim extending implant (green) indicating that by extending the acetabular coverage the implant adds stability to the hip.

Break-out/implant failure test

After the subluxation potential test the biomechanical setup was altered and the specimens were rotated along the longitudinal axis and rigidly fixated using clamp fixtures (Figure 4). The main weightbearing area of the implant (12.00 o'clock position) (Figure 2D) was pressed by the crosshead using a 6 mm diameter indentation attachment (Figure 4A) (Lloyd instruments LR5K). The compression force was generated with a crosshead speed of 1 mm/min until failure occurred. The outcome was the peak force before failure and was defined by a drop in pressure due to breaking or loosening of screws, fracture of the implant, or fracture of the pelvis.

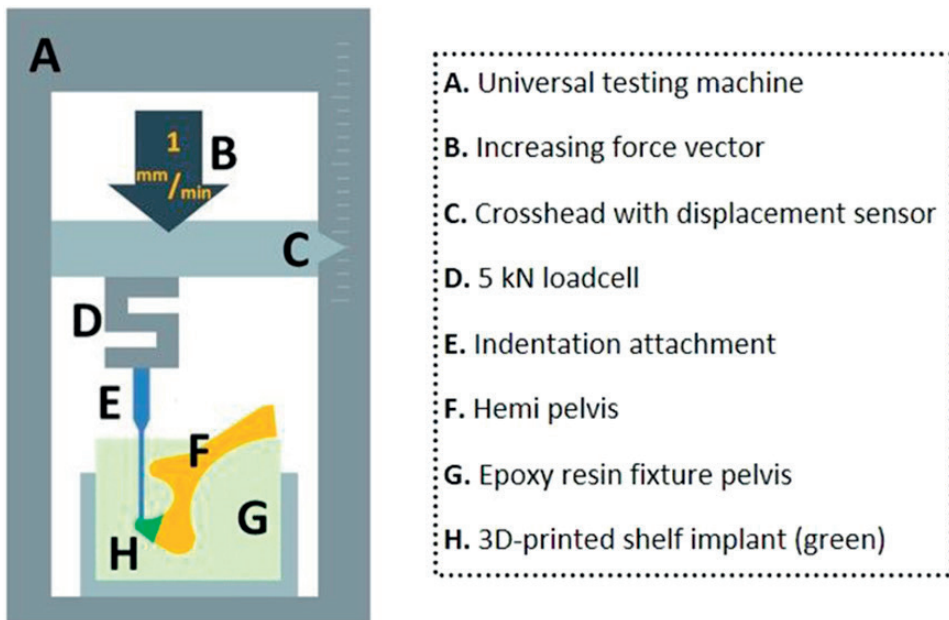


Figure 4. Schematic diagram of the custom-made testing set-up for measuring the implant failure force. An isolated stress force is applied on the most dorsal side of the implant (the 12.00 o'clock position) to investigate the peak force (Newton) for implant failure.

Statistical analysis

The hypothesis was tested that the angles of coverage and dislocation at the 12.00 o'clock position were statistically different when comparing the native to the intervention condition, with an alpha level of 0.05 and a power of 80%. Given that a relevant difference was 20°, with a SD of 10° in similar research,[28, 29] we needed six samples with paired measurements.[30] Statistics were performed in SPSS (v26, IBM) employing a paired student t-test. Statistics were conducted at the 12:00 o'clock position as this is the main biomechanical focus point for load bearing in the standing position.

Results

The acetabular coverage ($n=6$) at the 12.00 o'clock position significantly increased from $46 \pm 3\%$ in the native hip to $68 \pm 2\%$ in the hip with implant, which corresponds to Norberg angles of $88 \pm 3^\circ$ and $122 \pm 2^\circ$, respectively (Table 1). The total acetabular coverage in the main five weightbearing directions (10:00 to 02:00 clock positions) increased from $47 \pm 3\%$ to $65 \pm 4\%$ (Figure 5).

Table 1. Coverage and dislocation angles at the 12.00 clockface position of each native hip and hip with shelf implant. The dislocation angle is the average of three sublaxation measurements per hip. Hips 1-2, 3-4, and 5-6 were from the same dogs.

Hip#	Coverage (°)		Dislocation (°)	
	Native	Implant	Native	Implant
1	89	120	82	113
2	88	124	81	118
3	88	122	83	117
4	90	122	84	119
5	90	125	82	117
6	91	124	84	119
Mean±SD	88±3	122±2	83±2	117±2
<i>p-value:</i>	<0.001		<0.001	

The sublaxation angle ($n=6$) at the 12.00 o'clock position significantly increased from $83 \pm 2^\circ$ in the native hip to $117 \pm 2^\circ$ in the hip with implant (Table 1). The total sublaxation potential in the main five weightbearing directions (10:00 to 02:00 clock positions) increased from $77 \pm 4^\circ$ to $110 \pm 5^\circ$ (Figure 5).

During the break-out test the implants failed at 1330 ± 320 N (range: 955–1910 N) at a crosshead translation of 4.7 ± 1.4 mm (range: 2.5–6.3 mm), the equivalent of 283 s. In two cases the first sign of failure was a drop in pressure because of a slipping screw–bone interface at 1125 N and 1406 N at respectively 3.2 mm and 3.8 mm of translation. In four cases the first sign of failure was a drop in pressure because of a pelvic fracture surrounding the implant and screws at 1362 ± 392 N and mean 5.3 ± 0.9 mm crosshead translation (Figure 6).

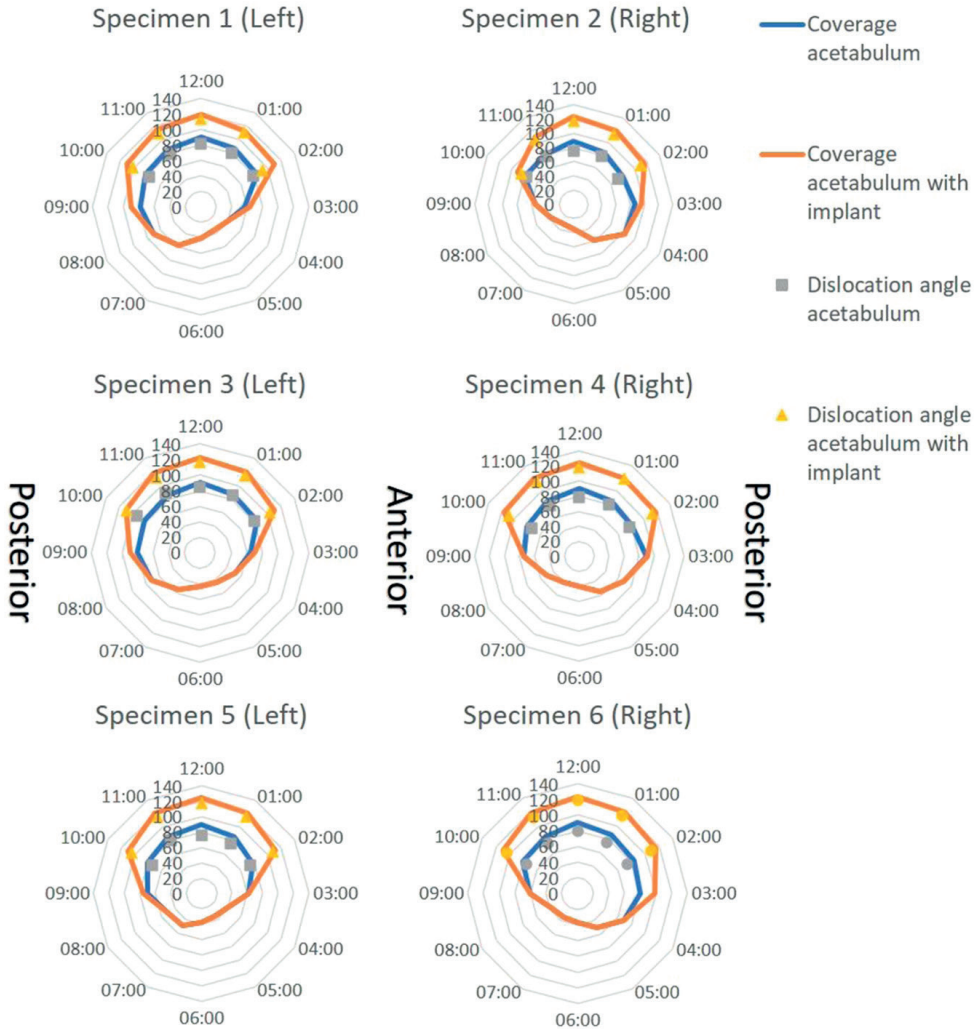


Figure 5. Clock face graphs of each biomechanical hip specimen. Hips 1&2, 3&4, and 5&6 were from the same dogs. The lines provide the Norberg angles calculated on reformatted CT images, so the modified planes align with the clock face positions. The markers show the dislocation angle at which the femur dislocated from the acetabulum in each load-bearing clock face position with (yellow) or without (grey) shelf implant

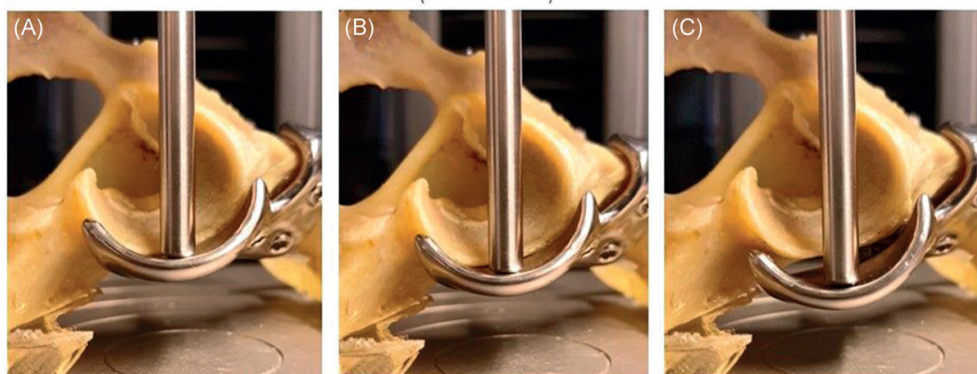
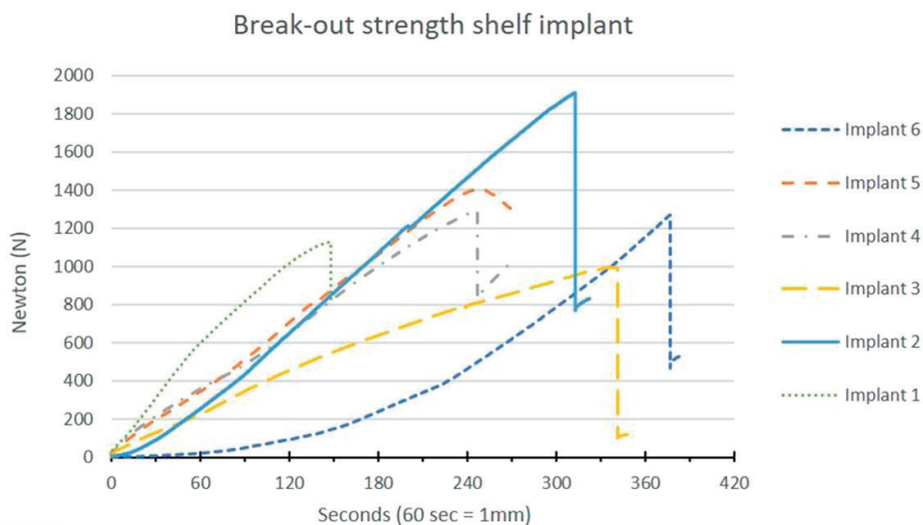


Figure 6. Break-out strength of the 3D-printed shelf implant. Hips 1&2, 3&4, and 5&6 were from the same dogs. The graph displays force versus time (displacement) curves in six dog pelvic specimens. All curves show a continued increase of the force until the force suddenly drops by bone-screw interface failure (#1 and 5) or by pelvic fracture (#2, 3, 4, and 6). The pictures show three consecutive timepoints (90, 180, and 270 s) during testing of specimen #5 (peak force 1405 N at 3.8 mm). At (A) 90 s (1.5 mm, 516 N), the implant is still attached to the bone; at (B) 180 Section (3 mm, 1070 N), the implant is still attached; at (C) 270 s (4.5 mm, 1303 N) there is a distinct reduction in force because of implant detachment by a bone-screw interface failure

Discussion

The present ex vivo study provides anatomical and biomechanical outcomes for a personalized 3D-printed titanium shelf implant to restore normal radiological parameters and stability to the canine dysplastic hip joint. The shelf implant augmented the acetabular rim and significantly improved the femoral head coverage of the dysplastic hip joint. Biomechanical ex vivo testing demonstrated that the stability of the dysplastic hip joint

improved significantly post-implantation. Furthermore, the failure test showed that the primary fixation of the personalized 3D-printed shelf implants was sufficient to withstand high forces.

The use of pre-planning to establish shelf size has never been reported to the best of the authors' knowledge. Likewise, the use of 3D printing to create the desired implant for shelf arthroplasty has never been reported. However, there are studies that research the applicability of 3D printed guides to assist peri-acetabular osteotomies surgery.[31,32] Nonetheless, the use of additive manufacturing techniques to create pre-planned and 3D printed (titanium) implants that restore dysplastic hips to normal radiological values is a first of its kind use.

In this study the Norberg angle and average acetabular coverage increased to normal values (Norberg > 105).[21] The in silico coverage planning was realized after insertion of the 3D shelf in the cadaveric dysplastic hips. This is an improvement in comparison to conventional free-hand shelf treatment where optimal shelf position and therefore acetabular coverage is frequently not accomplished.[1, 8] A high resolution 3D-printed implant in combination with a patient-specific anatomical fit makes this procedure a more reliable way of restoring healthy acetabular morphology. By employing subluxation potential test, that was set up to mimic the Ortolani test used in the clinic, it was demonstrated that the femur had to be adducted further to decentralize the femoral head indicating improved joint stability. Within this context, the patient-specific 3D shelf implant may prevent subluxations, reduce peak forces on the acetabular rim cartilage preventing cartilage micro fissures, and therefore reduce the risk of secondary osteoarthritis.[33,35]

The implant failure force of 1330 ± 320 Newton corresponds to approximately four times body weight (25 kg) of the tested canine cadavers. This easily exceeds the functional forces (1–2 times body weight) applied to the canine hip joint in daily life.[25, 26] In all specimens, the bone or bone–screw interface eventually failed which was expected since the ultimate strength of titanium is much higher than that of cortical bone.[26] When using these implants in dogs suffering from hip dysplasia, this primary fixation strength is important, as dogs are difficult to restrict in their direct postoperative weightbearing behaviour.

There are several limitations inherent to the cadaveric nature of this study. First, the small number of specimens tested might have affected the large range in implant failure between the different hips studied in distance and time (x-axis) and in the force needed (y-axis) needed to reach implant failure. However, this variability could also relate to the patient-specific nature of the implant and unique screw directions. The screw trajectories are unique for each implant and therefore the bone–screw interface could have had more

grip in one arrangement than the other. Within the context of safety, optimal arrangements of the screw corridors maximizing implant fixation remain to be determined. Furthermore, the change over time to soft tissues and dysplastic hip capsule, for example hypertrophy and metaplasia are considered to significantly contribute to tightening of the capsule and therefore reducing joint laxity after extension of the acetabular rim. However, this change to the soft tissue could not be studied due to the *ex vivo* nature of this study and therefore these tissues were removed to allow focus on the bony geometry and initial subluxation potential.

From a clinical perspective, caution is needed in translating the current results to human dysplastic hips. Although there are many similarities between the ball and socket hip joint anatomy in dogs and humans, there are marked functional differences with respect to loading. For example, the front/hind limb weight ratio logically differs between quadruped animals and biped humans.[25] However, the hip dysplasia morphology, diagnostics, and treatment options in both species are so similar that this study provides useful information for designs for human application.[18] Moreover, the high incidence of hip dysplasia in dogs may allow for future clinical veterinary studies exploring further the long term safety and efficacy of the 3D shelf implant.

Conclusion

This study provides anatomical and biomechanical outcomes for using the 3D-printed shelf in canine dysplastic hip joints to restore coverage and stability. For a next step, an *in vivo* experimental study is needed to evaluate the safety of the proof of concept of this surgical implantation and to streamline its introduction to the veterinary clinic and eventually the translation to the human clinic.

References

1. Willemsen K, Doelman CJ, Sam ASY, et al. Long-term outcomes of the hip shelf arthroplasty in adolescents and adults with residual hip dysplasia: a systematic review. *Acta Orthop.* 2020; 91(4):383-389.
2. Terjesen T. Residual hip dysplasia: is there a place for hip shelf operation? *J Child Orthop.* 2018;12(4):358-363.
3. Smith JT, Goodman SB, Fornasier VL. The histology of a failed shelf procedure. *Orthop Rev.* 1989;18(10):1069-1072.
4. Moll FK. Capsular change following Chiari innominate osteotomy. *J Pediatr Orthop.* 1982;2(5):573-576.
5. Hiranuma S, Higuchi F, Inoue A, Miyazaki M. Changes in the interposed capsule after Chiari osteotomy: an experimental study on rabbits with acetabular dysplasia. *J. Bone Jt. Surg. - Ser. B.* 1992; 74(3):463-467.
6. Diab M, Clark JM, Weis MA, Eyre DR. Acetabular augmentation at six- to 30-year follow-up: a biochemical and histological analysis. *J. Bone Jt. Surg. - Ser. B.* 2005;87(1):32-35.
7. Böhler N, Chiari K, Grundschober F, Niebauer G, Plenck H Jr. Guidelines for Chiari's osteotomy in the immature skeleton developed from a canine model. *Clin. Orthop. Relat. Res. NO.* 1985; 192(192):299-311.
8. Clohisy JC, Schutz AL, St John L, Schoenecker PL, Wright RW. Periacetabular osteotomy: a systematic literature review. *Clin Orthop Relat Res.* 2009;467(8):2041-2052.
9. Klaue K, Sherman M, Perren SM, Wallin A, Looser C, Ganz R. Extra-articular augmentation for residual hip dysplasia Radiological assessment after Chiari osteotomies and shelf procedures. *J. Bone Jt. Surg.—Ser. B.* 1993;75(5):750-754.
10. Nishimatsu H, Iida H, Kawanabe K, Tamura J, Nakamura T. The modified Spitzzy shelf operation for patients with dysplasia of the hip. *J. Bone Jt. Surg.—Ser. B.* 2002;84(5):647-652.
11. Summers BN, Turner A, Wynn-Jones CH. The shelf operation in the management of late presentation of congenital hip dysplasia. *J. Bone Jt. Surg. - Ser. B.* 1988;70(1):63-68.
12. Wolff J. *The law of bone remodelling.* Springer Science & Business Media; 2012.
13. Pauwels F. *Biomechanics of the Normal and Diseased Hip.* Biomech. Norm. Dis. Hip. 1976
14. Tanaka H, Chiba D, Mori Y, et al. Long-term results of a modified Spitzzy shelf operation for developmental dysplasia of the hip in adults and adolescents. *Eur. J. Orthop. Surg. Traumatol.* 2018;28(7): 1341-1347.
15. Bickel WH, Breivis JS. Shelf operation for congenital subluxation and dislocation of the hip. *Clin. Orthop.* 1975;No. 106:27-34.
16. Willemsen K, Nizak R, Noordmans HJ, Castelein RM, Weinans H, Kruyt MC. Challenges in the design and regulatory approval of 3D- printed surgical implants: a two-case series. *Lancet Digit. Heal.* 2019; 1(4):e163-e171.
17. Widmer KH, Zurfluh B. Compliant positioning of total hip components for optimal range of motion. *J Orthop Res.* 2004;22(4):815-821.

18. Pascual-Garrido C, Guilak F, Rai MF, et al. Canine hip dysplasia: a natural animal model for human developmental dysplasia of the hip. *J Orthop Res.* 2018;36(7):1807-1817.
19. Jensen DJ, Sertl GO. Sertl shelf arthroplasty (BOP procedure) in the treatment of canine hip dysplasia. *Vet Clin North Am Small Anim Pract.* 1992;22(3):683-701.
20. Oakes MG, Lewis DD, Elkins AD, Hosgood G, Dial SM, Oliver J. Evaluation of shelf arthroplasty as a treatment for hip dysplasia in dogs. *J Am Vet Med Assoc.* 1996;208(11):1838-1845.
21. Flückiger M. Scoring radiographs for canine hip dysplasia—the big three organizations in the world. *Eur J Companion Anim Pr.* 2007; 17(Table):135-140.
22. Larson CM, Moreau-Gaudry A, Kelly BT, et al. Are normal hips being labeled as pathologic? A CT-based method for defining normal acetabular coverage. *Clin Orthop Relat Res.* 2015;473(4):1247-1254.
23. King C, Birch W. Assessment of maceration techniques used to re- move soft tissue from bone in cut mark analysis. *J Forensic Sci.* 2015; 60(1):124-135.
24. Freiberg JA. Early diagnosis and treatment of congenital dislocation of the hip. *J Am Med Assoc.* 1934;102(2):89-93.
25. Chalman JA, Butler HC. Coxofemoral joint laxity and the Ortolani sign. *J Am Anim Hosp Assoc.* 1985;21(5):671-676.
26. Minihane KP, Turner TM, Urban RM, Williams JM, Thonar EJM, Sumner DR. Effect of hip hemiarthroplasty on articular cartilage and bone in a canine model. *Clin Orthop Relat Res.* 2005;437(437): 157-163.
27. Farese JP, Todhunter RJ, Lust G, Williams AJ, Dykes NL. Dorso- lateral subluxation of hip joints in dogs measured in a weight-bearing position with radiography and computed tomography. *Vet Surg.* 1998;27(5):393-405.
28. Comhaire FH, Schoonjans FA. Canine hip dysplasia: the significance of the Norberg angle for healthy breeding. *J Small Anim Pract.* 2011; 52(10):536-542.
29. Tomlinson JL, Cook JL. Effects of degree of acetabular rotation after triple pelvic osteotomy on the position of the femoral head in re- lationship to the acetabulum. *Vet Surg.* 2002;31(4):398-403.
30. Sanjeev B. *Fundamentals of Biostatistics.* 4th ed. Nelson Education; 2006:221.
31. Zhou Y, Kang X, Li C, et al. Application of a 3-dimensional printed navigation template in Bernese periacetabular osteotomies: a ca- daveric study. *Medicine (Baltimore).* 2016;95(50).
32. Otsuki B, Takemoto M, Kawanabe K, et al. Developing a novel custom cutting guide for curved peri-acetabular osteotomy. *Int Orthop.* 2013;37(6):1033-1038.
33. Kotlarsky P, Haber R, Bialik V, Eidelman M. Developmental dysplasia of the hip: what has changed in the last 20 years? *World J Orthop.* 2015;6(11):886-901.
34. Olmstead ML. *Small animal orthopedics.* 365–368. Mosby; 1995:368.
35. Vanden Berg-Foels WS, Todhunter RJ, Schwager SJ, Reeves AP. Effect of early postnatal body weight on femoral head ossification onset and hip osteoarthritis in a canine model of developmental dysplasia of the hip. *Pediatr Res.* 2006;60(5):549-554.



CHAPTER 7

3D-Printed regenerative magnesium phosphate implant ensures stability and restoration of hip dysplasia

Nasim Golafshan | Koen Willemsen | Firoz Babu Kadumudi |
Elke Vorndran | Alireza Dolatshahi-Pirouz | Harrie Weinans |
Bart C. H. van der Wal | Jos Malda | Miguel Castilho

Published in Advanced Healthcare Materials 10.21 (2021): 2101051
<https://doi.org/10.1002/adhm.202101051>

Abstract

Osteoarthritis of the hip is a painful and debilitating condition commonly occurring in humans and dogs. One of the main causes that leads to hip osteoarthritis is hip dysplasia. Although the current surgical methods to correct dysplasia work satisfactorily in many circumstances, these are associated with serious complications, tissue resorption, and degeneration. In this study, a one-step fabrication of a regenerative hip implant with a patient-specific design and load-bearing properties is reported. The regenerative hip implant is fabricated based on patient imaging files and by an extrusion assisted 3D printing process using a flexible, bone-inducing biomaterial. The novel implant can be fixed with metallic screws to host bone and can be loaded up to physiological loads without signs of critical permanent deformation or failure. Moreover, after exposing the hip implant to accelerated in vitro degradation, it is confirmed that it is still able to support physiological loads even after losing $\approx 40\%$ of its initial mass. In addition, the osteopromotive properties of the novel hip implant is demonstrated as shown by an increased expression of osteonectin and osteocalcin by cultured human mesenchymal stem cells after 21 days. Overall, the proposed hip implant provides an innovative regenerative and mechanically stable solution for hip dysplasia treatment.

Introduction

Osteoarthritis (OA) of the hip is a painful and debilitating condition that affects over 40 million people just in Europe.[1, 2] One of the main causes for hip OA is hip dysplasia (HD), which is an instability of the hip joint.[3] This instability is caused by incomplete coverage of the femoral hip by the acetabulum[4, 5] and is commonly observed in humans, including children, as well as in veterinary patients, mainly dogs.[6] The incorrect alignment of the hip joint in HD results in overload of the joint edges with subsequent degenerative changes of the cartilage and the acetabular labrum at a young age, leading ultimately to the development of osteoarthritis. Most HDs resolve without treatment or after bracing at early childhood.[7] If HD remains during puberty, a very high risk of osteoarthritis results and often surgical treatment is required to correct the dysplasia by, e.g., realignment of the hip socket (osteotomy) or the insertion of a bone graft (shelf arthroplasty) to enlarge the acetabular rim.[8] Osteotomies are technically demanding and invasive surgical procedures with associated complications, typically related to risk of nerve damage, inappropriate orientation of the acetabulum, and extensive rehabilitation periods.[9, 10] On the other hand, shelf arthroplasty is a less complex surgical procedure, but requires the use of bone grafts typically harvested from the patient's iliac crest, which can result in donor site morbidity.[11] Moreover, the success rate of this procedure is relatively low, about 40% to 60%, due to the challenges in shaping and positioning of the bone graft to the defect size with associated accelerated graft resorption or impingement of the femoral head.[12] There is thus, an urgent need for less invasive treatments that can overcome the drawbacks of the state-of-the-art procedures and subsequently ensure a near-perfect fit, facilitating optimal integration and durable restoration of the hip socket.

Progress in additive manufacturing (AM) techniques has provided new possibilities for the fabrication of individually shaped orthopedic implants. In particular, fabrication of titanium-based implants using a direct metal printing process has shown to generate personalized implants to treat hip dysplasia with a perfect repair of the bony defect and fit to the bone.[13] Such a procedure can overcome the need for an osteotomy or shelf arthroplasty procedure. However, the use of metallic implants cannot ensure complete integration with native bone due to their nonresorbable properties and the implants may be associated with infection or loosening. In addition, the use of nonresorbable implants is not preferred for the treatment of younger (pediatric) patients due to mismatch of the implant size after patient growth.

Here, we developed a regenerative, yet stable, patient-specific bone implant for the treatment of hip dysplasia. The external and internal architecture of the implant was rationally designed to increase femoral coverage and mechanical stability. To manufacture the implant, a flexible and bone-inducing biomaterial ink, based on a magnesium

phosphate (MgP) composite material,[14] was extruded using an extrusion-based 3D printing process and sacrificial support material. After implant fabrication, the effect of the internal structure on mechanical stability and fixation to host bone was extensively investigated by three-point flexure and compression mechanical testing. To confirm the biocompatibility and osteopromotive properties of the biomaterial, printed constructs were in vitro cultured over 21 days using human mesenchymal stem cells. Finally, to anticipate the in vivo mechanical performance of the resorbable implant, implants were loaded under physiological loading conditions using a custom-built bioreactor system and after exposed to accelerated in vitro enzymatic degradation.

Results

Extrusion 3D Printing of Anatomically Shaped Hip Implants

Based on imaging data, the external implant design was adapted to provide adequate attachment to the pelvis and to provide the largest acetabular extension without impairing the range of motion of the femur (Figure 1A–C). Before being finalized for 3D printing, the anatomically designed hip implant was confirmed to not induce femoroacetabular impingement and to ensure a perfect fit to the hip socket. Further, to allow for the fabrication of the implant's complex anatomical shape, we combined extrusion printing of a poloxamer hydrogel as a support material with extrusion of a MgPSr–poly(ϵ -caprolactone) (PCL) biomaterial ink in a single printing process using a printer set-up equipped with two printheads (Figure 1D). Both viscosity and density of the biomaterial ink were evaluated to ensure ink extrusion reproducibility. MgPSr–PCL showed a viscosity of ≈ 27.5 Pa s (Figure S1, Supporting Information) and a density of 1.7 g mL $^{-1}$.

Moreover, the implant's structure encompassed different architectures at the external and internal region of the implant (Figure 1E). The external region is made of a fully dense layer and the internal region is made of a porous region with an interfiber spacing of 1 and 0.7 mm (IFS-0.7 and IFS-1) (Figure 1F,G). These two interfiber spacings were investigated for optimal mechanical stability and have been selected based on best compromise between biomaterial ink printing accuracy and porosity (Figure S2, Supporting Information). We observed that independent of the internal architecture considered, the printed external architecture resembled well the CAD designed counterpart (Figure 1H, I). In addition, a final pore size of 606 ± 108 μ m and 319 ± 57 μ m was observed for IFS-1 and IFS-0.7 hip implants (Figure 1J), respectively. This resulted in a residual printing deviation from the CAD design for both internal architectures. Moreover, the final porosities of the IFS-1 and IFS-0.7 hip implants were observed to be $54.7 \pm 2.6\%$ and $46.1 \pm 1.2\%$, respectively (Figure 1K).

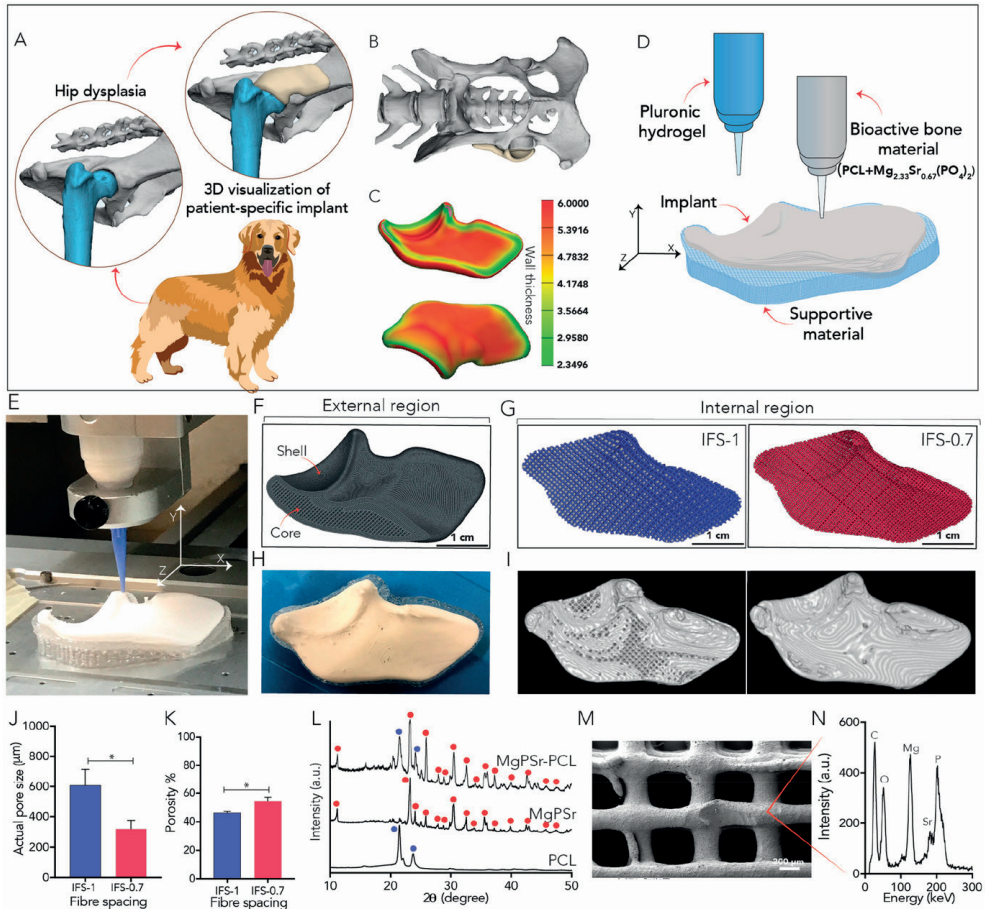


Figure 1. Design, fabrication, and respective printing accuracy and compositional analysis of the developed hip implants.

A) Schematic illustration of the hip dysplasia in a canine model. B) CAD design of anatomically shaped implant based on patient image data. C) The wall thickness of the designed hip implants. D) Schematic illustration of extrusion 3D printing using a bone-inducing biomaterial ink and support material. E) Room-temperature extrusion-based printing process showing support material (transparent) and hip implant (white). F) Hip implant external and internal architecture, where G) internal architecture encompassed two interfiber spacings: 1 mm (IFS-1) and 0.7 mm (IFS-0.7). H) Representative image-printed hip implant shell region. I) 3D reconstructed micro-CT images of hip implants with IFS-1 and IFS-0.7 core region. J) Printed pore size for IFS-1 and IFS-0.7 and respective K) porosity (significant differences were analyzed by t-test, $n = 3$ and $*p < 0.05$). L) X-ray diffraction pattern of printed hip implants, with PCL identified with blue dots and MgPSr with red dots. Plain PCL and MgPSr were analyzed as controls. M) Representative SEM image of the hip implant with IFS-0.7 microstructure and respective N) EDX elemental analysis.

Subsequently, X-ray diffraction (XRD) analysis confirmed the presence of an MgPSr inorganic phase and PCL organic phase on the printed implants (Figure 1L). Notably, Scanning Electron Microscope (SEM) analysis on the implant microstructure showed that the ceramic phase was highly exposed and not masked by the PCL phase (Figure 1M; Figure S3A, Supporting Information). This was also confirmed by elemental analysis, which revealed the presence of Mg, P, and Sr ions at the surface of the 3D-printed hip implants (Figure 1N; Figure S3B, Supporting Information).

Effect of Internal Architecture on Implant Three-Point Flexural Properties

In order to evaluate the internal porosity on the mechanical performance of the generated implants, three-point bending tests were performed. Both IFS-1 and IFS-0.7 implant structures presented similar load–displacement behavior. Load–displacement curves started with a steep slope in the elastic region, followed by an inflexion point after the yield until maximum force was reached. Afterward, the force decreased substantially and plateau after failure (Figure 2A). As expected, implant fractures were observed to occur in the regions that experienced high tensile stresses (Figure 2B, red arrow), and interestingly were observed to initiate at similar displacements for both implant porosities. The maximum flexural stress and flexural elastic modulus of the IFS-0.7 implant were ≈ 1.6 and 2.2 times higher than for the IFS-1 implant (Figure 2C,D), respectively. However, no significant differences were observed in flexure strain between both internal architectures (Figure 2E). In addition, the strain energy was 1.4 times higher for IFS-0.7 implants than for IFS-1 implants (Figure 2F).

Flexible Biomaterial Ink Allows Stable Implant Fixation

The successful fixation of hip implants to the saw-bones using metallic screws was demonstrated (Figure 3A). The effect of implant porosity on fixation and stability upon cyclic shear loading was investigated by quantifying dissipated energy after cyclic shear loading at 100 and 200 N (Figure 3B) and respective implant permanent deformation. Important to mention that a maximum shear load of 200 N was selected, as it would correspond to a force exerted on one of the hip quadrants of a dog with an average dog body weight of a 30 kg.

After the first loading cycle at 100 N, the energy dissipation is ≈ 1.2 times higher for the IFS-1 than IFS-0.7. Same trend was observed for samples loaded until 200 N, but with a significant higher dissipated energy, ≈ 2.3 times, for IFS-1 than for IFS-0.7 (Figure 3B). Furthermore, microcomputed tomography (micro-CT) analysis confirmed a higher permanent deformation of IFS-1 implants than of IFS-0.7 implants after cyclic loading (Figure 3C). The deformed shape of the fixation holes was approximated by an ellipsoid geometry and the deformation ratio quantified by $1+\epsilon_1$ (long axis) and $1+\epsilon_3$ (short axis) (Figure 3D,E). Permanent deformation was only statistically different between IFS-1 and IFS

0.7 implants at 200 N (Figure 3F). It should be noted that independently of the deformation observed, both internal architectures maintained their overall structural integrity through cyclic loading without failing even at higher applied forces than 200 N. Nevertheless, based on these fixation results and the results from three-point flexural characterization, we selected the IFS-0.7 implants for further evaluation since they presented negligible accumulated deformation and improved flexural properties.

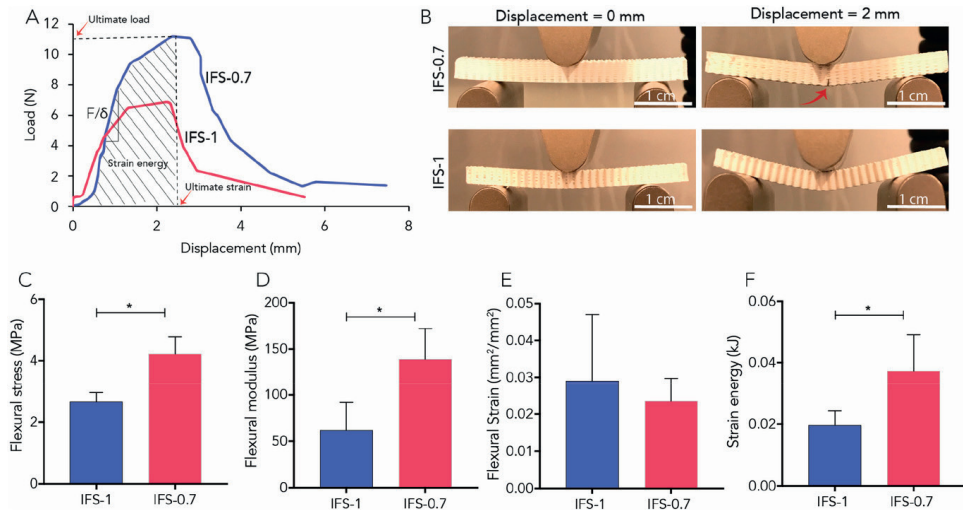


Figure 2. Flexure response under three-point loading of rectangular-shaped implant structures with different internal porosities. A) Representative load–displacement curves and B) corresponding photographs showing implants deformation before loading (displacement = 0 mm) and after loading (displacement = 2 mm). Determined C) flexural stress, D) flexural elastic modulus, E) flexural strain, and F) strain energy (significant differences were analyzed by one-way ANOVA, $n = 3$ and $*p < 0.05$).

Monitoring Implant Mechanical Integrity upon Degradation

We examined the microscopic features, as well as the mechanical performance of the implant internal structure upon accelerated in vitro enzymatic degradation. After 15 days of accelerated in vitro degradation, we observed that $38.5 \pm 1.1\%$ of the implant was degraded (Figure 4A). It is important to note that the lipase-enzyme medium solution used for the degradation tests catalyzes the implant degradation through hydrolysis, which is the major degradation mechanism in polymer-based scaffolds. Therefore, this allows us to resemble long term in vivo degradation in a relatively short in vitro experiment. In addition, the observed degradation was accompanied by a sustained release of Sr²⁺ and Mg²⁺ (Figure 4B) without MgPSr major ceramic phase transformation, as confirmed by XRD analysis (Figure 4C). However, it is important to note, that the presence of Mg(H₂PO₄)·2H₂O and Mg(H₂PO₄)·4H₂O were also detected in the degraded implants which might be attributed to the hydration product of MgPSr. Furthermore, from the

analysis of the flexural properties during in vitro degradation, we observed a significant decrease in maximal flexural stress and flexural modulus over the 15 days from 4.2 ± 0.6 MPa and 138.8 ± 33.2 MPa to 0.9 ± 0.5 MPa and 14.1 ± 4.7 MPa, respectively (Figure 4D*ε*). Interestingly, an increase in flexural strain was observed at day 10 and day 15. This might be attributed to the hydrolysis of the PCL bulk structure that resulted in high mobility of polymer chains and consequent increase in flexibility.

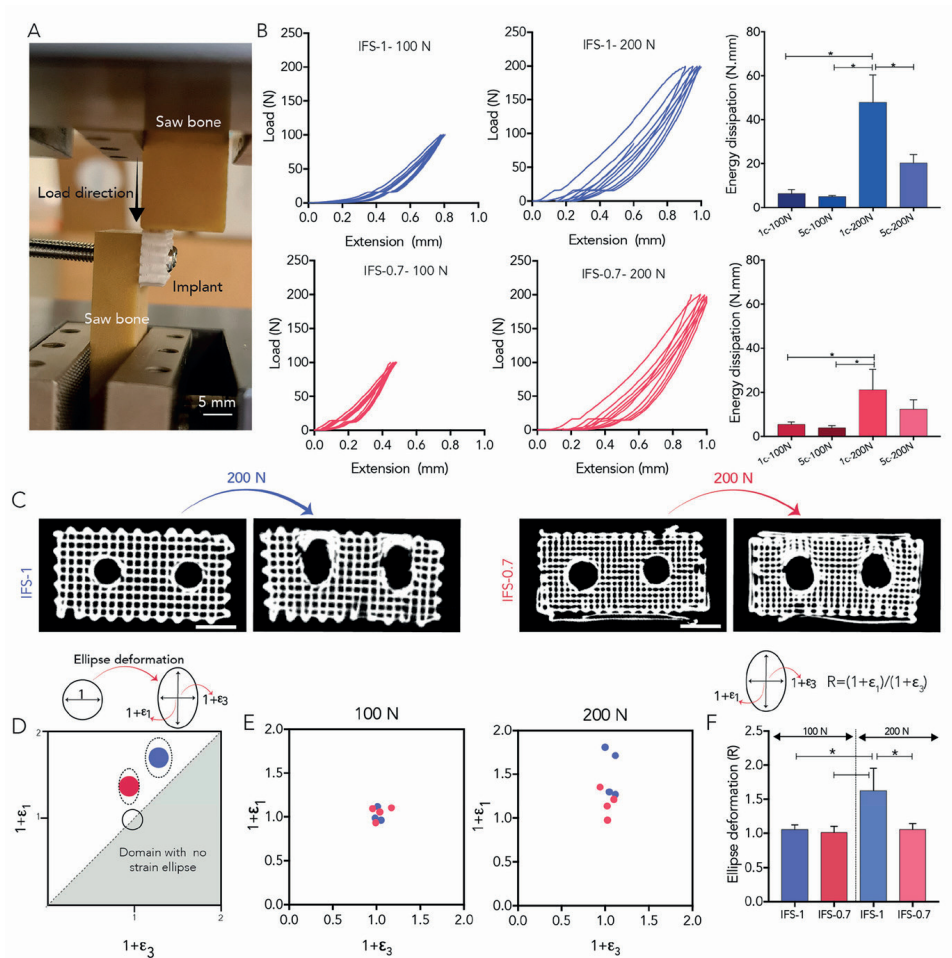


Figure 3. Fixation response of implants under cyclic shear loading.

A) Snapshot image of the fixation of IFS-0.7 and IFS-1 to the saw-bones prior to the test. B) Representative load–extension curves at 100 and 200 N applied shear load and energy dissipation of the implants after one and five loading cycles. C) Representative micro-CT images of the unloaded (left) and loaded (right) implants at maximum shear load of 200 N (scale bar = 5 mm). D) Schematic of ellipse deformation parameters along the major (ϵ_1) and minor ellipse axis (ϵ_3) and E) respective experimental measured values. F) Ellipsoid deformation parameter R (significant differences were analyzed by one-way ANOVA, $n = 5$ and $*p < 0.05$).

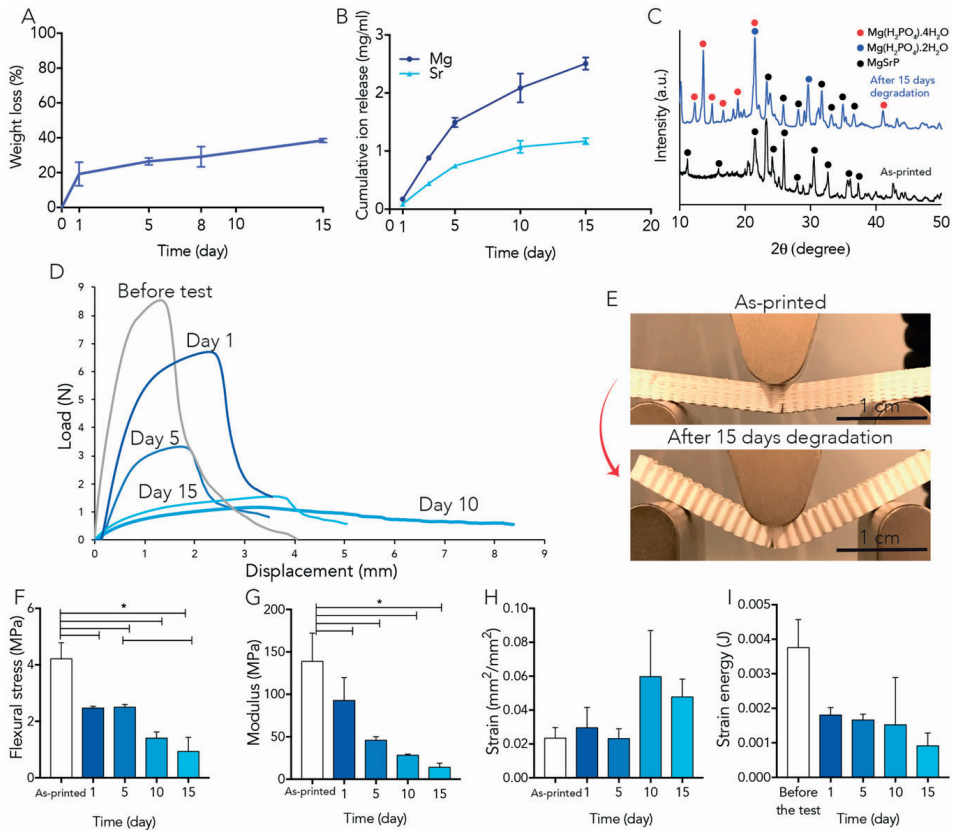


Figure 4. IFS-0.7 implant mechanical integrity and material composition stability upon in vitro enzymatic degradation.

A) Implant weight loss, B) cumulative ion release, and C) XRD composition. D) Representative flexural load–displacement curves of IFS-0.7 implants at different time points of in vitro degradation and E) representative snapshots of as-printed and 15 days degraded implants after the flexural test failing. Determined F) flexural stress, G) flexural elastic modulus, H) flexural strain, and I) strain energy (significant differences were analyzed by one-way ANOVA, $n = 5$ and $*p < 0.05$).

Cytocompatibility and Osteogenic Potential of Implants

In further analysis, we checked whether the biomaterial ink and 3D printing manufacturing strategy used resulted in toxicity of the produced implant or changes in their osteogenic potential. To investigate this, we benchmarked implants produced with biomaterial ink against PCL only implants. The human mesenchymal stem cells (hMSCs) proliferated faster on MgPSr–PCL implants than on PCL implants (Figure 5A). In addition, the metabolic activity analysis over 14 days also confirmed that the solvent-based printing approach did not affect cell activity and that cells, cultured on the MgPSr–PCL, were ≈ 1.4 times more active than when culture on pristine PCL implants after 14 days (Figure 5B). Furthermore, the alkaline phosphatase (ALP) activity, as a measure of the osteogenic potential of the

MgPSr-PCL implants, was three times higher than on PCL implants after 7 days of culture (Figure 5C,D). An upregulation of osteonectin (Figure 5E) and osteocalcin (Figure 5F), both markers of osteogenic differentiation, was also observed for cells cultured on the MgPSr-PCL scaffolds after 14 and 21 days of culture, confirming the osteoinductive potential of the hip implant biomaterial composition.

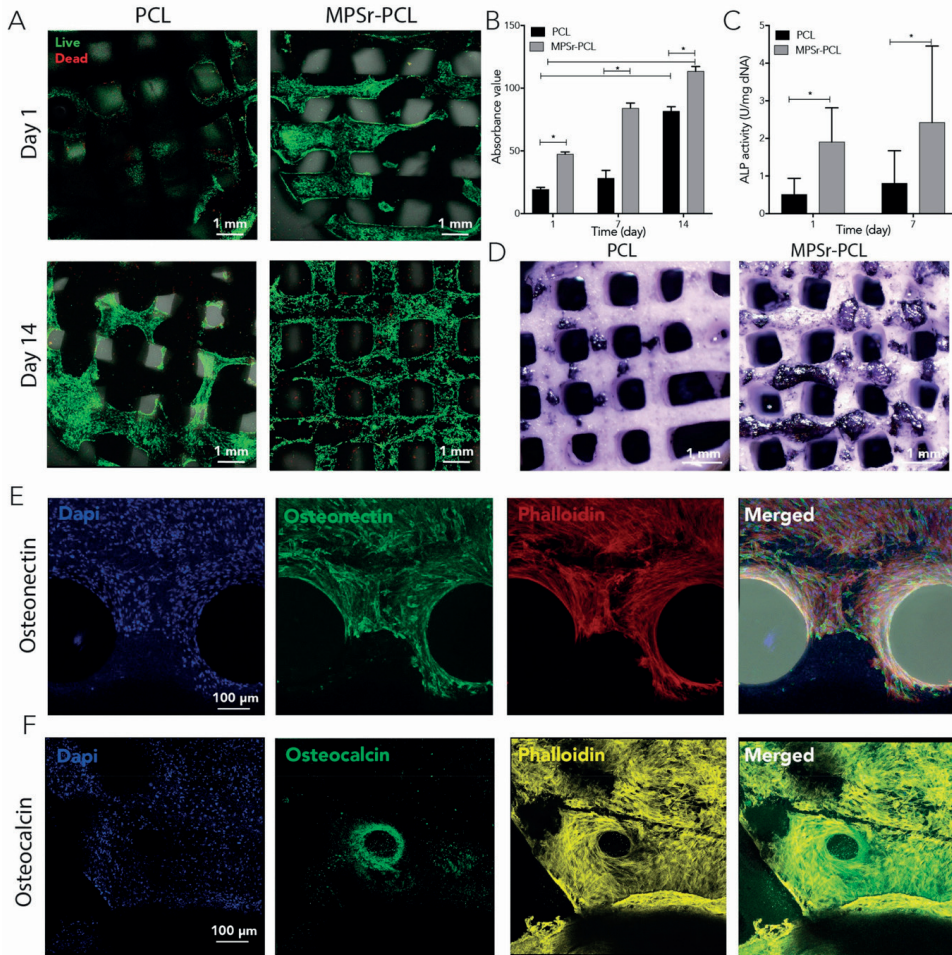


Figure 5. In vitro assessment of cytocompatibility and osteogenic potential of IFS-0.7 hip implants. A) Confocal images from the live–dead staining assay during 14 days culturing of hMSCs in basal media. B) Metabolic activity of hMSCs during 14 days culturing. C,D) Alkaline phosphatase (ALP) images of the printed samples. ALP activity levels were normalized to DNA content. E,F) Confocal images of osteonectin and osteocalcin expression in basal media after 14 and 21 days, respectively (significant differences were analyzed by two-way ANOVA, $n = 3$ and $*p < 0.05$).

Ex Vivo Biomechanical Evaluation under Physiological Loading

To confirm the mechanical integrity of the hip implants under physiological loading, implants were tested in a custom-made biomechanical setup before and after accelerated in vitro degradation (Figure S5, Supporting Information). After 15 days in enzymatic media, implants did not exhibit a significant deterioration of their internal and external architecture, although the presence of material voids and alternation of surface smoothness could be observed (Figure 6A). This material degradation resulted in a decrease in the overall mechanical performance of the implants when loaded under punctual compressive load (Figure 6A–E). In particular, after 15 days of degradation provided a material loss of 38.5% bringing the pore size from $(319 \pm 57) \mu\text{m}$ to $(524 \pm 21) \mu\text{m}$. At the same time the maximum load decreased from $(91.9 \pm 7.2) \text{ N}$ to $(18.7 \pm 2.9) \text{ N}$ ($p < 0.05$), while the overall implants stiffness dropped from $(36.8 \pm 6.9) \text{ N mm}^{-1}$ to $(13.4 \pm 1.2) \text{ N mm}^{-1}$. Moreover, a significant decrease in implants strain energy uptake from $(252.1 \pm 60.3) \text{ N mm}^{-1}$ to $(134.6 \pm 7.9) \text{ N mm}^{-1}$ was also observed. Local microscopic analysis of implants failure, revealed that failure was initiated close to the fixation screws (white arrows).

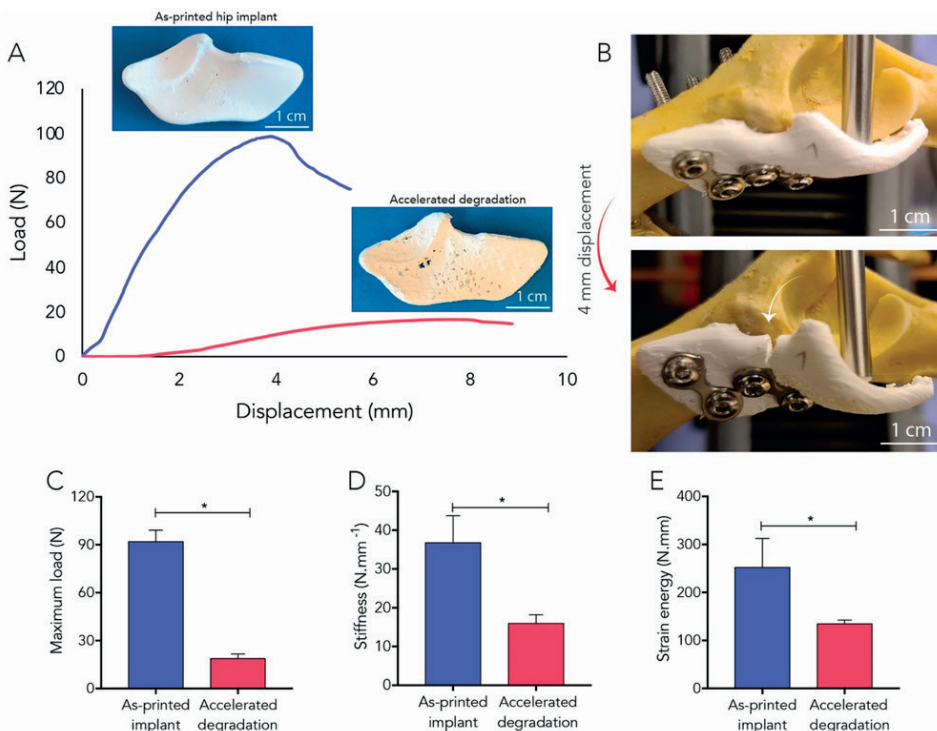


Figure 6. Mechanical performance of hip implants under physiological loading conditions for IFS-0.7.

A) Load–displacement curves of as-printed implants and after 15 days immersing in enzymatic solution (accelerated degradation) and corresponding images of the hip implants. B) The snapshots of the as-printed and 15 days degraded implants after the failure. Determined C) maximum load, D) stiffness, and E) strain energy (significant differences were analyzed by one-way ANOVA, $n = 3$ and $*p < 0.05$).

Although a significant decrease in mechanical properties was observed after 15 days of accelerated degradation, it was notable to observe that hip implant even after a loss in weight of material of $\approx 38\%$ did not lose completely its mechanical integrity.

Discussion

Currently, there is a great need for regenerative implants that could provide optimal integration and restoration of the hip socket as a regenerative and stable treatment for hip dysplasia. Here, we described the development of such implant by using extrusion 3D printing of a flexible, bone-inducing biomaterial ink and subsequently rigorously investigate its mechanical and (in vitro) biological performance.

The implant was designed based on CT scans of a dog hip joint. In an internal ongoing study, we have recently shown that a metallic hip implant with a similar design was able to provide an extension of the acetabular rim to keep the femoral head in its correct position, while still retained maximal range of motion of the hip joint. In the current work, local modifications on the implant thickness were specifically included to accommodate for its resorbable properties, without compromising its mechanical stability. Moreover, we observed that the one-step extrusion-based printing strategy and the bone-inducing material combined here could yield a hip implant that uniquely matched the anatomical designed counterpart, with minimal geometrical deviation from CAD design. Important to mention that fabrication of such anatomically shaped and size relevant ceramic-based implants is typically a limiting factor for the conventional extrusion-based printing processes when comparing to other technologies like 3D powder printing[15, 16] or stereolithography.[17, 18] The use of a sacrificial support material, together with the ceramic-based material ink that rapidly solidified due to presence of high volatile solvents, allowed to overcome this limitation.

In addition, through a rigorous mechanical evaluation, we confirmed that both the biomaterial ink and anatomically shaped implant with a highly porous and interconnected porosity can provide sufficient strength and resilience to support physiological loads. In particular, we first tested the effect of hip implants internal structure under three-point flexure. This allowed us to characterize both material and internal structure behavior, under simultaneous compression and tension loading, which the hip implants are known to be subjected to in vivo.[19] As expected, we observed that internal porosity plays a significant role in the final implants mechanical performance, and that the low porosity implants (IFS-0.7) resulted in higher strength and flexural modulus. The flexural strength was largely dictated by the size of pores, therefore, the mechanical properties of IFS-1 was inferior to the IFS-0.7. Moreover, the obtained flexural strength of the hip implant

internal architecture was approximately one order of magnitude higher than other previously reported ceramic-based bone implants.[20] For example, calcium phosphate-based scaffolds obtained by casting of the cement paste were reported to present flexural strengths ranging from 3.1 to 4 MPa for a macroporosity between 40% and 50%. Low flexural and tensile strength has so far restricted the application of ceramic-based materials to nonload bearing areas. Thus, our novel magnesium-based biomaterial demonstrates the potential not only to be shaped in complex geometry implants, but importantly to be used in load-bearing applications.

It is also important to notice that the flexible nature of the biomaterial ink allowed a stable fixation with metallic screws, which is not possible for most of the pure ceramic-based implants due to their brittle nature.[20, 21] Although a significant permanent deformation was observed upon loading on the IFS-1, which was mostly attributed to its highly porous internal architecture, the IFS-0.7 only showed only a residual permanent deformation at the implant fixation interface upon cyclic loading at 200 N (approximate maximum load exerted on one of the hip quadrants of a dog with an average bodyweight of 30 kg[22, 23]). Therefore, only hip implants with the internal porosity of IFS-0.7 were selected for in vitro biological evaluation and bioreactor study.

Through cytocompatibility and osteogenic differentiation studies, without the addition of osteogenic factors, we confirmed that the biomaterial ink (and printing strategy adopted) is not cytotoxic and can stimulate osteogenic differentiation of clinically relevant hMSCs. The cytocompatibility of the implants was attributed to the high volatility of the solvent combination used, which did not leave any toxic residues within the printed implant independent of its large volume and geometrical complex shape. This is particular important for future clinical translation of the hip implants. Furthermore, we were able to confirm the osteopromotive potential of the hip implants. The osteogenic differentiation of hMSCs was attributed to the high exposure of the MgPSr ceramic phase on the implant structure and to the consequent release of Mg²⁺ and Sr²⁺ ions, which are both known to significantly promote bone formation.[24, 25] Importantly, the degradable characteristics and osteopromotive properties of the biomaterial ink combined with its high porous internal architecture, is expect to maximize bone ingrowth and consequent hip implant stability and fast integration with host bone. This will finally offer a viable alternative to the existent metallic hip implants, with particular impact for pediatric patients.[26, 27]

Moreover, despite the regenerative and osteopromotive properties of the hip implant, it is also fundamental that the mechanical integrity of the implants is preserved during the degradation process and properly balanced with bone ingrowth speed.[14] We opted to study the in vitro acceleration degradation in the presence of lipase since it is known to hydrolyze PCL, which comes closer to the in vivo condition (as the degradation starts from

the surface) than other conventionally used enzymes, such as Cutinase.[28] Interestingly, the implants weigh loss here observed is in line with our previous findings in an in vivo study using an equine tuber coxae model.[14] Importantly, the decrease in mechanical properties followed by in vitro degradation is in line with other reports on ceramic-based implants.[29]

Our results also demonstrated that the developed hip implant can support a load exerted on the acetabulum of a dog with an approximate body weight of 30 kg, even after a material degradation of ≈ 38 wt% was observed. Important to mention, that the implant stability is expected to further improve after implantation due to resorbable nature and porous structure of the implant which will result in bone ingrowth into the porous structure, which typically occurs within 4–12 weeks post implantation.[30] Therefore, it is likely that any initiation of failure observed in our study, as a result of degradation of the implant, will be compensated by the additional stability provided by bone ingrowth.

Conclusion

In conclusion, we have designed, fabricated, and fully characterized a patient-specific hip implant for hip dysplasia treatment. The patient-specific design was precisely fabricated from a flexible bone-inducing biomaterial using printed (sacrificial) supporting structures. Moreover, the implant was strong and resilient enough to bear physiological loads, is cytocompatible, can stimulate in vitro bone growth, and has the ability to resorb in vivo. This new regenerative implant opens a new perspective for the treatment of hip dysplasia of both veterinary (and potentially) human patients.

Experimental Section

Preparation of the MgP Biomaterial Ink

Printable biomaterial ink was prepared by combining Mg_{2.33}Sr_{0.67}(PO₄)₂ powder and commercial medical grade poly(ϵ -caprolactone) (mPCL, Purasorb PC 12, Purac Biomaterials, The Netherlands) in weight ratios of 70:30 wt% of MgPSr to PCL, according to a procedure previously described.[14] Briefly, the ceramic component was synthesized by sintering (1050 °C, 5 h) a mixture of 0.6 mol magnesium hydrogen phosphate (MgHPO₄·3H₂O, Sigma-Aldrich, Steinheim, Germany), 0.1 mol magnesium hydroxide (Mg(OH)₂ (VWR International GmbH, Darmstadt, Germany), and 0.2 mol strontium carbonate (SrCO₃, Sigma-Aldrich, Steinheim, Germany). The sintered cake was manually crushed with pestle and mortar followed by wet grinding for 2 h in pure ethanol in a planetary ball mill (250 U min⁻¹) using 200 agate balls. Afterward, the cement powder was dried at room

temperature. Then, the MgPSr powder and mPCL were dispersed in a mixture of high volatile solvents (dichloromethane (Sigma-Aldrich, Germany), 2-BU-1-(4-(diethylamino) anilino)-3-me-pyrido(1,2-a) benzimidazole-4-carbonitrile (Sigma-Aldrich, Germany), and dibutyl phthalate (Sigma-Aldrich, Germany)) in a ratio of 10:2:1 wt%, at the concentration of 90 wt% of solid material in solvent. After dispersion, the composite paste was left for homogenizing for ≈ 4 days on a roller mixer at room temperature before printing.

Biomaterial ink printability was first accessed according to a protocol described elsewhere. [14] Briefly, a one-layer triangular-shaped structure with a fill-in pattern of straight lines at increasing interfilament spacings, from 0.5 to 1 mm, was printed. Then, the length of fused filament (fs), at each filament distance (fd), was quantified. Fs was normalized by the average of filament thickness (ft). Moreover, to evaluate effect of filament stacking on printing resolution, rectangular-shaped scaffolds (10 mm \times 20 mm \times 4 mm) with three different interfiber spacings were printed. As a measure of scaffolds printing accuracy, open pore ratio was quantified by

$$\text{Open pore ratio} = \frac{A_t - A_a}{A_t} \quad (1)$$

where A_t and A_a are a theoretical and actual pore areas, respectively. Open ratio varies between 0 (open) and 1 (close). All measurements were performed with Image J.

Design and Extrusion-Based 3D Printing of Implants

All dogs used for the current cadaveric research were terminated for other non-orthopedic related experiments by another research group from the same institution (UMCU) that worked under Ethical approval nr.2016.II.529.002. After termination, the cadavers were donated to our group to reduce the need for experimental animals. To design the hip implants, three cadaveric dogs (6 hips) were CT scanned (Siemens SOMATOM Definition AS, Siemens, Healthcare) with the following standardized parameters, 120 kV, 250 mAs, and 0.6 mm slice thickness. The segmentation was done semiautomatically using standardized bone threshold values (HU 226 - upper boundary) using an imaging processing software, Mimics Medical 21.0 (Medical v21.0, Materialise, Leuven, Belgium). The implant's rim was designed in 3-Matic software (Medical v12.0, Materialise, Leuven, Belgium) to add 30° of coverage to the dysplastic acetabular rim without interfering with the hip capsule or muscles (e.g., Rectus Femoris) when using the standard dorsolateral approach to the hip joint. Additionally, the external implant was designed to provide adequate scaffold material (average thickness, 4 mm) and surface area to fixate the implant to the pelvis with bone screws.

After assessment of the implant external geometry, BioCAM software was used to define the hip implant internal architecture and subsequently translate the design into a G-Code. The external region of the implant (shell) was kept closed, while for the internal region (core) of the implant, two interfiber spacings, 1 and 0.7 mm (abbreviated as IFS-1 and IFS-0.7, respectively), were considered (Figure S2, Supporting Information). Designed implants were fabricated by a multimaterial extrusion-based 3D-printing system (3D Discovery, regenHU, Switzerland) using the MgPSr–PCL biomaterial ink. The ink was transferred to a 10 mL syringe (Nordson EFD, USA) and extruded through a 22G conical nozzle, (diameter = 0.41 mm, Nordson EFD, USA) at pressure of 0.9 bar and collector speed of 6 mm s⁻¹. For the fabrication of the anatomically shaped hip implants, a supporting material, 40 wt% of poloxamer (Pluronic F-127, Sigma-Aldrich, Germany), was used. Poloxamer ink was dissolved for 24 h at 4 °C, transferred to 10 mL syringe, and extruded printed through a 27G conical nozzle (diameter = 0.2 mm) at room temperature. After the printing process using the poloxamer and biomaterial ink, the scaffolds were immersed in cold water for 3 h to remove the support material.

Physical and Chemical Characterization

Pore size and porosity were analyzed by micro-CT analysis. Micro-CT was performed using a Quantum FX-Perkin Elmer (μCT, Quantum FX, PerkinElmer, USA). Hip implants were scanned at 90 kV tube voltage, 180 mA tube current, 30 μm resolution, and 3 min scan time. Volume fraction and respective porosity of IFS-1 and IFS-0.7 was determined by measuring trabecular parameters in 3D μCT images according to a protocol described previously.[14] Briefly, the 3D scans of the implants were adjusted based on Bernsen thresholding method using ImageJ software. Next, the volume fraction (BV/TV) was measured with BoneJ plugin for a specific region of interest (ROI) and porosity (Φ) was determined as

$$\Phi = 1 - \frac{BV}{TV} \quad (2)$$

Moreover, the printing deviation of the prepared implants was quantified as

$$\text{Printing deviation} = \frac{V_P}{V_{CS}} \quad (3)$$

where V_P and V_{CS} represent volume of the printed implants (based on the micro-CT images) and CAD designed implants, respectively. The volumes were measured with Meshlab (v.2016). In addition, the phase composition of printed implants was analyzed by X-ray diffraction using monochromatic Cu-Kα radiation was utilized. X-ray measurements were collected from $2\theta = 10^\circ$ – 40° with a step size of 0.02° . The inorganic phase composition

of MgPSr was checked by reference patterns of the ICDD database (magnesium strontium phosphate, $\text{Mg}_2\text{Sr}(\text{PO}_4)_2$, PDF ref. 00-014-0206, $\text{Mg}(\text{H}_2\text{PO}_4)\cdot 2\text{H}_2\text{O}$, PDF ref. 00-39-0132, and $\text{Mg}(\text{H}_2\text{PO}_4)\cdot 4\text{H}_2\text{O}$, PDF ref. 01-075-1445).

3D-printed implant microstructure and elemental composition was analyzed by SEM (XL30SFEQ, FEI, USA) and energy-dispersive X-ray (EDX; Bruker AXS, Germany), respectively. Prior to imaging, samples were coated with gold (thickness = 6 nm). Both SEM and EDX were performed at an acceleration voltage of 10 kV.

Rheological evaluation of MgPSr–PCL ink was performed on a rheometer (Discovery HR-2, TA instruments). Biomaterial ink was placed between parallel plates (20 mm in diameter) at a gap distance of 0.5 mm. Viscosity was recorded during an oscillatory shear rate sweep test (10–100 s^{-1}). Density of MgPSr–PCL ink was calculated based on the mass of a unit volume of the ink.

Three-Point Flexural Tests

Three-point flexural tests were performed in a universal mechanical testing device (Instron, Model 5967, UK) with a 1 kN load cell. For both designs (IFS-1 and IFS-0.7), rectangular bars ($6 \times 1 \times 0.5$ cm) were printed with printing parameters described in “Design and Extrusion-Based 3D Printing of Implants” section and loaded at a crosshead speed of 2 mm min^{-1} , with support and loading span at 40 and 20 mm, respectively, according to a protocol previously described.[31] The flexural stress, strain, modulus, and strain energy were calculated according to the classic beam theory considering a linear elastic material behavior. In particular, flexural stress was estimated as

$$\sigma_f = \frac{3P_{max}L}{2bh^2} \quad (4)$$

where P_{max} is the maximum load on the beam, L is the length of the support span, and b and h are the width and thickness, respectively. Flexural strain (at P_{max}) was calculated as

$$\varepsilon_f = \frac{6b\delta}{L^2} \quad (5)$$

where δ is the beam deflection under P_{max} at the midspan. The flexural elastic modulus was determined from the load–displacement curve as

$$E_f = \frac{FL^3}{4b\delta h^3} \quad (6)$$

where F/δ is the tangent of the initial straight-line (linear) portion of the load–displacement curve. Moreover, the strain energy (U) was determined by the area below the load–

displacement curve until maximum peak load (Pmax). At least five samples for each group were tested.

Implant Fixation

To study the effect of initial implant fixation to the host bone, rectangular-shaped implants (2 × 1 × 0.4 cm) for both IFS-1 and IFS-0.7 internal architectures were fixed to rectangular-shaped saw-bone blocks (2 × 1 × 1 cm) using cortical screws (diameter = 3.5 mm) and loaded in shear with a customized loading device. A crosshead speed of 2 mm min⁻¹ was applied until a maximum shear force of 100 and 200 N was reached. At each maximum shear force, loading was repeated for five consecutive cycles to investigate the capacity of the material to recover. The applied load and deformation were monitored and the dissipated energy (U_d) after unloading at first and fifth cycle was quantified as

$$U_d = \int_0^{\delta_u} F_t(\delta) d\delta - \int_{\delta_0}^{\delta_u} F_e(\delta) d\delta \quad (7)$$

where $F_t(\delta)$ and $F_e(\delta)$ are the loading function and the unloading function, respectively. δ_u is the total strain at the unloading point, and δ_0 is the permanent strain after unloading. To further investigate permanent deformation of the tested samples, the area of the screw fixation holes, before and after loading, was quantified by micro-CT analysis. Shape of the fixation holes before loading was approximated as a circle of unit radius, and after loading as an ellipsoid. The deformed shape of ellipse (R) was quantified as:

$$R = (1 + \varepsilon_1)/(1 + \varepsilon_3) \quad (8)$$

where ε_1 and ε_3 represent deformation along X and Y axes (minor and major axis of the ellipse). At least, five samples for each group were tested.

In Vitro Degradation Experiments

The effect of enzymatically induced degradation of the implant material was evaluated in vitro over 15 days, with intermediate time points 1, 5, 10, and 15 days, following a protocol described elsewhere.[14] Rectangular-shaped samples (4 × 1 × 0.5 cm) were incubated in a 0.4 mg mL⁻¹ lipase solution (from *Pseudomonas cepacian*, Sigma-Aldrich, Germany) and 1 mg mL⁻¹ sodium azide (Sigma-Aldrich, Germany) at 37 °C. Incubation medium was refreshed every 4 days. At each intermediate time point samples were washed generously with milli-Q water and kept in the desiccator until 48 h prior mechanical testing and weight assessment. Subsequently, the effect of in vitro degradation on material mechanical performance was evaluated by flexural properties under three-point flexural testing, following the protocol described previously in “Three-Point Flexural Tests” section. In

addition, weight loss of the implants and pH of the incubation solution were monitored at each intermediate time. Finally, the cumulative ion release profile of magnesium and strontium ions was recorded utilizing inductively coupled plasma mass spectrometry (ICP-MS, Varian, Darmstadt, Germany) at each incubation time point.

In Vitro Cell Culture

To confirm the cytotoxicity and osteogenic potential of the bone-inducing implants, MgPSr-PCL and plain PCL cylindrical samples (diameter = 5 mm and height = 1 mm) with an internal architecture of IFS-0.7 were prepared and cultured in vitro with hMSCs (passage number 3) for 21 days. Samples were sterilized in 70 v/v% ethanol for 2 h followed by 30 min under ultraviolet (UV) light. hMSCs were first expanded for 7 days in α -MEM supplemented with 10% (v/v) fetal bovine serum (FBS), 0.2×10^{-3} M l-ascorbic-acid-2-phosphate (ASAP), and 1% (v/v) penicillin-streptomycin at 37 °C in a humidified atmosphere containing 5% CO₂, and then seeded (passage number 4) onto implants at a density of 150 000 cells cm⁻². After seeding hMSCs onto implants, constructs were cultured in basal media.

hMSCs viability was determined using a live-dead viability kit for mammalian cells (Invitrogen Life Technologies, USA), prepared according to the manufacturer's instructions. Stained cell-laden constructs were imaged using a confocal microscope (Leica SP8X Laser Scanning, Germany) with 494 nm (green, Calcein) and 528 nm (red, EthD-1) excitation filters. In addition, cell metabolic activity was quantified by Alamar blue, following manufacturer's instruction. Moreover, hMSCs osteogenic differentiation was measured using ALP analysis performed at day 1 and day 7 of in vitro culture, following a protocol described elsewhere. [14] Briefly, ALP activity was measured using conversion of the p-nitrophenyl phosphate liquid substrate system (pNPP, Sigma-Aldrich) and a serial dilution of calf intestinal ALP (Sigma-Aldrich, Germany) in TE-buffer. ALP results were normalized to DNA content from the same cell lysate used to measure ALP, using a Quan-iT-Picogreen-dsDNA kit (Molecular Probes, Invitrogen, Carlsbad, USA) following the manufacturer's instructions. In addition, ALP staining of hMSCs was assessed by utilizing a 5-bromo-4-chloro-3-indolyl phosphate/Nitro blue tetrazolium (BCIP/NBT, ThermoScientific, USA) solution. At least three samples were analyzed per group, i.e., MgPSr-PCL and plain PCL cylindrical samples.

The implants and attached hMSCs were fixed 30 min in formalin to prepare for osteonectin and osteocalcin immunocytochemistry. Then, the cell-laden implants constructs were incubated for 10 min in 0.2% (v/v) Triton X-100 in PBS, and thereafter blocked for 30 min with 5% (v/v) bovine serum albumin/PBS. The samples were incubated overnight at 4 °C with 10 mg mL⁻¹ rabbit monoclonal anti-SPARC antibody (osteonectin, ab225716) and mouse monoclonal antibody recognizing human osteocalcin (clone OCG4; Enzo Life Sciences), respectively. This was followed by incubation with 10 mg mL⁻¹ goat-antimouse

polyclonal antibody conjugated to Alexa Fluor 488 (Invitrogen). All cell-laden implants were also stained for F-actin (TRITC) and DAPI (FAK100 Kit; Merck Millipore), according to the manufacturer's protocol. All other fluorescence images were taken with a Leica SP8X Laser Scanning Confocal Microscope using a white light laser (470–670 nm) and Leica LASX acquisition software.

Ex Vivo Biomechanical Studies

To investigate the mechanical performance of hip implants under representative physiological loading conditions, hip implants (IFS-0.7 group) were mounted on an ex vivo macerated dog pelvis before and after accelerated in vitro degradation (15 days). The pelvis was embedded in epoxy resin (poly-pox THV 500, Poly-Service B.V. Amsterdam, The Netherlands) to facilitate implant loading. The implants were placed in their correct surgical position to repair the acetabular defect and mechanically loaded in Y-direction to mimic normal gait of the canine.

A universal mechanical testing device (Instron, Model 5967, UK) equipped with a 1 kN load cell was used. Implants were loaded at a compressive speed of 5 mm min⁻¹ until implant (or pelvis) failure was reached. From the load–displacement curves different mechanical parameters were determined, in particular the load at failure (defined as the maximum load before implant failure), the strain energy (determined as detailed in “Implant Fixation” section), and the stiffness (as the slope of the load–displacement curves between 2 and 3 mm deformation). A minimum batch of three samples before and after 15 days of in vitro degradation was tested.

Statistical Analysis

A one- or two-way ANOVA with post-hoc Tukey's test was performed to compare the means of the different groups. Only for the pore size and porosity, normality and homogeneity were first checked with Kolmogorov–Smirnov test and then means of the groups were compared with an independent t-test. Differences were considered significant at a probability error (p) of $p < 0.05$. Data were represented as mean \pm standard deviation (SD) and at least three samples were evaluated for each test. All statistical analysis was performed using GraphPad prism V6.

References

1. The Burden of Musculoskeletal Conditions at the Start of the New Millennium: Report of a WHO Scientific Group, World Health Organization, Geneva 2003, p. 218.
2. TS. R. Kingsbury, H. J. Gross, G. Isherwood, P. G. Conaghan, *Rheumatology* 2014, 53, 937.
3. TS. Jacobsen, S. Sonne-Holm, *Rheumatology* 2005, 44, 211.
4. TB. L. Gray, J. B. Stambough, G. R. Baca, P. L. Schoenecker, J. C. Clohisy, *Bone Jt. J.* 2015, 97-B, 1322.
5. TS. Pun, *Curr. Rev. Musculoskeletal Med.* 2016, 9, 427.
6. TC. Pascual-Garrido, F. Guilak, M. F. Rai, M. D. Harris, M. J. Lopez, R. J. Todhunter, J. C. Clohisy, *J. Orthop. Res.* 2018, 36, 1807.
7. TR. Sakkars, V. Pollet, *J. Child. Orthop.* 2018, 12, 302.
8. TR. Ganz, K. Klaue, T. S. Vinh, J. W. Mast, *Clin. Orthop. Relat. Res.* 1988, 232, 26.
9. TC. Clohisy, A. L. Schutz, L. St. John, P. L. Schoenecker, R. W. Wright, *Clin. Orthop. Relat. Res.* 2009, 467, 2041.
10. TZaltz, G. Baca, Y. J. Kim, P. Schoenecker, R. Trousdale, R. Sierra, D. Sucato, E. Sink, P. Beaulé, M. B. Millis, D. Podeszwa, J.C. Clohisy, *J. Bone Jt. Surg., Am. Vol.* 2014, 96, 1967.
11. D. R. Maldonado, V. Ortiz-Declet, A. W. Chen, A. C. Lall, M. R. Mohr, J. R. Laseter, B. G. Domb, *Arthrosc. Tech.* 2018, 7, e779.
12. Willemsen, C. J. Doelman, A. S. Y. Sam, P. R. Seevinck, R. J. B. Sakkars, H. Weinans, B. C. H. van Der Wal, *Acta Orthop.* 2020, 91, 383.
13. K. Willemsen, M. Tryfonidou, R. Sakkars, R. M. Castelein, A. A. Zadpoor, P. Seevinck, H. Weinans, B. Meji, B. C. H. van der Wal, *J. Orthop. Res.* 2021, 25133.
14. Golafshan, E. Vorndran, S. Zaharievski, H. Brommer, F. B. Kadumudi, A. Dolatshahi-Pirouz, U. Gbureck, R. van Weeren, M. Castilho, J. Malda, *Biomaterials* 2020, 261, 120302.
15. J. A. Inzana, D. Olvera, S. M. Fuller, J. P. Kelly, O. A. Graeve, E. M. Schwarz, S. L. Kates, H. A. Awad, *Biomaterials* 2014, 35, 4026.
16. M. Castilho, C. Moseke, A. Ewald, U. Gbureck, J. Groll, I. Pires, J. Teßmar, E. Vorndran, *Biofabrication* 2014, 6, 015006.
17. L. Elomaa, S. Teixeira, R. Hakala, H. Korhonen, D. W. Grijpma, J. V. Seppälä, *Acta Biomater.* 2011, 7, 3850.
18. K. Arcaute, B. Mann, R. Wicker, *Acta Biomater.* 2010, 6, 1047.
19. G. N. Duda, E. Schneider, E. Y. S. Chao, *J. Biomech.* 1997, 30, 933.
20. Paknahad, N. W. Kucko, S. C. G. Leeuwenburgh, L. J. Sluys, *J. Mech. Behav. Biomed. Mater.* 2020, 103, 103565.
21. S. de Lacerdas Schickert, J. A. Jansen, E. M. Bronkhorst, J. J. van den Beucken, S. C. Leeuwenburgh, *Acta Biomater.* 2020, 110, 280.
22. N. R. Ordway, K. J. Ash, M. A. Miller, K. A. Mann, K. Hayashi, *Vet. Comp. Orthop. Traumatol.* 2019, 32, 369.

23. S. N. Sangiorgio, D. B. Longjohn, J. L. Lee, J. D. Alexander, L. D. Dorr, E. Ebramzadeh, *J. Appl. Biomater. Biomech.* 2008, 6, 72.
24. L. Mao, L. Xia, J. Chang, J. Liu, L. Jiang, C. Wu, B. Fang, *Acta Biomater.* 2017, 61, 217.
25. S. Yoshizawa, A. Brown, A. Barchowsky, C. Sfeir, *Acta Biomater.* 2014, 10, 2834.
26. F. Mavrogenis, A. D. Kanellopoulos, G. N. Nomikos, P. J. Papagelopoulos, P. N. Soucacos, *Clin. Orthop. Relat. Res.* 2009, 467, 1591.
27. N. G. Grün, P. L. Holweg, N. Donohue, T. Klestil, A. M. Weinberg, *Innovative Surg. Sci.* 2020, 3, 119.
28. K. Shi, J. Jing, L. Song, T. Su, Z. Wang, *Enzymatic Hydrolysis of Polyester: Degradation of Poly(ϵ -Caprolactone) by Candida Antarctica Lipase and Fusarium Solani Cutinase*, Elsevier B.V, Amsterdam 2020.
29. R. M. Felfel, I. Ahmed, A. J. Parsons, G. S. Walker, C. D. Rudd, *J. Mech. Behav. Biomed. Mater.* 2011, 4, 1462.
30. Hofmann, R. D. Bloebaum, K. N. Bachus, *Acta Orthop. Scand.* 2009, 68, 161.
31. ASTM C1161 -02 Standard Test Method for Flexural Strength of Advanced Ceramics at Ambient Temperature, <https://www.astm.org/DATABASE.CART/HISTORICAL/C1161-02.htm>



CHAPTER 8

A novel treatment for anterior shoulder instability A biomechanical comparison between a patient-specific implant and the Latarjet procedure

Koen Willemsen | Thomas D. Berendes | Timon Geurkink |
Ronald L.A.W. Bleys | Marius A. Leeflang | Harrie Weinans |
René M. Castelein | Rob G.H.H. Nelissen | Bart C.H. van der Wal

Published in
The Journal of bone and joint surgery, American volume 101.14 (2019): e68.
<https://doi.org/10.2106/JBJS.18.00892>

Abstract

Background: Anterior glenohumeral instability with >20% glenoid bone loss is a disorder that can be treated with the Latarjet stabilizing procedure; however, complications are common. The purposes of this study were to (1) evaluate the effect of an anatomic-specific titanium implant produced by 3-dimensional (3D) printing as a treatment option for recurrent shoulder instability with substantial glenoid bone loss and (2) compare the use of that implant with the Latarjet procedure.

Methods: Ten fresh-frozen cadaveric shoulders (mean age at the time of death, 78 years) were tested in a biomechanical setup with the humerus in 30° of abduction and in neutral rotation. The shoulders were tested under 5 different conditions: (1) normal situation, (2) creation of an anterior glenoid defect, (3) implantation of an anatomic-specific titanium implant produced by 3D printing, and the Latarjet procedure (4) with and (5) without 10 N of load attached to the conjoined tendon. In each condition, the humerus was translated 10 mm anteriorly relative to the glenoid, and the maximum peak translational force that was necessary for this translation was measured.

Results: After creation of the glenoid defect, the mean translational peak force decreased by $30\% \pm 6\%$ compared with that for the normal shoulder. After restoration of the original glenoid anatomy, the translational force needed to dislocate the humeral head from the glenoid significantly increased compared with that in the defect condition-to $119\% \pm 16\%$ of normal ($p < 0.01$) with the 3D-printed anatomic-specific implant and to $121\% \pm 48\%$ of normal ($p < 0.01$) following the Latarjet procedure. No significant differences in mean translational force were found between the anatomic-specific implant and the Latarjet procedure ($p = 0.72$).

Conclusions: The mean translational peak force needed to dislocate the humerus 10 mm anteriorly on the glenoid was higher after glenoid restoration with the 3D-printed anatomic-specific implant compared with when the glenoid had a 20% surface defect but also compared with when the glenoid was intact. No differences in mean translational peak force were found between the 3D-printed anatomic-specific glenoid implant and the Latarjet procedure, although there was less variability in the 3D-implant condition.

Clinical Relevance: Novel 3D-printing technology could provide a reliable patient-specific alternative to solve problems related to traditional treatment methods for shoulder instability.

Introduction

Anterior glenohumeral instability is a common disorder, typically affecting the young and active population, with an overall prevalence of 2%[1,2]. The shoulder joint is the most mobile joint in the human body; however, this mobility comes at the expense of stability[1]. A first dislocation often has a traumatic origin and is often followed by a disabling course as recurrent (sub)luxations occur in up to 94% of patients, especially younger ones[3]. Eventually, this can lead to chronic anterior shoulder instability, with presentations ranging from minor symptoms to frequent (sub)luxations[1]. Without adequate treatment, this condition often leads to more rapid degenerative arthropathy of the shoulder and major limitations in daily life[2,4].

There are numerous surgical treatment options for the unstable shoulder joint, and they target different causes of a multifactorial problem. With all treatments, the aim is to lower the rate of recurrence of dislocations in combination with a low complication rate. The dynamic interactions of soft-tissues lesions and bone loss are an important factor in the choice of treatment[5]. The arthroscopic Bankart repair and the Latarjet procedure are the 2 most commonly used techniques[2,6]. Soft-tissue repairs such as the Bankart procedure often fail in the presence of substantial bone loss (>20% of the glenoid area), which is present in up to 67% of patients with recurrent shoulder instability[7]. In patients with severe glenoid loss, the Latarjet procedure seems to be the preferred treatment[1,2,8]. Currently, there are 2 commonly used and equivalent techniques for the Latarjet[9] procedure: (1) the classic technique, with which the inferior surface of the coracoid is transferred to the anterior surface of the glenoid, and (2) the congruent-arc technique, with which the coracoid is rotated 90° and transferred with the medial side against the glenoid[10].

The Latarjet procedure is known for its low rates of recurrent instability, even in high-intensity contact-sport athletes, but it can have severe complications in up to 30% of patients[11-14]. The recent literature contains claims of possible superiority of the Latarjet procedure relative to the Bankart repair[14,15]. However, although the split subscapularis tendon might provide dynamic stability by means of the sling effect by the coracobrachialis tendon, the bone block of the coracoid within the subscapularis tendon also prevents normal function of the subscapular muscles, which are major shoulder muscles. Another possible long-term problem with the Latarjet procedure is resorption of the coracoid bone block while it is fixed by 2 titanium screws[16]. Complications, donor site problems, and the nonanatomic nature of this procedure have spurred research on other graft sources, such as iliac crest autograft, allograft, and synthetics[17].

In this study, as part of the PROSPERoS (PRinting PERsonalized orthopaedic implantS) project group, the first author (K.W.) designed a 3-dimensional (3D)-printed titanium implant that could circumvent these potential issues. The implant is placed extracapsularly, flush with the bone, to fill in the exact defect and with the joint capsule acting as the articulating surface.

The primary aim of this study was to investigate, in a cadaveric model, if use of an anatomic-specific glenoid implant in a severe glenoid defect could restore glenohumeral morphology and stability. The secondary aim was to compare the anatomic implant and the classic Latarjet procedure with regard to the translational forces needed to dislocate the humerus 10 mm anteriorly on the glenoid after the operation[9]. Our hypothesis was that the anatomic implant would increase these translational forces relative to those after the creation of the glenoid bone defect and that the forces would be comparable with those in a normal shoulder and those after the classic Latarjet procedure.

Methods

Thirteen fresh-frozen human shoulders were originally inspected for use in this study. Exclusion criteria were osseous defects (humeral and/or glenoid), rotator cuff tears, and moderate to severe osteoarthritis as demonstrated by direct inspection and computed tomography (CT). After exclusion, 10 shoulders (5 left and 5 right, and 5 from male donors and 5 from female donors) from 8 cadavers with a mean age at the time of death of 78 years (range, 71 to 86 years) were included.

All specimens were disarticulated at the scapulothoracic joint and transected at the humeral shaft, about 15 cm distal to the greater tubercle. The shoulder girdle was dissected, with the deltoid muscle removed and the rotator cuff muscles, conjoined tendon, and joint capsule left intact. The scapula was rigidly fixed in a self-centering vice that was secured on 4 linear railed platforms (TRS15VN; TBI Motion Technology) placed parallel to the glenoid's posterior-anterior axis and attached by prestretched rope (high-modulus polyethylene [HMPE]; Dyneema) to the crosshead of an LR5K universal testing machine equipped with an XLC 5kN load cell (Lloyd Instruments).

The proximal part of the humerus was rigidly fastened at its shaft with a custom-made fixture that allowed 30° of abduction and neutral rotation of the humerus in relation to the glenoid cavity. In this position, the osseous anatomy largely provides the stability, rather than the dynamic stabilizers and the capsuloligamentous structures[18,19]. The humeral fixture was attached to 4 vertically placed linear railed platforms and loaded with weights to allow a downward force of 50 N[18-20] on the glenoid, ensuring that the humeral head

found its original neutral anatomic position in the glenoid cavity. This neutral position was defined as the starting position for each test. The glenoid platform moved posteriorly to cause anterior translation of the humerus at a set rate of 1.0 mm/sec for a total of 10 mm measured by calipers on the horizontal rail [21,22]. The loads were recorded with NEXYGEN data acquisition software (Lloyd Instruments) (Fig. 1).

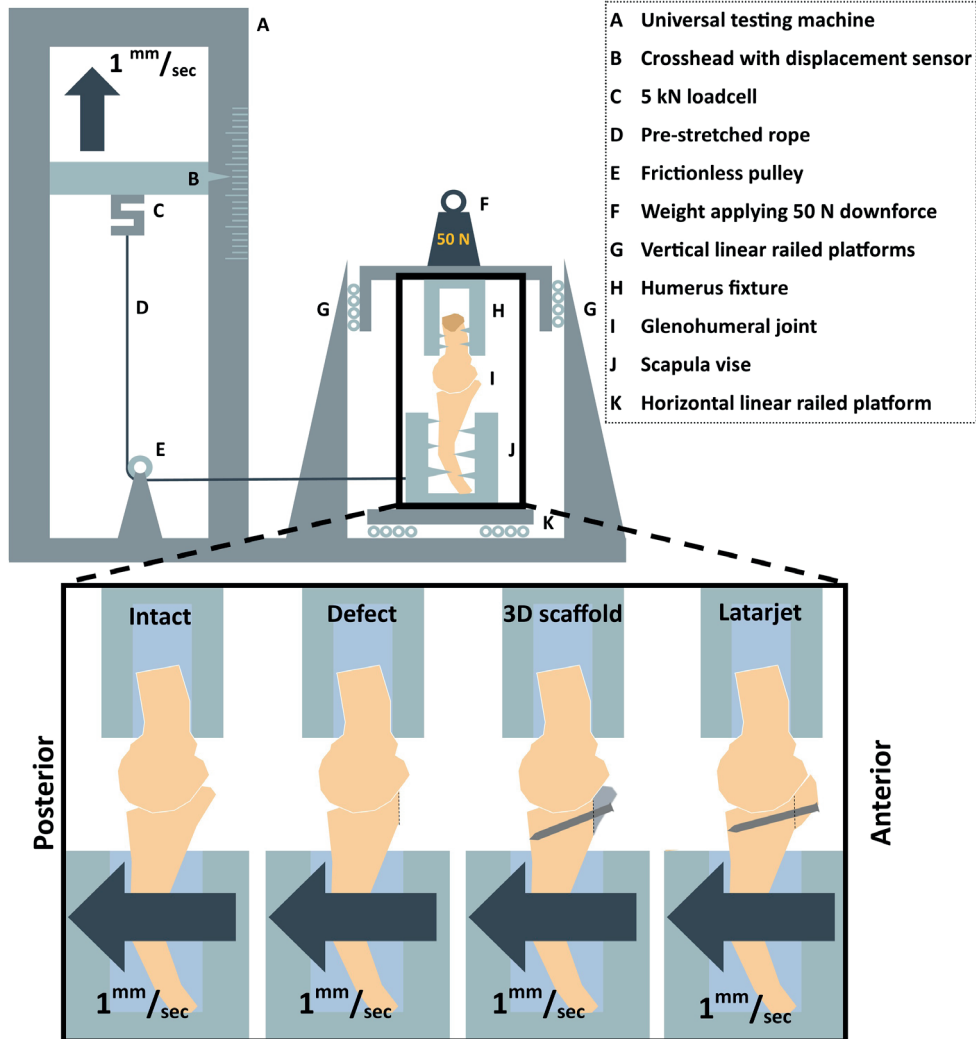


Figure 2. Top Schematic overview of the components of the custom-designed testing device. Bottom (enlarged area) The different testing conditions.

At the start of the study, a CT scan of the shoulder girdle was made. The images comprised the entire shoulder girdle and humerus with a slice thickness of 0.9 mm (250 mAs, 120 kV). The CT scans were transferred to commercially available image processing software

(Mimics Medical 20.0; Materialise), which was used to segment a pre-defect 3D model of the osseous structures using standardized bone threshold values (≥ 226 Hounsfield units).

After imaging, an anterior critical defect of 20% of the glenoid length was created[23] as described by Yamamoto et al.[18,24]. The anterior labrum was removed, and an osteotomy was made perpendicular to the joint surface using an anatomic-specific saw template (Fig. 2).

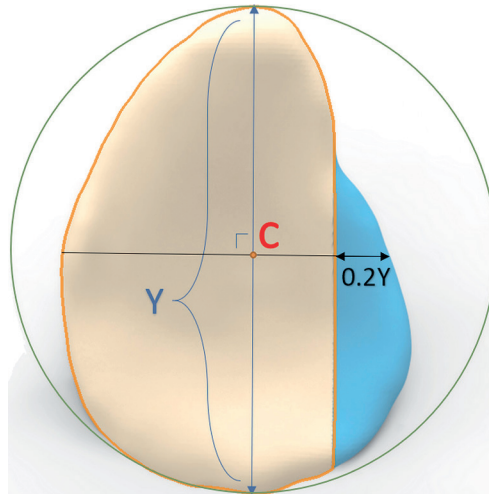


Figure 2. Schematic representation of the simulated glenoid defect as described by Yamamoto et al.^{18,24}. A circle was drawn around the pear-shaped glenoid. The y axis was drawn through the superior and inferior points. The x axis was drawn perpendicular to the y axis, through the center (C) of the glenoid circle. The osseous defect was created at the anterior side of the glenoid with a total width equal to 20% of the glenoid length ($0.2Y$).

As part of the the PRoSPERoS project, the defect-repairing titanium implants were designed by the first author (K.W.) using Geomagic Freeform Plus software (3D Systems). A simulation model of the glenoid defect was removed from the pre-defect model using CAD (computer-aided design) Boolean subtraction operatives, leaving the essential size of the implant. The created implant is therefore the size of the osteotomized glenoid rim and designed to be flush with the bone with the capsule as the overlying articulating surface. Additionally, 2 locking screws were added for angular stability, and their trajectories were digitally planned in the scaffold. The 3D printing was done with medical grade titanium (Ti-6Al-4V ELI [extra-low interstitial], grade 23) using an SLM (Selective Laser Melting) printer (ProX DMP 320; 3D Systems). Post-processing included polishing and screw wiretapping (Fig. 3).

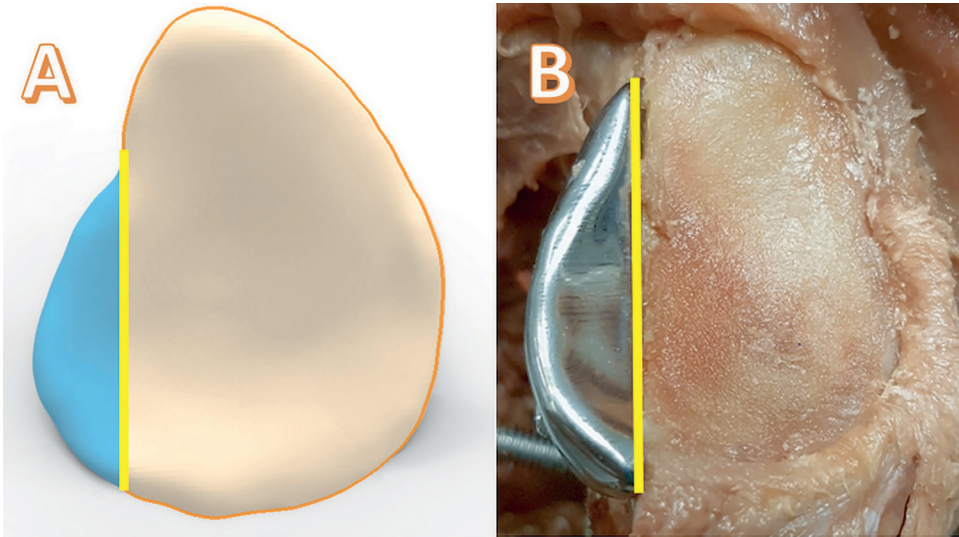


Figure 3-A. In silico simulation of the implant. The vertical line is the osteotomy or defect line. The implant is to the left of the osteotomy line, and the glenoid is to the right of the line. **Fig. 3-B** A specimen with an implanted scaffold. The shoulder capsule was removed for visualization purposes.

We tested 5 different conditions: (1) the “normal” situation, (2) after creation of an anterior glenoid bone defect, (3) after implantation of the 3D-printed titanium anatomic-specific implant (the “scaffold” condition), and after the classic Latarjet procedure (4) with and (5) without a 10-N load applied to the conjoined tendon by means of sutures to simulate the so-called sling effect[19] (Fig. 4). The specimens were tested in the situation with either the 3D implant first ($n = 5$) or the Latarjet procedure first ($n = 5$), depending on the randomization. Every specimen was tested under all 5 conditions 5 times in 1 day. The specimens were sprayed with a 0.9% NaCl solution to prevent the quality of the soft tissue from deteriorating. A detailed description of the surgical technique is available in the Appendix (Supplementary Data 1).

After stability testing, another CT scan was performed for 5 shoulders with the 3D-printed implant in situ and 5 shoulders after the Latarjet for evaluation of the geometry of the defect repair. The images were uploaded into Mimics Medical to compare the glenoid width (the widest anteroposterior diameter measured parallel to the superior-inferior axis) and the cavity depth (measured as described by Willemot et al.[25]) among the intact, defect, and post-reconstruction conditions.

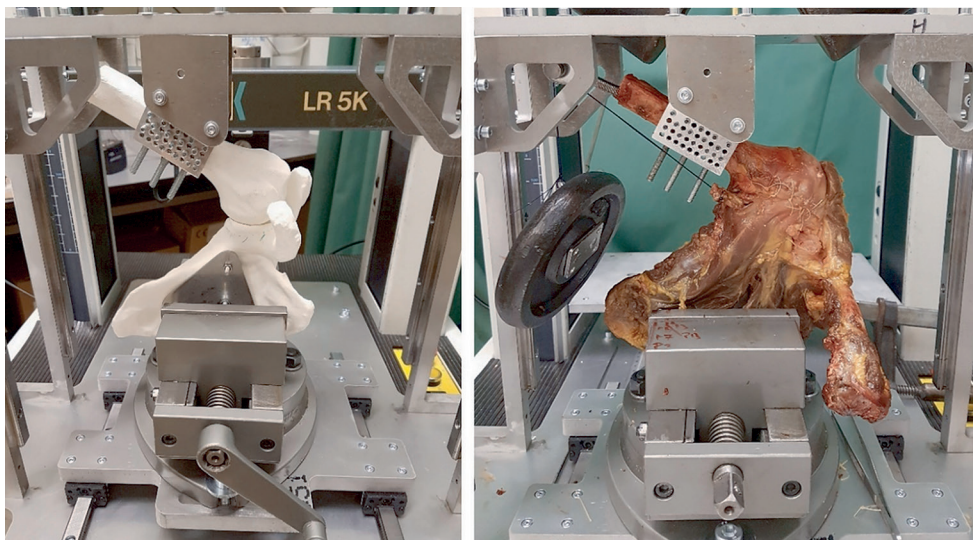


Figure 4. Left A 3D-printed sample used for optimizing the setup. Right A specimen that underwent a test cycle under condition 4: the Latarjet procedure with 10 N of pull on the conjoined tendon

Data Analysis

A nonparametric Friedman test was performed to compare the mean peak translational forces needed to translate the humeral head 10 mm and the glenoid cavity width and depth among all of the different conditions. When a significant value was found, the related-samples Wilcoxon signed-rank test (SPSS, version 24; IBM) was used as a post hoc analysis for the distinct research questions. The sample size was calculated on the basis of prior data[22,26-28]. A mean effect size of 30% and a standard deviation of 25% were chosen. A minimum of 8 samples was needed to show a significant difference in translational force with a power of 0.8 and an alpha of 0.05. Ten samples were included in this study

Results

After dissection, all shoulder capsules and labra were found to be intact. During testing, no signs of damage to the specimens were observed. The mean superior-inferior glenoid diameter (and standard deviation [SD]) of the 10 specimens was 37.1 ± 3.9 mm as measured on CT scans. Therefore, 7.4 ± 2.1 mm—or 20% of the superior-inferior glenoid diameter—was the desired average width of the glenoid defect. The actual created mean width of the glenoid defect was 7.4 ± 1.9 mm, equivalent to 19.9% of the glenoid diameter, which was not significantly different from the desired width ($p = 0.80$).

The glenoid width decreased significantly after creation of the bone defect in both the group that subsequently received the 3D-printed anatomic-specific scaffold (the “scaffold group”) ($p < 0.05$; $n = 5$) and the group that received the Latarjet procedure ($p < 0.05$; $n = 5$). The glenoid width increased to 100% and 96% of the normal width after restoration with the scaffold and Latarjet procedure, respectively. These widths did not differ significantly from the normal width in either the scaffold ($p = 0.50$) or Latarjet ($p = 0.14$) group (Fig. 5). The glenoid cavity depth decreased significantly after the creation of the bone defect in both the scaffold ($p < 0.05$) and the Latarjet ($p < 0.05$) group and increased to 118% of the normal depth after restoration with either procedure. This depth differed significantly from the normal depth in both the scaffold ($p = 0.05$) and the Latarjet ($p < 0.05$) group (Fig. 5).

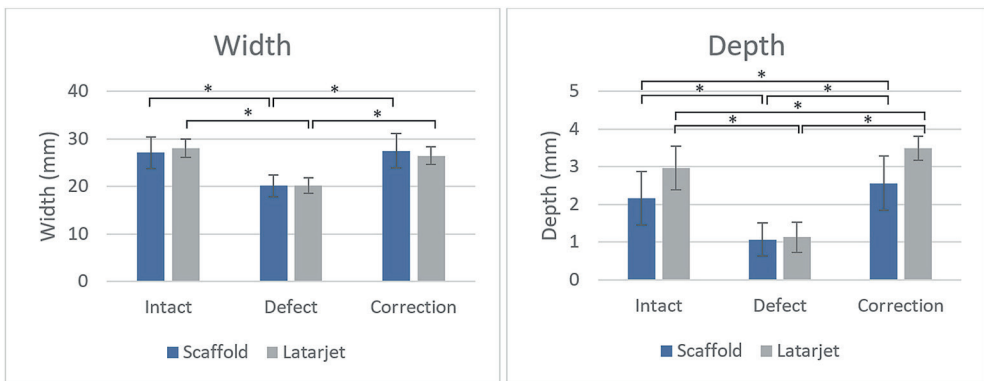


Figure 5. The mean (and standard deviation [SD]) glenoid cavity width and depth (mm) in the normal, defect, and reconstructed (correction) conditions (scaffold or Latarjet procedure). *A significant difference ($p \leq 0.05$).

Peak Translational Forces

The mean maximum peak force needed to translate the humeral head 10 mm anteriorly in the intact specimens was 48.6 ± 15.8 N, which decreased significantly (by $30\% \pm 6\%$) to 33.8 ± 10.1 N after creation of the bone defect ($p < 0.01$). The mean force in the defect condition significantly increased after reconstruction—to 56.0 ± 16.4 N ($p < 0.01$) in the scaffold group and to 55.0 ± 16.2 N ($p < 0.01$) in the Latarjet group. Also, the mean translational peak force was significantly higher after reconstruction with the scaffold compared with that in the normal situation ($p < 0.01$). No significant difference was found when the reconstructions with the scaffold and the Latarjet procedure were compared ($p = 0.72$) (Table I). A box plot showing the peak forces, as percentages of the normal situation, under all of the different conditions is shown in Figure 6.

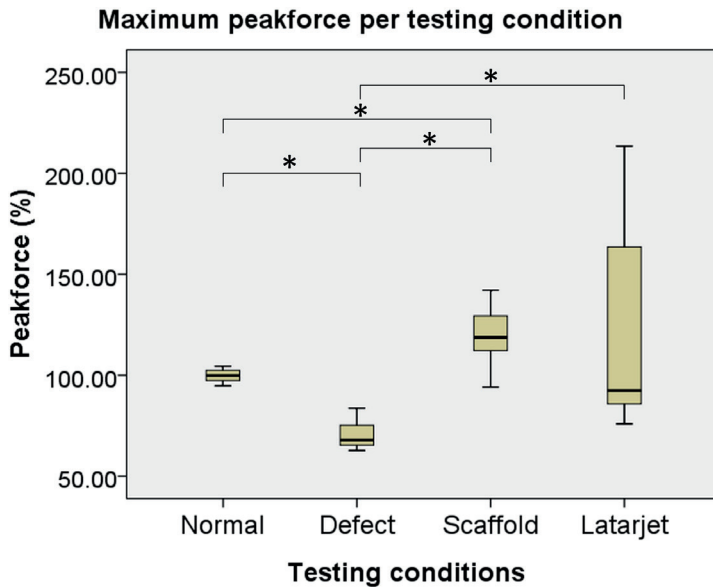


Figure 6. Maximum peak force (%) needed to translate the humeral head 10 mm anteriorly with respect to the glenoid in the normal, defect, scaffold, and Latarjet conditions. The humerus was in 30° of abduction and neutral rotation in all conditions. The normal healthy shoulder was used as the standard for the subsequent analyses. *A significant difference ($p < 0.05$). Horizontal line inside box = median, top and bottom of box = interquartile range, and top and bottom of whiskers = total range.

Table 1. Results of Related-Samples Wilcoxon Signed-Rank Test Comparing Various Testing Conditions*

	Z	P Value*
<i>Normal vs. defect</i>	-2,803 [†]	<0.01
<i>Scaffold vs. normal</i>	-2,497 [‡]	<0.01
<i>Scaffold vs. defect</i>	-2,803 [‡]	<0.01
<i>Latarjet vs. defect</i>	-2,803 [‡]	<0.01
<i>Latarjet vs. scaffold</i>	-0,357 [†]	0.72
<i>Latarjet vs. Latarjet without sling</i>	-2,666 [†]	<0.01

*The level of significance was $p < 0.05$.

[†]Based on positive ranks.

[‡]Based on negative ranks.

As an additional test, the translational forces were measured after the Latarjet procedure but without 10 N of load on the conjoined tendon. Under this condition, the force decreased by $21\% \pm 31\%$, compared with force in the Latarjet group with this load; this difference was significant ($p < 0.01$).

Discussion

The force necessary to translate the humeral head 10 mm anteriorly in the glenoid significantly decreased, to $70\% \pm 7\%$ of normal, after the creation of the glenoid defect. After restoration of the original glenoid anatomy with an anatomic-specific 3D-printed scaffold, the translational forces increased to $119\% \pm 16\%$ of the forces in the intact glenohumeral joint. This was not significantly different from the increase after the Latarjet procedure (to $121\% \pm 48\%$ of normal); however, this does not imply that the 2 procedures are the same (Fig. 6).

In 1947, Moseley described a metallic rim that could be fixed to the neck of the scapula[29]. This implant, which contained holes for suturing of the capsule to the bone on the joint side of the prosthesis, was placed in an extracapsular position[29]. More recently, Diederichs et al. presented an *in silico* method that compares the healthy contralateral glenoid with the affected glenoid to simulate the optimal reconstruction of a glenoid rim defect[30]. However, the current study is the first to use biomechanical testing of 3D-printed anatomic-specific titanium implants for reconstruction of severe glenoid defects in the human shoulder.

Since the 3D-printed glenoid scaffold should recreate the intact glenoid exactly it was expected that the mean translational peak force would be comparable between the 2 situations. However, several factors may have attributed to the greater forces measured after the scaffold reconstructions. First, although the bone cut used to create the glenoid defect was expected to be exactly parallel to the y axis and perpendicular to the glenoid surface, if the implant was not positioned perfectly perpendicular to the joint surface (i.e., if it was at a slight angle) the glenoid cavity could have become too wide and too deep. Second, capsular interposition and capsular suturing contribute to the translational force, as shown by Yamamoto et al.[22]. The capsule was envisioned to be as thick as the cartilage as the implant was placed and modeled to match the bone level. However, the thickness of the interpositioned capsule is difficult to predict as it is not visible on pre-defect CT. This might have affected the translational forces.

The secondary goal of this study was to compare the 3D-printed titanium implant with the classic Latarjet procedure, which is currently considered to be the standard for treating recurrent anterior glenohumeral instability when $>20\%$ of the glenoid bone has been lost[2,8]. However, the Latarjet procedure is not anatomically precise and has a high rate of complications, including malpositioning, problems with the screw trajectory, loss of the range of motion, and eventually the development of arthrosis[13]. A patient-specific implant can be a solution for some of these problems, as all aspects of the reconstruction can be planned with the aid of 3D-design software. However, this study was not performed to show inferiority or superiority of 1 procedure over the other; more research is needed for comparison of the 2 techniques.

Both clinical and biomechanical studies have demonstrated the working mechanism of the Latarjet procedure[15,19,22,26,27]. The downside of the 3D-printed scaffold method might be the absence of a dynamic muscle stabilizer, which is created during the Latarjet procedure using the conjoined tendon[22,27,31]. In our study, the conjoined tendon contributed approximately 21% of the force needed to translate the humerus. However, the variability in the restoration of glenohumeral stability by the Latarjet procedure was relatively large (Fig. 6), whereas the titanium implant was more predictable (had less variability) in the restoration of glenohumeral stability.

Some limitations must be considered when interpreting our findings. We performed a biomechanical cadaver study, thus eliminating large dynamic stabilizers (i.e., muscles), which may be 1 of the most important factors in shoulder instability. Also, the same specimens were used for both the Latarjet and the scaffold procedure, with the risk of tissue elongation during testing. However, no significant differences were found between the shoulders in which the scaffold was implanted after the primary Latarjet procedure and those in which the procedures were done in the reverse order. In addition, it would have been preferable for us to have created the defect before the implants were designed. However, we made a cutting template to accurately create the glenoid defects, which were nearly the same as the planned defects, with widths of 7.4 ± 1.9 mm and 7.3 ± 2.1 mm, respectively. By designing the implants before the creation of the defects, we were always able to perform all procedures within 24 hours after defrosting the specimen, thereby preventing degradation of the tissues as much as possible. Another limitation of the 3D-printed implant is that no soft-tissue lesions such as labral injuries were directly targeted.

In conclusion, the purpose of our study was to determine whether use of a 3D-printed anatomic-specific titanium implant in a severe glenoid defect would increase the mean peak force needed to translate the humerus 10 mm anteriorly to levels comparable with those in the healthy normal situation. We found that the mean translational peak force after restoration with the anatomic-specific implant was significantly higher than that in the normal situation. No significant difference in results was identified between the 3D-printed anatomic-specific implant and the classic Latarjet procedure. Restoration of glenohumeral stability with the 3D-printed anatomic-specific implant is not the same as the normal situation, although it is very consistent and is comparable with that following the Latarjet procedure.

Appendix

<http://links.lww.com/JBJS/F299>

References

1. Dodson CC, Cordasco FA. Anterior glenohumeral joint dislocations. *Orthop Clin North Am*. 2008. October;39(4):507-18, vii.
2. Sofu H, Gürsu S, Koçkara N, Oner A, İssin A, Camurcu Y. Recurrent anterior shoulder instability: review of the literature and current concepts. *World J Clin Cases*. 2014. November 16;2(11):676-82.
3. Leroux T, Wasserstein D, Veillette C, Khoshbin A, Henry P, Chahal J, Austin P, Mahomed N, Ogilvie-Harris D. Epidemiology of primary anterior shoulder dislocation requiring closed reduction in Ontario, Canada. *Am J Sports Med*. 2014. February;42(2):442-50. Epub 2013 Nov 25.
4. Hovelius L, Saeboe M. Neer Award 2008: arthropathy after primary anterior shoulder dislocation—223 shoulders prospectively followed up for twenty-five years. *J Shoulder Elbow Surg*. 2009. May-Jun;18(3):339-47. Epub 2009 Feb 28.
5. Momaya AM, Tokish JM. Applying the glenoid track concept in the management of patients with anterior shoulder instability. *Curr Rev Musculoskelet Med*. 2017. December;10(4):463-8.
6. Blonna D, Bellato E, Caranzano F, Assom M, Rossi R, Castoldi F. Arthroscopic Bankart repair versus open Bristow-Latarjet for shoulder instability: a matched-pair multicenter study focused on return to sport. *Am J Sports Med*. 2016. December;44(12):3198-205. Epub 2016 Aug 8
7. Pauzenberger L, Dyrna F, Obopilwe E, Heuberer PR, Arciero RA, Anderl W, Mazzocca AD. Biomechanical evaluation of glenoid reconstruction with an implant-free J-bone graft for anterior glenoid bone loss. *Am J Sports Med*. 2017. October;45(12):2849-57. Epub 2017 Aug 3.
8. Ramhamadany E, Modi CS. Current concepts in the management of recurrent anterior glenohumeral joint instability with bone loss. *World J Orthop*. 2016. June 18;7(6):343-54.
9. Montgomery SR, Katthagen JC, Mikula JD, Marchetti DC, Tahal DS, Dornan GJ, Dahl KD, Brady AW, Turnbull TL, Millett PJ. Anatomic and biomechanical comparison of the classic and congruent-arc techniques of the Latarjet procedure. *Am J Sports Med*. 2017. May;45(6):1252-60. Epub 2017 Feb 14.
10. Burkhart SS, De Beer JF, Barth JRH, Cresswell T, Roberts C, Richards DP. Results of modified Latarjet reconstruction in patients with anteroinferior instability and significant bone loss. *Arthroscopy*. 2007. October;23(10):1033-41.
11. Neyton L, Young A, Dawidziak B, Visona E, Hager JP, Fournier Y, Walch G. Surgical treatment of anterior instability in rugby union players: clinical and radiographic results of the Latarjet-Patte procedure with minimum 5-year follow-up. *J Shoulder Elbow Surg*. 2012. December;21(12):1721-7. Epub 2012 May 5.
12. Latarjet M. [Treatment of recurrent dislocation of the shoulder]. *Lyon Chir*. 1954. Nov-Dec;49(8):994-7. French.
13. Griesser MJ, Harris JD, McCoy BW, Hussain WM, Jones MH, Bishop JY, Miniaci A. Complications and re-operations after Bristow-Latarjet shoulder stabilization: a systematic review. *J Shoulder Elbow Surg*. 2013. February;22(2):286-92.

14. Longo U, Loppini M, Rizzello G, Ciuffreda M, Maffulli N, Denaro V. Latarjet, Bristow, and Eden-Hybinette procedures for anterior shoulder dislocation: systematic review and quantitative synthesis of the literature. *Arthroscopy*. 2014;30(9):1184-211.
15. An VVG, Sivakumar BS, Phan K, Trantalos J. A systematic review and meta-analysis of clinical and patient-reported outcomes following two procedures for recurrent traumatic anterior instability of the shoulder: Latarjet procedure vs. Bankart repair. *J Shoulder Elbow Surg*. 2016. May;25(5):853-63. Epub 2016 Jan 19.
16. Di Giacomo G, Costantini A, de Gasperis N, De Vita A, Lin BKH, Francone M, Rojas Beccaglia MA, Mastantuono M. Coracoid graft osteolysis after the Latarjet procedure for anteroinferior shoulder instability: a computed tomography scan study of twenty-six patients. *J Shoulder Elbow Surg*. 2011. September;20(6):989-95. Epub 2011 Mar 9.
17. Willemot LB, Elhassan BT, Verborgt O. Bony reconstruction of the anterior glenoid rim. *J Am Acad Orthop Surg*. 2018. May 15;26(10):e207-18.
18. Yamamoto N, Itoi E, Abe H, Kikuchi K, Seki N, Minagawa H, Tuoheti Y. Effect of an anterior glenoid defect on anterior shoulder stability: a cadaveric study. *Am J Sports Med*. 2009. May;37(5):949-54. Epub 2009 Mar 4.
19. Wellmann M, Petersen W, Zantop T, Herbort M, Kobbe P, Raschke MJ, Hurschler C. Open shoulder repair of osseous glenoid defects: biomechanical effectiveness of the Latarjet procedure versus a contoured structural bone graft. *Am J Sports Med*. 2009. January;37(1):87-94. Epub 2008 Dec 4
20. Itoi E, Lee SB, Berglund LJ, Berge LL, An KN. The effect of a glenoid defect on anteroinferior stability of the shoulder after Bankart repair: a cadaveric study. *J Bone Joint Surg Am*. 2000. January;82(1):35-46.
21. Itoi E, Yamamoto N, Kurokawa D, Sano H. Bone loss in anterior instability. *Curr Rev Musculoskelet Med*. 2013. March;6(1):88-94.
22. Yamamoto N, Muraki T, An KN, Sperling JW, Cofield RH, Itoi E, Walch G, Steinmann SP. The stabilizing mechanism of the Latarjet procedure: a cadaveric study. *J Bone Joint Surg Am*. 2013. August 7;95(15):1390-7.
23. Saito H, Itoi E, Sugaya H, Minagawa H, Yamamoto N, Tuoheti Y. Location of the glenoid defect in shoulders with recurrent anterior dislocation. *Am J Sports Med*. 2005. June;33(6):889-93. Epub 2005 Apr 12.
24. Yamamoto N, Itoi E. Osseous defects seen in patients with anterior shoulder instability. *Clin Orthop Surg*. 2015;7(4):425-9.
25. Willemot LB, Akbari-Shandiz M, Sanchez-Sotelo J, Zhao K, Verborgt O. Restoration of articular geometry using current graft options for large glenoid bone defects in anterior shoulder instability. *Arthroscopy*. 2017. September;33(9):1661-9. Epub 2017 Jun 15.
26. Patel RM, Walia P, Gottschalk L, Kuklis M, Jones MH, Fening SD, Miniaci A. The effects of Latarjet reconstruction on glenohumeral kinematics in the presence of combined bony defects: a cadaveric model. *Am J Sports Med*. 2016. July;44(7):1818-24. Epub 2016 Apr 15.

27. Barrett Payne W, Kleiner MT, McGarry MH, Tibone JE, Lee TQ. Biomechanical comparison of the Latarjet procedure with and without a coracoid bone block. *Knee Surg Sports Traumatol Arthrosc.* 2016. February;24(2):513-20. Epub 2015 Dec 12.
28. Kephart CJ, Abdulian MH, McGarry MH, Tibone JE, Lee TQ. Biomechanical analysis of the modified Bristow procedure for anterior shoulder instability: is the bone block necessary? *J Shoulder Elbow Surg.* 2014. December;23(12):1792-9. Epub 2014 Jun 9.
29. Moseley HF. The use of a metallic glenoid rim in recurrent dislocation of the shoulder. *Can Med Assoc J.* 1947. March;56(3):320.
30. Diederichs G, Seim H, Meyer H, Issever AS, Link TM, Schröder RJ, Scheibel M. CT-based patient-specific modeling of glenoid rim defects: a feasibility study. *AJR Am J Roentgenol.* 2008. November;191(5):1406-11.
31. Giles JW, Boons HW, Elkinson I, Faber KJ, Ferreira LM, Johnson JA, Athwal GS. Does the dynamic sling effect of the Latarjet procedure improve shoulder stability? A biomechanical evaluation. *J Shoulder Elbow Surg.* 2013. June;22(6):821-7. Epub 2012 Sep 28.



CHAPTER 9

Deformable titanium for acetabular revision surgery: a proof of concept

Joëll Magré | Koen Willemsen | Eline M.A. Kolken | Amir A. Zadpoor |
Charles Vogely | Bart C.H. van der Wal | Harrie Weinans

Under review at The Journal of Orthopaedic Research

Abstract

Aims: To overcome stress-shielding in increasingly popular custom-made triflange acetabular implants a new concept of deformable porous titanium is introduced to redirect forces from the acetabular rim to the bone stock behind the implant. This concept is tested for deformability and primary stability.

Methods: Three types of highly porous titanium cylinders with increasing unit cell (BCC) sizes (3-5 mm) were designed with three differently graded porosities and were tested under compression to determine their properties. The most promising dimensions were then used to design five acetabular revision implants either by incorporating a deformable layer (3) or by adding a separately produced generic deformable mesh behind the implant (2). All the implants were inserted into sawbones with acetabular defects followed by a cyclic compression test (100-1800N) for 1000 cycles.

Results: The structure with a strut thickness of 0.2mm (4x4x4mm unit cell size) performed the best and was applied for the design of the acetabular implants. An immediate primary fixation was realized in all three implants with an incorporated deformable layer. One of the two implants with a separate deformable mesh needed fixation with screws. Cyclic tests revealed an average additional implant subsidence of 0.253 ± 0.034 mm in the first 1000 cycles.

Conclusions: It is possible to realize primary implant fixation and stability in simulated large acetabular revision surgery using a deformable titanium layer. Additional research is needed to investigate the effects of such implants.

Introduction

Given the ever-increasing life expectancy, an increasing number of primary total hip arthroplasties are being performed each year. This, in turn, results in more revision surgeries, particularly in patients operated at a relatively young age. In the United States alone, revision arthroplasties are expected to grow by 137% by 2030 (1). The main reason for revision surgeries is aseptic loosening of the implant (55%) (2). For long-term fixation of uncemented acetabular cup bony ingrowth is required, which relies on the initial stability after implantation. There exist number of reasons that lead to insufficient fixation: i) micromotion at the bone-implant interface that results in fibrous tissue formation instead of bone ingrowth; ii) polyethylene wear particles that initiate an inflammatory response and subsequent bone loss; iii) infection related inflammation and bone loss; and iv) relative mechanically unloading (stress-shielding) of the bone stock under the acetabular implant (3,4). When acetabular bone loss exceeds 50% of the normal physiological bone stock, regular hemispherical acetabular cups have a high chance of failure due to the inefficiency to mechanically load and stimulate the deep acetabular bone (5,6).

To improve the success of revision total hip arthroplasties, multiple options are available, including structural allografts, (non-)cemented hemispherical cups, oblong cups, jumbo cups, anti-protrusio cages, and Trabecular Metal augments and shells (7–11). However, not every revision method and/or procedure is suitable for large acetabular defects, resulting in high re-revision rates due to the (recurrent) loosening or implant migration of the acetabular cup (12).

Due to the high failure rates associated with revision cases, complex acetabular defects (e.g., Paprosky 3A/3B) are nowadays often treated with a patients-specific implant that more or less precisely follows the actual shape of the acetabular cavity (13,14). They often mechanically rely on three flanges that are screwed onto the cortices of the ilium, ischium, and pubis to obtain initial stability directly after implantation (triflange cups). However, the design is challenging as a perfect fit can never be reached due to complex shaped bone defects and segmentation errors due to imaging artefacts. A slight oversize of the stiff cup will lead to a bad fit with local overload and chances of instability with subsequent wiggling and micromotion. Therefore, most triflange revision cups are slightly undersized and in particular in the deep central zone of the acetabulum there is no bone-implant contact. As a result, all loads are transferred via the flanges, leading to the stress-shielding of the trabecular bone located underneath the implanted cup (15–17). Hence, this lack of mechanical stimulus could eventually lead to even more bone resorption and might further destabilize the fixation of the acetabular cup and/or the stability of the entire pelvis (18,19).

The abovementioned shortcomings of the current designs motivated us to develop alternative designs for the acetabular component that helps achieve a more natural stress distribution, limiting stress-shielding while providing sufficient primary stability. Modern additive manufacturing technologies, including selective laser melting (SLM), can be used to manufacture patient-specific implants from ductile metals, such as commercially pure titanium (CP-Ti)(20). CP-Ti shows a mechanical behaviour that is somewhat similar to tantalum and outperforms its alloyed counterparts (e.g., Ti-6Al-4V) in terms of the normalized high cycle fatigue strength, making it a suitable material for cyclically loaded implants such as acetabular components (21). With the current 3D printing methods, elements as small as 200 μm can be manufactured at a reasonable accuracy, which present opportunities for highly porous lattice structures that undergo substantial plastic deformation under compression. Incorporating such a deformable zone in acetabular implants renders the under-sizing of the implant unnecessary, as the implant will 'deform' to match the patient's anatomy. Moreover, these lattice (i.e., trabecular bone-like) structures generally expand laterally in response to axial compression, filling up complicated bone defects during insertion of the implant (22), thereby creating substantial implant-bone interface surface and primary stability.

In this study, we will test the feasibility of the abovementioned approach. For this purpose, the mechanical properties of a CP-Ti Body Centred Cubic unit cell (BCC, Figure 1) are examined in terms of stiffness, strength, plastic deformation and its capability to precisely fill an acetabular bone defect during insertion. In previous studies this type of unit cell exhibited a low yield stress and high ductility with a large lateral expansion. It is, therefore, expected to exhibit promising space-filling properties too. In this study, we aim to increase the unit cell size to decrease the yield strength of the porous deformable layer and create a viable deformable acetabular cup. In addition to mechanical properties, we evaluated the initial stability (subsidence after placement) of such deformable acetabular designs under cyclic loading.

Methods

Study outline

This study contains three parts. First, the mechanical properties of lattice structures designed with different dimensions of the BCC unit cell were determined with compression tests on cylinders with varying porosities and strut thicknesses. Based on the results of the first part, one of the unit cell dimensions was chosen for the design of custom-made acetabulum implants, which were then inserted in the acetabulum of bone mimicking Sawbone pelvises (Sawbones, Limhamn, Sweden) with systematically created acetabular defects to evaluate the space-filling potential of the deformable titanium layers. Finally,

the inserted implants were cyclically loaded to measure their post-insertion migration to indicate primary stability.

Cylindrical test

Design

Three porous cylindrical samples were designed using 3-Matic (version 13.0, Materialise NV, Leuven, Belgium) (Figure 1). The samples were 81 mm in height and had a diameter of 40 mm. The infill with the BCC unit cells was done via a direct patterning approach, using a different unit cell size for each design (23). The cylinders were divided into three equal sections of 27 mm (Figure 2) with each a different strut thickness to create a graded porosity (percentage of solid volume).

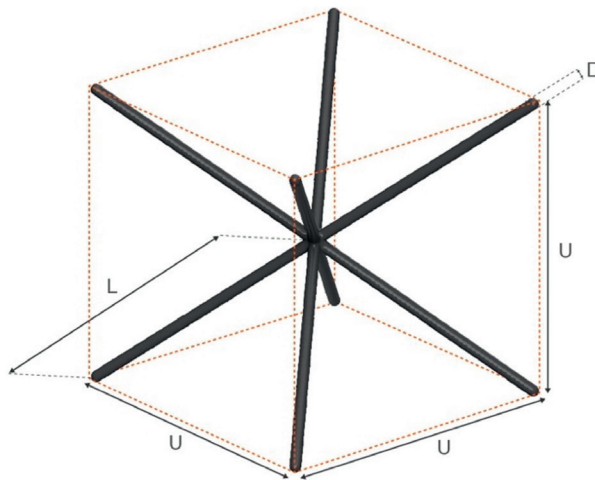


Figure 1. The design of the body centred cubic (BCC) unit cell with the representation of the strut length (L), strut diameter (D), and unit cell size (U).

Production

The specimens were manufactured with SLM using a ProX DMP 320 (3D Systems, Leuven, Belgium) machine (24). All specimens were tested as-manufactured without any additional post-processing, except for the removal of support material. Three specimens of each design were produced (nine specimens in total).

Test

Each specimen was subjected to a static compression test between two compression plates on a Lloyd LS 5 universal test machine (Amatek, Berwyn, United States) with a 5 kN load cell and at a rate of 2 mm/min up to a force of 4.9 kN. All the cylindrical specimens

were tested in the same manner and a video recording was made of the compression test of each specimen type.

Outcomes

The compressive yield strengths was determined from the stress-strain curves of the cylindrical specimens using the 0.2% offset method (ISO 13314-2011) as was done by Huang et al. for lattice structures (25). The stress (σ) was calculated by dividing the applied force by the initial cross-sectional area using the (apparent) full 40 mm diameter. The strain (ϵ) was defined as the displacement divided by the original sample height per section, so one third of the entire height of 81 mm (=27 mm) was taken. The elastic moduli were calculated from the stiffest part of the slope of the stress-strain curves in the linear elastic regions of the subsequent parts of the stress-strain curve. The strut length/thickness ratio was determined by dividing the strut length by its thickness.

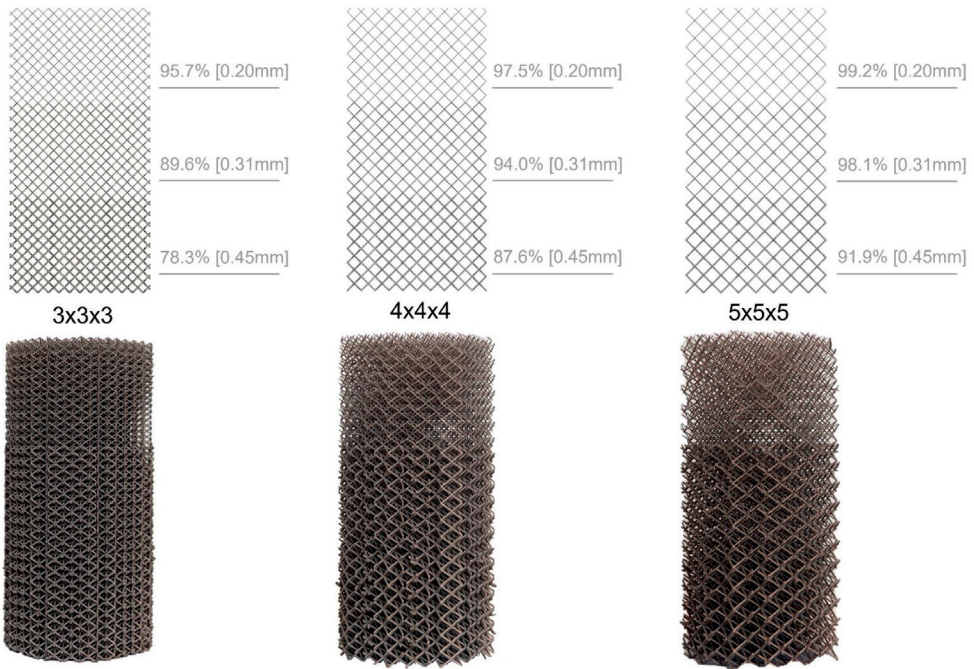


Figure 2. The design of the graded porous cylinders. Unit cell dimensions: left = 3x3x3 mm, middle = 4x4x4 mm, right = 5x5x5 mm. The porosity gradient is obtained by adjusting the strut thickness in the specimens (from top to bottom: 0.20 mm, 0.31 mm, and 0.45 mm).

Deformable acetabular implant test

Defect creation

Acetabular defects were systematically created into five right-sided biomechanical composite hemipelvis Sawbones (Hemi-Pelvis, 4th Gen., Composite, 10 PCF Solid Foam Core, Large, Sawbones, Limhamn, Sweden). The bone phantoms that were used have been specifically designed to mimic the material properties of native bone, simulating trabecular bone using a foam and a short fibre filled epoxy to simulate cortical bone (26–28). In all five hemipelvis, acetabular defects were created according to the Paprosky acetabular defect classification system (14,29). In two hemipelvis, an identical Paprosky type 3A defect was created while identical type 3B defects were created in three other hemipelvis (Figure 3).

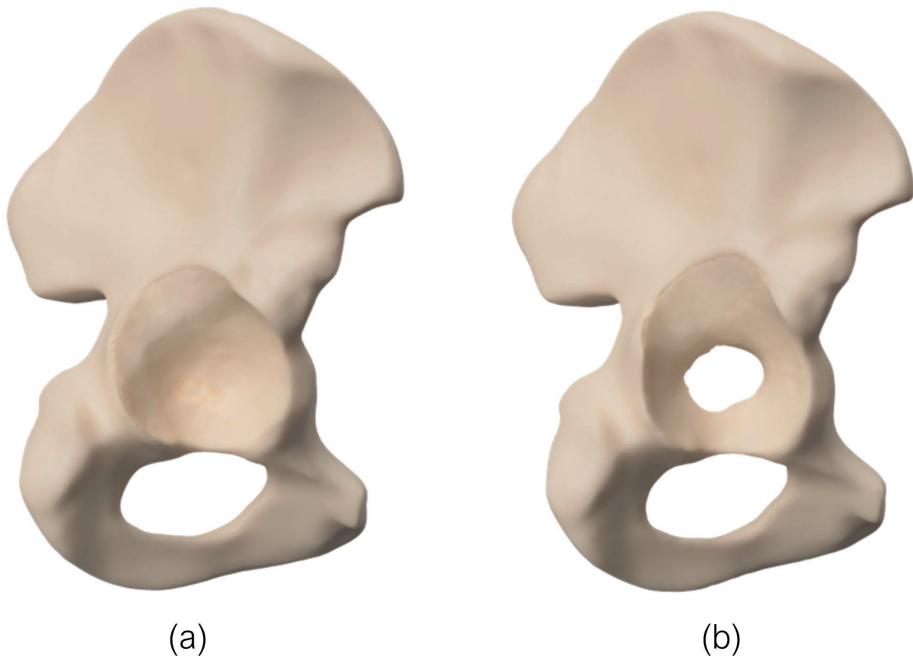


Figure 3. The rendered images of the acetabular defects created in the Sawbones hemipelvis. Paprosky type 3A (a), Paprosky type 3B (b).

Imaging and segmentation

After defect creation, a clinical CT-scan was made of all hemipelvis with a 0.8 mm slice thickness (80kV, 280mAs, IQon Spectral, Philips, Amsterdam, Netherlands). The DICOM files were imported and segmented in Mimics (version 23.0, Materialise, Leuven, Belgium) to create three-dimensional computer models of the acetabular defects.

Design

Using the 3D defect models of the Sawbones hemipelaves, five unique 'case-specific' acetabular cups were designed using 3-Matic (Version 15.0, Materialise, Leuven, Belgium). These cups can be divided into two main types: acetabular cups without flanges (flush) and acetabular triflange cups (Table 1). The triflange cups featured two design concepts: an oversized version with an incorporated deformable titanium layer and an undersized version that requires a separate deformable mesh being placed underneath the cup. The porous layers of the cups are made based on the 4x4x4mm BCC lattice structures. The lattice structures were oriented in the direction of cup insertion, thereby facilitating lateral expansion of the BCC unit cell under compression (30).

The solid titanium parts of the implants have an inner cup diameter of 44 mm and a thickness of 3 mm. The incorporated lattice structures of cup 1, 3, and 5 consisted of a low-porous layer with a strut thickness of 0.5 mm and were 4 mm undersized in the direction of insertion. To overcome this 4 mm gap to the bone, these three cups were designed to have an additional incorporated deformable layer with a strut thickness of 0.2 mm and a layer thickness of 8 mm. This made the total size of the cup 4 mm oversized in the direction of insertion. Alternatively, cups 2 and 4 incorporated low porous lattice structure with a strut thickness of 0.5 mm and were 6 mm undersized in the direction of insertion. To overcome this gap, these cups needed to be combined with a separate highly porous inlay mesh. These generic meshes were designed in SolidWorks (version 2017, Dassault Systems, France) and had a thickness of 10 mm and a strut thickness of 0.2 mm. Two types of meshes were designed for spherical and elongated bony defects. Both mesh types were produced in three diameters: 53 mm, 63 mm, and 73 mm (Figure 4). As a result, cup 2 and cup 4 were also 4 mm oversized in the direction of insertion, once combined with the deformable inlay.

As a substitute for clinically used polyethylene liners, polyamide liners were designed to be cemented into the acetabular cups. These liners, with a thickness of 6 mm, accommodated a 28 mm femoral head for cyclic testing.

Production

All CP-Ti implants were produced on a ProX DMP 320 machine (3D Systems, Leuven, Belgium) (24) and were tested as manufactured without any additional post processing except for the removal of support material. The 28 mm liners were produced using selective laser sintering (SLS) out of nylon (polyamide 12) (Oceanz, Ede, Netherlands).

Implant insertion

The acetabular cups were inserted into their corresponding Sawbones acetabula by two senior orthopaedic surgeons at UMC Utrecht. The acetabular cups with attached

deformable layer (1,3,5) were inserted directly into their position using an inserter and hammer from a standard hip insertion set (Zimmer). For the other two cups (2,4), a separate mesh was selected by the surgeon and pressed into the acetabulum and then the implant was inserted on top. After insertion of the acetabular implants, the liners were cemented into the cups using a bone cement (Zimmer Biomet Refobacin®) (31).

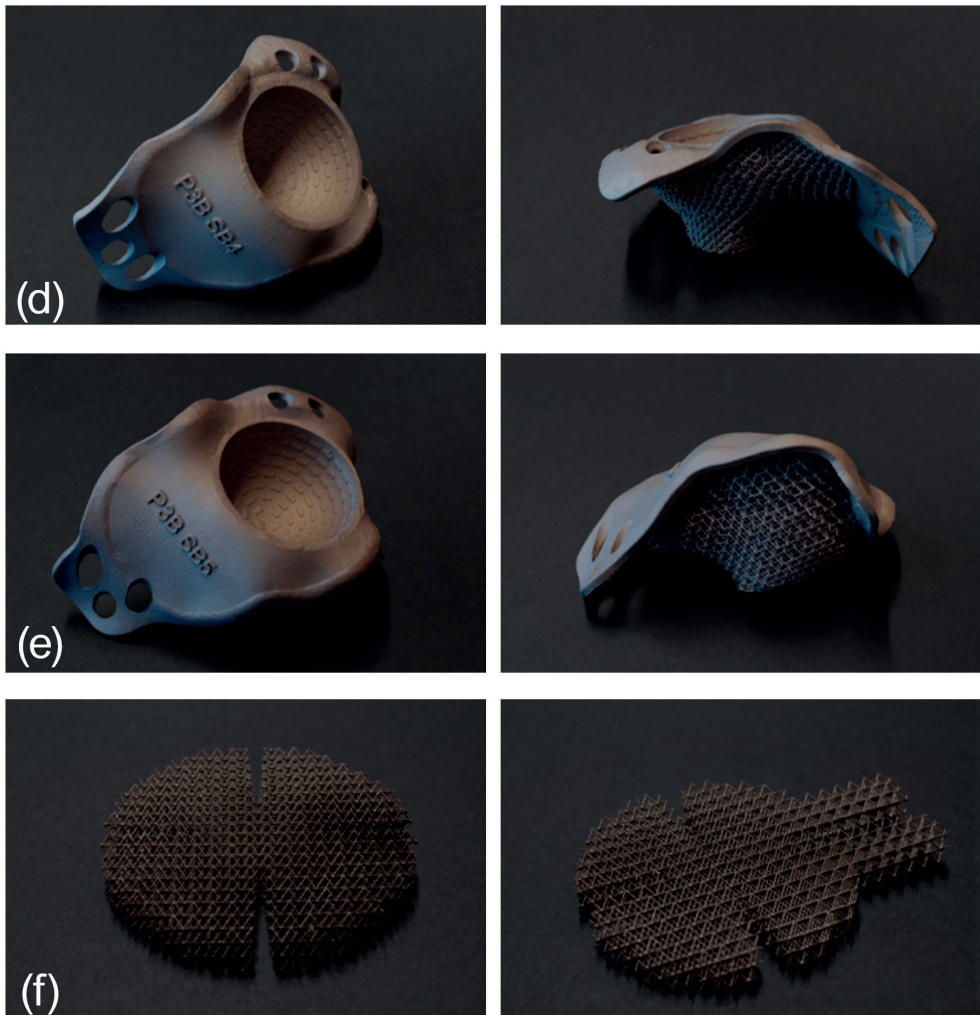


Figure 4. The photographs of the manufactured acetabular cups: implant 1 (a), implant 2 (b), implant 3 (c), implant 4 (d), implant 5 (e), deformable meshes (f). (figure continues on next page)

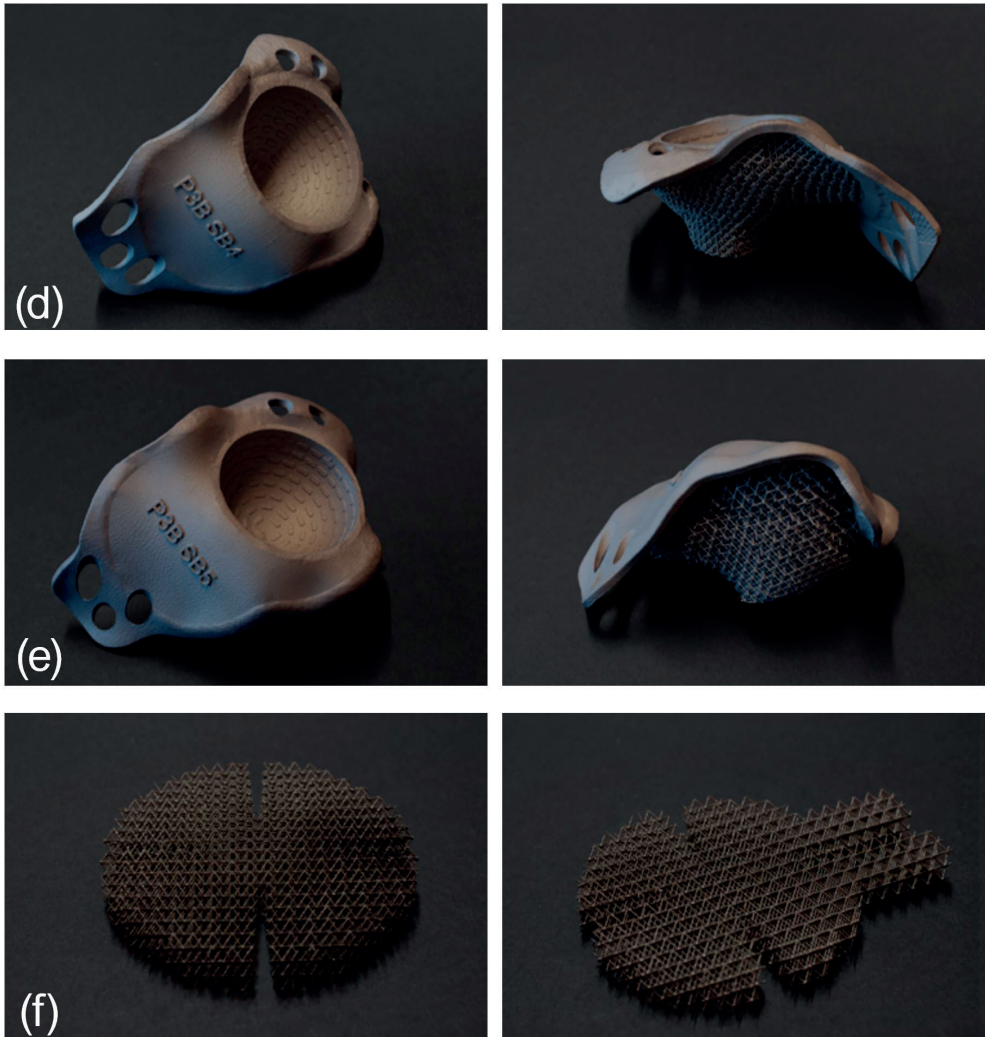


Figure 4 continued. The photographs of the manufactured acetabular cups: implant 1 (a), implant 2 (b), implant 3 (c), implant 4 (d), implant 5 (e), deformable meshes (f). (figure continues on next page).

Imaging of deformation

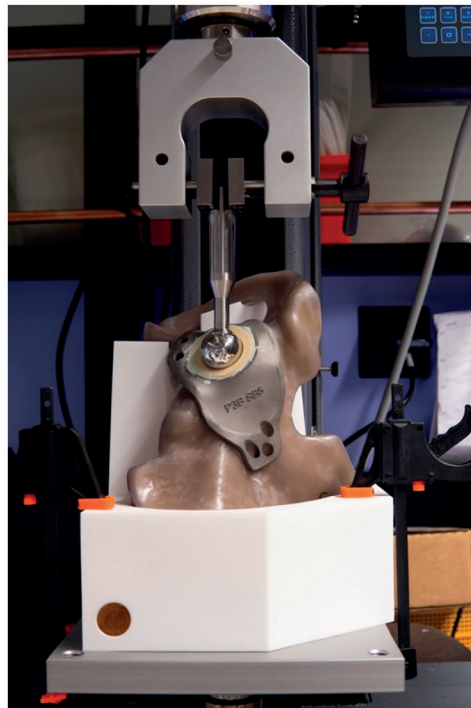
After insertion, the deformation of the deformable layer was assessed by making a new CT scan and segmenting the deformed acetabular implant from the CT using Mimics. The non-deformable solid flange of the segmented model was registered onto the original CAD model using a point-to-point registration method in 3-Matic in order to make a detailed analyses of the deformation.

Table 1. Different cup designs.

Acetabular cup	Defect type	Triflange/ flush	Deformable Type	Unit cell size [mm]	Strut thickness
1	Paprosky 3A	Flush	Incorporated	4x4x4 4x4x4	0.2 0.5
2	Paprosky 3A	Triflange	Incorporated Separate mesh	1.5x1.5x1.5 4x4x4	0.5 0.2
3	Paprosky 3B	Flush	Incorporated	4x4x4 4x4x4	0.2 0.5
4	Paprosky 3B	Triflange	Incorporated Separate mesh	2.5x2.5x2.5 4x4x4	0.5 0.2
5	Paprosky 3B	Triflange	Incorporated	4x4x4 4x4x4	0.2 0.5

Cyclic loading

To evaluate implant migration caused by cyclic loading, a cyclic test was performed on a Lloyd LS 5 universal testing machine (Amatek, Berwyn, United States). The hemipelves were positioned in an epoxy resin-filled (Polyservice, Amsterdam, Netherlands) negative mould of the pelvis that enabled a femoral head (28 mm) to deliver a cyclic force with a force vector described by Bergmann et al. on the cemented liner of the inserted implants (Figure 5) (32).

**Figure 5.** The setup used for the cyclic tests of the acetabular cups.

All acetabular cups were tested up to 1000 cycles with a sinusoidal loading between 100 N and 1800 N to simulate a gait cycle. A minimum load of 100 N was used to ensure the acetabular head did not lose contact with the liner. A maximum compressive force of 1800 N was selected based on the average peak load of gait for a body weight of 750 N (32). The crosshead velocity of the machine was kept constant at 60 mm/min.

Results

Cylindrical test

The smaller unit cell size specimens (e.g., 3x3x3 mm) resulted in a stiffer and stronger structure than those with a larger unit cell size (e.g., 5x5x5 mm). Three linear elastic sections and three plateau regions (plastic deformation) can clearly be differentiated in the case of the specimens with the 4x4x4 and 5x5x5 mm unit cell dimensions (Figure 6). The stress-strain plot of the 3x3x3 mm specimens does not show three, but two linear elastic sections as the maximum of the 5 kN could not reach the yield point of the strongest part of this specimen with the 450 microns strut thickness (see Figure 6). From the stress-strain plot the apparent values of the compressive yield stress and the Youngs modulus of elasticity can be estimated for each section (Table 2).

Table 2. The mechanical and morphological properties of the CAD designs of the cylindrical specimens.

Unit cell size [mm]	Strut thickness [mm]	Porosity %	Estimated Elastic modulus [MPa]	Compressive yield strength [MPa]	Strut ratio
3x3x3	0.20	95.7	0.224 ±0.013	0.499 ±0.014	12.990
3x3x3	0.31	89.6	0.380 ±0.037	2.368 ±0.090	8.381
3x3x3	0.45	78.3	-	-	-
4x4x4	0.20	97.5	0.066 ±0.007	0.168 ±0.006	17.321
4x4x4	0.31	94.0	0.145 ±0.006	0.857 ±0.030	11.175
4x4x4	0.45	87.6	0.190 ±0.017	2.462 ±0.043	7.698
5x5x5	0.20	99.2	0.026 ±0.001	0.076 ±0.007	21.651
5x5x5	0.31	98.1	0.039 ±0.008	0.383 ±0.030	13.968
5x5x5	0.45	91.9	0.087 ±0.012	1.029 ±0.021	9.623

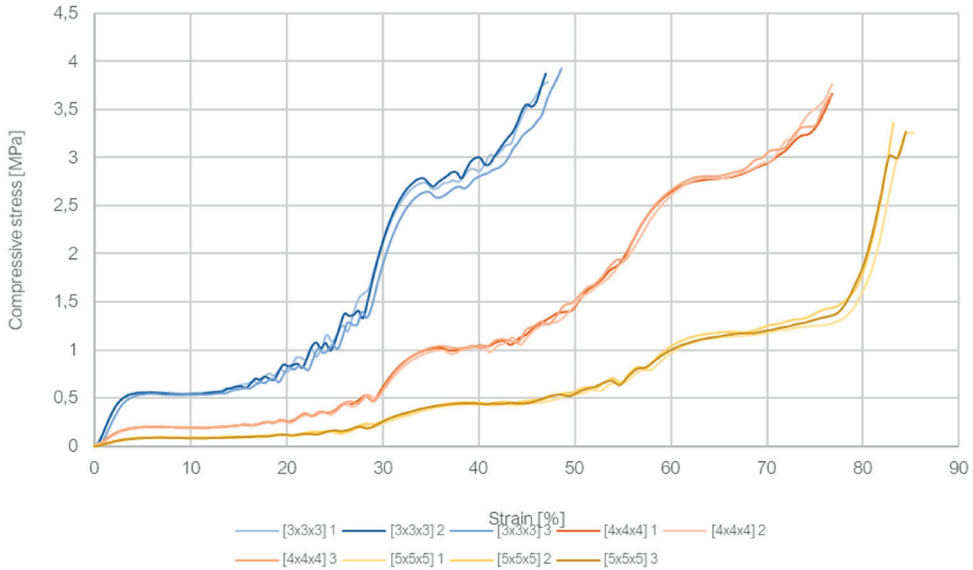


Figure 6. The stress-strain curves recorded during the compression tests of the cylindrical specimens. The 3x3x3 mm samples are displayed in blue, the 4x4x4 mm samples in orange, and the 5x5x5 mm samples in yellow.

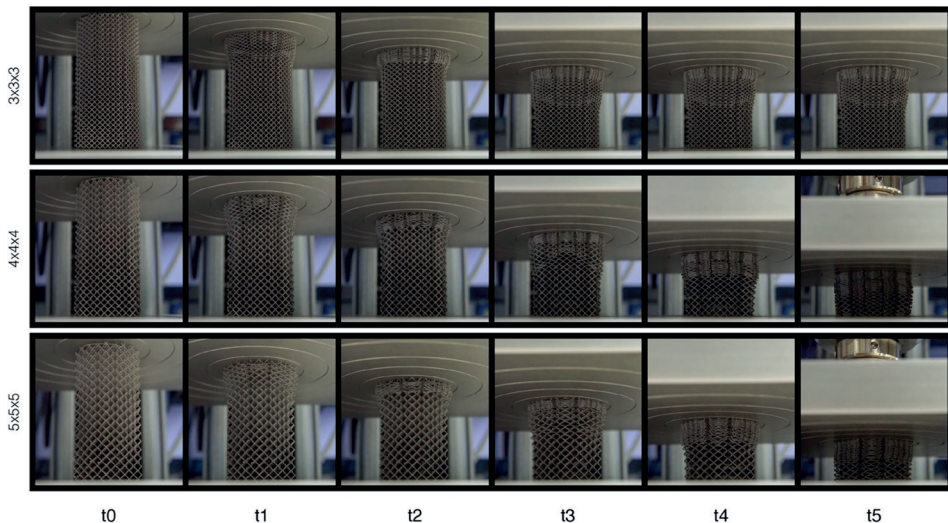


Figure 7. Compression of the cylindrical samples at different time intervals.

Top: 3x3x3 mm, middle: 4x4x4 mm and bottom: 5x5x5 mm. At t5 the maximum compression force of 5 kN is reached for the 4x4x4 mm and 5x5x5 mm samples. Note that at t3 a load of 5 kN is reached for the 3x3x3 mm sample.

All specimens deformed significantly under compression (Figure 7). Those with largest unit cell sizes (i.e., 5x5x5 mm) deformed the most. The height of the 3x3x3 mm specimens decreased 41.6% on average. For the 4x4x4 mm and 5x5x5 mm specimens, the decrease in the height was 71.1% and 79.2%, respectively. The average lateral expansion of the specimens at the fully deformed sections (end point) was 16.8% for the 3x3x3 mm specimens, 16.8% for the 4x4x4 mm specimens, and 17% for the 5x5x5 mm specimens.

The yield strength of the porous structure was a power function of the ratio of the strut length to the strut thickness (Figure 8).

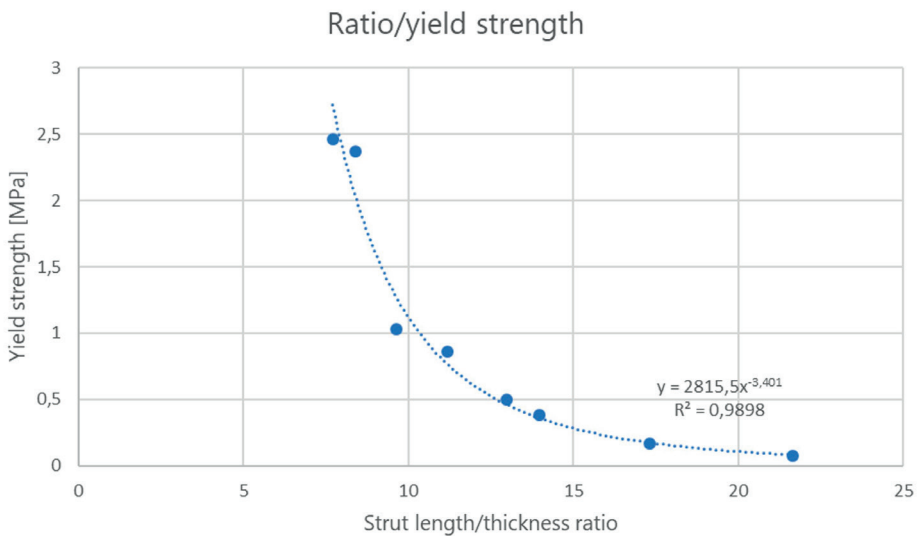


Figure 8. Strut length/thickness ratio plotted against the yield strength of the corresponding lattice structure.

Deformable implant insertion test

All five acetabular cups were implanted into their specific Sawbone defects (Table 1). Subjectively none of the surgeons felt that any of the cups required a larger impact force to insert than a regular hemispherical acetabular cup. For the undersized cups, the surgeons decided on a circular 53 mm deformable mesh for implant 2 and an elongated 53 mm mesh for implant 4. After insertion, no step-offs were observed for cups 1 and 3, which were flush with the defect border and no gaps were observed between the bone and the flanges of cups 2,4, and 5. After insertion, 4 out of 5 implants (1,2,3, and 5) were firmly in place and not manually removable. However, in the case of implant 4, fixation screws were

needed to provide initial implant stability. Additionally, some broken titanium struts were observed as they fell through the defect in the medial wall.

The post-insertion CT model of the acetabular cup was registered on the original model and showed a volumetric reduction of the deformable layer in all three acetabular cups with an attached deformable layer (Figure 9). All cups decreased in volume after implantation within a range of 2.7 to 7.5% (see Table 3).

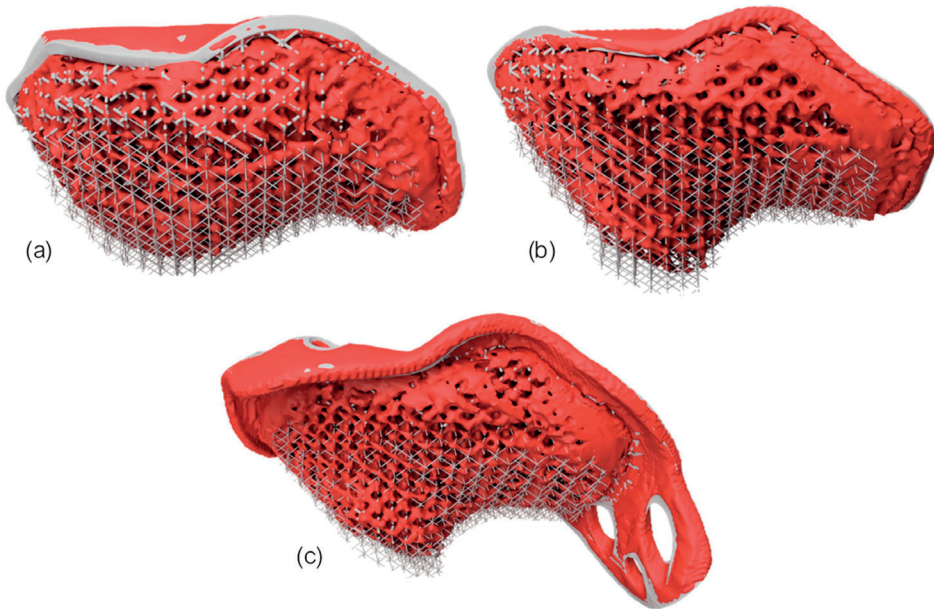


Figure 9. The rendered images of the CT-CAD registrations: implant 1 (a), implant 3 (b), implant 5 (c). The red part is the segmented cup after insertion, the grey part is the original CAD file.

Table 3. The volumes and volume reductions of the implants after the insertion of the acetabular cups.

Acetabular cup	Volume CAD (cm ³)	Volume CT (cm ³)	Volume reduction (cm ³)
1	61.98	58.68	3.3
3	65.99	61.03	4.97
5	85.60	83.26	2.35

Cyclic loading

Subsidence of the cups during cyclic loading after implantation was very small and reached on average up to 0.253 ± 0.034 mm, ranging from 0.1781 mm (implant 4) to 0.3793 mm (implant 1). Most of this subsidence (or migration) occurred during the first 1000 cycles of the experiment with a flattened curve approaching 1000 cycles.

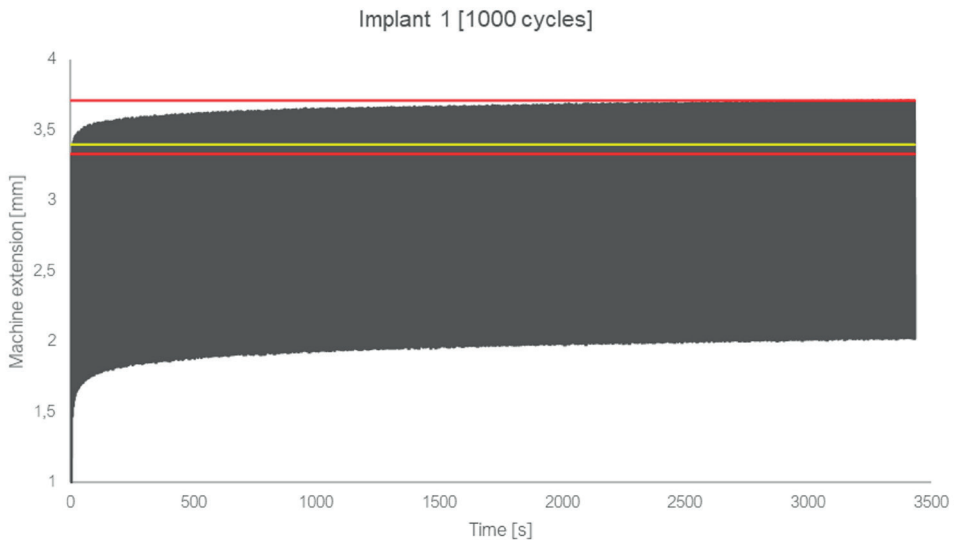


Figure 10. The time-extension curves for the cyclic test of implant 1.

The extension needed to reach 1800 N during the first compression is indicated by the lower red line, the second compression by the yellow line and the last compression by the upper red line.

Discussion

From the compression tests, we found very low yield stresses for the BCC lattice structures. A compressive yield strength below 0.2 MPa was required to have a material that can be deformed during the surgical procedure. Moreover, the strut length/thickness ratio correlated with the yield strength. A ratio higher than 17 was found to be viable for deformable implants. The most optimal design with a unit cell size of $4 \times 4 \times 4$ mm and a strut thickness of 0.2 mm (Figure 8) was therefore incorporated into five custom-made acetabular cups. A screwless implant fixation was realized in 4 out of 5 sawbones with Paprosky type 3A and 3B acetabular defects. The subsequent 1000 cycles of 1800 N compression onto the implant showed minimal additional implant migration.

The low elastic modulus and large deformation capacity of the BCC unit cell found in this study have been described in literature too (33). The stress strain curves resulting from the compression tests with cylindrical specimens show a linear elastic region and a plateau region as expected. The three porous sections are discernible in the plots of both the 4x4x4 mm and 5x5x5 mm unit cell sizes (Figure 6) as they plastically deform one by one. All the specimens exhibited the same type of stress-strain curve although they represent different stiffnesses and compressive strengths. However, it is apparent from the stress strain curves that the specimens with a higher porosity (thinner strut thicknesses or larger unit cell) showed a larger plateau region in the plastic deformation phase (Figure 6). Elastic moduli and compressive yield strengths as low as 0.026 MPa and 0.076 MPa, respectively, were found in this experiment. It should be realized that the yield stresses can be accurately determined with our specimen, while the elastic moduli a crude estimation based on the deformation of the entire specimen where the three parts are placed in series. Therefore, the elastic moduli in Table 3 represent an upper limit of the true values, as the displacement of the 1/3 region considered is less than the actual deformation used from the specimen as a whole in Figure 6. Moreover, lateral expansion of the unit cells under uniaxial compression creates lateral friction on the compression plates, resulting in artificial stiffening of the lattice structure, which compensated the above estimation. In addition, due to the graded porosity, thinner struts are connected to thicker struts at the transition, limiting lateral expansion of these thinner struts. This as well leads to stiffening of the lattice structure.

Usually, the material properties such as the elastic modulus and yield strength purely describe the intrinsic properties of the material and are unrelated to the morphological properties of the specimens. It is important to understand that the material properties described in these experiments describe a different concept when concerning highly porous lattice structures. When referring to highly porous lattice structures, such properties describe the effective macroscopic behaviour of the entire porous structure (34). In the case of graded designs, such effective properties deviate even further from the mechanical properties of a material, as they are highly dependent on the specifics of the graded design and are by definition dependent on the specimen dimensions. Altogether the elastic moduli should be considered as estimated values as they are not precise values for the above mentioned reasons.

The stress-strain curves also show some spikes at the most deformed part of the plateau regions. These spikes could indicate the failure of the struts, although no loose struts have been observed after compression. This may indicate that struts have fractured at one end only. At that point, the strut will not be bearing mechanical loads anymore. The specimens exhibited a layer-by-layer failure mode, starting from the highly porous top layers. This is consistent with the failure mechanism described in the literature

(35,36). The manufacturing irregularities caused by the additive manufacturing process significantly affect the mechanical properties of the resulting lattice structures (37). The lattice structures showed heterogeneous behaviour while, at the strut level, elevated local strains continue to accumulate at the weakest spots, resulting in strut failure.(38)

The deformable titanium layers in the implants were assumed to have deformed during insertion as the oversized implants were flush to the bone without gaps, indicating considerable deformation. This deformation was quantified by measuring the incurred volume reduction using post-insertion CT images. However, this (again) is an approximation as the exact value of the volume reduction is difficult to determine from a CT scan due to beam hardening and the partial volume effects (39).

During the cyclic tests, all the implants showed additional subsidence between the first and last compression up to 1800 N. In the literature, this is sometimes described as 'bedding-in' (or subsidence or migration) of the implant (40). We postulate that the implants 'settle' during the first cycles in which some extra deformation takes place. The additional migration between the first and last compressions was comparable to the values found in literature (41). Saffarini et al. have described migration values of between 0.05 and 0.27 mm of for cementless hemispherical cups (41). Moreover, the graphical illustration of the migration over time in the study of Saffarini et al. is consistent with the curves obtained during our experiments.

This study also has its limitations. First of all, using as-manufactured implants could have influenced the mechanical properties and strut failure during insertion of the implants. A recommended post-processing step is Hot Isostatic Pressing (HIP) (42). For CP-Ti, HIP treatment may further reduce the yield strength of the bulk material and increase its ductility (43). This will translate to increased deformability and will reduce the risk of strut failure in the deformed lattice structures.

Second limitation is the use of Sawbones hemipelves. The inner solid foam that represents the trabecular bone is isotropic whereas the trabecular bone found in the human pelvis can be considered as largely transversely isotropic (44). Furthermore, the yield strength of human pelvic trabecular bone is 3-10 times lower than the yield strength of the solid foam used in the Sawbones pelvises (Table 4). That said, Sawbones are one of the best ways to evaluate implant designs at the conceptual design stage because their mechanical behaviour is highly reproducible (as opposed to cadaveric specimens), enabling different design concepts to be objectively compared with each other.

Another limitation is the stress-strain plot of the 3x3x3 mm unit cell size that did not show three, but two linear elastic sections. This was likely caused by lack of sufficient deformation

in the least porous section (i.e., 0.45 mm strut thickness), which did not deform under a 5 kN load and therefore an elastic modulus and compressive yield strength could not be estimated.

The most optimal unit cell size we considered was 4x4x4 mm with a 200 microns thick strut thickness, leading to a yield stress of 0.168 MPa that worked well within the simulated clinical setting. However, the implant design is significantly restricted once whole 4 mm unit cells are incorporated into the structure. To effectively describe a volume with a lattice structure with this ratio, one would ideally like to work with shorter struts with an even smaller thickness than 200 microns. However, such thin structures are currently not possible with the most advanced additive manufacturing techniques (45).

Creating plastically deformable acetabular cups seems a technically viable solution for filling critical sized acetabular defects. The deformable layer will increase the load transfer through the acetabular cavity, as compared to flanges only. According to Wolff's law, the increased load transfer stimulates bone to grow into the highly porous structure providing a strong secondary fixation and ultimately will preserve the cancellous bone in the deep acetabular zone (46–48). In addition, the porous printed structure can be designed using architectures that lead to high expansion in the transverse directions, thereby filling gaps of the bone defects upon insertion.

Conclusions

It is possible to realize primary implant fixation in simulated acetabular revision surgery with bone defects, using acetabular cups with an incorporated deformable titanium scaffold. However, additional research is needed to investigate the effects of the deformable titanium on actual real bone specimen.

Appendix

https://1drv.ms/b/s!AjdWTaQAIFN0p4Nvm_wTawFhpekJ0w?e=s7uXKa

References

1. Kurtz S, Ong K, Lau E, Mowat F, Halpern M. Projections of Primary and Revision Hip and Knee Arthroplasty in the United States from 2005 to 2030. 2007;780–5.
2. Sadoghi P, Liebensteiner M, Agreiter M, Leithner A, Böhler N, Labek G. Revision surgery after total joint arthroplasty: A complication-based analysis using worldwide arthroplasty registers. *Journal of Arthroplasty*. 2013;28(8):1329–32.
3. Morsi E, Orth MS. Total Hip Arthroplasty With Shelf Grafts Using Uncemented Cups A Long-term Follow-up Study. 1996;11(1):81–5.
4. Hooten JP, Engh CA, Heekin RD, Vinh TN. Structural bulk allografts in acetabular reconstruction: Analysis of two grafts retrieved at post-mortem. *Journal of Bone and Joint Surgery - Series B*. 1996;78(2):270–5.
5. Boscainos PJ, Kellett CF, Maury AC, Backstein D, Gross AE. Management of periacetabular bone loss in revision hip arthroplasty. *Clinical Orthopaedics and Related Research*. 2007;(465):159–65.
6. Schulze C, Morgenroth R, Bader R, Kluess D, Haas H. Fixation Stability of Uncemented Acetabular Cups With Respect to Different Bone Defect Sizes. *Journal of Arthroplasty*. 2020;35(6):1720–8.
7. Brown NM, Morrison J, Sporer SM, Paprosky WG. The Use of Structural Distal Femoral Allograft for Acetabular Reconstruction of Paprosky Type IIIA Defects at a Mean 21 Years of Follow-Up. *Journal of Arthroplasty*. 2016;31(3):680–3.
8. Carroll FA, Kerry RM, Stockley I, Hoad-Reddick DA, Kerry RM, Stockley I. The survival of support rings in complex acetabular revision surgery. *Journal of Bone and Joint Surgery - Series B*. 2008;90(5):574–8.
9. Babis GC, Sakellariou VI, Chatziantoniou AN, Soucacos PN, Megas P. High complication rate in reconstruction of Paprosky type IIIa acetabular defects using an oblong implant with modular side plates and a hook. *Journal of Bone and Joint Surgery - Series B*. 2011;93 B(12):1592–6.
10. Gaiani L, Bertelli R, Palmonari M, Vicenzi G. Total hip arthroplasty revision in elderly people with cement and Burch-Schneider anti-protrusio cage. *La Chirurgia degli organi di movimento*. 2009;93(1):15–9.
11. Borland WS, Bhattacharya R, Holland JP, Brewster NT. Use of porous trabecular metal augments with impaction bone grafting in management of acetabular bone loss. *Acta orthopaedica*. 2012;83(4):347–52.
12. Baauw M, Van Hooff ML, Spruit M. Current construct options for revision of large acetabular defects: A systematic review. *JBJs Reviews*. 2016;4(11):e2.
13. Baauw M, Van Hellemond GG, Spruit M. A custom-made acetabular implant for paprosky type 3 defects. *Orthopedics*. 2017;40(1):e195–8.
14. Paprosky WG, Perona PG, Lawrence JM. Acetabular defect classification and surgical reconstruction in revision arthroplasty. A 6-year follow-up evaluation. *The Journal of Arthroplasty*. 1994;9(1):33–44.

15. Sumner DR. Long-term implant fixation and stress-shielding in total hip replacement. *Journal of Biomechanics*. 2015;48(5):797–800.
16. Huiskes R, Weinans H, Van Rietbergen B. The relationship between stress shielding and bone resorption around total hip stems and the effects of flexible materials. *Clinical Orthopaedics and Related Research*. 1992;(274):124–34.
17. Huiskes R, Rulmerman R, Van Lenthe GH, Janssen JD. Effects of mechanical forces on maintenance and adaptation of form in trabecular bone. *Nature*. 2000;405(6787):704–6.
18. Currey JD. *The Mechanical Adaptations of Bones*. Princeton university press; 1984.
19. Turner CH, Pavalko FM. Mechanotransduction and functional response of the skeleton to physical stress: The mechanisms and mechanics of bone adaptation. *Journal of Orthopaedic Science*. 1998;3(6):346–55.
20. Zadpoor AA, Malda J. Additive Manufacturing of Biomaterials, Tissues, and Organs. *Annals of Biomedical Engineering*. 2017;45(1):1–11.
21. ZWauthle R, Ahmadi SM, Amin Yavari S, Mulier M, Zadpoor AA, Weinans H, et al. Revival of pure titanium for dynamically loaded porous implants using additive manufacturing. *Materials Science and Engineering C*. 2015;54:94–100.
22. ZKolken HMA, Jonge CP de, Sloten T van der, Garcia AF, Pouran B, Weinans HH, et al. Additively manufactured space-filling meta-implants. (conditionally accepted) *Acta Biomaterialia*. 2020;
23. ZTao W, Leu MC. Design of lattice structure for additive manufacturing. *International Symposium on Flexible Automation, ISFA 2016*. 2016;(August 2016):325–32.
24. Z3D SYSTEMS. Metal Additive Manufacturing with the ProX[®] DMP 3D printers METAL ALLOYS FOR THE PROX[®] DMP 100 , 200 , 300. 2018;3-6.
25. ZHuang Y, Xue Y, Wang X, Han F. Mechanical behavior of three-dimensional pyramidal aluminum lattice materials. *Materials Science & Engineering A*. 2017;696(April):520–8.
26. ZChong ACM, Miller F, Buxton M, Friis EA. Fracture toughness and fatigue crack propagation rate of short fiber reinforced epoxy composites for analogue cortical bone. *Journal of Biomechanical Engineering*. 2007;129(4):487–93.
27. ZSzivek JA, Thomas M, Benjamin JB. Characterization of a synthetic foam as a model for human cancellous bone. *Journal of applied biomaterials : an official journal of the Society for Biomaterials*. 1993;4(3):269–72.
28. ZSawbones. TEST MATERIALS AND COMPOSITE BONES composite bones for test and.
29. ZZimmer. Zimmer[®] Trabecular MetalTM Acetabular Revision System. 2010;
30. ZLi X, Fan Z, Fan R, Lu Y. Two-dimensional mechanical metamaterials with bending-induced expansion behavior. *Applied Physics Letters*. 2020;117(1):011904.
31. Zimmer Biomet. Biomet Bone Cement R. Zimmer Biomet. 2017;1–4.
32. Bergmann G, Graichen F, Rohlmann A, Bender A, Heinlein B, Duda GN, et al. Realistic loads for testing hip implants. *Bio-Medical Materials and Engineering*. 2010;20(2):65–75.
33. Mazur M, Leary M, Sun S, Vcelka M, Shidid D, Brandt M. Deformation and failure behaviour of Ti-6Al-4V lattice structures manufactured by selective laser melting (SLM). *International Journal of Advanced Manufacturing Technology*. 2016;84(5–8):1391–411.

34. Zadpoor AA. Mechanical performance of additively manufactured meta-biomaterials. *Acta Biomaterialia*. 2019;85:41–59.
35. Liu L, Kamm P, García-Moreno F, Banhart J, Pasini D. Elastic and failure response of imperfect three-dimensional metallic lattices: the role of geometric defects induced by Selective Laser Melting. *Journal of the Mechanics and Physics of Solids*. 2017;107:160–84.
36. Kadkhodapour J, Montazerian H, Darabi AC, Anaraki AP, Ahmadi SM, Zadpoor AA, et al. Failure mechanisms of additively manufactured porous biomaterials: Effects of porosity and type of unit cell. *Journal of the mechanical behavior of biomedical materials*. 2015;50:180–91.
37. Campoli G, Borleffs MS, Amin Yavari S, Wauthle R, Weinans H, Zadpoor AA. Mechanical properties of open-cell metallic biomaterials manufactured using additive manufacturing. *Materials and Design*. 2013;49:957–65.
38. Genovese K, Leeflang S, Zadpoor AA. Microscopic full-field three-dimensional strain measurement during the mechanical testing of additively manufactured porous biomaterials. *Journal of the Mechanical Behavior of Biomedical Materials*. 2017;69(August 2016):327–41.
39. Park HS, Chung YE, Seo JK. Computed tomographic beam-hardening artefacts: mathematical characterization and analysis. *Philosophical Transactions of the Royal Society A: Mathematical, Physical and Engineering Sciences*. 2015;373(2043):20140388.
40. Christi, J., Sychterz, M.S.E., Anderson, C., Anthony Yang, B.S. and Charles A. Analysis of Temporal Wear Patterns of Porous-Coated Acetabular Components : Distinguishing Between True Wear and So-Called Bedding-in. *Journal of Bone and Joint Surgery - American Volume*. 1999;81(6).
41. Saffarini M, Gregory T, Vandenbussche E. Quantification of clearance and creep in acetabular wear measurements. *Annals of Translational Medicine*. 2016;4(7):1–8.
42. Atkinson HV., Davies S. Fundamental aspects of hot isostatic pressing: An overview. *Metallurgical and Materials Transactions A: Physical Metallurgy and Materials Science*. 2000;31(12):2981–3000.
43. Gr LT. LaserForm Ti Gr1 (A) LaserForm ® Ti Gr1 (A). 1:5-6.
44. Dalstra M, Huiskes R, Odgaard A, van Erning L. Mechanical and textural properties of pelvic trabecular bone. *Journal of Biomechanics*. 1993;26(4–5):523–35.
45. Van Bael S, Kerckhofs G, Moesen M, Pyka G, Schrooten J, Kruth J-P. Micro-CT-based improvement of geometrical and mechanical controllability of selective laser melted Ti6Al4V porous structures. *Materials Science and Engineering: A*. 2011;528(24):7423–31.
46. Prendergast PJ, Huiskes R. The Biomechanics of Wolff 's Law : Recent Advances. :9–11.
47. Huiskes R, Weinans H, Van Rietbergen B. The relationship between stress shielding and bone resorption around total hip stems and the effects of flexible materials. *Clinical Orthopaedics and Related Research*. 1992;(274):124–34.
48. Huiskes R, Rulmerman R, Van Lenthe GH, Janssen JD. Effects of mechanical forces on maintenance and adaptation of form in trabecular bone. *Nature*. 2000;405(6787):704–6.



The background is a solid blue color. It features several sets of parallel diagonal lines. One set of lines is white and runs from the top-left towards the bottom-right. Another set of lines is yellow and runs from the bottom-left towards the top-right. These lines are thin and spaced out, creating a modern, geometric aesthetic.

PART 3

ONE MEDICINE (TRANSLATION)



CHAPTER 10

Patient-specific 3D-printed shelf implant for the treatment of hip dysplasia tested in an experimental animal pilot in canines

Koen Willemsen | Marianna Tryfonidou | Ralph J. B. Sackers |
René M. Castelein | Martijn Beukers | Peter R. Seevinck |
Harrie Weinans | Bart C. H. van der Wal | Björn P. Meij

Published in Scientific Reports, (2022) 12, 3032
<https://doi.org/10.1038/s41598-022-06989-9>

Abstract

The concept of a novel patient-specific 3D-printed shelf implant should be evaluated in a relevant large animal model with hip dysplasia. Therefore, three dogs with radiographic bilateral hip dysplasia and a positive subluxation test underwent unilateral acetabular augmentation with a 3D-printed dog-specific titanium implant. The contralateral side served as control. The implants were designed on CT-based pelvic bone segmentations and extended the dysplastic acetabular rim to increase the weight bearing surface without impairing the range of motion. Outcome was assessed by clinical observation, manual subluxation testing, radiography, CT, and gait analysis from 6 weeks preoperatively until termination at 26 weeks postoperatively. Thereafter, all hip joints underwent histopathological examination. The implantation and recovery from surgery was uneventful. Clinical subluxation tests at the intervention side became negative. Imaging showed medialization of the femoral head at the intervention side and the mean (range) CE-angle increased from 94° (84°+/-99°) preoperative to 119° (117°+/-120°) postoperative. Gait analysis parameters returned to pre-operative levels after an average follow-up of 6 weeks. Histology showed a thickened synovial capsule between the implant and the femoral head without any evidence of additional damage to the articular cartilage compared to the control side. The surgical implantation of the 3D shelf was safe and feasible. The patient-specific 3D-printed shelf implants restored the femoral head coverage and stability of dysplastic hips without complications. The presented approach holds promise to treat residual hip dysplasia justifying future veterinary clinical trials to establish clinical effectiveness in a larger cohort to prepare for translation to human clinic.

Introduction

Hip dysplasia or developmental dysplasia of the hip affects as many as one in every 22 newborns[1]. However, cases that eventually need treatment have an incidence of 0.5%[2,3]. Over the last decades, treatment outcome has improved by treating young patients before their triradiate cartilage definitely closes at the age of approximately 16 years[4]. However, early detection and treatment sometimes fails, leading to (young) adolescents with residual dysplasia who present with pain or pre-osteoarthritic changes[5]. It is presumed that many osteoarthritic hips are the result of (subclinical) dysplastic hips[6,7]. In skeletal mature cases of hip dysplasia, surgical treatment is often indicated to prevent severe osteoarthritis at later age[6].

The gold standard surgical treatment option for hip dysplasia is Peri-Acetabular Osteotomy (PAO)[8]. PAO is an invasive surgery with an extensive learning curve and is associated with a high rate of complications[8]. Therefore, the concept of shelf arthroplasty[9] could be revisited by using titanium additive manufacturing technologies[10] to develop 3D-printed joint preserving implant in a personalized approach[11,12].

The titanium 3D-printed shelf implant was previously biomechanically tested in a cadaveric dog model and demonstrated to stabilize the dysplastic hip joint by creating an acetabular rim extension in a predictable and consistent manner[11]. Similar to the autologous shelf arthroplasty the 3D shelf implant is placed extra capsular with the synovial membrane lining the inner rim of the implant and thereby increasing the weight bearing surface of the dysplastic acetabulum.

An experimental animal model should be used to investigate the concept and feasibility of the 3D-printed shelf implant. Dogs are the animal of choice for a translational study as canine hip dysplasia has similar diagnostic and treatment strategies as developmental hip dysplasia in humans[13,14]. The primary aim of the study is to test the feasibility and safety of the 3D shelf implantation in a small pilot of three experimental dogs, because when implantation is proven safe an immediate translation is preferred to symptomatic patient dogs who consult the veterinarian. As secondary outcomes the post-operative rehabilitation of the implantation is followed and compared to the control side using clinical observation, manual subluxation testing, imaging, gait analysis and post mortem histology of the hip joint.

Materials and methods

Ethics approval

Animal handling was in accordance with the European Directive for the Protection of Vertebrate Animals Used for Experimental and Other Scientific Purposes (86/609/EU). The experiments were approved by the National Central Committee for Experiments on Animals (CCD) and a maximum of three experimental dogs could be used to evaluate safety (AVD1080020173505) after which a new clinical trial should be started to investigate effectiveness in symptomatic dog patients. The working protocol (WP3505-01-1) was further supervised by the local Animal Welfare Body and followed the ARRIVE guidelines.

Study design

Prior to the implantation of the personalized 3D-printed implant (T=0) and during the 6 months follow up period, clinical observation, manual subluxation testing, imaging, gait analysis were conducted. Upon termination of the study, histology of the hip joints was performed (Table 1).

Table 1. Study outline in weeks (W). T=0 is the time point of intervention.

Study Action	-6W	-5W(-2W)	-1W	T=0	1W	2W	4W	6W	8W	12W	16W	20W	26W
Imaging (CT + X-ray)													
Subluxation test (Ortolani)													
Gait analysis (training)													
Gait analysis (measurement)			*										
Intervention													
General health assessments, orthopedic examinations, and subjective locomotion evaluations													
Termination													
Histology													

*The preoperative baseline consisted of three measurements conducted on separate days during 1 week.

Animals

In this pilot study three female mongrel dogs (Marshall, North Rose, New York) with natural occurring, radiographically confirmed, asymptomatic bilateral hip dysplasia were included. The mean (range) age of the dogs was 25 (24–25) months and the mean body weight was 26

(24–29) kg. The hip with the worst dysplastic parameters[15] based on radiological examination and manual subluxation (Ortolani[16]) testing (Fig. 1A–D) was chosen as the intervention side for the 3D shelf implant (N=3) and the contralateral hip served as control (N=3) (Table 2). All subluxation tests were performed under general anesthesia by two board-certified veterinary surgeons who were blinded for each other's results. The three dogs were housed in a group enclosure with cage enrichment and were put on an ad libitum diet. Furthermore, the dogs were housed with a regular 24-h day-night rhythm and were allowed in an outdoor pen at least twice daily.

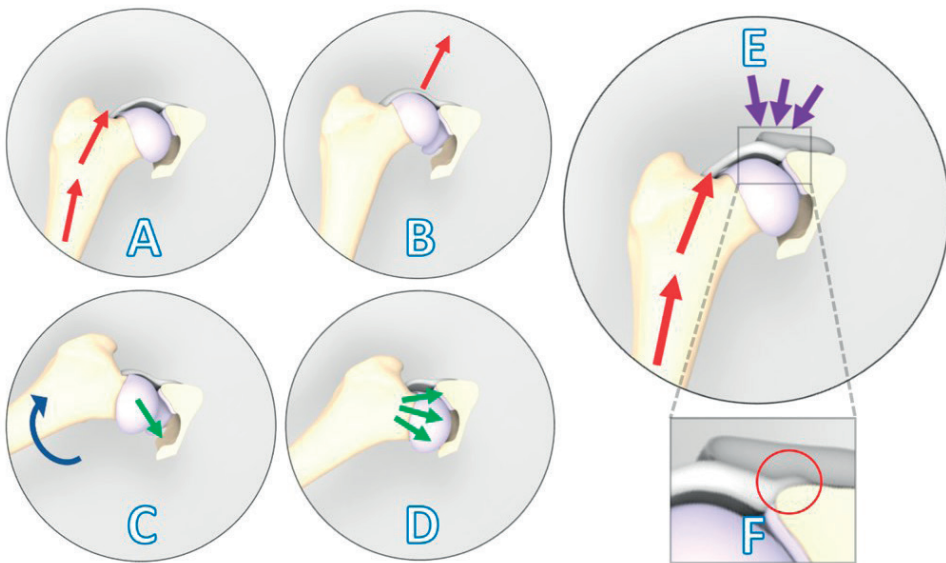


Figure 1. Laxity due to hip dysplasia is confirmed based on clinical examination (A–D) and is counteracted by implantation of the 3D-printed shelf implant (E). (A) The limb is in neutral flexion and in an adducted position, and force is applied toward the dorsum of the dog along the femoral axis (red arrows). (B) This force causes dorsal subluxation in a hip with joint laxity due to hip dysplasia. (C) During the Ortolani (reduction) test, the limb is slowly abducted (blue arrow) while force on the femur (red arrows) is maintained. (D) A positive Ortolani sign is evident when a click is heard or palpated as the subluxated femoral head reduces into the acetabulum (green arrows)[17]. (E) Introduction of the shelf implant ideally stabilizes the joint by reinforcing the hip capsule and labrum as a weight bearing and stabilizing surface (purple arrows). In close-up the internal 2 mm offset of the implant is visible that allows the capsule attachment to remain unaffected (F).

The intervention/imaging

At the initiation of the study (– 6 weeks), a CT-scan with a standardized protocol (Appendix 1) was made of the entire pelvic area and femora (120 kV, 250 mas, 0.6 mm slice thickness). The CT scans were semi-automatically segmented using imaging processing software, Mimics Medical 21.0 (Materialise, Leuven, Belgium). Standardized bone threshold values (HU 226—upper boundary) were used to guide the semi-automatic CT-based anatomical model. This model was saved and transferred using Stereolithography (STL file) to design the 3D shelf implant.

Table 2. Baseline and postoperative measurements (radiology and Ortolani test).

<i>Measurements</i>	Dog #1		Dog #2		Dog #3	
<i>Hip (L/R)</i>	Left	Right	Left	Right	Left	Right
<i>Operative side</i>	Control	Intervention	Control	Intervention	Intervention	Control
<i>Sex (F/M)</i>	F		F		F	
<i>Weight (kg)</i>	23.9		29.2		23.6	
<i>Age (months)</i>	24		25		25	
Baseline (– 6 weeks)						
<i>Ortolani</i>	+	+	+	+	+	+
<i>CE-angle (°) 12:00 o'clock</i>	105	98	92	84	99	107
<i>Femoral coverage</i>	53%	48%	46%	41%	50%	53%
<i>Radiographic hip joint incongruency</i>	Mild	Moderate	Moderate and sub-luxation	Moderate and sub-luxation	Moderate	Very mild
Direct post-operative (+ 0 days)						
<i>CE-angle (°)</i>	105	120	92	117	120	107
<i>Femoral coverage</i>	53%	61%	45%	59%	61%	53%
<i>Ortolani</i>	+	–	+	+	–	+
<i>Surgical accuracy</i>	–	1 mm	–	3 mm	–	1 mm
Intermediate follow-up (+ 6 weeks)						
<i>Ortolani</i>	+	–	+	+	–	–
Intermediate follow-up (+ 6 weeks)						
<i>Ortolani</i>	+	–	+	–	–	+
Final follow-up (+ 6 months)						
<i>CE-angle (°)</i>	104	120	92	116	119	108
<i>Femoral coverage</i>	52%	62%	46%	58%	60%	54%
<i>Ortolani</i>	+	–	–	–	–	+

L left, R right, F female, M male, CE center edge angle.

Implant design

The patient-specific 3D-printed acetabular shelf implants were designed, by the primary author using Freeform Plus software (Geomagic, 3D Systems, Leuven, Belgium), as described prior by Willemsen et al.[11] (Figs. 2 and 3). The implants consisted of two subsections; the 'rim extension part' and the 'implant-bone interface or attachment part'. For the rim extension part a 20°–30° increase in CE-angle was pursued and the effect on the range of motion was monitored by performing an in silico range of motion (ROM) simulation, for each individual hip. Thereafter, the outcomes were reviewed with a board-certified surgeon and the design was altered if clinically needed (Figs. 1E, 3) (Video 1). The rim of the acetabulum received an offset of 2 mm not to interfere with the attachment of the joint capsule on the acetabular rim and to allow the hip capsule to be interposed between the implant and the cartilage of the femoral head (Figs. 1F, 3).



Figure 2. Rendering of a canine pelvis with a 3D-designed acetabular rim implant for the left dysplastic hip. Orientation: left is cranial, top is dorsal.

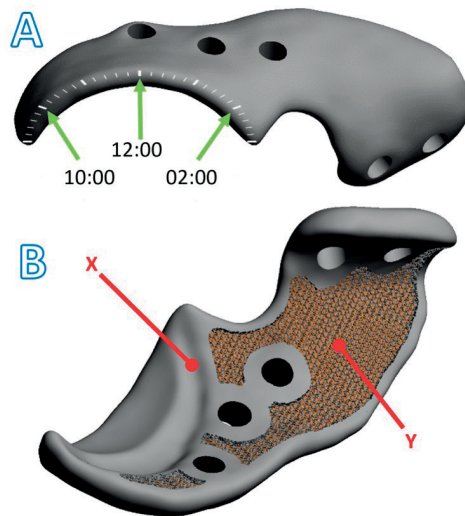


Figure 3. Digital rendering of the implant designed for dog #1.

(A) The external implant surface with the clockface positions (green arrows) on the rendered implant. (B) The internal implant surface shows the internal offset (X) that allows the capsule attachment to remain unaffected and the 70% porous inner shell (Y) allowing bone ingrowth for osseous integration and secondary implant fixation.

The implant-bone interface part was also designed patient specific to be able to incorporate 5 locking screws and an additional ilium flange for ease in positioning and for additional stability. Thereafter, the implant bone interface was designed with a porous (70%, 1 mm sized Dode-Medium unit cell) inner shell to optimize bone ingrowth, osseointegration and secondary implant fixation (Fig. 3). Locking screw holes were planned in the implant in such a way that the screw trajectory remained sufficiently distant from the acetabulum but at the same time purchasing the maximal possible bone stock for the preferred screw length. The screws were placed bi-cortical and generally not parallel to each other.

The implants were manufactured from medical grade titanium alloy Ti-6Al-4V ELI grade 23 by direct metal printing using a ProX DMP320 machine (3D Systems, Leuven, Belgium). Postprocessing included hot-isostatic-pressing, polishing, screw wiretapping and a standard intermediate cleaning step (incl. ultrasonic cleaning and automated cleaning) by the implant manufacturer. Additionally, final (manual) cleaning and autoclave sterilization was performed by our in-house sterilization facility.

Orthogonal radiographs and CT of the pelvis and hips were made at -6, 0, +6, +12, +26 weeks from the implantation (Table 1) and parameters such as the center-edge (CE)-angle[18] were assessed by a board-certified veterinary radiologist. Subsequently, the CT-scans were uploaded into image analysis software Mimics (Medical v20, Materialise,

Leuven, Belgium) to calculate the percentage of femoral head coverage by using multiplanar reconstruction¹⁹. The acetabular coverage was measured in +20° posterior pelvic tilt in relation to the cranial–caudal axis to simulate the functional standing posture of a dog[19]. Additionally, the accuracy of the placement was analyzed by rigidly overlaying the preplanning with the postoperative 3D models with an iterative closest point (ICP) algorithm[20] and subsequently calculating the average implant transformation matrix in mm[21].

The surgeries were performed by a board-certified veterinary surgeon under a standardized general anesthesia protocol (Appendix 2b) and consisted of a cranio-dorsal approach (Appendix 3) to the hip joint leaving the joint capsule intact[22]. The implant was fitted to the bone and positioned over the hip joint capsule and was fixated with five 3.5 mm locking screws (DePuy Synthes, Raynham, Massachusetts, USA). Full weight bearing was allowed directly postoperatively and reintroduction of the dog into the study group from an individual cage was done 24 h postoperatively. Due to the surgical nature of the intervention only blinding occurred during histological examination.

Outcomes

General health assessments, orthopedic examinations, and subjective locomotion evaluations were performed weekly during the whole experiment. The subluxation (Ortolani) tests of the hips were assessed under general anesthesia at –6, 0, 6, 12, 26 weeks (Fig. 1) (Table 1).

Gait analysis was performed using a standardized gait protocol (Appendix 4) using a force plate[23,24] for objective evaluation of vertical (F_z) ground reaction forces (N/kg) measuring differences between the intervention and control limb and the distribution ratio between front-limb and hind-limb loading before surgery at –1 (baseline) and after surgical intervention at 1, 2, 4, 8, 12, 16, 20, and 26 weeks (Table 1).

The dogs were followed for 26 weeks to allow enough time for initial surgical recovery, secondary implant fixation and to assess tissue changes to the joint capsule or cartilage after implant intervention. At final follow-up, the dogs were euthanized (Appendix 2c). Each hip joint was harvested and macroscopically evaluated before histological examination was performed on the capsule and femoral and acetabular cartilage of the decalcified joints using a standardized staining protocol for Hematoxylin and Eosin (HE) staining, and Safranin O/Fast Green staining[19] (Appendix 5).

Results

Preoperative

At baseline (6 weeks preoperative) all intervention and control hips exhibited a positive Ortolani test (Video 2) and femoral heads showed decreased acetabular coverage or subluxation on radiography. The mean CE-angle was 94° (range 84°–99°) for the intervention hips and 98° (range 92°–105°) for the control hips (Table 2; Fig. 4). General orthopedic examination and subjective locomotion evaluation revealed no other relevant joint abnormalities other than the findings related to hip dysplasia. Objective gait analysis showed no marked differences between the loading (Fz) of intervention and control hips (Fig. 5).

Postoperative

The implantation of the 3D shelf implant went uneventful. Two implants (dog #1 and dog #3) were placed within 1 mm of their planned position while the other implant (dog#2) was placed distally with a 3 mm offset. Directly post-operatively dog #1 and #3 displayed a negative Ortolani test at the intervention side (Video 3). The recovery of all animals was rapid, the dogs were fully weightbearing on the intervention limb the next day. The dogs were comfortable and were able to resume their normal daily activity. At final follow-up, all three intervention hips and one control hip (dog #2) displayed a negative Ortolani test (Table 2) and no screw failure or loosening was witnessed.

After surgery, the mean CE-angle of the treated hips improved, due to a combination of femoral head medialization and an increase in femoral head coverage by the acetabulum and implant (Fig. 4). The mean intervention side CE-angle increased to 119° (117°–120°), which is within the normal range¹⁸. The mean total femoral head coverage for the intervention hips increased from 46% (range 41–50%) preoperatively to 60% (58–62%) postoperatively (Table 2 and Fig. 4). The radiographic measurements on the control hips did not change over time (Table 2).

During gait analysis in the first two weeks postoperatively, all dogs showed a decrease in their intervention/control ratio of the ground reaction forces. After a mean of four weeks, the intervention/control ratios returned to preoperative levels (Fig. 5). Furthermore, all three dogs showed a decrease of the front limb/hind limb ratio of the ground reaction forces after surgery that returned to baseline levels after an average of 6 weeks (range 3–12 weeks) postoperatively (Fig. 5).

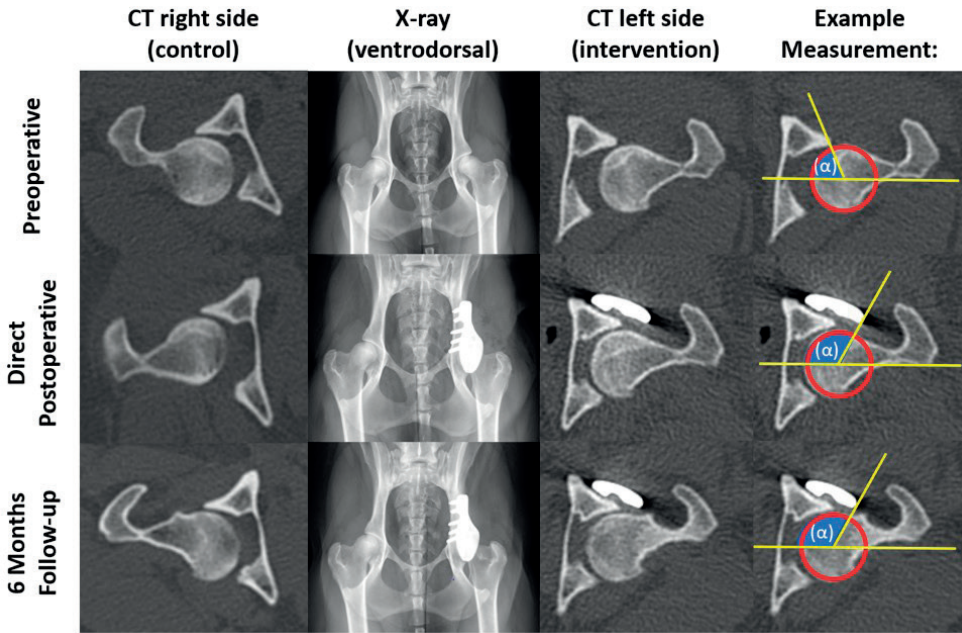


Figure 4. Imaging of dog #3. Preoperatively the intervention side is decentralized. The intervention hip becomes centralized directly postoperatively. On 6 months follow-up the intervention side is still centralized showing improvement in comparison to the preoperative situation. The control side remains unchanged. In the right column the change in center of edge (CE) angle (α) is measured on CT. On the postoperative images the head of the femur centralizes in the acetabulum and there is increased dorsolateral coverage of the femoral head which is reflected in an increased CE-angle (α) by measuring the combined rim of the native acetabulum and the rim extension implant. Also it should be mentioned that some osteophytes are visible in the femoral neck at 6 months follow-up, however these were not evidently more present at the control of intervention side.

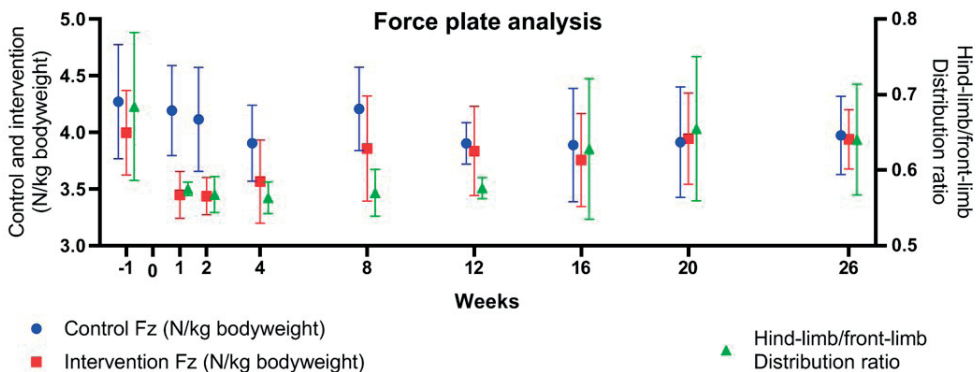


Figure 5. Objective gait analysis by force plate. Mean \pm standard deviation force (Fz) (N/kg body weight) on the control (red) and intervention (blue) side, and hind-limb/front-limb distribution ratio (green) before and after acetabular rim extension with a personalized 3D implant that was implanted (week 0) in 3 dogs with hip dysplasia.

Histopathology

Macroscopic evaluation of the hip joints showed that the hip implant was completely encapsulated by connective tissue. When the hips were separated in a cranial and caudal section there was a clear view of the hip capsule at the most dorsolateral (12:00 o'clock) position. The capsule interposed between the implant and the femoral head was markedly increased in thickness compared to control hips, and had a perceptible smooth transition to the macroscopically unaffected acetabular cartilage (Fig. 6). The samples presented variable pathologic changes of cartilage structure, varying from normal volume with smooth cartilage surface with all zones intact (OARSI grade A) to fissures to the mid zone and erosion of the surface (OARSI grade C). No additional histological damage to the acetabular or femoral cartilage, or metallosis due to the implant was observed in the intervention hips compared to the control hips (Fig. 7). Likewise, the synovial membrane presented with variable levels of absent (control hip dog#1 and all intervention hips) to mild synovitis (control hips of dog#2 and dog#3) evidenced by an increase in the number of cell layers (up to 3) and finger-like villous hyperplasia. Full histological results are presented in the Appendix 6

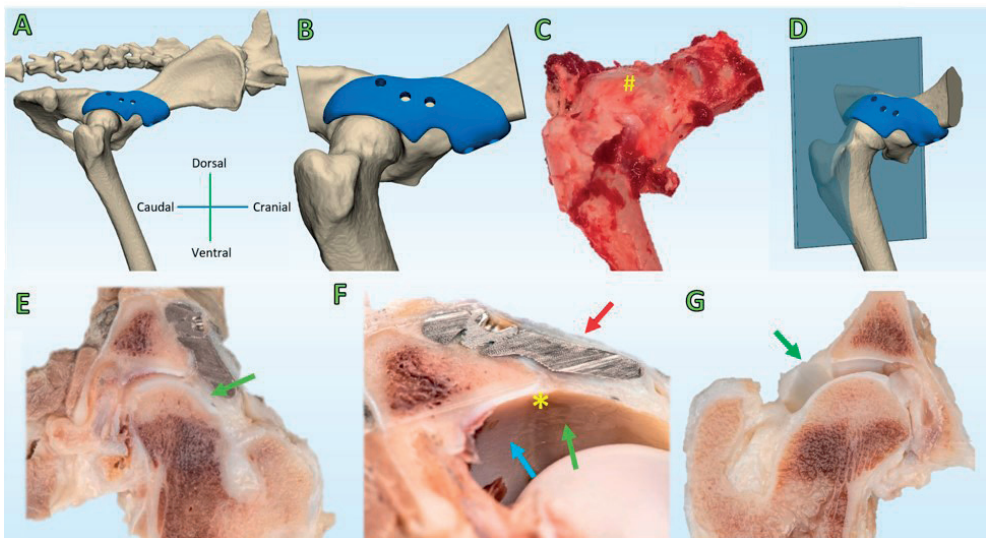


Figure 6. Macroscopy of the intervention and control hip joint of dog#1. (A) CT rendering overview of the pelvis with a view on the intervention side. (B) CT rendering overview of the size of the dissected specimen. (C) Overview of the dissected hip joint with the implant in situ (#). The implant is not distinguishable because it is entirely encapsulated by a thin layer of connective tissue (red arrow, F). (D) CT rendering overview of the cut hip plane (Blue) through the 12:00 o'clock position of the acetabulum. (E,F) Cross section through the 12:00 o'clock position of the acetabulum. The joint capsule shows hypertrophy (green arrow, E) and has incorporated the implant in-between layers (red arrow, F) allowing for a smooth transition (*, F) from the acetabular cartilage (blue arrow, F) into the weightbearing hip capsule (green arrow, F). (G) The control hip is depicted for reference in a cross section through the 12:00 o'clock position of the acetabulum. The hip capsule has a minimal thickness (green arrow, G) as compared to the intervention side (green arrows, E,F).

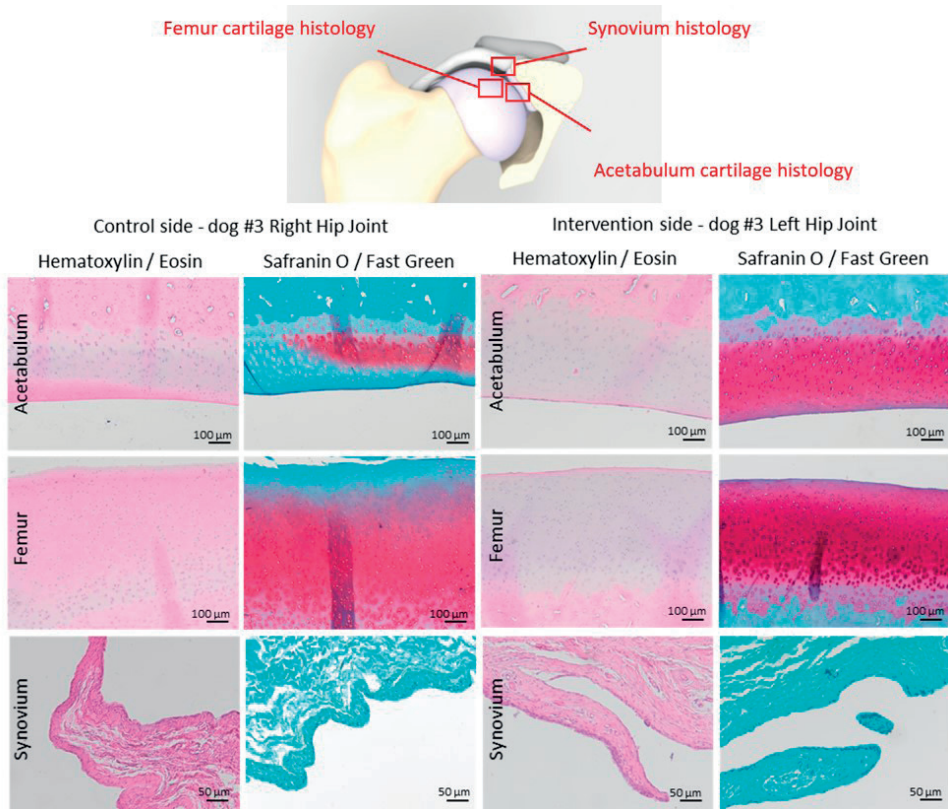


Figure 7. Representative histological images of the acetabular and femoral cartilage and synovium of dog #3. The control side demonstrates a fairly normal volume and smooth surface of acetabular and femoral cartilage, focal loss of proteoglycan staining into the deep zone of the acetabular cartilage, and global loss of proteoglycan staining into the upper zone of the femoral cartilage. The intervention side demonstrates a normal volume and smooth surface of acetabular and femoral cartilage, and unremarkable corresponding Safranin O/Fast Green staining. For both sides there are no abnormalities observed in the tide mark, nor subchondral changes. The synovial lining is composed of 2–3 layers of cells at the control side, whereas at the interventional side it is composed of 1–2 layers of cells. Both sides demonstrate absence of cell infiltrates, and proteoglycan deposition.

Discussion

The present study provides a *proof-of-concept* for a safe and feasible surgical approach to treat naturally occurring hip dysplasia with a personalized 3D-printed titanium shelf implant in a dog model. The shelf implant augmented the acetabular rim and was effective in increasing femoral head coverage and normalizing the CE-angle of the dysplastic hip joint. The *in vivo* implantation of the 3D shelf implants demonstrated minimal morbidity, uneventful recovery, and normalization of the gait of the dogs to baseline based on force plate analysis while preserving joint health.

The experimental dogs were allowed full weight-bearing immediately after implantation without clinical adverse effects, which confirmed the implant safety derived from the break-out test in the reported biomechanical study with cadaveric dysplastic dog hips[11]. Cartilage health remained preserved based on macroscopic and histological findings 6 months after implantation. Altogether these observations indicate that the 3D shelf implant can be used in a clinical setting to treat dogs suffering from hip dysplasia, and may not require postoperative lifestyle restrictions following a standard period of limited exercise restriction.

Surgical interventions in case of hip dysplasia are primarily meant to improve hip joint stability and preserve joint health[6]. The 3D shelf implant helped to improve the stability of the hip joints as all three intervention hips demonstrated negative Ortolani tests at final follow-up in combination with medialization of the femoral head to a normal position on CT scan images. This was in agreement with a prior biomechanical study which revealed that the 3D shelf implant added stability to the hip joint[25]. While the control hips of two dogs still showed hips with subluxation, one control hip (dog #2) also presented a negative Ortolani at 6 months postoperatively, albeit with evident signs of osteoarthritic changes on histology. This is a well-known phenomenon, as negative Ortolani testing is commonly seen in dogs with hip dysplasia that develop progressive secondary osteoarthritis commencing from their second year of adult life[26]. In future studies fluoroscopy examination under sedation and weight bearing conditions[27] or during treadmill walking[28] could be used to give more insight in hip joint stability during follow up of the 3D shelf implant.

Improved joint stability within 6 months after implantation of the 3D shelf implant is most probably achieved by a combination of increased femoral head coverage and soft tissue changes after implantation. In all three dogs, the capsule lining the inside of the titanium acetabular rim completely filled the (2 mm) gap between implant and femoral head and was remarkably thicker than the submillimeter natural thickness of the normal hip capsule[29]. This suggests that the increased biomechanical requirements of the capsule resulted in hyperplasia of the synovial membrane without inducing synovitis. Also in dog #2, where implant positioning was slightly imperfect, the space between the implant and femoral head was macroscopically filled with a relatively thick tissue layer. The latter probably contributed to the stabilization of the hip joint and resulted in a negative Ortolani test and facilitated the return to baseline locomotion in similar fashion as in the other two experimental hips. A further favoring of the treated (hind) limb was not anticipated as these experimental dogs were not (yet) clinically affected by their dysplasia and therefore a conversion to a clinically affected patient population is essential.

The 3D shelf implant as a treatment resembles the shelf arthroplasty that has been described in dogs using a biocompatible osteoconductive polymer (BOP)[30]. Although short-term clinical effectiveness of the BOP shelf arthroplasty was reported in dogs with hip dysplasia, a study in normal dogs showed that ossification around the BOP fibers was slow and unsatisfactory to recommend its use for the treatment of canine hip dysplasia[30]. In another prospective study, 10 dogs with bilateral hip dysplasia were treated with the BOP shelf arthroplasty on the right hip joint and a sham procedure on the left hip joint[31]. Large bony shelves failed to develop on the treated hips and the amount of periarticular bone even decreased over time. The BOP implants were encapsulated by fibrous tissue and there was no histologic evidence of osteoconduction by the bony implants[31]. Shelf arthroplasty using the 3D printed titanium implant in the present study has the advantage that it is not dependent on osteoconduction or osteoinduction, results in immediate patient-specific augmentation of the acetabular rim, and potentially limits uncontrolled bone proliferation. However, no histology was performed on the porous sections of the implant to review the amount of bone ingrowth and this is still recommended for future research in a clinically affected cohort with longer follow-up.

Hip dysplasia morphology, diagnostics, and treatment options in both man and dogs are comparable allowing for a translational study employing dogs as a model to show a proof-of-concept[13]. Ethical considerations prevented the use of a higher number of experimental dogs. Nonetheless, this study serves the veterinary dog patient suffering from canine hip dysplasia, to offer an alternative for invasive double or triple pelvic osteotomies, or prevent future femoral head and neck resection or hip joint replacement[32]. Long term follow up studies in patient dogs may give insight in whether this procedure may prevent the development of debilitating secondary hip osteoarthritis before evaluating this procedure for humans. Within this context, there are some limitations of the current study. First, the follow-up can be deemed as short and numbers treated small, however if no implant failure was witnessed in the first few months under full weight bearing, the ethical committee had enough confidence to allow a secondary trial in clinically affected canine patients in which the effect of the implant shall be further evaluated. Another limitation of this study with respect to its translation towards humans is the analogous hip anatomy of dogs and humans that exhibits marked functional differences with respect to loading in magnitude, direction and the front/hind limb weight ratio that logically differs between quadruped animals and biped humans[33]. Therefore, to prepare translation of this 3D shelf approach to human clinic a cadaveric proof of concept is required with a further biomechanical analysis.

This study showed a proof-of-concept of a patient-specific acetabular rim implant that restored the coverage and stability of dysplastic hip joints to a normal level without complications. This low invasive procedure holds promise to treat dog patients with hip

dysplasia. To compare this novel procedure to the gold-standard TPO and confirm long term safety and efficacy, a follow up study with a larger cohort in a clinically affected dog population suffering from hip dysplasia is indicated. To prepare translation of this 3D shelf approach to human clinic a cadaveric proof of concept is also required.

Appendix

<https://doi.org/10.1038/s41598-022-06989-9>

References

1. Peled, E., Eidelman, M., Katzman, A. & Bialik, V. Neonatal incidence of hip dysplasia. *Clin. Orthop. Relat. Res.* 466, 771–775 (2008).
2. Freiberg, J. A. Early diagnosis and treatment of congenital dislocation of the hip. *J. Am. Med. Assoc.* 102, 89–93 (1934).
3. Bialik, V. et al. Developmental dysplasia of the hip: A new approach to incidence. *Pediatrics* 103, 93–99 (1999).
4. Parvaresh, K. C., Pennock, A. T., Bomar, J. D., Wenger, D. R. & Upasani, V. V. Analysis of acetabular ossification from the triradiate cartilage and secondary centers. *J. Pediatr. Orthop.* 38, e145–e150 (2018).
5. Mavčič, B., Iglič, A., Kralj-Iglič, V., Brand, R. A. & Vengust, R. Cumulative hip contact stress predicts osteoarthritis in DDH. *Clin. Orthop. Relat. Res.* 466, 884–891 (2008).
6. Jacobsen, S. & Sonne-Holm, S. Hip dysplasia: A significant risk factor for the development of hip osteoarthritis. A cross-sectional survey. *Rheumatology* 44, 211–218 (2004).
7. Jessel, R. H. et al. Radiographic and patient factors associated with pre-radiographic osteoarthritis in hip dysplasia. *JBJS* 91, 1120–1129 (2009).
8. Clohisy, J. C., Schutz, A. L., John, L. S., Schoenecker, P. L. & Wright, R. W. Periacetabular osteotomy: A systematic literature review. *Clin. Orthop. Relat. Res.* 467, 2041–2052 (2009).
9. Willemsen, K. et al. Long-term outcomes of the hip shelf arthroplasty in adolescents and adults with residual hip dysplasia: A systematic review. *Acta Orthop.* 91, 383–389 (2020).
10. Willemsen, K. et al. Challenges in the design and regulatory approval of 3D-printed surgical implants: A two-case series. *Lancet Digit. Health* 1, e163–e171 (2019).
11. Willemsen, K. et al. Patient-specific 3D-printed shelf implant for the treatment of hip dysplasia: Anatomical and biomechanical outcomes in a canine model. *J. Orthop. Res.* <https://doi.org/10.1002/jor.25133> (2021).
12. Golafshan, N. et al. 3D-Printed regenerative magnesium phosphate implant ensures stability and restoration of hip dysplasia. *Adv. Healthc. Mater.* 10, e2101051 (2021).
13. Pascual-Garrido, C. et al. Canine hip dysplasia: A natural animal model for human developmental dysplasia of the hip. *J. Orthop. Res.* 36, 1807–1817 (2018).
14. Willemsen, K. et al. Comparing hip dysplasia in dogs and humans: A review. *Front. Vet. Sci.* <https://doi.org/10.3389/fvets.2021.791434> (2021).
15. Ginja, M. M. D. et al. Early hip laxity examination in predicting moderate and severe hip dysplasia in Estrela Mountain Dog. *J. Small Anim. Pract.* 49, 641–646 (2008).
16. Chalman, J. A. & Butler, H. C. Coxofemoral joint laxity and the Ortolani sign. *J. Am. Anim. Hosp. Assoc.* 21, 671–676 (1985).
17. Smith, G. K., Karbe, G. T., Agnello, K. A. & McDonald-Lynch, M. B. Pathogenesis, diagnosis and control of canine hip dysplasia. in *Veterinary Surgery: Small Animal* 824–848 (Elsevier, 2012).
18. Lopez, M. & Schachner, E. Diagnosis, prevention, and management of canine hip dysplasia: A review. *Vet. Med. Res. Rep.* 6, 181 (2015).

19. Larson, C. M. et al. Are normal hips being labeled as pathologic? A CT-based method for defining normal acetabular coverage. *Clin. Orthop. Relat. Res.* 473, 1247–1254 (2015).
20. Besl, P. J. & McKay, N. D. A method for registration of 3-D shapes. in *IEEE Transactions on Pattern Analysis and Machine Intelligence* vol. 14 239–256 (International Society for Optics and Photonics, 1992).
21. Kuo, H. Y., Su, H. R., Lai, S. H. & Wu, C. C. 3D object detection and pose estimation from depth image for robotic bin picking. In *IEEE International Conference on Automation Science and Engineering* vol. 2014, 1264–1269 (IEEE, 2014).
22. Gibson, N. An atlas of surgical approaches to the bones and joints of the dog and cat. *Aust. Vet. J.* 84, 301–338 (2006).
23. Tellegen, A. R., Willems, N., Tryfonidou, M. A. & Meij, B. P. Pedicle screw-rod fixation: A feasible treatment for dogs with severe degenerative lumbosacral stenosis. *BMC Vet. Res.* 11, 299 (2015).
24. Suwankong, N. et al. Assessment of decompressive surgery in dogs with degenerative lumbosacral stenosis using force plate analysis and questionnaires. *Vet. Surg.* 36, 423–431 (2007).
25. Authors & Blinded. Patient-specific 3D printed shelf implant for the treatment of hip dysplasia: anatomical and biomechanical outcomes in a canine model (under parallel submission for back-to-back publication at Bone Joint J.) (2021).
26. Adams, W. M. et al. Early detection of canine hip dysplasia: Comparison of two palpation and five radiographic methods. *J. Am. Anim. Hosp. Assoc.* 34, 339–347 (1998).
27. Farese, J. P., Todhunter, R. J., Lust, G., Williams, A. J. & Dykes, N. L. Dorsolateral subluxation of hip joints in dogs measured in a weight-bearing position with radiography and computed tomography. *Vet. Surg.* 27, 393–405 (1998).
28. Fischer, M. S., Lehmann, S. V. & Andrada, E. Tree-dimensional kinematics of canine hind limbs: In vivo, biplanar, high-frequency fluoroscopic analysis of four breeds during walking and trotting. *Sci. Rep.* 8, 1–22 (2018).
29. Page, A. E. et al. Determination of loading parameters in the canine hip in vivo. *J. Biomech.* 26, 571–579 (1993).
30. Oakes, M. G. et al. Evaluation of shelf arthroplasty as a treatment for hip dysplasia in dogs. *J. Am. Vet. Med. Assoc.* 208, 1838–1845 (1996).
31. Jensen, D. J. & Sertl, G. O. Sertl shelf arthroplasty (BOP procedure) in the treatment of canine hip dysplasia. *Vet. Clin. North Am. Small Anim. Pract.* 22, 683–701 (1992).
32. Bergh, M. S. & Budsberg, S. C. A systematic review of the literature describing the efficacy of surgical treatments for canine hip dysplasia (1948–2012). *Vet. Surg.* 43, 501–506 (2014).
33. Bergmann, G., Siraky, J., Rohlmann, A. & Koelbel, R. A comparison of hip joint forces in sheep, dog and man. *J. Biomech.* 17, 907–921 (1984).



CHAPTER 11

Acetabular rim extension using a patient-specific implant for the treatment of hip dysplasia in dogs

Koen Willemsen | Irin Kwananocha | Joëll Magré | Marianna Tryfonidou |
Harrie Weinans | Ralph J.B. Sakkers | Bart C.H van der Wal | Björn P. Meij

This manuscript contains preliminary data and is still under preparation

Abstract

Aim: A novel 3D-printed shelf implant for acetabular rim extension to treat dogs with hip dysplasia was introduced in previous biomechanical and experimental animal studies. The aim of the present study was to describe the surgical and clinical outcome of placement of this 3D-printed shelf implant in a cohort of dogs with hip dysplasia.

Method: Young dogs with hip laxity due to hip dysplasia with positive Ortolani tests and no or minimal osteoarthritis, were included for operative intervention with acetabular a rim extension implant. Primary outcomes were hip measurements on CT and radiographs, implant survival, and pain scores. Secondary outcomes were complications, surgery time, Ortolani tests and activity scores.

Results: 25 Dogs (42 hips) were treated with the 3D shelf implant and had a mean follow-up of 6 months. 8 Dogs received the implant unilaterally, 11 dogs bilaterally in one-stage and 6 dogs bilaterally in two-stages. In 3 dogs, the implant was placed suboptimal as was evident on postoperative CT and was readjusted. Shelf implants improved the radiographic hip measurements to normal levels. After surgery the pain scores by owner questionnaires improved, whereas on average the osteoarthritis score increased. In 3 hips the shelf implant was converted to total hip arthroplasty (THA) between 6-10 months: in 1 hip the shelf implant failed whereas in 2 other hips rapid progression of osteoarthritis causing clinical signs that necessitated THA.

Conclusion: Acetabular rim extension using a 3D-printed shelf implant is a feasible technique to treat hip laxity due to hip dysplasia in young dogs. The shelf implant is well tolerated after implantation, radiographic values and pain scores improved, while postoperative complications are rare. Mean osteoarthritis score slightly increased and further analysis is needed to assess the shelf implant's ability to delay OA and conversion to THA in the long term.

Introduction

Hip dysplasia is common in humans and dogs[1] and characterized by deficient formation of the acetabular rim and hip joint laxity. After closure of the triradiate growth plate of the acetabulum there are only a few surgical treatment options left.[1] One of the oldest hip dysplasia interventions is the shelf arthroplasty[2] and this procedure has also been tried in dogs, using biocompatible osteoconductive polymers (BOP).[3] Despite promising short term clinical results, the BOP procedure was abandoned due to uncontrolled bone proliferation of the acetabular rim. Therefore, to improve the shelf procedure for dogs a patient-specific 3D-printed titanium shelf implant designed from 3D CT images was introduced recently and tested in prior studies.[4]–[6]

First, an *ex-vivo* study was performed in cadaveric dysplastic hip joints and the 3D shelf increased the potential weight bearing surface of the acetabulum, the femoral head coverage percentage, and the Norberg angle. Moreover, the implants increased joint stability demonstrated by an Ortolani mimicking biomechanical dislocation-potential test.[4] Second, an *in vivo* pilot study was performed in three experimental dogs with subclinical hip dysplasia with hip laxity and positive Ortolani tests. The feasibility study showed safe surgical placement of the 3D-printed implants without complications, increased radiographic joint congruency and hip stability marked by negative Ortolani testing. Gait analysis showed that dogs returned to pre-operative baseline values within a few weeks until termination at 6 months. Histology showed no acetabular and femoral head cartilage deterioration with fibrous capsule metaplasia under the acetabular rim. Implantation in a larger clinically affected cohort of dogs with hip dysplasia was started thereafter to show efficacy of the implant in a clinical setting.

This study describes a cohort of dog patients with hip laxity due to hip dysplasia that visited the outpatient clinic and were treated with a 3D-printed titanium shelf implant that comprised of an acetabular rim extension made according to a patient-specific design. Clinical follow-up included the following primary outcome parameters: radiographic increase of femoral head coverage, radiographic osteoarthritis scores, implant survival and pain scores by owner questionnaires. Secondary outcomes were surgical complications, surgery time and Ortolani testing.

Methods

Ethical statement

The owners were informed about the novel aspects of the shelf procedure and the possible complications related to pelvic surgery using a metal implant. The owners of the

dogs consented to the surgical treatment under the same conditions as required for the triple pelvic osteotomy procedure.

Study outline

Table 1. Study outline with outcome parameters per patient. Double line represents the moment of intervention.

	T=-6W	T=0D	T=0D	T=6W	T=3M	T=12M
Radiography	x		x	x		
CT-scan	x		x		x	x
Ortolani test	x	x	x	x	x	x
Helsinki chronic pain index score		x		x	x	x
Orthopaedic examination	x	x	x	x	x	x

Patients

Client-owned dogs with hip dysplasia that were referred to the Small Animal Clinic of the Faculty of Veterinary Medicine of Utrecht University and were treated with the patient-specific shelf implant were included in this cohort. At the moment of inclusion for 3D shelf surgery all dogs had clinical signs of hip dysplasia such as lameness, exercise intolerance, hip pain, and difficulty getting up, with evidence of hip dysplasia from pre-operative x-ray and a positive Ortolani test. Exclusion criteria consisted of severe osteoarthritis (AO score >2) of the hip joint, open triradiate growth plate at pelvic bone, systemic disease, or infectious arthritis.

Hip dysplasia and osteoarthritis scoring

At baseline, radiographs and computed tomography (CT) scans were assessed by two examiners (BM&IK). Hip dysplasia scoring was done on ventrodorsal radiographs in (HD1 position) without distraction according to the guidelines of the Fédération Cynologique Internationale (FCI).[7] The FCI scoring scale was A (0), B (Tc=transitional case), C (\pm), D (+), E (++) included grading on congruence and osteoarthritis (OA). OA was also scored on the planning CT for the 3D-shelf implant and follow up CT scans and osteophytes were measured in mm at the femoral neck and caudal acetabular rim and graded 0 (no osteophytes), 1 (0-2 mm), 2 (2-5 mm) and 3 (> 5 mm)[8].

Implant Design

Pre-operatively CT-scan (1 mm slice thickness, 120 kV, 250 mAs, Siemens) of the complete pelvis and femoral heads was acquired in dorsal recumbency to assess the bilateral hip joints with special focus on the deficient femoral head coverage of the dorsal acetabular rim. Thereafter, the 3D shelf implants were designed (KW & JM) as described in prior studies.[4] Briefly, the implants consisted of a patient-specific acetabular rim extension

part and was attached to a flange in which screw holes were designed to allow implant-bone linking. In comparison to previous study,[4] the flange was altered and the number of screws were reduced from five to four of which one non-locking screw and three locking screws (Fig. 1). Also, the screw trajectories were placed in a more lateromedial direction instead of craniocaudal direction to facilitate insertion during the craniodorsal approach to the dorsal acetabular rim and hip capsule.

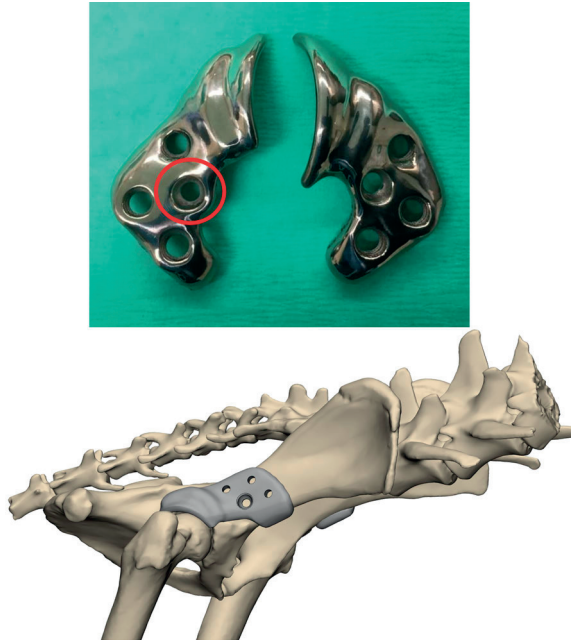


Figure 1. Examples of patient-specific shelf implant designs (left and right side) of two patients with hip dysplasia. Note the difference in design (top) of the acetabular rim extensions for these two patients. Within the red circle is shown a non-locking cortical screw hole design, whereas the other three holes are designed for locking cortical screws. In the image below an *in-silico* rendering of the shelf implant is shown on a CT scan of a dog pelvis.

Implant manufacturing

Implants were produced as described in prior studies.[4] Briefly, direct metal 3D-printing, Hot-Isostatic-Pressing (HIP), screw thread CNC milling, mirror polishing and an intermediate cleaning step. To decrease the lead time to surgery and shorten the production process the Hot-Isostatic-Pressure (HIP) treatment was replaced by an internal stress release procedure during the cohort study, reducing the lead time by 4 working days. This procedure was changed based on ongoing insight experiencing rapid progression of osteoarthritis in young dogs with severe laxity due to hip dysplasia.

Anaesthesia

Dogs were premedicated with intravenous dexmedetomidine 2 mg/kg and methadone hydrochloride 0.3 mg/kg. Induction of anaesthesia was done with intravenous propofol 2-4 mg/kg. Dogs were intubated and inhalation anaesthesia was maintained with isoflurane and oxygen. Analgesia was provided by an epidural block at the L7-S1 junction with Levobupivacaine 0.5 mg/kg and morphine 0.2 mg/kg.

The protocol for anaesthesia for CT scan was premedication with intravenous dexmedetomidine 2 mg/kg and butorphanol tartrate 0.3 mg/kg. Induction of anaesthesia was done with intravenous propofol 2-4 mg/kg and maintained with inhaled isoflurane.

Surgical approach and implantation

All surgeries were performed by one board certified veterinary surgeon (BM) and the craniodorsal approach to the hip^[9] was slightly modified to allow identification of landmarks for implant positioning. Briefly, skin incision was oriented in cranial aspect to the greater trochanter (Fig.2A) and incision was made in the superficial leaf of the fascia lata along the cranial border of the biceps femoris muscle (Fig.2B). The biceps femoris muscle was retracted caudally. Superficial and middle gluteal muscle were retracted dorsally. Tenotomy of deep gluteal muscle was done close to the insertion and a stay suture was preplaced (Fig. 2C). The deep gluteal muscle was retracted dorsally and carefully freed from the joint capsule and its attachment on the ilium. The articularis coxae muscle, and rectus femoris muscle attachments were identified and the ventral rim of the ilium just cranial to the acetabulum was freed for placement of the flange of the implant (Fig. 2D). The articularis coxae muscle was detached from the capsule and the rectus femoris muscle attachment was retracted caudally to make sure that the implant was positioned directly on the body of ilium (Fig. 2E). Periosteal elevation was used to remove all remaining soft tissue fibres from body of ilium preparing for implantation positioning and to stimulate bone in-growth in the porous layer. The shelf implant was fixated with 3 locking cortical screws and one non-locking cortical screw (Fig. 2F)(3.5 mm or 2.7 mm, Stainless steel, DePuy Synthes). Based on ongoing insight and experience, from hip number 13 onwards, implant positioning was confirmed after placement of the first screw using fluoroscopy (Philips[□] model NZS 229). During surgery Cefazolin sodium 20 mg/kg was used as prophylactic antibiotics and repeated every 90 minutes. Immediately after implantation within the same anaesthesia session a CT-scan and radiography was acquired to qualitative assess the accuracy of the implant placement.

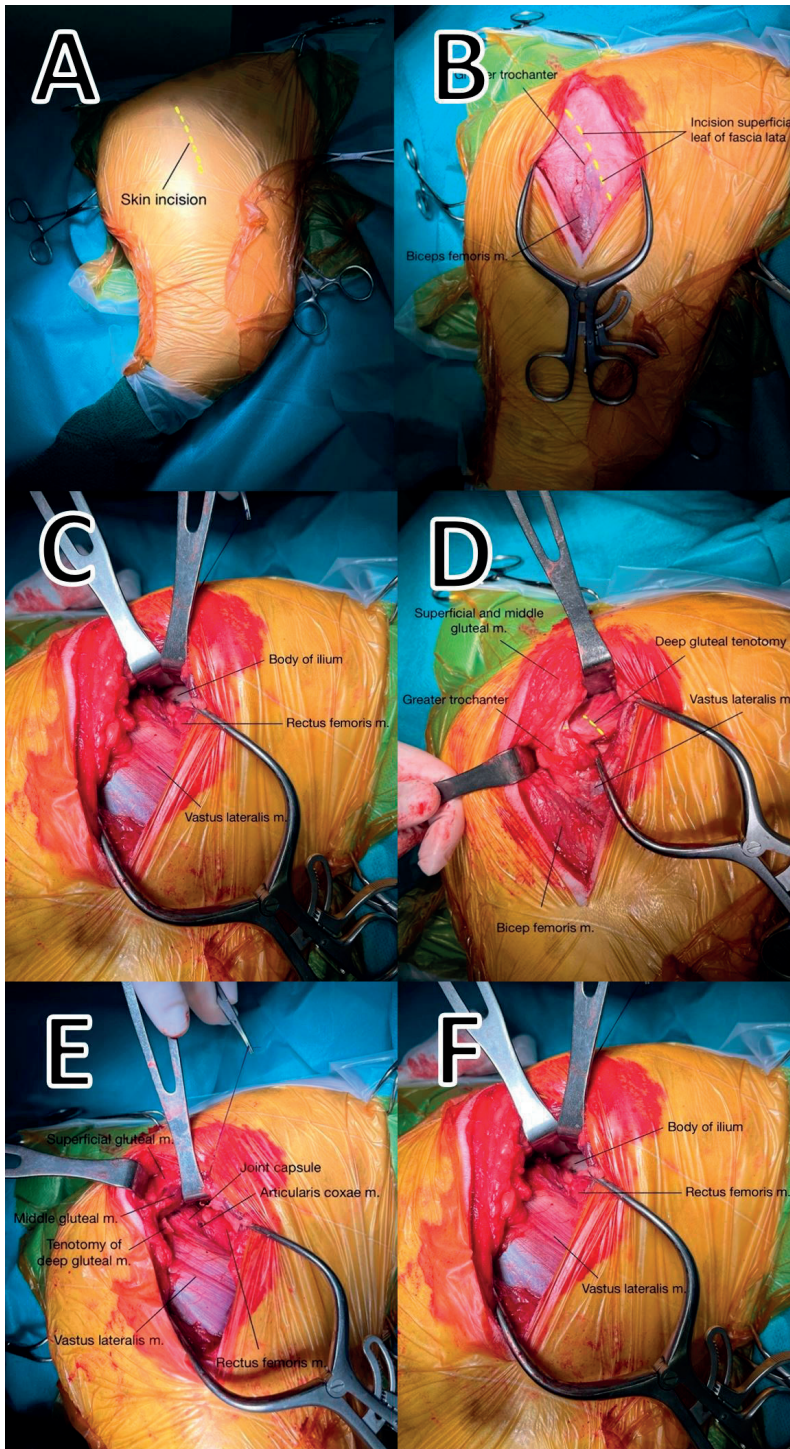


Figure 2. Craniodorsal approach to the right hip joint for acetabular rim extension using the 3D-shelf implant.

Rehabilitation & pain medication

Patients were observed overnight and when patients were walking with weight bearing on operated limb(s), urinated spontaneously, and were comfortable they were discharged the next day. Carprofen (2 mg/kg BID for 2 weeks) and Gabapentin (10 mg/kg TID, for 2 weeks) was orally administered. In case of very hyperactive dogs or at request of the owner Trazadone hydrochloride 2-5 mg/kg was administered for 1 to 2 weeks. Direct postoperative weightbearing was allowed during leash walking but high impact energy exercise (e.g. playing, running, jumping) was restricted for 6 weeks after surgery. During 6 weeks post operatively, the dog patient was allowed to walk 4 – 6 times per day with leash control begin with 5 – 10 minutes per walk in the first 2 weeks. The walking duration was increased 5 minutes every 2 weeks. Animal physiotherapy and or hydrotherapy was advised from the second week after surgery.

Outcomes

Helsinki pain score owner questionnaires[10] were voluntarily filled in pre-operatively and at 6 weeks and 3 and 12 months postoperatively. Orthogonal (lateral and ventrodorsal) radiographs were acquired pre-operatively, post-operatively and at 6 weeks post-operatively. CT scans were acquired preoperatively and at 3 and 12 months follow up to follow implant positioning, detect implant integrity, and assess development of osteoarthritis. General health assessments, orthopedic examinations, Ortolani test (awake and/or under sedation or general anesthesia), and subjective locomotion evaluations were performed during return visits to the outpatient clinic at 6 weeks and at 3 and 12 months of follow-up.

Radiographic evaluation

All measurements were performed by two independent observers (IK&BM) in XeroViewer (DICOM viewer) and for pre-operative radiographs from referring veterinarians that were stored as jpeg or pdf files in VetWare (medical patient data information system). Radiographs in JPEG formats were measured with IC Measure Software program. The FCI score[7], OA score[8], the Norberg angle, and the Radiological Coverage Percentage (RPC) were assessed on all ventrodorsal radiographs, CT-scans and reconstructed radiographs derived from coronal CT-scans with a thickness of 5 mm.

The Norberg angle was calculated as the angle between a line connecting both femoral head centers (FHCs) and a line from the FHC to the most (cranio)lateral point of the acetabular rim that was outside of the femoral head circle. The most (cranio)lateral point was determined as the most lateral point from the craniocaudal axis. If there was no single point but a line, the most cranial part of that line was chosen (Fig. 3).

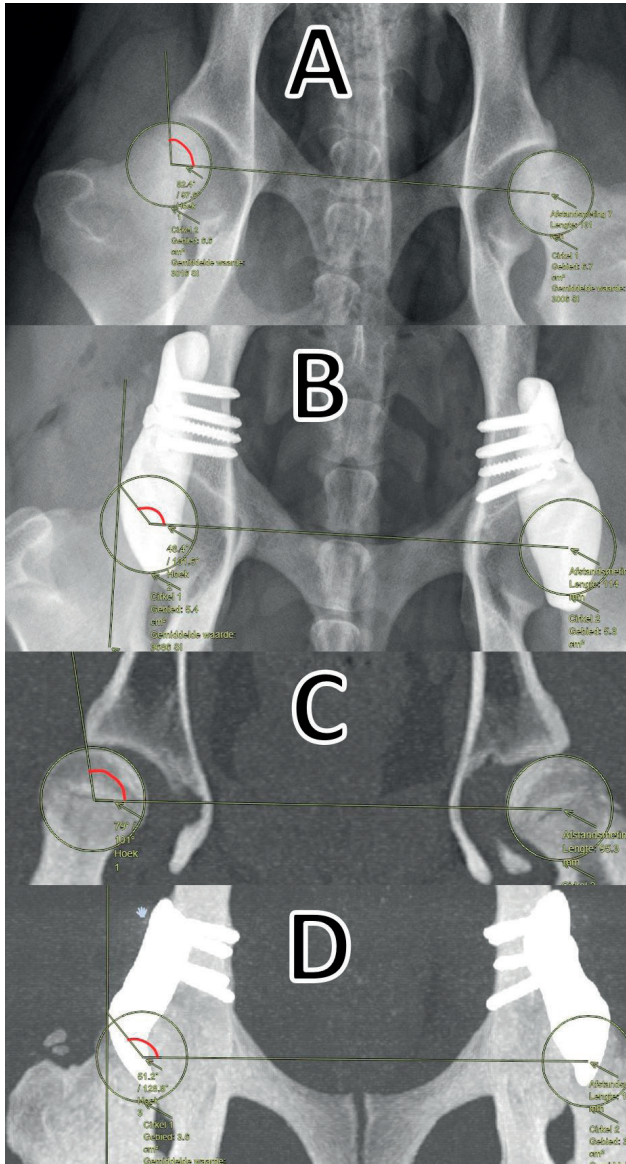


Figure 3. The Norberg Angle measurement before and after 3D shelf implantation on the right coxofemoral joint from the VD radiograph (A,B: 82.4°,131.6°) and the coronal CT-scan (C, single slice: 79°, D: reconstructed radiograph: 128.8°).

Radiographic/CT percentage coverage (RPC)[11] was calculated as the area of the femoral head circle that was covered by the acetabulum compared to the total area of the circle. This area was defined by a line that connects both points of the femoral head circle that are intersected by the most lateral edges of the dorsal acetabular rim (Fig. 4)

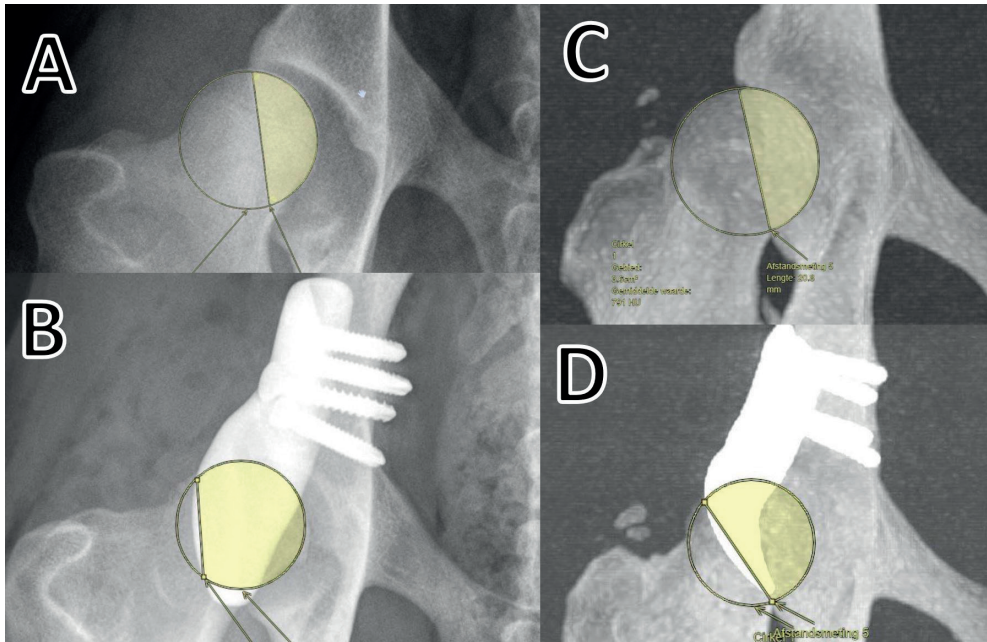


Figure 4. The percentage coverage measurement of before and after implantation on the right coxofemoral joint from the VD radiograph (A,B: 32.44%,89.6%) and the coronal CT-derived reconstructed radiograph (C,D: 36.97%,70.85%).

Statistics

This work is preparatory and no statistics on clinical outcome have been performed to prevent bias. A full analysis for which we anticipate 100 patients will occur once the gathering of the clinical data is completed.

Results

Cohort and surgery

Between August 2019 and December 2021 twenty-five client-owned dog patients (42 hips) were included in the study. The average age of the dogs was 14 ± 6 (7-32) months and body weight 31 ± 18 (11-86) kg. Full patient characteristics are available in the supplementary data. On the preoperative radiographs the FCI hip dysplasia scores were B (3 hips), C (11 hips), D (28 hips). The baseline radiographic osteoarthritis grading of 42 hips in 25 dogs was: 12 hips had an OA score of 0, 16 had a score of 1 and 14 had a score of 2. Furthermore, 10 out of 25 dogs (40%) had co-existing orthopaedic diseases (elbow dysplasia, osteochondritis dissecans of the shoulder and hock) for which they were surgically treated before or after 3D-shelf implantation. Full characteristics per dog and hip can be found in the supplementary data.

At first consultation and inclusion for the shelf implant all 42 hips had a positive Ortolani, however at the day of surgery 1 hip had become Ortolani negative.

The included 25 dogs received 42 shelf implants with a mean follow-up of 6 months (range: 3-12 months)(Fig. 5). Eight dogs received the 3D implant unilaterally, 11 dogs received the implant bilaterally in one surgical procedure and six dogs received their implant bilaterally in two separated surgical procedures, with an average time between sides of 5 ± 4 months.

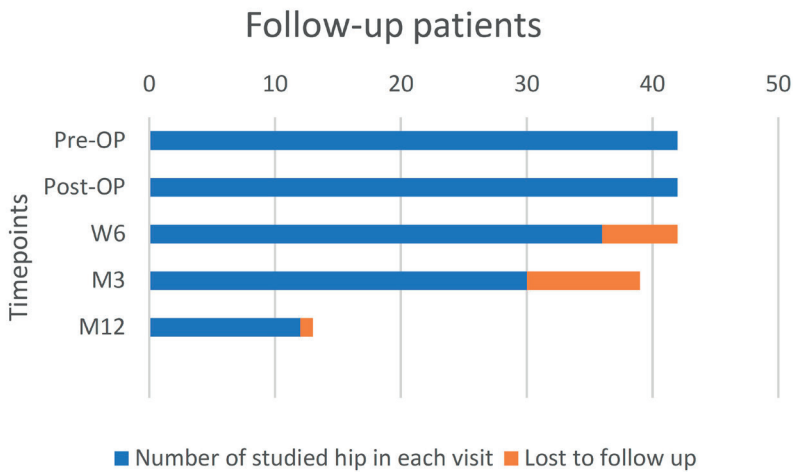


Figure 5. Follow-up time of 25 dogs (42 hips) that underwent acetabular rim extension using a 3D-printed titanium shelf implant. Pre-OP = moment of inclusion. Post-OP = after shelf placement (same day), W6 = 6 weeks follow-up, M3 = 3 Months follow-up. M12 = 12 months follow-up.

The surgery time was 90 ± 22 minutes per implant. The surgery cutting time per hip was similar when implants were placed bilaterally or unilaterally. Surgical implantation was considered acceptable in 39 of 42 hips on immediate postoperative imaging. In three (1L,2R) of the first 13 hips the implant placement was considered suboptimal (>2 mm from target) during the immediate post-operative CT scan, and in those three cases it was decided to return to surgery within the same anaesthesia session to adjust the position. To improve surgical positioning of the implant the protocol was adjusted from dog 8 (hip #13) onward and it was decided to use intraoperative fluoroscopy imaging routinely. After that all implants positions were considered satisfactory at immediate postoperative CT evaluation. Besides the suboptimal placement there were no other intra-operative complications. In 1 dog that initially presented because of severe hip laxity, bilateral implants were planned for a one-stage procedure. However, at the time of surgery only the right-sided implant (hip #37) was placed and the left side was abandoned because hip

dysplasia had progressed severely to the complete luxoid state. This dog received a left-sided total hip arthroplasty at a later date.

Recovery and rehabilitation

Orthopaedic examination of the hip joint was performed after closure and under anesthesia and revealed no impingement or crepitation. Of the 41 preoperative positive Ortolani hips 40 became Ortolani negative immediately after surgery. One hip stayed Ortolani positive after surgery despite the increase in Norberg angle from 83° preoperative to 100° postoperative. The one hip with a negative Ortolani on baseline stayed negative after surgery.

The returned owner questionnaires (Fig. 6) showed an improving trend when comparing the mean \pm standard deviation (SD) values over all 11 domains (Fig. 6). The total sum score of all domains improved from 11.2 \pm 6.2 (0-28) points at baseline (n=30) to 8.4 \pm 5 (2-18) points at 6 weeks (n=20) and further improved to 7.6 \pm 5.5 (0-18) points at 3 months follow-up (n=18). 12 months timepoint is excluded from the analysis as too few dogs reached this follow-up moment at time of writing.

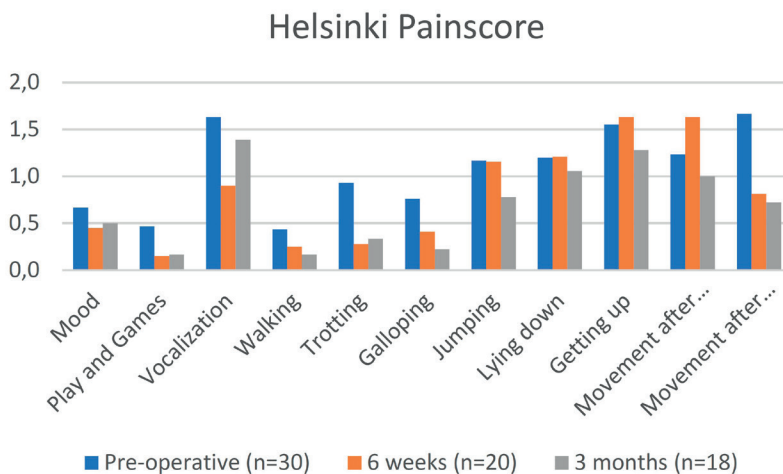


Figure 6. Helsinki pain score (lower score is better function) in 25 dogs with hip dysplasia that underwent acetabular rim extension.

Radiographic evaluation

Due to the ordinal nature of the AO score, the data is presented as cumulative columns in Figure 7. For an assessment per hip see the supplementary data. The mean \pm SD Norberg angle (CT) on baseline was 88 \pm 12° (range 62-111°) and this increased to 136 \pm 19° (range 97-167°) at direct postoperative CT examination and to 134 \pm 20° (range 97-169°) at 3

months postoperative CT (Fig. 8). All radiographic parameters are displayed in Table 2. All scores improved after intervention and remained so at 3 months follow-up.

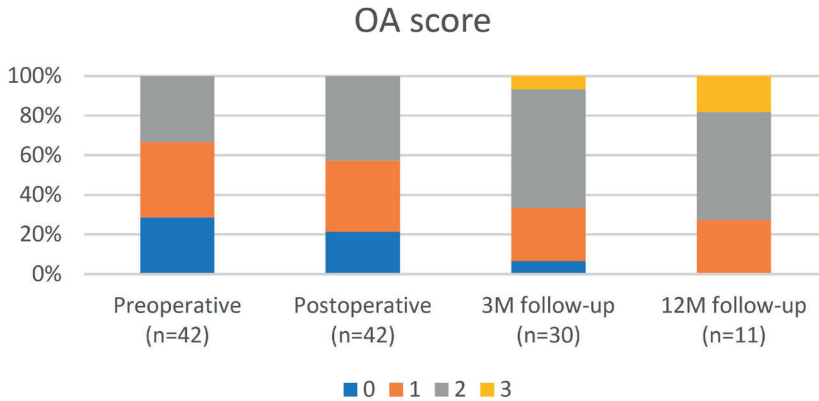


Figure 7. Osteoarthritis (OA) grading on computed tomography in 25 dogs (42 hips) with hip dysplasia that underwent acetabular rim extension. OA scoring: 0 (no osteophytes), 1 (0-2 mm), 2 (2-5 mm), 3 (> 5 mm).

Implant survival and conversion to THA

One 3D shelf out of the 42 operated hips fractured (2.4%) at six months after surgery and in 3 of 42 hips (7.1%), including the one that fractured, the shelf implant was replaced by total hip arthroplasty at respectively 6, 7, and 10 months after surgery.

The first failed case was a German Shepherd dog with a baseline OA score of 1 and a FCI score of D at first diagnosis at age of 5 months. Planning of bilateral acetabular rim extension was delayed due to open triradiate growth plates and planning CT was repeated at age of 6 months. Surgery with the shelf implant was performed at age 8 months. At that time OA score had progressed to 2. The dog received bilateral shelf implants, improved clinically on Helsinki pain score but then developed increasing lameness on the left side. The osteoarthritis score had further deteriorated to 3 and the left hip was converted (hip #25) to Zurich cementless THA 10 months after initial shelf implantation. The explanted implant and screws showed no immediate signs of failure. It is noteworthy that this was one of the two hips that did not reach a Norberg angle of >105 degrees after 3D shelf intervention.

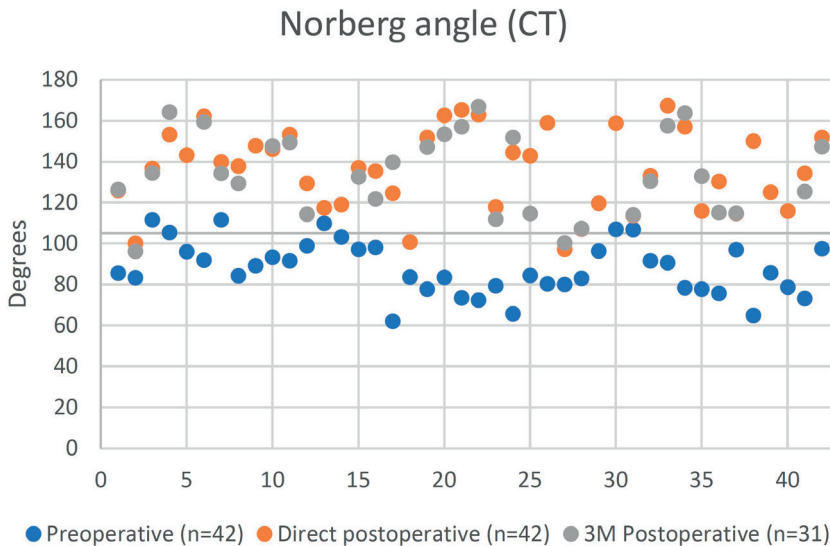


Figure 8. Norberg angle measured on CT-derived synthetic radiographs in 25 dogs (42 hips) with hip dysplasia that underwent acetabular rim extension using a 3D-printed shelf implant. Norberg angle (y-axis) per hip number (x-axis) was measured at baseline (preoperative planning CT), postoperative (T=0) and 3 months follow-up. 105 degrees is the threshold value for normal hips. 2 Hips remained under the 105 degrees threshold direct postoperatively and 3 months postoperatively (#2 & #27).

The second case, a Newfoundland dog, had a bilateral OA score of 2 that received bilateral shelf implantation, first on the left side and 3 months later on the right side. Thereafter the dog was treated for multiple concurrent orthopaedic diseases. Besides HD, this dog was also diagnosed with bilateral medial coronoid disease (MCD) for which it was treated on both sides by arthrotomy and medial coronoid fragment removal with a 6 week interval. Following improvement after elbow surgery, the dog suddenly within a 1 week period, developed severe non-weightbearing bilateral front limb lameness and was diagnosed with bilateral intra-articular fractures of the lateral humeral condyles (most likely due to undiagnosed incomplete ossification of the humeral condyles (IOHC)) for which the dog was bilaterally treated with intercondylar screw and lateral humeral plating. OA score of elbows had progressed to grade 3 and severe front limb lameness. Following internal fixation of the elbow joints the dog was able to walk again on the forelimbs and a right hindlimb lameness was noted. The radiograph of the right hip showed an implant fracture through the most caudal (locking) screw hole (Fig. 9). The dog underwent explantation of the broken shelf together with all 4 screws and this hip (hip #23) received a Zurich cementless dual mobility THA at age 1 year and 7 months, 6 months after shelf implantation.

Table 2. Radiographic evaluation in 25 dogs (42 hips) with hip dysplasia that underwent acetabular rim extension using a 3D-printed shelf implant.

<i>Modality</i>	<i>Measurement</i>	<i>Timepoint</i>	<i>Mean</i>	<i>SD±</i>	<i>Min</i>	<i>Max</i>
CT	NA	T=-6W	88.1	12.8	62.1	111.7
		T=0D	136.0	19.4	97.2	167.4
		T=3M	134.3	20.1	96.2	166.9
	RPC	T=-6W	34.2	16.1	6.8	70.8
		T=0D	80.1	20.2	23.4	100.0
		T=3M	79.1	19.5	18.0	100.0
X-ray	NA	T=-6W	89.6	10.7	66.7	118.4
		T=0D	135.8	19.8	96.9	169.6
		T=6W	134.7	19.3	97.3	169.1
	RPC	T=-6W	34.0	1.8	9.9	78.7
		T=0D	82.4	18.3	32.9	100.0
		T=6W	82.2	16.9	39.6	100.0

NA: Norberg angle

RPC: Radiographic Percentage Coverage

The third case also involved total hip arthroplasty conversion due to OA progression. This Border Collie was initially diagnosed with severe hip laxity and planned for bilateral shelf implants. The left hip had an OA score of 2 and FCI score D. The right hip had an OA score 1 and FCI score D. Both hips had an extreme tendency to luxate (luxoid hip). In this dog the planned shelf implantation was abandoned on the left side since because of progression to complete luxoid state at the time of surgery. Therefore, only the right hip received a shelf implant and the left hip received a THA 1 month after the right-sided shelf implantation. The dog clinically improved on both hind limbs but moderate right hind limb lameness recurred and follow-up radiography at 7 months after implantation showed that all 4 screws of the shelf implant had failed whereas the shelf implant remained in place. The radiographic OA score of the right hip had deteriorated to grade 2 and because of presumed future instability the broken screws and implant were removed and the hip (hip #37) was converted to Zurich cementless THA at 7 months after shelf implantation. The shelf implant showed no macroscopic signs of failure. No dogs died during the course of this study follow-up and the longest follow up period at time of writing is 25 months for the first dog that received the shelf implant.

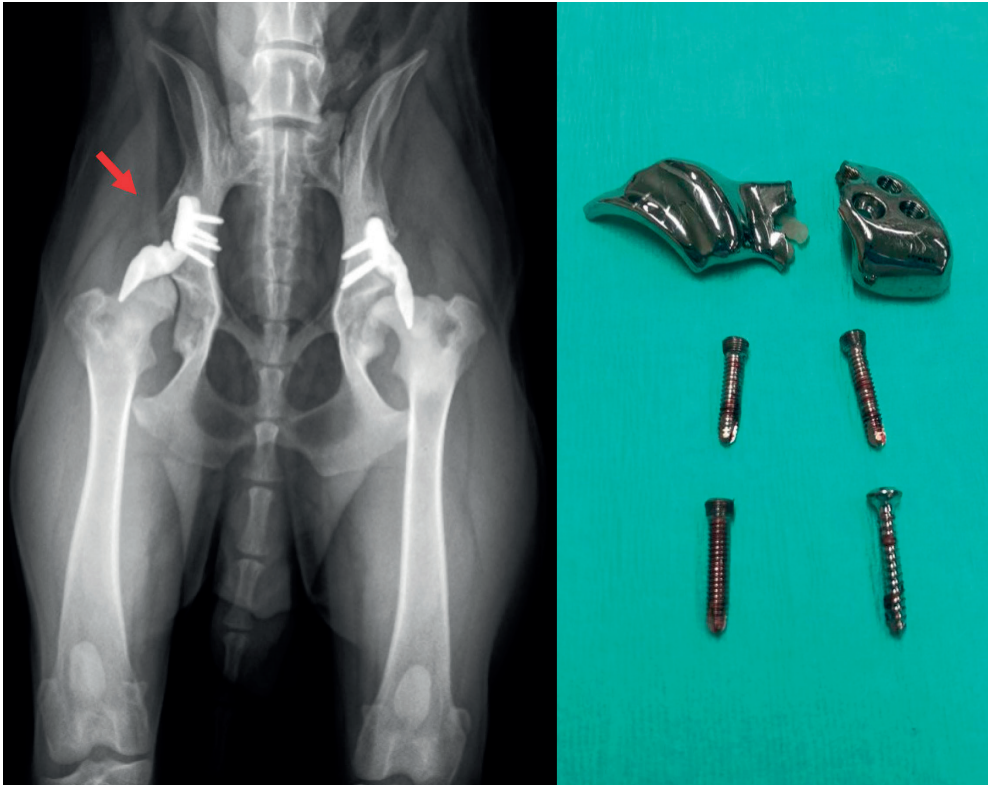


Figure 9. Left: Ventrodorsal radiograph showing fracture failure of the 3D-printed shelf implant (arrow). Right: explanted shelf implant with intact screws. The fracture occurred through 1 of the locking screw holes.

Discussion

At the moment of writing, the follow-up of the cohort is not completed and data is still being collected or under analysis up to a total inclusion of 100 cases. From the 3 dogs in which the implants were removed, the shelf implant and screws were saved and undergoing metallurgic analysis, whereas (capsular) tissues were collected for histological analysis. Also gait analysis was performed before and after surgery in all 25 dogs but not analysed yet. Therefore, the data in this manuscript presents the preliminary data of the first 25 dog patients (42 hips) receiving the shelf implant with a minimal follow-up of 3 months. Overall, the mean radiographic scores improved to normal values and the Helsinki pain scores showed an overall improvement at 6 weeks and 3 months after surgery, however osteoarthritis scores still advanced over time.

Besides suboptimal shelf placement in 3 dogs, there were no intra-operative complications, which is in line with results of the previous study with three experimental

dogs.[6] The 3D-printed shelf implant is patient-specific but the experiences during the first 13 hips revealed that exact placement was more challenging than expected. There are several factors that may play a role in precise placement. 1) During (increased) lead time between the planning CT and final implantation small changes may take place in the receiving bone bed due to progression of OA on the dorsal acetabular rim, thus hindering precise placement. 2) The soft tissue factor needs to be considered during surgery, since the implant is designed on a CT-based bone model. In surgery, the ilium cranial to the acetabulum can be cleared completely from muscular tissues, however the capsular attachment to the dorsal acetabular rim is preserved and when this actually turns out to be thicker than considered from the CT scan during the design, as crowding of capsular tissue may elevate the rim extension hindering precise placement. 3) The learning curve in the surgical approach to the dorsal acetabular rim. The deep gluteal muscle was completely separated from the joint capsule and the tendinous attachment of the m. rectus femoris was partially isolated to allow the implant to curve around this landmark. These soft tissues may prevent precise placement of the implant when they are not sufficiently cleared or matched to the implant. 4) The view of the hip (capsule) is limited due to the muscle separation approach creating a surgical tunnel view. With experience it was learned that abduction and exo-rotation of the femur decreased the tension on the gluteal muscle group and facilitated the surgical view on the hip capsule and implant insertion. These factors may have led to imperfect positioning in three cases as demonstrated on postoperative CT imaging, which required immediate amendment.

To prevent future revisions, from hip number 13 onwards it was decided to introduce intra operative fluoroscopy and in the remaining cases no immediate postoperative revisions were needed. The surgical team was able to assess implant positioning intraoperatively instead of relying on postoperative imaging after wound closure. Also, intraoperative fluoroscopy required a learning curve to confirm the perfect fit. After placing the first screw, imaging was performed to assess the perfect alignment of the curvature of the dorsal acetabular rim and the curvature of the shelf rim. Only when both curvatures were exactly congruent, placement was considered precise and the procedure continued. Also, in the perfect lateral position the rim extension of the shelf implant could be evaluated in relation to the deficient acetabular rim, whereas in the oblique view the distance between both curvatures were assessed. All imaging modalities such as intra operative fluoroscopy and postoperative CT added to the insight of the acetabular rim extension and the data that are collected will be assessed separately in more detail and eventually may lead to refinement and reduction of the imaging protocol.

When comparing the 3D-printed shelf arthroplasty to triple pelvic osteotomy (TPO) it is evident that the 3D printed shelf requires a longer lead time than the mass produced TPO plate, which comes in fixed sizes. The 3D-printed shelf implant needs to be designed (<1

week) and produced (2-3 weeks) by additive manufacturing.[4] In this study the lead time was further increased due to the unexpected COVID-19 pandemic in 2020, which severely affected industrial 3D printing facilities and surgical hospital facilities. This does not have to be a problem when the time between first consultation or diagnosis and the planned surgery date is shorter than 4 weeks, however the actual lead time was in reality closer to 3 months (supplementary data).

After the shelf arthroplasty surgeries that were performed unilaterally it was noted that recovery was much faster with less pain and discomfort than after TPO. This empiric assessment was considered reliable since TPOs have been performed in the same institution for more than 20 years. It was realized that shelf arthroplasty potentially held an enormous benefit, i.e., making it possible to treat both hips in a single surgical procedure, which is not routinely done or advised for TPO/DPO.[12] This allows a patient that is affected with bilateral dysplastic hips to be treated in a single procedure. Moreover, even considering the longer lead time, a bilateral 3D-printed shelf could be faster performed than two TPOs with a six-week rehabilitation in between. This has multiple benefits like reduction of anaesthesia events, reduction of postoperative recovery events, reduction of total costs and prevention of a second lead period in which hip dysplasia can dramatically progress to severe OA.

Another benefit of the 3D shelf in comparison to the TPO surgery is the fact that the shelf does not decrease the pelvic diameter as the DPO and TPO do.[13] Moreover, in comparison to the TPO, the 3D shelf seems to have a wider age window in which the surgery can be performed; the lower age is restricted to closure of the triradiate growth plate around age of 5 months, whereas CT planning can be done as early as 6 months. The upper age at which shelf arthroplasty is indicated is not really restricted. The only requirements for inclusion are positive Ortolani testing and no severe OA. Furthermore, due to the patient-specific nature of the 3D shelf it can be placed faster as it does not need three individual approaches and less screws (less costs) and therefore needs less time in the operation theatre (less costs) in comparison to the TPO. Also, to further reduce production costs new ideas are being tested to produce the implant with 3D-printed locking screw threads or as a generic implant.[14], [15] However, generic implants are likely more susceptible to the above-mentioned placement error and therefore introduces new challenges.

In the first dog patient in which the 3D-printed shelf was revised to THA due to severe progression of osteoarthritis, the radiographic threshold value for normal hips was not reached after surgery, which may have negatively influenced the weight bearing conditions of the native acetabulum resulting in progressive OA. This demonstrates the importance of trying to get the dysplastic hips back to normal values.

In the second case that was revised to THA, the implant fractured through a locking. However, a combination of three factors could have contributed to this implant fracture. First, the patient possibly overloaded the 3D-printed shelves in the pelvic limbs because of severe elbow complications requiring bilateral surgery of both forelimbs, consequently increasing the bodyweight load distribution to the hindlimbs. Secondly, the implant was not HIP treated making the implant more brittle and more susceptible to failure under elongation/stress. Finally, no torque limiting screwdriver was used in this study, which could indicate that some screws became over-torqued.[16] To overcome these kind of failures HIP treatment or torque limiting screw drivers should be (re-)introduced. [17] Furthermore, a root cause analysis and metallurgic failure is needed to check any procedural or manufacturing errors of the implant.

In the third failure case that needed conversion to THA the patient had severe joint laxity at baseline, close to the luxoid state. In retrospect this may have been a contraindication as the shelf implant is not made for full weight bearing but was designed to guide and keep the femoral head in the native acetabulum and only receive partial joint forces. This is reflected in the decision in abandoning shelf arthroplasty for one side that rapidly had developed to a complete luxoid state at the time of surgery. However, it can also be concluded that the shelf arthroplasty that was performed in one of the hips prevented the complete luxoid state in that hip, making it a better candidate for THA later on. Due to the novelty of this 3D-printed shelf concept these conditions should be followed with caution and inclusion criteria for implantation should be strict or the owner should be warned that the shelf implant procedure can be performed as an intermediate step for a THA later in life. In those cases, a consideration needs to be made whether the shelf implant needs to be removed before THA insertion. In the current case however, the shelf implant was explanted for metallurgic analysis on the implant.

Overall the shelf material complication rate in this article (4.8%, 2/42) remains in line with other hip dysplasia procedures such as the TPO. TPO complications vary between 4-29% of the procedures with screw loosening being the most frequent complication and total implant pull-out as the most severe one.[14], [18], [19]

This study also has some limitations. First, no gait analysis with measurement of ground reaction forces (GRFs) was reported yet. Objective measurements of GRFs before and after acetabular rim extension can support the clinical efficacy of the surgical technique,[20] although it must be realized that walking a dog over a force plate is not a complete representation of the functioning of a dog in a dog owner's household. Therefore, the combination of force plate analysis and questionnaires to owners - like the Helsinki brief chronic pain index or the Liverpool Osteoarthritis in Dogs - will give a more complete picture how the dog is functioning.[10]

Secondly, radiological measurements were performed to monitor the clinical efficacy, however for future studies also an additional 3D analysis can be performed to assess coverage in all clock positions and to define the true placement accuracy in six degrees of freedom. Lastly, no histology of the femoral head cartilage and capsular tissues was available after conversion of the hip to THA. For future appreciation of this new technique this could be helpful. If in the future dogs are converted to THA or die due to unrelated causes, it would be of added value to examine the joint with the implant in situ for histopathological findings. Therefore, all owners were informed at inclusion that we would like to examine the hip in case of unexpected death. The hip joint will then cosmetically be removed after which the dog can be cremated at the owner's request. First, it would be interesting to see how the hip capsule has developed and changed under long term loading in between the femoral head and the titanium shelf implant, because research data evaluating hip capsule differentiation or metaplasia are rare and should be well documented.[21], [22] Besides that, the state of the cartilage and ingrowth of bone into the porous scaffold of the implants can be examined.

In the light of One Health One Medicine it is interesting to translate this idea back for human application in young adolescents with hip dysplasia.[1], [23] However, to facilitate such a translation to humans, first a (biomechanical) proof of concept should be shown in cadaveric human pelvises.[4] New challenges will arise such as the well know biomechanical difference in stance and gate between dogs (quadruped) and humans (biped).[1] Regarding human translation, for young dysplastic children (3D-printed) titanium is not an option as the titanium shelf will not allow for growth, therefore a bioresorbable implant that is incorporated, osseointegrated, and modified by body own tissue could be of added benefit.[5]

Conclusion

This manuscript contains preliminary data of the first 25 dog patients (42 hips) that received a personalized 3D shelf implant. Dogs receiving the 3D shelf showed improved acetabular coverage and radiographic values. Recovery after bilateral surgery is rapid, clinical pain scores improved after implantation but osteoarthritis scores advanced. All dogs functioned well but after six months three dogs were converted to THA for material failure or severe osteoarthritis. We consider the personalized shelf implant successful so far and longer follow-up times are required to fully show the effectiveness of this potentially novel intervention.

Supplementary Data

<https://1drv.ms/x/s!AjdWTaQAIFN0p4YSzHBXNJKdCGGymQ?e=Rc4bcO>

References

1. K. Willemsen *et al.*, "Comparing hip dysplasia in dogs and humans: a review," *Frontiers in Veterinary Science*, p. 1491.
2. K. Willemsen *et al.*, "Long-term outcomes of the hip shelf arthroplasty in adolescents and adults with residual hip dysplasia: a systematic review," *Acta Orthopaedica*, vol. 91, no. 4, pp. 383–389, 2020, doi: 10.1080/17453674.2020.1747210.
3. D. J. Jensen and G. O. Sertl, "Sertl shelf arthroplasty (BOP procedure) in the treatment of canine hip dysplasia.," *The Veterinary clinics of North America. Small animal practice*, vol. 22, no. 3, pp. 683–701, 1992, doi: 10.1016/S0195-5616(92)50062-6.
4. K. Willemsen *et al.*, "Patient-specific 3D-printed shelf implant for the treatment of hip dysplasia: Anatomical and biomechanical outcomes in a canine model," *Journal of Orthopaedic Research*, p. jor.25133, Jul. 2021, doi: 10.1002/jor.25133.
5. N. Golafshan *et al.*, "3D-Printed Regenerative Magnesium Phosphate Implant Ensures Stability and Restoration of Hip Dysplasia," *Advanced Healthcare Materials*, p. 2101051.
6. K. Willemsen *et al.*, "Patient-specific 3D-printed shelf implant for the treatment of hip dysplasia tested in an experimental animal pilot in canines," *Scientific Reports*, vol. 12, no. 1, p. 3032, 2022, doi: 10.1038/s41598-022-06989-9.
7. M. Flückiger, "Scoring radiographs for canine hip dysplasia - the big three organizations in the world," *Eur J Companion Anim Pract*, vol. 17, no. Table 1, pp. 135-140., 2007.
8. M. Wessely, A. Brühshwein, and E. Schnabl-Feichter, "Evaluation of intra- and inter-observer measurement variability of a radiographic stifle osteoarthritis scoring system in dogs," *Veterinary and Comparative Orthopaedics and Traumatology*, vol. 30, no. 06, pp. 377–384, 2017.
9. K. A. Johnson, *Piermattei's Atlas of Surgical Approaches to the Bones and Joints of the Dog and Cat*, vol. 114. Elsevier Health Sciences, 2013.
10. A. K. Hielm-Björkman, H. Rita, and R.-M. Tulamo, "Psychometric testing of the Helsinki chronic pain index by completion of a questionnaire in Finnish by owners of dogs with chronic signs of pain caused by osteoarthritis," *American Journal of Veterinary Research*, vol. 70, no. 6, pp. 727–734, 2009.
11. M. Fujiki, K. Misumi, and H. Sakamoto, "Laxity of canine hip joint in two positions with computed tomography," *Journal of veterinary medical science*, vol. 66, no. 8, pp. 1003–1006, 2004.
12. D. A. Koch, H. A. W. Hazewinkel, R. C. Nap, B. P. Meij, and W. T. C. Wolvekamp, "Radiographic evaluation and comparison of plate fixation after triple pelvic osteotomy in 32 dogs with hip dysplasia," *Veterinary and Comparative Orthopaedics and Traumatology*, vol. 6, no. 01, pp. 9–15, 1993.
13. A. M. Remedios and C. L. Fries, "Implant complications in 20 triple pelvic osteotomies," *Veterinary and Comparative Orthopaedics and Traumatology*, vol. 6, no. 04, pp. 202–207, 1993.
14. R. D. Fischer, J. Klasen, and B. C. Prorok, "Implementing a Commercially Available Self-Locking Screw System in Additively Manufactured Medical Implants," in *Thermomechanics & Infrared*

- Imaging, Inverse Problem Methodologies and Mechanics of Additive & Advanced Manufactured Materials, Volume 7*, Springer, 2021, pp. 87–92.
15. R. D. Fischer, J. Klasen, A. Shmatok, and B. C. Prorok, "An additively manufactured locking fixation system for potential application in patient-specific implants," *Journal of the Mechanical Behavior of Biomedical Materials*, vol. 124, p. 104867, 2021.
 16. C. Kanchanomai, V. Phiphobmongkol, and P. Muanjan, "Fatigue failure of an orthopedic implant—A locking compression plate," *Engineering Failure Analysis*, vol. 15, no. 5, pp. 521–530, 2008.
 17. R. D. Fischer, J. Klasen, A. Shmatok, and B. C. Prorok, "An additively manufactured locking fixation system for potential application in patient-specific implants," *Journal of the Mechanical Behavior of Biomedical Materials*, vol. 124, p. 104867, 2021.
 18. M. T. Doornink, M. A. Nieves, and R. Evans, "Evaluation of ilial screw loosening after triple pelvic osteotomy in dogs: 227 cases (1991–1999)," *Journal of the American Veterinary Medical Association*, vol. 229, no. 4, pp. 535–541, 2006.
 19. S. A. Rose, K. A. Bruecker, S. W. Petersen, and N. Uddin, "Use of locking plate and screws for triple pelvic osteotomy," *Veterinary Surgery*, vol. 41, no. 1, pp. 114–120, 2012.
 20. A. R. Tellegen, N. Willems, M. A. Tryfonidou, and B. P. Meij, "Pedicle screw-rod fixation: a feasible treatment for dogs with severe degenerative lumbosacral stenosis," *BMC veterinary research*, vol. 11, no. 1, p. 299, 2015.
 21. S. Hiranuma, F. Higuchi, A. Inoue, and M. Miyazaki, "Changes in the interposed capsule after Chiari osteotomy. An experimental study on rabbits with acetabular dysplasia," *The Journal of Bone and Joint Surgery. British volume*, vol. 74, no. 3, pp. 463–467, 1992.
 22. P. Raab, J. Löhr, and R. Krauspe, "Remodeling of the acetabulum after experimental hip joint dislocation—an animal experiment study of the rabbit," *Zeitschrift für Orthopädie und Ihre Grenzgebiete*, vol. 136, no. 6, pp. 519–524, 1998.
 23. C. Pascual-Garrido *et al.*, "Canine hip dysplasia: A natural animal model for human developmental dysplasia of the hip," *Journal of Orthopaedic Research*, vol. 36, no. 7, pp. 1807–1817, 2018, doi: 10.1002/jor.23828.



CHAPTER 12

Additive manufacturing of titanium implants for skull reconstruction in canine oncological surgery

Eline J.C. van den Brink | Koen Willemsen | Floor Driessen |
Guy C.M. Grinwis | Susanne A.E.B. Boroffka | Björn P. Meij

Under review at Veterinary and Comparative Orthopaedics and Traumatology

Abstract

Two dogs were treated with a patient specific implant created by additive manufacturing (AM) for tumours of the skull. Both dogs presented with a space occupying mass in which standard excisional surgery without the use of implants would have been suboptimal due to extensive bone defects of the skull. The aim of the present case study is to describe the use of personalized 3D printed titanium implants for skull reconstructions following oncological surgery. The reconstructive implant-based surgeries performed in these patients extended the dog's quality of life without complications.

Introduction

AM has been introduced in the medical field in the last decade, gaining popularity specifically in the field of dentistry, maxillofacial, orthopedic, and spine surgery. The availability of materials and printers has led to lower costs of patient specific three-dimensional (3D) implants in human medicine bringing them also within the scope of the veterinary field (1).

The use of personalized implants is the latest development in osteosynthesis and offers a wide variety of opportunities and applications. To date, only few studies in veterinary medicine have used 3D personalized implants. Case reports have described 3D printed implants for dogs with atlanto-axial subluxation, angular limb deformity, in limb-sparing surgery and in mandibular and maxillary surgery (2-8). 3D printed customized cages have also been used for tibial tuberosity advancement and for treatment of cervical spondylomyelopathy (9, 10).

In contrast to fractures and defects in the appendicular skeleton, reconstruction of the skull and spine are often complicated due to the individual variety in anatomy or the lack of veterinary implants. The development of patient specific 3D printing will improve surgical planning and enable more successful surgical results in challenging veterinary patients. The use of AM offers new surgical possibilities for patients who cannot benefit from existing surgical treatments. Practical experience from cases treated using this technique is valuable to accelerate the development of patient specific 3D implants in the future (11). The aim of the present case study is to describe the use of personalized 3D printed titanium implants for skull reconstructions following oncological surgery.

Case description

Case 1

A 2-year-old female neutered Siberian Husky was presented for depression and a mass on the right rostral calvarium. For further evaluation of the extension of the mass and metastasis control, a pre- and postcontrast computed tomography (CT) of the head and thorax was performed. CT showed an ossifying mass originating from the right frontal sinus and adjacent frontal bone (Fig 1). The mass measured approximately 4.2x4.4x5.1 cm and had infiltrated the entire right frontal sinus and frontal neurocranium compressing the brain on the right side (Fig 1). Suspected CT diagnosis was a multilobular osteochondrosarcoma, osteosarcoma or osteoma. There was no evidence of metastases in the regional lymph nodes or the lungs.

The dog was premedicated with methadone (Insistor, Richter pharma, Wels, Austria) and acepromazine (Acepromazine, Pharmacy of Utrecht University, the Netherlands) and induced with midazolam (Midazolam, Aurobindo Pharma B.V., Baarn, the Netherlands) and propofol (Propofol, Fresenius Kabi, Zeist, the Netherlands). Anesthesia was maintained using sevoflurane (Sevorane, Abbvie, Hoofddorp, the Netherlands), lidocaine (Lidocaine HCL, Fresenius Kabi, Ziest, the Netherlands) and sufentanyl (Sufentanyl, Hameln Pharma plus gmbh, Germany). Mannitol (Osmosteril, Fresenius Kabi, Zeist, the Netherlands) and dexamethasone (Rapidexon, Dechra, Bladel, the Netherlands) were used at the start of anesthesia to reduce intracranial pressure. Right trans sinus frontalis craniectomy was performed with 5 mm bone margins and the tumor was removed as one solid mass. At the base of the tumor the dura mater was lost over 1 cm² and the defect was covered with a fascia latae transplant harvested from the right hind leg. The m. temporalis, the subcutis and skin were routinely closed. Recovery was uneventful and the patient was discharged 2 days after surgery with tramadol (Tralieve, Dechra, Bladel, the Netherlands), carprofen (Carporal, AST Farma, Oudewater, the Netherlands), gabapentin (Gabapentine, Pharmachemie BV, Haarlem, the Netherlands), paracetamol (Paracetamol, Sandoz, Almere, the Netherlands), omeprazole (Omeprazol, Sandoz, Almere, the Netherlands) and amoxicillin-clavulanic acid (Synulox, Zoetis, Rotterdam, the Netherlands). Histopathological examination showed proliferation of well-defined bony tissue, most likely an osteoma. A follow-up CT scan at 3 months after surgery showed possible regrowth of the tumor which was confirmed 6 months post-surgery at four locations around the original craniectomy (Fig 1) without evidence of metastasis. Because total excision of the tumor recurrences with 10 mm margins would lead to removal of more than half of the calvarium, the option of AM to close the defect with a personalized implant was explored.

To design an AM personalized implant, first the DICOM files of the most recent CT scan (250 mAs, 120 kV, 0.6 mm slice thickness) were exported from the imaging archive system to Mimics v21 (Materialise, Leuven, Belgium) for anatomical segmentation. Standard bone threshold values (226 HU – upper threshold) were taken to segment the bone. Furthermore, the recurring tumors were manually segmented together with a digitally grown resection margin that was used to simulate the minimal needed resection area. Thereafter the anatomical models were transferred using stereolithography (STL) files to 3-matic software in which the design took place. The resection guide was designed to resect the relapsing tumors, including the digitally simulated 10 mm resection margin, and reviewed by a board certified veterinarian surgeon. Thereafter the remaining skull was digitally reconstructed. The cranioplasty implant was designed as press fit and contained five extensions overlaying intact bone with screw holes for fixation to the skull and a porous mesh border (70% porous, 500-600 µm pore size, Diamond unit cell) to allow bony ingrowth at the implant bone interface (Fig 2)(12-13).

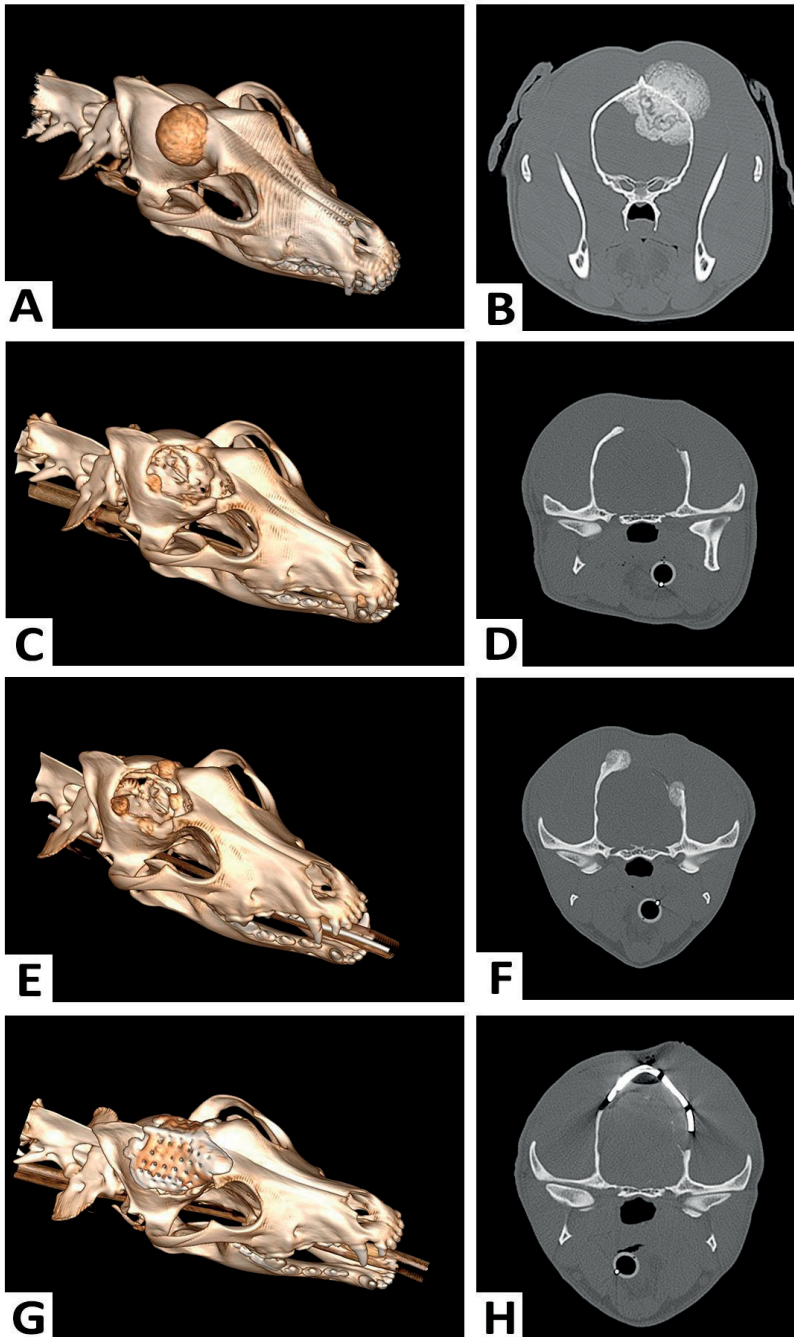


Figure 1. Case 1: 3D CT reconstruction (A,C,E,G) and transverse CT image (B,D,F,H) of a 2-year-old Siberian Husky with a calvarial neoplasm. Before surgery (A,B), at 3 months (C,D), and 6 months (E,F) after surgical resection, and after revision surgical resection followed by reconstruction with a 3D printed titanium implant (G,H).

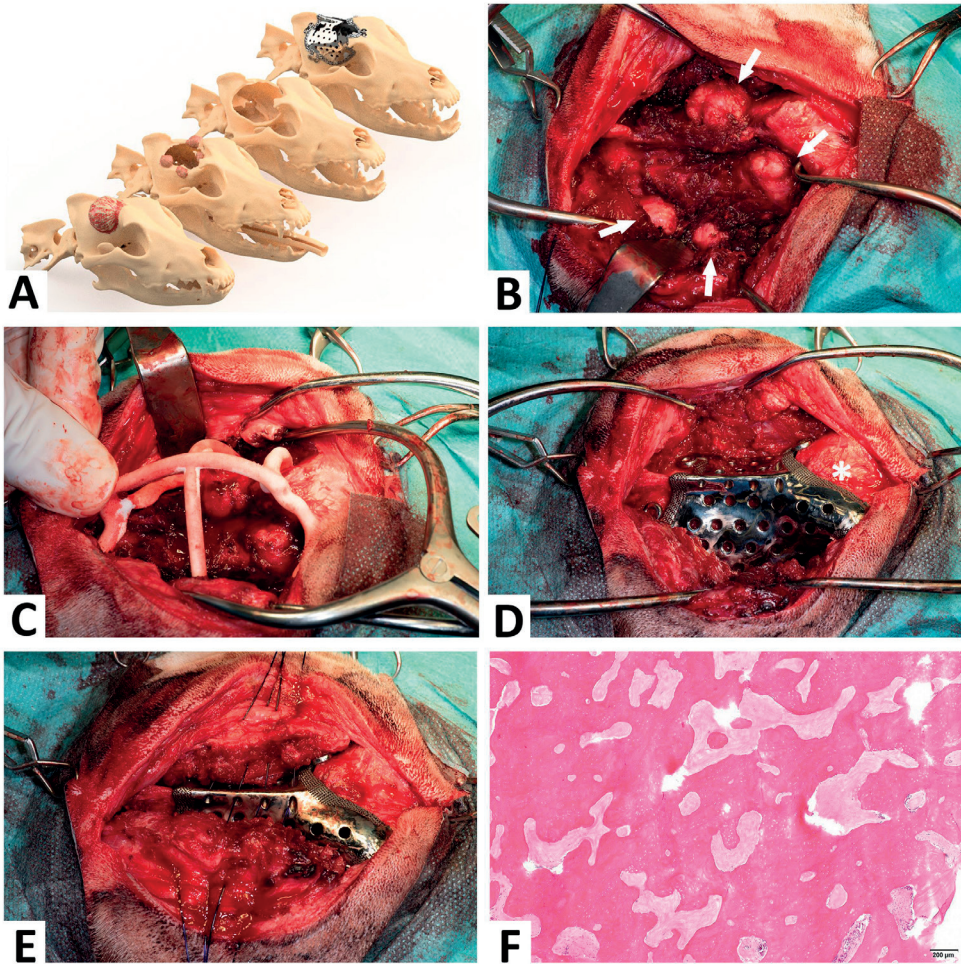


Figure 2. Case 1: Sequential steps in surgical treatment of a 2-year-old Siberian Husky with a calvarial neoplasm (A). Intra operative views at moment of revision surgical resection for quadruple recurrences (arrows) at first surgical rim (B). Placement of the saw guide (C) for the 3D printed titanium implant (D) extending over the right frontal sinus (*) and application of stay sutures for attachment of the temporal muscle to the dorsal implant ridge (E). Histology of the mass showed well-differentiated, mainly immature (woven) bone and a cell-poor fibrous component most consistent with an osteoma. Hematoxylin and eosin stain, size bar=200 μ m (F).

Additionally, the midline ridge of the implant contained designated holes for suture attachment of the temporal muscle fascia and suture anchors through which muscles could be reattached. The surgical guide was 3D-printed in Nylon (PA12) on an EOS P110 printer (EOS, Krailling, Germany) and the implant was 3D-printed in medical grade titanium alloy Ti-6Al-4V ELI grade 23 using direct metal printing on a ProX DMP320 printer (3D Systems, Leuven, Belgium). Post-processing included polishing, cleaning and sterilization.

Two months after the latest CT scan, the dog underwent second extended craniectomy where the tumor recurrences were removed using the saw guide (Fig 2). The implant was fitted and secured into place using six 2.0 mm self-tapping titanium cortical screws (Unilock®, DePuy Synthes, Johnson-Johnson, Oberdorf, Switzerland) ranging from 6 to 8 mm in length. The fascia of the temporal muscle was sutured through 4 holes on the sagittal ridge of the implant. The subcutis and cutis were routinely closed. A postoperative CT was performed to assess the position of the implant. The dog received post-operative analgesia, was monitored on our intensive care unit and was discharged two days after surgery with carprofen (Carproal, AST Farma, Oudewater, the Netherlands), gabapentin (Gabapentine, Pharmachemie BV, Haarlem, the Netherlands), paracetamol (Paracetamol, Sandoz, Almere, the Netherlands), omeprazole (Omeprazol, Sandoz, Almere, the Netherlands) and amoxicillin-clavulanic acid (Synulox, Zoetis, Rotterdam, the Netherlands). A follow-up CT was performed 4 months postoperatively and showed no signs of tumor regrowth and intact implant positioning identical to the immediate postoperative CT (Fig 1). The dog showed no clinical signs and survival time at time of writing is 943 days.

Case 2:

A 11-year-old female neutered Labrador retriever was presented for removal of a mass of the zygomatic arch causing problems with mastication. A CT was performed for surgical planning and the mass measured approximately 3 cm in diameter (Fig 3). Suspected CT diagnosis was a multilobular osteochondrosarcoma, osteoma or osteosarcoma. There was no evidence of metastases to the regional lymph nodes or the lungs.

Using the same AM workflow as in case 1, a patient specific 3D implant was designed based on the mirrored contralateral skull after complete tumor removal with 10 mm bone margins on the zygomatic arch and adjacent orbital and maxillar bones. Because of clear bony landmarks, there was no need for a saw guide in this patient. The implant consisted of polished titanium with an unpolished titanium mesh around the edges to facilitate bone ingrowth and was manufactured using the same parameters as in case 1.

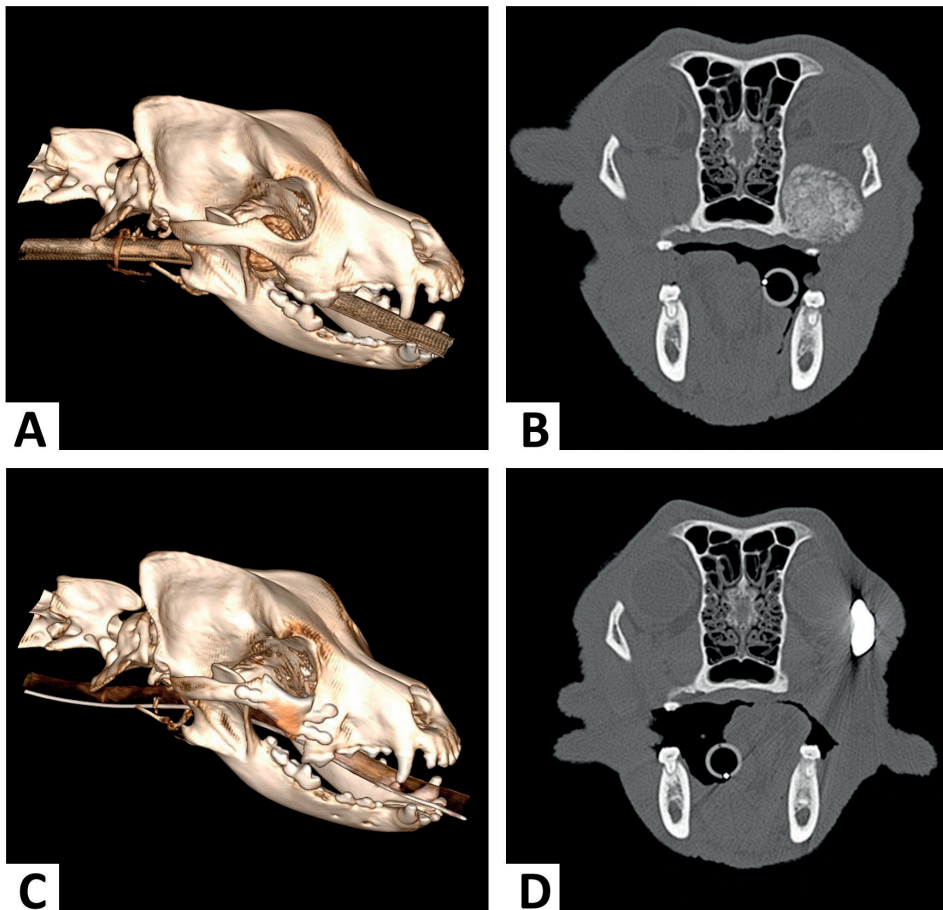


Figure 3. Case 2: 3D CT skull reconstruction (A,C) and transverse CT image (B,D) of a 11-year-old Labrador retriever with a right zygomatic arch neoplasm involving the maxillar and orbital bones. Before surgery (A,B) and after surgical resection of the mass and reconstruction with a 3D printed titanium implant (C,D).

Six weeks after the most recent CT scan the dog was premedicated with methadone (Insistor, Richter Pharma, Wels, Austria), induced with propofol (Propofol, Fresenius Kabi, Zeist, the Netherlands) and midazolam (Midazolam, Aurobindo Pharma B.V., Baarn, the Netherlands) and anesthesia was maintained with isoflurane (IsoFlo, Zoetis, Rotterdam, the Netherlands), sufentanyl (Sufentanyl, Hameln Pharma plus gmbh, Germany) and ketamine (Narketan, Vetoquinol, Breda, the Netherlands). The tumor was removed by approaching the zygomatic arch and cutting the bone with an oscillating saw at the predetermined land marks (Fig 4). The mass was removed in toto together with zygomatic arch and adjacent orbital bone and maxillar bone including molars 109 and 110 (Fig 4). The implant was secured using six 2.0mm self-tapping titanium cortical screws (Unilock®, DePuy Synthes, Johnson-Johnson, Oberdorf, Switzerland) ranging from 7 to 10 mm in

length. The subcutis and cutis were routinely closed. A post-operative CT scan showed anatomical placement of the 3D printed titanium implant (Fig 3). The patient was discharged 1 day after surgery with tramadol (Tralieve, Dechra, Bladel, the Netherlands), gabapentin (Gabapentine, Pharmachemie BV, Haarlem, the Netherlands), paracetamol (Paracetamol, Sandoz, Almere, the Netherlands), amoxicillin-clavulanic acid (Synulox, Zoetis, Rotterdam, the Netherlands). The dog was only offered soft food and was not allowed to chew on toys.

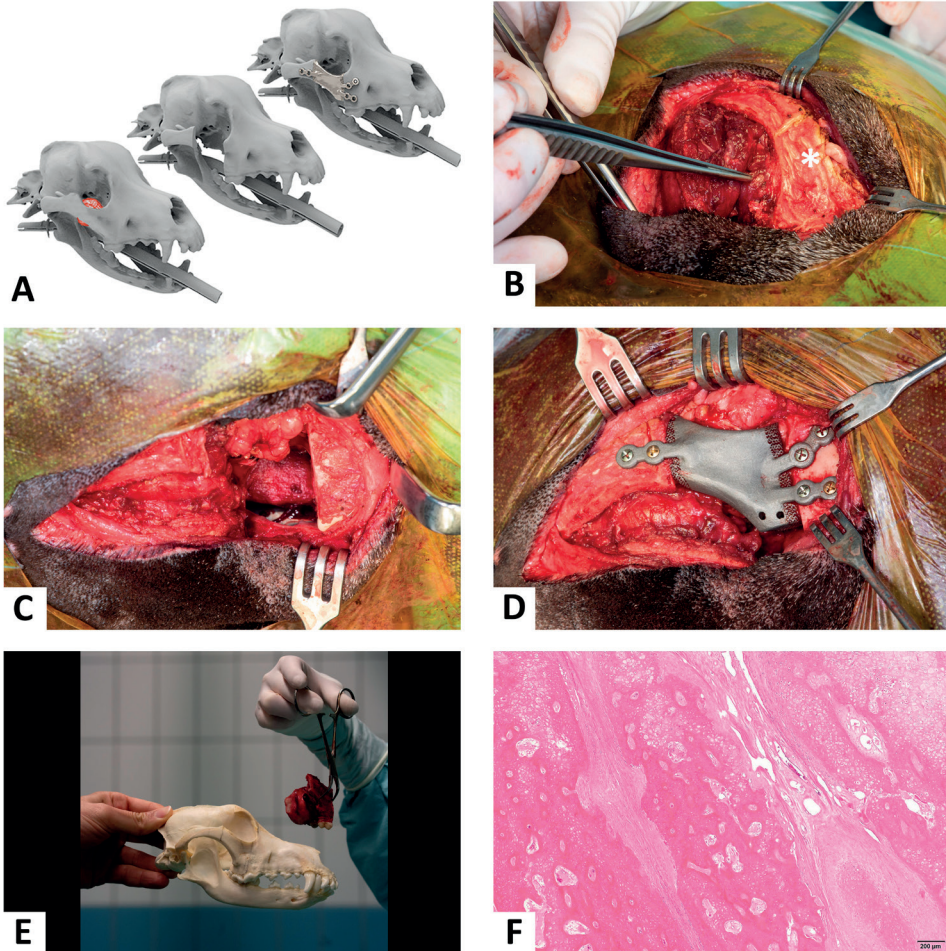


Figure 4. Case 2: Sequential skull views in surgical treatment of an 11-year-old Labrador retriever with a right zygomatic arch neoplasm (A). Intra operative view showing the right zygomatic arch (*) with the forceps indicating the neoplasm (B), followed by surgical resection of part of the zygomatic arch and maxilla together with the neoplasm (C) and placement of the 3D printed titanium implant (D). Tumor after excision next to canine skull (E). Histology of the mass showed a moderately cellular spindle cell proliferation with formation of woven bone and a cartilaginous component most consistent with a parosteal osteosarcoma. Hematoxylin and eosin stain, size bar=200 μ m (F).

One month after surgery, the patient showed no clinical signs and normal pellet food was reintroduced without problems. Histopathological diagnosis of the tumor was consistent with a parosteal osteosarcoma. A follow-up CT scan 4 months after surgery showed no signs of implant failure and some activity of bony ingrowth on the porous implant borders. The dog died 670 days after surgery of age related problems, until the day of death the dog showed no clinical signs associated with the tumor or implant.

Discussion

These two cases describe the feasibility and the use of patient specific customized implants in extensive reconstructive surgery of the skull. The implants in these patients were custom designed with medical software programs Mimics and 3-Matic (Materialise NV, Leuven, Belgium). The CT Dicom data were loaded into the software program, bones were segmented and design took place in silico. Excisional margins were planned in the 3D reconstructed skull specimens and implants were designed according to the created defects with the software program. Both implants were designed to precisely press fit into the craniectomy or ostectomy defect. This differs from the implant described by Oblak et al. (2019) who created a titanium implant that overlaid the frontal and temporal bones in a case with a reconstruction of the neurocranium after removal of a frontal bone tumor (14). Previous research has shown that the use of CT provides accurate models of the skull (15). The accuracy of the designer, the quality of the program, the collaboration with the manufacturer and surgeon are all of uttermost importance to achieve a high quality end result (11).

The borders of both implants were made of a porous titanium mesh allowing bone ingrowth and therefore permanently embedding the implant into the skull, adding to the long-term durability. Although we have no histological prove that bone in growth occurred in our cases, both in vivo and in vitro push-out tests, micro-CT and histopathology have proven that bone in-growth occurred in Ti6-Al4-V scaffolds in dogs. Bone ingrowth increased the strength in implant embedding (16-19).

The solid part of the implant was polished, the mesh surface was not polished. Polishing has proven to be beneficial in the reduction of the risk of biofilm formation compared to non-polished implants (20). To obtain a smooth surface implants can also be coated. Calcium-phosphate-coated porous titanium implants enhanced tissue ingrowth compared to porous implants without coating (21). Preliminary results of an in vitro study performed at our institution showed promising results on the prevention of growth of tumor cells on the margins of selenium-coated implants (22). For future cases, this could be of added benefit in oncological bone reconstruction.

Although strict asepsis is applied in orthopedic surgery using metal implants, there is always a risk for implant-related infections. In an in vivo study, significantly more bacteria were cultured from implants with rough surfaces than from those with a smooth surface (20). However, in non-coated implants with a porous mesh border that stimulated ingrowth of bone, an in vitro study showed that mesh also increased the risk of bacterial adhesion (23). In the present case series, there were no signs of implant-related infections, despite the use of a porous mesh at the borders of the implants.

As these were the first patients that received patient specific 3D printed implants in our hospital, the manufacturing and printing of the implants took more than 1 month. The commercial company that printed the implants usually does not have a priority lane for veterinary implants which resulted in a long lead time between CT and the surgery date. This similar problem has been experienced by other surgeons and presents a problem in oncological patients in which the tumor continues to grow after CT imaging (21). Further developments in AM for veterinary use and starting up companies with a veterinary focus on patient specific 3D printing should result in future decreased lead times for 3D printed implants.

Little is known about the long-term effects and durability of 3D printed implants. Although titanium has been used safely in osteosynthesis with long follow up times, there is currently no long-term data on patient specific implants in veterinary medicine. More research and veterinary clinical reports are needed to provide information on long term results and possible side-effects of the implants and the specific designs. Collaboration between human medicine and veterinary medicine accelerates development and broadens the knowledge on AM in the veterinary field, thereby adding more applications for patient specific implants in dogs and cats.

This short case series describes two cases of extensive reconstructions after tumor excision of the skull with patient specific customized titanium implants with porous edges. Three months post-operatively, both dogs were free of clinical signs and CT showed correct placement of implants without signs of tumor regrowth, implant loosening, or infection. These case series showed that the use of partly porous titanium implants in craniomaxillary surgery in two dogs resulted in excellent clinical outcome with long survival and therefore should be considered as a treatment option in similar future cases.

References

1. Willemsen K, Tryfonidou M, Sakkers R, et al. Patient-specific 3D-printed shelf implant for the treatment of hip dysplasia: anatomical and biomechanical outcomes in a canine model. *J Orthop Res* 2021;1-9
2. Kamishina H, Sugawara T, Nakata K et al. Clinical application of 3D printing technology to the surgical treatment of atlantoaxial subluxation in small breed dogs. *PLoS One* 2019;14(5)
3. Carwardine D, Gosling M, Burton N, O'Malley F, Parsons K. Three-Dimensional-Printed Patient-Specific Osteotomy Guides, Repositioning Guides and Titanium Plates for Acute Correction of Antebrachial Limb Deformities in Dogs. *Vet Comp Orthop Traumatol* 2020;34(01):043-052
4. Choi S, Oh Y, Park K, Lee J, Shim J, Kang B. New clinical application of three-dimensional-printed polycaprolactone/ β -tricalcium phosphate scaffold as an alternative to allograft bone for limb-sparing surgery in a dog with distal radial osteosarcoma. *J Vet Med Sci* 2019;81(3):434-439
5. Séguin B, Pinard C, Lussier B, et al. Limb-sparing in dogs using patient-specific, three-dimensional-printed endoprosthesis for distal radial osteosarcoma: a pilot study. *Vet Comp Oncol* 2019;18(1):92-104
6. Arzi B, Cissell D, Pollard R, Verstraete F. Regenerative approach to bilateral rostral mandibular reconstruction in a case series of dogs. *Front Vet Sci* 2015;2
7. Kim S, Mi Shim K, Jang K, Shim J, Kang S. Three-dimensional printing-based reconstruction of a maxillary bone defect in a dog following tumor removal. *In Vivo (Brooklyn)* 2018;32(1):63-70
8. Liptak J, Thatcher G, Bray J. Reconstruction of a mandibular segmental defect with a customized 3-dimensional-printed titanium prosthesis in a cat with a mandibular osteosarcoma. *J Am Vet Med Assoc* 2017;250(8):900-908
9. Castilho M, Dias M, Vorndran E, et al. Application of a 3D printed customized implant for canine cruciate ligament treatment by tibial tuberosity advancement. *Biofabrication* 2014;6(2):025005
10. Joffe M, Parr W, Tan C, Walsh W, Brunel L. Development of a customized interbody fusion device for treatment of canine disc-associated cervical spondylomyelopathy. *Vet Comp Orthop Traumatol* 2019;32(01):079-086.
11. Willemsen K, Nizak R, Noordmans HJ, Castelein RM, Weinans H, Kruyt MC. Challenges in the design and regulatory approval of 3D-printed surgical implants: a two-case series. *Lancet Digital Health* 2019;1(4):e163-171
12. Taniguchi N, Fujibayashi S, Takemoto M et al. Effect of pore size on bone ingrowth into porous titanium implants fabricated by additive manufacturing: an in vivo experiment. *Mater Sci Eng C* 2016;59:690-701
13. Van der Stok J, Van der Jagt OP, Yavari SA et al. Selective laser melting-produced porous titanium scaffolds regenerate bone in critical size cortical bone defects. *J Orthop Res* 2013;31(5):792-799
14. Oblak M, Hayes G. Use of a custom additive manufactured titanium plate for cranioplasty in a dog with multilobular osteochondrosarcoma. Abstract. European College Veterinary Surgeons 28th Annual Scientific Meeting, July 2–4, 2019, Budapest, Hungary.

15. Comrie M, Monteith G, Zur Linden A, Oblak M, Phillips J, James F. The accuracy of computed tomography scans for rapid prototyping of canine skulls. *PLoS One*. 2019;14(3)
16. Wang H, Su K, Su L, Liang P, Ji P, Wang C. The effect of 3D-printed Ti6Al4V scaffolds with various macropore structures on osteointegration and osteogenesis: a biomechanical evaluation. *J Mech Behav Biomed Mater* 2018;88:488-496
17. Wang H, Su K, Su L, Liang P, Ji P, Wang C. Comparison of 3D-printed porous tantalum and titanium scaffolds on osteointegration and osteogenesis. *Mater Sci Eng C* 2019;104:109908
18. Tanzer M, Chuang P, Ngo C, Song L, TenHuisen K. Characterization of bone ingrowth and interface mechanics of a new porous 3D printed biomaterial. *Bone Joint J*. 2019;101-B(6_Supple_B):62-67
19. Reints Bok T, Willemsen K, Rijen M, Grinwis G, Tryfonidou M, Meij B. Instrumented cervical fusion in nine dogs with caudal cervical spondylomyelopathy. *Vet Surg* 2019;48(7):1287-1298
20. McGaffey M, Zur Linden A, Bachynski N, Oblak M, James F, Weese J. Manual polishing of 3D printed metals produced by laser powder bed fusion reduces biofilm formation. *PLoS One* 2019;14(2):e0212995
21. Bose S, Banerjee D, Shivaram A, Tarafder S, Bandyopadhyay A. Calcium phosphate coated 3D printed porous titanium with nanoscale surface modification for orthopedic and dental applications. *Mater Des* 2018;151:102-112
22. Nimwegen B. Head & Neck tumors: diagnosis, staging, surgery, and multimodal treatment. Abstract. Voorjaarsdagen European Veterinary Conference, April 10-12, 2019, The Hague, The Netherlands.
23. Xie K, Guo Y, Zhao S, et al. Partially melted Ti6Al4V particles increase bacterial adhesion and inhibit osteogenic activity on 3D-printed implants: an in vitro study. *Clin Orthop Relat Res* 2019;477(12):2772-2782



CHAPTER 13

Additive titanium manufacturing to repair critically sized antebrachial bone defects in dogs

Sara D.S. Jansen | Koen Willemsen | Joëll Magré | Björn P. Meij

This manuscript is still under preparation

Abstract

Recent developments in the medical field of additive manufacturing (AM) allows printing of scaffolds to fill bone defects that cannot be bridged by the natural process of bone consolidation. Two dogs were presented with atrophic non-union of the proximal ulna involving the elbow joint due to previous orthopaedic procedures with severe complications that led to critical size bone defects. Computed tomography was performed and porous scaffolds and saw guides were designed in silico and printed by AM. Osteotomies in vital bone were guided by patient-specific 3D printed nylon saw guides allowing a perfect fit for the 3D printed titanium implant. In one case the scaffold was filled with bone morphogenic protein and held in place by two plates. In the other case the scaffold was filled with cancellous bone graft and held in place by a titanium plate that was part of the scaffold design. Both cases regained function and weight-bearing without lameness. Osseointegration of the implant was shown in both cases on follow-up CT and radiographs and macroscopically evident in the pores of the 3D implant after plate removal. One dog was euthanized for unrelated disease and micro-CT revealed solid bone bridging through the inner scaffold tunnel. This study shows the successful application of the design, fabrication, and clinical use of a patient-specific 3D printed titanium implant to repair critically sized bone defects of the antebrachium in two dogs.

Introduction

Failure to progress to osteosynthesis can be caused by insufficient mechanical stability, an inadequate biological environment, or both. Biological inactivity despite adequate fixation results in the absence of osteosynthesis and is defined as a nonunion. A subclassification of this nonviable nonunion is the atrophic nonunion, which is characterized by complete absence of restorative processes. [1] A nonunion can result in potential devastating complications like permanent lameness, osteomyelitis, osteoarthritis in case of joint involvement, angular limb deformities, tendon problems, and side effects of prolonged use of non-steroidal anti-inflammatory drugs (NSAIDs). Treatment of atrophic nonunions is often challenging and requires surgical debridement of all nonviable tissue. To stimulate new bone regeneration to bridge the segmental bone defect a rigid fixation is of vital importance. [1] In case the nonunion involves joint surface, segmental bone bridging should preferably also restore the anatomic joint surface to restore limb function without lameness. Biological activity can be promoted using autogenous cancellous bone together with recombinant human bone morphogenetic protein-2 (rhBMP-2) or rhBMP-7. [2,3] Due to a poor prognosis for return of function, high expenses and extensive efforts, owners are often forced to decide for limb amputation or euthanasia. However, recent innovations in AM offer a surgical solution when mass produced off-the-shelf implants with fixed sizes fail to reach an optimal solution to bridge critical-sized bone defects, especially in cases with involvement of joint surface that requires perfect anatomic restoration. [4,5]

AM is used for rapid prototyping and small series manufacturing. [4] Digital 3D models are in silico created by using medical imaging. Standard DICOM images are reconstructed to 3D models in readily available segmentation software. This AM technique enables the manufacturing of implants directly from a digital 3D model, stereolithography (STL) by printing material, usually on a layer-by-layer basis. [5] The main advantage of this technique is the ability to manufacture extremely complex 3D geometries that cannot be produced by other manufacturing techniques. This can expedite surgery with improved recovery. [4,5]

The last decade AM is gaining popularity in both human and veterinary medicine and multiple case studies have been reported. [6-22] In veterinary medicine this technique has mainly been used for the reconstruction of cranial defects but recently developments in treatment for hip dysplasia were published. [23-26]

The aim of this study was to describe the design and clinical use of patient-specific 3D printed osteotomy guides, and a patient-specific 3D printed porous titanium implant to bridge a critically sized antebrachial bone defect involving the elbow joint due to an atrophic nonunion in two dogs.

Case description

Case 1

A 1-year-old Bernese Mountain Dog was referred to the University clinic 11 weeks following bi-oblique dynamic proximal ulnar osteotomy (BOD-PUO) of the right antebrachium for elbow dysplasia with medial coronoid disease (MCD) and incongruency. The osteotomy in the ulna was performed too close to the elbow joint. Three weeks after the BOD-PUO the dog developed a surgical site infection (SSI), which was treated with broad-spectrum antibiotics. Despite conservative management with antibiotics and NSAIDs the dog developed a persistent lameness of the right thoracic limb grade 4 out of 5, moderate to severe muscle atrophy of the antebrachial musculature, and joint effusion of the elbow joint. [27] Concurrent orthopedic abnormalities included bilateral subluxations of the hip joints due to hip dysplasia. Radiographic examination revealed an atrophic nonunion defect of the right proximal ulna with malalignment and intra-articular extension (Fig. 1). There was severe osteoarthritis with subchondral bone lesions, joint effusion and incongruency of the right elbow. Computed tomography (CT) of both forelimbs revealed a chronic osteolytic defect of 10 mm of the right proximal ulna and severe right elbow osteoarthritis with fragmentation of the medial coronoid, incongruity and mineralization and erosion of cartilage and subchondral erosive lesions.

Design

A patient-specific 3D implant was designed to fill the critically sized defect in the right ulna and restore the ulnar elbow joint alignment. To develop the patient-specific implant, first the Digital Imaging and Communications in Medicine (DICOM) files of the CT scan (250 mAs, 120 kV, 0.6 mm slice thickness) were exported from the imaging archive system to Mimics (v21, Materialise NV., Leuven, Belgium) for anatomical segmentation. Standard bone threshold values (226 HU – upper threshold) were taken to segment the bone. The left ulna was mirrored to obtain an approximation of the original anatomy of the right ulna for the accomplishment of a 3D patient-specific implant for ulnar reconstruction (Fig. 1). Hereafter, the nonunion was manually segmented together with a digitally grown resection margin that was used to simulate the minimal needed resection area to obtain straight osteotomies enhancing the placement of the 3D patient-specific implant. Subsequently the anatomical models were transferred as STL files to 3-matic software (v13, Materialise NV., Leuven, Belgium) to design the guides and scaffold. The proximal and distal resection guides were designed, to remove the irregular non-viable bony edges of the nonunion and they were reviewed by a board-certified veterinary surgeon for approval. The resulting gap between the two osteotomies determined the size of the required implant (20 mm length x 18 mm in width). The ulnar reconstruction implant was designed as an anatomical sized porous titanium (70% porous, 500-600 µm pore size, Dodecahedron unit cell)

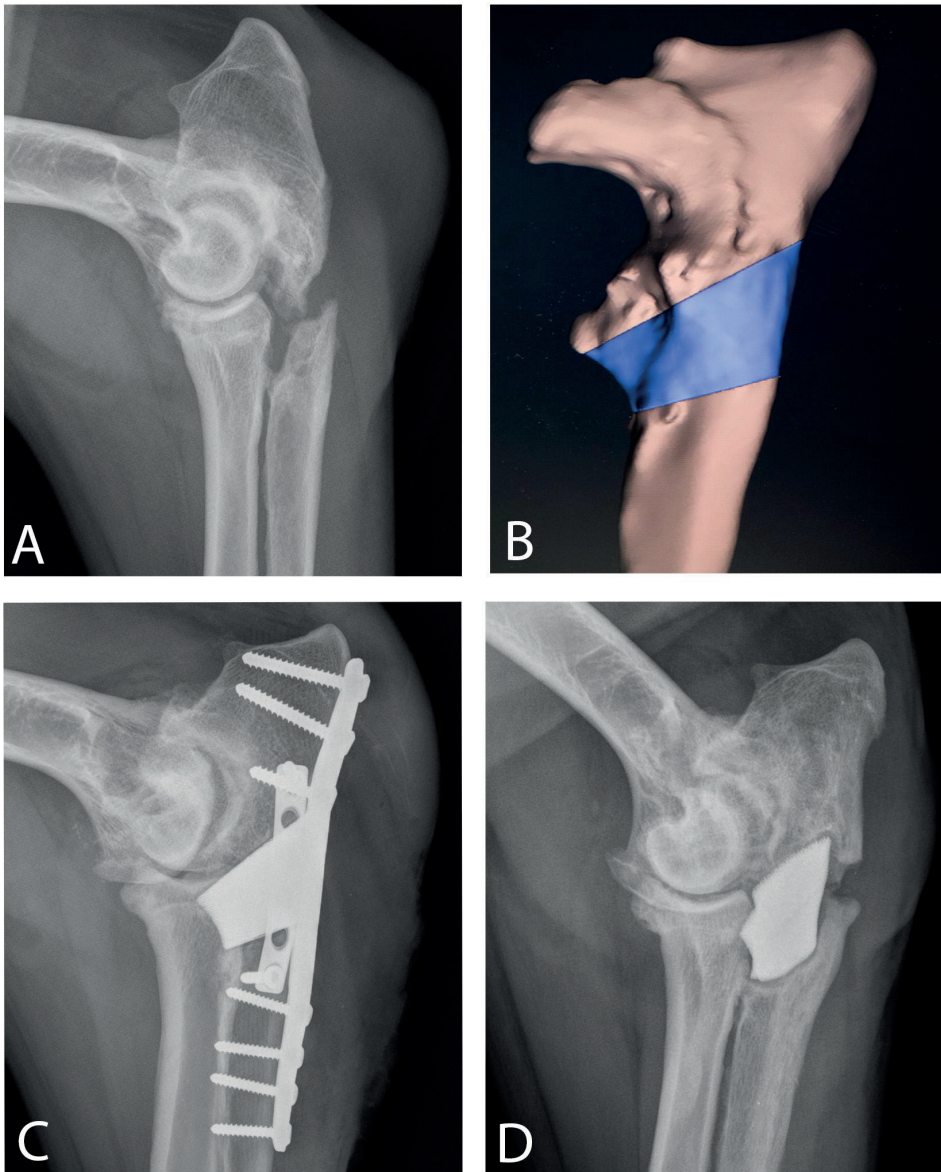


Figure 1. Case 1

- A – atrophic non-union defect of the right proximal ulna with cranioproximal malalignment and intra-articular extension and severe osteoarthritis
- B – The left ulna was mirrored to obtain an approximation of the original anatomy of the right ulna for the accomplishment of a 3D patient specific implant for ulnar reconstruction.
- C – Immediate postoperative radiograph
- D – 20 months postoperative radiograph after removal of fractured plates

to allow bony ingrowth at the implant bone interface. Additionally, the central region of the implant contained 2 holes for application of an autogenous cancellous bone graft together with demineralized bone matrix (Fig. 3).

Production and presurgical planning

The osteotomy saw guides and left, and right ulna were 3D printed in Nylon (PA12) on an EOS P110 printer (EOS, Krailling, Germany) and the implant was 3D printed from titanium alloy (Ti-6Al-4V ELI grade 23) using direct metal printing on a ProX DMP320 printer (3D Systems, Leuven, Belgium). Post-processing of the implant included scaffold removal and Hot Isostatic Pressing (HIP). Presurgical planning was done in the dry lab on another 3D printed bone model specimen together with the saw guides and titanium scaffold, allowing precise selection of the size and length of the plates and contouring to the bone and presurgical planning for the screw trajectories. Before surgery both the guides and the implant were manually cleaned, and underwent standardized autoclave sterilization at the in-house sterilization facility.

Surgery

The patient was placed in dorsal recumbency with the affected limb suspended and retracted caudally for draping. A caudal approach to the proximal shaft of the ulna was performed. [28] Subperiosteal elevation and medial retraction of the flexor carpi ulnaris muscle and lateral retraction of the extensor carpi ulnaris muscle exposed the ulnar shaft. After debridement of both fragments, the 3D printed surgical saw guides were applied to the caudal ulnar bone surface and perfect fit of the saw guide was confirmed before the distal and proximal osteotomies were performed with a 0.6 mm thick oscillating saw (DePuy Synthes, Johnson-Johnson, Oberdorf, Switzerland) (Fig. 2). Following removal of the ulnar nonunion, the newly formed bone ends were inspected for viability and bleeding. The patient-specific 3D implant was embedded with the autogenous cancellous bone graft harvested from the ipsilateral tuberculum majus and mixed with artificially engineered demineralized bone matrix (Attrax Putty, Nuvasive, San Diego, CA, USA). The titanium implant was fitted in between both ulnar fragments (Fig. 2) and after restoration of the ulnar alignment and elbow congruence a hybrid dynamic compression plate 3.5/2.7 mm (Hybrid DCP [HDCP]) (DePuy Synthes, Johnson-Johnson, Oberdorf, Switzerland) was placed caudally on the tension side of the ulna under fluoroscopic guidance. An additional 2.7 mm DCP (DePuy Synthes, Johnson-Johnson, Oberdorf, Switzerland) was applied medially and fixed with 2 bicortical cortical screws to prevent medial displacement of the titanium implant. Before routine closure, 4 x 32.5 mg gentamycin sponges (Garacol, SERB SA, Brussels, Belgium) were applied locally around the implant.

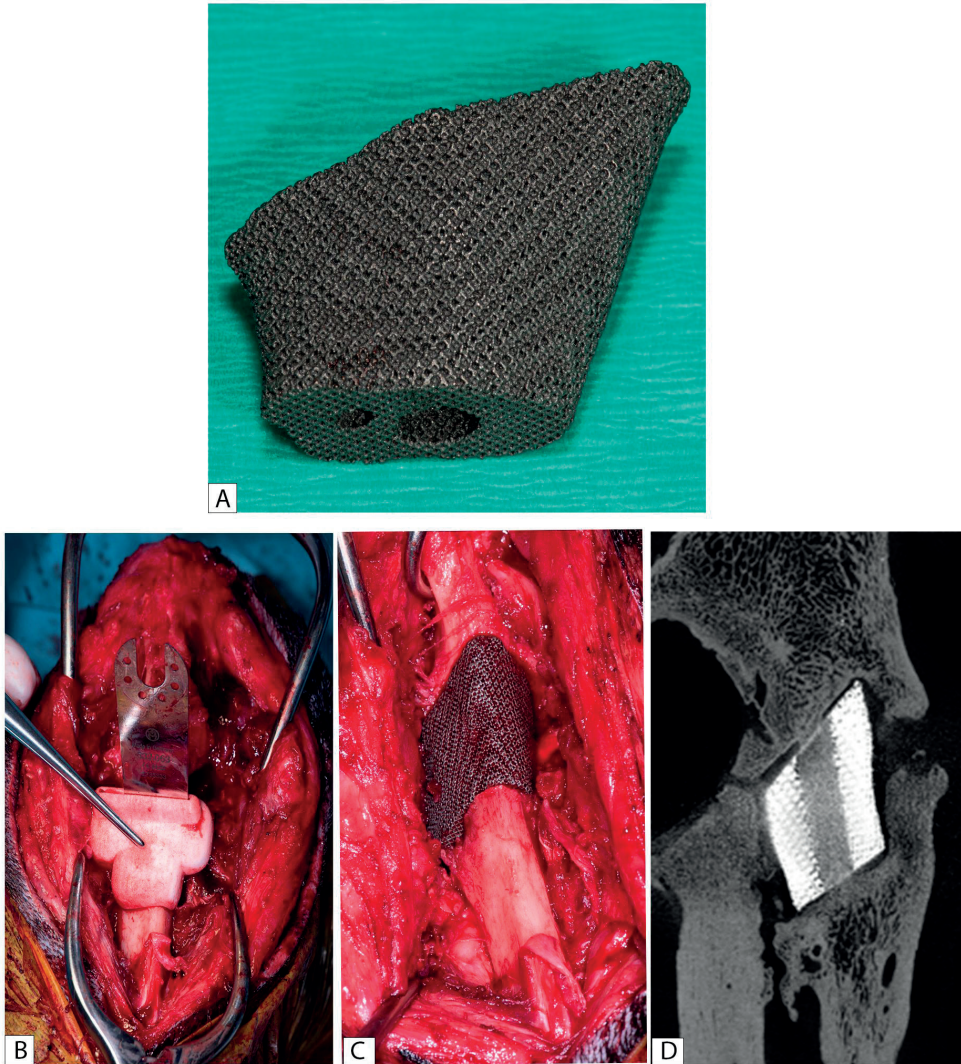


Figure 2. Case 1

- A - The titanium ulnar reconstruction porous implant with central canals for application of an autogenous cancellous bone graft with demineralized bone matrix.
- B - The 3D-printed surgical saw guides were applied.
- C - The patient-specific 3D implant was fitted in between both ulnar fragments.
- D - MicroCT cross section at 24 months postoperatively (after euthanasia). Bone ingrowth is seen through the large cannula.

Follow-up

Postoperative radiographs showed a stable construction (Fig. 2). At the four months postoperative check there was clinical improvement in use of the right thoracic limb and CT revealed no changes with postoperative radiographs. At five months postoperatively the dog developed a progressive worsening lameness at the right thoracic limb. HDCP plate failure with fracture of 5 out of 7 cortical screws was present. During surgical removal of the HDCP plate, inspection of the 3D implant showed complete osseointegration. Eleven months after surgery the medial DCP plate was removed because of failure of the 2 screws. During surgical removal of the DCP plate, inspection of the 3D implant showed continued complete osseointegration and fixation of the 3D implant. At twenty months follow-up (of the initial surgery) the owners reported clinical improvement. The 3D implant was radiologically stable without signs of implant failure (Fig. 1). There was a mild to moderate progression of the elbow joint arthrosis. Exactly two years postoperatively the dog developed right pelvic limb lameness. Radiographs of the stifle revealed an osteolytic process in the distal femur with aggressive characteristics. The owner decided for euthanasia of the dog and consented with postmortem collection of the antebrachial segment to study bone ingrowth. 3D micro-CT scan (VECTor6/CT system, MILabs B.V., Utrecht, The Netherlands) was obtained of the bone specimen with the following parameters: multi-circle 360 degrees acquisitions, tuber voltage of 55KV, tube current of 0.19 mA, exposure time of 75 ms per projection, angle increment of 0.5 degrees, and 50 μ m reconstructed isotropic voxel size using 3D Feldkamp filtered back-projection reconstruction. Micro-CT revealed bone in-growth in the medullar cavity of the porous segment (Fig. 2), however in-growth of bone in the smaller porous structure was too small for detection.

Case 2

A 4-year-old Schapendoes was presented with a history of a transverse olecranon fracture due to collision with a train three years ago which was treated with open reduction and internal fixation and complicated by osteomyelitis. Implants were removed after 12 weeks and with physiotherapy the dog regained some chronic non-weight bearing left thoracic limb lameness. Unfortunately, the dog suffered another road traffic accident and was referred to the University clinic two weeks later. Radiological examination revealed a chronic, complete, transverse, intra-articular nonunion of the left olecranon and a moderate amount of osteoarthritis of the elbow joint and sclerosis of the ulna (Fig. 3). A CT scan was performed as well as arthrocentesis to exclude an intra-articular infection. A chronic osteolytic defect of approximately 12 mm of the proximal left ulna was present with concurrent bilateral signs of medial coronoid disease. Prior to the surgery, and at 6 weeks and 10 weeks after surgery, ground reaction forces (GRF) were measured with a quartz crystal piezoelectric force plate (Kistler type 9261, charnwood Dynamics

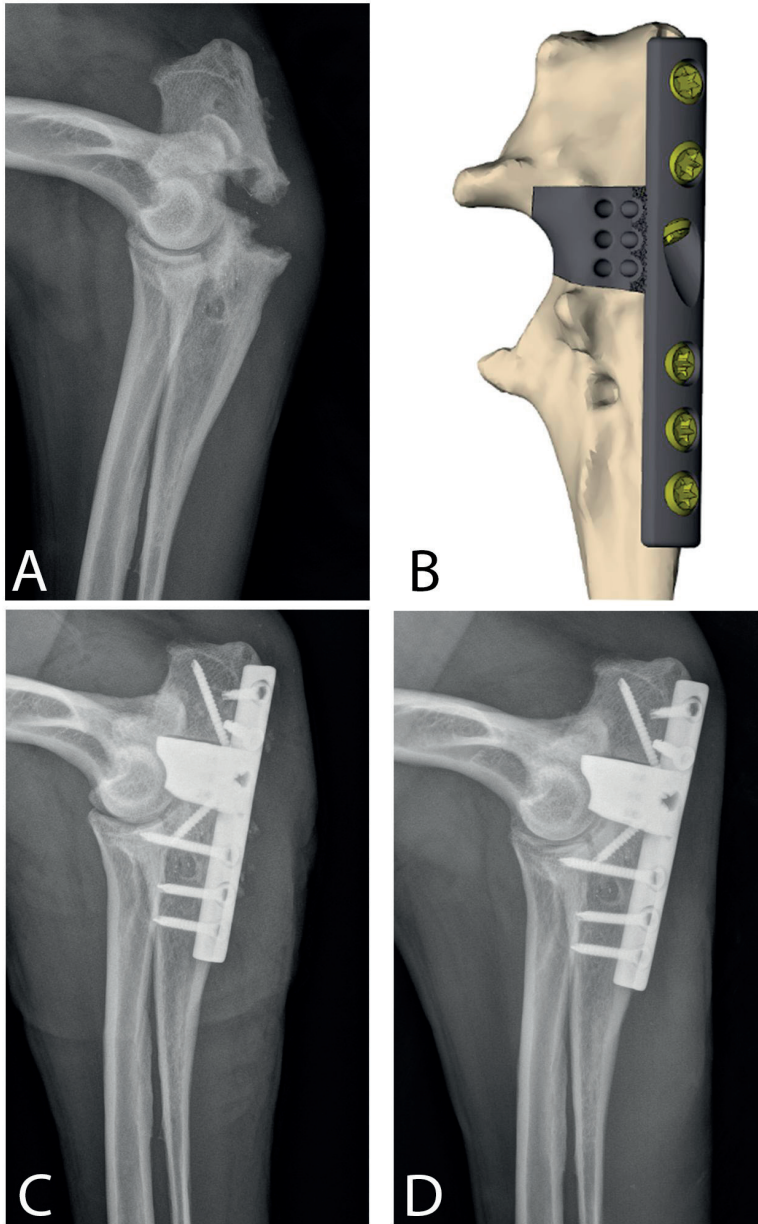


Figure 3. Case 2

- A – a chronic, complete, transverse, intra-articular non-union of the left olecranon and a moderate amount of osteoarthritis of the elbow joint and sclerosis of the ulna
- B – Design of the 3D patient specific implant with an incorporated plate with diagonal screws that allow compression of the distal and proximal fragments towards the implant.
- C – Immediate postoperative radiograph
- D – 6 weeks postoperative radiograph shows a stable presentation of the metallic implants without any lucent lines around the implants

Limited, Rothley UK) together with the Kistler 9865E charge amplifiers, as described previously.[29,30] Measurements were obtained with a frequency of 100 Hz. GRFs were measured in the mediolateral (Fx), craniocaudal (Fy), and vertical (Fz) direction. The presurgical measurement revealed a Fzmax of 12N/kg bodyweight of the right thoracic limb and a non-load bearing left thoracic limb.

Design

Saw guides and a patient-specific 3D implant were designed from the CT images in a similar manner as in case 1. The ulnar reconstruction implant was designed from porous titanium (70% porous, 500-600 μm pore size, Dodecahedron unit cell) to allow bony ingrowth at the implant bone interface. The porous titanium implant was modified in comparison to case 1 by adding/incorporating a 3D printed titanium 6-hole 2.7mm plate on the caudal site and designing two drill guides for the screws to capture the screw direction and screw length for optimal bone stock in the proximal and distal fragment (Fig. 3). Additionally, the central region of the bone bridging porous implant contained 1 hole for application of an autogenous cancellous bone graft. The surgical saw guides and drill guides were 3D printed in Nylon (PA12) on an EOS P110 printer (EOS, Krailling, Germany) and the implant was 3D printed from titanium alloy (Ti-6Al-4V ELI grade 23) using direct metal printing on a ProX DMP320 printer (3D Systems, Leuven, Belgium). Post-processing of the implant included polishing and HIP treatment. Before surgery both the guides and the implant were manually cleaned and sterilized at the in-house sterilization facility.

Surgery

Surgical approach to the caudal side of the ulna was performed in a similar fashion as in case 1. The anconeal process was luxated for additional exposure of the proximal fragment and to better assess the intra-articular ulnar defect. After debridement of both fragments, the 3D printed osteotomy saw guides were applied to the caudal ulnar bone surface and when perfect fit was confirmed, the saw guides were temporarily fixed with 1.6 mm K-wires (Fig. 4). Distal and proximal osteotomies were performed with a 0.6 mm thick oscillating saw and extra new bone formations on the caudal and medial part of the ulna were removed. The patient-specific 3D implant was filled with an autogenous cancellous bone graft harvested from the ipsilateral tuberculum majus and fitted in between both ulnar fragments. First the implant was fixated to the proximal fracture fragment using the proximal drill guide by placing a central 2.4 mm titanium MF cortex screw (Unilock, DePuy Synthes, Johnson-Johnson, Oberdorf, Switzerland). After reduction of the anconeal process and alignment of the proximal and distal ulnar fragments, fixation of the most proximal bone fragment occurred using one diagonal 2.4 mm titanium MF cortex screw (Unilock, DePuy Synthes, Johnson-Johnson, Oberdorf, Switzerland)

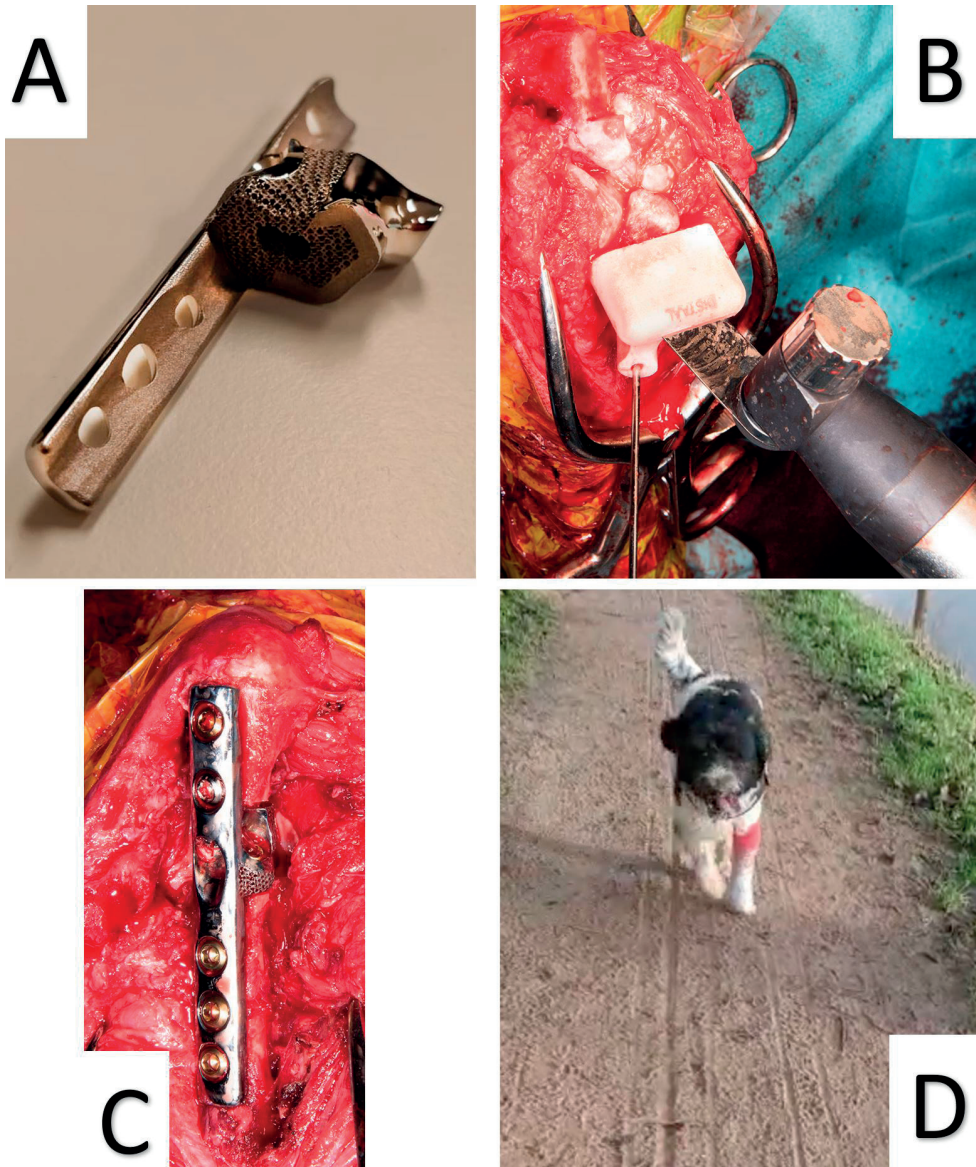


Figure 4. Case 1

- A – new edition porous titanium implant was modified by adding/incorporating a 3D printed titanium dynamic compression plate 2.7mm on the caudal site. Additionally, the central region of the implant contained 1 hole for application of an autogenous cancellous bone graft as well as two extra screw holes for 2.4mm locking titanium screws
- B – The 3D-printed surgical saw guides were applied
- C – The patient-specific 3D implant was fitted in between both ulnar fragments
- D – A still frame from a movie of the Patient dog walking at 1 year of follow-up

that was placed from distal to proximal and therefore gave compression between the bone and implant interface. Thereafter another 2.4 mm titanium screw was placed on the medial side of the plate through the porous implant in distal direction using the proximal drill guide (Fig. 4) which also gave compression on the bone implant interface. Thereafter the distal drill guide was used and three 2.7 mm titanium screws were placed (Kyon, Zürich, Switzerland) under fluoroscopic guidance for elbow congruency. Fixation of the plate was completed by filling the remaining proximal screw holes with one 2.7 mm titanium screw (Kyon, Zürich, Switzerland) and one 2.7 mm 316L stainless steel cortical screw using the proximal drill guide. The latter screw placed was a 316L stainless steel screw, because there wasn't a 2.7mm titanium screw in the correct length available. Before closure an autologous bone graft was applied around the implant.

Follow-up

Postoperative radiographs showed a stable construction (Fig. 3). The patient was discharged from the hospital with a Modified Robert Jones bandage including a splint. Bandage changes were performed on a weekly base for 6 weeks. The dog started to use the thoracic limb during the 6-week bandage period and after bandage removal it showed a gradual return to full weightbearing without lameness up to 15 months follow-up at time of writing. Radiographs at 6 and 10 weeks showed a stable presentation of the metallic implants and congruent elbow with stable osteoarthrotic changes (Fig. 3). Six- and ten-weeks postoperative force plate analysis was rechecked. At six weeks F_{zmax} of the left thoracic limb was 3.5 N/kg and F_{zmax} of the right thoracic limb was 9N/kg. Measurements were repeated at ten weeks postoperative and showed an increase in F_{zmax} of the left thoracic limb of 5.5 N/kg and a F_{zmax} of the right thoracic limb of 8N/kg.

Discussion

This case series described the use and feasibility of additive titanium manufacturing to create a patient-specific implant for repair of critically sized bone defects in dogs. Both patients were presented with critically sized bone defects the first in close vicinity of the elbow joint and the second including the elbow joint. Both cases due to atrophic nonunion of the ulna as a result of failed previous orthopedic procedures. Alternative treatments like the use of standard sized of-the-shelf implants or limb amputation would result in increased morbidity because of respectively absence of a complete articular surface or functional limb loading.[31] Amputation of the antebrachium was prevented and reconstruction of ulna with the 3D patient-specific implant led to functional limb use and excellent clinical outcome.

Both implants were made of highly porous titanium scaffolds allowing bone ingrowth and which ultimately leads to permanent osseointegration of the implant in the ulna, adding to the long-term durability.[32-35] However, the use of metal implants and plates can also lead to stress shielding of the bone by the implant. The changed stress distribution could lead to bone resorption and implant failure in time.[36] To avoid stress shielding at the bone-implant interface Gibson and Ashby (1997/1999) suggested to adjust the relative density of the materials.[31,37] Metal alloys like titanium (Ti-6Al-4V) are used extensively in orthopedic surgery as it is known for its good biocompatibility, satisfactory mechanical strength, and superior corrosion resistance. Characteristics of importance in bone scaffolds are: (1) biocompatibility; (2) suitable surface for cell attachment, proliferation, and differentiation; (3) highly porous with an interconnected pore network for cell ingrowth and transport of nutrients and metabolic waste; (4) mechanical properties to match the requirements of the surrounding tissues to reduce or eliminate stress shielding, and to meet anatomic loading requirements to avoid mechanical failure. The anisotropic character of bone with variable stiffness and strength in different directions pose challenges to create suitable porous metals to approximate the exact stiffness of surrounding bones.[38] The porous structure of implants at the bone-implant interface makes them effective for load transfer and alleviating the stress shielding effect.[39-43]

Fracture repair of the proximal ulna can be addressed by using an interlocking nail, hybrid external fixator or a trans articular external fixator, plate fixation or a combination of these techniques. The forces that need to be addressed are torsion, bending, and shearing. In this case with a chronic nonunion combined with a critically sized non bridging bone defect extending into the elbow joint, the use of an interlocking nail, hybrid external fixator or a trans articular external fixator, plate fixation or a combination of these techniques would not have resulted in a clinical anatomic union. Also the abovementioned methods won't be suitable for restoring the articular surface of the elbow joint. The use of a porous 3D patient-specific implant combined with a plate on the tension side of the ulna resulted in a stable construction. In both cases the dog started to use the limb again and near full weight bearing was achieved with good clinical function. However, in case 1 the bone bridging implant was not connected to the plates that acted as buttress plates, making them probably more susceptible to mechanical failure. This resulted in multiple failures of plate screws which necessitated plate and screw removal at 5 and 11 months after surgery. At the time of plate removal, it was possible to macroscopically assess osseointegration of the porous implant and this was found to be a solid component of the ulna and micro-CT at 24 months confirmed bone bridging through the central hole in the titanium scaffold. At that time bone bridging was not complete caudal to the implant which may be due to remaining micromotion on the tension site of the ulna or simply because the dog did not survive long enough because of euthanasia for an aggressive pelvic limb bone tumor.

Ongoing insight in patient-specific implants and their application together with experience of the implant failures in case 1 resulted in adaptations of the design of the implant in case 2. The modification consisted of incorporating a 3D printed 2.7 mm titanium plate on the caudal site of the porous titanium implant as well as the design of two screw holes through the porous implant itself, creating a compressive force on the bone-implant interface. The porous scaffold between the bone parts contained one central hole for application of a cancellous bone graft and 2 screw holes so the implant itself was also fixated to the bone but was also an integral part with the caudal plate that was additionally fixated with screws to the ulna. The incorporation of a plate on the caudal side of the scaffold has added stability to the construct and the design likely reduced stress shielding that has prevented implant failure in case 2 up to the follow-up at time of writing. In addition, in case 2 drill guides were designed pre-surgically for screw placement which allowed precise selection of screw direction and screw length in relation to the optimal bone stock avoiding the joint surface of the elbow. This may have led to optimal distribution of scaffold and plate fixation forces and therefore help bone and implant survival.

In case 1 bone ingrowth was seen in and around the 3D printed scaffold. This in line with previous experimental implantations in mice. [44,45] The strength in implant embedding is increased by bone ingrowth. [46-49] Another technique to evaluate bone formation in the scaffolds is histomorphometry of the non-decalcified sections using traditional light- and epifluorescent microscopy.[50] Li et al (2007) concluded that increase of porosity and pore size of titanium alloy implants have a positive influence on osteoconductive properties. The hydromechanical properties of porous scaffolds were investigated by Ouyang et al. (2019) in distal femoral condyle models in rabbits. [51] They concluded that the permeability, flow velocity, and the inflow of fluid linearly increase with the pore size and therefore influence performances in cell penetration, adhesion, proliferation, and differentiation, to optimize bone in-growth in scaffold. Histology of the bone specimen in case 1 is ongoing but may further give insight in the osseointegration of the scaffold in the ulnar bone.

Force plate analysis was performed in case 2 and showed preoperatively overcompensation of the right thoracic limb. Postoperatively at six weeks there was an improved but noticeable difference in Fzmax between both the left and the right thoracic limbs, whereas at ten weeks the absolute difference in Fzmax between both thoracic limbs decreased further. One can conclude that these results indicate a clinical improvement of the left thoracic limb lameness. However, a force plate analysis is a snapshot of a particular moment in time and provides little information about the use of the limb during the entire day, e.g., while playing, lying down, and standing (up). Because the limited value of the gait analysis to analyze the well-being of the dog it is not routinely prescribed and currently

more preference is given to owner (pain score) questionnaires, however in this case the gait analysis objectively confirmed improvement from preoperative to postoperative.[52]

In these 2 cases, the lead time for the implants between imaging and surgery was approximately 3 months and is due to time needed for design, feedback to the surgeon and adapting the design, manufacturing of the implant, post processing and quality control, transportation, and sterilization procedures. Popescu et al. (2015) described a platform to exchange medical and technical information between surgeon and engineer to facilitate the process of manufacturing and decreasing the lead time.[53] Also protocols and algorithms can be written to have a faster design process. However, the patient-specific nature of these implants and their low occurrence makes them inherently difficult for algorithms. The patient-specific nature causes an inherent delay in the availability of implants, and this should be considered in the surgical planning and when addressing the owner's expectations.

There are several limitations of this case series. The limited number of dogs makes it difficult to draw firm conclusions. This study is descriptive in nature and ongoing insight and experiences with case 1 has changed the design for case 2. Histopathology of the bone specimen of case 1 is not available at time of writing. Imaging at follow-up is not uniform and depends on financial willingness of owners. Minimal requirements for follow-up are radiography to monitor implant position and implant failure, however, CT is considered of added benefit to assess bone in-growth in the titanium scaffold. For more detail on bone ingrowth histology is advised. However, this is difficult when dealing with patients. In case bone specimens become available like in case 1 histopathology is a challenge and difficult due to the size of the scaffold (>3cm). Routine histopathology laboratories cannot deal with the implant-bone specimen and a specialized laboratory is needed to cut the bone-titanium implant specimen without disturbing the bone in-growth in the titanium pores or at the metal-bone interface which are the focus of attention. Therefore, when available, micro-CT should be performed first before proceeding to histopathology processing in case the specimen is lost because of technical difficulties.

Conclusion

This case series described the use and feasibility of additive titanium manufacturing to create a patient-specific implant for repair of critically sized bone defects in dogs. The availability and experience with these techniques is important to treat future cases. Follow-up of treated patients remains important to optimize the design of scaffold structures for complete osseointegration and implant durability for lifetime use in dogs.

References

1. Willemsen K, Tryfonidou M, Sakkars R, et al. Patient-specific 3D-printed shelf implant for the treatment of hip dysplasia: anatomical and biomechanical outcomes in a canine model. *J Orthop Res* 2021;1-9
2. Kamishina H, Sugawara T, Nakata K et al. Clinical application of 3D printing technology to the surgical treatment of atlantoaxial subluxation in small breed dogs. *PLoS One* 2019;14(5)
3. Carwardine D, Gosling M, Burton N, O'Malley F, Parsons K. Three-Dimensional-Printed Patient-Specific Osteotomy Guides, Repositioning Guides and Titanium Plates for Acute Correction of Antebrachial Limb Deformities in Dogs. *Vet Comp Orthop Traumatol* 2020;34(01):043-052
4. Choi S, Oh Y, Park K, Lee J, Shim J, Kang B. New clinical application of three-dimensional-printed polycaprolactone/ β -tricalcium phosphate scaffold as an alternative to allograft bone for limb-sparing surgery in a dog with distal radial osteosarcoma. *J Vet Med Sci* 2019;81(3):434-439
5. Séguin B, Pinard C, Lussier B, et al. Limb-sparing in dogs using patient-specific, three-dimensional-printed endoprosthesis for distal radial osteosarcoma: a pilot study. *Vet Comp Oncol* 2019;18(1):92-104
6. Arzi B, Cissell D, Pollard R, Verstraete F. Regenerative approach to bilateral rostral mandibular reconstruction in a case series of dogs. *Front Vet Sci* 2015;2
7. Kim S, Mi Shim K, Jang K, Shim J, Kang S. Three-dimensional printing-based reconstruction of a maxillary bone defect in a dog following tumor removal. *In Vivo (Brooklyn)* 2018;32(1):63-70
8. Liptak J, Thatcher G, Bray J. Reconstruction of a mandibular segmental defect with a customized 3-dimensional-printed titanium prosthesis in a cat with a mandibular osteosarcoma. *J Am Vet Med Assoc* 2017;250(8):900-908
9. Castilho M, Dias M, Vorndran E, et al. Application of a 3D printed customized implant for canine cruciate ligament treatment by tibial tuberosity advancement. *Biofabrication* 2014;6(2):025005
10. Joffe M, Parr W, Tan C, Walsh W, Brunel L. Development of a customized interbody fusion device for treatment of canine disc-associated cervical spondylomyelopathy. *Vet Comp Orthop Traumatol* 2019;32(01):079-086.
11. Willemsen K, Nizak R, Noordmans HJ, Castelein RM, Weinans H, Kruyt MC. Challenges in the design and regulatory approval of 3D-printed surgical implants: a two-case series. *Lancet Digital Health* 2019;1(4):e163-171
12. Taniguchi N, Fujibayashi S, Takemoto M et al. Effect of pore size on bone ingrowth into porous titanium implants fabricated by additive manufacturing: an in vivo experiment. *Mater Sci Eng C* 2016;59:690-701
13. Van der Stok J, Van der Jagt OP, Yavari SA et al. Selective laser melting-produced porous titanium scaffolds regenerate bone in critical size cortical bone defects. *J Orthop Res* 2013;31(5):792-799
14. Oblak M, Hayes G. Use of a custom additive manufactured titanium plate for cranioplasty in a dog with multilobular osteochondrosarcoma. Abstract. European College Veterinary Surgeons 28th Annual Scientific Meeting, July 2–4, 2019, Budapest, Hungary.

15. Comrie M, Monteith G, Zur Linden A, Oblak M, Phillips J, James F. The accuracy of computed tomography scans for rapid prototyping of canine skulls. *PLoS One*. 2019;14(3)
16. Wang H, Su K, Su L, Liang P, Ji P, Wang C. The effect of 3D-printed Ti6Al4V scaffolds with various macropore structures on osteointegration and osteogenesis: a biomechanical evaluation. *J Mech Behav Biomed Mater* 2018;88:488-496
17. Wang H, Su K, Su L, Liang P, Ji P, Wang C. Comparison of 3D-printed porous tantalum and titanium scaffolds on osteointegration and osteogenesis. *Mater Sci Eng C* 2019;104:109908
17. Tanzer M, Chuang P, Ngo C, Song L, TenHuisen K. Characterization of bone ingrowth and interface mechanics of a new porous 3D printed biomaterial. *Bone Joint J*. 2019;101-B(6_Supple_B):62-67
19. Reints Bok T, Willemsen K, Rijen M, Grinwis G, Tryfonidou M, Meij B. Instrumented cervical fusion in nine dogs with caudal cervical spondylomyelopathy. *Vet Surg* 2019;48(7):1287-1298
20. McGaffey M, Zur Linden A, Bachynski N, Oblak M, James F, Weese J. Manual polishing of 3D printed metals produced by laser powder bed fusion reduces biofilm formation. *PLoS One* 2019;14(2):e0212995
21. Bose S, Banerjee D, Shivaram A, Tarafder S, Bandyopadhyay A. Calcium phosphate coated 3D printed porous titanium with nanoscale surface modification for orthopedic and dental applications. *Mater Des* 2018;151:102-112
22. Nimwegen B. Head & Neck tumors: diagnosis, staging, surgery, and multimodal treatment. Abstract. Voorjaarsdagen European Veterinary Conference, April 10-12, 2019, The Hague, The Netherlands.
23. Xie K, Guo Y, Zhao S, et al. Partially melted Ti6Al4V particles increase bacterial adhesion and inhibit osteogenic activity on 3D-printed implants: an in vitro study. *Clin Orthop Relat Res* 2019;477(12):2772-2782
24. Harrysson OL, Marcellin-Little DJ, Horn TJ. Applications of metal additive manufacturing in veterinary orthopedic surgery. *JOM*. 2015;67(3):647-654
25. Golafshan N, Willemsen K, Kadumudi FB, et al. 3D-Printed regenerative magnesium phosphate implant ensures stability and restoration of hip dysplasia. *Adv Healthc Mater* 2021;10(21):2101051
26. Willemsen K, Tryfonidou M, Sackers R, et al. Patient-specific 3D-printed shelf implant for the treatment of hip dysplasia: Anatomical and biomechanical outcomes in a canine model. *J Orthop Res* 2021
27. Vasseur PB, Johnson AL, Budsberg SC, et al: Randomized, controlled trial of the efficacy of carprofen, a nonsteroidal anti-inflammatory drug, in the treatment of osteoarthritis in dogs. *J Am Vet Med Assoc* 1995; 206: 807-811
28. Piermattei DL, Johnson KA. Approach to the Distal Femur and Stifle Joint through a Lateral Incision: An Atlas of Surgical Approaches to the Bones and Joints of the Dog and Cat, 4th ed. Philadelphia, PA: Saunders; 2004:338–341

29. Suwankong N, Meij BP, Van Klaveren NJ, et al. Assessment of Decompressive Surgery in Dogs with Degenerative Lumbosacral Stenosis Using Force Plate Analysis and Questionnaires. *Vet Surg* 2007; 36, 423–431
30. Tellegen AR, Willems N, Tryfonidou MA, Meij BP. Pedicle screw-rod fixation: A feasible treatment for dogs with severe degenerative lumbosacral stenosis. *BMC Vet Res* 2015; 11: 299
31. Long M, Rack HJ. Titanium alloys in total joint replacement—a materials science perspective. *Biomater* 1998;19(18):1621-1639
32. Currey JD. *Bones: Structure and mechanics*. Princeton university press; 2006.
33. Choi K, Kuhn JL, Ciarelli MJ, Goldstein SA. The elastic moduli of human subchondral, trabecular, and cortical bone tissue and the size-dependency of cortical bone modulus. *J Biomech* 1990;23(11):1103-1113
34. Rho J, Kuhn-Spearing L, Zioupos P. Mechanical properties and the hierarchical structure of bone. *Med Eng Phys* 1998;20(2):92-102
35. Rho JY, Ashman RB, Turner CH. Young's modulus of trabecular and cortical bone material: Ultrasonic and microtensile measurements. *J Biomech* 1993;26(2): 111-119
36. Mie, Keiichiro, et al. "Impaired bone quality characterized by apatite orientation under stress shielding following fixing of a fracture of the radius with a 3D printed Ti-6Al-4V custom-made bone plate in dogs." *Plos one* 15.9 (2020): e0237678.
37. Gibson LJ, Ashby MF. *Cellular solids: Structure and properties*. Cambridge University Press, Cambridge, UK. 1997.
38. Bernard S, Grimal Q, Laugier P. Accurate measurement of cortical bone elasticity tensor with resonant ultrasound spectroscopy. *J Mech Behav Biomed Mater* 2013; 18: 12-19
39. Hollister SJ. Scaffold design and manufacturing: From concept to clinic. *Adv Mater*. 2009;21(32-33):3330-3342.
40. Langer R, Vacanti JP: *Tissue engineering*. Science. 1993;260(5110):920-926.
41. Langer RS, Vacanti JP. *Tissue engineering: The challenges ahead*. *Sci Am*. 1999;280(4):86-89.
42. Cima LG, Vacanti JP, Vacanti C, Ingber D, Mooney D, Langer R. *Tissue engineering by cell transplantation using degradable polymer substrates*. . 1991.
43. Langer R, Cima LG, Tamada JA, Wintermantel E. *Future directions in biomaterials*. *Biomaterials*. 1990;11(9):738-745.
44. Yavari SA, van der Stok J, Chai YC, et al. Bone regeneration performance of surface-treated porous titanium. *Biomaterials*. 2014;35(24):6172-6181.
45. Wauthle R, Van Der Stok J, Yavari SA, et al. Additively manufactured porous tantalum implants. *Acta biomaterialia*. 2015;14:217-225.
46. Wang H, Su K, Su L, Liang P, Ji P, Wang C. The effect of 3D-printed Ti6Al4V scaffolds with various macropore structures on osteointegration and osteogenesis: a biomechanical evaluation. *J Mech Behav Biomed Mater* 2018;88:488-496
47. Wang H, Su K, Su L, Liang P, Ji P, Wang C. Comparison of 3D-printed porous tantalum and titanium scaffolds on osteointegration and osteogenesis. *Mater Sci Eng C Biomim Supramol Syst* 2019;104:109908

48. Tanzer M, Chuang P, Ngo C, Song L, TenHuisen K. Characterization of bone ingrowth and interface mechanics of a new porous 3D printed biomaterial. *Bone Joint J.* 2019;101-B(6_Supple_B):62-67
49. Reints Bok T, Willemsen K, Rijen M, Grinwis G, Tryfonidou M, Meij B. Instrumented cervical fusion in nine dogs with caudal cervical spondylomyelopathy. *Vet Surg* 2019;48(7):1287-1298
50. Li JP, Habibovic P, van den Doel M, et al. Bone ingrowth in porous titanium implants produced by 3D fiber deposition. *Biomaterials.* 2007;28(18):2810-2820.
51. Ouyang P, Dong H, He X, et al. Hydromechanical mechanism behind the effect of pore size of porous titanium scaffolds on osteoblast response and bone ingrowth. *Mater Des.* 2019;183:108151
52. Hielm-Björkman, Anna K., Hannu Rita, and Riitta-Mari Tulamo. "Psychometric testing of the Helsinki chronic pain index by completion of a questionnaire in Finnish by owners of dogs with chronic signs of pain caused by osteoarthritis." *American Journal of Veterinary Research* 70.6 (2009): 727-734.
53. Popescu, Diana, et al. "Workflow for additive manufacturing of an individualized surgical template." *Proceedings in Manufacturing Systems* 10.3 (2015): 131.



The background is a solid blue color. It features several sets of thin, parallel lines that run diagonally across the page. One set of lines is in the top-left corner, another set is in the bottom-left corner, and a third set is in the bottom-right corner. The lines are light blue and create a sense of movement and depth.

PART 4

BEDSIDE



CHAPTER 14

MRI-based synthetic CT shows equivalence to conventional CT for the morphological assessment of the hip joint

Mateusz C. Florkow | Koen Willemsen | Frank Zijlstra | Wouter Foppen |
Bart C. H. van der Wal | Jochem R. N. van der Voort van Zyp |
Max A. Viergever | René M. Castelein | Harrie Weinans |
Marijn van Stralen | Ralph J. B. Sakkers | Peter R. Seevinck

Published in Journal of Orthopaedic Research (2021)
<https://doi.org/10.1002/jor.25127>

Abstract

This study evaluated the accuracy of synthetic computed tomography (sCT), as compared to CT, for the 3D assessment of the hip morphology. Thirty male patients with asymptomatic hips, referred for magnetic resonance (MR) imaging and CT, were included in this retrospective study. sCT images were generated from three-dimensional radiofrequency-spoiled T1-weighted multi-echo gradient-echo MR images using a commercially available deep learning-enabled software and were compared with CT images through mean error and surface distance computation and by means of eight clinical morphometric parameters relevant for hip care. Parameters included center-edge angle (CEA), sharp angle, acetabular index, extrusion index, femoral head center-to-midline distance, acetabular version (AV), and anterior and posterior acetabular sector angles. They were measured by two senior orthopedic surgeons and a radiologist in-training on CT and sCT images. The reliability and agreement of CT- and sCT-based measurements were assessed using intraclass correlation coefficients (ICCs) for absolute agreement, Bland–Altman plots, and two one-sided tests for equivalence. The surface distance between CT- and sCT-based bone models were on average submillimeter. CT- and sCT-based measurements showed moderate to excellent interobserver and intraobserver correlation ($0.56 < \text{ICC} < 0.99$). In particular, the inter/intraobserver agreements were good for AV ($\text{ICC} > 0.75$). For CEA, the intraobserver agreement was good ($\text{ICC} > 0.75$) and the interobserver agreement was moderate ($\text{ICC} > 0.69$). Limits of agreements were similar between intraobserver CT and intermodal measurements. All measurements were found statistically equivalent, with average intermodal differences within the intraobserver limits of agreement. In conclusion, sCT and CT were equivalent for the assessment of the hip joint bone morphology.

Introduction

The initial diagnosis and evaluation of hip structural disorders, such as hip dysplasia or femoral acetabular impingement, are generally performed on anteroposterior and lateral radiographs. However, because radiographs only represent a two-dimensional (2D) projection, they might not reflect the full 3D variation in bone shape resulting from the disorder.[1]

3D imaging techniques provide a visualization of the entire hip anatomy and enable postacquisition 3D reformatting to standardize patient positioning,[2] as patient positioning might affect the diagnosis.[3] As a result, 3D imaging, whether based on magnetic resonance imaging (MRI) or on computed tomography (CT), has been shown to improve the diagnosis[4, 5] and the surgical planning[6, 7] of hip morphological disorders. In addition, MR and CT have similar diagnostic power, providing accurate bone models[8, 9] and morphometric measurements of the hip which correlate well with each other[10, 11] and with radiography-based measurements.[12, 13]

MR images are commonly used for diagnostic purposes in orthopedic care[14, 15] due to their ability to expose defects in periarticular and intraarticular soft tissues.[16] However, the nonselective visualization of bone on common MR images complicates both bone modeling and the measurement of diagnostic parameters as extra care needs to be taken to discriminate bone from soft tissues such as the labrum[13] or ligaments.[17] CT has traditionally been the modality of choice for the assessment of osseous structures, enabling 3D bone visualization for diagnostic purposes[18] and for a range of motion analysis[5, 19] with bone models generated faster than with MR images.[20] However, CT imaging introduces an adverse radiation burden,[11] especially for younger populations. Low-dose CT techniques have been developed in the last decade to limit the radiation burden[21] but when bone and soft tissue information is required, two modalities still have to be acquired and processed.

To produce a radiation-free alternative that would provide accurate morphometric measurements for diagnosis whilst enabling fast and accurate bone modeling for planning, CT surrogates could be obtained from MR. Such a unimodal workflow would reduce patients' burden and simplify clinical workflow. Accordingly, MR sequences have been developed to acquire images with CT-like contrast, of which the most promising is zero-echo time (ZTE) imaging.[10, 22] However, this technique is not quantitative, requires dedicated hardware, and is prone to false-positive bone identification at water-fat interfaces and fascia.[22] Alternatively, MR-based synthetic computed tomography (sCT) offers a quantitative CT-like contrast, intrinsically registered to the MR images. Although thoroughly investigated for radiotherapy treatment planning and positron emission

tomography–MRI attenuation correction,[23] the use of sCT for orthopedic purposes is limited. Recent studies reported promising results, demonstrating overall accurate bone geometry on sCT in lower arms in an ex vivo setting,[24] and in vivo in the cervical spine,[25] lumbar spine,[26] and in the sacroiliac joint.[27]

The aim of this study was to evaluate the accuracy of sCT, as compared to CT, for the 3D assessment of the hip morphology. We compared the morphology of the hip joint as assessed on CT and sCT using global surface distance metrics and local morphometric parameters that are clinically relevant for diagnostic indications in orthopedic care. It was hypothesized that bone morphology and contrast are reconstructed accurately by sCT generation models, thus providing a radiation-free time effective method for diagnostic and planning in hip care.

Methods

This retrospective equivalence study was performed in accordance with the regulations of the local medical ethical committee, and waiver of written informed consent was obtained (18-381/C).

Data collection

Imaging datasets of male patients were randomly collected from an existing radiotherapy database containing patients who underwent CT and MRI between October 2017 and April 2018 for the treatment of prostate cancer. Only patients without any implants were included.

MR images were acquired using a 3T scanner (Ingenia; Philips Healthcare), using a torso coil in combination with a multi-echo gradient-echo sequence. Acquisition parameters included echo times of 2.1, 3.5, and 4.8 ms, a repetition time of 6.5 ms, a total acquisition time of 2 min 38 s, and a flip angle of 10°. Images were acquired axially at a resolution of 1.2 mm × 1.2 mm × 2 mm and were reconstructed from the k-space by the scanner at a resolution of 0.97 mm × 0.97 mm × 1 mm, in a 448 × 448 × 160 matrix.

CT scans (Brilliance CT Big Bore; Philips Healthcare) were reconstructed at a slice spacing of 3 mm and a pixel spacing ranging from 0.8 to 1.1 mm as per the standard radiotherapy clinical protocol. MR and CT images have been acquired within 1 h, in head-first supine position.

sCT images were generated fully automatically from the first two MR echoes using a deep learning-enabled software for sCT generation (BoneMRI v1.1; MRGuidance B.V.). The

software is based on a 3D patch-based UNet-like neural network[28, 29] that was trained on patients from a similar cohort (radiotherapy patients). Images thus generated have the same resolution, orientation, and matrix size as the MR images. sCT images were generated in 2 min 53 s on a GeForce RTX 2080 Ti (NVIDIA) graphics processing unit.

Bone morphology and contrast

Bone morphology and contrast on sCT images were validated against CT by means of mean error and surface distance metrics. Mean error expresses the voxel-wise difference between CT and sCT and reflects the difference in contrasts between both modalities. Surface distance measures the distance for each vertex on a CT-based bone model to the closest point on the sCT-based bone model and vice versa (sCT to CT). The root-mean-square error (RMSE) of the surface distance was computed as an overall indication of the morphological differences between bone structures in CT and sCT. To compute these metrics, bones were semi-automatically segmented on CT and sCT images. The segmentation was initialized with in-house deep learning software, extensively manually edited using 3D Slicer[30] and manually checked by a second observer. Then CT and sCT images were rigidly registered using the Elastix registration toolbox.[31] The registration process applied an Euler transform on the bones to minimize the intermodal advanced Mattes mutual information using adaptive stochastic gradient descent.[31] The registration was done independently for the femoral and pelvic bones.

Hip joint morphometric parameters

The local geometry of the hip joint as visualized on sCT images was validated by means of eight morphometric parameters that were measured by visual annotation on CT and sCT images.

Processing

Before measuring the parameters, images were first reformatted on Mimics (Mimics medical v.22; Materialize) to correct for interscan changes in body position. The reformatting process included the alignment of the centers of the femoral heads in the coronal and axial planes, followed by the sagittal correction of the tilt to the anterior pelvic plane. [2] The anterior pelvic plane was defined as the plane containing the pubic symphysis and the anterior superior iliac spines[2] and was aligned with the coronal plane. These processing steps were applied manually and independently on the CT and sCT images. For these measurements, CT and sCT images were not registered.

After the corrections, the axial and coronal planes containing the centers of the femoral heads were extracted and used to perform clinical measurements. As a result, all the measurements presented hereinafter were done in predefined axial and coronal planes, facilitating a one-to-one comparison between modalities and between observers.

Morphometric parameters

Parameters measured in the coronal plane included central center-edge angle (CEA), acetabular index (AI) (also known as Tönnis angle, or “horizontal toit externe”), sharp angle (SA), extrusion index (EI), and femoral head center-to-midline distance (FHCM). [32, 33] Measurements done in the axial plane included anterior acetabular sector angle (AASA), posterior acetabular sector angle (PASA), and acetabular version (AV), [33] all measured cranially and centrally. Schematic definitions of these parameters are given in Figures 1B and 1D. These parameters were measured as they are used in the management and preoperative assessment of orthopedic disorders. [33-36]

To extract the aforementioned parameters, anatomical landmarks were annotated by three readers on the images as presented in Figures 1A and 1C. The desired distances and angles were subsequently automatically computed using Matlab 2017a (MathWorks, Inc.) using the coordinates of the annotations.

Readers

Two senior orthopedic surgeons (R.S. and B.W., with a specialist experience of 23 and 12 years, respectively) and a radiologist in-training with a specialization in musculoskeletal radiology (W.F.) independently identified the anatomical landmarks on the images. Readers annotated the landmarks independently and were blinded to the other readers' measurements. CT and sCT were randomly shuffled for the annotations and no mention was given to whether a CT or sCT was being annotated. For the assessment of the intraobserver variability, R.S. repeated his annotations with a 1-month interval.

Statistical analysis

Reliability was measured by means of intraclass correlation coefficients (ICCs) for absolute agreement for the inter- and intraobserver variabilities. [37] The CT-to-sCT intermodal agreement was assessed using a Bland–Altman analysis. [38]

The equivalence between CT and sCT was tested for each measurement using paired two-sided tests (TOST). [39] This test checked whether the average difference between the CT- and sCT-based measures differed by more than a user-defined equivalency margins ($\pm\Delta$). Δ was defined as the intraobserver limit of agreement (LoA), computed as $1.96 * \sigma_{\text{intra}}$, where σ_{intra} is the intraobserver standard deviation obtained from the literature. When σ_{intra} was not available, the standard deviation of the interobserver variability, σ_{inter} , was used instead. Values for the reference inter- and intraobserver LoAs are given in Figures 1B and 1D. [10, 36, 40, 41] TOSTs were performed separately on the left and right hips to meet the data independence assumption required by the statistical test. A Bonferroni correction was applied to correct for the 16 repeated comparisons (8 parameters, left/right for data independence). As such, $p < 1.6E-3$

was considered significant. The normality of the data was determined using a Shapiro–Wilk test and homoscedasticity using a two-sample *F*-test.

Before the study, a sample size calculation had been performed as described by Chow et al.[42] for a one-sample design, given the mean (1.2°) and standard deviation (4.1°) of the CT-to-MR difference previously reported in the literature for CEA.[10] It resulted in a required sample size of 30 paired measurements for the CEA. All statistical tests were done in Matlab 2017a (MathWorks, Inc.).

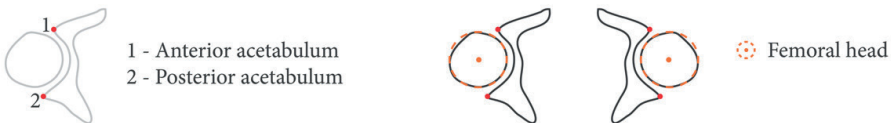
(A) Coronal plane annotations:



(B) Coronal plane measurements:

Center edge angle (CEA)	Acetabular index (AI)	Sharp angle (SA)	Extrusion index (EI)	Femoral head center mid-line distance (FHCM)
± 4.2° / 6.4° Engesaeter, 2012	± 5.6° / 6.3° Engesaeter, 2012	± 2.9° / 3.5° Engesaeter, 2012	± 6.1 / 9.2 Engesaeter, 2012	± 4.5 mm* Alazzawi, 2012

(C) Axial plane annotations:



(D) Axial plane measurements:

Anterior acetabular sector angle (AASA)	Posterior acetabular sector angle (PASA)	Acetabular anteversion (AV)
± 4.9°** Hingsammer, 2014	± 4.9°** Hingsammer, 2014	± 4.3°* Breighner, 2019

Figure 1. Anatomical landmarks annotated by the readers in the (A) coronal and (C) axial planes. Points defined remarkable anatomical landmarks, circles modeled femoral heads, and a line defined the pubic symphysis. (B and D) Measurements derived from these landmarks in the (B) coronal and (D) axial planes. For each measurement, literature values of ±1.96* standard deviation (σ) of the intra/interobserver variability are given. * = only the interobserver values were found in the literature. σ_{inter} was reported as <3°. Dashed lines indicate the horizontal and vertical in the corrected images.

Results

Demographics

Thirty male patients were included in the study accounting for 60 hip joints. The median age was 74 years (range: 59–83 years), the median weight was 82 kg (range: 66–112 kg), the median height was 175 cm (range: 150–184 cm) for a median BMI of 27.1 kg/m² (range: 23.4–43.5 kg/m²).

Bone contrast

Table 1 reports the average values of mean error and surface distance obtained between the CT and sCT. The negative mean error indicated that the HU of bone on sCT was on average underestimated.

Table 1. Root-mean-square error (RMSE) and mean error (mean ± standard deviation) obtained across the entire population to assess CT-to-sCT difference in bone morphology and contrast

Measurement	Femur	Pelvis
<i>Bilateral surface distance (RMSE in mm)</i>	0.81 ± 0.07	0.79 ± 0.16
<i>Mean error (HU)</i>	−23 ± 24	−15 ± 29

Abbreviations: CT, computed tomography; sCT, synthetic computed tomography.

Bone morphology

The average surface distance was below the image resolution with a submillimeter residual error as shown by the RMSE in Table 1. Figure 2 shows four views of the bone models obtained from the CT and sCT images together with the sCT-to-CT surface distance map. Errors were mostly located on the edge of the image, where less information is available, around the trochanter and around the ischium. A 360° view is available in Video [S1](#).

Figure 3 compares CT and sCT radial reformats of a femoral head with a bone growth around the femoral neck. Qualitatively, Figure [3A,B](#) shows no major differences between both modalities with the bump around the femoral neck correctly represented on the sCT images. The corresponding 3D bone renderings show no higher error in the region of the bump (Figure [3C](#)).

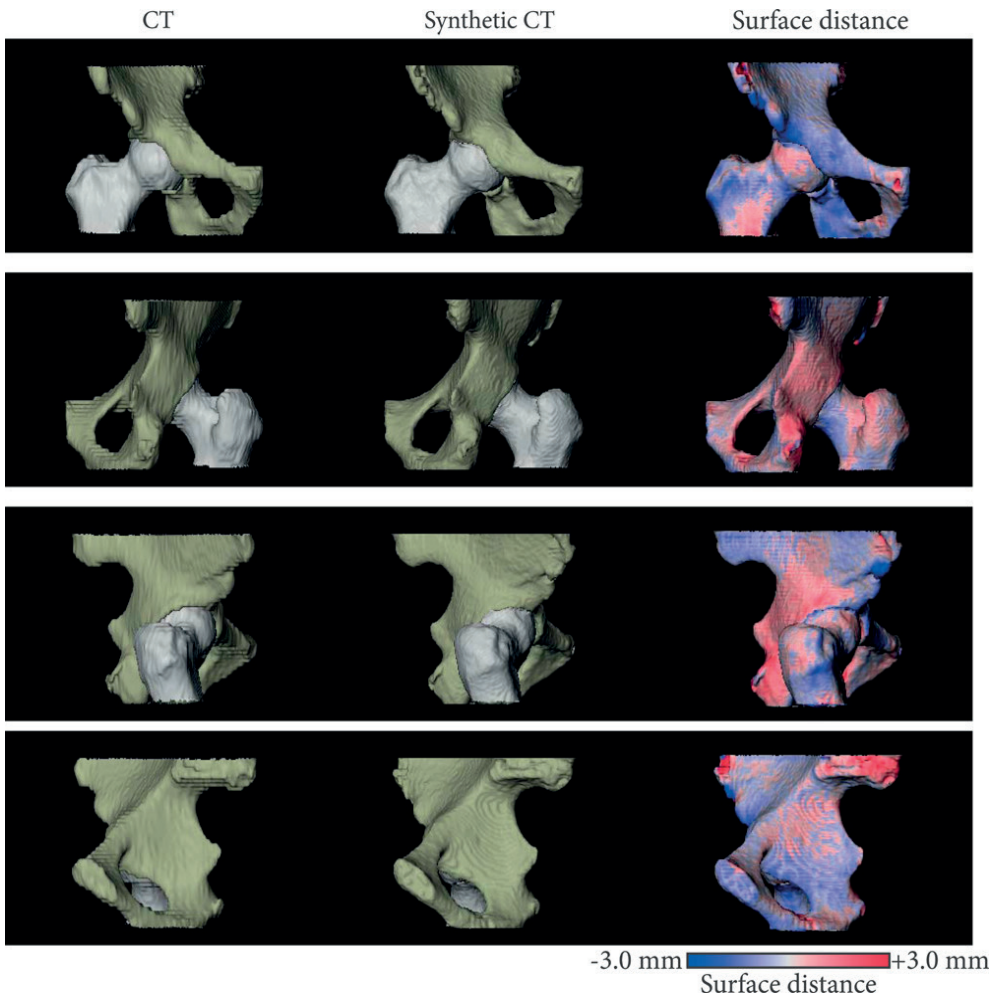


Figure 2. Bone models obtained for a right femur and pelvis as seen from four different views (from top to bottom: anterior, posterior, right, and left views). The corresponding sCT-to-CT surface distances are mapped on the sCT bone model. Negative values indicate the sCT model is larger. CT, computed tomography; sCT, synthetic computed tomography

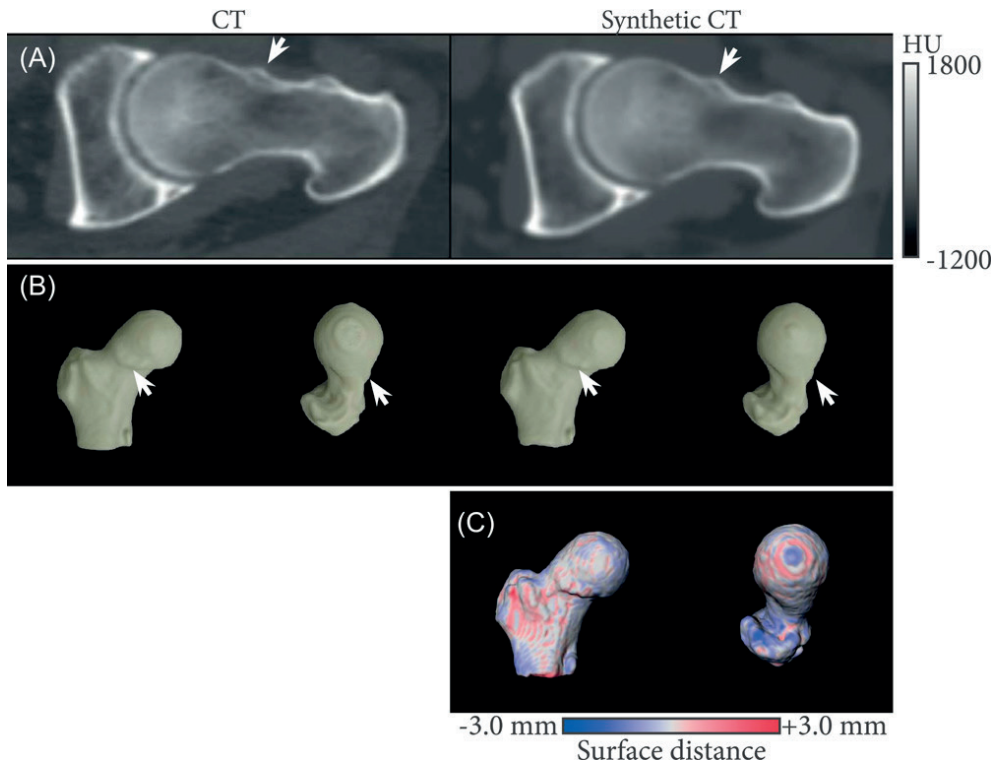


Figure 3. Qualitative comparison between CT and sCT. (A) Radial CT and sCT- based 3 o'clock reformats of the left femur obtained for one patient (where 12 o'clock indicates the superior location of the acetabulum and 3 o'clock indicates its anterior location). (B) Corresponding three-dimensional (3D) femur reconstructions as seen from anterior and superior locations. White arrows indicate a bump around the femoral neck, with good correspondence between CT and sCT images and bone 3D renderings. (C) Surface distance from the sCT bone model to the CT bone model mapped on the sCT bone model. Negative values indicate the sCT model is larger. CT, computed tomography; sCT, synthetic computed tomography

Hip joint morphometric parameters

Table 2 reports the average values (\pm standard deviation [range], CT vs. sCT) obtained for the morphometric parameters across all patients and readers. Detailed descriptive statistics per reader are given in Table S1.

Table 2. Mean, standard deviation, and range pooled across readers for all morphometric parameters for CT and sCT

Measurement	CT		sCT	
	Mean \pm SD	Range	Mean \pm SD	Range
CEA ($^{\circ}$)	35.2 \pm 6.4	[19.5–52.5]	35.6 \pm 6.8	[19.6–53.0]
SA ($^{\circ}$)	37.0 \pm 2.6	[28.1–42.7]	36.3 \pm 2.7	[27.8–42.9]
EI (%)	91.6 \pm 5.6	[77.2–106.7]	91.5 \pm 6.1	[78.2–109.2]
AI ($^{\circ}$)	4.8 \pm 3.6	[0.0–17.4]	4.8 \pm 3.6	[0.0–17.8]
FHCM (mm)	89.2 \pm 5.1	[78.2–99.7]	88.8 \pm 5.1	[77.3–97.8]
AV ($^{\circ}$)	19.1 \pm 5.2	[10.3–33.4]	19.3 \pm 5.3	[9.2–36.9]
AASA ($^{\circ}$)	61.5 \pm 7.8	[40.9–83.7]	61.5 \pm 8.3	[38.3–78.9]
PASA ($^{\circ}$)	99.5 \pm 9.1	[80.8–134.7]	99.9 \pm 7.9	[81.3–126.2]

Abbreviations: AASA, anterior acetabular sector angle; AI, acetabular index; AV, acetabular version; CEA, center-edge angle; CT, computed tomography; EI, extrusion index; FHCM, femoral head center-to-midline distance; PASA, posterior acetabular sector angle; SA, sharp angle; sCT, synthetic computed tomography.

Figure 4 presents CT and sCT images with landmarks annotated by Reader 2 for four patients in the coronal (Figure 4A) and axial (Figure 4B) planes. It exposes osteophytes (bone spurs), present around the acetabular rim of some patients and visible on both the CT and sCT. Intermodal differences were mainly observed in the identification of the medial part of the acetabular sourcil and of the lateral and posterior parts of the acetabular rim.

Figure 4C shows the pairwise differences between the measurements performed by Reader 2 on CT and sCT on the 60 hip joints. For comparative purposes, measurements are displayed relatively to the intra- and interobserver variability. No patient presented considerable differences in all measurements which indicates that the overall morphology was conserved in sCT reconstructions. The most important differences were observed for CEA, SA, AASA, and PASA, on patients with osteophytes (Figure 4A,B).

Statistical analysis

The interobserver ICC ranged from 0.56 (AI) to 0.99 (FHCM) for CT and from 0.62 (PASA) to 0.97 (FHCM) for sCT. The intraobserver ICC ranged from 0.68 (EI) to 0.99 (FHCM) for CT and from 0.62 (EI) to 0.97 (FHCM) for sCT. According to Koo et al.,[43] these values indicate moderate ($ICC > 0.5$) to excellent ($ICC > 0.9$) correlation between and within observers. Detailed values per measurement are given in Table 3. The CT intraobserver average difference (\pm standard deviation) pooled across patients was $-0.9^{\circ} \pm 4.1^{\circ}$ for CEA, $1.1^{\circ} \pm 1.7^{\circ}$ for SA, -0.3 ± 5.6 for EI, $-0.4^{\circ} \pm 2.9^{\circ}$ for AI, 0.1 ± 1.0 for FHCM, $0.7^{\circ} \pm 2.5^{\circ}$ for AV, $3.3^{\circ} \pm 3.1^{\circ}$ for AASA, and $4.9^{\circ} \pm 5.2^{\circ}$ for PASA.

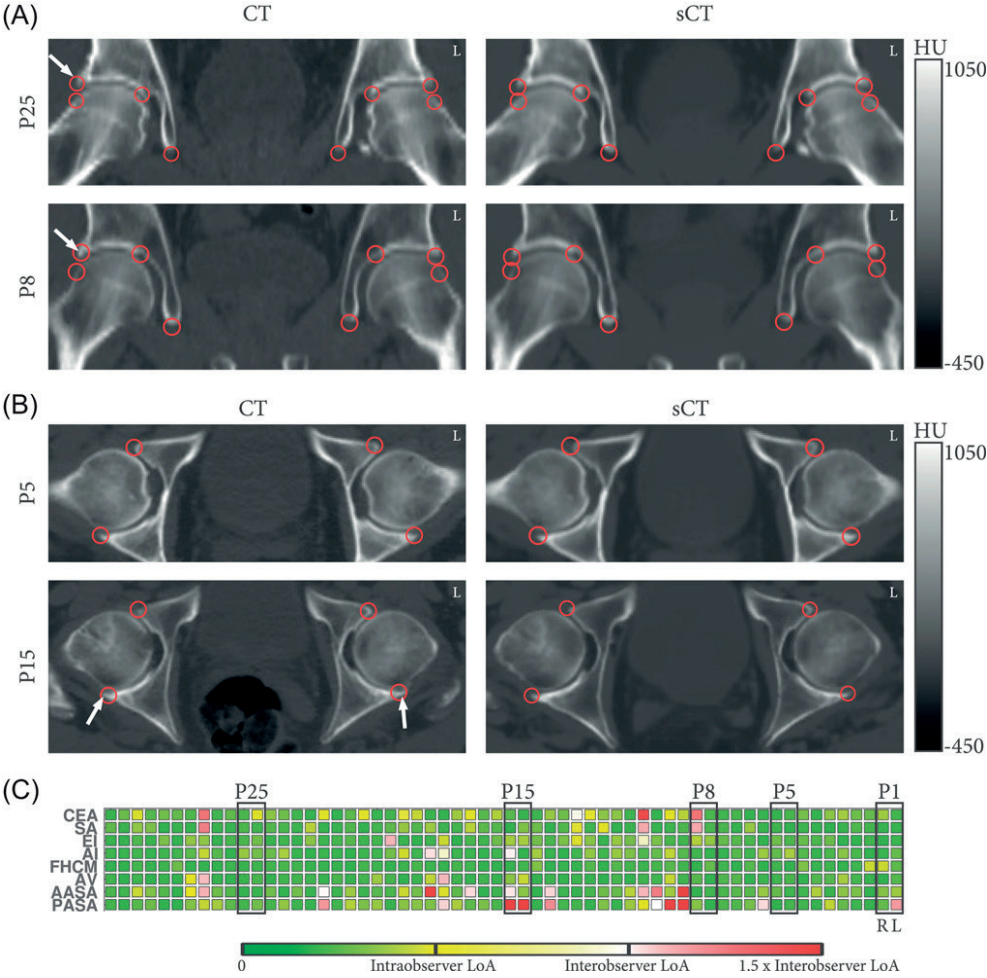


Figure 4. Bone models obtained for a right femur and pelvis as seen from four different views (from top to bottom: anterior, posterior, right, and left views). The corresponding sCT-to-CT surface distances are mapped on the sCT bone model. Negative values indicate the sCT model is larger. CT, computed tomography; sCT, synthetic computed tomography

Figure 5 presents Bland–Altman plots between CT and sCT for each measurement. The agreement between CT- and sCT-based measurements was similar to the intraobserver agreement as obtained by Reader 1. In addition, for most parameters, the LoAs of the difference between CT and sCT were similar to the LoA of the intra- and interobserver variability found in the literature, confirming the agreement between CT- and sCT-based measurements.

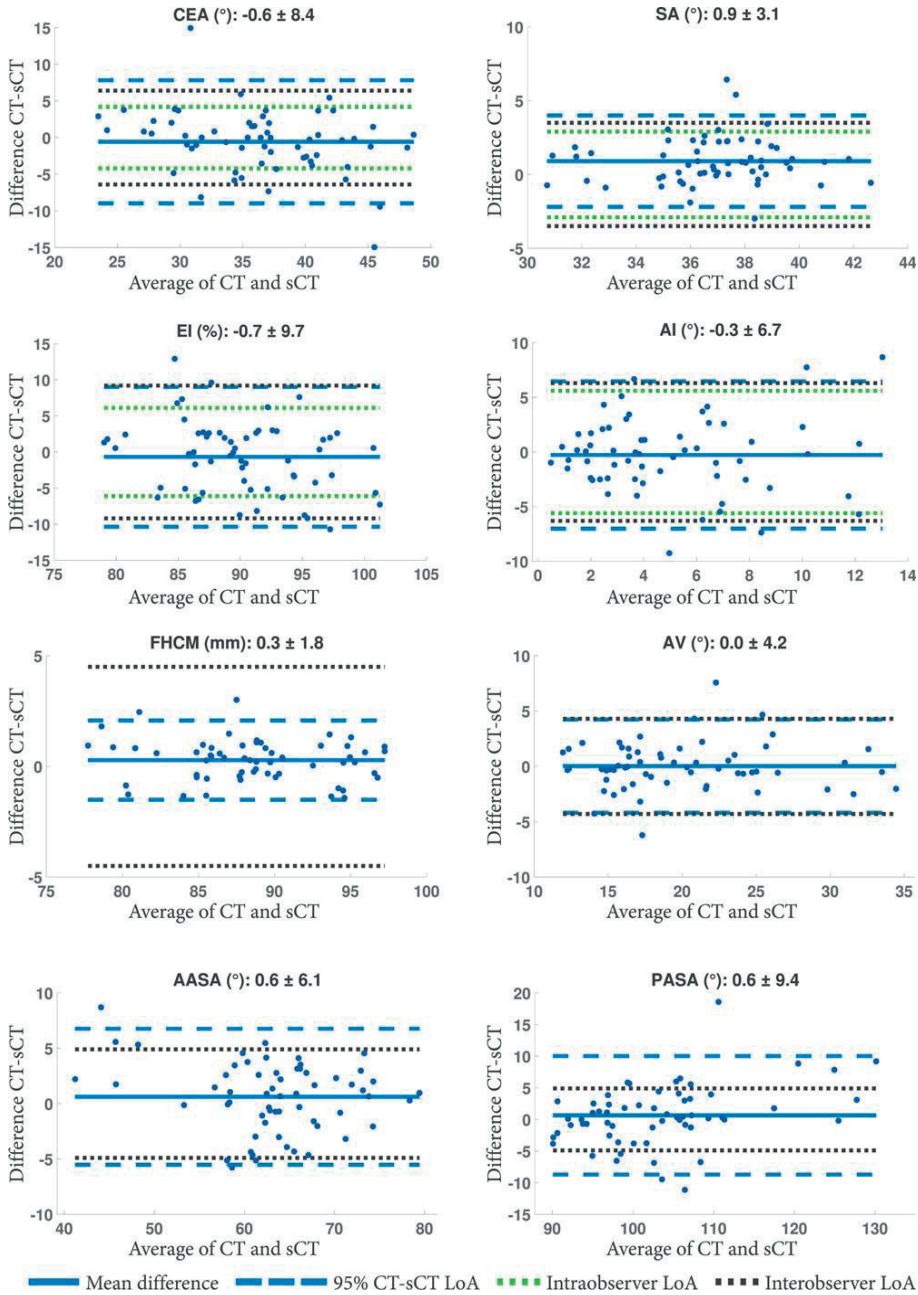


Figure 5. Bland–Altman plots for the agreement between the CT and sCT measurements (bias ± limit of agreement [LoA]). LoA of the inter/intraobserver variability found in the literature are given when available. AASA, anterior acetabular sector angle; AI, acetabular index; AV, acetabular version; CEA, center-edge angle; CT, computed tomography; EI, extrusion index; FHCM, femoral head center-to-midline distance; PASA, posterior acetabular sector angle; SA, sharp angle; sCT, synthetic computed tomography

Table 3. Interobserver and intraobserver variability obtained for each parameter as measured by the intraclass correlation coefficient (ICC) for absolute agreement

Measurement	Interobserver				Intraobserver			
	CT		sCT		CT		sCT	
	ICC	95% CI	ICC	95% CI	ICC	95% CI	ICC	95% CI
CEA	0.77	[0.57, 0.87]	0.69	[0.36, 0.84]	0.84	[0.75, 0.90]	0.79	[0.67, 0.87]
SA	0.83	[0.75, 0.88]	0.75	[0.60, 0.84]	0.82	[0.63, 0.91]	0.72	[0.52, 0.83]
EI	0.67	[0.52, 0.79]	0.65	[0.51, 0.76]	0.68	[0.52, 0.80]	0.62	[0.43, 0.75]
AI	0.56	[0.41, 0.69]	0.72	[0.61, 0.81]	0.77	[0.64, 0.85]	0.71	[0.56, 0.82]
FHCM	0.99	[0.98, 0.99]	0.97	[0.91, 0.98]	0.99	[0.98, 0.99]	0.97	[0.95, 0.98]
AV	0.85	[0.76, 0.91]	0.88	[0.82, 0.92]	0.88	[0.80, 0.93]	0.88	[0.81, 0.93]
AASA	0.91	[0.77, 0.96]	0.82	[0.70, 0.89]	0.89	[0.58, 0.96]	0.86	[0.40, 0.95]
PASA	0.66	[0.34, 0.81]	0.62	[0.41, 0.76]	0.76	[0.23, 0.90]	0.72	[0.28, 0.87]

Note: Confidence intervals (CIs) were computed at a 95% confidence level.

Abbreviations: AASA, anterior acetabular sector angle; AI, acetabular index; AV, acetabular version; CEA, center-edge angle; CT, computed tomography; EI, extrusion index; FHCM, femoral head center-to-midline distance; PASA, posterior acetabular sector angle; SA, sharp angle; sCT, synthetic computed tomography.

The average difference (\pm standard deviation) between CT- and sCT-based measurements pooled across readers and patients was $-0.8^\circ \pm 3.4^\circ$ for CEA, $0.7^\circ \pm 1.4^\circ$ for SA, 0.2 ± 3.3 for EI, $-0.1^\circ \pm 2.9^\circ$ for AI, 0.7 ± 1.2 for FHCM, $-0.5^\circ \pm 1.7^\circ$ for AV, $-0.4^\circ \pm 3.6^\circ$ for AASA, and $-1.5^\circ \pm 3.9^\circ$ for PASA. All measurements performed on sCT were statistically equivalent to CT measurements at the considered equivalency margins. The detailed mean difference between the CT- and sCT-based measurements obtained for each reader, together with the Bonferroni-corrected 95% confidence interval (CI) of the TOST are given in Table S2.

Discussion

Abnormalities of the hip joint morphology are associated with various hip disorders affecting the bone and periarticular and intraarticular soft tissues. 3D bone morphology is usually assessed using CT images despite their radiation burden and poor soft tissue visualization. In this study, we investigated the accuracy of an MR-based sCT method for assessing bone morphology in the hip joint. sCT was automatically generated by a commercial software running on a server connected to a picture archiving and communication system. By comparing 3D bone models and measuring eight morphometric parameters relevant for hip care, we confirmed the equivalence of CT and sCT for the morphological assessment of the hip joint.

The surface distance between CT- and sCT-based bone models were on average below the MRI voxel resolution and the residual errors were on average submillimetre. Hence, the overall bone geometry was reconstructed accurately on sCT images. On a local scale, the average values of the morphometric parameters representing the 3D morphology reported in the present study were found to be comparable between CT and sCT. In addition, these values were in agreement with a recent study reporting reference values for hip morphometric parameters in male asymptomatic patients⁴⁴: $33^\circ \pm 6^\circ$ for CEA, $3^\circ \pm 5^\circ$ for AI, $15^\circ \pm 5^\circ$ for AV, $60^\circ \pm 7^\circ$ for AASA, and $92^\circ \pm 7^\circ$ for PASA.

Statistical analyses showed strong reliability between and within readers, with ICC values indicating moderate to excellent correlations. The intraobserver ICC was in line with a study by Air et al.,^[12] which reported values of 0.83 [CI: 0.70–0.90] for CEA (vs. 0.84 present study) and of 0.75 [CI: 0.55–0.86] for AI (vs. 0.77). The interobserver ICC was within the values reported in the literature, knowing that, in patients with hip disorders, the interobserver ICC can vary from 0.78 [CI: 0.69–0.85] to 0.95 [CI: 0.91–0.98] for CEA (vs. 0.77), from 0.87 [CI: 0.80–0.92] to 0.98 [CI: 0.93–0.99] for AI (vs. 0.56) and from 0.68 [CI: 0.55–0.78] to 0.95 [CI: 0.81–0.99] for AV (vs. 0.85).^[10, 12, 45] The interobserver ICC reported in this study might be in the literature lower range for several reasons. First, the inclusion of elderly patients, prone to degenerative changes such as osteophytes which would not be present in the younger population. Despite being visible on both modalities, osteophytes made the identification of the acetabular rim more challenging and less consistent. Second, annotations were performed by readers with different backgrounds (orthopedic surgery and musculoskeletal radiology), which could have increased the interobserver variability. Finally, the 3 mm slice spacing on the CT images made the landmark identification in the coronal plane less precise. As the sCT generation model was trained to reproduce CT images with such slice spacing, sCT images were probably not favored over CT images for identifying anatomical landmarks.

The degree of agreement and equivalence between CT- and sCT-based measurements were assessed using reference values of intraobserver and interobserver variability. Intra- and interobserver LoAs defined the acceptable CT-to-sCT difference, suggesting that, for sCT to be clinically acceptable, the error made when annotating sCT images should not be larger than the error made when repeating measurements. As radiography is the current standard for diagnosing hip disorders, literature values of radiography-based variability were used as a reference for measurements in the coronal plane. For measurements in the axial plane, CT-based variability was used as a reference.

Concerning the agreement between CT and sCT, the Bland–Altman analysis did not expose any biases for any measurements, indicating no systematic difference. Limits of agreements between CT and sCT were similar to the reference intraobserver LoAs for SA, EI, AI, FHCM,

and AASA and to the interobserver LoA for CEA and AV. Therefore, the presented results suggest the interchangeability[38] of CT and sCT to perform these measurements if the inter- and intraobserver differences are considered clinically acceptable. The LoAs were marginally larger for the CEA, AV, and PASA probably due to a less consistent annotation of the lateral and posterior acetabular rims, but were still within the literature limits with Breighner et al.[10] reporting CT-to-MRI intermodal LoA of $\pm 8.0^\circ$ for CEA and $\pm 7.0^\circ$ for AV. Differences in annotations might have resulted from the presence of osteophytes as suggested by the high intraobserver variability obtained for PASA in this study. As for the equivalence, the TOST demonstrated a statistical equivalence between CT and sCT with the estimated average intermodal differences within the intraobserver variability of the measurements. These results are in line with previous studies demonstrating similar diagnostic power for CT and MRI for assessment of bone anatomy[11] and morphometric parameters. In particular, CT and ZTE MR images have been demonstrated to have a good to excellent agreement.[10] Compared to ZTE imaging which is an acquisition-based method for bone visualization, sCT is a postprocessing technique that provides CT-like Hounsfield units. Therefore, any common radiological processing done on CT images should be doable on sCT images. No additional learning and development should be required. Furthermore, although becoming increasingly available,[46] ZTE imaging still requires hardware that is not available in all hospitals.

The presented study has some limitations. The study focused on the acetabular morphology of asymptomatic male patients. The inclusion of femoral parameters, such as the alpha angle,[47] was limited by the field of view of the MR images which did not fully cover the femoral neck, nor the pelvis. However, as a surrogate for the femoral parameters, the overall femoral morphology deviation between CT- and sCT-based bone renderings was computed. Although only asymptomatic patients were considered, based on these results, measurements made on sCT for this patient population are within the submillimetre accuracy of CT. Given the ability of the sCT generation model to capture morphological variations (osteophytes, bumps), we expect measurements made on sCT images for symptomatic patients (e.g., with cam lesions) to be similarly comparable to CT. Furthermore, the age and sex distribution were not representative of the patient population with hip disorders. Femoroacetabular impingement and hip dysplasia are more prevalent in adolescents and young adults. However, the purpose of this study was to assess the agreement between CT and sCT and we do not expect relevant differences in sCT generation between our study population and the target population. Sex-related changes in bone shape should not affect the model as it is a patch-based method, not prone to global morphological changes as demonstrated in a study performed in canines of various shapes and sizes that used a similar method.[29] Another factor that could potentially influence the voxel-wise accuracy of sCT generation is bone density. However,

as bone density is expected to be in the same range in elderly males and young adults, the intermodal differences should be similar between the two groups.

In conclusion, sCT is a promising alternative to CT for the assessment of hip disorders. It provided a submillimeter 3D assessment of bone morphology compared to CT and enabled the measurement of acetabular parameters equivalently to CT, without the ionizing radiation burden. In combination with the soft tissue information of the original MRI sequences, this opens new possibilities in the diagnosis and surgical planning of hip disorders.

Supplementary Information

<https://doi.org/10.1002/jor.25127>

References

1. Atkins PR, Shin Y, Agrawal P, et al. Which two-dimensional radio-graphic measurements of cam femoroacetabular impingement best describe the three-dimensional shape of the proximal femur? *ClinOrthop Relat Res.* 2019;477(1):242-253.
2. Larson CM, Moreau-Gaudry A, Kelly BT, et al. Are normal hips being labeled as pathologic? A CT-based method for defining normal acetabular coverage. *Clin Orthop Relat Res.* 2015;473(4): 1247-1254.
3. Ross J, Nepple J, Philippon M, Kelly B, Larson C, Bedi A. The influence of pelvic tilt on common acetabular parameters and range of motion in patients with femoroacetabular impingement (FAI). *Arthroscopy.* 2013;29(12):e203.
4. Mascarenhas VV, Rego P, Dantas P, Gaspar A, Soldado F, Consciência JG. Cam deformity and the omega angle, a novel quantitative measurement of femoral head-neck morphology: a 3D CT gender analysis in asymptomatic subjects. *Eur Radiol.* 2017;27(5): 2011-2023.
5. Kraeutler MJ, Chadayammuri V, Garabekyan T, Mei-Dan O. Femoral version abnormalities significantly outweigh effect of cam impingement on hip internal rotation. *J Bone Joint Surg Am.* 2018; 100(3):205-210.
6. Smet MH, Marchal GJ, Baert AL, et al. Three-dimensional imaging of acetabular dysplasia: diagnostic value and impact on surgical type classification. *Eur J Radiol.* 2000;34(1):26-31.
7. Audenaert EA, Mahieu P, Pattyn C. Three-dimensional assessment of cam engagement in femoroacetabular impingement. *Arthroscopy.* 2011;27(2):167-171.
8. Malloy P, Gasienica J, Dawe R, et al. 1.5 T magnetic resonance imaging generates accurate 3D proximal femoral models: Surgical planning implications for femoroacetabular impingement. *J Orthop Res.* 2020;38(9):2050-2056.
9. Stephen JM, Calder JD, Williams A, El Daou H. Comparative accuracy of lower limb bone geometry determined using MRI, CT, and direct bone 3D models [online ahead of print]. *J Orthop Res.* 2020.
10. Breighner RE, Bogner EA, Lee SC, Koff MF, Potter HG. Evaluation of osseous morphology of the hip using zero echo time magnetic resonance imaging. *Am J Sports Med.* 2019;47(14):3460-3468.
11. Samim M, Eftekhary N, Vigdorichik JM, et al. 3D-MRI versus 3D-CT in the evaluation of osseous anatomy in femoroacetabular impingement using Dixon 3D FLASH sequence. *Skeletal Radiol.* 2019; 48(3):429-436.
12. Air ME, Harrison JR, Nguyen JT, Kelly BT, Bogner EA, Moley PJ. Correlation of measurements of the prearthritic hip between plain radiography and computed tomography. *PM R.* 2018;11:158-166.
13. Stelzener D, Hingsammer A, Bixby SD, Kim Y-J. Can radiographic morphometric parameters for the hip be assessed on MRI? *ClinOrthop Relat Res.* 2013;471(3):989-999.
14. Mascarenhas VV, Rego P, Dantas P, et al. Imaging prevalence of femoroacetabular impingement in symptomatic patients, athletes, and asymptomatic individuals: a systematic review. *Eur J Radiol.* 2016;85(1):73-95.
15. Sutter R, Pfirrmann CWA. Update on femoroacetabular impingement: what is new, and how should we assess it? *Semin Musculoskelet Radiol.* 2017;21(5):518-528.

16. Bredella MA, Stoller DW. MR imaging of femoroacetabular impingement. *Magn Reson Imaging Clin N Am*. 2005;13(4):653-664.
17. Ollivier M, Stelzlen C, Boisrenoult P, Pujol N, Beaufile P. Poor re- producibility of the MRI measurement of distal femoral torsion. *Orthop Traumatol Surg Res*. 2015;101(8):937-940.
18. Lopes DS, Pires SM, Mascarenhas VV, Silva MT, Jorge JA. On a "Columbus' Egg": modeling the shape of asymptomatic, dysplastic and impinged hip joints. *Med Eng Phys*. 2018;59:50-55.
19. Röling MA, Visser MI, Oei EH, Pilot P, Kleinrensink GJ, Bloem RM. A quantitative non-invasive assessment of femoroacetabular im- pingement with CT-based dynamic simulation—cadaveric validation study clinical diagnostics and imaging. *BMC Musculoskelet Disord*. 2015;16(1):50.
20. Lerch TD, Degonda C, Schmaranzer F, et al. Patient-specific 3-D magnetic resonance imaging-based dynamic simulation of hip im- pingement and range of motion can replace 3-D computed tomography-based simulation for patients with femoroacetabular impingement: implications for planning open hip reservation sur- gery and hip arthroscopy. *Am J Sports Med*. 2019;47(12):2966-2977.
22. Su AW, Hillen TJ, Eutsler EP, et al. Low-dose computed tomography reduces radiation exposure by 90% compared with traditional computed tomography among patients undergoing hip-preservation surgery. *Arthroscopy*. 2019;35(5):1385-1392.
22. Argentieri EC, Koff MF, Breighner RE, Endo Y, Shah PH, Sneag DB. Diagnostic accuracy of zero-echo time MRI for the evaluation of cervical neural foraminal stenosis. *Spine (Phila Pa 1976)*. 2018; 43(13):928-933.
23. Edmund JM, Nyholm T. A review of substitute CT generation for MRI-only radiation therapy. *Radiat Oncol*. 2017;12(1):28.
24. Zijlstra F, Willemsen K, Florkow MC, et al. CT synthesis from MR images for orthopedic applications in the lower arm using a condi- tional generative adversarial network. In *SPIE, Medical Imaging 2019:Image Processing*. San Diego, CA; 2019. p. 109491J.
25. van der Kolk B, van Stralen M, Podlogar M, et al. Reconstruction of osseous structures in MRI scans of the cervical spine with BoneMRI: a quantitative analysis. In *58th Annual Meeting of the American So- ciety of Neuroradiology*. Boston, MA; 2019.
26. Staartjes VE, Seevinck PR, Vandertop WP, van Stralen M, Schröder ML. Magnetic resonance imaging-based synthetic com- puted tomography of the lumbar spine for surgical planning: a clinical proof-of-concept. *Neurosurg Focus*. 2021;50(1):E13.
27. Jans LBO, Chen M, Elewaut D, et al. MRI-based synthetic CT in the detection of structural lesions in patients with suspected sacroiliitis: comparison with MRI. *Radiology*. 2021;298(2):343-349.
28. Ronneberger O, Fischer P, Brox T. U-net: Convolutional networks for biomedical image segmentation. In: Navab N, Hornegger J, Wells WM, Frangi AF, eds. *Lecture Notes in Computer Science*. Cham: Springer International Publishing; 2015:234-241.
29. Florkow MC, Zijlstra F, Willemsen K, et al. Deep learning-based MR-to-CT synthesis: the influence of varying gradient echo-based MR images as input channels. *Magn Reson Med*. 2020;83(4):1429-1441.
30. Fedorov A, Beichel R, Kalpathy-Cramer J, et al. 3D slicer as an image computing platform for the quantitative imaging network. *Magn Reson Imaging*. 2012;30(9):1323-1341.

31. Klein S, Staring M, Murphy K, Viergever MA, Pluim JP. Elastix: a toolbox for intensity-based medical image registration. *IEEE Trans Med Imaging*. 2010;29(1):196-205.
32. Rabari YB, Sanap A, Prasad DV, Thadeshwar KH. The distance of the centre of femoral head relative to the midline of the pelvis: a prospective X-ray study of 500 adults. *Int J Res Orthop*. 2017;3(3):565.
33. Mascarenhas VV, Ayeni OR, Egund N, et al. Imaging methodology for hip preservation: techniques, parameters, and thresholds. *Semin Musculoskelet Radiol*. 2019;23(3):197-226.
34. Delaunay S, Dussault RG, Kaplan PA, Alford BA. Radiographic measurements of dysplastic adult hips. *Skeletal Radiol*. 1997;26(2):75-81.
35. Ömeroğlu H, Ağuş H, Biçimoğlu A, Tümer Y. Evaluation of experienced surgeons' decisions regarding the need for secondary surgery in developmental dysplasia of the hip. *J Pediatr Orthop*. 2012;32(1):58-63.
35. Alazzawi S, Field MH, Bardakos NV, Freeman MA, Field RE. The position of the centre of the femoral head relative to the midline of the pelvis: a consistent landmark in total knee replacement surgery. *Knee*. 2012;19(6):827-831.
36. Shrout PE, Fleiss JL. Intraclass correlations: uses in assessing rater reliability. *Psychol Bull*. 1979;86(2):420-428.
37. Bland JM, Altman DG. Statistical methods for assessing agreement between two methods of clinical measurement. *Lancet*. 1986; 1(8476):307-310.
39. Lakens D. Equivalence tests: a practical primer for *t* tests, correlations, and meta-analyses. *Soc Psychol Personal Sci*. 2017;8(4):355-362.
40. Engesæter IØ, Laborie LB, Lehmann TG, et al. Radiological findings for hip dysplasia at skeletal maturity. Validation of digital and manual measurement techniques. *Skeletal Radiol*. 2012;41:775-785.
41. Hingsammer AM, Bixby S, Zurakowski D, Yen YM, Kim YJ. How do acetabular version and femoral head coverage change with skeletal maturity? *Clin Orthop Relat Res*. 2015;473(4):1224-1233.
42. Chow SC, Shao J, Wang H. A note on sample size calculation for mean comparisons based on noncentral *t*-statistics. *J Biopharm Stat*. 2002;12(4):441-456.
43. Koo TK, Li MY. A guideline of selecting and reporting intraclass correlation coefficients for reliability research. *J Chiropr Med*. 2016; 15(2):155-163.
44. Mechlenburg I, Stilling M, Rømer L, de Bruijne M, Søballe K, de Raedt S. Reference values and variation of acetabular angles measured by computed tomography in 170 asymptomatic hips. *Acta Radiol*. 2019;60:895-901.
45. Heyworth BE, Dolan MM, Nguyen JT, Chen NC, Kelly BT. Preoperative three-dimensional CT predicts intraoperative findings in hip arthroscopy. *Clin Orthop Relat Res*. 2012;470(7):1950-1957.
46. de Mello RAF, Ma YJ, Ashir A, et al. Three-dimensional zero echo time magnetic resonance imaging versus 3-dimensional computed tomography for glenoid bone assessment. *Arthroscopy*. 2020;36(9): 2391-2400.
47. Nötzli HP, Wyss TF, Stoecklin CH, Schmid MR, Treiber K, Hodler J. The contour of the femoral head-neck junction as a predictor for the risk of anterior impingement. *J Bone Joint Surg Br*. 2002;84(4):556-560.



CHAPTER 15

3D-printed saw guides for lower arm osteotomy A comparison between a synthetic CT and CT-based workflow

Koen Willemsen | Mirte HM Ketel | Frank Zijlstra | Mateusz C Florkow |
Ruurd JA Kuiper | Bart CH van der Wal | Harrie Weinans | Behdad Pouran |
Freek J Beekman | Peter R Seevinck | Ralph JB Sackers

Published in 3D Printing in Medicine 7.1 (2021): 1-12.
<https://doi.org/10.1186/s41205-021-00103-x>

Abstract

Background: Three-dimensional (3D)-printed saw guides are frequently used to optimize osteotomy results and are usually designed based on computed tomography (CT), despite the radiation burden, as radiation-less alternatives like magnetic resonance imaging (MRI) have inferior bone visualization capabilities. This study investigated the usability of MR-based synthetic-CT (sCT), a novel radiation-less bone visualization technique for 3D planning and design of patient-specific saw guides.

Methods: Eight human cadaveric lower arms (mean age: 78y) received MRI and CT scans as well as high-resolution micro-CT. From the MRI scans, sCT were generated using a conditional generative adversarial network. Digital 3D bone surface models based on the sCT and general CT were compared to the surface model from the micro-CT that was used as ground truth for image resolution. From both the sCT and CT digital bone models saw guides were designed and 3D-printed in nylon for one proximal and one distal bone position for each radius and ulna. Six blinded observers placed these saw guides as accurately as possible on dissected bones. The position of each guide was assessed by optical 3D-scanning of each bone with positioned saw guide and compared to the preplanning. Eight placement errors were evaluated: three translational errors (along each axis), three rotational errors (around each axis), a total translation (ΔT) and a total rotation error (ΔR).

Results: Surface models derived from micro-CT were on average smaller than sCT and CT-based models with average differences of 0.27 ± 0.30 mm for sCT and 0.24 ± 0.12 mm for CT. No statistically significant positioning differences on the bones were found between sCT- and CT-based saw guides for any axis specific translational or rotational errors nor between the ΔT ($p = .284$) and ΔR ($p = .216$). On Bland-Altman plots, the ΔT and ΔR limits of agreement (LoA) were within the inter-observer variability LoA.

Conclusions: This research showed a similar error for sCT and CT digital surface models when comparing to ground truth micro-CT models. Additionally, the saw guide study showed equivalent CT- and sCT-based saw guide placement errors. Therefore, MRI-based synthetic CT is a promising radiation-less alternative to CT for the creation of patient-specific osteotomy surgical saw guides.

Introduction

Three-dimensional (3D) preoperative planning and 3D-printed patient-specific implants and saw guides are increasingly used during orthopedic procedures [1,2,3]. Besides a better understanding of complex anatomies, the use of 3D-printing during surgical procedures can improve surgical results, decrease operating time and decrease radiological exposure [4]. A lower arm osteotomy is one of the orthopedic applications where 3D planning tools and patient-specific saw guides show a significant clinical improvement [5]. For the 3D planning and saw guide design [6, 7], a computed tomography (CT) scan is most commonly used to create a bone model because of its excellent hard tissue contrast and high spatial resolution [8]. However, the CT's ionizing radiation is harmful, especially for young patients [9]. Even low-dose radiation increases the cancer risk and should be kept as low as possible and alternative procedures should be considered [10, 11].

A radiation-less alternative to CT is Magnetic Resonance Imaging (MRI). MRI-scans generate 3D information without ionizing radiation and provide good quality soft tissue information. Currently, MRI-scans are rarely used for 3D bone modelling and related saw guide design as their lesser bone contrast requires intensive processing to generate 3D bone renderings [12, 13]. Therefore, novel deep learning based models are developed to enhance the bone contrast: MRI-based synthetic CT (sCT) [14]. These deep learning based sCT models use convolutional neural networks (CNN) that translate MRI data into Hounsfield Units (HU). Eventually, with the MRI-scan and simultaneously generated sCT, both good quality soft tissue and hard tissue information is provided with one radiation free acquisition. However, studies investigating sCT for orthopaedic care are scarce and a validation is needed to evaluate the impact of CT-to-sCT differences [15] on 3D digital bone surface modelling and saw guide design.

The primary aim was to investigate whether the sCT-scan provides sufficiently accurate bone surface information for saw guide development when compared to micro-CT (ground truth for image resolution) and how accurate saw guide positioning is when a sCT workflow is used compared to a CT workflow. Therefore, the research question states: 'Is the precision of the synthetic-CT, compared to the precision of currently used CT, sufficient for the accurate placement of 3D printed patient-specific lower arm osteotomy saw guides?' We hypothesized that the sCT-based models would have similar performance to CT-based methods in terms of bone surface modelling and saw guide positioning.

Materials and methods

Specimens

Eight healthy fresh-frozen human cadaver lower arms (4 left and 4 right, 4 women and 4 men, mean age 78y, ranged 71-86y) were obtained via the Human Body Donation program of the University of Utrecht (Fig. 1).

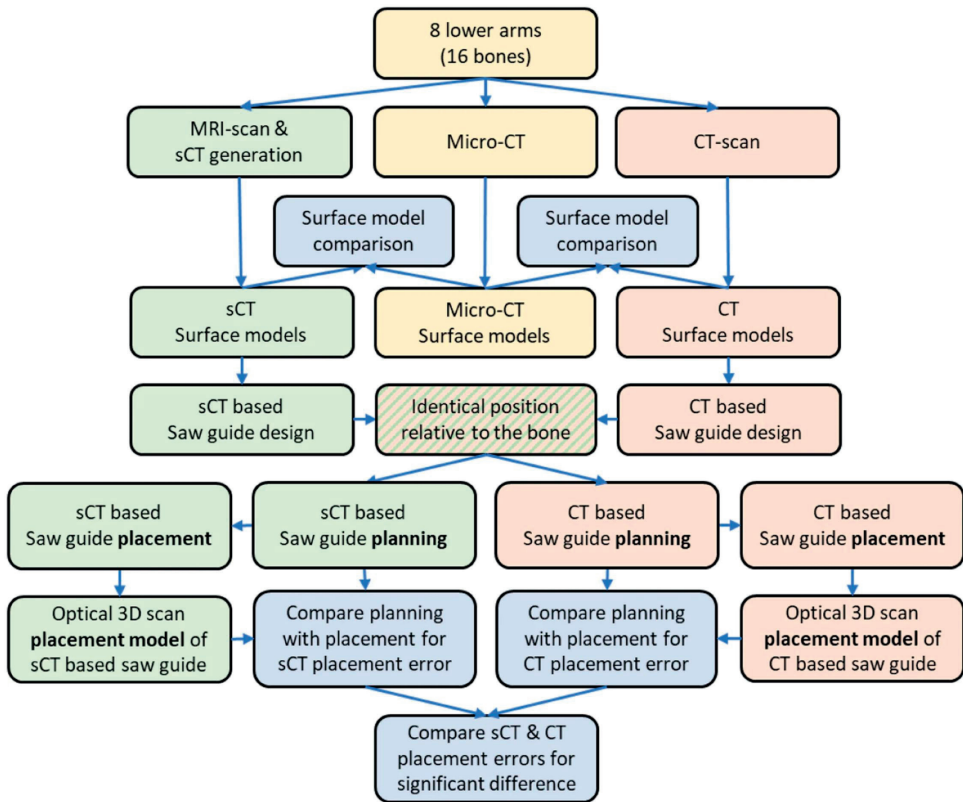


Figure 1. Study overview flowchart. The sCT pipeline is presented in green, the CT pipeline in red and the micro-CT pipeline (ground truth) in yellow. The blue boxes represent the main study outcomes.

Imaging

With the 24-h thawed intact lower arms fixed in an extended and pronated position, a CT-scan and MRI-scan were acquired in immediately succeeding sessions. The CT-scans (Philips Healthcare, Best, The Netherlands; 120 kV and 250mAs) were obtained with the following parameters: 0.3×0.3 mm pixel spacing, 0.8 mm slice thickness and 0.4 mm slice spacing (Fig. 2a). The MRI-images were obtained with a 3T scanner (Ingenua, Philips Healthcare, Best, The Netherlands) with the following parameters: 1.2 mm isotropic resolution

(reconstructed to 0.6 mm), 313x103x128mm field of view, echo times 2.1/3.25/4.4 ms, repetition time 6.9 ms, flip angle 15°, and a total scan duration of 151 s (Fig. 2b).

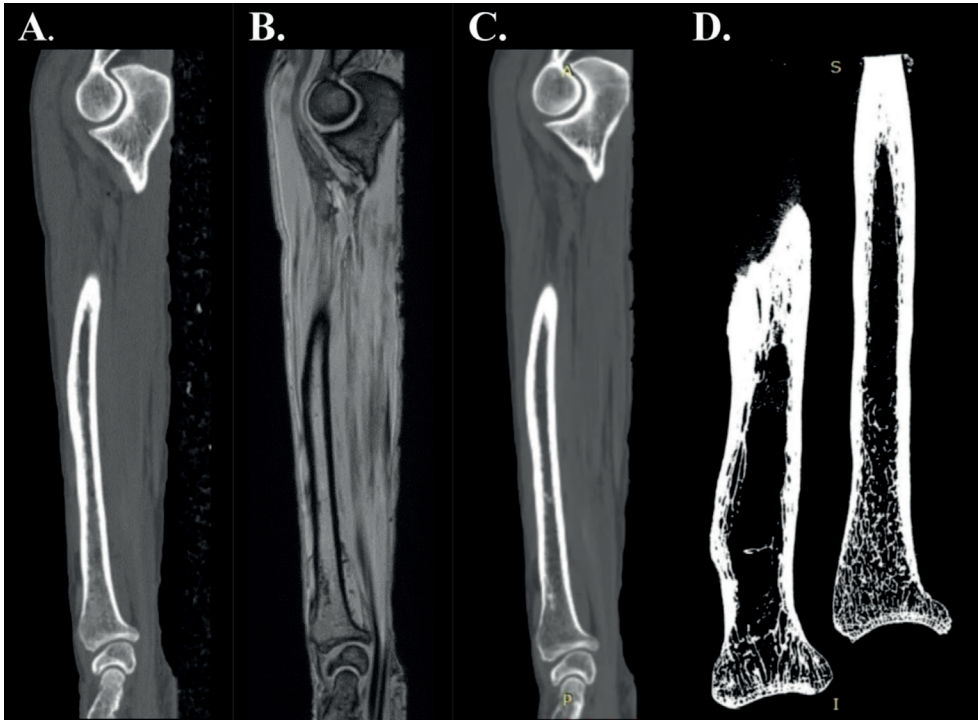


Figure 2. Various imaging modalities from the same left lower arm (P1) a Lower arm CT image, b Lower arm MRI image, c Lower arm sCT image. d Micro-CT image of two dissected halves of the same radius bone.

sCT-scans (Fig. 2c) were generated from the MRI-scans using a 2D conditional generative adversarial network (cGAN) in Python (Python Software Foundation, Wilmington, DE, USA) as previously described by Zijlstra et al. [15]. As ground truth, a 3D micro-CT scan (VECToR6/CT system, MILabs B.V., Utrecht, The Netherlands) was obtained of every bone with the following parameters: multi-circle 360 degrees acquisitions, tuber voltage of 55KV, tube current of 0.19 mA, exposure time of 75 ms per projection, angle increment of 0.5 degrees, and 50 μ m reconstructed isotropic voxel size using 3D Feldkamp filtered back-projection reconstruction (Fig. 2d). To fit the arms through the bore and in the micro-CT chamber the bones were cut in half and soft tissue was roughly dissected with standard dissection equipment (i.e. scalpels). After the micro-CT acquisition, the bones were simmered [16] to allow further processing. The influence of simmering on the bone surface was evaluated using a second micro-CT scan (Appendix).

3D bone model generation and comparison

A 3D-bone model comparison was performed on semi-automatic bone segmentations of the sCT-, CT- and micro-CT scans generated in Mimics (v21, Materialize NV, Leuven, Belgium). sCT- and CT-segmentations were created based on the thresholding method from Van den Broeck et al. [17] and the micro-CT with Otsu's [18] automatic thresholding based on Rovaris et al. [19] (Fig. 3). For direct comparison, the generated 3D models were rigidly registered [17]. After registration, the average distances between the 3D model vertices of the ground truth micro-CT and the sCT or CT were calculated in millimeters in 3-matics (v. 13, Materialize NV, Leuven, Belgium). A positive value indicates a larger sCT- or CT-model as compared to the micro-CT model.

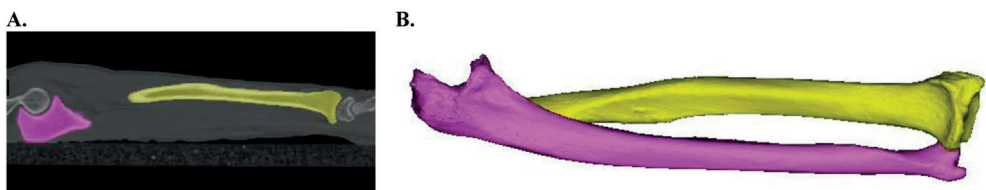


Figure 3. 3D-model generation. All scans were segmented (a) and the subsequent segmentations were converted in 3D bone models (b) in Mimics software. The following settings were used: interpolation method 'contour', preferred 'continuity', shell reduction to 1, no matrix reduction applied and smoothing factor 0.3 using 2 iterations and exported as binary stereolithography (STL) file. Radius (yellow) and ulna (purple).

Saw guide generation

For all eight radius and ulna bones, one proximal and one distal saw guide was designed per imaging modality, resulting in 32 sCT and 32 CT-based saw guides (Fig. 4). The 40 mm long saw guides [6] were systematically designed (MK) in 3-matic with a reference box ($20 \times 5 \times 10$ mm) on top. The relative position to the bone of each saw guide with reference box was identical for both imaging modalities. The 64 saw guides were pseudonymized and 3D-printed using selective laser sintering of nylon powder (PA12) with a printing accuracy 0.12 mm in all directions (P110, EOS, Krailing, Germany). One lateral and one frontal screenshot of the saw guide planning was printed on A4 paper and used as a guide for the observers.

Observers

Six blinded observers (two orthopedic surgeons, two orthopedic residents in training and two orthopedic researchers) placed the 64 saw guides on the corresponding bone parts, with sCT and CT-based saw guides randomly assigned over two rounds of 32 guides to reduce repetition bias. Observer #3 conducted the study two times with one-week interval, to analyze the intra-observer variability.

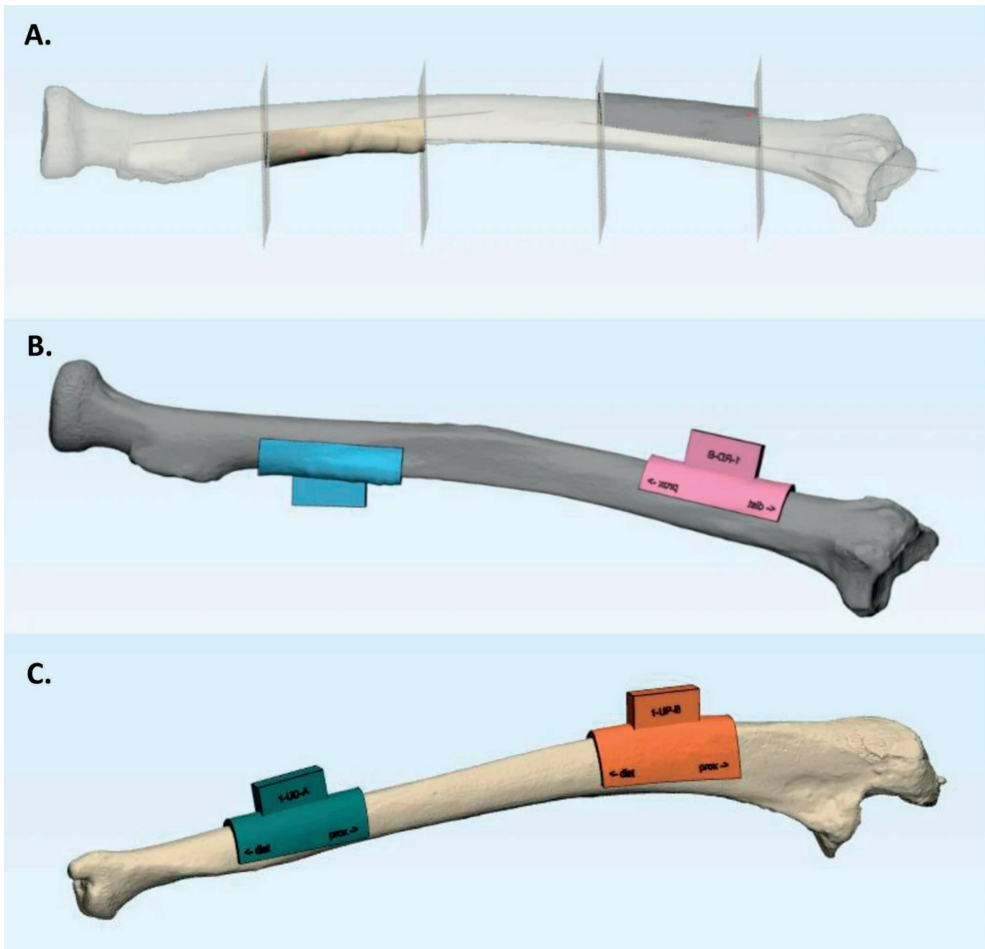


Figure 4. Saw guide generation. a A radius CT-3D model with two half cylinders located proximal and distal on the bone, created with the 4 perpendicular and 2 parallel cut-off planes in 3-matic. b A radius CT-3D model with its distal (pink) and proximal (blue) saw guide. c A ulna CT-3D model with its distal (green) and proximal (orange) saw guides in 3-matic.

Measuring the position of saw guides

To measure the saw guide placement accuracy of each observer, a 0.1 mm voxel size accurate white-light optical 3D scanner (Artec Space Spider, 4C, Emmen, The Netherlands) was used to scan the position of each saw guide relative to the bone and create a corresponding optical 3D bone with saw guide surface model (Fig. 5).

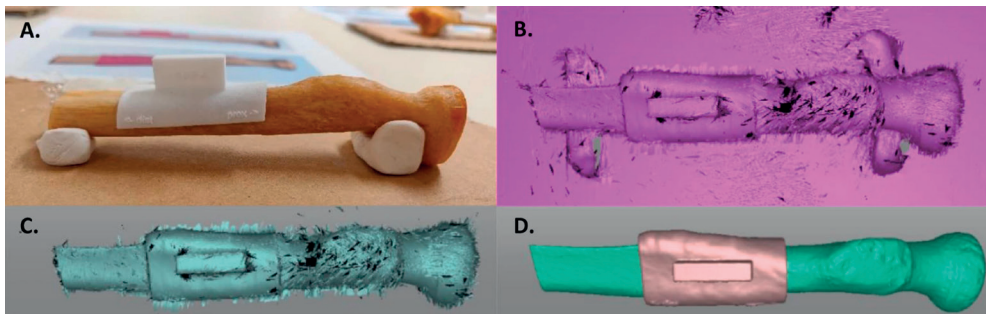


Figure 5. Generation of optical 3D models of a proximal radius bone half and corresponding saw guide after placement. a Proximal radius with saw guide after observer placement during the saw guide study. b Raw image made by the optical scanner, including the ground, bone holder, bone and saw guide. c During post-processing in Artec Studio the regions of interest are selected (saw guide and bone). d The final optical scan 3D models of the bone (green) and the saw guide 3D (pink)

Comparing saw guide placement with planning

The position of the placed sCT and CT based saw guides on the optical 3D scan were compared to the saw guide position on the planning [6]. The bone models from these optical 3D models were rigidly registered to the bones on the micro-CT in MATLAB (MathWorks, Natick, USA) with an iterative closest point (ICP) algorithm [20]. After registration with the ICP-algorithm, the displacement between the sCT or CT placement reference boxes and the corresponding planning reference box was calculated in a transformation matrix T (Fig. 6). From this matrix, eight displacement errors were determined: axis specific translational errors in the x , y and z -direction (Δx , Δy , Δz) and a total translation error $\Delta T = \sqrt{(\Delta x)^2 + (\Delta y)^2 + (\Delta z)^2}$ in mm and axis specific rotation errors around the x , y and z -axis (ϕ_x , ϕ_y , ϕ_z) and a total rotation $\Delta R = \sqrt{(\phi_x)^2 + (\phi_y)^2 + (\phi_z)^2}$ in degrees [21].

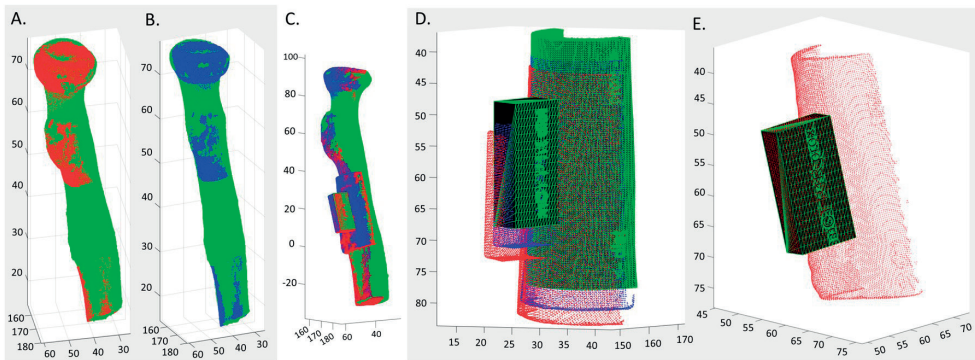


Figure 6. Example calculation of proximal radius saw guide placement error. Registration of the CT (a red) and sCT (b blue) optical scan bone model (without saw guide) to the micro-CT surface model (green). c The registered CT (red) and sCT (blue) optical scan 3D bone models including the relative position of each optical scan's saw guide model. d. The isolated saw guides with their relative positions, revealing the displacements of the CT saw guide (red) and sCT saw guide (blue) relative to the saw guide planning (green). e The reference box (black) is selected as the region of interest on the optical scan (red) to compare to the reference box of the planning (green) in order to calculate the transformation matrix T with eight corresponding placement errors. Relative to the planning position: Z-value increases when translating in proximal direction, Y-value increases when translating away from the bone, X-increases when translating to the left.

Statistics

Results were statistically analyzed with SPSS v.25 (IBM Corp, Armonk, NY, USA). A repeated measure analysis of variance (rANOVA) investigated between observers and between subjects differences in mean translation and rotation displacements of the sCT saw guides compared to the CT saw guides. Secondly, Bland-Altman plots of the ΔT and ΔR were created in order to assess to what extent sCT-based saw guide placement agreed with the CT-based saw guide placement. For this, two types of limits of agreement (LoA) were calculated and displayed: $1.96 \times$ standard deviation (SD) of the intra- and inter-observer variability, with the inter-observer variability as the maximum difference. If 95% of the data of the ΔT and ΔR lies within the calculated LoA, the displacement errors of the CT and sCT-based saw guides were regarded equivalent. Thirdly, box plots were created to analyze differences between saw guide locations.

The hypothesis that mean absolute placement errors would be equivalent for both CT and sCT was tested against the alternative hypothesis of significantly different errors. We aimed to detect a true difference of a 1 mm translational or 2 degrees of rotational error [22] with a SD of 1 mm or 2 degrees [6] with 80% power at a significance level of 0.05. This resulted in a required sample size of 16 per group [23].

Results

Bone model comparison

The average surface difference was 0.27 ± 0.30 mm between the micro-CT and sCT models and 0.24 ± 0.12 mm between the micro-CT and CT models. The positive number indicates a small overestimation of bone by the sCT and CT when compared to the ground truth micro-CT (Fig. 7). Differences were largest and most frequently seen near the joints at the proximal and distal bone ends of both CT and sCT (Fig. 7a,b). However, in one case, a sizable difference was found in the sCT surface model due to a false positive identification of a (calcified) tendon as bone (Fig. 7c,d).

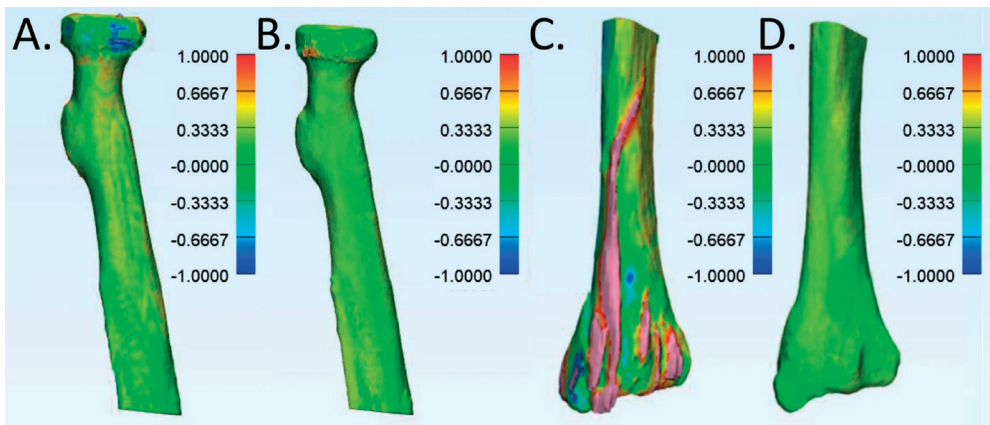


Figure 7. Distance mapping of surface model comparison. sCT (a) and CT (b) surface models compared to the micro-CT surface model of proximal radius. The color bar indicates differences (mm) between the micro-CT and the sCT or CT within a -1 and 1 mm range. A positive value indicates a larger sCT or CT model than the micro-CT model. c Exhibits an inconsistency in the sCT surface model compared to the micro-CT surface model of a distal radius. The corresponding sCT saw guide was a placement outlier during the saw guide placement study. d Shows the CT surface model compared to the micro-CT surface model of the same distal radius

Influence bone simmering

The additional surface distance analysis between the pre- and post-simmering micro-CT showed an average surface difference of -0.04 ± 0.12 mm indicating only a minimal shrinkage and therefore likely had a negligible effect on the study results (Appendix).

Saw guide placement

Saw guide placement error for both sCT- and CT-based designs were assessed. The rANOVA showed no statistically significant difference in sCT and CT placement for all axis-specific translational and rotational errors as well for the ΔT and ΔR errors (Table 1). Additionally, no significant difference was found between observers. The average translation and

rotation placement errors were the largest in the z-direction for both sCT and CT based designs (Fig. 8).

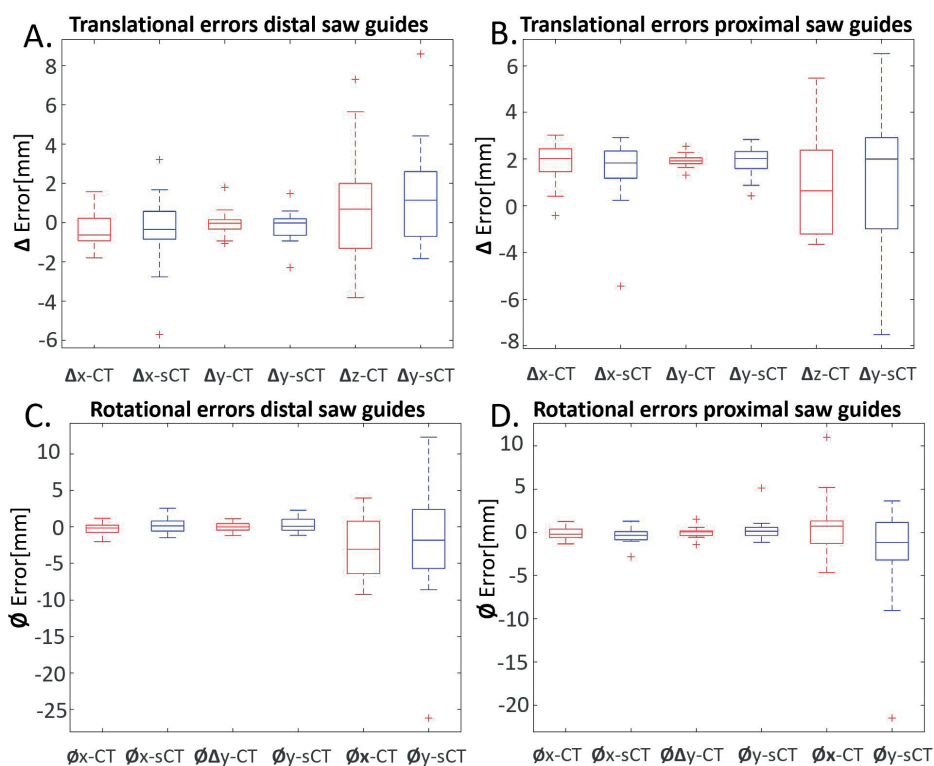


Figure 8. Box plots of a translation errors of distal guides, b translation errors proximal guides, c rotational errors of distal guides and d rotational errors proximal guides with a stratification for CT (red) and sCT-based (blue) saw guide types. The central mark in the box indicates the mean, the top (Q3) and bottom (Q1) box edges are the 25th and 75th percentile. The whiskers extend to the most extreme data not considering outliers; outliers are defined as > 1.5 times the interquartile range and are marked with a red '+' sign

The placements errors ΔT and ΔR were stratified for individual observers (Table 2) and outliers were defined as values that were > 1.5 times the interquartile range of that observer (Fig. 9). Observer 1 and 4 are orthopedic surgeons, observers 5 and 6 are orthopedic surgeons in training and observer 2 and 3 are orthopedic researchers. In total 51 of the 768 (64 saw guides \times 6 observers \times 2 errors [ΔT and ΔR]) placements errors were defined as outliers (7%). Of these 51 outliers 51% were CT, 49% were sCT, 33% were outliers on both CT and sCT within one location, 36% unique for CT and 31% unique for sCT, 78% were ulna saw guides, 71% were distal located ulna saw guides, 53% were rotational errors of distal located ulna saw guides.

Table 1. Average (Standard deviation (SD)) absolute translation and rotation errors of the CT- and sCT-based saw guides placed by the six observers.

Saw guide type	Translation: mm (SD)					Rotation: degrees (SD)				
	Δx	Δy	Δz	ΔT average	ΔT max diff	x	y	z	ΔR average	ΔR max diff
CT-based	0.8 (± 1.1)	0.4 (± 0.6)	2.1 (± 2.3)	2.4 (± 2.4)	4.5 (± 3.4)	0.6 (± 0.7)	0.5 (± 0.6)	3.5 (± 4.8)	3.8 (± 4.8)	6.9 (± 6.8)
sCT-based	1.0 (± 1.3)	0.5 (± 0.6)	2.3 (± 2.4)	2.8 (± 2.5)	4.5 (± 2.8)	0.7 (± 0.6)	0.8 (± 0.7)	4.6 (± 6.0)	4.9 (± 6.0)	7.0 (± 6.8)
p-value	.892	.687	.752	.284	-	.245	.167	.227	.216	-

The p-value was calculated with a rANOVA on the between subjects differences of each parameter, with $p < 0.025$ being significantly different

Table 2. Average errors ΔT and ΔR (SD) of CT- and sCT-based saw guides found per observer

	Observer 1	Observer 2	Observer 3	Observer 4	Observer 5	Observer 6
ΔT_{CT}	3.9 (± 3.5)	1.8 (± 1.2)	1.1 (± 1.0)	2.4 (± 2.6)	2.9 (± 2.9)	2.5 (± 1.5)
ΔT_{sCT}	3.8 (± 3.1)	2.1 (± 1.9)	1.8 (± 1.4)	3.4 (± 3.1)	3.0 (± 2.3)	2.8 (± 2.2)
ΔR_{CT}	4.0 (± 6.9)	3.6 (± 3.9)	2.4 (± 2.7)	4.4 (± 6.1)	4.6 (± 4.5)	3.4 (± 2.8)
ΔR_{sCT}	6.0 (± 6.8)	4.5 (± 6.2)	3.8 (± 4.0)	4.6 (± 5.6)	5.4 (± 7.0)	5.1 (± 5.9)

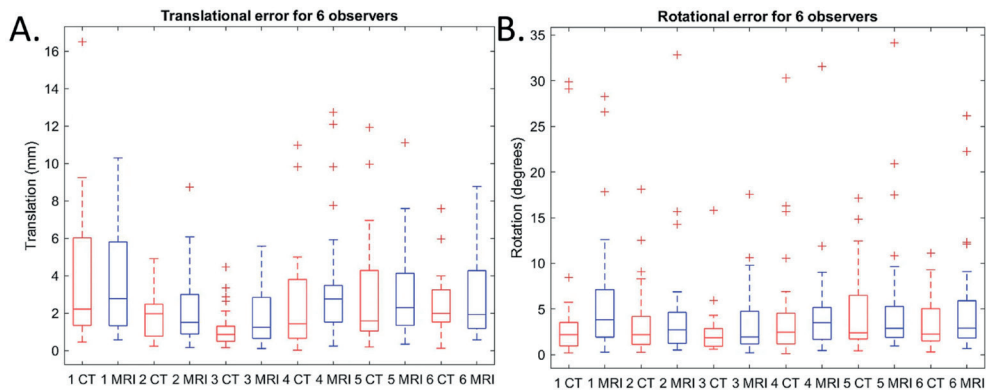


Figure 9. Box plots of the a total translation error ΔT and the b total translation error ΔR , stratified for the six observers and for CT based (red) or sCT-based (blue) saw guide design. The central mark in the box indicates the mean, the top (Q3) and bottom (Q1) box edges are the 25th and 75th percentile. The whiskers extend to the most extreme data not considering outliers; outliers are defined as > 1.5 times the interquartile range and are marked with a red '+' sign

Bland-Altman plots were computed containing the average differences between the CT and sCT-based saw guide ΔT and ΔR errors (Fig. 10). In addition to the standard LoA, the $1.96 \times SD$ of the intra- and inter-observer variability limits of agreement are displayed. For both the ΔT and ΔR errors all values fall between the inter-observer LoA and almost all (30/32) values fall between the intra-observer LoA which was based on the best scoring observer #3 (Fig. 9).

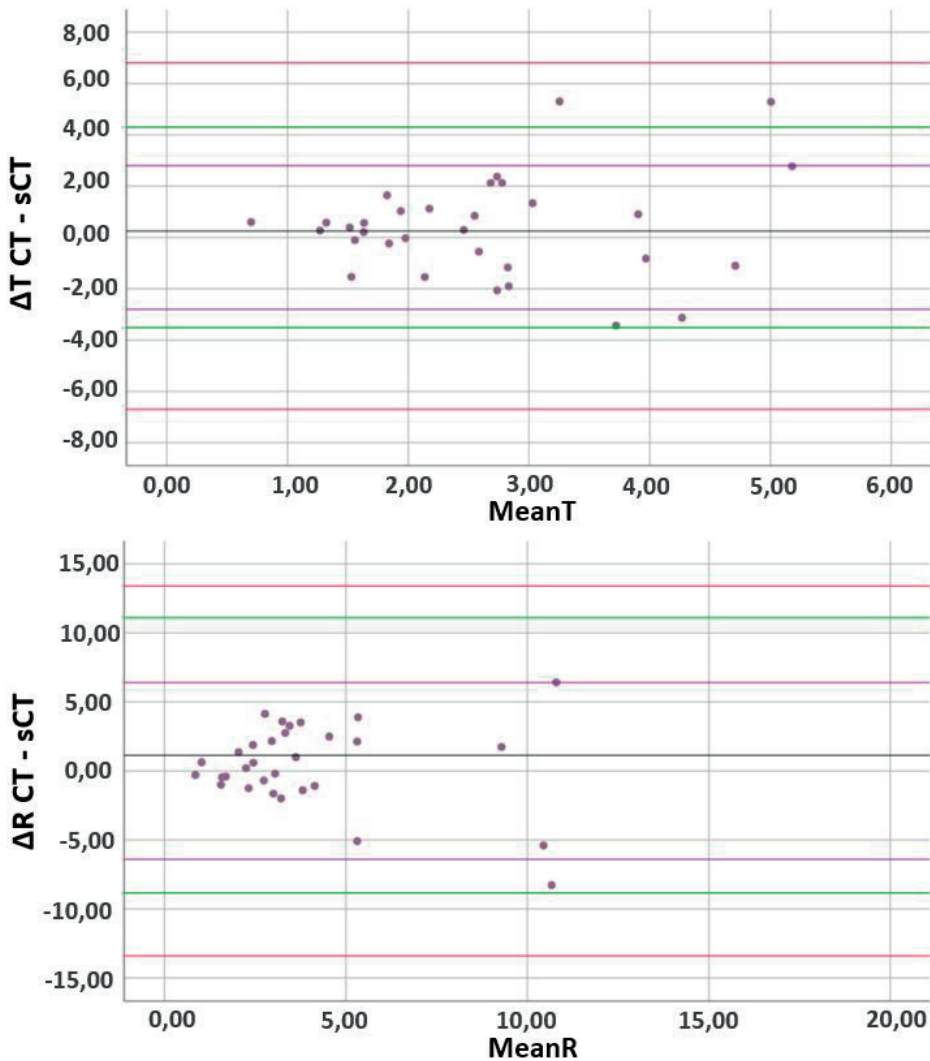


Figure 10. Bland-Altman plots. a The total translation error ΔT difference between CT- and sCT-based saw guides. The greyline represents the mean of 0.38mm and b the total rotation error ΔR difference found between CT- and sCT-based saw guides with a mean of 1.13 degrees (grey line). Green lines display the 95% confidence interval of LoA $1.96 \times SD$. The purple and red lines are respectively the intra- and interobserver variability LoA ($1.96 \times SD$)

Discussion

The 3D model surface distance comparison showed similar errors for sCT and CT with respect to the ground truth micro-CT. The similarity between both imaging modalities was in line with the fact that no statistically significant differences were found when comparing all translational and all rotational saw guide placement errors of both modalities. Furthermore, Bland-Altman plots of the total rotation and total translation displacement showed that the LoA of these displacements were within the LoA of the inter-observer variability. These results indicate that the positioning errors of the CT- and sCT-based saw guides are comparable in the context of its relevance for clinical application.

In another publication on surgical guides design, Caiti et al. [6] analyzed positioning errors of distal, mid-shaft and proximal radius saw guides in vitro and also found the largest translation and rotation errors in the z-axis. Additionally, Caiti et al. showed that distal guides have the smallest total translation (ranged 0.25–1.8 mm) and rotation (ranged 0.2–1.6 degrees) errors when compared to proximal (respectively ranged 0.15–2.25 mm and 0.3–5.7 degrees) or mid-shaft guides (respectively ranged 0.4–3.2 mm and 1.3–7.3 degrees). These values are slightly smaller than the results of our current study, which might be explained by several aspects. First of all, Caiti et al. 3D-printed plastic radius bone models to place the saw guides on, while these models were also used to design the saw guides themselves. Our study used the actual cadaveric specimens. Secondly, different anatomical locations were used: Caiti et al. investigated three locations merely on the radius, while this study focused on two locations (distal and proximal) for both radius and ulna bones. In our study the distal ulna had the largest placement errors, which is probably due to the distal ulna being more circular shaped and largely anchorless. Thirdly, different saw guide lengths were used; the guides of Caiti et al. were slightly longer (> 50 mm) than our saw guides (40 mm), which may be expected to influence the stability as longer guide length have had more attachment anchors and thus result in smaller positioning errors. Note however that longer saw guides are not often clinically used [2]. Besides the differences, both studies used a simplistic design of the saw guides that allowed for high reproducibility but made them prone to placement errors on the mainly tubular shaped bones. Therefore, the placement accuracy of both sCT and CT generated saw guides might even better when used for actual clinical cases because the guides can be designed with a more three-dimensional fit accompanying specific surgical identifiable landmarks.

There are several study limitations and recommendations that should be noted. First, the initial resolution of the CT-scan was higher than the resolution of the MRI-scan used for sCT reconstruction: 0.3 versus 0.7 mm pixel spacing, 0.8 versus 1.2 mm slice thickness and 0.4 versus 0.6 mm spacing between slices. This relative high CT resolution and mAs was used to get a best case surface model, though is not often clinically used because of

the radiation burden. Therefore, this could have positively influenced the accuracy of the CT-guides in comparison to the sCT-guides and may have caused the smaller standard deviation in the bone surface evaluation. However, despite these initial resolution differences, no statistically significant differences were found in saw guide placement. As a result, we can conclude that the MRI resolution was sufficient for sCT-based saw guide design and planning.

Furthermore, the currently used version for sCT generation may still contain inconsistencies [15]. Firstly, in one case, calcified tendons or vessels adjacent to the bone were falsely interpreted by the sCT model and presented as bone (Fig. 7c). However, no large average differences were found between sCT and CT placement errors for this bone, respectively ΔT of 1.0 mm versus 2.8 mm and ΔR 5.7 versus 4.0 degrees. Second, because the neural network is trained to generate the sCT with different data sets with each comprising a slightly different field of view, the network has the least (training) data on border visualizations, therefore the sCT sometimes delivers inhomogeneous densities near the distal or proximal bone ends (Fig. 7a,b) [15]. These inhomogeneities influenced the surface distance comparison, but should not have affected the accuracy of the saw guides as these were positioned further away from the joints (bone ends). Nevertheless, future research should focus on optimizing the sCT-algorithm with additional training data to further minimize false positive structures and errors in the sCT.

Another limitation is the difficulty of translating the results to clinically relevant outcomes for a lower arm osteotomy. The results in this study show displacement errors, where a larger displacement indicates a less accurate cutting plane compared to the planning. Ma et al. [22] showed the clinical relevance of distal radius osteotomy guides by translating the displacement errors to correction errors of the ulnar variance, radial inclination and volar tilt. A recommendation is to compare future results to those of Ma et al. by creating a virtual lower arm osteotomy model with the generated 3D models and translate the calculated displacement errors to clinical corrections. However, the main focus of this study was to assess the placement accuracy differences of the two different imaging modalities (MRI/sCT versus CT). For future use, the sCT scan should be validated with a sCT-based saw guide patient study.

Finally, this research on the accuracy of sCT generated saw guides for lower arm osteotomies sets an example for other areas with a high saw guide turnover (e.g. knee and craniomaxillofacial surgery) to also implement sCT. However, to get to the clinical application sCT training data should be acquired and validated in a similar fashion.

In conclusion, in this research we showed that sCT and CT provided similar digital models, as the surface distance with respect to the ground truth micro-CT was not significantly

different in lower arms. Furthermore, the positioning of saw guides based on these sCT and CT models did not demonstrate significant differences in a cadaveric lower arm study and indicate that both methods are clinically equal. Therefore, a first important step is made in enabling radiation-less 3D planning and design of patient-specific saw surgical guides facilitated by MRI-based synthetic CT.

Appendix

<https://doi.org/10.1186/s41205-021-00103-x>

References

1. Mulford JS, Babazadeh S, Mackay N. Three-dimensional printing in orthopaedic surgery: review of current and future applications. *ANZ J Surg.* 2016;86(9):648–53. <https://doi.org/10.1111/ans.13533>.
2. Dobbe JGG, Strackee SD, Schreurs AW, Jonges R, Carelsen B, Vroemen JC, et al. Computer-assisted planning and navigation for corrective distal radius osteotomy, based on pre-and intraoperative imaging. *IEEE Trans Biomed Eng.* 2010;58(1):182–90. <https://doi.org/10.1109/TBME.2010.2084576>.
3. Willemsen K, Nizak R, Noordmans HJ, Castelein RM, Weinans H, Kruyt MC. Challenges in the design and regulatory approval of 3D-printed surgical implants: a two-case series. *Lancet Digit Heal.* 2019;1(4):e163-71.
4. Martelli N, Serrano C, Van Den Brink H, Pineau J, Prognon P, Borget I, et al. Advantages and disadvantages of 3-dimensional printing in surgery: a systematic review. *Surg (United States).* 2016;159(6):1485–500.
5. de Muinck Keizer RJO, Lechner KM, Mulders MAM, Schep NWL, Eygendaal D, Goslings JC. Three-dimensional virtual planning of corrective osteotomies of distal radius malunions: a systematic review and meta-analysis. *Strateg Trauma Limb Reconstr.* 2017;12(2):77–89.
6. Caiti G, Dobbe JGG, Strijkers GJ, Strackee SD, Streekstra GJ. Positioning error of custom 3D-printed surgical guides for the radius: influence of fitting location and guide design. *Int J Comput Assist Radiol Surg.* 06-11th–2017th ed. 2018;13(4):507–18.
7. Kunz M, Ma B, Rudan JF, Ellis RE, Pichora DR. Image-guided distal radius osteotomy using patient-specific instrument guides. *J Hand Surg.* 2013;38:1618–24.
8. Dirix P, Haustermans K, Vandecaveye V. The value of magnetic resonance imaging for radiotherapy planning. Ménard C, editor. *Semin Radiat Oncol.* 2014;24(3):151-9. <https://doi.org/10.1016/j.semradonc.2014.02.003>.
9. Vittas D, Larsen E, Torp-Pedersen S. Angular remodeling of midshaft forearm fractures in children. *Clin Orthop Relat Res.* 1991;265:261–4.
10. De Gonzalez AB, Salotti JA, McHugh K, Little MP, Harbron RW, Lee C, et al. Relationship between paediatric CT scans and subsequent risk of leukaemia and brain tumours: assessment of the impact of underlying conditions. *Br J Cancer.* 2016;114(4):388–94. <https://doi.org/10.1038/bjc.2015.415>.
11. Pearce MS, Salotti JA, Little MP, McHugh K, Lee C, Kim KP, et al. Radiation exposure from CT scans in childhood and subsequent risk of leukaemia and brain tumours: a retrospective cohort study. *Lancet.* 2012;380(9840):499–505. [https://doi.org/10.1016/S0140-6736\(12\)60815-0](https://doi.org/10.1016/S0140-6736(12)60815-0).
12. Kwon OR, Kang KT, Son J, Choi YJ, Suh DS, Koh YG. The effect of femoral cutting guide design improvements for patient-specific instruments. *Biomed Res Int.* 2015;2015:1–8. <https://doi.org/10.1155/2015/978686>.
13. Eley KA, Watt-Smith SR, Golding SJ. “black Bone” MRI: A novel imaging technique for 3D printing. *Dentomaxillofacial Radiol.* 2017;46(3):20160407.

14. Florkow MC, Zijlstra F, Kerkmeijer LGW, Maspero M, van den Berg CAT, van Stralen M, et al. The impact of MRI-CT registration errors on deep learning-based synthetic CT generation. In: *Medical Imaging 2019: Image Processing*, vol. 10949. International Society for Optics and Photonics; 2019. p. 1094938.
15. Zijlstra F, Willemsen K, Florkow MC, Sakkers RJB, Weinans HHH, Van Der Wal BCH, et al. CT synthesis from MR images for orthopedic applications in the lower arm using a conditional generative adversarial network [Internet]. In: *Progress in Biomedical Optics and Imaging - Proceedings of SPIE SPIE-Intl Soc Optical Eng*; 2019. p. 54. Available from: <http://arxiv.org/abs/1901.08449>.
16. Gelaude F, Vander Sloten J, Lauwers B. Accuracy assessment of CT-based outer surface femur meshes. *Comput Aided Surg*. 2008;13(4):188–99. <https://doi.org/10.3109/10929080802195783>.
17. Van den Broeck J, Vereecke E, Wirix-Speetjens R, Vander SJ. Segmentation accuracy of long bones. *Med Eng Phys*. 2014;36(7):949–53. <https://doi.org/10.1016/j.medengphy.2014.03.016>.
18. Otsu N. A threshold selection method from gray-level histograms. *IEEE Trans Syst Man Cybern*. 1996;9(1):62–6.
19. Rovaris K, Queiroz PM, Vasconcelos K. de F, Corpas L dos S, da Silveira BM, Freitas DQ. Segmentation methods for micro CT images: a comparative study using human bone samples. *Braz Dent J*. 2018;29(2):150–3. <https://doi.org/10.1590/0103-6440201801385>.
20. Besl PJ, McKay ND. Method for registration of 3-D shapes. *Proc. SPIE 1611, Sensor Fusion IV: Control Paradigms and Data Structures*, (30 April 1992); Event: Robotics '91, 1991, Boston, MA, United States. <https://doi.org/10.1117/12.57955>.
21. Kuo HY, Su HR, Lai SH, Wu CC. 3D object detection and pose estimation from depth image for robotic bin picking. In: *IEEE International Conference on Automation Science and Engineering: IEEE*; 2014. p. 1264–9.
22. Ma B, Kunz M, Gammon B, Ellis RE, Pichora DR. A laboratory comparison of computer navigation and individualized guides for distal radius osteotomy. *Int J Comput Assist Radiol Surg*. 2014;9(4):713–24. <https://doi.org/10.1007/s11548-013-0966-8>.
23. Chow SC, Liu JP. *Design and analysis of bioavailability and bioequivalence studies*. 3rd ed: CRC press; 2008. p. 1–735. <https://doi.org/10.1201/9781420011678>.



CHAPTER 16

Challenges in the design and regulatory approval of 3D-printed surgical implants: a two-case series

Koen Willemsen | Razmara Nizak | Herke Jan Noordmans |
René M Castelein | Harrie Weinans | Moyo C Kruyt

*Published in The Lancet, section Digital Health, 1.4 (2019): e163-e171.
[http://dx.doi.org/10.1016/S2589-7500\(19\)30067-6](http://dx.doi.org/10.1016/S2589-7500(19)30067-6)*

Abstract

Background: Additive manufacturing or three-dimensional (3D) printing of metal implants can provide novel solutions for difficult-to-treat conditions, yet legislation concerning patient-specific implants complicates the implementation of these techniques in daily practice. In this Article, we share our acquired knowledge of the logistical and legal challenges associated with the use of patient-specific 3D-printed implants to treat spinal instabilities.

Methods: Two patients with semiurgent cases of spinal instability presented to our hospital in the Netherlands. In case 1, severe kyphotic deformity of the thoracic spine due to neurofibromatosis type 1 had led to incomplete paralysis, and a strong metallic strut extending from C6 to T11 was deemed necessary to provide long-term anterior support. In case 2, the patient presented with progressive paralysis caused by cervicothoracic dissociation due to vanishing bone disease. As the C5–T1 vertebral bodies had mostly vanished, an implant spanning the anterior spine from C4 to T2 was required. Because of the complex and challenging nature of both cases, conventional approaches were deemed inadequate; instead, patient-specific implants were designed with use of CT scans and computer-aided design software, and 3D printed in titanium with direct metal printing. For each implant, to ensure patient safety, a comprehensive technical file (describing the clinical substantiation, technical and design considerations, risk analysis, manufacturing process, and labelling) was produced in collaboration with a university department certified for the development and manufacturing of medical devices. Because the implants were categorised as custom-made or personalised devices under the EU Medical Device Regulation, the usual procedures for review and approval of medical devices by a notified body were not required. Finite-element analyses, compression strength tests, and cadaveric experiments were also done to ensure the devices were safe to use.

Findings: The planning, design, production, and insertion of the 3D-printed personalised implant took around 6 months in the first patient, but, given the experience from the first case, only took around 6 weeks in the second patient. In both patients, the surgeries went as planned and good positioning of each implant was confirmed. Both patients were discharged home within 1 week after the surgery. In the first patient, a fatigue fracture occurred in one of the conventional posterior fusion rods after 10 months, which we repaired, without any deformation of the spine or signs of failure of the personalised implant observed. No other adverse events occurred up to 25 months of follow-up in case 1 and 6 months of follow-up in case 2.

Interpretation: Patient-specific treatment approaches incorporating 3D-printed implants can be helpful in carefully selected cases when conventional methods are not an option. Comprehensive and efficient interactions between medical engineers and physicians are essential to establish well designed frameworks to navigate the logistical and regulatory aspects of technology development to ensure the safety and legal validity of patient-specific treatments. The framework described here could encourage physicians to treat (once untreatable) patients with novel personalised techniques.

Research in context

Evidence before this study: Three-dimensional (3D) printing has the potential to provide personalised implant solutions for patients with difficult-to-treat conditions. However, the regulatory channels related to the application of these techniques are often unclear and bureaucratic. As a result, medical professionals often use suboptimal standardised techniques to treat patients with unique deformities. Based on a 2017 systematic review, we did an updated search of PubMed, Cochrane, and Embase (to Dec 1, 2018) using the following search terms: ((3D* or three*dimension* or 3* dimension*) adj1 (print* or model* or reprod* or manufactur* or templat* or mould or prototyp* or framework or represent*)).tw.; (additive* manufactur* or stereolithograph* or biomodel*).tw.; (computer* aided manufacturing or CAM or computer* aided engineer* or CAE or computer* aided design or computer-assisted design or CAD).tw.; (patient* adj1 (specific or adapt* or customi* or personali* or individuali*)).tw.; (implant* or prosthe* or insert* or model* or guid*).tw.; 9 adj1 10 (surg* adj1 (guid* or templ* or model*)).tw.; 6 OR 7 OR 8 OR 11 OR 12. The 2017 systematic review identified only seven published articles on 3D-printed implants for the spine, four of which did not investigate the challenges of regulatory frameworks, whereas three only theorised about a new treatment method without introducing it into a clinical situation. Our updated search found no new articles. Therefore, further guidance on how to navigate these regulatory frameworks is needed for physicians treating patients with unique conditions that require personalised 3D-printed solutions.

Added value of this study: In this report, we describe the challenges associated with the production of personalised 3D-printed implants in a hospital setting, from medical, organisational, and legal perspectives. With two case examples, we show the feasibility and relative ease of using 3D-implant solutions after a development workflow has been established. These examples may serve as guidance to physicians in similar situations to establish in-house development pathways and to create technical files describing the clinical substantiation, technical and design considerations, risk analysis, manufacturing process, and labelling for regulatory and legal purposes.

Implications of all the available evidence: Surgeons have been hesitant to treat patients with use of personalised 3D-printed implants, partly because of the challenges of navigating the applicable legislative regulations. However, patients with unique or difficult-to-treat defects can be effectively treated with such personalised approaches. These approaches will be facilitated if physicians familiarise themselves with setting up technical files and collaborate with mechanical engineers to establish workflows for the development of new 3D-printed personalised techniques.

Introduction

With advances in three-dimensional (3D) printing technology and the increasing availability of user-friendly software to design almost any shape, opportunities for customized surgical implants have emerged.[1, 2] We can now treat clinical conditions that could not previously be treated, and ineffective and demanding treatments for extreme conditions (such as tumor site reconstruction or extreme scoliosis) can be substantially improved with use of patient-specific implants and cutting guides.[3, 4] As a consequence, more unique situations are amenable to unprecedented solutions than ever before.[3, 5, 6]

Any new technology is—by definition—explorative, and guidelines and legislation for the use of such new techniques are imperative to mitigate the risk of mistakes.[6] However, these regulations tend to be restrictive, and can even impede innovative and improved patient care. As a result, surgeons are seeing a widening gap between the technical possibilities of personalized techniques and the extent to which these techniques can be realized. Furthermore, the pathways for navigating these regulations are often unclear and always bureaucratic,[2, 7, 8] a scenario that is especially problematic in semi urgent situations that preclude a time-consuming approval procedure.[2] Consequently, surgeons often opt not for the best (ie, personalized) treatment, but for the more convenient, conventional approach.

An exemption from the usual approval procedure for the use of personalized implants can be obtained in an emergency or exceptional-use situation, when specific safety requirements are met.[9, 10] We believe that thorough and efficient interactions between medical engineers and physicians to establish well designed frameworks to navigate the logistical and regulatory aspects of personalized implant development are necessary. These frameworks can be locally administered and managed to obtain legal clearance for personalized implants in an optimal manner; only then can the possibilities be effectively exploited and the expected increase in personalized solutions accommodated. [6] However, time and investment are required to understand the needs and language of physicians, engineers, government administrators, hospital management, and legal representatives to facilitate interactions between the relevant parties.

Previous studies of 3D-printed implants in the clinical setting have scarcely described the legal aspects and inherent decision-making dilemmas associated with these techniques,[2, 3, 6] while studies that have investigated the legal aspects have not shown this application in the clinical setting.[2, 6, 11] In this Article, we elaborate on the possibilities of 3D printing for complex spinal surgery as illustrated by two semi-urgent cases for which we were able to create personalized solutions using 3D metal printing technology. We also describe the associated procedural workflow and regulatory

framework that we had to navigate to achieve these solutions, as well as the advantages of thoroughly documenting these processes. We designed, manufactured, and implanted patient-specific, bone-integrating titanium implants for patients with severe destruction of the spine. As both cases were exceptional, no standard devices, procedures, or regulations were available; yet the surgical implantations had to be done within months in both cases to prevent paraplegia, during which time the spines were protected with an external orthosis. In terms of strength, invasiveness, fit, and efficacy, we consider these personalized treatments to have been far better than if we had attempted to use any conventional treatment options (such as placing posterior fusion rods anteriorly) in these unique cases. This report provides information that could encourage other surgeons with similar unconventional cases to use patient-specific approaches and provides guidance on how to develop the necessary regulatory frameworks to ensure patient safety.

Methods

Case 1

Case background

A 16-year-old boy presented to the emergency department and subsequently to the department of orthopaedics of the University Medical Centre Utrecht (Utrecht, Netherlands) in January, 2017, with incomplete paralysis (American Spinal Injury Association impairment scale [AIS] grade C) due to severe kyphotic deformity of the thoracic spine resulting from neuro-fibromatosis type 1 (figure 1).[12] Neurofibromatosis type 1 is a single-gene disorder that affects around one in every 2500–3000 people, with scoliosis present in 10–26% of cases.[12, 13] Because of the development of dystrophic deformities, surgical management can be very challenging in these cases.[14] Our patient had been treated for severe dystrophic scoliosis with a short posterior fusion (of vertebra T1–T10) 5 years earlier, in February, 2012. However, the proximal fixation progressively failed over a period of 5 years in the absence of sufficiently supportive vertebral bodies from T4 through T9, which were damaged by extensive and increasing dystrophic changes of the bone and dural ectasia (figure 1), eventually leading to incomplete paralysis and neurological symptoms. After urgent reduction with halo-gravity traction, the patient recovered neurologically (AIS grade D), and the spine was aligned and stabilized with posterior fixation extending from C4 to L1 using lateral mass and pedicle screws, together with transition rods in January, 2017. Although this treatment was initially effective, the slender posterior fixation would not be mechanically sufficient for a long period and failure of the construct was deemed to be inevitable. Therefore, a more rigorous support at the anterior side of the spine was needed, which required a personalized approach. To allow time to develop a permanent solution, a temporary orthosis was used to protect the spine. Meanwhile, the patient was allowed to ambulate and to go home.

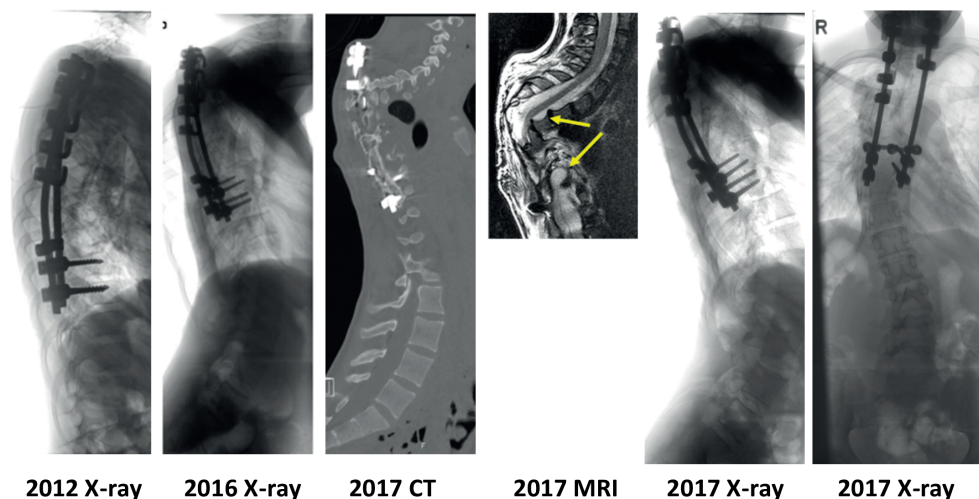


Figure 1. Pre-implantation imaging findings (case 1). (A) Lateral x-ray in 2012, in which short segment fixation with rods for dystrophic scoliosis was visible. (B) Lateral x-ray (2016) showing considerable loss of alignment of the spine to the fixation rods with progressive kyphosis at T2–T3 due to proximal failure. (C) CT scan (2017) showing total collapse of the spine due to proximal failure, which was causing paralysis. (D) MRI (2017) showing the cord at risk, with destruction of the T3–T9 vertebrae due to dural ectasias (arrows). (E) Lateral x-ray (2017) showing extensive loss of alignment due to proximal failure. (F) Anterior-posterior x-ray (2017) showing considerable loss of alignment due to proximal failure.

Anterior support

For provision of the necessary anterior support, structural bone grafting would be very difficult and unreliable because of the dystrophic nature of the neurofibromatosis and the large dural ectasias that would prevent bone integration.[15] Standard anterior hardware would also be problematic: first because of the difficulty in shaping it properly in the presence of the bony deformation, and second because the hardware was not anticipated to match the mechanical demands of the spinal column over time. We concluded that a strong and solid metallic strut would be needed at the anterior side to assure reliable long-term support. Such a prosthesis had to be fixed and would ultimately need to integrate into the proximal and distal viable vertebral bone without interfering with vital structures such as the heart, lungs, and bronchi. The shape of the prosthesis had to be customized to ensure a perfect fit with the surrounding intact vertebrae and to bridge the diseased bone, as well as to allow the least amount of mobilization and dissection of the vital anatomy, especially around the structures of the mediastinum. The only way to achieve this was by designing a personalized implant with use of computer-aided design and 3D-print manufacturing. After extensive examination of the CT and MRI images, the surgical team decided that a personalized implant that spanned the anterior spine from C6 to T11 would be necessary to stabilize the spine. During a cadaveric trial surgery, we

established that such an implant could be inserted through a standard right anterior approach to C6 and a separate right-sided thoracotomy through the bed of the eighth rib.

Regulatory framework

To allow the implantation of a personalized prosthesis, certain criteria needed to be met. The design and production process had to be lawful, using the proper regulatory channels, imaging requirements, design steps, and implant production. However, because of the semi-urgent nature of the situation, these steps had to be taken quickly and simultaneously to allow prioritization of our time for the design process and preparation of printing. This scenario precluded extensive procedures and formal tests of the implant.

According to the EU Medical Device Regulation, an orthopaedic implant is a medical device of class III, the highest risk class.[7] Normally, a class III medical device should be provided with an extensive technical file that is reviewed by a notified body. This approval process usually takes years to complete and involves extensive clinical trials before approval is granted, which was impossible in this case. However, because the medical device for our patient was made specifically for one exceptional case, it fell into a different category: custom-made or personalized devices.[7] For a custom-made device, a technical file must be made in accordance with the procedures described in annex XIII of the Medical Device Regulation,[7] although sufficient justification allows for deviation from the usual performance and safety demands. In the Netherlands, the technical file for a custom device does not have to be reviewed by a notified body. Therefore, we made a technical file in collaboration with the Department of Medical Technology and Clinical Physics of the University Medical Centre Utrecht (appendix pp 1–5). This department is ISO 13485 certified for the development and manufacturing of medical devices. The technical file described the clinical substantiation, all technical and design considerations (Table 1), the risk analysis, manufacturing process, and labelling according to an Investigational Medicinal Device Dossier (appendix pp 1–5). We documented all the steps involved in creating this file.

Imaging

A conventional CT scan with a slice thickness of 1 mm (35 mAs, 120 kV) was used to create a Dicom file that was segmented in 3D Slicer (version 4.5.0, revision 24735) to produce a 3D model of the bony structures. An initial threshold of 226 Hounsfield units was used for bone segmentation. The acquired model was exported in standard tessellation language (STL) format (a native file format for stereo-lithography software) for the design step.

Table 1. Considerations in the risk analysis of personalized implants

	Requirements	Variables	Justification
<i>Surgical approach</i>			
<i>Anatomical positioning of the implant</i>	Must not interfere with anatomical structures in the cervical and thoracic spine	Size of implant, thickness of implant	Cadaveric trial surgery before implantation, experience of the surgical team, literature
<i>Anatomical free space</i>	Must allow positioning without great difficulties in the surgical approach	Drill guides, fitting guides for optimal placement on desired position	Cadaveric trial surgery before implantation, experience of the surgical team, literature
<i>Implant specifications</i>			
<i>Material properties</i>	Must not cause adverse tissue reaction	Material, hot isostatic pressing (metal stress-relieving treatment)	Literature
<i>Implant strength</i>	Must provide support for lifetime of patient, must provide axial compressive mechanical support	Size of implant, thickness of implant, weight of patient	Finite-element analysis, biomechanical compression test
<i>Optimization of bone-implant interface</i>	Should have porous interface with bone to facilitate ingrowth	Pore-sizes, porosity, unit-cell structure	Literature
<i>Screws</i>	Must allow compressive fixation to the spine and provide rotational stability	Quantity, lengths, thickness, type, and trajectories of screws	Computer-aided design and three-dimensional analysis, finite-element analysis, literature
<i>Alternatives</i>			
<i>Off-the-shelf implant and fixation rods</i>	Should not be an equal or better treatment option than the personalized treatment	Size of spinal rods, osteosynthesis material	Literature, experience of the surgical team, biomechanical compression test

Implant design

With regard to the size and geometry of the implant, we used a specific implant rationale to determine the design requirements (Table 1). The implant had to be long enough to cover the destabilized portion of the spine, but small enough to allow a straightforward surgical approach. It had to be thick enough to withstand the estimated forces of the spine for a lifetime, but must not interfere with anatomical structures. A prerequisite for a rapid design phase is a close collaboration with an (in-house) designer and mechanical engineer. The patient-specific implant was designed in close collaboration with the surgical team, using Blender software (version 2.78; Blender, Amsterdam, Netherlands).

The implant consisted of a solid cylindrical part stretching from C6 to T11 (figure 2). A proximal protrusion supported the inferior endplate of C6 and a distal protrusion rested on the superior endplate of T11. The protrusions were made partially porous at the bone-implant interface to allow bone ingrowth. A pore size of 500–600µm with an overall

porosity of 70% was used.[16, 17] For initial fixation of the implant and to accommodate bony integration, two proximal and distal screw holes were included in the implant; the preferred trajectory and optimal screw length were calculated and planned with use of computer-aided design software. To determine global strength, an in-silico finite-element analysis of the implant was done, which showed that the implant easily sustained axial stress of 500 N (appendix p2)—far more than the mechanical forces exerted on the implant in the body. Finally, a biomechanical compression test was done on a supplementary prototype. This compression test showed that the implant had about ten-times higher stiffness and strength compared with a conventional 5.5-mm titanium rod (appendix p2). To ensure an optimal fit and to check the implant, a 3D print of the spine and the prosthesis in plastic was made. After approval by the surgical team, the files of the final implant were sent in STL format to the implant manufacturer, together with two oversized implants (with an additional 2 mm or 4 mm added in the axial direction) to accommodate for slight size differences and unpredictable posture changes during surgery.[18]

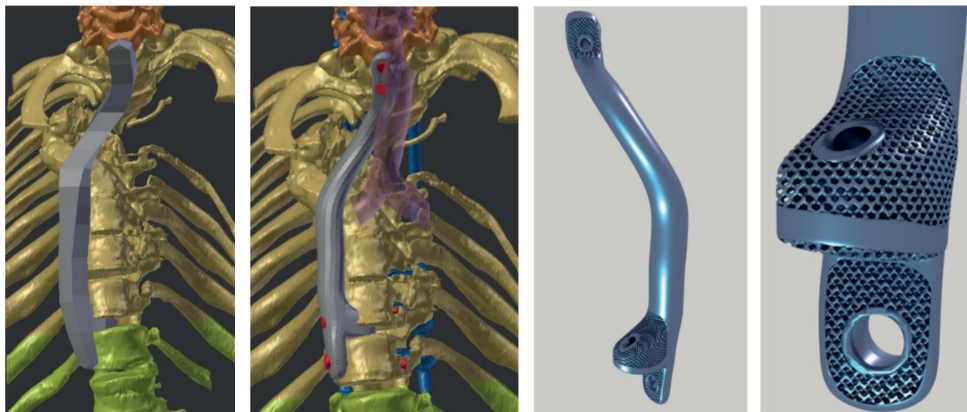


Figure 2. Design of personalized prosthesis (case 1). (A) First step in the design process: a prototype that follows the mechanical axis near the spine, attaching to the last mechanically stable vertebrae in the cervical spine (C4–C5) and bridging the unstable part (C6–T11) to the first mechanically stable vertebra distal of the defect (T12). (B) Restructured prototype with addition of screw holes and their trajectories. (C) Final implant design (rendered picture). (D) Close-up view of the porous mesh structure to allow bone ingrowth, with distal screw holes.

Implant production

The implants were manufactured at a CE-certified 3D-printing facility, with ISO 9001:2008, ISO 13485:2003, and EN ISO 13485:2012 certificates for the scope of modelling and production of metal additively manufactured medical products (3D Systems, Leuven, Belgium). Printed products come with a manufacturer's declaration of conformity to ensure the required quality of the 3D-printing process (direct metal printing) and base

materials (appendix p1). The implants were 3D printed using medical grade titanium (Ti6Al4V ELI grade 23). The printing was done with a direct metal printing titanium 3D-printer DMP320 (3D Systems, Leuven, Belgium). Post-processing included hot isostatic pressing treatment,[19] polishing, and screw hole finishing. Sterilization of the implants was done at in-house sterilization facility of the University Medical Centre Utrecht by manual cleaning, additional autoclave sterilization, and sterile packaging.

Surgical procedure

After a standard right-sided anterior approach of the cervical spine to expose C6 and a mini thoracotomy through the bed of the eighth rib, with mobilization of the right lung, a passage could be created with blunt finger dissection from proximal into the pleural cavity under endoscopic guidance. The docking sites were created by partial dissection of the intervertebral discs C6–C7 and T10–T11. Additional proximal and distal ends of the prosthesis were printed in polyamide to serve as a docking trial guide. The normal-sized implant had the best fit and was inserted from distal to proximal end. The fit was precise, and, after drilling and measuring, the predetermined screws were inserted. Three 3.5-mm standard small fragment cancellous screws were used (two at the proximal side and one at the distal side), with an additional 6.5-mm fully threaded cancellous bone screw used at the distal side (DePuy Synthes, West Chester, PA, USA).

Case 2

Case background

The second patient, a 68-year-old woman with progressive paralysis (AIS grade C) due to a severe cervicothoracic dissociation, presented around 18 months after case 1, in October, 2018. The cervicothoracic dissociation was a consequence of vanishing bone disease,[20] which was diagnosed 20 years earlier and had resulted in multiple surgeries before the patient's condition was finally stabilized with a posterior C2–T5 fixation. Gorham's vanishing bone disease is a disease of unknown cause that is characterized by the destruction and absorption of bone, much like lytic metastasis but without oncological cells.[20] Eventually, in October, 2018, the posterior fixation failed proximally, possibly because of a minor trauma 2 months before. Because of the (partial) absence of the C5–T1 vertebral bodies, the cervical spine slowly deviated and collapsed, which caused neurological symptoms (figure 3). The patient was first treated with halo traction and posterior C2–T5 spinal fusion with allograft bone in October, 2018. She recovered remarkably well in the next weeks (to AIS grade E) and was discharged home. However, she needed to maintain the halo frame while the surgical team planned for anterior support because the C5–T1 vertebral bodies had mostly vanished.

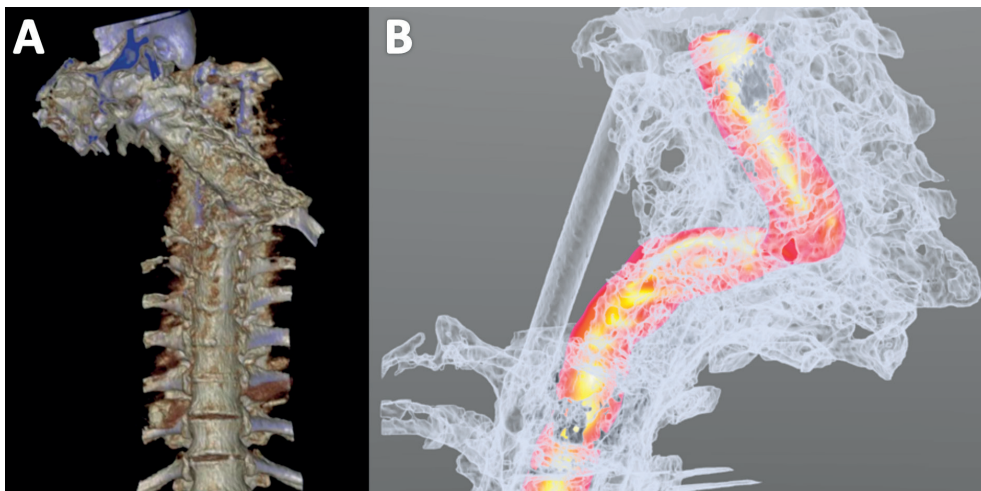


Figure 3. Pre-implantation imaging findings (case 2). (A) CT reconstruction of severe cervicothoracic dislocation with deviation of the distal cervical spine to the left where it was resting on the first rib. The failed posterior fixation rods are shown in blue. (B) CT reconstruction with the spinal cord segmented (in red). The cord was curved into a syphon, with severe compression causing paralysis. White translucent structures shown are the bones and posterior fixation.

Planning, design, and production of implant

We replicated the procedure followed in case 1 for the development of the anterior 3D-printed personalized prosthesis, including producing the technical file (appendix pp 1–5). Given the experience from the previous case, the team was better prepared, and we were able to complete the design, production, and regulatory procedures within weeks instead of months. We used commercially available software for segmentation (Mimics Medical 21.0; Materialise, Leuven, Belgium) and for implant design (3-Matic Medical 13.0; Materialise, Leuven, Belgium). An implant was designed that spanned the anterior spine from C4 to T2. Because of the smaller anatomical space, the implant was downsized compared with case 1. The solid part of the design was approximately 10 mm in width, 5 mm in depth, and 88 mm in height, and curved in the axial plane to allow close positioning against the curved shape of the remaining anterior vertebral bodies. The proximal protrusion supported the inferior endplate of the lowest proximal healthy vertebra (C4) and the distal protrusion rested on the superior endplate of the T2 vertebra. As was done for case 1, the models of the spine and prosthesis were printed in plastic to verify shape and size. After approval from the surgical team, the personalized implant and one oversized version (with an additional 3 mm in height) were printed in titanium following the same production method as that for case 1.

Surgical procedure

The personalized prosthesis was inserted using a standard anterior approach to the lower cervical spine that gave excellent access to the fixation points at C4–C5 and T1–T2. Polyamide docking guides were again used. This time, the 3-mm oversized version of the implant was used with additional printed polyamide drill guides that facilitated precise predrilling of the screw holes (figure 4). At the proximal side, two 3.5-mm standard small fragment cancellous screws were used, and one 6.5-mm fully threaded cancellous bone screw (DePuy Synthes, West Chester, PA, USA) was used at the distal side.

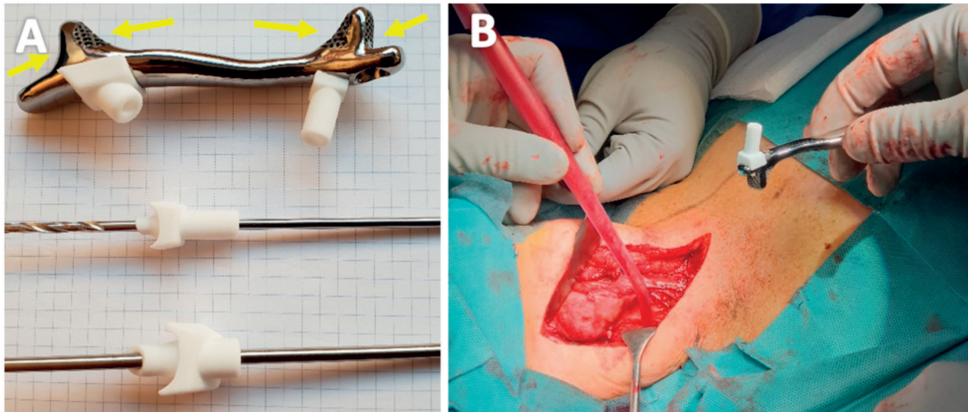


Figure 4. Prosthesis and surgery (case 2). (A) Titanium prosthesis with polyamide drill guides for case 2. The prosthesis was made with porous ends (arrows) to allow bone integration. (B) Intraoperative image of the implant (arrow) before insertion; a right-sided standard anterior approach to the lower cervical spine was used (the patient's head is situated on the left side of the image).

Ethical approval

Both patients gave their consent for the procedures after being extensively informed about the first-in-human nature of these devices; patients were provided with information on the different treatment options, with a consent period, after which another appointment was made to answer additional questions before confirmation was acquired for these procedures. The patients also gave explicit consent for their cases and outcomes to be presented in this Article. Following Dutch legislation, a waiver for ethical review was granted by the Institutional Review Board of the University Medical Centre Utrecht (approval protocol number 19-371), as these treatments were not intended as clinical research.

Results

Case 1

After the consideration of multiple treatment approaches during the first weeks after the emergency treatment, the legal and regulatory possibilities were explored from week 3 onwards to initiate the patient-specific implant treatment plan. The official design process commenced around week 8, with multiple design and five evaluation sessions with the surgical team. Two cadaveric sessions were planned to test the feasibility of the design, after which the implant was approved for production (around week 16). The design was sent for manufacturing at around week 18, with production and shipping taking 2 weeks. In week 20 the implant was delivered to the hospital facility for sterilization and was made ready for the surgery.

The 3D-printed anterior implant was eventually inserted around 6 months after the emergency posterior stabilization surgery. This procedure was uneventful and went as planned. Total surgery time after positioning of the patient was about 150 min, and blood loss was around 300ml. Perioperatively, there were no complications, and postoperative CT confirmed good positioning of the prosthesis (figure 5). The patient recovered well and was discharged within 1 week. He was able to mobilize without further support, and returned to school 4 weeks after the surgery. Due to the patients' neurofibromatosis, frequent imaging and PET-CT scans were available up to 25 months post-surgery and showed good incorporation of the prosthesis, without signs of loosening of the implant. The patient's AIS grade improved from grade C to grade D after the emergency reduction and posterior refixation surgery, and subsequently showed gradual recovery over time (within AIS grade D), although some muscle weakness in his leg remained.

At 10 months post-surgery, a fatigue fracture occurred in the thin section of one of the conventional posterior fixation rods, without any deformation of the spine or signs of failure of the personalized anterior prosthesis. This fracture was probably the result of some remaining internal stress in the posterior system. Without the anterior stabilizing implant, the spine may have collapsed further. In March, 2018, we repaired the rod with a small inline connector, and observed no other adverse events (figure 5). Frequent yearly follow-up and monitoring of the implant and function will be done as part of the monitoring planned for the patient's neurofibromatosis.

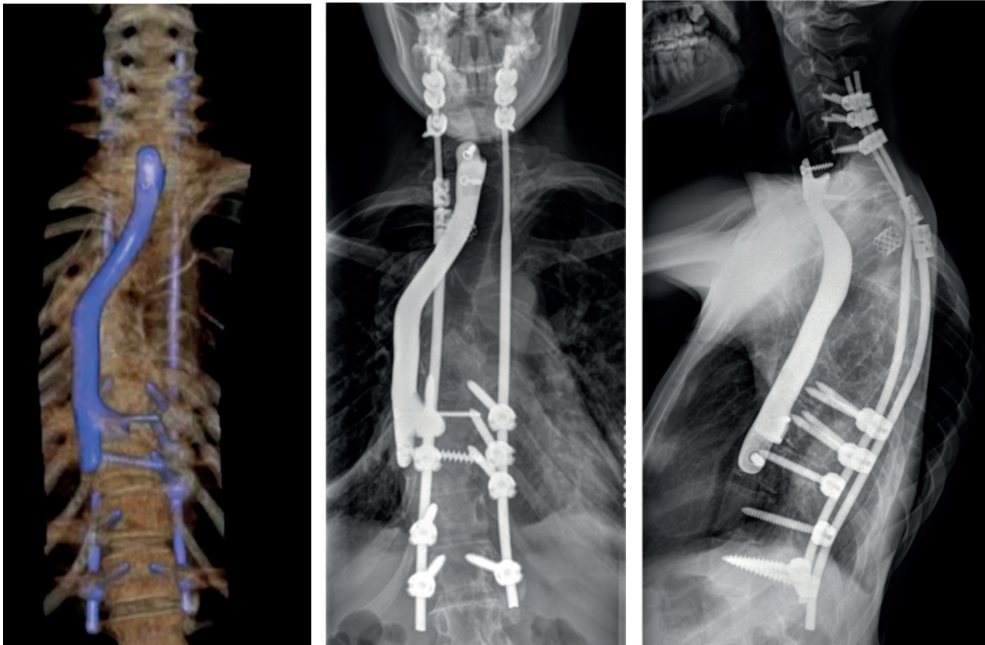


Figure 5. Post-implantation imaging findings (case 1) (A) Three-dimensional reconstruction of the CT scan (anteroposterior view) of the spine after insertion of the personalized implant (shown in blue), showing good positioning of the implant. (B) Anteroposterior radiograph, 1.5 years after implantation, showing unaltered position of the prosthesis and no signs of failure. (C) Lateral radiograph at 1.5 years, showing the optimal anatomical position of the prosthesis.

Case 2

In the first week after the emergency reduction and posterior re-fixation, a CT was done and the anatomy of the patient was segmented (including the spine, ribs, trachea, carotids, and oesophagus). This process was time consuming as the bone–tissue interface was not sharply defined because of the vanishing bone disease, and because the metallic posterior fixation induced a lot of beam hardening, necessitating intensive manual segmentation. In week 2, the implant was designed, with immediate in-house evaluation with the surgical team, after which the implant underwent two additional evaluation rounds. The implant was approved and physically printed at the beginning of week 4, and heat treated in week 5, followed by polishing and sterilization before surgery.

The 3D-printed anterior implant was eventually inserted 6 weeks after the emergency posterior stabilization surgery. The surgery went as planned and there were no perioperative complications. The duration of the surgery was about 120 min and blood loss was 200 mL. The patient did well after surgery. CT and x-ray confirmed correct positioning of the prosthesis and screws (figure 6), after which the halo frame could be removed. The patient was discharged home without restrictions within 1 week post-surgery. At 6 months post-surgery, the situation was unchanged and the patient was walking normally (AIS grade E).

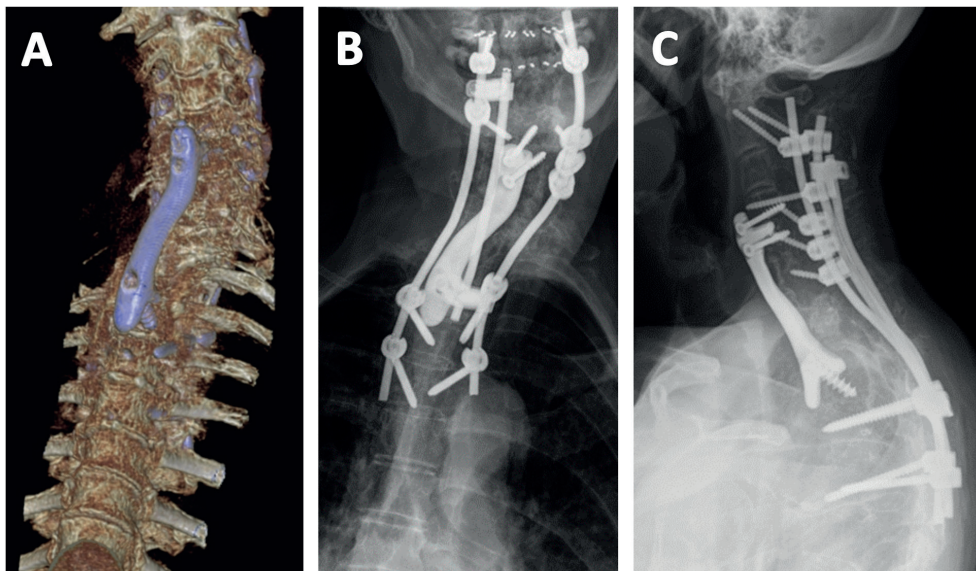


Figure 6. Post-implantation imaging findings (case 2). (A) Three-dimensional reconstruction of CT scan (anteroposterior view) of the spine after insertion of the personalized implant, showing good positioning of the implant. Anteroposterior radiograph (B) and lateral radiograph (C) at 3 months after the surgery, showing unchanged position and no signs of failure of the implant.

Discussion

The emergence of 3D imaging and direct metal printing techniques creates new possibilities for the surgical treatment of complex cases. Many papers have described the use of these technologies for preoperative planning[26] or for producing perioperative saw or drill guides.[1, 2, 6] Additionally, commercial 3D-printed implants for spinal cages or acetabulum revision implants are available.[2] However, relatively few papers have described the use of patient-specific permanent spinal implants.[6, 21] One of the reasons that surgeons are hesitant to use the personalized 3D-printing technology is that there are many regulatory impediments to the implementation of this technology, resulting from the uncertain or extensive regulation of such implants, and the scarcity of in-house expertise for implant design and subsequent in-house production logistics.[2, 18]

In our cases, the process of ensuring compliance with the EU Medical Device Regulation was extensive but straightforward, requiring a procedural blueprint (figure 7) and a technical file with a detailed description of all steps and procedures (appendix pp 1–5). When this process has been done and documented well, it can be replicated and followed easily in subsequent cases, as shown in our two cases (in which the planning, design, approval, and production of the implants took 6 months for case 1 but only 6

weeks for case 2). The current EU Medical Device Directive annex XIII and the upcoming new Medical Device Regulation leave enough flexibility for hospitals to organize their own development process for personalized implants. This process requires a team with surgeons and engineers, in close collaboration with the department of medical technology, which has extensive knowledge of implant legislation and legal matters. For such approaches to become more routine, ISO 13485 certification is advantageous as it allows for the production of medical devices, and the accompanying knowledge could help in the production of patient-specific medical devices. Furthermore, the regulatory procedures outlined in this Article are widely translatable in other EU countries, which are subject to the same regulations on medical devices. In the USA, the Food and Drug Administration also allows for a patient-centered approach: the special custom device exemption act allows use of custom-made devices for patients with special needs with a rare and unique pathology for which no conventional treatment is available.[10]

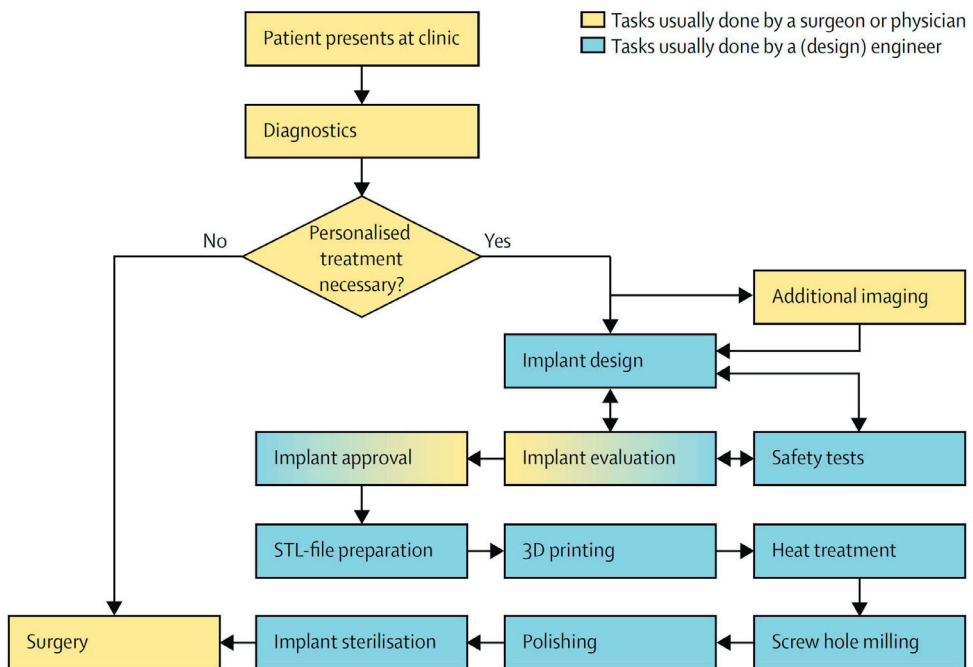


Figure 7. Workflow for development of personalized 3D implants. After a patient has been identified as needing personalized treatment, additional imaging is occasionally required to obtain higher-resolution images to allow optimal segmenting of the anatomical model. On this model, an implant is designed. After the design process, the implant needs to undergo formal (prototype) testing, after which a critical evaluation of the implant is made. Then, either the implant is approved for production or needs to be redesigned before undergoing another safety test and subsequent evaluation. The production requires STL-file preparation, which is uploaded to the 3D printer for physical 3D-printing. In our cases, we used hot isostatic pressing of the implant as a stress relieving treatment. After the heat treatment, the screw holes were finished, the implant was polished, and finally the implant was sterilized before surgery. 3D=three-dimensional. STL=standard tessellation language.

To fulfil all requirements from annex XIII of the EU Medical Device Regulation, all procedures involved in the design and production of the device must be registered for medical use. This requirement might be difficult to meet if using software packages, which are not always registered for medical use, although the EU Medical Device Regulation is not clear about whether the segmentation software and design software are medical devices themselves. In our cases, we had to guarantee that the shape and size of the 3D-printed implant would precisely fit to ensure no problems would occur during the operative procedure. Therefore, we thoroughly inspected and verified the size and shape of a plastic printed version of both the vertebrae and the implant. With respect to extensive mechanical tests, it was reasonable to presume that the implants would be stronger than conventional rods because of the increased diameter of the patient-specific implants; in fact, we maximized the size of the implants only on the basis of anatomical limitations. The finite-element analysis was done to confirm the hypothesis that the patient-specific implant would be stronger than a conventional rod. Because of time restrictions, the compression test was not done before the implantation for case 1. Nevertheless, a pro-forma compression test was done on one of the remaining oversized implants to confirm the safety and to act as a precedent for future cases, including case 2 (appendix p 2).

When the primary concern is the health of the patient, the surgeon can take responsibility for decisions that might deviate from the typical regulations, as long as they verify the safety of the treatment approach by providing argumentation and the rationale in the technical file for the implant. Whereas review by an ethics board is mandatory for experimental devices in clinical studies, it is not required for the application of new techniques and devices when patients are not participating in a clinical study.[22] For such applications, the physician is responsible for ethical considerations, and for providing extensive information to the patient and acquiring their consent.[7, 22]

To allow the advancing technical possibilities of custom medical devices to be realized in spite of the increasingly strict legislation on its use, close collaborations between physicians and engineers are essential, as are well documented technical files.[18] In this regard, in-house knowledge on the design of 3D-printed implants is extremely helpful, and can even be a prerequisite in cases where time is limited. Face-to-face meetings among all parties involved in the planning and production of the device, as well as of generation of prototypes in-house, can speed up development.[23] The coordinator of the development workflow should preferably be either a physician who has received extensive training in design engineering, or a biomedical engineer who is trained to understand anatomy and surgical procedures.[18] In many countries, medical technicians or design engineers are educated to design custom medical devices and guides for commercial companies. Incorporation of all the required services (engineering, legal, anatomy, and surgical) within one medical facility is of great value, especially for urgent cases.

When conventional methods are not an option, patient-specific treatment approaches can be helpful in carefully selected cases. A valid technical file with all necessary documents is essential to ensure the safety and legal validity of the approach. In this article, we have provided a blueprint technical file based on two consecutive cases in which patient-specific implants were used with excellent results. We hope that this information can accelerate the introduction of personalized implants for other physicians. However, consideration must be given to local ethics and governmental legislation in other regions.

Supplementary Material:

[http://dx.doi.org/10.1016/S2589-7500\(19\)30067-6](http://dx.doi.org/10.1016/S2589-7500(19)30067-6)

References

1. Hoang D, Perrault D, Stevanovic M, Ghiassi A. Surgical applications of three-dimensional printing: a review of the current literature & how to get started. *Ann Transl Med* 2016; 4: 456.
2. Martelli N, Serrano C, van den Brink H, et al. Advantages and disadvantages of 3-dimensional printing in surgery: a systematic review. *Surgery* 2016; 159: 1485–500.
3. Xu N, Wei F, Liu X, et al. Reconstruction of the upper cervical spine using a personalized 3D-printed vertebral body in an adolescent with Ewing sarcoma. *Spine* 2016; 41: E50–54.
4. Pijpker PA, Kuijlen MA, Kraeima J, Faber C. Three-dimensional planning and use of individualized osteotomy-guiding templates for surgical correction of kyphoscoliosis: A technical case report. *World Neurosurg* 2018; 119: 113–17.
5. Parker SL, Wolinsky JP, Tufaro AP, Gokaslan ZL, Witham TF. Five-level cervical corpectomy for neurofibromatosis-associated spinal deformity: case report. *Eur Spine J* 2015; 24 (suppl 4): 544–50.
6. Wilcox B, Mobbs RJ, Wu AM, Phan K. Systematic review of 3D printing in spinal surgery: the current state of play. *J Spine Surg* 2017; 3: 433–43.
7. European Parliament, Council of the European Union. Regulation (EU) 2017/745 of the European Parliament and of the Council of 5 April 2017 on medical devices, amending Directive 2001/83/EC, Regulation (EC) no 178/2002 and Regulation (EC) no 1223/2009 and repealing Council Directives 90/385/EEC and 93/42/EEC. <https://www.emergogroup.com/sites/default/files/europe-medical-devices-regulation.pdf> (accessed Feb 21, 2019).
8. Phan K, Sgro A, Maharaj MM, D'Urso P, Mobbs RJ. Application of a 3D custom printed patient specific spinal implant for C1/2 arthrodesis. *J Spine Surg* 2016; 2: 314–18.
9. Bracci R, Maccaroni E, Cascinu S. Transient sunitinib resistance in gastrointestinal stromal tumors. *N Engl J Med* 2013; 368: 2042–43.
10. US Food and Drug Administration. Custom device exemption: guidance for industry and Food and Drug Administration staff. Sept 24, 2014. <https://www.fda.gov/media/89897/download> (accessed June 3, 2019).
11. de Beer N, Van Der Merwe A. Patient-specific intervertebral disc implants using rapid manufacturing technology. *Rapid Prototyping J* 2013; 19: 126–39.
12. Williams VC, Lucas J, Babcock MA, Gutmann DH, Korf B, Maria BL. Neurofibromatosis type 1 revisited. *Pediatrics* 2009; 123: 124–33. Akbarnia BA, Gabriel KR, Beckman E, Chalk D. Prevalence of scoliosis in neurofibromatosis. *Spine* 1992; 17 (suppl): S244–48.
13. Duhem-Tonnelle V, Vinchon M, Defachelles AS, Cotten A, Dhellemmes P. Mature neuroblastic tumors with spinal cord compression: report of five pediatric cases. *Childs Nerv Syst* 2006; 22: 500–05.
14. Yilmaz K, Ozmen M, Goksan SB, Eskiyurt N. Bone mineral density in children with neurofibromatosis 1. *Acta Paediatr* 2007; 96: 1220–22. Taniguchi N, Fujibayashi S, Takemoto M, et al. Effect of pore size on bone ingrowth into porous titanium implants fabricated by additive manufacturing: an in vivo experiment. *Mater Sci Eng C* 2016; 59: 690–701.

15. Van der Stok J, Van der Jagt OP, Amin Yavari S, et al. Selective laser melting-produced porous titanium scaffolds regenerate bone in critical size cortical bone defects. *J Orthop Res* 2013; 31: 792–99.
16. Choy WJ, Mobbs RJ, Wilcox B, Phan S, Phan K, Sutterlin CE 3rd. Reconstruction of thoracic spine using a personalized 3D-printed vertebral body in adolescent with T9 primary bone tumor. *World Neurosurg* 2017; 105: 1032.e13–17.
17. Benedetti M, Torresani E, Leoni M, et al. The effect of post-sintering treatments on the fatigue and biological behavior of Ti-6Al-4V ELI parts made by selective laser melting. *J Mech Behav Biomed Mater* 2017; 71: 295–306.
18. Nikolaou VS, Chytas D, Korres D, Efstathopoulos N. Vanishing bone disease (Gorham-Stout syndrome): a review of a rare entity. *World J Orthop* 2014; 5: 694–98.
19. Choy WJ, Parr WCH, Phan K, Walsh WR, Mobbs RJ. 3-dimensional printing for anterior cervical surgery: a review. *J Spine Surg* 2018; 4: 757–69.
20. ACOG Committee on Ethics. ACOG Committee opinion no 352: innovative practice: ethical guidelines. *Obstet Gynecol* 2006; 108: 1589–95.
21. Krause FL, Ciesla M, Stiel C, Ulbrich A. Enhanced rapid prototyping for faster product development processes. *CIRP Ann* 1997; 46: 93–96



CHAPTER 17

Vital role of in-house 3D lab to
create unprecedented solutions for
challenges in spinal surgery
Practical guidelines and clinical
case series

Koen Willemsen | J. Magré | J. Mol | E. Hekman | H.J. Noordmans |
H. Weinans | M.C Kruyt

Published in:
Journal of Personalized Medicine, special issue: Personalized Spine Surgery (2022)
<https://doi.org/10.3390/jpm12030395>

Abstract

For decades, the advantages of rapid prototyping for clinical use have been recognized. However, demonstrations of potential solutions to treat spinal problems that cannot be solved otherwise are scarce. In this paper, we describe the development, regulatory process, and clinical application of two types of patient specific 3D-printed devices that were developed in an in-house 3D point-of-care facility. This 3D lab made it possible to elegantly treat patients with spinal problems that could not have been treated in a conventional manner. The first device, applied in three patients, is a printed nylon drill guide, with such accuracy that it can be used for insertion of cervical pedicle screws in very young children, which has been applied even in semi-acute setting. The other is a 3D-printed titanium spinal column prosthesis that was used to treat progressive and severe deformities due to lysis of the anterior column in three patients. The unique opportunity to control size, shape and material characteristics allowed a relatively easy solution for these patients, who were developing paraplegia. In this paper, we discuss the pathway towards the design and final application, including technical file creation for dossier building and challenges within a point-of-care lab.

Introduction

Additive manufacturing, commonly known as 3D printing, has been adopted as one of the key elements of future medical care. The entire process has evolved and progressed over the last 20 years, first in labs for fundamental research and subsequently for actual clinical care.[1]–[3] 3D technology provides new tools to treat complex and previously untreatable surgical problems while increasing accuracy.[4] However, to optimally benefit from such front-running technological enhancement, close interaction between all stakeholders and especially between technical and medical personnel is mandatory.[3]

Therefore, an increasing number of hospitals are establishing a 3D printing point-of-care facility in which the opportunities of 3D printing, in terms of technical possibilities and legal/regulatory challenges, can be fully explored.[5], [6] Such a facility, frequently known as a (point-of-care) 3D lab, uses the output of established state-of-the-art clinical image modalities such as the newest CT and MRI and subsequently post-processes the data into digital anatomical models to better embody the patient and to allow interaction with surgeons for the development of custom-made medical devices.[7]–[10] To enable this, the 3D lab personnel is a multidisciplinary team to remove boundaries such as jargon, and should be able to quickly produce 3D models, prototypes and even implants under governance of an appropriate quality management system (ISO 13485:2016).[5]

This 3D technology is especially important for tertiary referral hospitals, which primarily functions as a specialized center for complex cases and ultimately functions as a safety net for last-resort cases.[6], [11] These hospitals have an academic setting where research, innovation and unique treatments come together.[11] As a result, exceptional cases which demand exceptional solutions are referred to these hospitals. To optimally serve this academic role, medical doctors, engineers and researchers are working together closely in fundamental and innovative research projects within the 3D lab.[3]

In this paper we demonstrate two additive manufacturing pathways that were created as a collaboration between a tertiary spinal surgery unit and an established point-of-care 3D lab within one academic hospital. The first pathway is a patient-specific device to guide cervical pedicle screws in very young children or patients with extraordinary spinal anatomy. The second pathway is an additively manufactured implant that is used as a spinal prosthesis to bypass the severely distorted and mechanically instable spinal column. For both pathways background information is given, followed by the methodology and clinical results.

Pathway 1: Click-on guide for cervical pedicle screws

Background

For spinal surgery, pedicle screws that run from posterior to anterior are currently the most used fixation technique. Since the ground-breaking work of Suk et al. in 1995[12], spine surgeons also adopted its use for challenging locations such as the scoliotic thoracic spine.[13], [14] Although the pedicle screw trajectory seems dangerous, as it passes immediately next to the spinal canal (Fig. 1), its use has been demonstrated to be safe in experienced hands, even when the screws are not positioned perfectly. About 10% of the free-hand-positioned screws show some breaching of the pedicle, medially or laterally, without clinical consequences.[15] For the cervical spine, mispositioned pedicle screws are less forgiving as the vertebral artery constitutes the lateral border of the trajectory, which makes a “lateral breaching” intolerable (Fig. 1). For that reason, most surgeons prefer the weaker lateral mass screws for cervical spine fixation.[16] In young children, the lateral mass has not yet developed and cannot serve as a foundation for screws, especially if distraction or pull-out forces are expected.[16] Alternative options such as hooks and wires, can be used but have serious risk of neurological complications. Consequently, placement of cervical pedicle screws to obtain strong cervical spine foundations is currently a high-risk procedure in very young children.[17], [18] Even 3D navigation, which can be used for this application in adults, may not allow sufficient accuracy due to the movement introduced by mechanical ventilation and the limited intraoperative image resolution.[17]–[19]

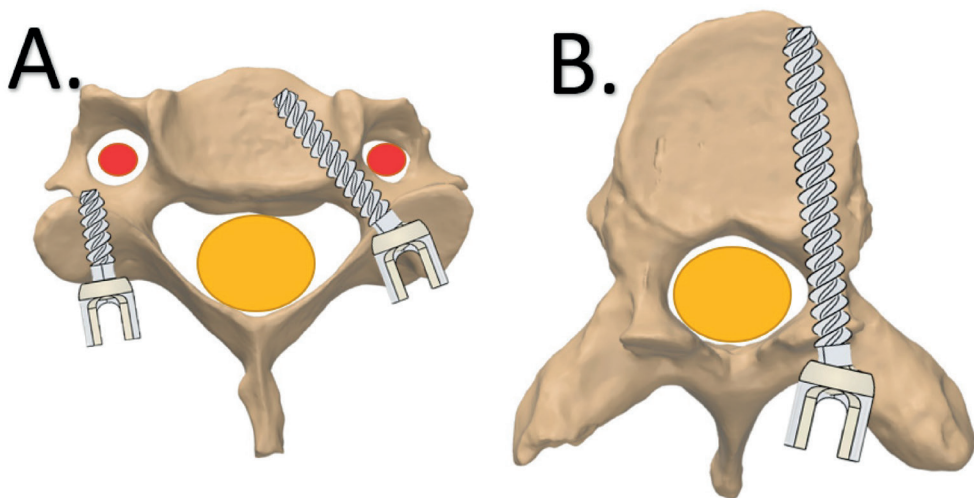


Figure 1. Screw placement in vertebrae, axial view. A. cervical vertebrae with a lateral mass screw (left) and pedicle screw (right). B. thoracic vertebrae with a right sided pedicle screw. The red area is the cervical artery and the yellow area is the spinal cord.

To aid surgeons with pedicle screw positioning in adults, patient specific 3D printed drill guides have been developed by several groups.[16], [20]–[22] These drill guides are based on direct surface contact on the laminae and transverse and spinous processes of one or sequential vertebrae, but this does not always reach the required accuracy for cervical use.[23]–[26] In both metal and polyamide lay-on drill guides screw tip deviation can still be $>2\text{mm}$ (Fig. 2)[23]–[26], which is unacceptable in the axial plane of cervical vertebrae, especially in young and small children.[17], [18]

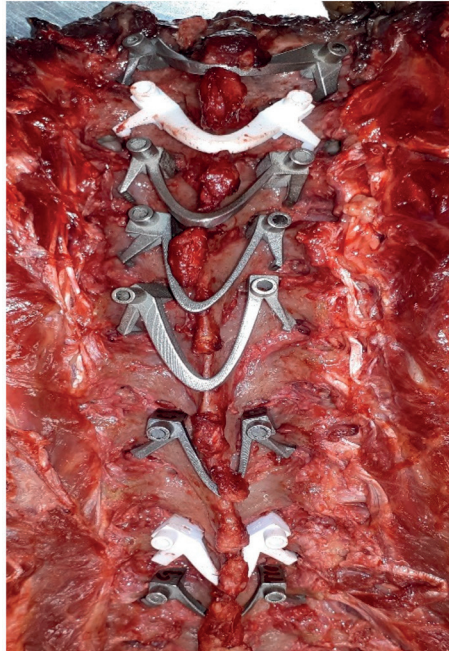


Figure 2. Examples of metal and polymer lay-on spine guides in thoracic cadaveric spine.

Moreover, the surface of the lateral apical processes, needed for optimal rotational stability, is difficult to clean from soft tissue, especially in the pediatric cervical spine where apophyseal cartilage is present. This soft tissue component hampers a perfect fit between the lay-on guide and vertebra. Additionally, the spinous process needed for sagittal stability cannot be used in the pediatric cervical spine. The only and most accessible smooth bone surfaces of the pediatric cervical spine are found at the laminae. However, the more medial laminae do not allow sufficient stabilization of the lay-on guide. Therefore, since the laminae is oval in cross-section, a clamp which is placed around it, will effectively block all degrees of freedom except perpendicular to the sagittal plane. This motion can be blocked with extensions that rests on the entry point of the pedicles. Consequently, we designed a click-on assembly that can be clamped around the bilateral laminae and harbors a drill guide in the upper part (Fig 3).

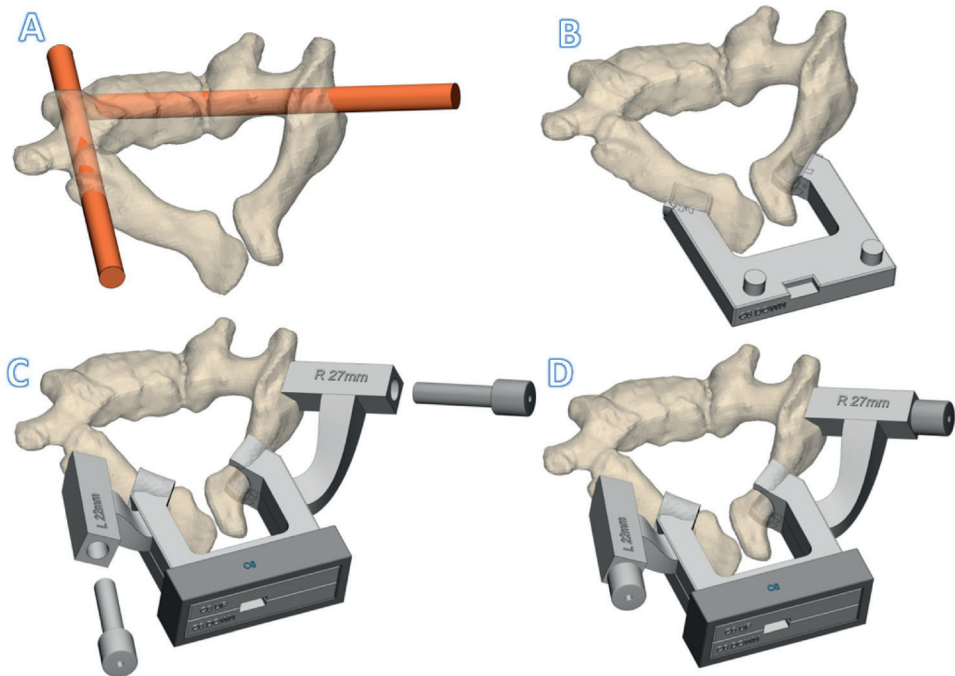


Figure 3. Rendering of a C6 click-on spine guide

A. The preferred screw trajectories B. The interconnected lamina hooks of the caudal part C The cranial part including the drill guide cavities and the (metallic) drill guides D. Fixation of the assembly with the fixation box, included the inserted drill guides.

Device description of click-on pedicle guides

Anatomical data acquisition

First a CT scan is made of the patient with $\leq 1\text{mm}$ slice thickness (250mAs, 120kV). We consider this resolution sufficient and in accordance with the “as low as reasonable possible” principle for radiation. Thereafter, the DICOM data are transferred to medical licensed segmentation software (Mimics, Materialise NV, Leuven, Belgium) to create an anatomical model of the spine of the patient. Together with the surgeon the screw trajectory is planned for the desired vertebrae. Thereafter, the anatomical models and screw trajectories are exported to medical certified CAD-CAM software (3-matic, Materialise NV, Leuven, Belgium) to design the click-on pedicle guides.

Design

The patient specific cervical pedicle click-on guide consists of three components that are assembled on the laminae during the surgery. First, the lower part contains two lamina hooks which are designed to exactly fit the caudal side of the laminae. Then the top part is designed which has two laminar hooks that exactly fit on the cranial side. Moreover, the top part also contains two extensions with cylindrical cavities for metallic drill guides. The exact trajectories of those drill guides are established in collaboration with the surgeon. Thereafter, the lower and top parts dock and can be rigidly fixed to each other using a simple fixation box (Fig. 3). Finally, cylindrical metal drill guides are inserted in the guide cavities. More details on the design are provided in the supplementary data.

Guide production

All three parts of the guide were 3D-printed under the ISO13485 quality management system. The guides were produced using selective laser sintering of nylon powder (PA12) with a printing accuracy of 0.12 mm in all directions (P110, EOS, Krailing, Germany). Before sterilization, the accuracy of the assembly was checked on the receiving cervical vertebrae that were printed separately with the same resolution. Thereafter, the guides were sterilized at our in-house sterilization facility by manual cleaning and standard autoclave sterilization (ISO 17665-1:2016 and EN 285) and sterile packaging (ISO 11607-1:2019).

Preclinical tests

The nylon versions of the click-on spine guides showed excellent stability and acceptable accuracy in cadaveric tests (Fig. 4). The average entry point deviation was 0.98 ± 0.38 mm and average angular deviation from the midline was $1.75 \pm 0.62^\circ$ (n=4).

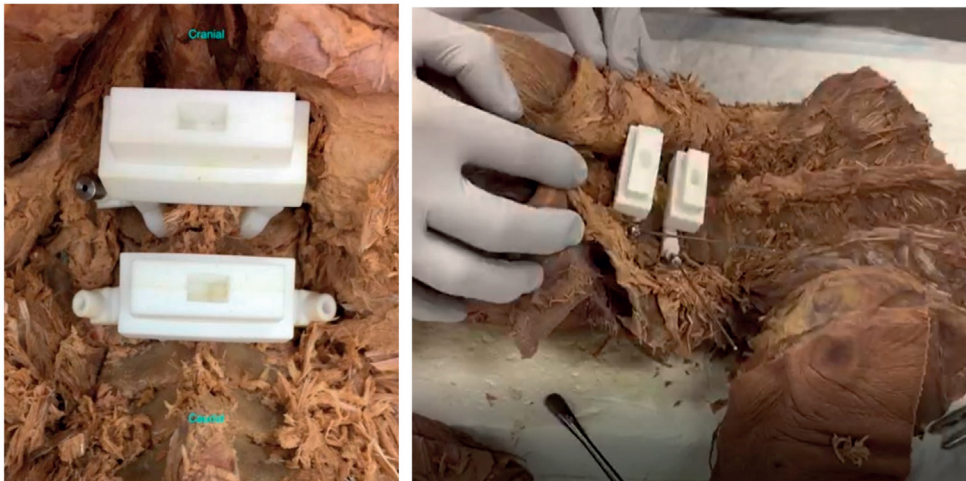


Figure 4. Photos of the cadaveric experimental set-up to test the accuracy of the click-on pedicle guides.

Clinical application

The cervical guide has been applied in two cases of spinal distraction and one case of emergency treatment. In our center we use spring distraction as a growth guidance technique for severe deformities that cannot be controlled with less invasive techniques such as braces or halo vests.[27] For cervicothoracic congenital deformities especially, the technique has shown the potential to not only control but even to reduce the deformity. [28] To allow continuous distraction forces on the cervical vertebrae a strong and reliable foundation is a prerequisite. Two patients (age 4 years) have currently been treated with spring distraction delivered to cervical pedicle anchors and in both cases a click-on spine guide was designed and used intraoperatively.

The first case was a 4-year-old boy with congenital scoliosis. For safety reasons, the C5 and C6 pedicle screws were only inserted unilaterally at the distraction side. Intraoperatively, after insertion of the K-wire, the position was checked with radiographs, after which 3.5 mm pedicle screws were placed. The procedure went well however, on the postoperative CT, we noticed a slight cranial deviation in the sagittal plane. This was likely caused by forces on the device due to insufficient exposure proximally, something that we took care of in the later procedures. There were no medial or lateral breaches and the distraction force (of 75N) was well sustained. This case has been followed up for almost 3 years now (Fig. 5).

The second case was a 4-year-old boy with Pierre Robin syndrome and severe high thoracic scoliosis. A halo vest had failed to control the curve; therefore, the spring distraction system was considered the best treatment. Unilateral placement of C6 and C7 pedicle screws was uneventful and smooth (<10 minutes per screw) with use of the click-on guides (Fig. 6). The latest follow-up is 9 months (Fig. 7).

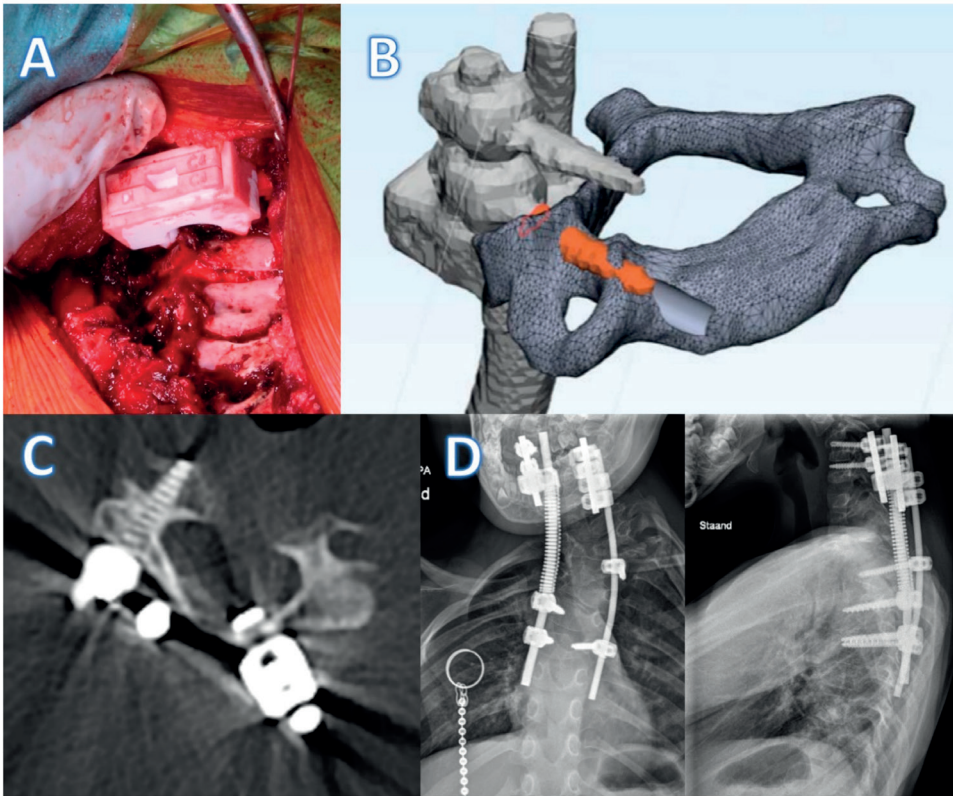


Figure 5. Click-on guide case 1.

A. Intraoperative use of the click-on guide, exposure of the operative site limited due to interference with the posterior skull. B. Slight upward deviation of the C6 screw (orange) in comparison to the planned trajectory (gray). C. Post-operative axial CT reconstruction with the screw precisely through the pedicle. D. Post-operative radiographs of the instrumented spine

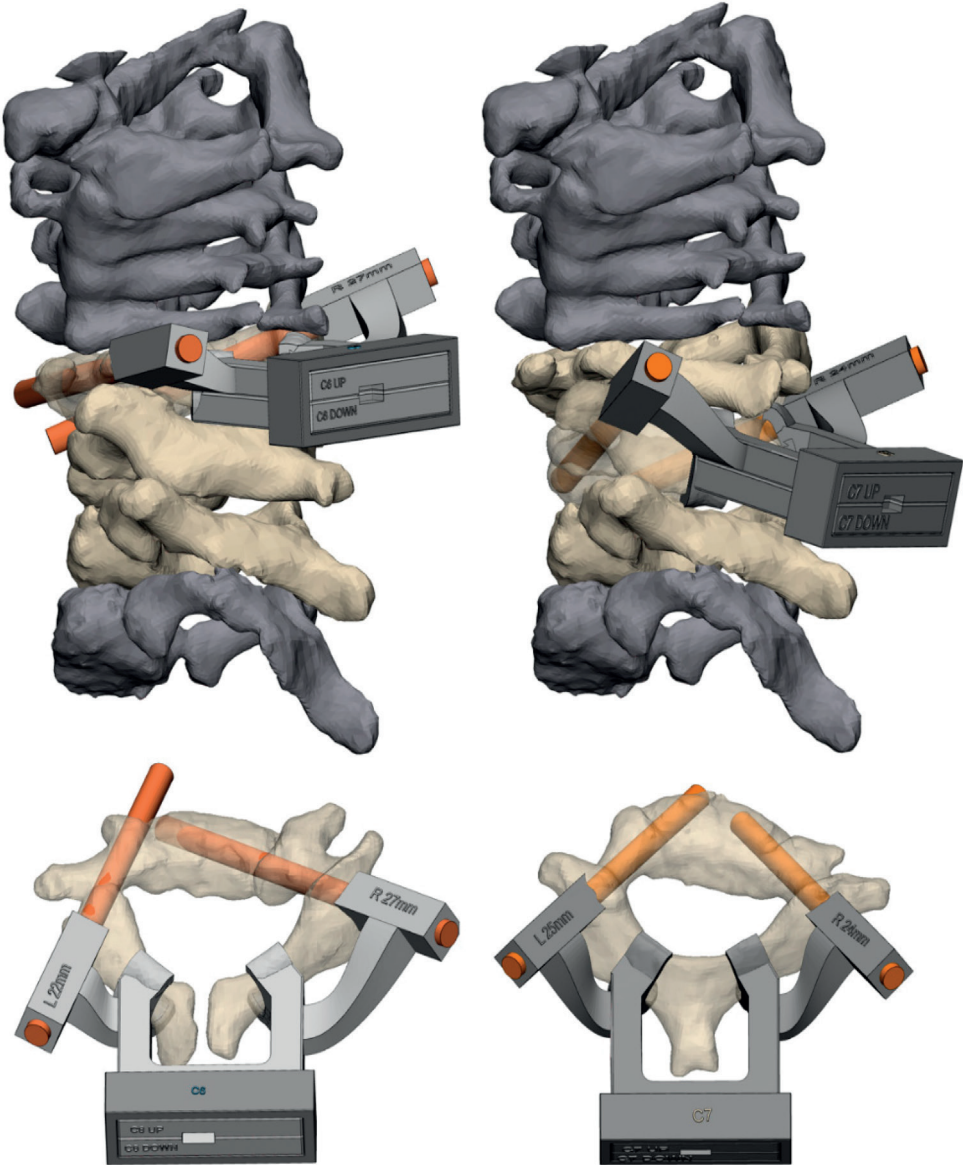


Figure 6. Click-on guide case 2. On the left side, the guide for C6; on the right side, C7. The orange cylinders are the target screw trajectories in the design.

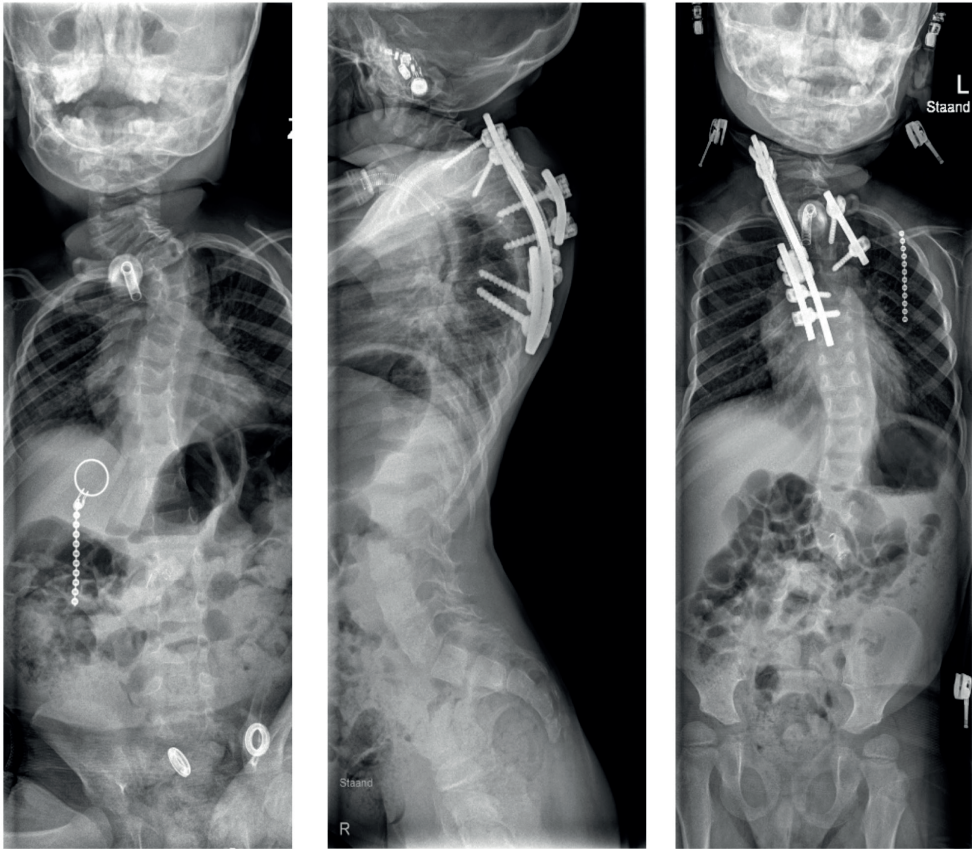


Figure 7. Case 2: preoperative AP sitting radiograph (**left**) and postoperative lateral (**middle**) and AP (**right**) standing radiographs

The third case did not receive a spring distraction; it had a more urgent situation. This 8-year-old girl presented in the emergency setting for basilar impression and impeding paraplegia due to high cervical congenital anomalies. Decompression of the C1 lamina was needed and due to the absence of C2 pedicles, an occiput to C3 fusion was performed. We mistakenly used only lateral mass screws (6 mm), which could not prevent recurrence of kyphosis and signs of paraplegia within 3 weeks. Therefore, immediate halo traction was provided, which reduced the head and reversed the paraplegia. Because this was not a permanent solution, we decided to revise the internal fixation with C5-6 pedicle screws and a free-hand C2-to-C1 fixation screw. Due to the available template for the click-on guides and especially the in-house availability of the 3D lab, the guide was produced within 1 week, which allowed for successful semi-acute revision. In this case, there was a fusion of certain vertebrae, which resulted in a combined guide for two levels of vertebrae

(C5-6) within one system (Fig. 8). Currently at 9 months follow-up, the patient is fully recovered and does not show signs of fixation failure.

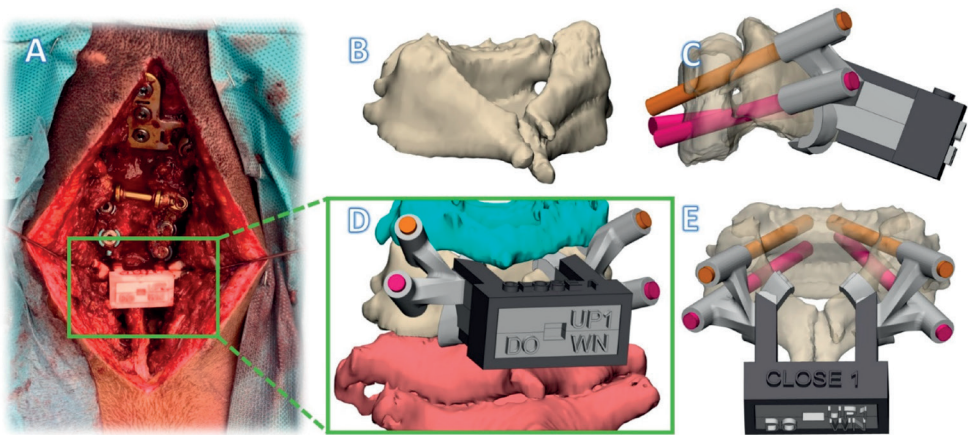


Figure 8. Click-on guide case 3.

A. Intraoperative photo B. Fused vertebrae C5-C6 C. Lateral view of alternative guide design with four pedicle guides from two levels in one click-on guide system D. Rendering of guide with cranial and caudal vertebrae also visible E. Posterior view of the guide system.

Pathway 2: Spinal cmn prosthesis

Background

The spinal column has been described as a mechanical construction that resembles a crane (Fig. 9). The metaphor of a crane is especially helpful to determine the cause of instability after spinal trauma. The key elements of a stable construction are the anterior column to support axial compressive forces and the posterior ligamentous complex that functions as a tether.[29], [30] As long as the posterior tether mechanism and facet joints are intact, kyphosis is prevented even when individual vertebral bodies collapse. However, when anterior support fails, for instance, due to a lytic disease involving several vertebrae and/or the facet joints, the posterior tether cannot stabilize the construction and progressive kyphosis results, often inducing paraplegia. Classic examples of this are lytic metastases, tuberculosis and neurofibromatosis. Additionally, neurofibromatosis causes severe scoliosis, which leads to a complex 3D deformity. When kyphosis occurs in such a complex deformity, it extends over several vertebrae and involves the cervicothoracic region. In this case, restoration of anterior support with fibular or rib grafts is extremely difficult, very invasive, and has a high chance of complications.[31] This is because internal chest structures such as the heart and bronchi do not allow a bulky implant and incorporation of the graft bone over a long distance is hampered.

To circumvent these difficulties, we developed the a 3D-printed personalized spinal prosthesis. The custom-made implant, can be inserted in a way which that is mini-mally invasive and, allows for the incorporation of bone into the porous ends of the implant. It and has a massive titanium stem that exactly follows the spinal contour with a substantial cross-sectional surface to prevent fatigue failure in time [3].

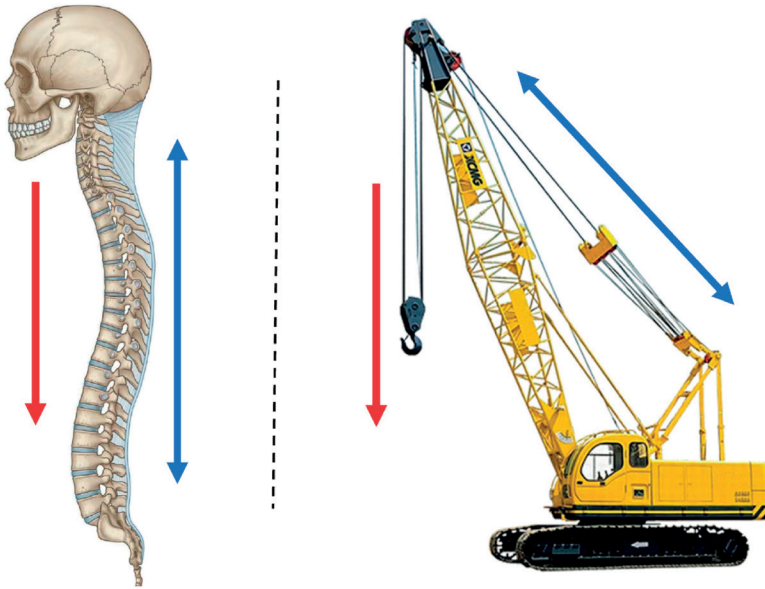


Figure 9. Resemblance of spinal balance equilibrium with a crane.

Red arrows represent (body) weight carried by the vertebrae (left) and crane arm (right). The blue arrows represent the stabilizing counterforce (tension) by the posterior ligamentary complex (left) and tension cables (right).

Device Description of Spinal Prosthesis

Anatomical Data Acquisition

First, a CT scan is made of the patient with ≤ 1 mm slice thickness (250 mAs, 120 kV). Thereafter, the DICOM data are transferred to medical licensed segmentation software (Mimics, version 24.0, Materialise NV, Leuven, Belgium) to create an anatomical model of the spine of the patient. Together with the surgeon, the appropriate vertebrae above and below the scoliotic segment are selected, after which the anatomical model containing the selected vertebrae are exported to medical certified CAD-CAM software (3-matic, version 15.0, Materialise NV, Leuven, Belgium) to design the bridging spine implant.

Design

The biomechanical spinal strut or bridge prosthesis consists of two docking parts with a porous interface (Figure 10A) and a solid bridging part (Figure 10B). A more de-tailed design description of the prosthesis is provided in the Supplementary Data. As part of the recommended dossier building for any medical device, a risk analysis was performed by a multidisciplinary team.

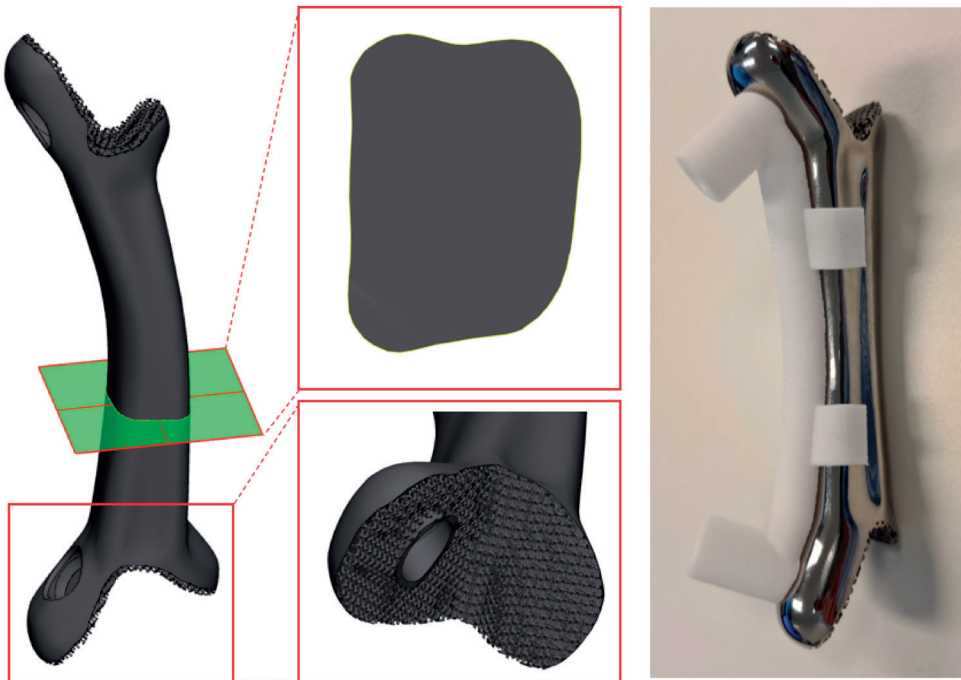


Figure 10. The implant design. Left is a rendered model of the implant. In the middle a cross section and a close up of the porous interface. On the right side the actual 3D-printed implant with a nylon drill guide attached.

Implant Production

The implants were 3D-printed using medical-grade titanium alloy (Ti6Al4V ELI grade 23). The printing was done performed with a direct-metal-printing 3D-printer DMP320 (3D Systems, Leuven, Belgium). Post-processing included hot isostatic pressing treatment, mirror polishing, ultrasonic cleaning, and quality control. Final (manual) cleaning and standard autoclave sterilization of the implants was done performed in-house. All accompanying drill guides, dummies, and trial implants were produced from nylon PA12 following the same production steps as the click-on pedicle screw guides.

Clinical Experience with Spinal Prosthesis

The spinal bridge prosthesis has been applied in three cases with spinal instability and posterior rod failure. The first two patients of this pathway were described previously in a paper on regulatory issues involved in developing 3D printed implants [3]. The first patient was a 16-year-old male suffering from neurofibromatosis type 1 and recurrence of kyphosis despite previous attempts of posterior fusion. He presented with paraplegia for which he was treated with halo gravity traction and revision of posterior instrumentation. Since this would definitely fail in time, we searched for a possibility to provide anterior support from C6 to T11. The main difficulties were the complicated 3D anatomy including the position of the vena cava and right bronchus and the absence of a bone bed. The 3D prosthesis that we made, after a 6-month design process that went back and forth between designer and surgeon, could be inserted within 2 hour via two separate incisions and had an excellent fit [3]. Follow-up is three years now without signs of failure.

The second case was a 69-year-old woman with vanishing bone disease of the lower cervical spine. She had several treatments for vertebral stability within the last 20 years, but the posterior instrumentation repeatedly failed and she presented with severe deformation and paraplegia. Fortunately, paraplegia recovered after halo traction and the spine was temporarily stabilized with posterior instrumentation and a halo vest. Using the procedural template of the first patient concerning design as well as regulatory, safety, and dossier implementation, we could produce a prosthesis within 6 weeks. This prosthesis provided support from C5 to T2 and was inserted with an extended anterolateral cervical approach [3]. This case has been followed up for 2.5 years now.

The third patient was referred in time, before paraplegia had occurred. This 20-year-old man had a posterior stabilization of his NF1 associated dystrophic ky-phoscoliosis (similar to the first patient) five years earlier, but the rods fractured and the kyphosis increased due to absence of anterior support. This timely referral made the procedure much easier, especially for the patient, as halo traction was not required and a two-stage treatment could be planned. With the revision of the posterior system, we deliberately inserted a screw that protruded anteriorly to serve as a reference for the anterior prosthesis that would be placed in the second stage. Due to the nature of the deformity, the prosthesis had to be inserted posterior to the heart on the left side, extending from T2 to T8 (Figures 11 and 12). Before actual surgery, the exposure and order of events of the procedure were simulated in the 3D lab using a HoloLens (Microsoft, Redmond, Washington, DC, USA). We used a posterolateral approach with partial resection of rib 3, 4, and 5. The three-hour procedure happened without issues and resulted in a tight fit of the implant. At 3 months follow-up the implant was stable, and no material breakage occurred. Clinical follow-up is 6 months now.

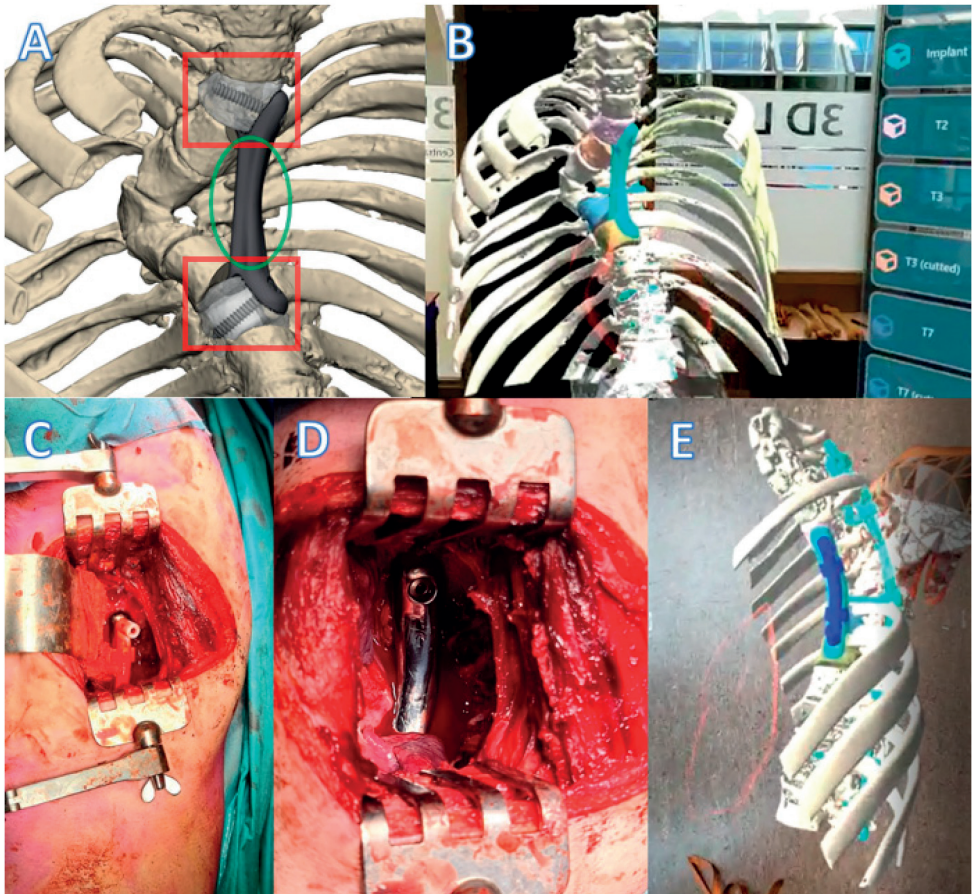


Figure 11. Spinal column prosthesis case 3. **A.** Design of the spinal column prosthesis. Within the red squares are the partially porous bone connectors. In the green circle the bridging part of the implant is visible. **B.** A still from a recording of a pre-operative HoloLens surgical training. **C.** Intraoperative photo of the prosthesis with a drill guide in situ (left anterior, right posterior). **D.** close-up after screw fixation. **E.** A still from a recording of the pre-operative HoloLens surgical training (same approach as picture **D**).

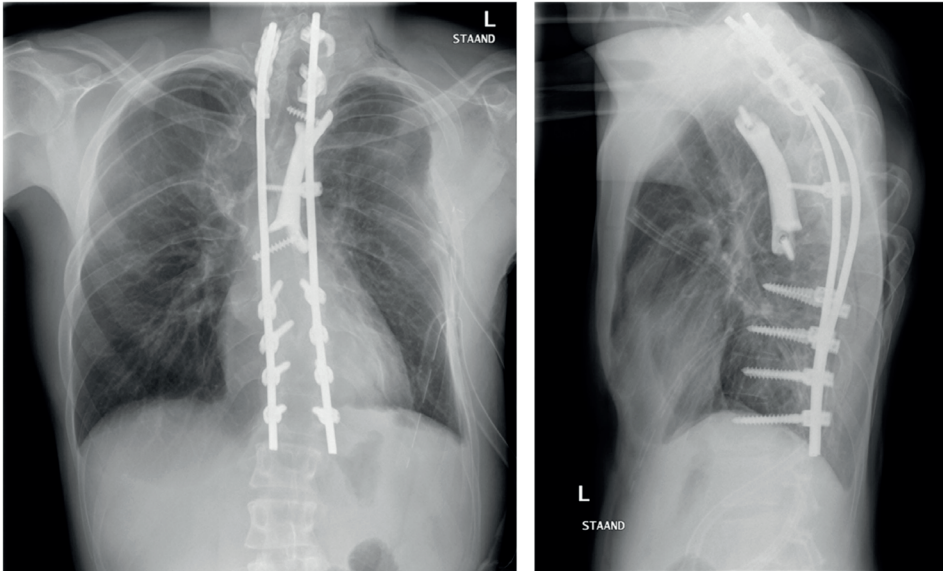


Figure 12. Case 3: Anterior-posterior (left) and sagittal (right) radiographs post-op.

Discussion

To treat exceptional spinal cases, exceptional solutions are needed. In this paper, we described the application of patient-specific 3D-printed devices for such solutions and strived to emphasize the potential of this technology, especially when available at an in-house 3D lab. To optimally explore the opportunities of additive manufacturing and 3D personalized design technology in terms of unrecognized possibilities and unmet needs, medical doctors, engineers, and researchers are working closely together in fundamental and innovative research projects.

Medical technology is a fast-growing sector with new devices entering the market each day [32,33]. To protect patients from poorly designed or not sufficiently tested medical devices, new legislation was introduced in 2021. The European Medical Device Regulations (MDRs) describe the precise legislation regarding the development of all medical devices [34]. Moreover, in the MDRs, there is a special section (Annex 13) for the production of patient-specific medical devices, which is important as the growing additive manufacturing industry has enabled an increasing number of hospitals to produce their own in-house-designed products [34]. The MDR dictates that hospitals that produce such patients-specific devices are now also the legal manufacturer of these devices, making them responsible for their quality. This includes the devices presented in this study, which were developed to treat rare cases. To mitigate risks and comply with this new legislation,

all in-house development of medical devices needs an appropriate Quality Management System (ISO13485) and multidisciplinary expertise for dossier building. Thankfully, we anticipated this change and started early with a multidisciplinary collaboration for 3D technology within our hospital and with affiliated technical universities [5]. This collaboration resulted in the current 3D lab with medically trained staff and engineers and had support of the Medical Technology and Clinical Physics department that was already ISO-13485-accredited for medical device development. Factors that need to be considered according to the ISO standard include risk analysis, traceability of procedures and implants, ISO certifications of critical suppliers, and a technical rationale per medical device.

Nowadays, our 3D lab has a Quality Management System in place that allows us to produce these devices under the current MDR, including fully supported dossier building. This way, we can deliver patient-specific solutions for specific (spine surgery) problems that previously could not be treated. Another major benefit of having an in-house design process is the intensive interaction between the 3D lab and the surgeons. During the design of these devices, we regularly have multidisciplinary meetings, sometimes multiple times per week. Visual models can be printed in-house, quickly obtaining a better insight into patient anatomy. This allows us to accelerate the iterative steps in the design process and shorten the lead time from scan to surgery [35,36].

This 3D technology can help hospitals with perioperative models for surgical training and patient awareness [37,38]. Furthermore, 3D technology helps physicians to increase their accuracy and allow for options that were previously not possible using conventional manufacturing methods [39,40]. However, there are also limitations for the point-of-care production of in-house-developed devices. Physicians should only opt for patient-specific medical devices when a conventional commercially available treatment is not available or would not have the desired outcome, as commercial implants are considered safer due to even stricter registration conditions. Furthermore, the treating physician should weigh the added value of a personalized implant against the costs, which are especially high as a result of the laboriousness of the process. However, the labor decreases with established pathways and the costs for production decrease as the market matures.

Another limitation of implementing 3D-printed patient-specific implants into regular clinical care is the lack of reimbursement of costs by the insurance companies. In many countries, the use of patient-specific medical devices, as described in this paper, are not part of standard care [41]. One of the reasons for this is the lack of evidence, which is hard to establish for exceptional and very diverse cases. However, as the custom-made devices market matures, the advantages will become evident, followed by reimbursement solutions [41].

Conclusions

In this paper, we showed two successfully implemented 3D-printed patient-specific device pathways that were developed in collaboration with a point-of-care 3D laboratory in an academic hospital, leading to short lead times for products that comply with current (inter)national regulations. The establishment of such a 3D lab for in-house development demonstrated great value for tertiary referral hospitals that regularly see exceptional cases, which demand fast and exceptional solutions.

Supplementary Material:

https://1drv.ms/b/s!AjdWTaQAIFN0p4NzM2VXCu1n_oRp3g?e=2DWQ7C

References

1. Aimar A, Palermo A, Innocenti B. The role of 3D printing in medical applications: a state of the art. *Journal of healthcare engineering*. 2019;2019.
2. Wilson CE, de Bruijn JD, van Blitterswijk CA, Verbout AJ, Dhert WJA. Design and fabrication of standardized hydroxyapatite scaffolds with a defined macro-architecture by rapid prototyping for bone-tissue-engineering research. *Journal of Biomedical Materials Research Part A: An Official Journal of The Society for Biomaterials, The Japanese Society for Biomaterials, and The Australian Society for Biomaterials and the Korean Society for Biomaterials*. 2004;68(1):123-132.
3. Willemsen K, Nizak R, Noordmans HJ, Castelein RM, Weinans H, Kruyt MC. Challenges in the design and regulatory approval of 3D-printed surgical implants: a two-case series. *The Lancet Digital Health*. 2019;1(4). doi:10.1016/S2589-7500(19)30067-6
4. Vlachopoulos L, Schweizer A, Graf M, Nagy L, Fürnstahl P. Three-dimensional postoperative accuracy of extra-articular forearm osteotomies using CT-scan based patient-specific surgical guides. *BMC musculoskeletal disorders*. 2015;16(1):1-8.
5. Calvo-Haro JA, Pascau J, Asencio-Pascual JM, et al. Point-of-care manufacturing: a single university hospital's initial experience. *3D Printing in Medicine*. 2021;7(1):1-14.
6. Lander B, Atkinson-Grosjean J. Translational science and the hidden research system in universities and academic hospitals: A case study. *Social Science & Medicine*. 2011;72(4):537-544.
7. van den Broeck J, Vereecke E, Wirix-Speetjens R, vander Sloten J. Segmentation accuracy of long bones. *Medical Engineering and Physics*. 2014;36(7):949-953. doi:10.1016/j.medengphy.2014.03.016
8. Gelaude F, vander Sloten J, Lauwers B. Accuracy assessment of CT-based outer surface femur meshes. *Computer Aided Surgery*. 2008;13(4):188-199. doi:10.1080/10929080802195783
9. Ballard DH, Mills P, Duszak Jr R, Weisman JA, Rybicki FJ, Woodard PK. Medical 3D printing cost-savings in orthopedic and maxillofacial surgery: cost analysis of operating room time saved with 3D printed anatomic models and surgical guides. *Academic radiology*. 2020;27(8):1103-1113.
10. Fang C, Cai H, Kuong E, et al. Surgical applications of three-dimensional printing in the pelvis and acetabulum: from models and tools to implants. *Unfallchirurg*. 2019;122(4):278-285. doi:10.1007/s00113-019-0626-8
13. Dickler HB, Korn D, Gabbe SG. Promoting translational and clinical science: the critical role of medical schools and teaching hospitals. *PLoS medicine*. 2006;3(9):e378.
12. Suk S il, Lee CK, Kim WJ, Park YB, Chung YJ, Song KY. Segmental pedicle screw fixation in the treatment of thoracic idiopathic scoliosis. *Journal of the Korean Orthopaedic Association*. 1995;30(1):49-58.
13. Garg B, Gupta M, Singh M, Kalyanasundaram D. Outcome and safety analysis of 3D-printed patient-specific pedicle screw jigs for complex spinal deformities: a comparative study. *The Spine Journal*. 2019;19(1):56-64.

14. Liu K, Zhang Q, Li X, et al. Preliminary application of a multi-level 3D printing drill guide template for pedicle screw placement in severe and rigid scoliosis. *European Spine Journal*. 2017;26(6):1684-1689.
15. Polly Jr DW, Yaszemski AK, Jones KE. Placement of thoracic pedicle screws. *JBJS essential surgical techniques*. 2016;6(1).
16. Pijpker PAJ, Kraeima J, Witjes MJH, et al. Accuracy assessment of pedicle and lateral mass screw insertion assisted by customized 3D-Printed drill guides: a human cadaver study. *Operative Neurosurgery*. 2019;16(1):94-102.
17. Nakashima H, Yukawa Y, Imagama S, et al. Complications of cervical pedicle screw fixation for nontraumatic lesions: a multicenter study of 84 patients. *Journal of Neurosurgery: Spine*. 2012;16(3):238-247.
18. Abumi K, Shono Y, Ito M, Taneichi H, Kotani Y, Kaneda K. Complications of pedicle screw fixation in reconstructive surgery of the cervical spine. *Spine*. 2000;25(8):962-969.
19. Ishikawa Y, Kanemura T, Yoshida G, Ito Z, Muramoto A, Ohno S. Clinical accuracy of three-dimensional fluoroscopy-based computer-assisted cervical pedicle screw placement: a retrospective comparative study of conventional versus computer-assisted cervical pedicle screw placement. *Journal of Neurosurgery: Spine*. 2010;13(5):606-611.
20. Pijpker PAJ, Kraeima J, Witjes MJH, et al. Accuracy of Patient-Specific 3D-Printed Drill Guides for Pedicle and Lateral Mass Screw Insertion: An Analysis of 76 Cervical and Thoracic Screw Trajectories. *Spine*. 2021;46(3):160.
21. Yu Z, Zhang G, Chen X, et al. Application of a novel 3D drill template for cervical pedicle screw tunnel design: a cadaveric study. *European Spine Journal*. 2017;26(9):2348-2356.
22. Kotani Y, Abumi K, Ito M, Minami A. Improved accuracy of computer-assisted cervical pedicle screw insertion. *Journal of Neurosurgery: Spine*. 2003;99(3):257-263.
23. Richter M, Cakir B, Schmidt R. Cervical pedicle screws: conventional versus computer-assisted placement of cannulated screws. *Spine*. 2005;30(20):2280-2287.
24. Ishikawa Y, Kanemura T, Yoshida G, et al. Intraoperative, full-rotation, three-dimensional image (O-arm)-based navigation system for cervical pedicle screw insertion. *Journal of Neurosurgery: Spine*. 2011;15(5):472-478.
25. Ito H, Neo M, Yoshida M, Fujibayashi S, Yoshitomi H, Nakamura T. Efficacy of computer-assisted pedicle screw insertion for cervical instability in RA patients. *Rheumatology international*. 2007;27(6):567-574.
26. Lee GYF, Massicotte EM, Rampersaud YR. Clinical accuracy of cervicothoracic pedicle screw placement: a comparison of the "open" lamino-foraminotomy and computer-assisted techniques. *Clinical Spine Surgery*. 2007;20(1):25-32.
27. Lemans JVC, Wijdicks SPJ, Castelein RM, Kruyt MC. Spring distraction system for dynamic growth guidance of early onset scoliosis: two-year prospective follow-up of 24 patients. *The Spine Journal*. 2021;21(4):671-681.

28. Wijdicks SPJ, Lemans JVC, Verkerke GJ, Noordmans HJ, Castelein RM, Kruyt MC. The potential of spring distraction to dynamically correct complex spinal deformities in the growing child. *European Spine Journal*. 2021;30(3):714-723.
29. Gillespie KA, Dickey JP. Biomechanical role of lumbar spine ligaments in flexion and extension: determination using a parallel linkage robot and a porcine model. *Spine*. 2004;29(11):1208-1216.
30. Wu CC, Jin HM, Yan YZ, et al. Biomechanical role of the thoracolumbar ligaments of the posterior ligamentous complex: a finite element study. *World neurosurgery*. 2018;112:e125-e133.
31. Kawabata S, Watanabe K, Hosogane N, et al. Surgical correction of severe cervical kyphosis in patients with neurofibromatosis Type 1: report of 3 cases. *Journal of Neurosurgery: Spine*. 2013;18(3):274-279.
32. Cutler DM. The lifetime costs and benefits of medical technology. *Journal of Health Economics*. 2007;26(6):1081-1100.
33. Callahan D. Health care costs and medical technology. *From birth to death and bench to clinic: The Hastings center bioethics briefing book for journalists, policymakers, and campaigns*. Published online 2008:79-82.
34. EUR-Lex. *Regulation (EU) 2017/745 of the European Parliament and of the Council of 5 April 2017 on Medical Devices, Amending Directive 2001/83/EC, Regulation (EC) No 178/2002 and Regulation (EC) No 1223/2009 and Repealing Council Directives 90/385/EEC and 93/42/EEC*; 201
35. Calvo-Haro JA, Pascau J, Mediavilla-Santos L, et al. Conceptual evolution of 3D printing in orthopedic surgery and traumatology: from “do it yourself” to “point of care manufacturing.” *BMC Musculoskeletal Disorders*. 2021;22(1):1-10.
36. Williams FC, Hammer DA, Wentland TR, Kim RY. Immediate teeth in fibulas: planning and digital workflow with point-of-care 3D printing. *Journal of Oral and Maxillofacial Surgery*. 2020;78(8):1320-1327.
37. Li KHC, Kui C, Lee EKM, et al. The role of 3D printing in anatomy education and surgical training: A narrative review. *MedEdPublish*. 2017;6.
38. Izard SG, Juanes JA, Peñalvo FJG, Estella JMG, Ledesma MJS, Ruisoto P. Virtual reality as an educational and training tool for medicine. *Journal of medical systems*. 2018;42(3):1-5.
39. Tack P, Victor J, Gemmel P, Annemans L. 3D-printing techniques in a medical setting: a systematic literature review. *Biomedical engineering online*. 2016;15(1):1-21.
40. George E, Liacouras P, Rybicki FJ, Mitsouras D. Measuring and establishing the accuracy and reproducibility of 3D printed medical models. *Radiographics*. 2017;37(5):1424-1450.
41. Govaert GAM, Hietbrink F, Willemsen K. Three-Dimensional Manufacturing of Personalized Implants in Orthopedic Trauma Surgery—Feasible Future or Fake News? *JAMA Network Open*. 2021;4(2):e210149-e210149.



The background is a solid blue color with several sets of thin, parallel diagonal lines. One set of lines is in the top-left corner, another in the bottom-left corner, and a third set is in the middle-left area, all extending towards the right side of the page.

PART 5

CLOSINGS



CHAPTER 18

Three-Dimensional Manufacturing of Personalized Implants in Orthopedic Trauma Surgery—Feasible Future or Fake News?

Geertje AM Govaert | Falco Hietbrink | Koen Willemsen

*Published in JAMA Network Open 4.2 (2021): e210149.
<http://dx.doi.org/10.1001/jamanetworkopen.2021.0149>*

Invited Commentary

Until recently, producing medical-grade osteosynthesis devices was solely done by (mostly large) orthopaedic medical device companies. Although a wide variety of osteosynthesis devices are commercially available, in reality, hospitals are bound by legal contracts, production and supply issues, and a need to reduce costs, which limits flexibility and availability. Ijpma et al¹ report on the feasibility of on-demand patient-specific osteosynthesis plates and drilling guides for acetabular fracture surgery that are designed in house and regionally produced. In a cohort of 10 patients with complex acetabular fractures, they managed to plan, design, and manufacture the implants within 4 days and reported easy handling and no need for additional intraoperative contouring of the plates. Each patient's computed tomography (CT) data were used to create a 3-dimensional (3-D) model that was virtually reduced and then used as a template to design patient-specific plates. Fracture reduction and implant position were evaluated by postoperative CT scans, and clinical outcomes were assessed by Short Musculoskeletal Function Assessment questionnaires. Excellent results in both domains were reported. Details regarding legal legislation and cost efficacy of this procedure were not provided. The question that remains after reading this article is: is this a gimmick for the happy few or is it the future? Will we soon all move to an era of self-designed and locally (ie, in-house) produced patient-specific osteosynthesis implants? Particularly for complex skeletal reconstructions—but also in austere environments or mass casualty situations—a readily available, affordable, and always-appropriate implant can make the difference between failure and success.

The surgical benefits of 3-D visualization and fabrication of bone models are beyond dispute, and their use during the last decade has gained popularity in orthopaedic trauma surgery. Particularly for the complex anatomy in reconstructive intra-articular acetabular procedures, preoperative printed pelvic models are regarded as valuable supplements to standard medical imaging techniques.² The physically printed bone models can also be used for preoperative planning and practicing, such as for fracture reduction techniques and precontouring of commercially available implants. This allows for reductions in operating time, which is financially attractive and might result in better outcomes.^{3,4} It would be interesting to compare this outcome to the results of the study by Ijpma et al¹; however, costs of surgery and time reduction were not part of their study. Technical possibilities have progressed toward the production of personalized implants. This is done not only for fracture surgery but also, for example, for revision of arthroplasties and skeletal stabilization of congenital deformities or after tumour resections in various clinical scenarios.⁵ All these indications demonstrate potential for these new techniques to stay and conquer a specific area in standard medical care.

It seems that personalized care within trauma surgery has no downsides; however, it must be noted that compared with conventional methods, these new techniques necessitate additional actions by the surgical team. The preparation of anatomical models, the design and planning of the surgical intervention, and the production of the implants all require added commitment and training and some extra costs. There is a delicate balance between the needed investment for software, materials, equipment, and the personnel to operate it on the one hand and the added treatment quality or reduced surgery time on the other. These key factors will ultimately determine whether these new techniques are here to stay and for which indications they are used.

Apart from the feasibility and costs of local (i.e., in-house) production facilities, another major challenge for the treating team is obtaining regulatory approval for the production of patient-specific surgical implants, including sterilization certificates. The pathways for navigating these regulations are often unclear, frequently bureaucratic, and always time consuming.⁶ It is clear that there has to be a system in place that represents patients' interests and allows for the safe production and use of medical implants. However, these regulations currently form a very worrisome barrier for the use of personalized fracture care in clinical practice. In trauma surgery, we simply do not have the luxury of elaborating a complex route for procedures that need to be done in a timely fashion. If we learned anything from the COVID-19 pandemic, it is that with the right perseverance, medical legislation can be accelerated when necessary.

Therefore, it is commendable to Ijpm et al¹ that they managed to plan, produce, and use these patient-specific implants in an actual, day-to-day trauma surgical setting. The study's concept of personalized fracture care is very interesting because it is also widely applicable in various subdisciplines of surgery. However, to further determine whether fast-track osteosynthesis is a gimmick for the happy few or the future for trauma surgery, we need well-designed and sufficiently powered prospective studies that compare patient-specific osteosynthesis implants targeting clinical outcomes and patient safety with a transparent impression of the costs.

References

1. Ijpma FFA, Meesters AML, Merema BBJ, et al. Feasibility of imaging-based 3-dimensional models to design patient-specific osteosynthesis plates and drilling guides. *JAMA Netw Open*. 2021;4(2):e2037519. doi:10.1001/jamanetworkopen.2020.37519
2. Fang C, Cai H, Kuong E, et al. Surgical applications of three-dimensional printing in the pelvis and acetabulum: from models and tools to implants. *Unfallchirurg*. 2019;122(4):278-285. doi:10.1007/s00113-019-0626-8
3. Maini L, Sharma A, Jha S, Sharma A, Tiwari A. Three-dimensional printing and patient-specific pre-contoured plate: future of acetabulum fracture fixation? *Eur J Trauma Emerg Surg*. 2018;44(2):215-224. doi:10.1007/s00068-016-0738-6
4. Ballard DH, Mills P, Duszak R Jr, Weisman JA, Rybicki FJ, Woodard PK. Medical 3D printing cost-savings in orthopedic and maxillofacial surgery: cost analysis of operating room time saved with 3D printed anatomic models and surgical guides. *Acad Radiol*. 2020;27(8):1103-1113. doi:10.1016/j.acra.2019.08.011
5. Ma L, Zhou Y, Zhu Y, et al. 3D printed personalized titanium plates improve clinical outcome in microwave ablation of bone tumors around the knee. *Sci Rep*. 2017;7(1):7626. doi:10.1038/s41598-017-07243-3
6. Willemsen K, Nizak R, Noordmans HJ, Castelein RM, Weinans H, Kruyt MC. Challenges in the design and regulatory approval of 3D-printed surgical implants: a two-case series. *Lancet Digit Health*. 2019;1(4):e163-e171. doi:10.1016/S2589-7500(19)30067-6



The background is a solid blue color. It features several sets of parallel diagonal lines. One set of lines is white and runs from the top-left towards the bottom-right. Another set of lines is yellow and runs from the bottom-left towards the top-right. There are also some faint, thin white lines scattered across the background.

CHAPTER 19

Summary, general discussion,
future perspectives and
concluding remarks

Summary and General Discussion

As technology in general advances exponentially, medical 3D technology is also generating more momentum in hospitals.[1], [2] This thesis addresses challenges and provides solutions for transferring new 3D techniques from the laboratory bench to the patient's bedside. First, an evaluation was made of current challenges based on extensive review of the literature. Second, biomechanical and imaging studies were conducted to assess new innovations. Third, bench research was translated into (experimental) animal research and eventually to regular clinical treatment in dogs. Fourth, increasing insights allowed us to introduce a new medical 3D technology-based workflow in human patients as a regulatory approved patient-specific treatment method. In other words: 'Medical 3D technology, from bench to bedside'. In the fifth and last part all the presented chapters are evaluated and discussed, and future perspectives are given to continue and improve on the current research.

In the first part of this thesis (**Chapter 1**) the current background of medical 3D technology was assessed. A frequently used quote is 'If you think you can do it, you can (make it)!'. This quote has some merit for 3D printing as 3D printing makes the production of complex geometries possible that were previously (near) impossible to produce with conventional manufacturing techniques.[3], [4] This allows surgeons to envision new treatment methods that were previously simply not possible.[5], [6] However, it is not clear which new ideas and solutions are truly of added benefit for the patient and which are not. [7], [8] One possible way medical 3D technology could improve current treatments is by improving their accuracy. Therefore, in this thesis some established treatment methods were reviewed to see whether adding additive manufacturing techniques could increase surgical accuracy and therefore hopefully its success and effectiveness.[9] One of these treatments is the shelf arthroplasty[10], which is (one of) the oldest surgical treatment methods for hip dysplasia and partly relies on the surgeon's craftsmanship using a bone autograft to extent the acetabular roof. Until this day not much effort is undertaken to increase the accuracy of this method. However, to investigate what the added benefit of 3D technology could be for this treatment, this thesis started with a thorough review of all literature to document the data on the long-term outcomes of shelf arthroplasty surgery and the key factors influencing the outcome parameters (**Chapter 2**).[11] If factors could be identified that could be improved by 3D planning or additive manufacturing these could be addressed with new methods. The systematic review (**Chapter 2**) showed that the shelf arthroplasty in well-defined indications has a comparable survival rate with the peri-acetabular osteotomy as the current gold standard.[12] Predictive for outcome parameters and survival were the (in)correct placement and size of the shelf implant and the surgeon's targets (accuracy) were frequently not achieved.[11] Therefore, the shelf arthroplasty might greatly benefit from 3D additive manufacturing technology as

obviously the fit of the implant will be much better predictable. One adaptation of the shelf arthroplasty might be the creation and use of a cutting guide[13] for the exact positioning of the shelf. Another adaptation for the shelf implant could be an implant that has the optimal, personalized dimensions of the patient.[14] This last option has been examined in **Chapters 6, 7, 10 and 11**. The systematic review of **Chapter 2** also describes the risk of impingement between the femur and the newly formed - and commonly oversized - acetabular shelf/roof.[11] The risk on impingement can be minimized by a preoperative 3D-simulation to determine the optimal dimensions of the shelf for an optimal balance between coverage of the femoral head and range of motion.[15], [16]·[17] These kind of planning tools are becoming more and more common in medical practice in which these pre-operative simulations[15] produce the parameters for the boundaries for cutting guides[13] and implants, not only for hip dysplasia but for a whole range of anatomies and products.[18] In **Chapter 3** the Chiari pelvic osteotomy, another classic salvage treatment for hip dysplasia, was systematically reviewed. Both the shelf arthroplasty and Chiari osteotomy rely on extra bony support on the hip capsule to increase the weight-bearing surface of the acetabulum. The review of the Chiari osteotomy showed that carefully selected patients on a young age, and with a low osteoarthritis score, have a good survival of the hip. The level of the osteotomy appeared to be an important determinant for the survival of the hip and might be better guided with additive manufactured surgical instruments.

In **Chapter 4** a comparison was made between human hip dysplasia and canine hip dysplasia.[19] There are similarities in etiology, anatomy and treatments between dogs and children as well as (young) adults.[20] Many of the surgical treatments for hip dysplasia that are developed for humans were first tested in dogs. Conversely, procedures that became successful in humans found their way to the veterinary field and are now commonly used in companion animal clinics. In this PhD-thesis the dog was chosen as the ideal animal to test improvements on the shelf hip dysplasia treatment (examined in chapter 2),[11] with the intention to work according to the One Medicine principle,[21] that could lead to a new treatment for both dogs and humans.[20]

The required steps towards human introduction of 3D technology also produce new challenges. One of the drawbacks of medical 3D technology is the need for 3D imaging, which is essential to produce virtual or physical anatomic representations of the patient.[18] The current most used 3D imaging methods are computed tomography (CT) and magnetic resonance (MR) imaging, both containing their pros and cons. CT is a medical imaging technique that uses x-ray beams shot from 360 degrees onto the patient in order to digitally reconstruct axial images of the patient.[22] MR-imaging is a medical imaging technique that uses magnetic field gradients and radio waves for volumetric (3D) imaging of the patient.[23] Hence, both imaging methods can provide a full 3D image of (part

of) the patient, making them suited to generate anatomical 3D models of individual organs by segmenting the connected voxels.[24] The limitations of the current CT-scan techniques are the use of harmful x-rays, and the inferior depiction of the soft tissues compared to MR.[25] Low dose CT scans reduce the level of radiation, but their accuracy for 3D modelling is not yet equivalent to normal dose CT imaging.[26] MR imaging does not make use of harmful radiation but consumes significantly more time per investigation, is more expensive and has a lower bone contrast for the making of segmentations needed for 3D skeletal models. Many different research groups are trying to increase the bony resolution of MR by creating favourable contrast settings or by creating algorithms that can be trained to convert MR imaging data into CT-like images, so called synthetic CT. **Chapter 5** compares MRI and CT for 3D-visualizing skeletal pathologies. New developments in MRI seem promising as a radiation-free alternative to CT for the diagnosis and treatment of bony pathologies. The value of a bone and soft tissue component within a single modality (MRI) would be of added benefit. In this PhD-thesis, it was described that data from MR imaging can be used for diagnosing hip dysplasia or to create accurate 3D saw guides on the depicted anatomy of long bones. The algorithms for synthetic CT (also referred to as bone MRI) need to be validated with sufficient amounts of data for training before it can be used clinically. Two of those validation steps for synthetic CT pathways are presented in **Chapters 14 and 15**. It seems obvious that modern 3D-technologies might provide extensive benefits for surgical planning and treatments in orthopaedics[19], [27] but it is not always clear how this will be implemented or developed.

In the second part of the thesis new ideas were tested in a more basic research setting to examine the feasibility of 3D concepts for hip and shoulder surgery with the use of biomechanical tests. Chapter 6 describes the testing of a proof of principle of a new implant for hip dysplasia (**Chapter 6**)[6]. The patient-specific shelf implant for hip dysplasia was designed to restore the dysplastic acetabular rim to the optimal 3D parameters using a method introduced by Larson et al. [28] This 3D evaluation method is preferred above the 2D centre-edge angle measured on a coronal radiograph, as it provides information on all quadrants of the acetabulum.[28] By restoring the hip coverage to values within the normal range, the hip became more stable. This was proven in a biomechanical set-up that tested the subluxation potential of cadaveric hips before and after receiving a titanium shelf implant. Also, the implant fixation of the personalized titanium shelf implant was biomechanically tested in order to proof the adequate resistance to physiological loads. [6]

After introducing the proof of principle of the 3D printed titanium shelf (**chapter 6**), the question arose whether the relatively stiff titanium metal,[29] would be the best choice for a treatment that targets mainly young patients. In growing patients, material that fully integrates with the bone and resorbs after the host bone has adapted via the implant to

its healthy geometry would be a far better choice. Therefore, a bioresorbable material was introduced in **Chapter 7**.^[30] The same principle as in **Chapter 6** was tested but made from 3D-printed biodegradable magnesium-phosphate^[31]. This material that has shown bone ingrowth in a prior pilot study^[30], exhibited less but still sufficient load bearing capacities compared to titanium in a canine cadaveric hip joint with hip dysplasia.^{[30]–[32]}

In **Chapter 8** the idea of the 3D-printed hip dysplasia implant was translated^[33] to repair and restore stability in an unstable shoulder. One of the benefits of computer aided design programs is that when mastered for one anatomy the technology is easily translated to another.^[34] Shoulders can become unstable as a result of a bone deficiency e.g. in the glenoid.^[35] Similarly to the hip,³³ the optimal socket dimensions can be reconstructed with an extracapsular implant that requires a dedicated patient-specific design. This concept was biomechanically tested in human cadaveric specimen and gave comparable results to the gold standard Latarjet procedure with a smaller variance between the results, making the outcome of the 3D-printed implant more consistent.^[35]

In **Chapter 9** a new scaffold design for porous deformable titanium was evaluated to allow clay-like high deformation that can penetrate in regions of bony defects with an irregular shape. In particular in acetabular cup revision surgery irregular shapes are often encountered in the deep acetabular zones. Better fit with a deformable material that forms towards these irregular shapes will allow better stability and potential implant integration and therefore reduce stress-shielding.^[5], ^[36] The results showed that the porous titanium sections of the acetabular revision implants highly deform after insertion in a saw bone pelvis. Good stability was observed during subsequent cyclic loading. To keep improving on these porous structures, 3D-printing of very thin struts preferably in the range of 100 to 200 μm will be explored, however certain techniques are still limited to what is currently possible. Additional tests in cadavers are needed to further evaluate the current advancement.^[5]

Concluding, **Chapters 6-9** have shown how to evaluate novel ideas in a bench research setting.^[31], ^[35], ^[37] Before translating these ideas to the bedside, a bridging step is needed e.g. an in vivo assessment in an (experimental) animal model. The next section of this thesis will focus on this translation and when successful, these novel concepts might lead to new treatments for both animal and human in a true “One health, One Medicine” concept.^[21]

In the third part of the thesis three types of patient-specific implants were tested and applied in veterinary (dog) surgery. In **Chapter 10** the hip dysplasia shelf implant that was biomechanically tested in chapter 6, was implanted in three dogs with hip dysplasia as

part of a pilot trial and the procedure proved to be feasible and safe. Subsequently, based on the outcomes presented in Chapters 6 and 10, a first cohort of 25 dog patients (with 42 implants) was operated with this implant and the data were presented as a first-in-patient application of the 3D shelf implant for hip dysplasia in patient dogs in **Chapter 11**. Overall the average pain scores (owner questionnaires) improved and radiographic hip dysplasia measurements returned to healthy values daily activities, showing the effectiveness of the personalized shelf implant in a clinically relevant patient cohort. However, the average osteoarthritis score also increased, which led to the conversion of one hip to THA, questioning the effectiveness of the implant to prevent long-term development of degenerative changes of the hip joint, or delays this development. Though it is also known that other dysplasia interventions, such as the rotational osteotomies, have limited capabilities to fully stop osteoarthritic developments. Whether the worsening of the osteoarthritis score is correlated to the placement accuracy of the shelf implant or how the grade of the preoperative hip dysplasia correlates with hip laxity, long-term outcomes and survival of the hip, needs further analyses.

Comparable to Part 2 where an anatomical translation was made to the shoulder, in Part 3 an *in vivo* anatomical translation of 3D technology was made to the skull (**chapter 12**)[38] and the antebrachium (**Chapter 13**). In **Chapter 12** two dog cases were presented, the first case with a massive osteoma in the skull that needed to be removed. The procedure left a huge gap in the skull that required surgical reconstruction with a patient specific implant to allow for normal functioning of the dog. The second case had an osteosarcoma in the jaw near the orbital socket and eye. This sarcoma was removed and this dog received a 3D-printed titanium implant to reconstruct the bony defect in the same surgery in order for the dog to retain normal function of the jaw and protection of the eye.[38] Both implants were created with a porous scaffold on the implant-bone interface to allow bone ingrowth. In **Chapter 13** other canine applications of titanium 3D printing were explored, e.g. the use of a 3D-printed scaffold for repairing a critically sized bone defect after an ulnar fracture non-union due to osteomyelitis in two dogs. These dogs had a non-weightbearing lameness, but returned to normal gait after surgery and showed good bony ingrowth of the prosthesis on follow-up CT imaging. One of the dogs died of unrelated causes allowing additional micro-CT analysis to study the bone ingrowth on a higher magnification. Micro-CT showed a large amount of new bone around and in the prosthesis, although complete bony fusion through the largest hole of the implant was not (yet) present. The ideal porous micro structure of titanium scaffolds for bony ingrowth still has to be determined.[39]

In the fourth part, a translational step towards the bedside is made. However, the question, '*are the results using 3D technology truly better than conventional treatments or are the physicians only happy that they can be involved in the process of developing something incredibly novel?*'[8] remains, and more research and evidence is required. If we look at

the “hype cycle” and what place medical 3D technology currently fills on the chart (Fig. 1) we might be still in the “peak of inflated expectations” or we might be entering the “slope of enlightenment” or even a “plateau of productivity”? In the last decade, due to the rapid expansion of technology and advances in engineering there has been a frequent and continuous flow of new devices entering the (medical) market and claiming clinical feasibility and thus creating a peak of inflated expectations.

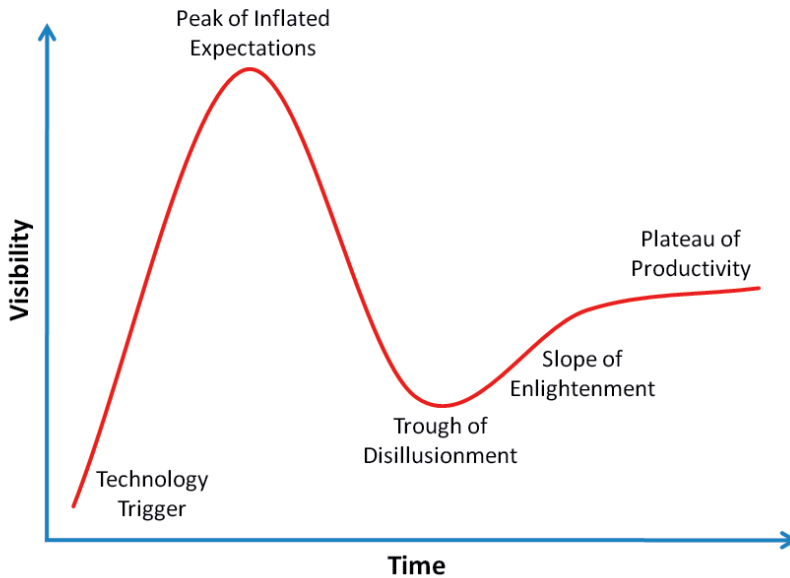


Figure 1. The hype cycle

With the rise of 3D printing even more devices enter the market, as budget consumer desktop 3D printers are available even under €100,- and segmentation and design software is available in open sources.[40] Consequently, everyone who is able to use a computer and an additive design (CAD) program is capable of 3D printing a guide or a device without much investments, documentation or even the necessary knowledge[41], [42]. This movement has grown into an even greater peak of inflated expectations with the inevitable drawback that some devices and software that had entered the market are flawed[43]–[45] or not-sufficiently legally backed.[46] With this thesis examples are given to validate new 3D devices and 3D techniques so that they are sufficiently legally backed. Two of those validation steps are presented in **Chapters 14 and 15**, two novel clinical applications of MRI-based synthetic-CT pathways are examined to see whether they can be used at the patient’s bedside. First in **Chapter 14** a comparison was made between the MRI-based sCT and conventional CT for the morphological assessment of the hip joint.[47] The sCT showed equivalence to conventional CT and therefore highlights the clinical applicability of this new

radiation-free pathway for hip joint diagnostics.[47] In **Chapter 15** another MRI-based sCT workflow was compared to a regular CT workflow in relation to lower arm osteotomy saw guides used for correction of misaligned bones. This was tested on cadaveric specimens and both workflows showed the same accuracy when their placement accuracy was compared with the measurements done with the (ground-truth) micro-CT.[48]

Moreover to protect patients from unqualified medical device manufacturers, the European authority came up with a new Medical Device Regulation (MDR).[49] This new MDR was enforced from May 2021 onward and ensured that the years of simple 'trial and error' were over and that every guide or device on the market needs to be sufficiently backed by necessary (stacks of) documentation.[45], [49] These regulations have as a downside that a lot of (human) experimental applications are no longer allowed, therefore creating a "valley of disillusionment" under users or medical device manufacturers (Fig. 1). This was especially troublesome in the medical 3D printing industry where there are a lot of low volume users and hospitals are now forced by the MDR to comply to all these new rules and documentations. Not every hospital has the knowledge or means to comply[50] and many will not be able to provide this 3D technology enhanced service to its patients. In this thesis the translation of 3D technology to the human clinic was presented as a tool to overcome this "valley of disillusionment" and enter a phase of productivity (the slope of enlightenment /the plateau of productivity) (Fig. 1). In this PhD-thesis 3D medical technology users are shown exemplar pathways, e.g. in **Chapter 16** a first-in-man application was presented of a titanium 3D-printed multi-segment/vertebrae bridging anterior spine implant.[51] The required rules and regulations that needed to be documented to comply to the new collective European laws (MDR)[49] are explained. With this chapter clinicians are provided with a workflow that allows a swifter process for future (comparable) cases that need a patient specific approach. Next, in **Chapter 17** the implant pathway presented in chapter 16 is expanded and another patient specific pathway is presented, the 'click-on spine guide'. Besides presenting these unprecedented pathways, extra emphasis is given to the required infrastructure needed within a tertiary referral centre and university hospital to facilitate these type of products.

The fifth part of this thesis starts with an invited commentary (**Chapter 18**) on the usability and applicability of novel 3D technology for orthopaedic (trauma)surgery, showing the importance of rules and regulations and the need for transparency of the costs of a 3D enhanced workflow.[52] Yet, in this thesis there has been no specific evaluation of the cost-effectiveness of the proposed treatments.[7] For example, if the 3D shelf implant, is being introduced in either animal or human practice, it should be backed by a cost analysis.[53] The main target hitherto was the safety and feasibility of certain applications of medical 3D technology. The financial background will be briefly discussed further in the next section, under 'future perspectives'.

Future Perspectives

This thesis addresses an innovative topic, however is 3D technology a gimmick for the happy few or is it the future of medicine? In other words, is 3D technology a feasible future or a “hype”? This is an important question, especially when considering the costs of these tailor-made methods.[7], [52] How should these 3D-derived products be paid?[7] Is there a valid business case for 3D technology? Most medical costs are reimbursed by insurance companies, but most insurance companies would like to see randomized controlled trials to get indisputable evidence that proves the (cost-)effectiveness of these new and fast growing applied technologies.[54] However, a major limitation in the research of personalized medical 3D technology, is the often patient specific nature of the applied techniques.[55] Making products personalized increases the number of variables and therefore makes it difficult to compare in high-level evidence trials.[56] Therefore, this should be one of the focus points for future research. Because when missing the financial reimbursement, 3D technology enhanced care has a difficult time to get (widely) accepted as a proven solution for the conservative medical stream. However, when a technology gets more adopted, e.g. computer technology, the price of this technologies will drop,[57] making it easier to find matching funds.[58] Eventually, could 3D printing become so affordable that it can be used for every implant? It seems a realistic option as already some spinal implants and acetabular cups get mass produced using 3D-printing technology.[59], [60] If so, does every hospital need their own 3D printers or can they still rely on critical suppliers? Even so, finding reimbursement for 3D technology is not the only challenge. It should be considered whether everything that can be made, should be made. Moreover, there are some ethical considerations, e.g. whether helping patients with low life expectancy with costly tailor-made solutions is helpful and sustainable for society.[61]

To further research the cost-effectiveness of a treatment, also the clinical effectiveness of the treatment needs to be considered.[62] Is being more accurate at performing an osteotomy with a saw-guide also clinically relevant? Does that patient have a faster recovery and therefore less consumption of medical care or is the added accuracy not clinically relevant because the human body is rather forgivable? These are challenges that should be tackled, for instance by performing large clinical trials with a long follow-up comparing different treatment methods.

3D Technology helped us to see beyond the limitations of 2D imaging, however 3D is merely a timely perspective of a 4D representation.[63]–[65] For example, 3D technology helps for planning the realignment of the biomechanical axis of a leg of a patient, when lying in the CT or MRI. But what happens when also time as a fourth dimension is evaluated?[63] What happens if movement or weightbearing is introduced into the mix.

With 3D technology becoming increasingly accessible and increasing computing power and related software options, the ability to account for that fourth dimension is getting closer.[65]

Introduction of 3D technology in clinic brings along a large amount of legislation. However, because of the novelty of this legislation (MDR) no precedent is known or jurisprudence is available.[51] Therefore, with this thesis clinicians and researchers are provided with examples of how to tackle the challenges concerned with the development and introduction of new 3D-derived technologies. More collaboration both at the national and international level will contribute to create uniform obligatory standards and influence and inspire policy makers in this regard.[66] As a result, 3D guiding software will adopt such standards and subsequently it will become easier to use and widely available.

One kind of software or tool that is becoming increasingly available in clinic is virtual reality[67]–[70] and augmented reality[71]–[74]. Virtual reality is a closed virtual environment most often entered by looking into virtual reality goggles.[69] In medical care virtual reality is most frequently used for educational purposes for surgeons and clinicians.[68] Thereby, they can practice certain skills in a safe environment before they practice their skills on ‘real life’ patients.[68]–[70] Another application is the use of virtual reality as therapy for (young) patients to e.g. overcome a frightening situation. Augmented reality is a tool which projects visual information over or besides your normal view of the world.[71]–[74] This is more helpful when you like to accomplish a task on a patient with guidance of extra information, e.g. by viewing an anatomical 3D model derived from a patient’s CT image projected on top of the actual patient.[71]–[74] Currently, a shift is seen from 3D printing to 3D visualisation.[69], [71] Surgeons don’t require a physically 3D-printed model in their hands anymore but they suffice with a visualisation in a virtual or augmented reality goggle. Both virtual reality and augmented reality are 3D tools that revolutionize medical care, but they still need to meet the same rules and regulations as other physical devices, especially when patients are involved. Not all goggles are validated or even calibrated for clinical use.[68], [69]

A software movement that is gaining momentum in medical care is the use of artificial intelligence and machine learning.[47], [75]–[77] Especially in medical imaging, appraisal machine learning algorithms can be of added benefit. Computer algorithms can be trained with imaging data with matching and manually produced segmentations of anatomical regions of interest.[78]–[80] Subsequently, these algorithms can produce their own segmentation and related 3D models. Also, these algorithms need to comply to the same rules and regulations as all medical devices and need to be validated before they can be clinically used.[49]

An opportunity, but also a big challenge is the forthcoming medical segment of 3D bioprinting.[29]–[32], [81], [82] The ultimate goal of bioprinting is to master the techniques to manufacture living organs such as a heart or liver.[29], [81] However, these techniques are still in their early stages of development.[29], [81] Nevertheless, the 3D printing of bone and cartilage mimicking substances has gone fast over the last few years.[30] Bone for example has a relative easy composition and is therefore easier to mimic in a laboratory environment. Adding more delicate tissues as cartilage is already becoming increasingly difficult. In this thesis a surgical application of a bone mimicking scaffold made from magnesium phosphate was presented.[31] However, to get these substances to a level where clinical introduction is imminent is still a challenge.[30], [31]

Medical 3D technology has been a quite specialized field, reserved for academical hospitals or specialized companies. Currently an increasing amount of start-up companies are emerging that try to conquer a very specific and specialized part of the medical 3D technology market and the medical device market.[83], [84] This shift in knowledge and input has its benefits as private enterprises help the 3D sector to grow. However, hospitals, especially the university hospitals, need to act as the medical safety net for patients[85], [86], because when a patient can't find treatment in one of the community hospitals they will be referred to the university or last resort hospitals.[51] Therefore collaboration between private enterprises and university hospitals is preferred.[85], [86] To facilitate such collaborations, it is important to create 'medical technology hubs' to allow this freedom to operate and quickly identify the right patients for these advanced therapies.[51], [52] Times will be challenging to create such hubs and find ways to position such a place in the current medical system.

Concluding remarks

This thesis describes 3D medical technology and its increasing importance in every day hospital care. The overall results of this thesis can be used for further exploration of medical 3D technology, giving examples for basic research to further the technology as well as provide guidelines needed to allow for regulatory approval when translating these techniques from bench to bedside. In daily practice, innovations are continuously being introduced. Unfortunately, history has repeatedly proven that many innovations are frequently not (enough) justifiable and as a consequence, to protect patients, healthcare can be rather conservative. Therefore 3D medical researchers should collaborate to quickly create uniform standards for hospitals and medical device manufacturers thereby helping the transition to 3D (personalized) healthcare and eventually create the bridge to imminent 4D healthcare solutions.

References

1. C. Sorenson, M. Drummond, and B. B. Khan, "Medical technology as a key driver of rising health expenditure: disentangling the relationship," *ClinicoEconomics and outcomes research: CEOR*, vol. 5, p. 223, 2013.
2. P. J. Neumann and M. C. Weinstein, "The diffusion of new technology: costs and benefits to health care," *The changing economics of medical technology*, vol. 2, pp. 21–34, 1991.
3. D. Lin *et al.*, "Three-dimensional printing of complex structures: man made or toward nature?," *ACS nano*, vol. 8, no. 10, pp. 9710–9715, 2014.
4. S. M. Ahmadi *et al.*, "Mechanical behavior of regular open-cell porous biomaterials made of diamond lattice unit cells," *Journal of the mechanical behavior of biomedical materials*, vol. 34, pp. 106–115, 2014.
5. H. M. A. Kolken *et al.*, "Additively manufactured space-filling meta-implants," *Acta Biomaterialia*, vol. 125, pp. 345–357, 2021.
6. K. Willemsen *et al.*, "Patient-specific 3D-printed shelf implant for the treatment of hip dysplasia: Anatomical and biomechanical outcomes in a canine model," *Journal of Orthopaedic Research®*, 2021.
7. P. Tack, J. Victor, P. Gemmel, and L. Annemans, "3D-printing techniques in a medical setting: a systematic literature review," *Biomedical engineering online*, vol. 15, no. 1, pp. 1–21, 2016.
8. K. R. Foster, "3-Dimensional printing in medicine: Hype, hope, and the challenge of personalized medicine," *Philosophy and Engineering*, pp. 211–228, 2017.
9. K. Klaue, M. Sherman, S. M. Perren, A. Wallin, C. Looser, and R. Ganz, "Extra-articular augmentation for residual hip dysplasia Radiological assessment after Chiari osteotomies and shelf procedures," *Journal of Bone and Joint Surgery - Series B*, vol. 75, no. 5, pp. 750–754, 1993, doi: 10.1302/0301-620x.75b5.8376432.
10. P. M. Lance, "Constitution d'une butee osteoplastique dans les luxations et subluxations de la hanche," *Presse Med Bd*, vol. 33, pp. 945–948, 1925.
11. K. Willemsen *et al.*, "Long-term outcomes of the hip shelf arthroplasty in adolescents and adults with residual hip dysplasia: a systematic review," *Acta Orthopaedica*, vol. 91, no. 4, pp. 383–389, 2020, doi: 10.1080/17453674.2020.1747210.
12. J. C. Clohisy, A. L. Schutz, L. S. John, P. L. Schoenecker, and R. W. Wright, "Periacetabular osteotomy: a systematic literature review," *Clinical Orthopaedics and Related Research®*, vol. 467, no. 8, pp. 2041–2052, 2009.
13. X. Wang *et al.*, "Development of a novel customized cutting and rotating template for Bernese periacetabular osteotomy," *Journal of orthopaedic surgery and research*, vol. 14, no. 1, pp. 1–10, 2019.
14. E. Morsi, D. Garbuz, and A. E. Gross, "Revision total hip arthroplasty with shelf bulk allografts: a long-term follow-up study," *The Journal of arthroplasty*, vol. 11, no. 1, pp. 86–90, 1996.

15. A. Bedi *et al.*, "Surgical treatment of femoroacetabular impingement improves hip kinematics: a computer-assisted model," *The American journal of sports medicine*, vol. 39, no. 1_suppl, pp. 43–49, 2011.
16. M. Kubiak-Langer,;MoritzTannast,;SB Murphy,;KA Siebenrock, and F.Langlotz,"Range of Motion in Anterior Femoroacetabular Impingement," 2007, doi: 10.1097/BLO.0b013e318031c595.
17. S. Hayashi *et al.*, "Preoperative anterior coverage of the medial acetabulum can predict postoperative anterior coverage and range of motion after periacetabular osteotomy: a cohort study," *Journal of Orthopaedic Surgery and Research*, vol. 15, no. 1, pp. 1–6, 2020.
18. J. R. Fredieu, J. Kerbo, M. Herron, R. Klatte, and M. Cooke, "Anatomical models: a digital revolution," *Medical science educator*, vol. 25, no. 2, pp. 183–194, 2015.
19. K. Willemsen *et al.*, "Comparing hip dysplasia in dogs and humans: a review," *Frontiers in Veterinary Science*, p. 1491.
20. C. Pascual-Garrido *et al.*, "Canine hip dysplasia: A natural animal model for human developmental dysplasia of the hip," *Journal of Orthopaedic Research*, vol. 36, no. 7, pp. 1807–1817, 2018, doi: 10.1002/jor.23828.
21. S. Hinchliffe, "More than one world, more than one health: Re-configuring interspecies health," *Social science & medicine*, vol. 129, pp. 28–35, 2015.
22. L. W. Goldman, "Principles of CT and CT technology," *Journal of nuclear medicine technology*, vol. 35, no. 3, pp. 115–128, 2007.
23. D. Weishaupt, V. D. Köchli, and B. Marincek, *How does MRI work?: an introduction to the physics and function of magnetic resonance imaging*. Springer Science & Business Media, 2008.
24. D. J. Withey and Z. J. Koles, "A review of medical image segmentation: methods and available software," *International Journal of Bioelectromagnetism*, vol. 10, no. 3, pp. 125–148, 2008.
25. W. Mazrani, K. McHugh, and P. J. Marsden, "The radiation burden of radiological investigations," *Archives of disease in childhood*, vol. 92, no. 12, pp. 1127–1131, 2007.
26. C. B. Nauer, A. Rieke, C. Zubler, C. Candreia, A. Arnold, and P. Senn, "Low-dose temporal bone CT in infants and young children: effective dose and image quality," *American journal of neuroradiology*, vol. 32, no. 8, pp. 1375–1380, 2011.
27. K. Willemsen *et al.*, "Long-term outcomes of the hip shelf arthroplasty in adolescents and adults with residual hip dysplasia: a systematic review," *Acta orthopaedica*, vol. 91, no. 4, pp. 383–389, 2020.
28. C. M. Larson *et al.*, "Are normal hips being labeled as pathologic? A CT-based method for defining normal acetabular coverage," *Clinical Orthopaedics and Related Research*, vol. 473, no. 4, pp. 1247–1254, 2015, doi: 10.1007/s11999-014-4055-2.
29. L. Moroni *et al.*, "Biofabrication: a guide to technology and terminology," *Trends in biotechnology*, vol. 36, no. 4, pp. 384–402, 2018.
30. N. Golafshan *et al.*, "Tough magnesium phosphate-based 3D-printed implants induce bone regeneration in an equine defect model," *Biomaterials*, vol. 261, p. 120302, 2020.
31. N. Golafshan *et al.*, "3D-Printed Regenerative Magnesium Phosphate Implant Ensures Stability and Restoration of Hip Dysplasia," *Advanced Healthcare Materials*, p. 2101051.

32. L. Moroni *et al.*, "Biofabrication: a guide to technology and terminology," *Trends in biotechnology*, vol. 36, no. 4, pp. 384–402, 2018.
33. T. D. Berendes, T. Geurkink, K. Willemsen, H. Weinans, and R. M. Castelein, "Labral (pathologic) similarities for the human shoulder and hip joint," *Open Access J Ortho*, vol. 1, p. 101, 2018.
34. D. J. Withey and Z. J. Koles, "Medical image segmentation: Methods and software," in *2007 Joint Meeting of the 6th International Symposium on Noninvasive Functional Source Imaging of the Brain and Heart and the International Conference on Functional Biomedical Imaging*, 2007, pp. 140–143.
35. K. Willemsen *et al.*, "A Novel Treatment for Anterior Shoulder Instability: A Biomechanical Comparison between a Patient-Specific Implant and the Latarjet Procedure," *Journal of Bone and Joint Surgery - American Volume*, vol. 101, no. 14, 2019, doi: 10.2106/JBJS.18.00892.
36. H. M. A. Kolken, S. Janbaz, S. M. A. Leeflang, K. Lietaert, H. H. Weinans, and A. A. Zadpoor, "Rationally designed meta-implants: a combination of auxetic and conventional meta-biomaterials," *Materials Horizons*, vol. 5, no. 1, pp. 28–35, 2018.
37. K. Willemsen *et al.*, "Patient-specific 3D-printed shelf implant for the treatment of hip dysplasia: Anatomical and biomechanical outcomes in a canine model," *Journal of Orthopaedic Research*, p. jor.25133, Jul. 2021, doi: 10.1002/jor.25133.
38. P. Dodier *et al.*, "Single-stage bone resection and cranioplastic reconstruction: comparison of a novel software-derived PEEK workflow with the standard reconstructive method," *International journal of oral and maxillofacial surgery*, vol. 49, no. 8, pp. 1007–1015, 2020.
39. J. van der Stok *et al.*, "Enhanced bone regeneration of cortical segmental bone defects using porous titanium scaffolds incorporated with colloidal gelatin gels for time-and dose-controlled delivery of dual growth factors," *Tissue Engineering Part A*, vol. 19, no. 23–24, pp. 2605–2614, 2013.
40. S. Pieper, M. Halle, and R. Kikinis, "3D Slicer," in *2004 2nd IEEE international symposium on biomedical imaging: nano to macro (IEEE Cat No. 04EX821)*, 2004, pp. 632–635.
41. R. Pérez-Mañanes, J. A. Burró, J. R. Manaute, F. C. Rodriguez, and J. V. Martín, "3D surgical printing cutting guides for open-wedge high tibial osteotomy: do it yourself," *The journal of knee surgery*, vol. 29, no. 08, pp. 690–695, 2016.
42. I. I. López-Torres, P. Sanz-Ruiz, V. E. León-Román, F. Navarro-García, R. Priego-Sánchez, and J. Vaquero-Martín, "3D printing in experimental orthopaedic surgery: do it yourself," *European Journal of Orthopaedic Surgery & Traumatology*, vol. 29, no. 5, pp. 967–973, 2019.
43. A. Sarkissian, "An exploratory analysis of US FDA Class I medical device recalls: 2014–2018," *Journal of medical engineering & technology*, vol. 42, no. 8, pp. 595–603, 2018.
44. J. W. Salazar and R. F. Redberg, "Leading the call for reform of medical device safety surveillance," *JAMA internal medicine*, vol. 180, no. 2, pp. 179–180, 2020.
45. L. Lin, K. J. Vicente, and D. J. Doyle, "Patient safety, potential adverse drug events, and medical device design: a human factors engineering approach," *Journal of biomedical informatics*, vol. 34, no. 4, pp. 274–284, 2001.

46. J. R. Ward and P. J. Clarkson, "An analysis of medical device-related errors: prevalence and possible solutions," *Journal of medical engineering & technology*, vol. 28, no. 1, pp. 2–21, 2004.
47. M. C. Florkow *et al.*, "MRI-based synthetic CT shows equivalence to conventional CT for the morphological assessment of the hip joint," *Journal of Orthopaedic Research*[®], 2021.
48. K. Willemsen *et al.*, "3D-printed saw guides for lower arm osteotomy, a comparison between a synthetic CT and CT-based workflow," *3D Printing in Medicine*, vol. 7, no. 1, pp. 1–12, 2021.
49. EUR-Lex, *Regulation (EU) 2017/745 of the European parliament and of the council of 5 April 2017 on medical devices, amending Directive 2001/83/EC, Regulation (EC) No 178/2002 and Regulation (EC) No 1223/2009 and repealing Council Directives 90/385/EEC and 93/42/EE*. 2017. [Online]. Available: <https://eur-lex.europa.eu/legal-content/EN/TXT/PDF/?uri=CELEX:32017R0745&from=EN>
50. S. Bastawrous *et al.*, "Establishing quality and safety in hospital-based 3D printing programs: patient-first approach," *RadioGraphics*, vol. 41, no. 4, pp. 1208–1229, 2021.
51. K. Willemsen, R. Nizak, H. J. Noordmans, R. M. Castelein, H. Weinans, and M. C. Kruyt, "Challenges in the design and regulatory approval of 3D-printed surgical implants: a two-case series," *The Lancet Digital Health*, vol. 1, no. 4, 2019, doi: 10.1016/S2589-7500(19)30067-6.
52. G. A. M. Govaert, F. Hietbrink, and K. Willemsen, "Three-Dimensional Manufacturing of Personalized Implants in Orthopedic Trauma Surgery—Feasible Future or Fake News?," *JAMA Network Open*, vol. 4, no. 2, pp. e210149–e210149, 2021.
53. B. K. Brockman, V. A. Taylor, and C. M. Brockman, "The price of unconditional love: Consumer decision making for high-dollar veterinary care," *Journal of Business Research*, vol. 61, no. 5, pp. 397–405, 2008.
54. D. H. Ballard, P. Mills, R. Duszak Jr, J. A. Weisman, F. J. Rybicki, and P. K. Woodard, "Medical 3D printing cost-savings in orthopedic and maxillofacial surgery: cost analysis of operating room time saved with 3D printed anatomic models and surgical guides," *Academic radiology*, vol. 27, no. 8, pp. 1103–1113, 2020.
55. V. M. Vaz and L. Kumar, "3D printing as a promising tool in personalized medicine," *AAPS PharmSciTech*, vol. 22, no. 1, pp. 1–20, 2021.
56. P. Tack, J. Victor, P. Gemmel, and L. Annemans, "3D-printing techniques in a medical setting: a systematic literature review," *Biomedical engineering online*, vol. 15, no. 1, pp. 1–21, 2016.
57. A. Copeland and A. H. Shapiro, "Price setting and rapid technology adoption: The case of the PC industry," *Review of Economics and Statistics*, vol. 98, no. 3, pp. 601–616, 2016.
58. M. Goyen and J. F. Debatin, "Healthcare costs for new technologies," *European journal of nuclear medicine and molecular imaging*, vol. 36, no. 1, pp. 139–143, 2009.
59. A. Aimar, A. Palermo, and B. Innocenti, "The role of 3D printing in medical applications: a state of the art," *Journal of healthcare engineering*, vol. 2019, 2019.
60. E. D. Sheha, S. D. Gandhi, and M. W. Colman, "3D printing in spine surgery," *Annals of translational medicine*, vol. 7, no. Suppl 5, 2019.
61. E. L. Neely, "The risks of revolution: ethical dilemmas in 3D printing from a US perspective," *Science and engineering ethics*, vol. 22, no. 5, pp. 1285–1297, 2016.

62. H. Hoekstra, W. Rosseels, A. Sermon, and S. Nijs, "Corrective limb osteotomy using patient specific 3D-printed guides: a technical note," *Injury*, vol. 47, no. 10, pp. 2375–2380, 2016.
63. M. Javaid and A. Haleem, "4D printing applications in medical field: a brief review," *Clinical Epidemiology and Global Health*, vol. 7, no. 3, pp. 317–321, 2019.
64. S. K. Sinha, "Additive manufacturing (AM) of medical devices and scaffolds for tissue engineering based on 3D and 4D printing," in *3D and 4D printing of polymer nanocomposite materials*, Elsevier, 2020, pp. 119–160.
65. G. Li *et al.*, "Advances in 4D medical imaging and 4D radiation therapy," *Technology in cancer research & treatment*, vol. 7, no. 1, pp. 67–81, 2008.
66. I. Abuhav, *ISO 13485:2016: a complete guide to quality management in the medical device industry*. CRC Press, 2018.
67. G. Riva, B. K. Wiederhold, and F. Mantovani, "Neuroscience of virtual reality: from virtual exposure to embodied medicine," *Cyberpsychology, Behavior, and Social Networking*, vol. 22, no. 1, pp. 82–96, 2019.
68. S. G. Izard, J. A. Juanes, F. J. G. Peñalvo, J. M. G. Estella, M. J. S. Ledesma, and P. Ruisoto, "Virtual reality as an educational and training tool for medicine," *Journal of medical systems*, vol. 42, no. 3, pp. 1–5, 2018.
69. R. Riener and M. Harders, *Virtual reality in medicine*. Springer Science & Business Media, 2012.
70. L. Li *et al.*, "Application of virtual reality technology in clinical medicine," *American journal of translational research*, vol. 9, no. 9, p. 3867, 2017.
71. S. Bin, S. Masood, and Y. Jung, "Virtual and augmented reality in medicine," in *Biomedical Information Technology*, Elsevier, 2020, pp. 673–686.
72. T. M. Peters, C. A. Linte, Z. Yaniv, and J. Williams, *Mixed and augmented reality in medicine*. CRC Press, 2018.
73. M. Eckert, J. S. Volmerg, and C. M. Friedrich, "Augmented reality in medicine: systematic and bibliographic review," *JMIR mHealth and uHealth*, vol. 7, no. 4, p. e10967, 2019.
74. H.-G. Ha and J. Hong, "Augmented reality in medicine," *Hanyang Medical Reviews*, vol. 36, no. 4, pp. 242–247, 2016.
75. F. Zijlstra *et al.*, "CT synthesis from MR images for orthopedic applications in the lower arm using a conditional generative adversarial network," in *Progress in Biomedical Optics and Imaging - Proceedings of SPIE*, 2019, vol. 10949. doi: 10.1117/12.2512857.
76. M. C. Florkow *et al.*, "The impact of MRI-CT registration errors on deep learning-based synthetic CT generation," Mar. 2019, p. 116. doi: 10.1117/12.2512747.
77. M. C. Florkow *et al.*, "Deep learning-based MR-to-CT synthesis: The influence of varying gradient echo-based MR images as input channels," *Magnetic Resonance in Medicine*, vol. 83, no. 4, 2020, doi: 10.1002/mrm.28008.
78. M. J. Willemink *et al.*, "Preparing medical imaging data for machine learning," *Radiology*, vol. 295, no. 1, pp. 4–15, 2020.

79. H. Seo *et al.*, "Machine learning techniques for biomedical image segmentation: An overview of technical aspects and introduction to state-of-art applications," *Medical physics*, vol. 47, no. 5, pp. e148–e167, 2020.
80. D. Zhang, G. Wu, and L. Zhou, *Machine learning in medical imaging*. Springer, 2014.
81. A. A. Zadpoor and J. Malda, "Additive Manufacturing of Biomaterials, Tissues, and Organs," *Annals of Biomedical Engineering*, vol. 45, no. 1, pp. 1–11, 2017, doi: 10.1007/s10439-016-1719-y.
82. R. Levato, J. Visser, J. A. Planell, E. Engel, J. Malda, and M. A. Mateos-Timoneda, "Biofabrication of tissue constructs by 3D bioprinting of cell-laden microcarriers," *Biofabrication*, vol. 6, no. 3, p. 35020, 2014.
83. A. Manbachi *et al.*, "Starting a medical technology venture as a young academic innovator or student entrepreneur," *Annals of biomedical engineering*, vol. 46, no. 1, pp. 1–13, 2018.
84. O. Burgel and G. C. Murray, "The international market entry choices of start-up companies in high-technology industries," *Journal of International Marketing*, vol. 8, no. 2, pp. 33–62, 2000.
85. B. Lander and J. Atkinson-Grosjean, "Translational science and the hidden research system in universities and academic hospitals: A case study," *Social Science & Medicine*, vol. 72, no. 4, pp. 537–544, 2011.
86. H. B. Dickler, D. Korn, and S. G. Gabbe, "Promoting translational and clinical science: the critical role of medical schools and teaching hospitals," *PLoS medicine*, vol. 3, no. 9, p. e378, 2006.



The background is a solid blue color with several sets of thin, parallel diagonal lines. One set of lines is in the top-left corner, another in the bottom-left corner, and a third set is in the bottom-right corner. The lines are light blue and create a sense of movement and depth.

PART 6

APPENDICES



APPENDICES

Dutch Summary /
Nederlandse Samenvatting

List of publications

Non-scientific communication

PhD-Portfolio

Acknowledgements

Curriculum Vitae

Nederlandse samenvatting

Medische 3D technologie, van het lab naar de kliniek

Deel 1: Introductie en visie

Een leven zonder de nieuwste technologische ontwikkelingen is niet meer reëel. Een mobieltje in iedere broekzak, een laptop in de rugzak, een teamvergadering tijdens het thuiswerken. Dit is vrij normaal geworden. Maar ook in de medische wereld hebben de ontwikkelingen niet stil gestaan. De technologische ontwikkeling waar dit proefschrift zich op richt is de introductie van de derde dimensie (3D) in de medische sector en hoe dit uiteindelijk heeft geleid tot medisch 3D printen en de verfijning van 3D-diagnostiek. De nadruk is gelegd op de benodigheden voor het transleren van deze nieuwe technieken van het lab, via diermodellen, naar de behandeling van patiënten.

In hoofdstuk 1 wordt een introductie gegeven van 3D-technologie. Voor het ontstaan van 3D-technologie werd een gebroken arm gediagnostiseerd met conventionele röntgenfoto's. Röntgenfoto's bestaan al langer dan honderd jaar en zijn sinds het ontstaan van de techniek niet veel meer veranderd. Röntgenstraling gaat makkelijker door weefsel met lucht erin, zoals longen maar moeilijker door stevig of hard weefsel zoals botten. Hierdoor ontstaat er contrast op de röntgenfoto. Bij een breuk in de arm zal straling makkelijker door de breuk heen passeren waardoor een donker streepje zal ontstaan in een verder wit bot. Een van de voordelen van deze techniek is dat het makkelijk te gebruiken is. Een van de nadelen van deze techniek is dat de röntgenfoto een twee dimensionale ofwel 'platte' foto geeft terwijl we in een driedimensionale wereld leven. Om dit probleem te ondervangen worden er vaak meerdere foto's gemaakt uit verschillende hoeken om zo een steeds beter beeld te krijgen van de werkelijke situatie. Een werkelijk 3D-beeld kan dit nog niet genoemd worden. Na het ontstaan van steeds krachtigere computers werd het uiteindelijk mogelijk om foto's uit verschillende richtingen (360 graden) te reconstrueren in een CT-scan. Met deze reconstructies kan men de derde (axiale) dimensie beoordelen. Niet lang daarna werd ook een andere techniek geïntroduceerd die deze derde axiale dimensie kan weergeven, de MRI-scan. MRI-techniek werkt niet met röntgenstraling maar met magnetische velden. Door dit verschil tussen de MRI en CT-techniek is de toepassing net wat anders.

In het begin werden deze CT en MRI-technieken vooral gebruikt voor het stellen van diagnoses, de resolutie was namelijk nog niet hoog genoeg voor het doen van verdere beeldbewerkingen. Uiteindelijk zorgden steeds krachtiger en sneller wordende computers voor een doorbraak. De resolutie van de gemaakte beelden ging omhoog en het werd mogelijk om deze beelden te reconstrueren in 3D modellen. Uiteindelijk werd het zelfs mogelijk om deze 3D modellen uit te printen met een 3D-printer. Deze innovatie

zorgde ervoor dat er ineens veel meer 3D-toepassingen binnen het bereik van de arts kwamen. Denk hierbij aan anatomische modellen die perfect de patiënt weerspiegelen, boor- en zaagmallen die de chirurg kunnen helpen bij het uitvoeren van een operatie, of maatwerk implantaten die specifiek voor een patiënt zijn ontworpen. In dit proefschrift worden de verschillende stadia van verschillende technieken besproken die toewerken naar een introductie in het ziekenhuis.

In het eerste gedeelte van dit proefschrift wordt er gekeken naar conventionele (operatie) technieken die nog niet 3D ondersteund worden. Er wordt gekeken hoelang het succes van bepaalde operaties aanhoudt en of er factoren aanwezig zijn die het succes beïnvloeden. Indien deze factoren te verbeteren zijn door de introductie van 3D-technologie dan wordt dit verder onderzocht. In het eerste gedeelte van het proefschrift is de focus komen te liggen op de behandeling van heupdysplasie. Heupdysplasie is een aandoening die vaak voorkomt en de gevolgen kunnen vrij ernstig zijn. Heupdysplasie kan leiden tot artrose (gewrichtsslijtage) en pijn. De standaard operaties, de 'triple osteotomie' of 'Ganz osteotomie' zijn erg ingrijpend. Op diverse plaatsen wordt in het bekken gezaagd om vervolgens het acetabulum van positie te veranderen. Deze operaties gaan gepaard met een lange herstelperiode en in veel gevallen herstelt de patiënt niet volledig. Om deze redenen is het belangrijk om ook te kijken naar alternatieven, al dan niet ondersteund met 3D-technologie.

Er zijn ook minder ingrijpende operaties beschikbaar voor heupdysplasie zoals de 'pandak plastiek' en de 'Chiari osteotomie'. Het succes van deze operaties is echter nooit goed uitgezocht. Daarom wordt in hoofdstuk 2 het succes van de pandak plastiek onderzocht en in hoofdstuk 3 het succes van de Chiari osteotomie. Eerst wordt er een systematische analyse gemaakt van de beschikbare data over de pandak plastiek (hoofdstuk 2). De pandak plastiek is een heupdysplasie operatie waarbij een stuk bot wordt weggehaald uit de bekkenkam en getransplanteerd naar het heupgewricht. Bij deze operatie wordt het stuk bot net boven het heupkapsel geplaatst, waardoor het heupkapsel hypothetisch zal functioneren als een alternatief stuk gewrichtskraakbeen. Hierdoor wordt het gewicht-verdelende oppervlak van de kom groter en dit zal het ontstaan van artrose verminderen. Het succes van de pandak plastiek bleek gecorreleerd met de exact goede plaatsing van het stuk donorbot. Te laag en er ontstaat inklemming, te hoog en het geeft te weinig versteviging, te klein en het bot resorbeert of te dun en het breekt. Dit zijn factoren die moeilijk vast te stellen zijn tijdens een operatie maar goed te plannen zijn met 3D-technologie. Een mogelijke oplossing is een pandak implantaat specifiek ontworpen voor individuele patiënten en geproduceerd met een 3D printer. Dit idee voor een 3D pandak implantaat is later in dit proefschrift verder uitgewerkt tot een 3D geprint titanium implantaat.

Verder wordt er een systematische analyse gemaakt van de beschikbare data over de Chiari osteotomie (hoofdstuk 3). De Chiari osteotomie is een operatie voor heup dysplasie waarbij een osteotomie wordt gemaakt iets boven het heupkapsel. Vervolgens wordt het heupgewricht iets naar binnen geduwd waardoor het bovengelegen stuk bot net iets boven het heupkapsel komt te liggen. Eveneens als bij de pandak plastiek bestaat bij de Chiari de hypothese dat het heupkapsel zal functioneren als een alternatief stuk gewrichtskraakbeen. Het succes van de Chiari osteotomie bleek gecorreleerd met de exact goede hoogte en richting van de botsnede. Te hoog en het ondersteunt het kapsel niet genoeg en te laag en dit zal het gewricht te veel inklemmen. Intra-operatief kan dit moeilijk vast te stellen zijn, maar met behulp van 3D-technologie zou die begeleid kunnen worden. Dit kan bijvoorbeeld door het maken van een boor- en zaagmal waarmee de hoogte en richting van de zaagsnede exact bepaald kan worden.

Om uit de literatuur afgeleide verbeteringen (zoals hierboven voorgesteld) te vertalen naar de mens, is er eerst vervolgonderzoek nodig. Dit kan bijvoorbeeld door testen te doen in een biomechanische opstelling of door te testen in een diermodel. Voor het 3D pandak implantaat was er een unieke kans om deze eerst te testen in een diermodel. Honden hebben net als mensen vaak last van heupdysplasie en worden hier ook vaak voor behandeld. Echter, literatuur die de overeenkomsten en verschillen tussen heupdysplasie bij mensen en honden bespreken ontbreekt. In hoofdstuk 4 wordt daarom een vergelijking gemaakt tussen heupdysplasie bij honden en mensen. Hierbij is er specifiek aandacht voor de anatomie, etiologie, diagnostiek en behandeling. Uit hoofdstuk 4 blijkt dat de maatschappelijke impact van heupdysplasie groot is, zowel bij mens als hond. Bij beide wordt pijn veroorzaakt door artrose van het heupgewricht ten gevolge van een ongewenst hoge krachtverdeling in het heupgewricht. Voor mens en hond zijn zeer vergelijkbare ingrijpende operaties voorhanden, die voor beide gepaard gaan met hoge kosten en een lange hersteltijd. De overeenkomsten tussen hond en mens zoals beschreven in dit hoofdstuk gaf de doorslag om de hond te gebruiken voor het exploreren van een 3D pandak implantaat. In deel twee van deze thesis wordt dit 3D pandak implantaat uitgebreider besproken.

Doordat 3D imaging zoals MRI en CT-scans steeds belangrijker zijn geworden, is het goed om te weten wat de verschillen zijn tussen de twee. CT-scans worden vaker gemaakt in de acute/trauma situatie, maar hebben de beperking dat ze voornamelijk het botweefsel goed weergeven en minder goed onderscheid maken tussen de diverse soorten zachte weefsels. MRI's worden vaker gemaakt als er diagnostiek nodig is van de zachtere organen, zoals kraakbeen, de interne organen of bijvoorbeeld de hersenen. Soms zijn beide scans nodig. CT is momenteel nog de gouden standaard voor het weergeven van harde structuren zoals bot, maar vanwege de schadelijke röntgenstraling zou dit zoveel mogelijk vervangen moeten worden door MRI. Wat is er op dit moment bekend over de toepassing

van MRI voor het visualiseren van bot? Een uitgebreide review van de beschikbare MRI-technieken m.b.t. het afbeelden van botweefsel is nog nooit gedaan. In hoofdstuk 5 is een uitgebreide analyse gemaakt per lichaamsdeel om te kijken of huidige MRI-technieken al bruikbaar zijn voor het weergeven van het menselijk skelet. Hieruit blijkt dat met name MRI-opnamen aangevuld met zogenaamde 'machine-learning' algoritmen botweefsel goed kunnen weergegeven. Bij 'machine learning' worden computer algoritmen eerst getraind met zowel MRI als CT-data en daarna kunnen deze getrainde algoritmen nieuwe MRI-scans zelfstandig omzetten in zogenoemde synthetische-CT scans (namaak CT). Vervolgens kan deze synthetische-CT weer gebruikt worden voor het makkelijker omzetten naar een 3D-model van botstructuren. Deze bot 3D-modellen gemaakt uit synthetische-CT doen soms al niet onder voor de 3D-modellen gemaakt uit originele CT-data. In deel 4 van dit proefschrift zullen twee nieuwe toepassingen van synthetische-CT verder worden onderzocht voor hun klinische toepasbaarheid.

Deel 2: Lab

In deel 2 van deze thesis worden de gevonden verbeteringen uit literatuur (deel 1) nader onderzocht. In hoofdstuk 6 van deze thesis wordt er gekeken naar de mogelijkheid van een 3D-geprinte pandakprothese om heupdysplasie te behandelen. Er is gezocht naar bekkens van overleden honden met heupdysplasie, zodat het idee van een pandak implantaat radiologisch en biomechanisch getest kon worden. In de database van de veterinaire kliniek van de UU zijn zes hondenheupen gevonden (drie honden) met heupdysplasie die vanwege niet-orthopedische redenen zijn overleden. Voor alle zes bekkens werd een 3D-geprint titanium heupdysplasie-implantaat gemaakt waarna deze werd getest. Na het plaatsen van de implantaten verbeterde het percentage heupoverkapping, zoals vooraf berekend, van dysplastisch naar gezond. Deze toename in overkapping zorgde er ook voor dat de heupen mechanisch stabielere waren dan zonder het implantaat. Ook kon het implantaat genoeg kracht weerstaan tijdens een mechanische test, waarmee de maximale fysiologische belasting op de hondenheup wordt gesimuleerd. Dit maakt de weg vrij voor het transleren van dit implantaat naar een levend diermodel in deel 3 van dit proefschrift.

Omdat de in hoofdstuk 6 geprinte implantaten van titanium zijn, kunnen ze niet geplaatst worden bij kinderen die nog in de groei zijn. Daarom is er gekeken naar materialen die enerzijds botingroei faciliteren maar in loop van tijd ook resorberen, waardoor de groei over langere tijd gegarandeerd kan worden. In hoofdstuk 7 wordt daarom een pandak implantaat getest van een biologisch resorberend materiaal; magnesiumstrontiumfosfaat (MgPSr) met polycaprolacton (PCL). Dit materiaal is niet zo stevig als het titanium implantaat getest in het voorgaande hoofdstuk en zal doorontwikkeld moeten worden om de krachten van normale dagelijkse bewegingen op te vangen. Daarnaast zijn er meer

testen nodig zodat het inzichtelijk wordt hoe snel dit materiaal resorbeert en in welke mate het eigen botweefsel ingroeit en of dit de vorm en functie van het implantaat overneemt. Een van de voordelen van 3D-ontwerpprogramma's is dat de techniek gemakkelijk kan worden toegepast op meerdere manieren. Zo wordt in hoofdstuk 8 het idee van het 3D-geprinte heupdysplasie implantaat getransleerd naar de schouder. Schouders kunnen onstabiel worden als gevolg van een botdeficiëntie, bijvoorbeeld in de kom, het glenoid. Net als bij de heup kunnen de optimale afmetingen van de kom worden gereconstrueerd met een extracapsulair implantaat dat een exact patiënt-specifiek ontwerp vereist. Dit concept is biomechanisch getest in menselijk kadavermateriaal en gaf vergelijkbare resultaten als de gouden standaard Latarjet-procedure met een kleinere variantie tussen de resultaten, waardoor de uitkomst van het 3D-geprinte implantaat consistent was.

In hoofdstuk 9 wordt een nieuw ontwerp voor poreus vervormbaar titanium geëvalueerd. De titanium implantaten zijn zo hoog poreus dat het hypothetisch kleiachtige kan vervormen. Deze vervorming kan helpen om implantaten te plaatsen in grote botdefecten met een onregelmatige vorm. Een plek waar grote defecten kunnen ontstaan is achter de totale heupprothese cup door stress shielding (spanningsafscherming). Dit kan een probleem geven bij revisieoperaties in de heup. Het vervormbare titanium zorgt daar voor een betere pasvorm, betere stabiliteit en daardoor betere implantaatintegratie (bot ingroei). In potentie vermindert daardoor de stress-shielding in deze diepe zones achter de cup. De resultaten van dit onderzoek toonden aan dat de hoog poreuze titaniumsecties van de 3D-geprinte acetabulumrevisie-implantaten sterk vervormen na implanteren in sawbones (kunstbotten). Eveneens werd een goede stabiliteit waargenomen van de implantaten tijdens daaropvolgende cyclische belasting. Om deze poreuze structuren te blijven verbeteren zal het 3D-printen van zeer dunne structuren, bij voorkeur in het bereik van 100 tot 200 μm , moeten worden onderzocht. Echter 3D-printtechnieken zijn beperkt tot wat momenteel haalbaar is. Daarnaast zijn aanvullende testen in menselijk materiaal nodig om het huidige vervormbare titanium verder te evalueren voordat het kan geïntroduceerd worden in de kliniek.

Concluderend hebben de hoofdstukken 6 tot 9 laten zien hoe nieuwe ideeën kunnen worden geëvalueerd in een lab- en onderzoeksomgeving. Voordat deze ideeën naar de kliniek worden vertaald, is een overbruggingsstap nodig, bijvoorbeeld een evaluatie in een (experimenteel) diermodel. Het volgende deel van dit proefschrift zal zich daarom concentreren op deze vertaling naar dieren. Indien deze nieuwe concepten dan succesvol zijn, kunnen ze leiden tot nieuwe behandelingen voor zowel dier als mens in een echt "One Health, One Medicine" concept.

Deel 3: One Medicine (translatie)

In het derde deel van het proefschrift zijn drie typen patiënt-specifieke implantaten getest en toegepast in veterinaire (honden)chirurgie. In hoofdstuk 10 wordt het heupdysplasie pandak implantaat, dat al biomechanisch werd getest in hoofdstuk 6, geïmplanteerd bij drie honden met heupdysplasie als onderdeel van een pilot-onderzoek. De procedure met de 3D pandak bleek haalbaar en veilig. Echter, verder onderzoek is nodig om te kijken hoe effectief het implantaat is in het voorkomen of vertragen van degeneratieve veranderingen van het heupgewricht op lange termijn. Dit moet onderzocht worden in een grotere groep patiëntdieren. Dit wordt vervolgens onderzocht in hoofdstuk 11. Hierbij worden de resultaten gepresenteerd van de eerste patiënthonden behandeld met het 3D pandak implantaat. Daarnaast moet er in de toekomst worden gekeken of het verschil in artroscore gecorreleerd is met de plaatsingsnauwkeurigheid van het implantaat en/ of de mate van de preoperatieve heupdysplasie correleert met de langetermijnresultaten en overleving van deze behandeling.

Vergelijkbaar met deel 2, waar een anatomische vertaling naar de schouder werd gemaakt, wordt in deel 3 een anatomische vertaling gemaakt naar de schedel (hoofdstuk 12) en het antebrachium (hoofdstuk 13). In hoofdstuk 12 worden twee patiënthonden gepresenteerd; de eerste casus had een massief osteoom in de schedel dat verwijderd moest worden. De procedure liet een enorme opening in de schedel achter die een chirurgische reconstructie met een patiënt-specifiek implantaat vereiste om normaal functioneren van de hond mogelijk te maken. De tweede casus had een osteosaroom in de kaak nabij de oogkas en oog. Dit sarcoom werd verwijderd en deze hond kreeg een 3D-geprint titanium implantaat om het benige defect in dezelfde operatie te reconstrueren. Op deze manier kon deze hond de normale functie van de kaak behouden en kon het oog behouden blijven. Beide implantaten zijn gemaakt met een poreuze rand op het implantaat-bot grensgebied om botingroei mogelijk te maken. In hoofdstuk 13 worden andere toepassingen van titanium 3D-printen onderzocht; het gebruik van een 3D-geprint poreus implantaat voor het repareren van een botdefect van kritieke grootte bij honden. Deze botdefecten waren ontstaan na een ulnaire fractuur met daaropvolgend een osteomyelitis met een non-union. Deze honden hadden een niet-belastbare poot, maar keerden na de operatie terug naar een normale gang en vertoonden een goede benige ingroei van de prothese bij follow-up met CT-beeldvorming. Een van de honden stierf aan niet-verwante oorzaken waardoor met aanvullende micro-CT-analyse de botingroei op een hogere vergroting kon bestudeerd worden. Micro-CT toonde een grote hoeveelheid nieuw bot aan rond en in het poreuze deel van de prothese, hoewel volledige botfusie door de grootste opening van het implantaat (nog) niet aanwezig was. De ideale poreuze microstructuur van 3D-geprint titanium voor benige ingroei blijft daarom onderwerp van onderzoek.

Deel 4: Kliniek

In het vierde deel wordt een translatiestap naar de kliniek ('bedside') gemaakt. Echter, dit is een stap die niet zomaar genomen kan te worden. Een nieuw technologisch product moet goed getest zijn wanneer deze de (medische) markt betreedt. Kortom er is valide onderzoek en bewijs nodig naar de effectiviteit van nieuwe 3D ondersteunde behandelingen bij de mens. Daarom worden in de hoofdstukken 14 en 15 twee nieuwe klinische toepassingen van op MRI-gebaseerde synthetische CT-werkwijzen nauwkeuring onderzocht om te zien of ze klaar zijn om op patiënten te worden gebruikt.

Eerst wordt in hoofdstuk 14 een vergelijking gemaakt, tussen de op MRI-gebaseerde synthetische-CT (sCT) en de conventionele CT, voor de morfologische beoordeling van het heupgewricht en pelvis. De sCT toonde zich gelijkwaardig aan de conventionele CT en benadrukt daarom de klinische toepasbaarheid van deze nieuwe stralingsvrije sCT-route voor beoordeling van het heupgewricht.

In hoofdstuk 15 wordt een andere op MRI gebaseerde sCT-werkwijze vergeleken met een reguliere CT-workflow. Dit keer met betrekking tot zaaggeleiders voor de onderarm-osteotomie. De vraag was of beide technieken gelijkwaardig zijn voor gebruik bij de correctie van kromme botten. Dit werd getest op kadavermateriaal en beide werkwijzen vertoonden dezelfde nauwkeurigheid voor plaatsing van de zaaggeleiders (vergeleken met hoge-resolutie micro-CT als gouden standaard).

Verder is een voordeel van medisch 3D printen de toegankelijkheid van de techniek. Een goedkope desktop 3D-printer (voor consumenten) is al beschikbaar onder de €100,- en segmentatie- en ontwerpsoftware is veelal open-source beschikbaar. Daardoor kan iedereen met kennis van 3D-ontwerpprogramma's (CAD) producten ontwerpen en 3D-printen zonder veel investeringen. Het nadeel van dit soort technologische ontwikkelingen is dat niet ieder product ook voldoende is getest voor de (medische) markt. Om patiënten te beschermen tegen ongekwalificeerde fabrikanten van medische hulpmiddelen kwam de Europese Autoriteit met een nieuwe Medical Device Regulation (MDR) die per mei 2021 actief werd. Hierdoor wordt het lastiger om op basis van 'trial and error' nieuwe medische hulpmiddelen op de markt te brengen. Ieder implantaat of apparaat dat na introductie van de MDR op de markt komt moet voldoende worden ondersteund met vereiste documentatie en wetenschappelijk bewijs. Deze extra bewijslast en administratie kan gebruikers en fabrikanten van medische hulpmiddelen ontmoedigen om nieuwe producten te ontwikkelen (Fig. 1). Dit is met name jammer voor de medische 3D-printindustrie waar veel kleine gebruikers zoals ziekenhuizen actief zijn. Niet alle ziekenhuizen hebben deze kennis of de middelen in huis om dit uit te zoeken en zijn daardoor niet meer in staat om 3D-technologie ondersteunde zorg aan hun patiënten aan te bieden. Daarom worden in dit proefschrift de ontwikkelingsstappen van

3D-technologie naar de kliniek gepresenteerd. Dit kan als hulpmiddel dienen voor andere onderzoekers en artsen om deze techniek ook te gaan gebruiken in hun ziekenhuis.

In hoofdstuk 16 is een 'first-in-man' applicatie gepresenteerd van een titanium 3D-geprint implantaat dat meerdere wervels van de anterieure wervelkolom overbrugt. Er wordt een uitleg gegeven welke regels en voorschriften er gevolgd moet worden om aan de nieuwe Europese wetten (MDR) te voldoen. Met dit hoofdstuk krijgen ontwikkelaars van patiënt-specifieke producten een workflow die een sneller proces mogelijk maakt voor toekomstige (vergelijkbare) gevallen. Vervolgens wordt deze werkwijze verder uitgebreid in hoofdstuk 17. Er wordt een patiënt-specifieke toepassing gepresenteerd van een boormal, de zogenaamde 'click-on pedikel boorgeleider'. Naast het presenteren van deze toepassing, wordt er extra nadruk gelegd op de benodigde infrastructuur die nodig is binnen een tertiair verwijzingscentrum zoals een universitair ziekenhuis om dit soort producten te faciliteren en veilig aan te bieden aan patiënten.

Deel 5: Afsluiting

Het vijfde deel van dit proefschrift begint met een geïnviteerd commentaarstuk (hoofdstuk 18) over de bruikbaarheid en toepasbaarheid van nieuwe 3D-technologie voor orthopedische (trauma)chirurgie, waarbij het belang van regels en voorschriften onder de aandacht wordt gebracht. Daarnaast wordt er gesproken over de behoefte aan transparantie van de kosten van een 3D-workflow in het ziekenhuis. Toch is er in dit proefschrift geen specifieke evaluatie gemaakt van de kosteneffectiviteit van de onderzochte behandelingen. Kortom, bij verdere introductie in de kliniek dient er nog wel een analyse te komen van de kosteneffectiviteit; dit om een dergelijk nieuw product daadwerkelijk een klinisch en commercieel succes te maken. Echter het belangrijkste doel voor dit proefschrift was de veiligheid en haalbaarheid van bepaalde toepassingen van medische 3D-technologie. De financiële achtergrond wordt verder besproken in de volgende paragraaf 'toekomstperspectieven'.

Toekomstperspectieven

Dit proefschrift behandelt een innovatief onderwerp; personaliseerde 3D-technologie. Blijft deze techniek voorbehouden voor specifieke patiënten of wordt het de toekomstige norm van de geneeskunde? Dit is een belangrijke vraag, zeker als je kijkt naar de kosten van deze op maat gemaakte medische hulpmiddelen. Hoe moeten deze door 3D-ondersteunde producten worden betaald? Is er een valide businesscase voor 3D-technologie? De meeste medische kosten worden vergoed door verzekeringsmaatschappijen, maar deze willen graag gerandomiseerde gecontroleerde studies als onbetwistbaar bewijs van de (kosten)effectiviteit van deze nieuwe technologieën. Echter, een grote beperking in het onderzoek van gepersonaliseerde medische 3D-technologie is de patiënt-specifieke aard van de producten, waardoor het aantal variabelen sterk verhoogd is. Hierdoor

is het moeilijk om hoogwaardig ‘evidence-based’ onderzoek te doen. Dit zou daarom een van de aandachtspunten moeten zijn voor toekomstig onderzoek. Want als de financiële vergoeding ontbreekt, heeft zorg met 3D-technologie het moeilijk om breed geaccepteerd te worden binnen de veelal conservatieve medische wereld. Wanneer een technologie echter meer wordt geadopteerd zal de prijs van deze technologie dalen, waardoor het steeds makkelijker wordt om voldoende vergoeding te vinden. De vraag dringt zich op of 3D-prints uiteindelijk zo betaalbaar wordt dat het voor elk implantaat kan worden gebruikt. Wordt het concurrerend met de huidige in massa geproduceerde en kant-en-klare implantaten? Sommige massa-geproduceerde implantaten worden nu namelijk al in grote aantallen geproduceerd met behulp van 3D-printtechnologie. En zo ja, heeft elk ziekenhuis dan zijn eigen 3D-printers nodig of kunnen ze beter vertrouwen op externe leveranciers? Het vinden van vergoedingen voor 3D-technologie is niet de enige uitdaging. Er moet worden afgewogen of alles wat gemaakt kan worden, ook gemaakt moet worden. Zo zijn er enkele ethische overwegingen, bijvoorbeeld of het helpen van patiënten met een lage levensverwachting met dure op maat gemaakte oplossingen, duurzaam is voor de samenleving als geheel.

Om de kosteneffectiviteit van een behandeling verder te onderzoeken, dient ook de klinische effectiviteit van de behandeling in ogenschouw te worden genomen. Is het nauwkeuriger uitvoeren van een osteotomie met een zaaggeleider ook klinisch relevant? Herstelt die patiënt sneller en is er minder medische zorg nodig of is de toegevoegde nauwkeurigheid klinisch niet relevant, omdat het menselijk lichaam ook redelijk vergeeflijk is? Dit zijn uitdagingen die in de toekomst verder onderzocht moeten worden. Bijvoorbeeld door grotere klinische onderzoeken op te zetten met een langere follow-up, waarbij verschillende methoden worden vergeleken in de gehele zorgketen.

3D-technologie helpt ons verder te kijken dan de beperkingen van 2D-beeldvorming, maar 3D is weer slechts een momentweergave van een 4D-situatie, waarbij de vierde dimensie tijd of beweging is. 3D-technologie helpt bijvoorbeeld bij het plannen van de herschikking van de biomechanische as van een been van een patiënt, wanneer liggend in de CT of MRI. Maar wat gebeurt er als we 4D gaan evalueren? In het voorbeeld van de osteotomie spelen bijvoorbeeld ook tijdsafhankelijke aspecten zoals beweging en belasting t.g.v. zwaartekracht en spieren een belangrijke rol. Nu 3D-technologie steeds toegankelijker wordt, is het steeds vaker mogelijk om rekening te houden met die vierde dimensie.

Introductie van 3D-technologie in de kliniek brengt een grote hoeveelheid wetgeving met zich mee. Vanwege de onervarenheid met deze wetgeving (MDR) is er echter geen precedent bekend of is er geen jurisprudentie beschikbaar. Daarom krijgen klinici en onderzoekers in dit proefschrift voorbeelden van hoe ze de uitdagingen kunnen

aanpakken die te maken hebben met de ontwikkeling en introductie van nieuwe 3D-ondersteunde technologieën. In de toekomst is meer samenwerking nodig, zowel nationaal als internationaal, om uniform geaccepteerde standaarden te creëren. Hierbij zal 3D-ondersteunende software steeds belangrijker, gebruiksvriendelijker en breder beschikbaar moeten worden.

Een tool die steeds meer beschikbaar komt in de kliniek is virtual reality en augmented reality. Virtual reality is een gesloten virtuele omgeving die kan worden bekeken in een virtual reality-bril. In de medische zorg wordt virtual reality het meest gebruikt voor educatieve doeleinden voor chirurgen en klinici, zodat bepaalde vaardigheden in een veilige omgeving geoefend kunnen worden voordat deze op 'real life' patiënten toegepast worden. Een andere toepassing is het gebruik van virtual reality als therapie voor (jonge) patiënten om bijvoorbeeld een trauma te verwerken. Augmented reality is een hulpmiddel dat visuele informatie projecteert bovenop of naast de 'normale' kijk op de wereld. Dit is handiger wanneer er een taak bij een echte patiënt moet worden uitgevoerd, maar met begeleiding van extra informatie. Bijvoorbeeld door een anatomisch 3D-model te bekijken dat is afgeleid van de CT-beelden van een patiënt en op de patiënt is geprojecteerd. Momenteel is er een verschuiving waar te nemen van 3D-prints naar 3D-visualisatie. Chirurgen hebben geen fysiek 3D-geprint model meer nodig, maar ze volstaan met een visualisatie middels een virtual of augmented reality-bril. Zowel virtual reality als augmented reality zijn 3D-tools die een nieuwe revolutie teweeg kunnen brengen in de zorg. Echter deze tools moeten nog steeds aan dezelfde regels en voorschriften voldoen als andere medische hulpmiddelen, zeker wanneer er patiënten betrokken zijn. Want niet alle brillen zijn gevalideerd of zelfs gekalibreerd voor klinisch gebruik.

Kunstmatige intelligentie is in de medische zorg bezig aan een enorme opmars. Vooral bij beoordeling van medische beeldvorming kan kunstmatige intelligentie zoals algoritmen die gebruik maken van zogenaamde 'machine learning' of 'deep learning' van grote toegevoegde waarde zijn. Computeralgoritmen kunnen worden getraind door het aanbieden van beeldgegevens met gepaarde (semiautomatisch) segmentaties van anatomische regio's. Vervolgens kunnen deze algoritmen hun eigen segmentatie algoritme 'schrijven' waarna ze bij aanbieden van alleen de beeldgegevens hun eigen 3D-modellen kunnen produceren. Maar deze zelflerende algoritmen moeten aan dezelfde regels en voorschriften voldoen als andere medische hulpmiddelen en moeten daarom gevalideerd worden voor klinisch gebruik. Aangezien het niet altijd duidelijk is wat het exacte algoritme is dat toegepast wordt, is het een grote uitdaging om dergelijke methoden veilig en juridisch waterdicht geïmplementeerd te krijgen.

Een kans, maar ook moeilijk te realiseren is het 3D-bioprinten voor medisch gebruik. Het uiteindelijke doel van bioprinten is om functionerende levende organen zoals een hart of lever te vervaardigen. Echter, deze technieken bevinden zich nog in de beginfase van ontwikkeling. Toch is het 3D-printen van bot- en kraakbeen-nabootsende materialen de laatste jaren snel gegaan. Bot heeft een relatief eenvoudige samenstelling en is daardoor makkelijker na te bootsen in een laboratoriumomgeving. Het toevoegen van meer delicate weefsels als kraakbeen wordt al moeilijker. In dit proefschrift wordt een chirurgische toepassing van een bot-nabootsend materiaal (magnesiumfosfaat) onderzocht. Het blijft een uitdaging om deze materialen op een niveau te krijgen waarbij klinische introductie mogelijk en toegestaan is.

Ontwikkeling van medische 3D-technologie was tot nu toe vaak gereserveerd voor academische ziekenhuizen of gespecialiseerde bedrijven maar momenteel ontstaan er steeds meer startup bedrijven die een deel van de medische 3D-technologiemarkt proberen te veroveren. Deze verschuiving in kennis en input heeft voordelen aangezien particuliere ondernemingen de 3D-sector kunnen laten groeien. Echter ziekenhuizen, met name de universitaire ziekenhuizen, moeten kunnen blijven fungeren als medisch vangnet voor patiënten en daarom voor de samenleving. Immers, wanneer een patiënt geen behandeling kan vinden in de streekziekenhuizen, wordt hij doorverwezen naar de universiteit voor een mogelijk laatste behandelingsoptie. Daarom is het belangrijk dat er samenwerking blijft bestaan tussen deze particuliere (startup) ondernemingen en de universitaire ziekenhuizen. Om samenwerkingen mogelijk te maken, is het belangrijk om medisch-technologische hubs te creëren binnen academische ziekenhuizen. Deze hubs kunnen op de werkvloer de specialisten ondersteunen met bijvoorbeeld 3D implantaten gemaakt met software ontwikkeld door bedrijven. Maar wat is er nodig om zo'n hub te creëren en hoe positioneer je zo'n plek in het bestaande medische systeem? Dit zijn uitdagingen voor de toekomst.

Conclusie

Dit proefschrift beschrijft de ontwikkeling van medische 3D-technologie en welke rol het inneemt in het ziekenhuis. De algemene resultaten van dit proefschrift kunnen worden gebruikt voor verdere verkenning van medische 3D-technologie; hierbij worden voorbeelden gegeven van fundamenteel onderzoek, diermodel onderzoek en het uiteindelijke klinisch gebruik. Om in de toekomst 3D-technieken nog beter te laten integreren in de zorg zal er meer samenwerking nodig zijn tussen ziekenhuizen. Deze investeringen zullen helpen bij de transitie van 2D naar 3D-zorg om vervolgens een brug te slaan naar de toekomst: 4D-zorg.

List of Publications

Manuscripts are presented in reversed chronological order

Manuscripts marked with (@) are included in this thesis

1. (@) Acetabular rim extension using a patient specific implant for the treatment of hip dysplasia in dogs
-Koen Willemsen, Irin Kwananocha, Joëll Magré, Marianna Tryfonidou, Harrie. Weinans, Ralph Sakkers, Bart van der Wal, Björn Meij
 -Manuscript in preparation
2. (@) Additive manufacturing of titanium implants for reconstruction of the ulna in two dogs with critically sized- bone defects due to nonunion
 -Sara Jansen, **Koen Willemsen**, Joëll Magré, Björn P. Meij
 -Manuscript in preparation
3. Preoperative CT volume measurement of the temporal bone cortex: predictive analysis for mastoid obliteration
 -Sanne F. Westerhout; **Koen Willemsen**; Louise V. Straatman; Ronald L.A.W. Bleys; Hans G.X.M. Thomeer
 -Submitted: Advances in Therapy
4. (@) Additive manufacturing of titanium implants for skull reconstruction in canine oncological surgery
 -Eline J.C. van den Brink, **Koen Willemsen**, Floor Driessen, Guy C.M. Grinwis, Susanne A.E.B. Boroffka, Björn P. Meij
 -Revisions: Veterinary and Comparative Orthopaedics and Traumatology
5. Sternal erosion as a rare complication of hemoclipping the perfusion branch of the aortic graft prosthesis after type A dissection surgery.
 -S. Harbish, T.C. Dessing, **K. Willemsen**, L.M. de Heer, W.J.L. Suyker
 -Under review: The Annals of Thoracic Surgery
6. (@) Deformable titanium for acetabular revision surgery: a proof of concept
 -Joëll Magré, **Koen Willemsen**, Amir A. Zadpoor, Peter Seevinck, Bart C.H. van der Wal, Charles Vogely, Harrie Weinans
 -Under review: Journal of Orthopaedic Research

7. Endoscopic versus microscopic stapes surgery: an anatomical feasibility study; stapes surgery: endoscopic versus microscopic
-Esther E. Blijleven, **Koen Willemsen**, Ronald L.A.W. Bleys, Robert J. Stokroos, Inge Wegner, Henricus G.X.M. Thomeer
-Under review: *Otology & Neurotology*
8. (@) The vital role of an in-house 3D lab to create unprecedented solutions for challenges in spinal surgery, practical guidelines and clinical case series
-**Koen Willemsen**, Joëll Magré, Jeroen Mol, Herke-Jan Noordmans, Harrie Weinans, Moyo C. Kruyt
-Published: *Journal of Personalized Medicine*, special issue: Personalized Spine Surgery
<https://doi.org/10.3390/jpm12030395>
9. (@) Patient-specific 3D-printed shelf implant for the treatment of hip dysplasia tested in an experimental animal pilot in canines
-**Koen Willemsen**, Marianna A. Tryfonidou, Ralph J. B. Sakkers, René M. Castelein, Martijn Beukers, Peter R. Seevinck, Harrie Weinans, Bart C. H. van der Wal, Björn P. Meij
-Published: *Scientific Reports*
<https://doi.org/10.1038/s41598-022-06989-9>
10. (@) Magnetic resonance imaging versus computed tomography for three-dimensional bone imaging of musculoskeletal pathologies: a review
-Mateusz C. Florkow, **Koen Willemsen**, Vasco V. Mascarenhas, Edwin H.G. Oei; Marijn van Stralen, Peter R. Seevinck
-Published: *Journal of Magnetic Resonance Imaging*
<https://doi.org/10.1002/jmri.28067>
11. (@) Good long-term outcomes of the hip Chiari osteotomy in adolescents and adults with hip dysplasia: a systematic review
-**Koen Willemsen**, Said Sadiqi, Menco Niemeyer, Peter Seevinck, Ralph Sakkers, Harrie Weinans, Bart van der Wal.
-Published: *Acta Orthopaedica*
<https://doi.org/10.1080/17453674.2020.1747210>
12. (@) Comparing hip dysplasia in dogs and humans: a review
-**Koen Willemsen**, Michelle Möring, Marianna Tryfonidou, Ralph Sakkers, Harrie Weinans, Björn Meij, Bart C.H. van der Wal.
-Published: *Frontiers in Veterinary Science* (2021)

- <https://doi.org/10.3389/fvets.2021.791434>
13. (@) 3D-Printed Regenerative Magnesium Phosphate Implant Ensures Stability and Restoration of Hip Dysplasia
-Nasim Golafshan, **Koen Willemsen**, Firoz Babu Kadumudi, Elke Vorndran, Alireza Dolatshahi-Pirouz, Harrie Weinans, Bart CH van der Wal, Jos Malda, Miguel Castilho
-Published: *Advanced Healthcare Materials* (2021)
<https://doi.org/10.1002/adhm.202101051>

 14. (@) Patient-specific 3D-printed shelf implant for the treatment of hip dysplasia: anatomical and biomechanical outcomes in a canine model
-**Koen Willemsen**, Marianna Tryfonidou, Ralph Sakkers, René M. Castelein, Martijn Beukers, Amir A. Zadpoor, Peter Seevinck, Harrie Weinans, Shared last author: Björn Meij & Bart C.H. van der Wal.
-Published: *Journal of Orthopaedic Research* (2021)
<https://doi.org/10.1002/jor.25133>

 15. (@) MRI-based synthetic CT shows equivalence to conventional CT for the morphological assessment of the hip joint
-M.C. Florkow, **K. Willemsen**, F. Zijlstra, W. Foppen, B.C.H. van der Wal, J.R.N van der Voort van Zyp, M.A. Viergever, R.M. Castelein, H. Weinans, M. van Stralen, R.J.B. Sakkers, P.R. Seevinck.
-Published: *Journal of Orthopedic Research* (2021)
<https://doi.org/10.1002/jor.25127>

 16. (@) 3D-printed saw guides for lower arm osteotomy, a comparison between a synthetic and conventional CT-based method;
-**Koen Willemsen**, Mirte H. M. Ketel, Franck Zijlstra, Mateusz Florkow, Ruurd Kuijpers, Bart C. H. van der Wal, Harrie Weinans, Peter R. Seevinck, Ralph J. B. Sakkers.
-Published: *3D printing in medicine* (2021)
<https://doi.org/10.1186/s41205-021-00103-x>

 17. Additively manufactured space-filling meta-implants
-H.M.A. Kolken, C.P. de Jonge, T. van der Sloten, A. Fontecha Garcia, B. Pouran, **K. Willemsen**, H. Weinans, A.A. Zadpoor
-Published: *Acta Biomaterialia* (2021)
<https://doi.org/10.1016/j.actbio.2021.02.020>

18. (@) Three-Dimensional Manufacturing of Personalized Implants in Orthopedic Trauma Surgery—Feasible Future or Fake News?
-Geertje AM Govaert, Falco Hietbrink, **Koen Willemsen**
-Published: JAMA Network Open (2021)
<https://doi.org/10.1001/jamanetworkopen.2021.0149>
19. Lumbosacral Fusion Using Instrumented Cage Distraction–Fixation in a Dog with Degenerative Lumbosacral Stenosis
-Tjarda E Reints Bok, Lucinda van Stee, **Koen Willemsen**, Martijn Beukers, Guy CM Grinwis, Björn P Meij
-Published: Veterinary and Comparative Orthopaedics and Traumatology Open (2020)
<https://doi.org/10.1055/s-0040-1713824>
20. (@) Long-term outcomes of the hip shelf arthroplasty in adolescents and adults with residual hip dysplasia: a systematic review;
-**Willemsen K**, Doelman CJ, Sam AS, Seevinck PR, Sakkers RJ, Weinans H, van Der Wal BC.
-Published: Acta Orthopaedica (2020)
<https://doi.org/10.1080/17453674.2020.1747210>
21. Deep learning–based MR-to-CT synthesis: The influence of varying gradient echo–based MR images as input channels;
-Florkow MC, Zijlstra F, **Willemsen K**, Maspero M, van den Berg CA, Kerkmeijer LG, Castelein RM, Weinans H, Viergever MA, van Stralen M, Seevinck PR.
-Published: Magnetic resonance in medicine. (2020)
<https://doi.org/10.1002/mrm.28008>
22. Instrumented cervical fusion in nine dogs with caudal cervical spondylomyelopathy;
-Reints Bok TE, **Willemsen K**, van Rijen MH, Grinwis GC, Tryfonidou MA, Meij BP.
-Published: Veterinary Surgery. (2019)
<https://doi.org/10.1111/vsu.13312>
23. (@) Challenges in the design and regulatory approval of 3D-printed surgical implants: a two-case series;
-**Willemsen K**, Nizak R, Noordmans HJ, Castelein RM, Weinans H, Kruyt MC.
-Published: The Lancet, Digital Health (2019)
[https://doi.org/10.1016/S2589-7500\(19\)30067-6](https://doi.org/10.1016/S2589-7500(19)30067-6)

24. (@) A Novel Treatment for Anterior Shoulder Instability: A Biomechanical Comparison Between a Patient-Specific Implant and the Latarjet Procedure;
-**Willemsen K**, Berendes TD, Geurkink T, Bleys RL, Leeftang MA, Weinans H, Castelein RM, Nelissen RG, van der Wal BC.
-Published: The Journal of bone and joint surgery (2019)
<https://doi.org/10.2106/JBJS.18.00892>
25. CT synthesis from MR images for orthopedic applications in the lower arm using a conditional generative adversarial network;
-Zijlstra F, **Willemsen K**, Florkow MC, Sakkers RJ, Weinans HH, van der Wal BC, van Stralen M, Seevinck PR.
-Published: Image Processing (2019)
<https://doi.org/10.1117/12.2512857>
26. Lack of consensus on optimal acetabular cup orientation because of variation in assessment methods in total hip arthroplasty: a systematic review;
-Snijders TE, **Willemsen K**, van Gaalen SM, Castelein RM, Weinans H, de Gast A.
-Published: HIP International. (2019)
<https://doi.org/10.1177/1120700018759306>
27. Labral (pathologic) Similarities for the Human Shoulder and Hip Joint;
-Berendes TD, Geurkink T, **Willemsen K**, Weinans H, Castelein RM.
-Published: Open Access J Ortho. (2018); 1:101

Non-scientific and Societal communications

National television and radio:

- Guest at the talkshow of Art Rooijarkers to talk about the first 3D printed spine implant.
RTL 4, 24-07-2019
- Interview and item about the first 3D printed dog skull replacement.
SBS, 05-02-2019
- Interview and item about the 3D printing of a spine implant.
RTL Z, 17-12-2019
- Interview about 3D printed spine implants.
BNR Nieuwsuur, 25-07-2019

National newspaper coverage:

- 'Reserve ribben uit de printer'
Financieel Dagblad, 22-02-2019
- 'Implantaten uit de 3D printer laten Utrechtse patiënt weer lopen'
Volkskrant, 24-07-2019
- 'Unieke operatie: Sienny (70) heeft een wervelkolom van titanium'
Algemeen Dagblad, 24-07-2019
- 'Hond krijgt 3D-geprint schedeldak'
Telegraaf, 04-02-2019
- 'Rugbyers zijn doorzetter en teamspelers'
Medisch Contact, 12-10-2016
- 'Weer lopen door gepersonaliseerd 3D-geprint implantaat'
Medisch Contact, 24-07-2019

Internet news articles:

- 'UMC laat patiënten weer lopen dankzij 3D-geprint implantaat'
NU.nl, 24-07-2022
- 'Labrador krijgt nieuwe 3D-geprinte kaak in Utrecht'
NU.nl, 27-03-2019
- 'Neushoornvogel in Texel Zoo heeft een 3D-geprinte hoorn'
-NOS.nl, 03-04-2020

UMCU Communications:

<https://www.umcutrecht.nl/nl/3d-lab>, <https://youtu.be/RKe-jxv3e38>

<https://werkenbijumcutrecht.nl/onze-verhalen/werken-als-arts-voor-het-3d-lab/>

PhD-Portfolio

Graduate school of Life Sciences:
Participant of the Medical Imaging graduate school

List of educational activities:

Courses:

"Certificate to conduct animal experiments, (Article 9)"	5 ECTS
"Medische Beeldvormende Technieken"	5 ECTS
"Physics and Physiology behind Medical Technology"	3 ECTS
"Stralingsbescherming"	3 ECTS
"Veiligheidskunde en risicoanalyse"	3 ECTS
"Management and Organization in the healthcare sector"	3 ECTS
"Technology Entrepreneurship"	2 ECTS
"Leiden van projecten"	1 ECTS
"Scientific Integrity"	0,2 ECTS
"Art of presenting science"	1 ECTS
"Academic Writing"	2 ECTS
"Art of scientific writing"	2 ECTS
"Giving Effective oral presentations"	1 ECTS
"Ontwerpen in de zorg"	1 ECTS
"Lean"	2 ECTS
"Introduction in Clinical Information Systems"	3 ECTS
"Electrical safety concerning medical equipment"	0,3 ECTS
"Rules and Regulations"	1 ECTS
"Zelfreflectie en communicatie"	1 ECTS
"Interactie en attitude training"	3 ECTS
"Medische Ethiek"	3 ECTS

Lectures & Meetings:

2017

- Conference lecture: "Jaarvergadering Nederlandse Orthopaedische Vereniging (NOV)" 'A new treatment for hip dysplasia. A cadaveric proof of concept'
• Nomination for the "Rick Huyskens" Price

2018

- Conference lecture: "Symposium Experimenteel Onderzoek Heelkundige Specialismen (SEOHS)", '3D adaptations for the treatment of orthopedic diseases'.
- Conference lecture: "Najaarsvergadering Nederlandse Orthopaedische Vereniging (NOV)", 'A new treatment for shoulder instability. A comparison between the patient specific implant and the Latarjet procedure.'
- Conference lecture: Medical Imaging (Imago), Nomination for 'best abstract' and 'best presentation'
- Conference lecture: "Nederlands Wetenschappelijke Organisatie (NWO)", National project day. 'Challenges in the design and regulatory approval of 3D printed surgical implants'
• First price: Best project presentation

2019

- Best Abstract: WSE-scientific award "Nederlandse Orthopaedische Vereniging", '3D treatment for shoulder instability'
- Lecture, ROGO Noord-West, 'Medical innovations, 3D and Robotic surgery'
- Invited speaker, PINK lecture, '3D printing in hospitals'
- Invited speaker, Innovatie Platform Federatie Medisch Specialisten, 'Lessen geleerd uit 3D printen voor zeldzame casuïstiek'
- Workgroup: ZonMW & ministerie van VWS: 'Alternatieven voor weefsel en orgaan transplantatie' Pakketleider: 'Bone and Cartilage' –
- Conference Lecture: Technical Innovations in Medicine (TiiM) 'Medisch 3D printen en wetgeving'

2020

- Lecture, 'Symposium Revalidatie Kliniek Hoogstraat Utrecht', Invited speaker, •'3D printing of a biomechanical spine implant'
- Invited speaker, Symposium, Paradox, '3D printing of a new musculoskeletal system'
- Conference Lecture: 3D Medical printing conference & expo '3D printing challenges within an academic hospital'
- Value Based Health Care (VHBC) 2020
 - Genomineerd voor de 'Dragon's Grant' met het initiatief 'M3Dical'

2021

- Panelist for Expert symposium Materialise 3D Printing in hospital.
- Health innovation World Summit (cancelled due to Covid-19), Invited speaker 'Is 3D printing the solution hospitals need?'

2022

- NFU workgroup "3D printing and in-house manufacturing"
- Member NEN commission: surgical implants
- Invited Speaker, Materialise Global Event, 'Expertise on 3D printing in an academic hospital'
- Member of the Europeans Special Interest Group (SIG) on 'In hospital 3D printing.'

Acknowledgements

Teamwork makes the dream work, daarom wil ik graag bedanken:

Mijn promotieteam:

Prof. Dr. H. Weinans, Beste Harrie. Jij was diegene waardoor ik mijn ogen op het UMCU heb laten vallen. Orthopedie trok altijd al mijn aandacht door het vakmanschap van het specialisme, maar voor mij was het allemaal nog iets te grijs. Ik wilde het vak technisch uitdiepen, iets wat jij met je biomechanische achtergrond al jaren verdienstelijk deed. Met jou kon ik praten over de soms vreemde beslissingen van artsen en hoe het soms technisch toch anders aangepakt zou moeten worden. Als mijn promotor ben je belangrijk geweest voor dit proefschrift maar daarnaast heb je als mentor altijd klaar gestaan voor het ondersteunen van mijn volgende loopbaan stappen, waarvoor dank! Hopelijk blijven we nog lang samen werken op het gebied van onderzoek, kliniek en “ons kindje”: het 3D lab.

Prof. Dr. B.P. Meij, Beste Björn. Voor je aanstekelijke enthousiasme en je aanpakkersmentaliteit. Bedankt voor het vertrouwen dat je in mijn kwaliteiten had waardoor jij het mogelijk hebt gemaakt ideeën te transleren via jouw patiënten, maar ook voor jouw patiënten. Van een kat met 5 poten tot een nieuwe snavel voor een neushoornvogel, ik ben iedere dag weer benieuwd wat we nu weer gaan ontdekken.

Dr. B.C.H. van der Wal, Beste Bart. Jij was vanaf mijn eerste UMCU-meeting gelijk betrokken. Jij had vertrouwen in mij als persoon en hebt er ervoor gezorgd dat ik een plekje kon verdienen als promovendus. Daarnaast heb jij mij altijd je mening laten horen, ook als ik die liever niet wilde horen. Bedankt, dat was nodig. Mede door jouw enthousiasme en doorzettingsvermogen heeft dit proefschrift de omvang die het vandaag heeft.

Dr. R.J.B. Sackers, Beste Ralph. Met jouw jarenlange ervaring in de (kinder)orthopedie heb je altijd een kritische blik klaar gehad. Mijn papers kwamen altijd rood kleurend terug maar dit heeft de kwaliteit goed gedaan. Daarnaast bedankt voor de vele skikilometers die we samen hebben afgelegd, want na de arbeid hoort ook de nodige lichamelijke ontspanning!

Prof. Dr. M.A. Tryfonidou, Beste Marianna. Ondanks dat je niet direct als (co-)promotor onderdeel was van mijn promotieteam ben je wel zeker op deze manier betrokken geweest. Wanneer de bovenstaande leden van het promotieteam weer eens onrealistische plannings op mij af vuurden was jij vaak diegene die aan mijn kant stond. Zo heb jij meermalen mij weer terug op het juiste (promotie)pad gekregen. Daarnaast bedankt

voor alle hulp bij onze dierstudie, zonder jouw hulp bij o.a. de DEC, histologie en logistiek was ik mogelijk nog bezig geweest!

Geachte leden van de leescommissie, prof. dr. L. van Rhijn, prof. dr. W.J.A. Dhert, prof. dr. L.C. Heyligers, dr. S.H.A.J. Tytgat, prof. dr. P.R. van Weeren, hartelijk dank voor het lezen en beoordelen van mijn proefschrift.

Prof. Dr. M.C. Kruyt, Beste Moyo, bedankt voor je eeuwige enthousiasme voor mijn werkzaamheden, het 3D lab en onze vele samenwerkingen. Jij bent diegene die het hoofdstuk kliniek kleur heeft gegeven in dit proefschrift. De deur van het 3D lab staat altijd voor je open, al denk ik dat we dan nooit stoppen met groeien!

Prof. Dr. R.L.A.W. Bleys, Beste Ronald, dank voor de samenwerking met de anatomie afdeling en het gebruik van de snijzalen. Speciale dank aan Marco en Simon voor hun voortdurende steun voor mijn (te) gekke projecten en het faciliteren van vele van mijn (huidige) onderzoeken.

Prof. Dr. A.A. Zadpoor, Beste Amir, dank voor de vele samenwerkingen met de TU Delft gedurende het Prosperos project. Ik voelde me altijd zeer welkom. Speciale dank aan Sander Leeftang voor zijn steun bij het ontwerpen van de biomechanische opstellingen.

Geachte collega's van het Mirror NWO project / Image Science Institute, beste dr. Peter Seevinck en dr. Marijn van Stralen, Mateusz Florkow, Ruurd Kuiper en dr. Frank Zijlstra. Bedankt voor de leuke meetings en de fijne samenwerking tijdens én na ons project.

Geachte Prosperos collega's, Beste Raymond en Chris, bedankt voor jullie support gedurende ons project. Hopelijk kunnen we snel verder met Prosperos 2!

Acknowledgements: Prof. Dr. E.J.E. Cottaar en Dr. I.M.M. Lammerts, Beste Ward en Ivonne, bedankt voor jullie steun tijdens mijn QME traject. De drempel voor mijn proefschrift leek al gehaald voordat ik aan het traineeship begon maar de kennis die ik sindsdien heb opgedaan - op de TUE - is zeker terug te vinden in een paar van de later gepubliceerde hoofdstukken in mijn proefschrift.

Dank aan alle co-auteurs voor jullie bijdrage.

Beste studenten, veel dank voor jullie werk bij het ontwikkelen van nieuwe producten, papers screenen voor de systematic reviews, helpen bij de hondenstudie en alle hulp op de anatomie zaal. Veel dank voor deze bijdrage.

Bedankt Lexa, Relexa en Rexa voor het offer dat jullie gebracht hebben voor de voortgang van de wetenschap.

Beste collega's van de orthopedie, specialisten, AIOS, ANIOS, secretaresses en onderzoekers, bedankt voor al jullie support tijdens mijn PhD-periode en jullie steun voor het ontwikkelen van nieuwe technieken. Speciale dank aan Q304, Jonneke ten eerste bedankt voor mijn verhuizing van Q2 naar Q3, hierdoor kwam ik in een warm bad van gezellige collega's. Bedankt voor je gezelligheid en wat vrouwelijk tegenwicht in de kamer (dat was af en toe ook wel nodig). Floris bedankt voor je energie, ongezouten mening en je talent om van alle dingen een groepsgeprek te maken binnen de kamer, maar wat hebben we gelachen waardoor ik menig keer te laat vertrok voor mijn meetings. Bedankt Razmara voor je enthousiasme voor techniek en het zijn van een sparringpartner voor nieuwe innovatieve ideeën. Justin bedankt voor je fanatisme bij de pingpong, je photoshop talenten en de altijd aanwezige verrassingen in onze veroverde koelkast. Tenslotte bedankt Chella, ook al was je geen voltijd bezetter van onze kamer, je bracht altijd een hoop gezelligheid mee en altijd een luisterend oor.

Bedankt Mattie voor het zijn van de rots in de branding. De consequente factor waar je op kan rekenen. Zowel als het gaat om labwerk als wanneer het gaat om een gezellige borrel op vrijdagmiddag. Ik hoop dat we nog vele Orthoski gaan meemaken!

Bedankt Q-leggas: Jelle, Rob, Sebastiaan, Jasmijn, Bruce, Willem-Paul, Esmee, Chien, Steven, Anneli, Joëll, Casper, Paul, Erin, Bas, Lorenzo, Hubrecht: Saber, Margot, Margot, Jasper, Barbara, Stafgang, Mechteld, Pauline en Hilde. Voor de gezellige lunches, de uitgelopen vrijdagmiddagborrels, de NK Kubbweekendjes, ping-pong battles, Q-meetings en de vele memorabele tripjes.

Bedankt 3D-Lab-team, ondanks het nog moeten afronden van mijn proefschrift, gaf mijn proefschrift wel aanleiding tot het opzetten van een 3D lab. Binnen het 3D lab staat patiëntenzorg op nummer één maar dit proberen we zoveel als mogelijk te combineren met research. Bedankt voor dit mogelijk maken, Harrie, Harmien, Stefaan, Joëll, Jaap, Chien, Jan, Maartje, Matthijs, Joël, Harm, Klijs, Robbie, Moyo, Bart en Ferry. Tijd voor het afdelingsuitje!

Bedankt Vrienden,

Bedankt AAC rugbyteam, trainers en supporters voor de sportieve uitdaging tussen alle arbeid door, de gezellige familiesfeer op de club en de mooie activiteiten. Bedankt Rugbyvrienden, Matthijs, Anthony, Cuppy, Yordi, Sander, Paolo en Stuart voor de vele gezellige weekendjes, borrels, boottochtjes en gezelligheid. Vo! Bedankt Curaçao Rugby

Federation, Rob en Tamara, voor hun vertrouwen in mij waardoor ik over de jaren buitengewoon mooie tripjes heb mogen maken over heel Europa, de Caribische eilanden en Noord-Amerika.

Bedankt N.E.B. Leden, Jasper, Wouter, Robin en Inne voor de mooie borrels, fancy etentjes en weekendjes Grolloo. Wanneer gaan we weer!? Bedankt Tilburgse vriendjes, Lieke, Andy, Joost, Eef, Giuli, Kim, Mayke, Fabian, Irina, Loek, Jhan, Jorik, Patrick, Remco, Thomas en Tim voor de overenthousiaste weekendjes, vliegende gourmetstellen, borrels en feestjes. Bedankt "Jan Wier vriendjes", Tom, Gavin, Martijn, Jaap, Jeroen, Luc, Thijs, Kevin, Eddy, Tobias, Eefje, Billy, Pepijn voor de onvoorwaardelijke vriendschap, 'de tour de carnaval', de mooie borrels, squash en de mountainbike en vriendenweekendjes.

Bedankt Familie,

Bedankt Familie Willemsen en Familie van Mierlo voor jullie onvoorwaardelijke liefde en gezelligheid. Bedankt schoonfamilie, Rian, Ton, Baudyn en oma, voor de interesse in mijn werk, de welkome sfeer, skireisje en de vele gezellige etentjes! Bedankt Nichtjes Puk, Lot, Fay, Liv en Sue voor jullie vrolijkheid en afleiding tussen alle werkstress door.

Bedankt Klavertje, Bedankt Bart voor je eeuwige gastvrijheid, je energie, je feestmodus en het zijn van mijn vriend. Bedankt Karlijn voor je goede zorgen als de vrouw van de familie, je bezorgdheid wat betreft mijn werkdruk en je onvoorwaardelijke (moeder) liefde. Bedankt Gijs voor het zijn van de grote broer, je rationele gedachten maar ook de voorliefde voor festivals, op naar Lowlands! Bedankt ook Renate en Paul voor jullie interesse en support!

Bedankt Papa, voor je eeuwige kritische blik, voor je interesse in mijn proefschrift. Voor het stellen van de vragen die ik soms niet wil horen en voor de vragen die ik juist wel moet horen. Bedankt voor het zijn van het luisterend oor als het gaat om mijn zorgen, stress, werkdruk, carrièrekeuzes en sociale dilemma's. Bedankt voor je liefde en het al die jaren zijn van zowel Papa als Mama.

Bedankt Mama, je zou zo trots zijn op mij voor het leveren van deze prestatie, maar ik ben jou eeuwig dankbaar voor het maken van wie ik ben, want ondanks dat ik nog wel kneedbaar ben, heb jij, samen met papa, mij vormgegeven!

Liefste Max, zolang we elkaar kennen is er altijd 'dat proefschrift' geweest. Hopelijk vind je me ook nog leuk nu het is afgerond;) Bedankt voor je steun om mij te blijven ontwikkelen maar bovenal bedankt voor het zijn van diegene die ik op verschillende momenten nodig heb. Jouw liefde en warmte maakt het na een dag werken een feestje om thuis te komen. Op naar nog meer nieuwe avonturen samen!

Curriculum Vitae

Koen Willemsen was born on the 2nd of February 1991 in Tilburg, the Netherlands. He graduated from a bilingual (English/Dutch) high school program in 2009 (VWO, 2College Durendael & ROC Tilburg) and subsequently moved to Amsterdam to start his medical studies at the Vrije Universiteit. During his study he participated in several extracurricular activities. He interrupted his studies for a year to play top-level sport (rugby, international level) and to participate as a board member of a student association. During his master he also participated in extracurricular research projects with prof. dr.



H. Weinans and dr. B.C.H van der Wal at the Orthopedics Department at the University Medical Center Utrecht. After graduation in 2016 he was awarded a PhD-position at the research group of prof. Weinans. There he worked full-time as a medical doctor and PhD-student as part of a large consortium in which novel 3D-printed implants and MRI-based diagnostic tools were developed. After two years of bench and translational animal research Koen's newly developed techniques were implemented in the human clinic. Thereafter, he was frequently consulted to support difficult to treat patients or reform conventional treatment methods with the use of medical 3D technology. Next to his clinical consultations and work as a PhD-candidate, Koen remained active as an (inter)national rugby player and simultaneously contributed as team physician at various international tournaments. In 2019 he co-founded the UMCU's 3D lab at which he was appointed full-time as coordinator and this allowed him to keep working as a consultant for medical specialists as well as advance his research lines. In 2020 he started a post-graduate traineeship as a Qualified Medical Engineer at the Technical University Eindhoven next to his work as 3D lab coordinator to further professionalize the 3D lab and work towards his Doctor of Engineering degree (Eng.D.). After the defense of his Ph.D. Koen will travel to the Mayo Clinic (Rochester, Minnesota, USA) as a visiting scholar to gain experience and learn from their personalized approach to treat patients.

